

ERS-1 GEOPHYSICAL VALIDATION



Workshop Proceedings

27-30 April 1992
Penhors, Bretagne, France

europaean space agency / agence spatiale européenne
8-10 rue Mario Nikis, F-75738 Paris, France

ERS-1 GEOPHYSICAL VALIDATION

Workshop Proceedings

27-30 April 1992

Penhors, Bretagne, France

Workshop Organisers

Evert Attema,
ESA/ESTEC,
Postbus 229,
2200 AG Noordwijk,
The Netherlands

Jean-Claude Morin,
GDTA,
18 Avenue Edouard Belin,
31055 Toulouse Cedex,
France

Editor

Mike Wooding,
Remote Sensing Applications Consultants,
Merlin Court,
82 Alexandra Road,
Farnborough, GU14 6QF
UK

Cover based on graphic by
DLR, Oberpfaffenhofen, Germany

Disclaimer

This document is published in the ESA WPP (Workshop Preliminary Proceedings) series. This is an informal series and the documents do not necessarily carry the full authority of the formal ESA publication series. Such documents are intended for issue to workshop participants and as working documents. Some papers in the ESA WPP series may be selected for editing and inclusion in a formal ESA publication at a later date.

There is no formal distribution of ESA WPP publications; distribution is arranged by the workshop organisers.

Copyright 1992 European Space Agency

CONTENTS

	Page
INTRODUCTORY PAPER	
THE ERS-1 GEOPHYSICAL VALIDATION PROGRAMME FOR WIND AND WAVE DATA PRODUCTS E.Attema, <i>ESTEC, The Netherlands</i>	1
 SESSION I - DEDICATED CAMPAIGNS	
WIND MEASUREMENTS OVER THE OCEAN WITH AN AIRBORNE C-BAND SCATTEROMETER DURING THE ERS-1 CALIBRATION AND VALIDATION CAMPAIGN V.Wismann, <i>Universität Hamburg, Germany</i>	5
WIND MEASUREMENTS FROM THE MRF C-130 AND THE DERIVATION OF ANALYSES FROM RENE-91 WINDS D.Offiler, <i>Meteorological Office, Bracknell, UK</i>	11
WIND AND WAVE MEASUREMENTS DURING EXTREME SITUATIONS T.I.Bern & S.Barstow, <i>Oceanographic Company of Norway</i>	17
EVALUATION OF WIND AND WAVE MEASUREMENTS FROM THE TOBIS BUOY NETWORK DURING RENE -91 P.Queffeuilou & A.Bentamy, <i>IFREMER, Plouzane, France</i>	29
TWO DIMENSIONAL WAVE FIELD MEASUREMENTS AS SEA TRUTH FOR ERS-1 SAR F.Ziemer, W.Rosenthal, <i>GKSS, Geesthacht, Germany;</i> & K.Richter, D.Schrader, <i>Bundesamt für Seeschifffahrt und Hydrographie, Hamburg, Germany</i>	35
VALIDATION OF WAVENUMBER SPECTRA FROM ERS-1 WITH DUTCH AIRBORNE AND GROUND BASED RADAR DATA OBTAINED IN RENE91 J.C.M.Kleijweg, <i>Physics and Electroics Lab TNO, The Hague, The Netherlands,</i> & D.Schrader, <i>Bundesamt für Seeschifffahrt und Hydrographie, Hamburg, Germany</i>	41
OBSERVATIONS WITH THE RESSEC AIRBORNE RADAR DURING RENE91 D.Hauser, G.Caudal, <i>CRPE/CNET/CNRS, Issy-les-Moulineaux, France</i> & B.Chapron, <i>INFREMER, Brest, France</i>	47
DATA COLLECTION OR DATA MANAGEMENT? A.V.Edward, <i>Serco Space, ESA/ESRIN, Frascati, Italy</i>	55
VALIDATION OF THE OCEAN SURFACE WIND FIELD AND WAVE HEIGHT MEASUREMENTS DERIVED FROM DATA OF THE ERS-1 SCATTEROMETER AND RADAR ALTIMETER (EARLY RESULTS) M.A.Goodberlet & C.T.Swift, <i>University of Massachusetts, Amherst, MA, USA,</i> & J.C.Wilkinson, <i>NOAA, Washington D.C., USA</i>	61
AIRBORNE C-BAND SCATTEROMETER MEASUREMENTS OBTAINED DURING UNDER FLIGHTS OF THE ERS-1 SATELLITE IN THE GULF OF MEXICO S.C.Carson, R.E.McIntosh, M.A.Goodberlet & C.T.Swift, <i>University of Massachusetts, Amherst, MA, USA,</i> & J.C.Wilkinson, <i>NOAA, Washington D.C., USA</i>	65

THE GRAND BANKS ERS-1 SAR VALIDATION EXPERIMENT	71
<i>P.W.Vachon, CCRS, Ottawa, Canada, F.W.Dobson, Bedford Institute of Oceanography, Dartmouth, N.S., Canada, J.R.Buckley, Royal Roads Military College, Victoria, B.C., Canada, D.Vandemark & E.J.Walsh, Wallops Flight Facility, NASA/Goddard Space Flight Centre, VA, USA</i>	
VALIDATION OF ERS-1 SCATTEROMETER WIND DATA DURING CALIBRATION/VALIDATION CAMPAIGN RENE-91	77
<i>A.Bentamy, IFREMER, Plouzane, France</i>	
 SESSION II - WIND SCATTEROMETER MODELS	
ERS-1 SCATTEROMETER CALIBRATION AND VALIDATION ACTIVITIES AT ECMWF:	83
A. THE QUALITY AND CHARACTERISTICS OF THE RADAR BACKSCATTER MEASUREMENTS	
<i>A.Stoffelen, European Centre for Medium-range Weather forecasts, Reading, UK & D.L.T.Anderson, Clarendon LABORATORY, Oxford, UK</i>	
ERS-1 SCATTEROMETER CALIBRATION AND VALIDATION ACTIVITIES AT ECMWF:	89
B. FROM RADAR BACKSCATTER CHARACTERISTICS TO WIND VECTOR SOLUTIONS	
<i>A.Stoffelen, European Centre for Medium-range Weather forecasts, Reading, UK & D.L.T.Anderson, Clarendon LABORATORY, Oxford, UK & P.M.Woiceshyn, JPL, Pasadena, USA</i>	
FROM SIMULATED DATA, TO REAL DATA	95
<i>C.Gaffard, CNRM/GMAP/AAD, Toulouse, France, J.M.Lefèvre, SCEM,/PREVI/MAR, Toulouse, France, & V.Cassé, CNRM/GMAP/AAD, Toulouse, France</i>	
TOWARDS AN EMPIRICAL ERS-1 WIND SCATTEROMETER MODEL	101
<i>V.Wismann, Universität Hamburg, Germany</i>	
VALIDATION AND QUALITY OF ERS-1 SCATTEROMETER WIND DATA	107
<i>Y.Quilfen, IFREMER, Plouzané, France</i>	
C-BAND V-POLARISED RADAR SEA-ECHO MODEL FROM ERS-1 HALTENBANKEN CAMPAIGN	113
<i>A.E.Long, ESA/ESTEC, The Netherlands</i>	
EVALUATION OF ERS-1 SCATTEROMETER WIND INFORMATION AT THE NORWEGIAN METEOROLOGICAL INSTITUTE	119
<i>L-A.Breivik, Norwegian Meteorological Institute, Oslo, Norway</i>	
VALIDATION AND COMPARISONS OF ALTERNATIVE WIND SCATTEROMETER MODELS	125
<i>D.Offiler, Meteorological Office, Bracknell, UK</i>	
SENSITIVITY STUDY - SCATTEROMETER RETRIEVALS WITH WAVE AGE PARAMETER	133
<i>P.Woiceshyn & P.Janssen, ECMWF, Reading, UK</i>	
WAVE AGE AND THE SCATTEROMETER WIND RETRIEVAL ALGORITHM	141
<i>P.Woiceshyn & P.Janssen, ECMWF, Reading, UK</i>	

SESSION III - RADAR ALTIMETER VALIDATION

THE HEIGHT CALIBRATION OF THE ERS-1 RADAR ALTIMETER C.R.Francis, <i>ESA/ESTEC, The Netherlands</i>	147
VALIDATION OF ERS-1 IN THE ICELAND-FAEROES REGION OF THE NORTH ATLANTIC P.D.Cotton, M.A.Srokosz, T.H.Guymer & R.T.Tokmakian, <i>James Rennel Centre for Ocean Circulation, Southampton, UK</i>	151
ERS-1 RADAR ALTIMETER VALIDATION WITH THE WAM MODEL B.Hansen, <i>ECMWF, Reading, UK</i> , & H.Günther, <i>ECMWF, Reading, UK /GKSS, Hamburg, Germany</i>	157
VALIDATION OF ERS-1 ALTIMETER WAVE AND WIND FAST DELIVERY PRODUCT P.Queffeuilou, <i>IFREMER, Plouzane, France</i> , & J.M.Lefevre, <i>METEO-FRANCE/SCEM, Toulouse, France</i>	163

SESSION IV - SAR WAVE AND CURRENT OBSERVATION

OCEAN WAVE IMAGING BY ERS-1 SYNTHETIC APERTURE RADAR: FIRST RESULTS FROM THE HALTENBANKEN CALIBRATION/VALIDATION CAMPAIGN C.Brüning, W.Alpers & A.Wilde, <i>Universität Hamburg, Germany</i>	169
SEA TRUTH AND MODEL DATA FOR SURFACE WAVES COMPARED WITH ERS-1 SAR W.Rosenthal, V.Atanassov, W.Koch, F.Ziemer, <i>GKSS, Geesthacht, Germany</i> , & K.Richter, <i>Bundesamt für Seeschifffahrt und Hydrographie, Hamburg, Germany</i>	179
DIRECTIONAL WAVE SPECTRA BY INVERSION OF ERS-1 SAR IMAGERY H.Johnsen & G.Engen, <i>FORUT Information Technology, Tromsø, Norway</i> , H.E.Krogstad, <i>SINTEF Industrial Mathematics, Trondheim, Norway</i> , & S.F.Barstow, <i>OCEANOR, Trondheim, Norway</i>	187
COASTAL OCEAN STUDIES WITH ERS-1 SAR DURING NORCSEX'91 J.A.Johannessen, <i>NERSC, Bergen, Norway</i> , R.A.Shuchman, <i>ERIM, Ann Arbor, USA</i> , K.Davidson, <i>NPS, Monterey, USA</i> , Ø. Frette, <i>NERSC, Bergen, Norway</i> , R.Ønstott, <i>ERIM, Ann Arbor, USA</i> , & O.M. Johannessen, <i>NERSC, Bergen, Norway</i>	193

SESSION V - SPECIAL TOPICS

INTERPRETATION OF ERS-1 SCATTEROMETER DATA OVER SEA ICE A.Cavanié & F.Gohin, <i>INFREMER, Brest, France</i>	199
--	-----

WORKSHOP CONCLUSIONS

WORKSHOP CONCLUSIONS AND FUTURE PLANS E.Attema, <i>ESA/ESTEC, The Netherlands</i>	203
--	-----

WORKSHOP PARTICIPANTS

LIST OF WORKSHOP PARTICIPANTS	205
-------------------------------	-----



INTRODUCTORY PAPER

THE ERS-1 GEOPHYSICAL VALIDATION PROGRAMME FOR WIND AND WAVE DATA PRODUCTS

Evert Attema
ESA/ESTEC
Postbus 229, 2200 AG Noordwijk,
The Netherlands

Abstract

The primary ERS-1 Wind and Wave data products are windspeed and direction at the ocean surface, the directional spectrum of the ocean waves and the significant wave height, derived from the primary outputs of ERS-1's radar altimeter, wind scatterometer and synthetic aperture radar. Geophysical validation is necessary to demonstrate the accuracy of the derived data products. After careful calibration of the satellite sensors, a large number of independent wind and wave measurements were collected to compare with satellite data. After some software modification in the ERS-1 ground processors and tuning of geophysical inversion models, all ERS-1 wind and wave data products show good consistency with selected high quality surface datasets, and with operational meteorological and oceanographic model outputs.

1. INTRODUCTION

The ERS-1 satellite was successfully launched in July 1991. It carries a suite of microwave and infrared instruments for the observation of ocean, ice and land surfaces, as well as for the determination of atmospheric water vapour [1]. Wind and wave information over the ocean is obtained by the radar altimeter and the active microwave instrument, which is a combination of a synthetic aperture radar and a wind scatterometer [2]. The basic measurements made by these instruments are the radar backscatter from the earth's surface, the time delay between transmission and echo reception, and the doppler shift of the radar echo signals induced by the relative motion of the satellite with respect to the surface under observation. Geophysical data products are derived from these

measurements, including windspeed and direction at the ocean surface, directional spectra of ocean waves and significant wave height. Geophysical validation is necessary to verify that these wind and wave products meet the required accuracy, and is defined as the process of assessing the accuracy of geophysical parameters derived from calibrated sensor outputs by independent means [3].

2. PROGRAMME ORGANISATION

More than five years before the launch of ERS-1 it was recognised that the preparation of suitable in-situ datasets, erroneously referred to as 'ground truth', was a particular challenge for meteorology and oceanography, and required close cooperation between earth observation specialists and experts in the scientific user community. In view of this, the European Space Agency convened an ERS-1 Wind and Wave Calibration Workshop in 1986 to discuss the available options. The following recommendations were made:

- A. The use of outputs from meteorological and oceanographic models on both regional and global scales.
- B. The use of World Weather Watch data from ships of opportunity and buoys.
- C. The use of complementary datasets from other satellites.
- D. Statistical analysis methods applied to the ERS-1 data themselves.
- E. The use of data from platforms of opportunity, including buoys, ships, aircraft, oilrigs, research platforms, tide gauges and onshore radar stations.

- F. Dedicated campaigns using instrumented ships, buoys and aircraft, supplemented by sky-wave radar observations and information from other satellites.
- G. To review the possibilities for acquiring useful in-situ data from any established scientifically autonomous international experiment.

Following the workshop, the technical feasibility and cost aspects of the proposed methods were examined, and the possibilities of collaboration with application oriented research institutes were explored. Particular attention was paid to validation elements of investigations proposed within the framework of the ERS-1 Announcement of Opportunity.

An ERS-1 Geophysical Validation Team was formed by ESA (Table 1). Each member of this team agreed to perform data analysis using one or more of the above methods.

Table 1: The ERS-1 Geophysical Validation Analysis Team

Name	Affiliation
W.Alpers	Univ.Hamburg - IFMEE
V.Casse	Meteo France
A.Cavanie	IFREMER
J.Guddal	DMNI
T.Guymer	James Rennell Centre for Ocean Circulation
A.Hollingsworth	ECMWF
D.Offiler	UK Met Office
W.Rosenthal	GKSS
I.Jones	DSTO WSRL Australia
P.Vachon	CCRS Canada
J.Wilkerson	NOAA USA
P.Woiceshyn	JPL USA

In addition, an ERS-1 Geophysical Validation Experiment Team was formed for the implementation of a dedicated validation campaign in Europe (Table 2).

Table 2: The ERS-1 Geophysical Validation Experimenters Team

Name	Affiliation
M.Andre	DMN
T.I.Bern	OCEANOR
R.Ezraty	IFREMER
H.Finkenzeller	DLR
D.Hauser	CRPE
J.A.Johannessen	NRSC
J.C.M.Kleijweg	FELTNO
J.C.Morin	GDTA
D.Offiler	UK Met Office
W.Rosenthal	GKSS
W.Wismann	Univ.Hamburg - IFMEE

3. SATELLITE DATA CALIBRATION

An important prerequisite for the geophysical validation work is that the ERS-1 data are fully calibrated. Data calibration involves two distinct stages; firstly, engineering calibration, and secondly, geophysical calibration.

Engineering calibration is carried out to relate the primary sensor outputs (volts, digital counts, etc.) to physical units within known limits of accuracy; e.g. radar backscatter coefficient ($m^2 \times m^2$), satellite height (m), measurement location (lat./long.) and time of measurement. This encompasses pre-launch and in-flight determination and monitoring of sensor characteristics as well as data processing activities, whereby the actual conversion of primary outputs into physical units takes place. For the radar altimeter, height calibration was carried out in-flight, while radar backscatter coefficient calibration relied mainly on pre-launch measurements [4]. For the AMI, a combination of pre-launch, internal and external measurements, was used [5].

After engineering calibration, geophysical calibration involves the conversion of calibrated sensor outputs into geophysical parameters using suitable inversion models. Only once this is achieved, can the satellite derived geophysical parameters be compared to parameter values obtained by independent means (e.g. in-situ measurements). Observed discrepancies between satellite estimates and in-situ measurements are indicative of uncertainties in both datasets. Consistent biases can be removed by adjusting the parameters of the geophysical inversion models, a procedure known as model tuning. Prior to model tuning, the robustness of the engineering calibration has to be established, because flaws in engineering calibration will otherwise lead to inversion model errors.

4. IN-SITU DATASETS

Geophysical validation activities carried out during the ERS-1 Commissioning phase have included methodological approaches A to F listed above in Section 2.

Surface wind fields were obtained as meteorological model outputs by ECMWF, DNMI and Meteo France. Ocean wave spectra were obtained as oceanographic model outputs by ECMWF (THE WAM model) and DNMI (the WINCH model).

Collocation files were compiled by ECMWF for a selected set of high quality data from ships, platforms, and islands available through the GTS network.

The complementary use of data from ERS-1 and the ALMAZ satellite has been explored by B.Beal [6].

Statistical analysis of ERS-1 data has been carried out by ECWMF.

Data were collected from the NOAA buoy network and from ship and platforms involved in the European dedicated campaign. Datasets for radar altimeter and wind scatterometer validation were collected by the James Rennell Centre for Ocean Circulation in Southampton, UK.

Dedicated campaigns were carried out in Europe (RENE campaign), in Canada (The Grand Banks campaign) [7] and in the US in the Gulf of Mexico [8].

By far the major effort in terms of data acquisition has been the dedicated RENE campaign organised by ESA in the area of the Hantenbanken off the coast of Norway from 16th September to 10th December 1991. This campaign involved a very large number of measurements made from aircraft, ships and ocean buoys, details of which are given in Table 3. Data from all sources were available at the end of the data acquisition period in a common database [9].

Table 3: RENE '91 DATASETS

Platform Type	Owner/name	Experimental Data
Aircraft	UK Met /C-130 DLR/Do-228 IFMEE/Racs	Windspeed & Dir. Windspeed & Dir. Windspeed & Dir./ σ°
	Meteo France/ Merlin-4 CRPE/Ressac NLR/Meteo TNO/Phars	Windspeed & Dir. Radar Wave Spectra SAR Imagery
Ship	DMNI/Mike BSH/Gauss TNO/Shira	Wind/Wave Obs. Wind/Wave Obs. Radar Wave Spectra
	GKSS/Gauss FWG/Planet NRSC/Hakon Mosby	Radar Wave Spectra Wind/Wave Obs. Wind/Wave Obs.
Oil Platform	Statoil/Gullfaks	Wind/Wave Obs. Wave Ht & Dir. Radar Wave Spectra
Ocean Buoy	Oceanor/Tobis	Windspeed & Dir Wave Ht & Period Wave Ht & Dir.
	GKSS/Wavec	Wave Ht & Dir.
Met./Ocean Analysis	ECMWF/ 6 Hr. Analysis	Wind Speed & Dir.
	DNMI/ 6 Hr Analysis	Wind Speed & Dir. Wave Field Analysis
Collocation Analysis	UK Met. Office	Wind Speed & Dir.

5. DATA ANALYSIS

The number and quality of the research papers presented within these workshop proceedings are testimony to the considerable efforts made by

members of the ERS-1 Validation Analysis and Experiment Teams during the first 9 months of ERS-1 operation.

A summary of the main results and plans for future activities are presented in the concluding paper of the workshop proceedings.

6. REFERENCES

1. R.Francis et al., *The ERS-1 Spacecraft and its payload*, ESA Bulletin No 65 pp26 - 48, Feb. 1991.
2. E.Attema, *The active microwave instrument on-board the ERS-1 satellite*, Proc. IEEE, Vol 79 No6, 1991, pp791 - 799.
3. E.Attema and R.Francis, *ERS-1 calibration and validation*, ESA Bulletin, No 65, pp 80 - 86 Feb., 1991.
4. R.Francis, *Height calibration of the ERS-1 radar altimeter*, IGARSS '92, Houston, Texas, May 26 - 29, 1992.
5. J.P.Guignard, *ERS-1 in-flight calibration and performance verification*, IGARSS '92, Houston, Texas, May 26 - 29, 1992.
6. R.C.Beal and P.G.Tilley, *ERS-1 and ALMAZ Ocean wave monitoring experiments*, IGARSS '92, Houston, Texas, May 26 - 29, 1992.
7. P.W.Vachon et al, *High Sea State Validation of the ERS-1 SAR*, IGARSS '92, Houston, Texas, May 26 - 29, 1992.
8. J.C.Wilkerson et al., *Airborne C-band scatterometer measurements obtained during underflights of the ERS-1 satellite in the Gulf of Mexico*, ERS-1 Geophysical Validation Workshop, Penhors, April 27 - 30, 1992.
9. A.Edward, *Data collection or data management*, ERS-1 Geophysical Validation Workshop, Penhors, April 27 - 30, 1992.

SESSION - I
DEDICATED CAMPAIGNS

WIND MEASUREMENTS OVER THE OCEAN WITH AN AIRBORNE C-BAND SCATTEROMETER DURING THE ERS-1 CALIBRATION AND VALIDATION CAMPAIGN

Volkmar Wismann

Universität Hamburg, Institut für Meereskunde, Troplowitzstr. 7, 2000 Hamburg 54, Germany

Abstract

The First European Remote Sensing Satellite (ERS-1) was launched from Korou, French-Guyana, on July 17, 1991. A geophysical calibration and validation of the Active Microwave Instrument (AMI) aboard the ERS-1 was performed in the Norwegian Sea in the period from September 15 to December 10, 1991. A total of 46 underflights of the ERS-1 satellite were performed with the Rotating Antenna C-band Scatterometer (RACS) of the University of Hamburg. The instrument was operated aboard a Donier Do-228 aircraft of the German Aerospace Research Establishment (DLR) in order to measure the normalized radar cross section (NRCS) of the ocean surface from which the wind speed $U_{10\text{ neutral}}$ can be inferred.

Wind measurements were also performed by anemometers mounted on 10 buoys, 3 research vessels and 2 aircrafts.

A good agreement was found between most of the wind measurements. The data set obtained during this experiment is being used for tuning the prelaunch wind retrieval algorithm for the ERS-1 scatterometer.

Introduction

Radar backscattering from the ocean surface is determined primarily by the short-scale surface roughness. The dominant factor determining this roughness is the local wind. Thus it is possible to infer ocean surface winds from the normalized radar cross section (NRCS). A C-band scatterometer is presently flying aboard the First European Remote Sensing Satellite (ERS-1) to measure ocean surface winds. In preparation of this satellite mission, the European Space Agency (ESA) has conducted a number of airborne C-band scatterometer campaigns over the North Sea, the Atlantic Ocean and the Mediterranean Sea [1]. Based on

the data collected during these campaigns an empirical prelaunch C-band wind scatterometer model for ERS-1 has been developed [2].

An airborne Rotating Antenna C-band Scatterometer (RACS) [3] has been constructed at the University of Hamburg which allows measurements of the wind field along flight tracks. During several experiments over the Atlantic in 1987 [4], the Mediterranean Sea in 1989 [5], and the rehearsal experiment for the ERS-1 Calibration and Validation Campaign over the Norwegian Sea in 1990 [6] RACS has demonstrated its capability of measuring ocean surface winds in quasi real time.

During the ERS-1 Geophysical Calibration and Validation Campaign in the Norwegian Sea between September 15 and December 10, 1991, 46 underflights of the ERS-1 were performed with RACS. Wind measurements were also carried out by a network of 10 meteorological buoys of the oceanographic institute OCEANOR (Norway), the research vessels Hakon Mosby (Norway), Planet and Gauss (Germany), the Hercules C-130 aircraft of the UK Meteorological Office (UK) and the navigation system of the Do-228 aircraft (Germany).

The Scatterometer

The scatterometer is a superheterodyne Doppler radar operating at 5.3 GHz. The microwave part of the instrument is very similar to the scatterometer described by Feindt et al. [7]. The output power and the gating of the transmitter and receiver allows measurements at flight altitudes between 500 and 15.000 ft. The beam axis of the vertical polarized planar microstrip antenna is squinted 45 degrees off the antenna normal. The one-way half-power beamwidth is 6.0° in elevation and 5.6° in azimuth. A special antenna mount for the Do-228 aircraft allows the antenna to rotate during flight at 1 revolution per minute. Thus the beam scans the surface conically at an incidence angle of 45 degrees.

The normalized radar cross section (NRCS) of the ocean at VV polarization is measured as a function of

antenna look direction. The surface wind vector is retrieved from the measured NRCS values for each revolution by fitting them to the empirical C-band backscatter model of Wismann [8].

Calibration of the Scatterometer

The technique for calibrating the airborne scatterometer employed during this campaign was developed and tested in several previous experiments. Seven corner reflectors (radar cross section : 650 m²) were placed alongside the runway of the airfield at Vaernes (Norway). Normally, calibration flights over the corner reflectors were carried out after each mission. In few cases turbulences or a high cross track wind component impeded accurate flight tracks over the corner reflectors. During the corner overflights the antenna was fixed to a look direction of 180 degrees (backward looking beam). The altitude during the calibration flights was 1,500 feet and the incidence angle 45 degrees.

Flight missions

During the experiment the ERS-1 satellite was in a 3 day repeat orbit. Within these 3 days two underflights of the ERS-1 were performed during which the AMI was operated in the scatterometer mode. In addition, 6 underflights of the full image SAR mode were performed during the intensive ocean wave phase between November 18 and 28, 1991 [9,10].

The flight missions were performed either across the ERS-1 scatterometer swath in order to cover all incidence angles or along the satellite track following the 45 degrees of incidence angle of the fore- and aft-beam antennae. One flight mission consisted of four parts. During the first part the flight altitude was 12,000 feet, and only RACS was used for measuring the ocean surface wind vector. At the turnpoint the vertical wind profile was measured by the navigation system of the aircraft during a descent down to 20 - 500 feet, depending on visibility and sea state. The return track was flown at 500 ft altitude using the navigation system of the Do-228 aircraft for the wind measurements. A boundary layer model was applied to these measurements in order to compute the 10 meters neutral winds [11]. At the end of the track another vertical wind profile was measured during an ascent up to 12,000 feet. As an example, Fig. 1 shows a very homogeneous wind field as measured by RACS on October 18. The wind is blowing with approx. 20 m/s from North. Figure 2 depicts the variation of the wind vector when crossing a meteorological front on November 11. There is a strong change in wind direction of 90 degrees across the front.

Results

During the 3 months of the experiment wind speeds between 8 and 15 m/s prevailed. But also very low wind speeds and wind speeds up to 25 m/s were encountered. Generally, a very good agreement was found between the wind fields obtained from RACS and those measured by the navigation system of the Do-228 aircraft.

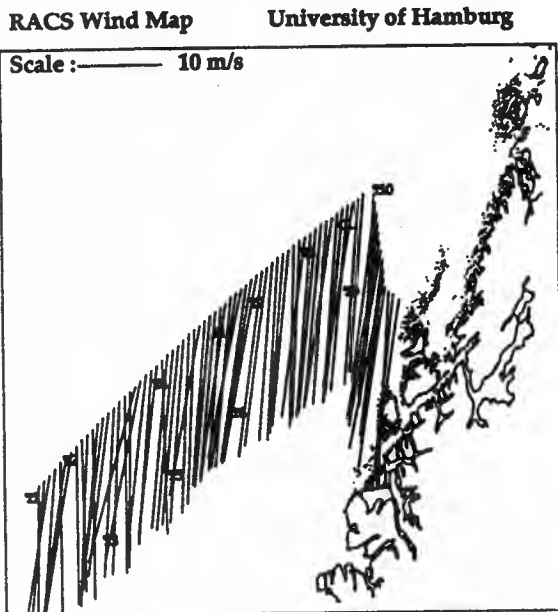


Fig. 1 Example of a very homogeneous wind field measured by RACS on October 18, 1991. The wind is blowing with approx. 20 m/s from North. The positions of the buoys T1 - T10 are inserted in the map.

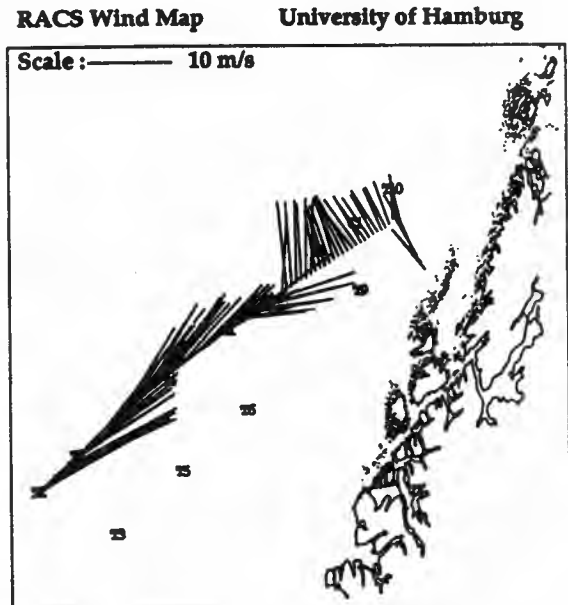


Fig. 2 Same as Fig. 1, but for a very inhomogeneous wind field encountered on November 11, 1991.

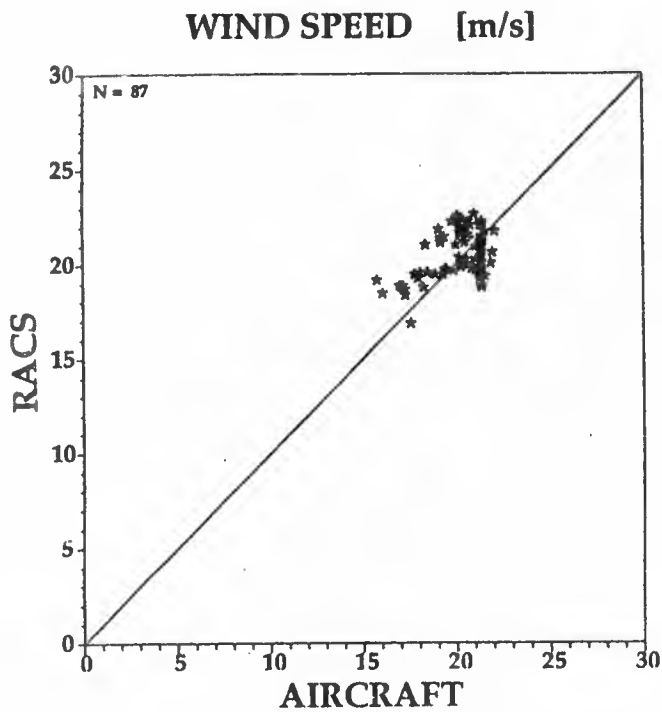


Fig. 3 Comparisons of the collocated wind speeds measured by the navigation system of the Do-228 aircraft and by RACS for a homogeneous wind field encountered on Oct. 18, 1991.

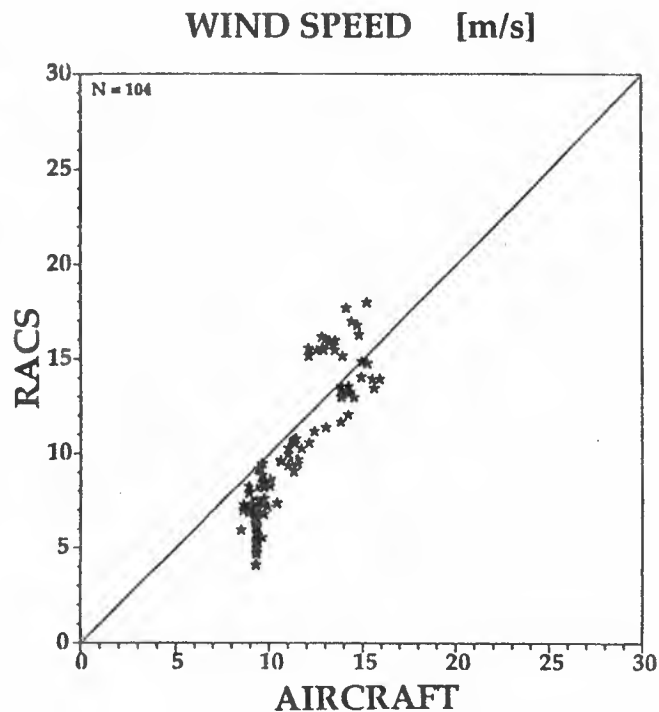


Fig. 4 Comparisons of the collocated wind speeds measured by the navigation system of the Do-228 aircraft and by RACS for a inhomogeneous wind field on Nov. 14, 1991.

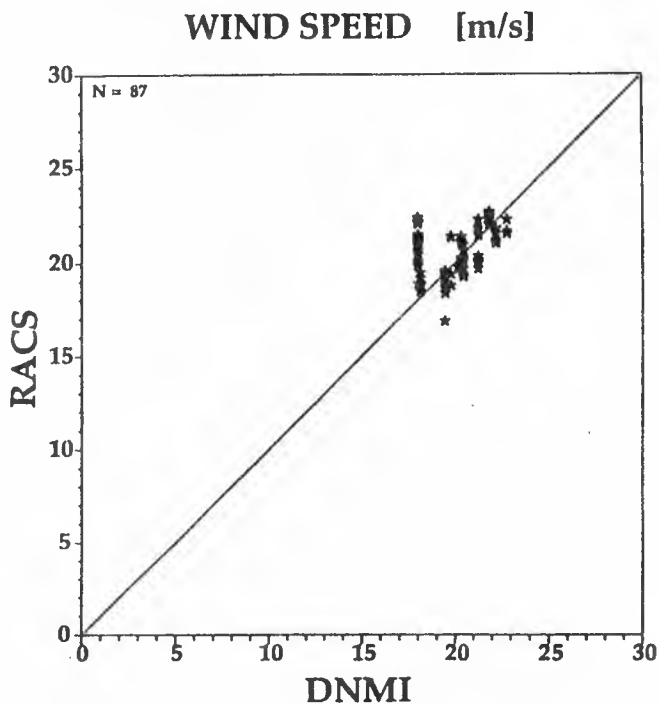


Fig. 5 Comparisons of the collocated wind speeds of the DNMI analysis and measured by RACS for a homogeneous wind field on Oct. 18, 1991.

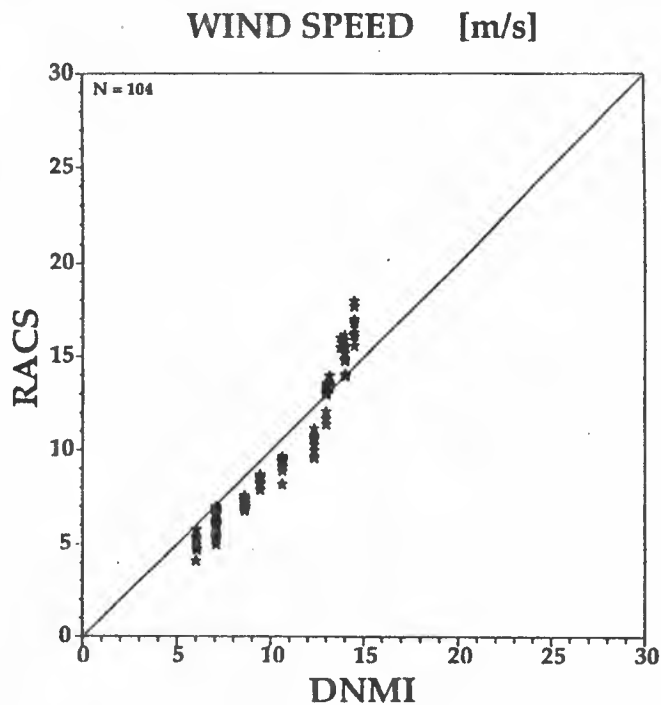


Fig. 6 Comparisons of the collocated wind speeds of the DNMI analysis and measured by RACS for a inhomogeneous wind field on Nov. 14, 1991.

Comparisons of the collocated wind speeds measured by the navigation system of the Do-228 aircraft and by RACS for a homogeneous (Oct. 18) and an inhomogeneous (Nov. 14) wind field are shown in Figures 3 and 4, respectively. In both cases a very good agreement between both measurements was found.

In order to extend the aircraft measurements for comparisons with the ERS-1 data over a larger area, the wind field analysis of the Norwegian Meteorological Office (DNMI) was used. Comparisons of the collocated wind speeds obtained from the DNMI analysis and measured by RACS are shown in Figures 5 and 6 for October 18 and November 14, respectively. The same good agreement was found.

During the ERS-1 Calibration and Validation Campaign in the Norwegian Sea the airborne C-band scatterometer system RACS demonstrated its capability of measuring the ocean surface wind along the track of the aircraft in quasi real time. Together with other sensors operated from other platforms a high quality data set of wind measurements over the open ocean was collected. A very high correlation is found between data obtained by all independent instruments and measurement techniques for 14 of the 46 underflights of the ERS-1 satellite. Discrepancies between single measurements encountered for the other 32 underflights could be explained by great variabilities in the wind fields in space and time. In several cases the measurements of the vertical wind profile indicated that the boundary layer model, that was applied to the aircraft measurements and the wind field analysis, was not valid. As an example, Fig 7. shows the vertical wind speed profile as measured by the navigation system of the Do-228 on December 2, 1991, at position T1.

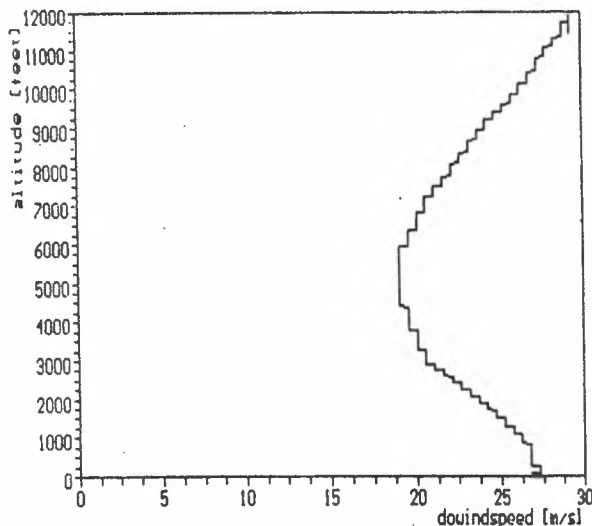


Fig 7. The vertical wind speed profile as measured by the navigation system of the Do-228 on December 2, 1991, at position T1.

The data set obtained during the Calibration and Validation Campaign is a very valuable tool for tuning the ERS-1 prelaunch wind scatterometer algorithm.

Acknowledgements

This research was supported by the Bundesministerium für Forschung und Technologie under grant 01QS90144 and by the European Space Agency under Contract No. 8398/89/NL/BI. We thank E. Attema from ESTEC, J.C. Morin from GDTA, H. Finkenzeller and G. Christner from DLR for the logistic support and the crews of the Do-228 aircraft H. Brockstieger, A. Eisenhut, M. Karg, W. Meier, F. Rösler, M. Scherdel, U. Schönbach, P. Vogel, R. Welser and R. Ziegler from DLR for their engaged collaboration.

The wind field analyses were provided by the Norwegian Meteorological Office DNMI as their contribution to the ERS-1 Calibration and Validation Campaign.

Furthermore, the hospitality of OCEANOR in Trondheim is acknowledged.

References

- [1] Attema, E.P.W., A.E. Long and A.L. Gray: "Results of the ESA Airborne C-Band Scatterometer Campaigns, Proceedings of IGARSS' 86 Symposium, Zürich, 8-11 Sept. 1986, Ref. ESA SP-254 ESA Publications Division, pp 381-387, 1986.
- [2] Long, A.E.: "Towards a C-Band Radar Sea Echo Model for the ERS-1 Scatterometer", Proceedings of the 3rd International Colloquium on Spectral Signatures of Objects in Remote Sensing, Les Arcs, France, 16-20 Dec. 1985, ESA SP-247, pp 29-34, 1985.
- [3] Wismann, V.: "Ocean Wind Field Measurements with a Rotating Antenna Airborne C-Band Scatterometer", Proceedings of IGARSS' 89 Symposium, Vancouver, Canada, 10-14 July, 1989, pp 1470-1473, 1989.
- [4] Wismann, V. and R. Stöwing: "Measurements of the Ocean Radar Cross Section at 5.3 GHz by an Airborne Scatterometer with a Rotating Antenna during the Toscane 2/Front 87 Experiment", Report to ESA, University of Bremen, 1988.
- [5] Wismann, V., S. Rieger and B. Friderici: "Tyrrhenian Eddy Multi-Platform Observations (TEMPO Experiment) Airborne Measurements", Experiment Report, University of Bremen, 1989.

- [6] Wismann, V. and S.Rieger: "Ocean Wind Vector Measurements with the Rotating Antenna C-Band Scatterometer during the ERS-1 Rehearsal Experiment", Report to ESA, University of Hamburg, 1990.
- [7] Feindt, F., V. Wismann, W. Alpers and W.C. Keller: "Airborne Measurements of the Ocean Radar Cross Section at 5.3 GHz as a Function of Wind Speed", Radio Science, 21, no. 5, pp 845-856, 1986.
- [8] Wismann, V.: "Messung der Windgeschwindigkeit über dem Meer mit einem flugzeuggetragenen 5.3 GHz Scatterometer", Dissertation, University of Bremen, 1989.
- [9] Wismann, V., A.Schmidt, R.Romeiser, B.Geisler, A.Wilde and K. Boehnke: "Ocean Wind Vector Measurements with the Rotating Antenna C-Band Scatterometer during the ERS-1 Calibration and Validation Experiment", Report to ESA, Contract 8398/89/NL/BI, University of Hamburg, 1992.
- [10] Morin, J.C.: "CAL-VAL Operation Plan RENE 1991 Campaign 15.09.91-09.12.91 Version No. 5", Trondheim, Norway, November 1992.
- [11] Ezraty, R.: "ETUDE DE L'ALGORITHME D'ESTIMATION DE LA VITESSE DE FROTTEMENT A LA SURFACE DE LA MER", Contract ESA/ESTEC N 6155/85/NL/BI, 1985.

Wind Measurements from the MRF C-130 and the Derivation of Analyses from RENE-91 Winds

D. Offiler, Meteorological Office, Bracknell, UK

Abstract

This paper describes the contribution made to the RENE-91 campaign by the Meteorological Research Flight (MRF) C-130 aircraft, including its instrumentation, wind vector determination and post-flight analysis. Also discussed is an objective analysis scheme which uses all available in situ wind information to form the best estimate of the local wind field for comparison with the ERS-1 scatterometer data.

1 Introduction

During the period 16 September to 10 December 1991, a campaign was coordinated by ESA to assist in the geophysical calibration of wind and wave products derived from the ERS-1 satellite. The campaign, known as *RENE-91*, involved making *in situ* measurements off the coast of Norway in the Haltenbanken area using a variety of platforms, including buoys, ships and aircraft. Details of the campaign — its objectives, participants and data handling and results — are given elsewhere in this volume.

For a period of three weeks at the beginning of the campaign, and for nearly two weeks at the end, the Meteorological Office's MRF C-130 (Hercules) instrumented aircraft was based in Trondheim, the campaign's operations centre. During this time, low-level measurements of the winds were made over the Haltenbanken area when the ERS-1 scatterometer was also operating.

Data from most of the platforms participating in the campaign, together with numerical analyses made by the Norwegian Meteorological Institute (DNMI) and ERS-1 fast delivery products were delivered to a local database, generally within 24 hours of their measurement time. This database was used to form a 'best-estimate' wind field around the Haltenbanken area, which could be used (a) to quickly compare with the ERS-1 winds for day-to-day quality monitoring, (b) to form a high-quality dataset which could be used for calibrating or tuning the scatterometer wind retrieval algorithms and (c) to validate such tuning.

2 C-130 Wind Measurements

2.1 Instrumentation

Depending on the needs of particular experiments, the C-130 can carry a wide range of instruments for measuring various atmospheric parameters, including chemistry, radiation (in the infra-red and microwave) and clouds [1].

However, for winds, only the standard sensors were required; principally —

- the Inertial Navigation System (INS), giving
 - aircraft position (latitude and longitude)
 - aircraft ground velocity (N and E components)
 - aircraft heading from True North
- wind vanes for angle of side slip and angle of attack
- dynamic (pitot) pressure for air speed.

In addition, to derive the most accurate winds, additional measurements are made using:

- other nav aids such as Global Positioning System (GPS), Omega, Decca and Doppler radar
- INS pitch and roll plus INS pitch, roll and yaw rates
- compensated air temperature and static pressure

The other nav aids (in particular GPS) are used during ground processing to correct for INS drifts and Schuler oscillations to obtain the best aircraft ground velocities; the true air temperature and static pressure are used to derive the true air speed. The wind speed and direction can then be calculated by the vector difference of ground and air velocities, and converting from an aircraft frame of reference to a geographic frame [2]. On an error budget analysis, it is expected that the flight level wind can be determined to $\sim 0.5\text{ms}^{-1}$ (rms vector error).

2.2 10-m wind

The scatterometer-derived wind speeds are specified to be those equivalent to a measurement at a height of 10 metres in a neutrally-stable atmosphere (U_{10}). In order to compare — and geophysically calibrate — the scatterometer winds, all the *in situ* measurements are required to be the same quantity. In the case of the C-130 data, the flight level winds were converted to U_{10} using the agreed Ezraty boundary layer model, which assumes a logarithmic wind profile, with corrections for the actual atmospheric stability. Full atmospheric compensation was be applied using:

- derived flight level wind speed
- measured flight level temperature, humidity and static pressure
- radiometric sea-surface temperature
- radar altitude (up to 5000 ft)
- temperature lapse rate



C-130 10-m Winds

Flight A154 02.12.91 08:03 - 14:24 10km averages

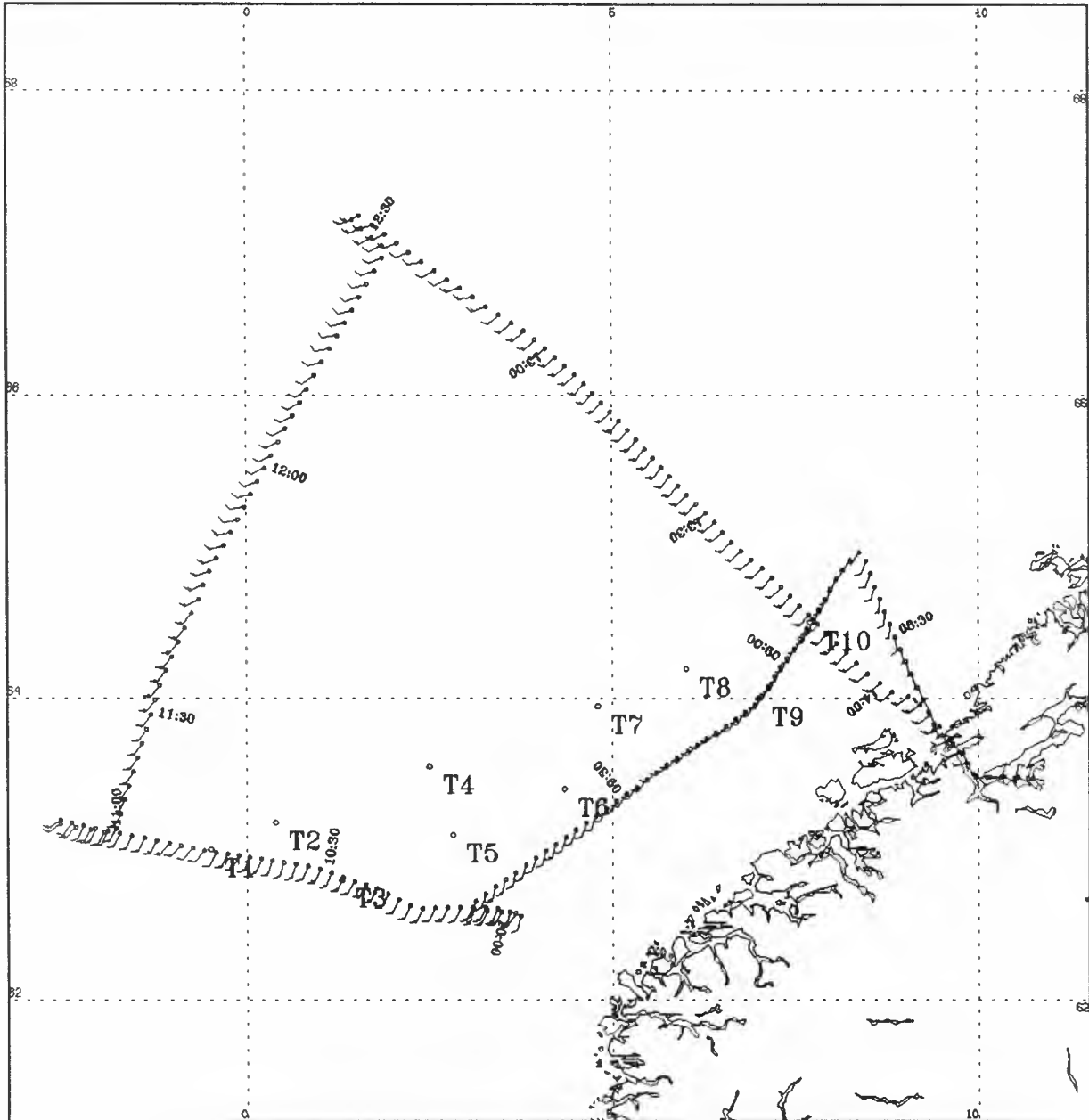


Figure 1: Example C-130 flight track and derived 10m winds



10-m Winds for 10:49 UT 02-DEC-1991

(Data measured below 2000ft and within 3.0hrs of pass time)

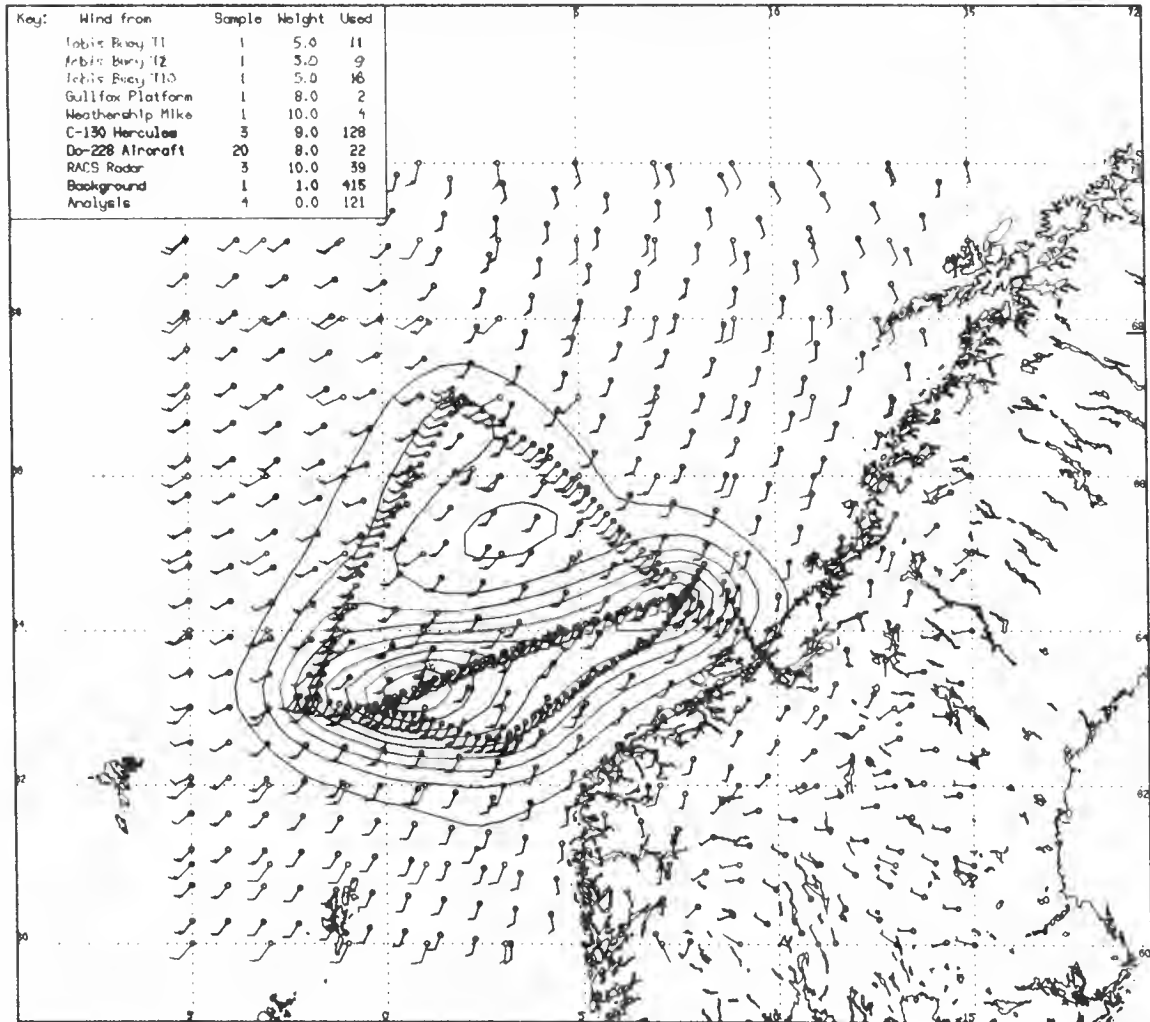


Figure 2: Analysis made from all sources of *RENE-91* data over the same time period as the C-130 flight shown in Figure 1

Because the aircraft parameters are logged at different rates (from 1 to 32 Hz) all were first averaged over equivalent 5 km lengths of flight track, with various quality control criteria applied. The temperature lapse rate was calculated from the last aircraft profile, usually from 4000 ft to 50 ft. Although some profiles showed highly non-logarithmic wind speeds with height, such deviations were generally above the nominal flight level of 200 ft, and are not thought to contribute significant error to the derived U_{10} in the majority of cases. The wind direction at 10m is assumed to be the same as at the flight level; profiles confirmed that this was usually the case in the lowest 200m of the atmosphere.

The final datasets from each flight were delivered to the local database in Trondheim in the agreed 'Ar Mor' format [3] the day following a flight.

2.3 Flights

While ERS-1 was in its commissioning phase 3-day orbit, scatterometer passes were scheduled to give good coverage of the Haltenbanken area three times every three days. The C-130 flew missions on two of these opportunities — the 'Day 1' descending pass at around 10:50 UT and the 'Day 2' descending pass at around 10:15 UT. Each flight covered as much of the swath as was practical, underflying all incidence angles and a length of the swath sufficient to determine the two-dimensional wind field — Figure 1 gives an example flight track and the derived winds for a Day 1 pattern. The nominal flight altitude was 200–250 ft (70–80m), with a profile between 4000 ft and 50 ft at each corner of the pattern, and passing over at least two buoys for cross-comparisons.

The Day 1 flight duration was around 6 hours, so there is obviously a time difference between the aircraft and scatterometer measurements; the flight was planned so that the C-130 (and the Do-228 when flying its own pattern) would be over the buoy position T1 at the time of the ERS-1 overpass.

On the Day 2 passes, the swath was closer to the coast and further north. On these flights, the rendezvous point was T10, travelling up-swath.

2.4 Summary of C-130 data

In all, 18 successful flights were made when good data were obtained; on two flights, the INS drifted badly, and although the aircraft position could be recovered with the GPS, the aircraft velocities could not be derived with sufficient accuracy to obtain good winds. Only one planned mission was not flown because of engine problems. Over 100 science-hours were flown during the campaign.

3 Analyses

3.1 Comparison methods

When comparing meteorological satellite data with *in situ* measurements, it has been traditional to use one of two methods:

1. collocate one *in situ* measurement with one or more nearest satellite point and within some time limit,

on an essentially one-for-one basis. This has the disadvantage of introducing collocation errors because of spatial or time differences, and also not comparing like with like, since the *in situ* measurement is usually taken at a point over a time average, and the satellite is an areal average at an instant in time. Such collocations or 'hits' tend to be few in number and rarely cover the whole range of desired parameters.

2. some of the above disadvantages can be reduced by first assimilating the *in situ* data into numerical models and interpolating the required parameter from the analysis grid to the satellite footprint location. However, such models tend to have rather coarse horizontal resolution compared to that of the satellite, and are generally tuned to the synoptic scale, which tends to smear out or miss small-scale features which might be represented in the satellite swath.

In the case of the *RENE-91* campaign, the *in situ* data, although gathered quickly by campaign standards, could not be delivered to weather centres in time for their numerical models' operational runs, so this collocation method could not be used during the campaign.

3.2 RENE analyses

So, if the data could not be sent to the analysis, the analysis must go to the data... An existing single-variable, two-dimensional, recursive filter, objective analysis scheme described in [4] was tuned to use the *RENE-91* winds, with the DNMI wind fields as a background; a 25 km grid size was chosen as comparable with the scatterometer node spacing, with the grid covering the area 60° to 70°N and 5°W to 15°E.

Because all the *RENE-91* datasets were supplied in the Ar Mor format, winds from all available sources could be incorporated into the analysis simply; the actual sources and quantities varied from day to day, but the following have been used in at least one analysis:

Aircraft	—	C-130, Do-228
Radar	—	RACS (on Do-228)
Buoys	—	up to 6 Tobis-3 buoys
Ships	—	WeatherShip Mike, — R/V Gauss, Håkon Mosby
Platforms	—	Gullfax
Models	—	DNMI wind field analyses

All of these data contain U_{10} wind speeds or have measurements made close to 10m; each data source is complementary in that they are made at many different locations over the analysis area and by different sensor and sampling systems. Of course, not all sources are available for every scatterometer pass.

Each data source is assigned a relative weight depending on its perceived *a priori* quality; for instance most of the *in situ* data is weighted with values 8–10, but the DNMI background (which should not significantly influence the analysis in the presence of *in situ* data) is weighted at 1. In addition, the weighting value is reduced by an amount depending on the time difference of the

measurement from the scatterometer overpass time and also by an amount related to the altitude of the platform (for aircraft). These weights are such that data more than three hours from the satellite pass or when an aircraft was above 2000 ft are not used. For the Tobis buoys, where both lower and upper sensor were available, the one with the smallest variability has been used.

The analysis software also calculates a 'quality index' (QI); this is an arbitrary number in the range 0–100, and at each grid point is a measure of:

- the expected errors of individual data sources contributing to that grid point
- individual observation weightings due to the time difference from satellite overpass time, or due to aircraft altitude
- the local density of observations
- the local consistency between observations

The higher the QI value, the higher the confidence in the analysis. The relative source weightings were also chosen such that a QI value of around 5 indicates a rough threshold where higher values indicate that the *in situ* winds have influenced the analysis, and lower values that only the DNMI background has been used.

Figure 2 shows an example of an analysis. In this case, the C-130 track from Figure 1 is seen, as is the Do-228 track though the centre of the C-130 loop. This track actually contains RACS winds outbound and Do-228 navaid winds back. This case also uses winds from three Tobis buoys, Weathership Mike (just below the northernmost part C-130 track) and the Gullfax platform to the south. The slightly sloping grid shows the DNMI background winds; the derived analyses (only plotted every fourth grid point for clarity) are the winds aligned with the latitude and longitude grid. Contours of the QI value are also plotted every 10 units.

The advantages of this analysis method are that

- it maximises the number of collocations, particularly by covering the whole width of the swath
- it minimises errors in any one platform or individual observation
- there should not be any systematic errors
- the spatial average is more comparable to a scatterometer measurement

although there will still be a tendency to smooth very small scale features or sharp gradients over one or two grid lengths, or where there are rapid changes in time.

3.3 Collocations

The analysed winds are bi-linearly interpolated from the four surrounding grid points to each of the scatterometer cell locations within the grid's area.

Figure 3 shows the *RENE-91* analysis of Figure 2 together with the ERS-1 fast delivery winds. The contour is the QI=5 value, inside which the analysis is almost entirely derived from the *in situ* measurements, and outside is influenced only by the DNMI background wind field. Over most of the swath, the scatterometer shows good agreement with the analysis except in the NW part of

the contour, where there are difference in wind direction of 20–30°; this is probably due to an active front passing through the area between the time of the satellite pass and the C-130 track 1–2 hours later. The frontal position can be identified from the wind direction changes in Figure 1 along the NE-bound and SE-bound C-130 legs.

3.4 Summary of analyses

A total of 77 scatterometer passes have been processed with analyses made using the technique described here, creating nearly 17,000 individual collocations (scatterometer cells) with a QI ≥ 5 . Not all of these passes have good coverage of *in situ* data, and not all have DNMI backgrounds available, but the QI value is a good filter for poorly covered cases. Some cases, like the one shown in the figures, have frontal systems which may give rise to 'errors' in the analyses — these may need to be excluded by inspection of the data and by consulting the synoptic patterns analysed by DNMI (which are available as part of the campaign operations documentation) before being used for calibration purposes.

These analyses cover the wind speed range 1–21ms⁻¹ with directions mainly from the SW to N; but as the passes are both ascending and descending, and three scatterometer beams cover 90° in azimuth, the wind directions relative to any beam have a more uniform spread. Taken over all 77 cases (17,000 collocations), the rms differences between the scatterometer winds and analysed winds are:

$$\begin{aligned} \text{Speed} &: 3.0\text{ms}^{-1} \\ \text{Direction} &: 21^\circ \text{ (ambiguity removed)} \\ \text{Vector} &: 4.3\text{ms}^{-1} \end{aligned}$$

This shows that against the *RENE-91* analyses, the ERS-1 wind directions are probably acceptable, but the wind speed retrieval from the current 'CMOD2' wind model requires tuning if the scatterometer specification of 2ms⁻¹ is to be met. A detailed appraisal of these collocations and some results of model tuning are given in [5].

The collocated scatterometer parameters (as found in the ESA UWI fast delivery products) and analysis winds have also been delivered to the ERS-1 database in the Ar Mor format for further use, some of which are described in other papers in this proceedings volume.

References

- [1] CJ Readings. The use of aircraft to study the atmosphere: the Hercules of the Meteorological Research Flight. *Meteorological Magazine*, 114:66–77, 1985.
- [2] DN Axford. On the accuracy of wind measurements using an inertial platform in an aircraft and an example of the measurement of vertical meso-structure of the atmosphere. *Journal of Applied Meteorology*, 7:645–666, 1968.
- [3] A Edward. ERS-1 geophysical campaign data format. ESA document ER-SR-EPO-GP-1111, Issue 3, Rev. 0, February 1992.

- [4] CM Hayden and RJ Purser. Three-dimensional recursive filter objective analysis of meteorological fields. *CIMSS View*, IV(1), Spring 1988.
- [5] D Offler. The validation and comparison of alternative wind scatterometer models. In *ERS-1 Geophysical Calibration Workshop, Penhors, France, 26-30 April, 1992*. ESA, 1992.

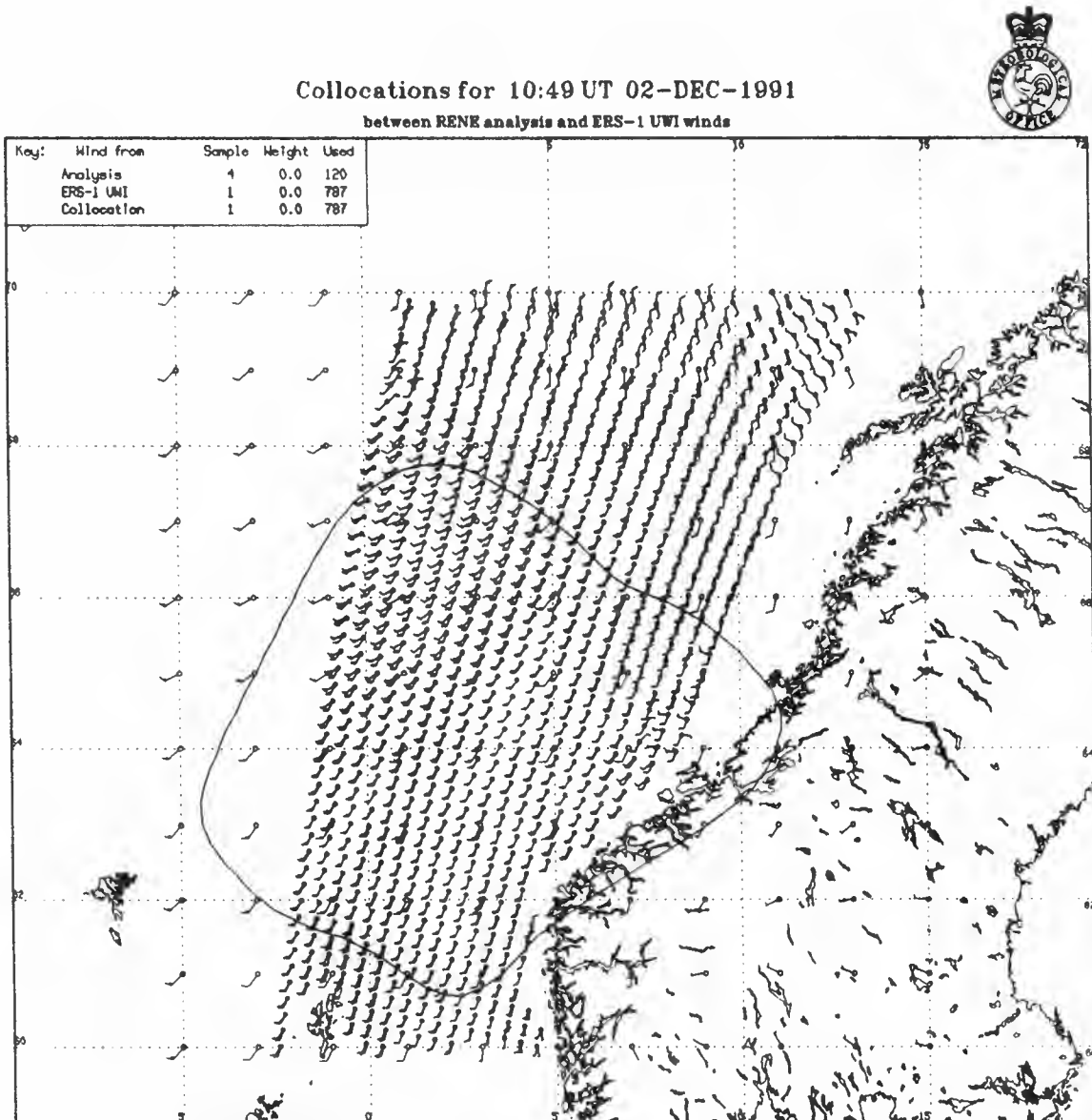


Figure 3: Collocated scatterometer and *RENE-91* analysed winds from Figure 2

ERS-1 CAL/VAL IN-SITU MEASUREMENT

WIND AND WAVE MEASUREMENTS DURING EXTREME SITUATIONS

BY

TOM-IVAR BERN AND STEPHEN BARSTOW

OCEANOGRAPHIC COMPANY OF NORWAY A/S

ABSTRACT

During the commissioning phase of the ERS-1, a dedicated wind and wave campaign, RENE-91, was staged in the Haltenbanken area off mid-Norway. This area is renowned for its severe winter weather, and long swells exposed as it is to the full force of the Atlantic Ocean and the Norwegian Sea..

A buoy net work consisting of ten wind and wave measuring buoys was deployed and maintained from September 16, 1991 until February 18, 1992, prolonged after the official closing of RENE-91 campaign which ended December 14.

On January 1, a major storm passed over the buoy network before it hit the coast of Norway. Hurricane force wind were reported along the coast leading to severe damage to property and forestry.

In this paper the observations gathered by the buoy network are reviewed with special emphasis on the major storm events.

INTRODUCTION

The buoy network

The buoy network consisted of 10 TOBIS buoys. In addition OCEANOR deployed a Directional Waverider, and a Wavescan buoy. An overview of the buoy network is given both in the Table 1, and in the map in Fig. 1.

The TOBIS buoy, sensors and geophysical parameters.

T01 to T10 are TOBIS buoys equipped with duplicate wind sensors and a non-directional Waverider. Fig. 2 gives an outline of the buoy and a sketch of the mooring system used. Details concerning the observations provided by the buoy and respective sensors on board these buoys are listed in Tables 2 and 3.

The buoys were operated with two time scales for data delivery. In the following table and overview is given of the measured parameters with *nrt* used as an abbreviation for *near real time*, (Argos transmitted data) while *ac* for *after campaign* (on board recorded data)

T11 is a directional Waverider supplied by OCEANOR to compensate for the faulty wave sensor on T04. In agreement with ESA, the buoy was not deployed alongside T04, but in a position both on the altimeter track and within the SAR swath.

T10a is a Wavescan buoy supplying both directional wave and wind measurements. It was deployed to provide OCEANOR with an independent wind measurement to be used for control of the ERS-1 buoys.

THE STORMS ENCOUNTERED

The area off mid-Norway is well known for its severe winter weather. Long term directional wave and wind measurements have been carried out by OCEANOR in this area from 1980 to 1988 with up to 16 m significant wave height recorded. In particular swell wave energy is particularly high in this area due to the open exposure to the Atlantic Ocean and Norwegian Sea. Under the ERS-1 related experiment, high waves (up to 14.2 m significant) were also encountered.

Nevertheless, surprises were kept in store for the RENE-91 campaign measurement period. In particular, a severe storm occurred on October 17 with unusual wave direction, a storm on December 18, had peak wave period recorded as high as 20 seconds. Finally, a cyclone like storm hit the campaign area on January 1st with extremely high winds causing considerable damage along the Norwegian Coast. The measurements from two of these two storms are discussed in more detail in the following:

October 17, storm

Buoy observations

A storm hit the experiment area on October 17th to 19th. In Table 4 peak significant wave heights and associated wave periods encountered by the buoy network during the passage of the storm are given.

The meteorological picture during this storm was that a deep low moved on a south eastward track from Iceland to Southern Norway during the 16th to 18th. An area of strong north to north east winds stretching from Spitsbergen to the central North Sea were present on the rear of the low leading to the up to 13 meter significant wave heights recorded. The measurements in this area had not previously recorded over 10 meters from this direction. Damage was caused on the Norwegian coast to coastal works exposed to the north. A lighthouse keeper at Halten fyr reported the worst conditions in his 40 years service.

January 1, 1992 storm.

Buoy observations

A very severe storm hit the buoy array and the west coast of Norway during January 1. The storm caused considerable wind damage to property and forestry. The insurance companies has received reports on damage worth 1,5 billion Norwegian Kroner. The 8 buoys in position endured the storm and transmitted data throughout the period with wind speed u_{10} (i.e. 10 m neutral wind) up to and partly above 30 m/s. The peak conditions are listed in Table 5.

This storm was very different from the October 17th storm event resulting from a fast moving powerful cyclone like storm which moved north eastwards from the Faeroe Islands on New Years Eve, the storm centre moving over the Norwegian Coast to the north of the buoy array on the evening of the 1st. On the morning of the 1st the storm central air pressure was below 950 hPa and hurricane force (Beaufort 12) winds were measured along the Norwegian coast at several locations east of the buoy array. Significant wave

heights during this storm reached 14.2 meters at three locations, but high waves were of short duration as a result of the rapid passage of the storm and its limited extent. This is in sharp contrast to the October 17th event which had somewhat lower winds over a very long fetch. In contrast to the severe nature of the wind damage, wave damage was apparently minor during the January 1st storm.

The ERS-1 satellite passed over the buoy network on January 1, at 10:54. Table 6 gives the wind speed and direction at the time of over flight of the satellite.

Figures

Figures 1, 2 and 3 gives the buoy network layout and a sketch of the buoy.

Figures 4 and 5 gives the timeseries of the significant waveheight for the buoy array. The data presented are from on board storage for the TOBIS buoys (hourly measurements). For station 10a and T11, the data has been transmitted via the Argos system (threehourly measurements). Erroneous data (spikes etc.) has not been removed.

Figures 6 and 7 gives the timeseries of wind speed and direction during the storm January 1.

CONCLUSIONS

During the RENE-91 measurement campaign OCEANOR deployed altogether three different buoys. They were deployed in water depths ranging from 255 to 1540 meters. The campaign has proven that all three buoy types are capable of providing wind and wave observations even during the most severe wave and wind conditions likely to be encountered. However, some problems were encountered particularly during the October storm with respect to mechanical failure of the wind sensors and perhaps as a result of breaking waves.

The weather conditions encountered during the RENE-91 were extremely variable from almost calm to hurricane force winds. In particular, two of the most severe storms ever encountered off mid-Norway were experienced. Further, very long swells were measured and crossing seas were common. The excellent spatial coverage over the buoy array both in normal and extreme conditions will be a valuable source of data for both the ERS-1 sensor calibration and validation and other studies such as numerical wave model calibration.

ACKNOWLEDGEMENTS

The work presented here was undertaken as a part of the ESTEC contract no 85/89/NL/BI between the European Space Agency, ESA through the European Space Research and Technology Centre, ESTEC, and the Oceanographic Company of Norway A/S, OCEANOR. The work has also been financed by the Norwegian Space Centre, NSC, through separate agreements between NSC and OCEANOR.

Table 1: The buoy network

Station	Deployed	Retrieved	Nominal position		Sounder depth	Comments
T01	91.09.10	91.09.26	63°00'N	00°30'W	1540 m	Drifted out of position with working sensors, provided data up to recovery 91.11.23
T01	91.11.24	91.12.07	63°00'N	00°30'W	1540 m	Drifted out of position with working sensors, recovered and re deployed at T03.
T02	91.09.11	91.12.20	63°11'N	00°24'E	1520 m	Drifted out of position with working sensors, provided data up to 92.01.01
T03	91.09.11	91.11.09	62°48'N	01°18'E	910 m	Originally deployed buoy lost
T03	91.12.08	92.02.18	62°48'N	01°18'E	910 m	Buoy from T01 deployed.
T04	91.09.11	92.02.18	63°33'N	02°30'E	1320 m	Both wind sensors missing at recovery
T05	91.09.15	91.12.07	63°06'N	02°49'E	940 m	Recovered and brought to shore since the wave-sensor was broken and the wind sensor carrier was damaged beyond field repair.
T06	91.09.16	92.02.18	63°24'N	04°20'E	1270 m	Propellers on both wind sensors missing
T07	91.09.14	92.02.18	63°57'N	04°48'E	1240 m	Propellers on one wind sensor missing
T08	91.09.12	92.01.03	64°12'N	06°00'E	392 m	
T09	91.09.12	91.12.13	64°00'N	07°00'E	333 m	Mooring cut with sharp knife.
T10	91.09.14	92.02.18	64°30'N	07°42'E	255 m	One complete wind sensor missing. On the other missing propeller
T10a	91.11.22	92.02.18	64°30'N	07°42'E	255 m	
T11	91.09.30	92.01.31	66°21'N	07°08'E		

Table 2: The TOBIS buoy sensor package

Manufacturer	Sensor	Measured variable	Location
Young	Model 05103 propeller anemometer	Wind speed Wind direction Wind variability, S_{1000} Wind variability, S_{100}	3.7 m above sea surface
Young	Model 05103 propeller anemometer	Wind speed Wind direction Wind variability, S_{1000} Wind variability, S_{100}	3.2 m above sea surface
Brookes and Gatehouse	Halcyon 3 flux gate compass	Buoy direction	3.0 m above sea surface
Datawell	Waverider 6000-9	Surface elevation Wave height Wave period Peak period	At buoy water line

Table 3: TOBIS buoy geophysical parameters

Measured variable	Sample length	Sample interval	Algorithm
Wind speed, nrt	20 minutes	Continuous	Vector average
Wind speed, ac	2 minutes	Continuous	Vector average
Wind direction, nrt	20 minutes	Continuous	Vector average
Wind direction, ac	2 minutes	Continuous	Vector average
Wind variability S_{wind} , nrt	20 minutes	Continuous	Component standard deviation
Wind variability S_{wind} , ac	20 minutes	Continuous	Component standard deviation
Wind variability S_{wind} , nrt	20 minutes	Continuous	Component standard deviation
Wind variability S_{wind} , ac	20 minutes	Continuous	Component standard deviation
Wave height, H_{m0} , nrt	34 minutes 8s	Every 3 hours	Fourier analysis
Wave height, H_{m0} , ac	34 minutes 8s	Every 1 hours	Fourier analysis
Wave period, T_{m02} , nrt	34 minutes 8s	Every 3 hours	Fourier analysis
Wave period, T_{m02} , ac	34 minutes 8s	Every 1 hours	Fourier analysis
Peak period, T_n , nrt	34 minutes 8s	Every 3 hours	Spectrum shape analysis
Peak period, T_n , ac	34 minutes 8s	Every 1 hours	Spectrum shape analysis
Height variance spectrum, ac	34 minutes 8s	Every 1 hours	Fourier analysis

Table 4: Wave observations during October 17th storm

Station	Date	H_{m0}	T_{m02}	T_n
T01	91.10.17-20:25	11.1	11.0	15.0
T02	91.10.17-16:25	12.7	11.2	15.0
T03	91.10.17-16:25	12.0	10.8	15.0
T05	91.10.17-20:25	12.5	11.4	15.0
T06	91.10.18-09:25	12.3	11.5	17.0
T07	91.10.18-04:25	13.0	11.8	15.0
T08	91.10.18-03:25	13.0	11.8	15.0
T09	91.10.18-04:25	11.4	11.4	15.0
T10	91.10.18-05:25	11.6	11.6	15.0

Table 5: Peak wind and wave measurements during January 1st storm

Station	Position	Wind speed	u_{10}	Wind direction	H_{m0}^*	T_n
T02	63.290°N 7.290°E	22.1	25.7	250.6°	14.2	17.0
T03	62.791°N 1.346°E	26.3	30.2	267.0°	14.2	17.0
T04	63.544°N 2.537°E	26.5	31.2	288.5°	N/A	N/A
T06	63.393°N 4.345°E	25.0	29.3	279.0°	12.8	15.0
T07	63.951°N 4.814°E	23.4	27.3	295.2°	12.9	17.0
T08	64.197°N 6.008°E	23.2	27.1	285.5°	14.2	15.0
T10	64.503°N 7.706°E	23.6	27.0	284.1°	10.2	16.8
T11	66.350°N 7.133°E	N/A	N/A	N/A	11.8	N/A

*Hourly peak conditions apart from T10 which is 3 hourly.

Table 6: Wind conditions at satellite passage January 1.

Station	Position	Wind speed	u_{10}	Wind direction
T02	63.290°N 7.290°E	21.0 m/s	24.4 m/s	253.4°
T03	62.791°N 1.346°E	18.7 m/s	21.4 m/s	278.2°
T04	63.544°N 2.537°E	19.6 m/s	22.7 m/s	281.2°
T06	63.393°N 4.345°E	20.5 m/s	23.8 m/s	282.3°
T07	63.951°N 4.814°E	22.7 m/s	26.0 m/s	274.1°
T10	64.503°N 7.706°E	16.5 m/s	18.6 m/s	267.2°

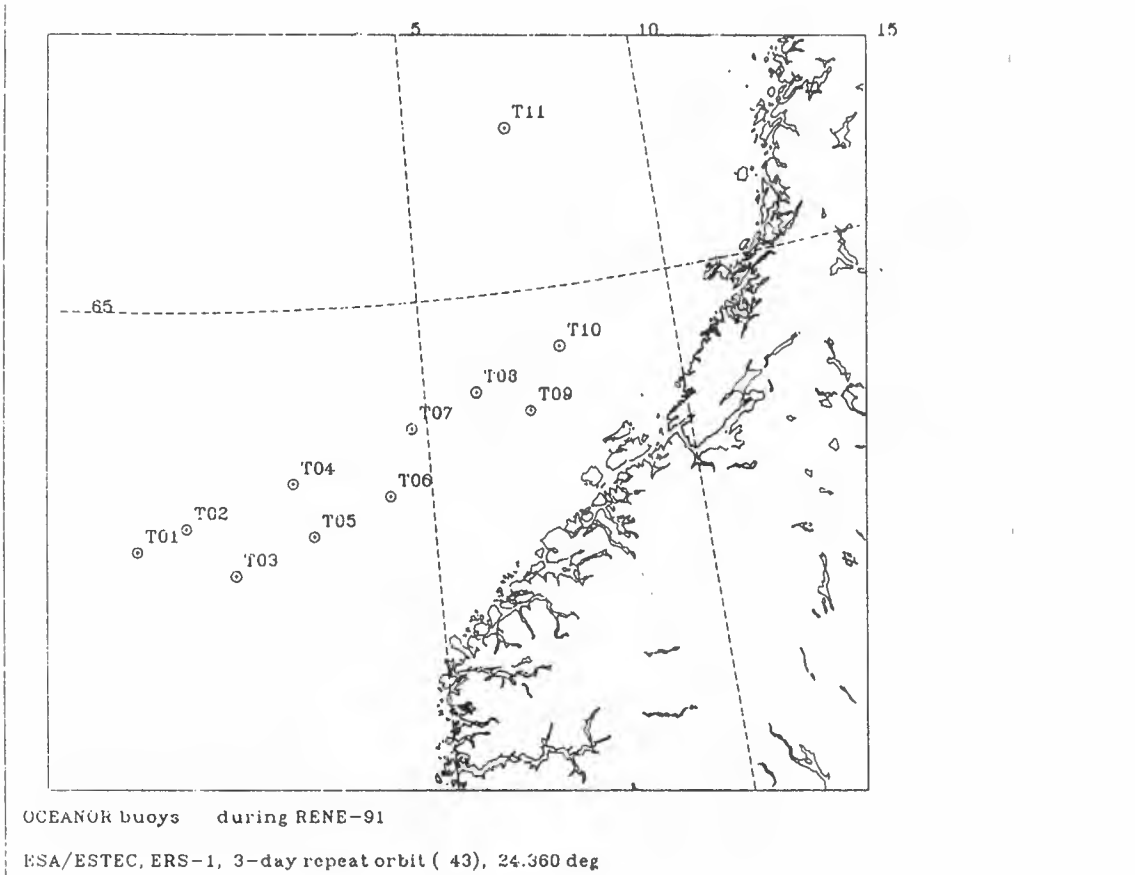


Figure 1

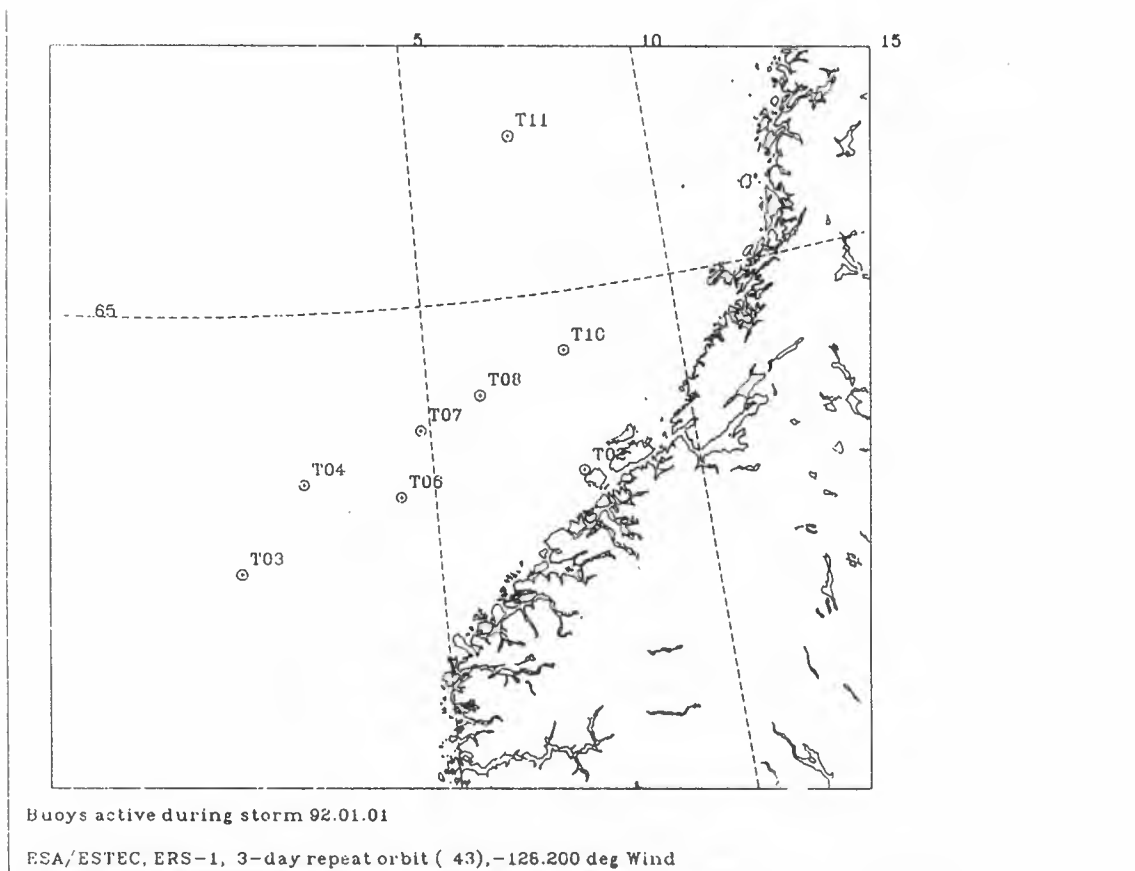


Figure 3

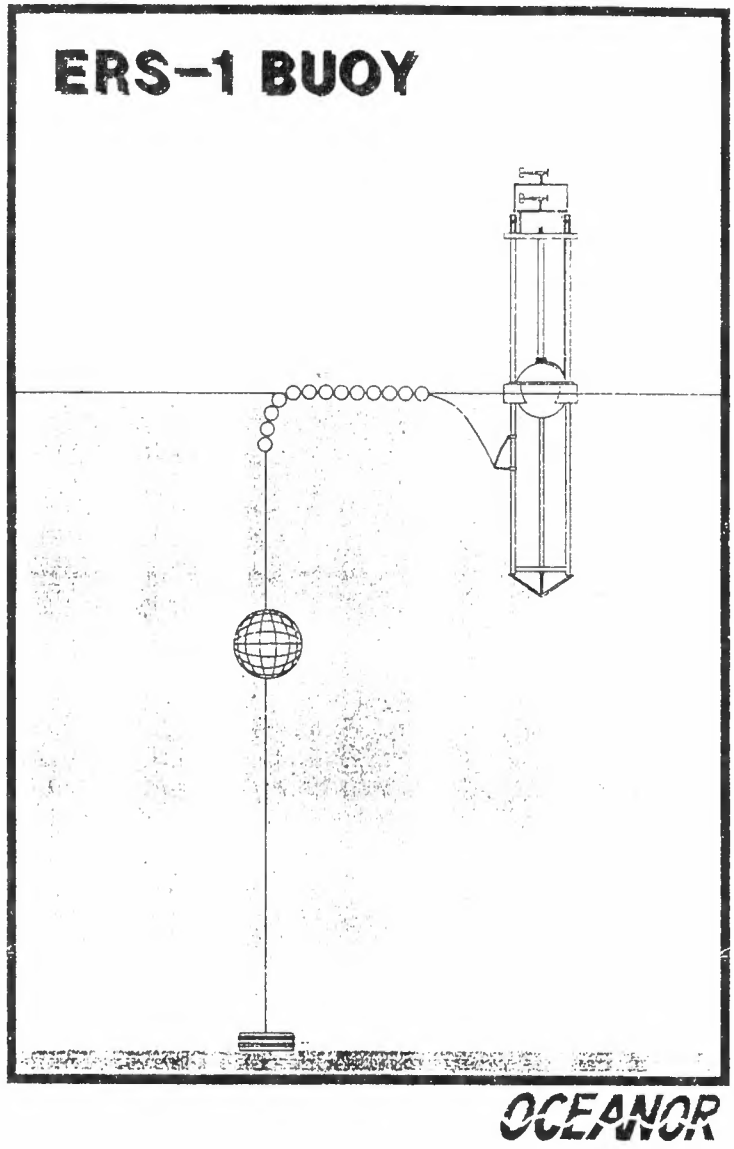


Figure 2

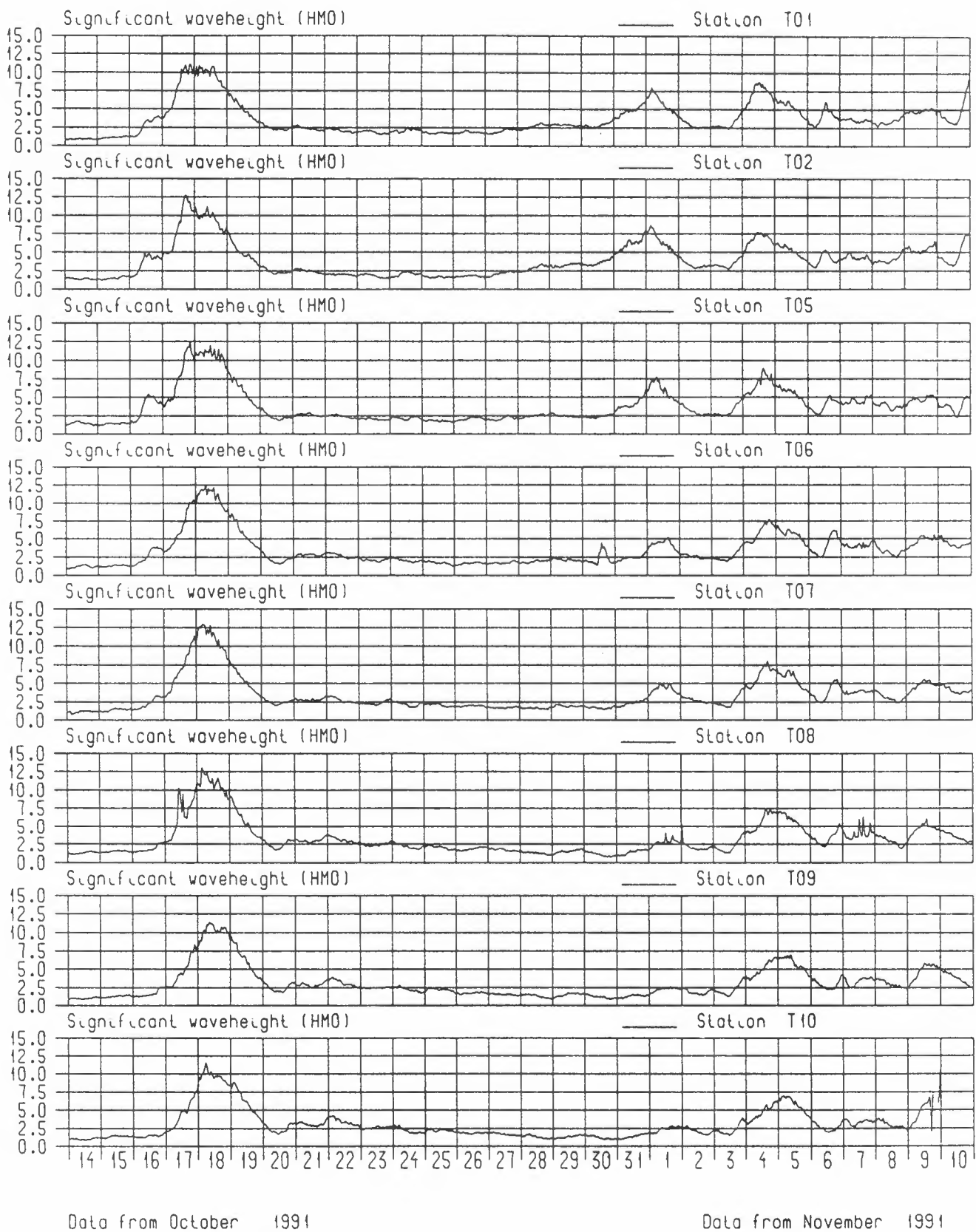
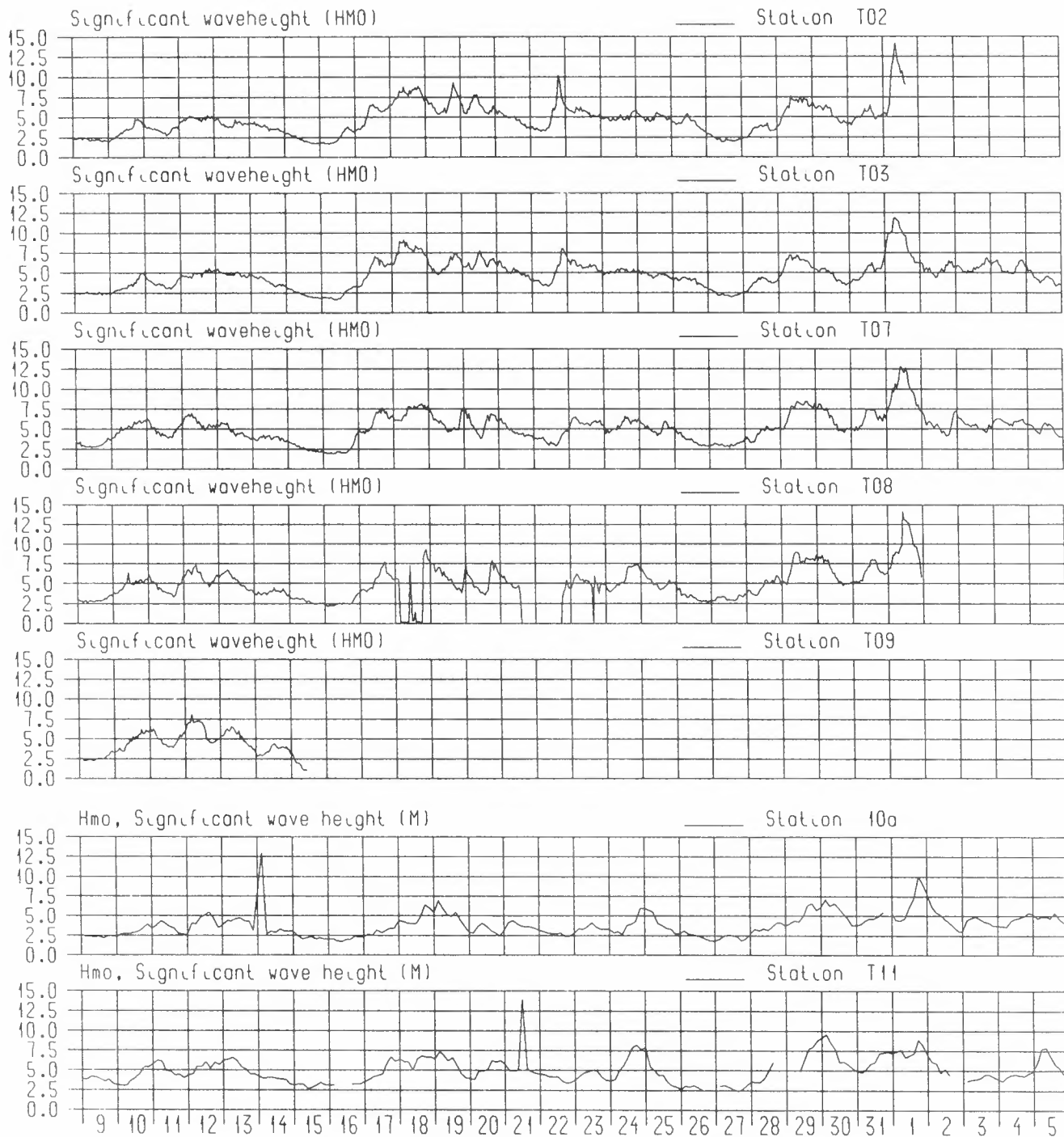


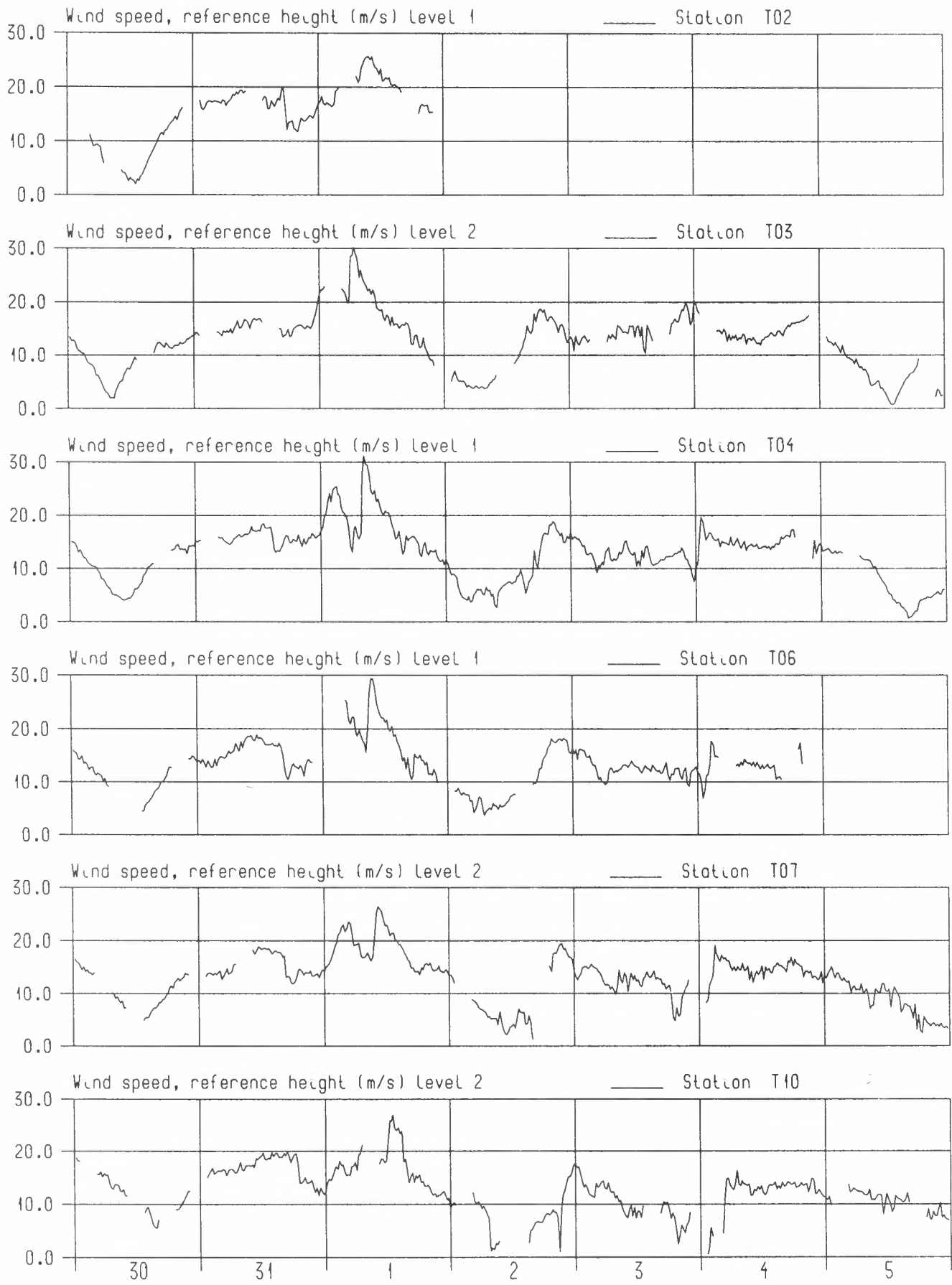
Figure 4



Data from December 1991

Data from January 1992

Figure 5



Data from December 1991

Data from January 1992

Figure 6

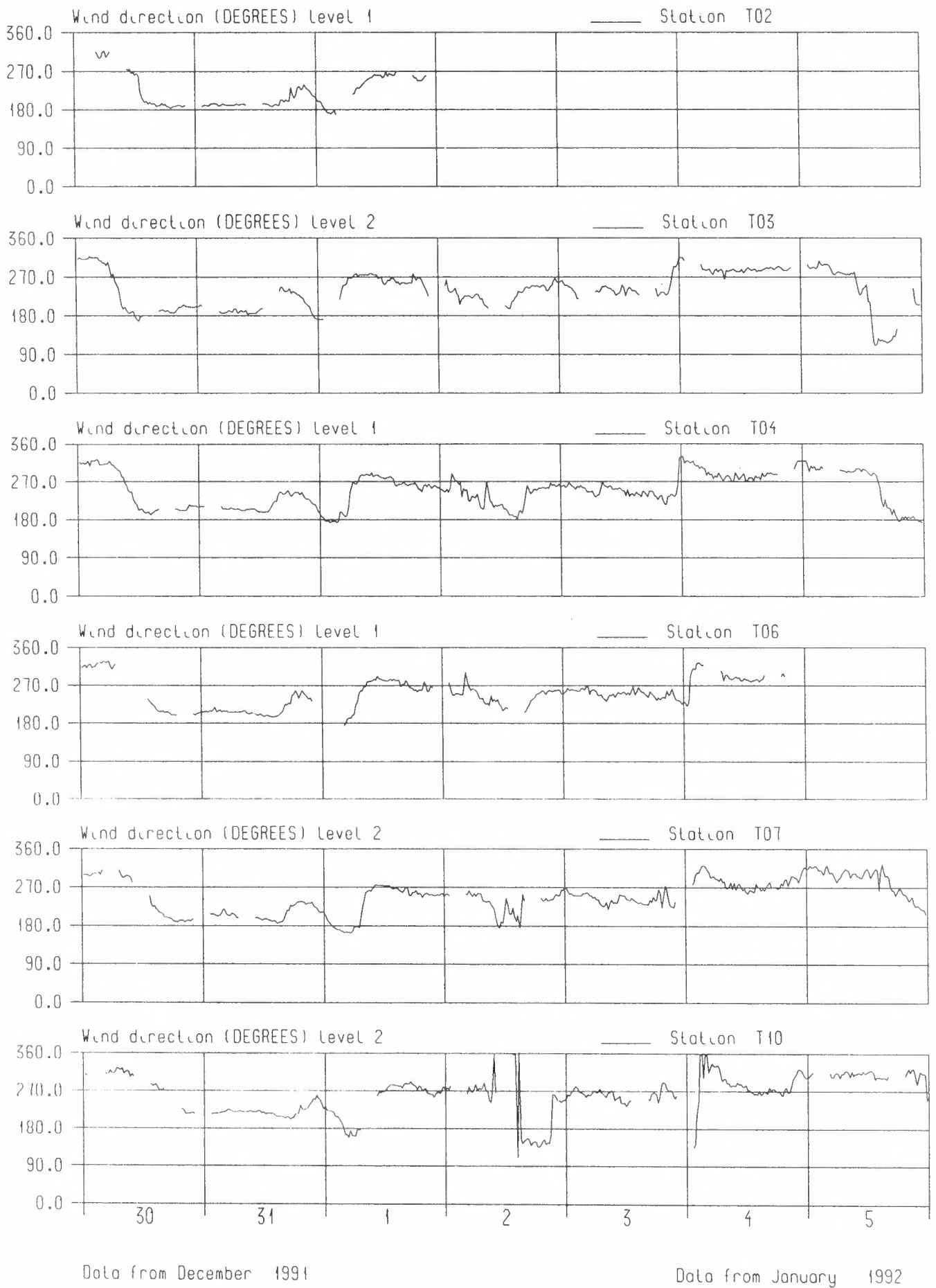


Figure 7

EVALUATION OF WIND AND WAVE MEASUREMENTS FROM THE TOBIS BUOY NETWORK DURING RENE-91

P. Queffeulou and A. Bentamy
IFREMER, BP 70, 29280 Plouzane, FRANCE

June 5, 1992

Abstract

During the ERS-1 calibration and validation experiment, RENE-91, a buoy network was deployed in the Norwegian Sea. Wind and wave measurements of these buoys were stored onboard and also transmitted in near real time through Argos link. Before using the buoy data for validation of the ERS-1 altimeter and scatterometer measurements, the accuracy of the near real time buoy data is analyzed in term of wind, speed and direction, and of significant wave height. Wave height measurements are shown to be of very good and homogeneous quality, long term averaging leading to differences less than 0.5 m over the network. For the wind measurements, though the real time data set is short, some corrections are proposed to improve the consistency over the network, but further analysis of onboard stored data are need to check the absolute accuracy, particularly for high wind and sea states.

Keywords : wind, wave, buoy-network, ERS-1, altimeter, scatterometer, validation

INTRODUCTION

During the European Space Agency calibration and validation dedicated experiment, RENE-91, a network of ten wind and wave measuring buoys was deployed by the OCEANOR company in the Norwegian Sea, from september 15th, 1991, to the end of february 1992. One of the goals of this buoy deployment was to validate the wind and wave Fast Delivery Product of the ERS-1 altimeter and scatterometer. IFREMER was in charge of this validation and, before this task, it has been necessary to test the buoy measurements and to estimate their accuracy. Some results of this work are presented hereunder.

THE TOBIS BUOYS

The buoy network (Fig.1) was designed taking into account the scatterometer swath geometry (range of incidence angles), scatterometer calibration simulations

[1], the altimeter footprint location (some buoys immediately beneath the satellite) and some logistic constraints as for instance the possibility of aircraft overflights of the network. Each buoy, TOBIS 3 type [2], was equipped with a Datawell waverider sensor and two independent wind measuring stations using two R. M. Young wind monitor, integral horizontal axis propeller and vane, respectively located at 3.2 m and 3.7 m above sea level. For both wind and wave measurements, two data processing were performed, resulting on one hand in onboard stored data and on the other hand in near real time (nrt) data transmitted through ARGOS link. For wind measurements onboard data consist of con-

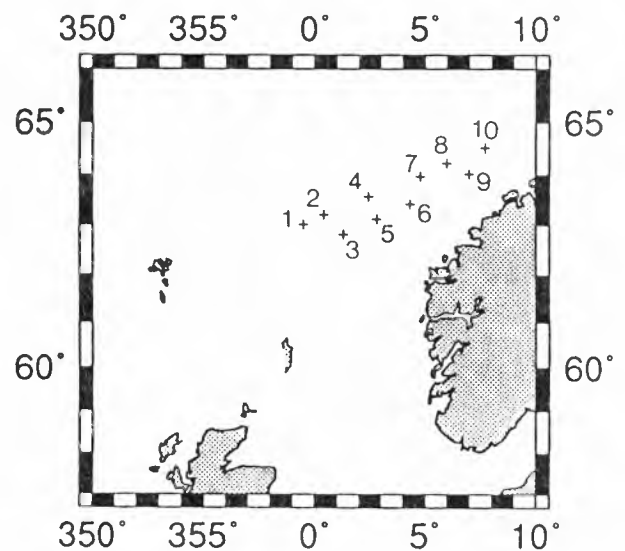


Figure 1: The RENE-91 buoy network.

tinuous 2 min wind vector averages and the nrt data set, analyzed here, consist of continuous 20 min averaged vectors. Wave spectra were computed every hour, from 34 min long record, and stored onboard. Significant wave height (swlh), mean period and peak period of sea state were computed and nrt transmitted every 3 hours, with the exception of one hour shift (near 2000 UT) in order to avoid some data losses during

the night, inherent in Argos system at this latitude. Details for internal wind and wave sampling and processing, together with the ARGOS formats and data transmission, can be found in [3] and [4].

WIND DATA

Data return. At the beginning of the experiment it appeared that there were some problems with the internal software for wind vector computation, and the first realistic wind data were only available at the end of november. The network data return is summarized in Table 1, showing, for each buoy, the beginning and the end of the time period for which the nrt wind data were received and the total length of the period, in day. The last two columns give the data returns in percentage of the total period for the two wind sensors (up and low). Missing data correspond either to erroneous data or to wrong Argos transmission. The following comments will be useful for potential users of nrt wind data set: there is a 80 min time lag between the up and low sensors on buoys 1 and 3 (in fact the same buoy, moored in two different locations during the experiment), the time data of the upper sensor is late and must be corrected; buoy 1 was drifting during operation (buoy positions are in the nrt data files); buoy 2 was also drifting after 1991/12/19; buoy 4 up sensor returned no data; buoy 6 up sensor and buoy 10 low sensor have poor data return.

buoy	start	end	duration day	return (%) up - low
1	91/11/24	91/12/07	13.1	80.1 - 49.3
2	91/11/25	92/01/02	38.7	77.9 - 81.6
3	91/12/07	92/01/13	37.6	79.6 - 82.4
4	91/12/04	92/01/12	40.0	0.0 - 63.4
5	no data			
6	91/12/04	92/01/05	33.0	19.7 - 75.6
7	91/12/09	92/02/09	63.0	79.5 - 60.3
8	no data			
9	no data			
10	91/11/25	92/02/09	77.0	77.5 - 14.6

Table 1: Wind buoy data return.

Up and low sensor comparison. All the following wind speed comparisons were performed on data at the measurement level and not on 10 m neutral corrected data. A first check of the data consistency was achieved in comparing the 20 min individual wind vectors measured by the two sensors on each buoy. Figure 2 is an example of scatter plots comparing speed and direction of the two sensors on buoy 10, and shows a good correlation between the measurements (about 500 data points are reported). Results for the whole

buoy network are given respectively in Tables 2 and 3 for speed and direction. These tables give, for each buoy, the number of data, mean value and standard deviation (std) of differences between up and low sensor data, the correlation coefficient (cor) and the slope (a) and intercept (b) parameters of the regression lines $Low = a * Up + b$.

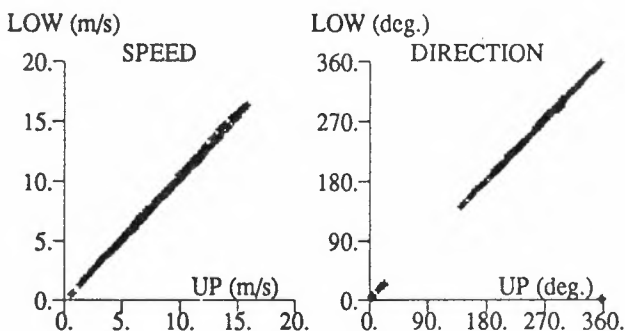


Figure 2: Comparison of wind measurements from the two sensors on buoy 10.

buoy	n	mean ms^{-1}	std ms^{-1}	cor %	a	b ms^{-1}
1	370	0.28	0.22	99.7	0.971	-0.05
2	1746	-0.71	0.73	98.6	1.117	-0.35
3	1801	0.43	0.39	99.6	0.947	0.11
6	408	0.71	0.54	99.8	0.889	0.21
7	2315	-0.32	0.55	99.1	1.020	0.11
10	615	-0.29	0.21	99.9	1.034	0.00

Table 2: Statistics on differences between up and low sensor wind speed measurements, correlation and regression coefficients $V_{low} = a * V_{up} + b$.

For speed, the mean values of differences are generally less than $0.5 ms^{-1}$, with the exception of buoys 2 and 6. Correlation coefficients are higher than 0.98. The slope coefficients, a , are close to unity, varying from 0.889 for buoy 6, to 1.117 for buoy 2, indicating some significant trend (about 12%) between the two sensors on these buoys. In fact, further buoy to buoy comparisons show that for these two buoys the low sensor measurements lead to best agreements.

For direction, the mean values of up-low differences are less than 5° , with the exception of buoy 7 for which a mean difference of 25° is observed. When comparing to other buoys it appears that both sensors of buoy 7 are biased in direction: about 12° to be subtracted

from the low direction and 12° to be added to the up one. The correlation coefficients are higher than 0.99 and the slope coefficients are very close to unity.

The above sensor comparisons can be summarized as follows: direction measurements from both sensors can be used indifferently with the exception of buoy 7 for which corrections have to be applied; for speed, it may be better to use data from low sensor on buoys 2 and 6 (or to correct the up measurement with the a and b coefficients given in Table 2); for buoys 1,3,7, and 10, both sensors can be used indifferently for speed.

buoy	n	mean °	std °	cor %	a	b °
1	370	-3.4	2.4	99.9	1.003	2.7
2	1746	3.9	3.1	99.9	0.982	0.3
3	1801	-4.2	3.4	99.9	1.004	3.2
6	408	-3.9	2.6	99.9	1.017	-0.2
7	2315	-25.0	7.1	99.5	0.998	25.3
10	615	-4.7	7.5	99.2	0.995	6.0

Table 3: Statistics on differences between up and low sensor wind direction.

Buoy to buoy comparisons. Buoy to buoy comparisons were then performed to test the homogeneity of wind measurements over the network.

buoy	averaging time (day)	mean (ms^{-1})	std (ms^{-1})	mean °	std °
1 up	8.08	9.05	2.99	236.8	54.0
2 low	8.08	9.30	3.29	234.6	53.3
2 low	17.36	10.06	3.81	248.4	72.8
3 low	17.36	9.46	3.89	248.2	78.4
3 low	19.62	9.21	3.62	254.1	76.7
4 low	19.62	9.80	3.62	259.3	72.5
4 low	15.19	9.00	3.56	267.6	77.2
6 low	15.19	8.58	3.59	271.7	78.0
6 low	17.93	9.40	4.40	267.9	68.0
7 up	17.93	10.33	3.92	255.6	67.2
7 up	40.12	10.37	3.62	251.1	57.7
10 up	40.12	9.48	3.72	260.5	62.8

Table 4: Long term comparison of wind speed (ms^{-1}) and direction ($^\circ$) for pairs of buoys.

The separation distance between two neighbouring buoys is of the order of 100 km and the network spread over 500 km so that, for measurement comparisons, the data have to be averaged over a time period long enough to filter the geophysical wind fluctuations in the involved spatial range [5]. Even when averaged over one month, for instance, winds from 500 km separated locations in the Norwegian Sea may differ significantly [6]. In order to shorten the spatial scale range and to increase the averaging time as much as possible, comparisons were achieved for pairs of neighbouring buoys only. Results of these comparisons, for selected sensors, are shown in Table 4, giving, for each pair of buoys, the averaging time length, mean value and standard deviation of wind speed and direction over the concerned time period. The common data time periods range from 8 days (buoys 1-2) to 40 days (buoys 7-10). Standard deviations within each pair are very close, indicating that the noise of measurement is roughly the same from one buoy to another. The differences between the mean values within each pair are less than $0.6 ms^{-1}$ for the four first pairs. The last two pairs show larger differences and it can be observed that buoy 7 gives the highest mean values, yet less than $1 ms^{-1}$, for the two pairs. For direction measurements (two last columns of Table 4), the differences between the mean values within each pair are less than 6° with the exception of buoy 7 for which biases about 12° and 9° are observed relatively to buoys 6 and 10. As for the speed, values of standard deviations within each pair are very close, indicating that the noise of measurement is roughly the same from one buoy to another.

Absolute accuracy. It is not easy to check the absolute accuracy of buoy wind speed data, nevertheless some comparisons were achieved with the Norwegian Meteorological Institut (DNMI) numerical weather model. An example of such a comparison is shown on

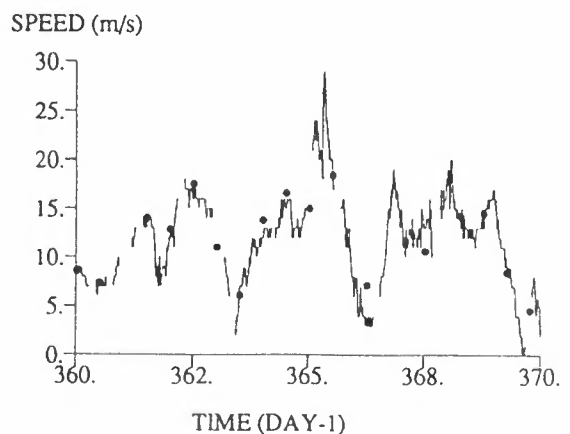


Figure 3: 10 day comparison of buoy (full line) and DNMI model (circles) wind speed.

Figure 3, where are reported the 10 m neutral 20 min

averaged wind speed from buoy 3 (full line) and the closest (separation distance less than 25 km) DNMI grid point wind data (circles). The correlation between the two data sets is very good but it is rather surprising that, for high winds, model data are equal to or even slightly larger than buoy data: one would expect the opposite because of some smoothing introduced, in both time and space, by the model. Results obtained from comparisons between ERS-1 altimeter wind data, Tobis buoy data and french meteorological wind model [7], also seem to indicate some underestimation of buoy wind speed measurements, at high speed. Nevertheless the nrt data set is not large enough to conclude but this will have to be investigated using the onboard stored data (2 min averaged wind vector and hourly wave spectra). It might be particularly interesting to analyze the 2 min wind signal for some storm events encountered during RENE-91 and for which significant wave height larger than 10 m were measured (significant number of individual wave heights between 15 m and 20 m), in comparison of the 3.5 m height of the buoy anemometers above sea level.

WAVE DATA

Data return. The wave buoy data acquisition and data return (near real time Argos transmitted data) are described in Table 5. Buoy 4 returned no data, the

buoy	start	end	duration day	data return %
1	91/09/16	91/12/07	82.4	96.5
2	91/09/17	92/01/02	107.2	92.0
3	91/09/17	92/01/13	118.5	70.3
4	no data			
5	91/09/16	91/11/17	62.5	97.0
6	91/09/16	91/11/17	62.9	94.6
7	91/09/16	92/02/09	146.9	95.4
8	91/09/16	91/11/30	75.5	71.7
9	91/09/16	91/12/13	88.0	90.3
10	91/09/16	91/11/17	62.9	95.4

Table 5: Wave buoy data return.

wave sensor being damaged during the mooring. The lowest data return is observed for buoy 8, the main part of missing data occurring after october 29th, 1991. Buoy 7 returned the longest data set, 95.4% of about 147 days. The following comments will be useful for potential users of nrt wave data set: buoy 1 was drifting during operation; buoy 2 was also drifting after 1991/12/19; buoy 6 wave data become very noisy after 1991/11/15 0000 UT and also for buoy 10 wave data after 1991/11/09 1200 UT, these data set were discarded for the following statistical analysis.

Consistency of swh measurements over the buoy network. As for the wind, in order to filter spatial fluctuations of swh, long term averages were performed for buoy to buoy comparison. An example of such a procedure is given on Figure 4, comparing swh data from buoys 9 and 10. A "mean" value of swh (lower graph) and the associated standard deviation (upper graph) are computed over time intervals of increasing width, here from 34 min to 56 days. The "mean" swh is estimated in term of energy as the root mean square of the swh time serie.

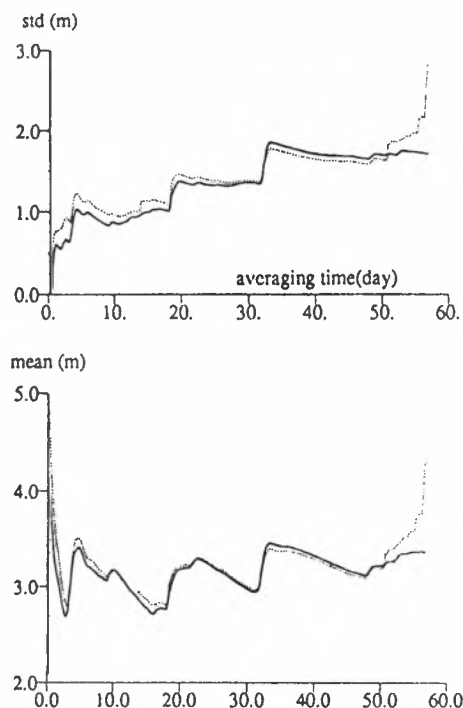


Figure 4: Comparison of wave measurements on buoys 9 (full line) and 10 (dashed line).

Assuming that long term averaging filters the spatial variability of sea state, the curves obtained for buoys at different locations must converge if the sensors performed identically. On the given example, the difference between the two buoy swh is about 1 m at the beginning and then decreases to a few centimeters after some days of averaging. Large variations observed on the curves, as for instance about 32 days, correspond to particular meteorological events, here for instance to a storm occurring on october 18th, during which the swh reached values higher than 12 m. After 50 days, a sharp divergence of the buoy 10 curves is observed, corresponding to measurement problems encountered on this buoy after 1991/11/09 1200 UT and, as already mentioned, these data have to be discarded.

The buoys were then compared two by two. Results of these comparisons are shown in Table 6, indicating, for each pair of buoys, the length of the averaged data set (in day) and the computed mean value and stan-

standard deviation of swl. The maximum of differences between mean values of swl occurs for the couple of buoys (7,8) and is equal to 0.22 m. The values of long-term standard deviation are very close within each pair of buoys (differences less than 0.1 m) showing that the noise is very similar from one buoy to the next one.

buoy	averaging time (day)	mean (m)	std (m)
1	72.50	3.88	1.80
2	72.50	4.07	1.83
2	67.25	4.32	2.06
3	67.25	4.42	2.13
3	49.50	4.07	2.06
5	49.50	4.01	2.05
5	55.87	4.05	1.98
6	55.87	3.89	1.98
6	55.50	3.90	1.99
7	55.50	3.83	1.93
7	53.12	3.98	1.95
8	53.12	3.76	1.86
8	51.25	3.66	1.76
9	51.25	3.51	1.75
9	50.25	3.23	1.69
10	50.25	3.21	1.63

Table 6: Long term comparison of swl measurements from pairs of TOBIS buoys.

The above values of mean and standard deviation cannot be compared from one pair to another because the data time periods are not similar for the whole pairs of buoys, involving consequently different meteorological events. This was then avoided in selecting the common data set to the whole network and in computing the mean value and standard deviations of swl for this data set. Results for the 9 operating buoys are given in Table 7: the swl mean values are within a short range, 3.17 m to 3.66 m, and so for standard deviations, between 1.62 m and 1.95 m. These results, over more than 32 days, are coherent and might reflect, at the present state of analysis, small biases between buoys as well as spatial fluctuations of sea state over the network: it can be observed that the mean value of swl homogeneously increases from buoy 1 to buoy

5 and then homogeneously decreases toward the east, from buoy 5 to buoy 10.

The above results indicate that the swl measurements are of good and homogeneous quality over the buoy network and that no serious general anomaly was detected on this data set. The absolute accuracy of the data cannot be tested, though the Datawell Waverider technology is well known, nevertheless a rough order of magnitude can be obtained through comparisons to wave model analysis.

buoy	averaging time (day)	mean (m)	std (m)
1	32.125	3.17	1.63
2	32.125	3.36	1.62
3	32.125	3.59	1.85
5	32.125	3.66	1.95
6	32.125	3.51	1.95
7	32.125	3.48	1.87
8	32.125	3.35	1.82
9	32.125	3.34	1.90
10	32.125	3.30	1.82

Table 7: Long term comparison of TOBIS buoy swl measurements, for the common data set over the network.

Comparison to wave model. The Norwegian Meteorological Institut (DNMI) wave field analysis (twice a day) were collected from PCS_SPAN directory on HAVTOR in Oceanor. The swl from DNMI and TOBIS buoys were then compared for the period september 28th to october 23rd, 1991. Swl time series of Figure 5, comparing swl from buoy 7 and from a neighbouring model grid point, indicate a rather good agreement, particularly during the storm on october 18th. This storm was a short and intense event since, at buoy 7, swl increased from 4 m, on october 17th at 0500 UT, to a maximum value of 12.7 m, on the 18th at 0800 UT, and then decreased back to 4 m, on the 19th at 2100 UT. The maximum value of swl given by the DNMI model is 9.3 m, on october 18th at 1200 UT. It is lower than the measured value but might be because, during this storm, the swl increase was very steep and too fast to be correctly modelled. Nevertheless, the agreement between the model and the measurement is very good during the decreasing period over the next 48 h following the maximum.

Statistical comparisons on 40 data points (20 days), including the above storm, give the following result: the mean value of differences between TOBIS buoy 2 and DNMI swl is 0.32 m, with a standard deviation of

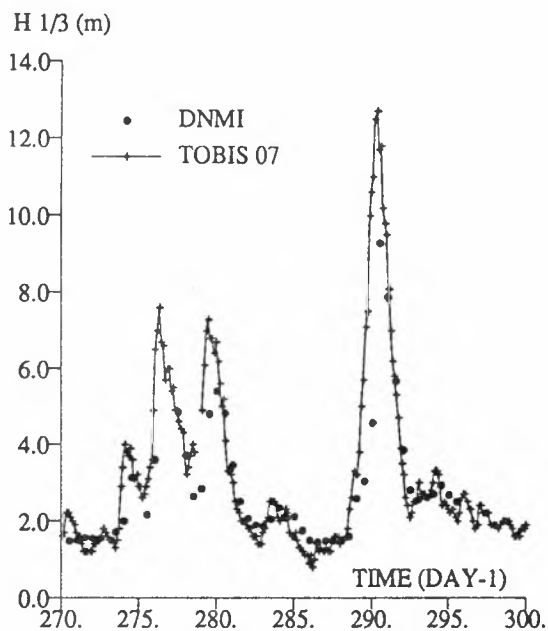


Figure 5: Comparison of buoy 7 wave measurements and DNMI model wave data.

1.18 m. For buoy 7, these values are respectively 0.45 m and 1.36 m.

CONCLUSION

Due to internal processing problems with the TOBIS wind buoy measurements, the wind data set was not as large as expected. Sensor comparisons on a same buoy and long term buoy to buoy comparisons show consistency of wind data over the network. Mean values of differences between two anemometer 20 min wind averages, on a same buoy, are less than about 0.7 ms^{-1} for speed and 5° for direction, with the exception of one buoy for which a 25° bias was observed. Buoy to buoy comparisons show differences less than 1 ms^{-1} and 6° (exceptionnaly 12° for the same buoy as above). The proposed linear corrections can be used to improve the homogeneity over the network. Nevertheless, as shown through meteorological wind model comparisons, the absolute accuracy of the buoy wind measurements is still questionnable, particularly for high wind and sea state conditions. This point has to be tested, using the onboard stored data (2 min averaged wind vector and hourly wave spectra).

For wave data, the near real time transmitted wave height measurements from the TOBIS buoys are of good and homogeneous quality over the network. Though the data return varies from one buoy to another, long term buoy to buoy comparisons show that swl measurements are accurate, differences between two neigh-

bouring buoy swl being less than 0.22 m. The measurement noise level is also very homogeneous, differences between standard deviations, from one buoy to the next one, being less than 0.10 m. The above wave analysis will be completed using onboard data (hourly rate and no ARGOS gaps) and also testing onboard computed wave spectra. Nevertheless, at present, the near real time wave data set can be used as a reference for validation of the ERS-1 altimeter swl measurements.

REFERENCES

- [1] Bentamy A., 1991 : calibration and validation of scatterometer measurement of sea surface wind, proc. *International Geoscience and Remote Sensing Symposium, Helsinki*, june 1991, pp 473-476.
- [2] Commissioning campaign report, OCEANOR report n° OCN-92064, 12 may 1992, OCEANOR, PIR-SENERET, N-7005 Trondheim, Norway.
- [3] Ezraty, R. and H. Schyberg, 1988 : Proposal for Onboard Buoy Data Processing and an Argos Message to be used during the ERS-1 Calibration/validation Campaign, IFREMER-OCEANOR report, Institut Français de Recherche pour l'Exploitation de la Mer, BP 70 29263 Plouzané, France.
- [4] Groupe Toscane/Espadons, Rapport d'avancement des travaux n° 1, contrat ESTEC 8698/89/NL/BI, juin 1990, Institut Français de Recherche pour l'Exploitation de la Mer, BP 70 29263 Plouzané, France.
- [5] Queffeuilou, P., 1991 : Accuracy of Wind Measurements performed on Buoys, Ship and Island, during the TOSCANE-2 experiment, *J. Atmos. Oceanic Technol.*, vol 8, n 6, pp 835-855, December 1991
- [6] Schyberg, H. and R. Ezraty, 1988 : A survey of the Surface Flux Climatology in the Faroe Islands - Haltenbanken ERS-1 Calibration Validation Area, and a Proposal for a model for computing the 10 m Neutral Wind, IFREMER-OCEANOR report, Institut Français de Recherche pour l'Exploitation de la Mer, BP 70 29263 Plouzané, France.
- [7] Queffeuilou, P. and J. M. Lefevre, 1992 : validation of the ERS-1 altimeter wave and wind fast delivery product, this issue.

Two-Dimensional Wave Field Measurements as Sea Truth for ERS-1 SAR

Friedwart Ziemer, Wolfgang Rosenthal

GKSS Forschungszentrum Geesthacht, Institut für Physik

Max-Planck-Strasse 1, 2054 Geesthacht, Germany

Karl Richter, Dieter Schrader

Bundesamt für Seeschifffahrt und Hydrographie

Bernhard-Nocht-Straße 78, 2000 Hamburg 4, Germany

In-Situ measurements of two-dimensional wave spectra were conducted for the estimation of the 'sea truth' during ERS-1 SAR missions by 'GKSS Research Centre' in cooperation with 'Bundesamt für Seeschifffahrt und Hydrographie (BSH)' and 'the Norwegian Meteorological Institute (DNMI)'. In parallel to 6 imaging SAR missions of ERS-1 in the second half of November 91 onboard the research vessel GAUSS (BSH) radar image spectra could be sampled at the position: 64° 30'N; 7° 42'E (T10). During the 30 minutes sampling and averaging period of buoy measurements the image spectra were sampled and averaged as well. For the transfer of the radar image spectra to wave energy spectra the measurements from the buoy were used for calibration.

1. Introduction

The Wave Monitoring Radar (WMR) that was mounted during the ERS-1 CAL/VAL campaign onboard Gauss was an experimental version of the 'GKSS WMR' system. The system contains a standard navigation radar with an extra memory for the radar signal storage and a PC for the wave field analysis [1]. In addition to the WMR a directional waverider was used to detect the absolute scaling of the wave field parameters. The buoy data were used to estimate the transferfunction for each single measurement. Thus the 'sea truth' of the two dimensional wave-spectra was composed by the buoy and the radar results. Due to sampling variability in the wave field in time and space a comparison between time sampling and imaging systems is always a problem. Therefore the radar samples were taken every 6 to 7 minutes and the spectra were smoothed by averaging over the same time period that was taken for the buoy spectra.

In figure 1 four wave field parameters measured by the buoy are given as time series. The plotted period is that time R.V. Gauss was close to position T10. The arrows mark these time instants when ERS-1 SAR missions were flown. This plot shows that the sea state was much more complicated in the first week compared to the second week. The directional spread is higher than 45° for the first three SAR missions, which is a clear hint that the wave field was dominated by multimodal seastates during this period. This situation was caused by different swell systems coming from changing directions, their energies were within the same order of quantity. During the second week the wave field had a more stationary behaviour with mean directions mainly from SW. The buoy derived low spread values and the sharply peaked radar image spectra indicate a structure in the wave field which is dominated by a unimodal windsea energy peak.

2. The Instruments

The Wave Monitoring Radar (WMR) is constructed to detect long waves (in the range between 30 m to 600 m). The most important technical details of the navigation radar that was mounted onboard the R.V. GAUSS for wave detection are given in table 1.

Table 1: The radar system parameters

Frequency:	9.4 GHz
PRF:	2.0 kHz
Antenna type:	2.4 m slotted wave guide
Antenna rotation:	2.7 sec
Polarisation:	HH
Pulse length:	70 nsec at 3 nm
Range resolution:	10.5 m
Azimuthal res.:	10.0 m at 0.75 nm

While the range resolution is constant over the full image the azimuthal resolution is a function of the distance. But within the scanned area (1400 m x 1400 m) the mean spatial resolution has the same order of quantity in range and azimuth. The radar image is stored in an internal memory on a cartesian grid (RASTER). For each rotation of the antenna (2.7 sec) the information of 5400 radial radar scannings (equidistant in azimuth) are transformed from range and azimuth to a cartesian grid with a 5 m x 5 m resolution. For the purpose of wave detection the digital information of 32 antenna rotations is written into an extra memory. It is described in [1] and [2] how the wave information is extracted from a time series of scatterfields of successive antenna rotations.

The sensors of the 'directional waverider' (produced by Datawell bv) are housed in a small spherical buoy of 90 cm diameter. The buoy is moored to response linearly on the orbital motions of the wave field in the wave-length range between $L = 600$ m to $L = 6$ m in deep water. For the detection of the wave direction parameter the vertical and horizontal motions of the buoy together with the buoys orientation are measured and analysed. The spectral estimates of the wave energy $F(f)$, the wave propagation direction $\theta(f)$ and the directional spread $s(f)$ are calculated by cross spectral analysis following the method introduced by Longuet Higgins et al. [3]. As 8 time series over 200 sec with 256 samples each have been used for the analysis, each spectral value has 16 degrees of freedom. For the 70% confidence interval we thus get: $\Pr\{0.75 < 1 < 1.4\} = 70\%$. The spectra are stored up to a frequency of 0.6 Hz, which is well apart from the Nyquist

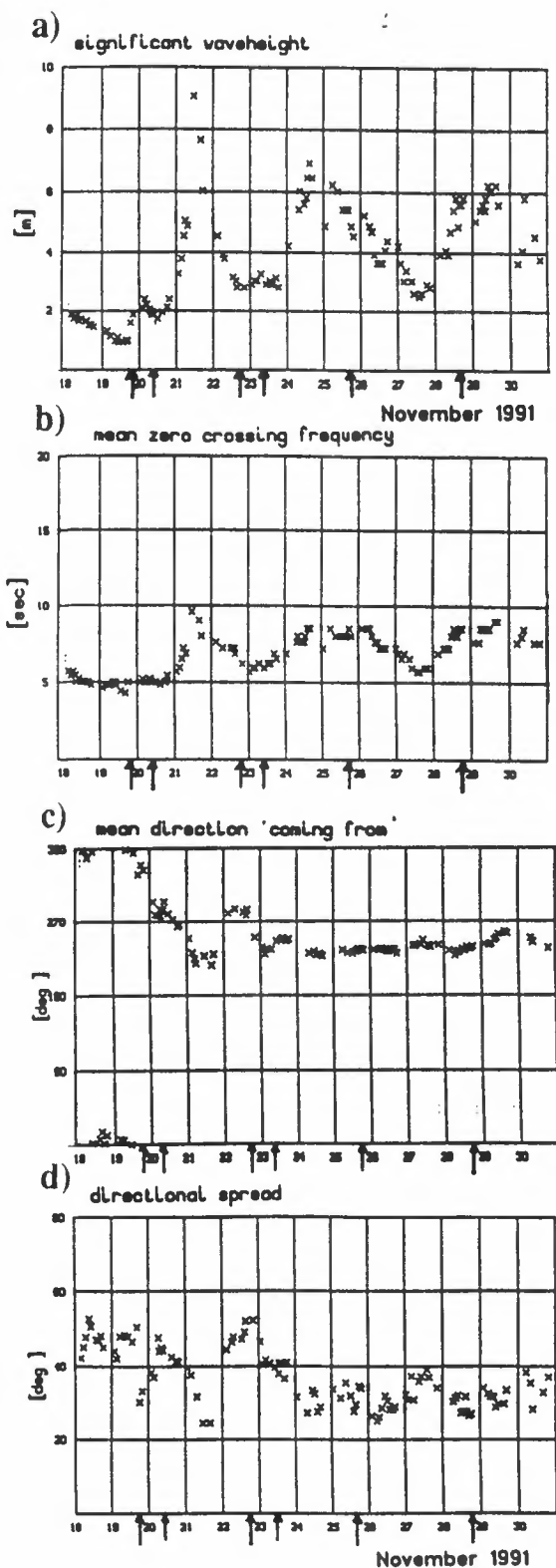


Figure 1: Time series of integrated parameters derived from the measurement of the "Directional Waverider". The definition of the parameters are given in the text. The arrows mark the ERS-1 SAR missions.

limit at 1.28 Hz. The spectral densities are given over 0.005 Hz intervals between 0.025 Hz and 0.11 Hz and in 0.01 Hz intervals for the rest. As long as the ship was not further than 10 nm from the buoy the transmission of the data was done by a normal telemetry at 29 MHz. An additional data link via a satellite (ARGOS) was used during the time with no ship in receiving range.

The wave parameters given as time series in figure 1 have been calculated from the following spectral parameters:

$$m_i = \int F(f) f^i df$$

$$c_0 = \int F(f) \cos\theta(f) df$$

$$s_0 = \int F(f) \sin\theta(f) df$$

The definition for the wave field parameters are:

$$H_s = 4\sqrt{m_0} \quad , \text{ for the significant wave height;}$$

$$T_z = \sqrt{m_0 / m_2} \quad \text{for the zero crossing period;}$$

$$\bar{\theta} = \arctg(s_0 / c_0) \quad \text{for the mean wave direction and}$$

$$\bar{s} = \sqrt{2} \sqrt{1 - \sqrt{s_0^2 + c_0^2} / m_0} \quad \text{for the directional spread.}$$

3. The Image Transfer Function

If $I(k_x, k_y)$ is the two-dimensional result of the radar measurement and $F(k_x, k_y)$ is the wave energy spectrum in wave number domain, then the image transferfunction (see: [2]) may be defined by:

$$(1) F(k_x, k_y) = T^{-1}(k_x, k_y, u, \dots) I(k_x, k_y).$$

As in the scope of this paper for each measurement an extra transferfunction is evaluated by the use of the buoy data, the functional dependency of T from the wind u and other geophysical parameters is of minor interest. The dependency of T from the relative view direction of the antenna to the wave direction is minimized by merging the results from an upwind and a crosswind window with 90° each. Therefore we write the image transferfunction as a function of the modulus of the wave number alone: $T = T(|k|)$. The one-dimensional wave energy spectrum as it is measured by the buoy is thus combined with the image spectrum by

$$(2) E(\omega) = \{k dk / d\omega\} \int_0^{2\pi} T^{-1}(k) I(k_x, k_y) d\theta$$

The transformation of wave energy from the wave number domain to the one-dimensional frequency domain is conducted by the Jacobian: $\{k dk / d\omega\}$. In (2) the wave number k is a function of ω , as given by the dispersion relationship for ocean waves. We approximate the transferfunction by: $T(k(\omega)) = A^{-1} k^\beta$ where A is a scaling factor that is deduced from the buoy spectra. One possible way to estimate a good value for the exponent β is to fit the spectral shape of the one-dimensional radar spectrum by evaluating: $\text{MIN} [Tz_{\text{buoy}} - Tz_{\text{radar}}]$ iteratively.

GKSS - radar No.: 100 - 25.11.1991 21:12:00

GKSS - buoy T10 - 25.11.1991 21:08:00

energy at peak 35.77 m²/Hz

significant wave height: 4.54 m

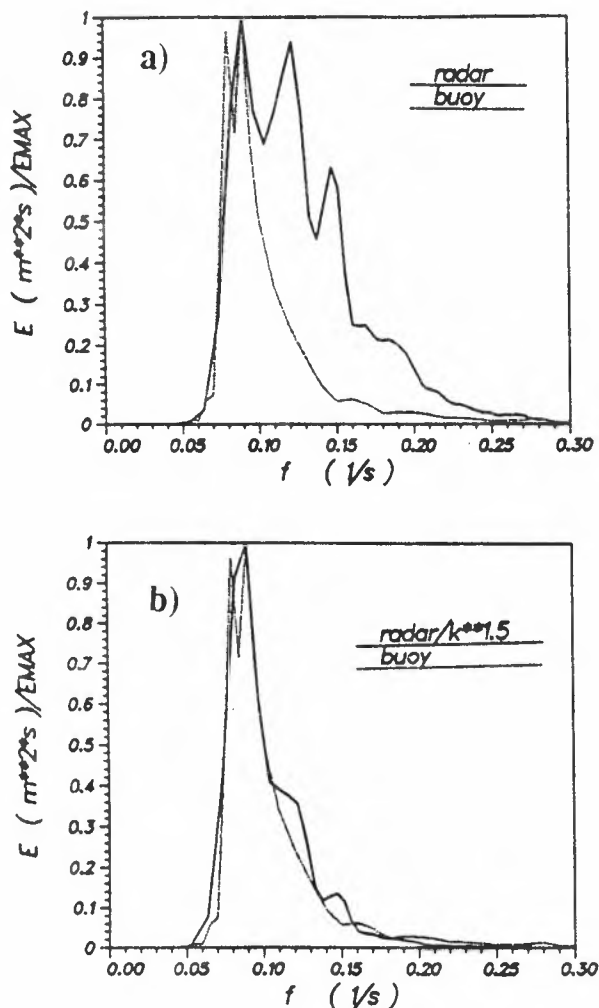


Figure 2: Example for the evaluation of the image transfer-function. The quotient: $36/k^{1.5}$ was fitted as given in the text. The radar spectrum is calculated out of one sample taken during 84 seconds at 21:12 UTC on 25 November 1991.

The estimated values for A and β were used for the estimation of the wave energy in the wavenumber domain by using the following formula:

$$(3) E(k_x, k_y) = A k^\beta I(k_x, k_y).$$

Figure 2 is a comparison of the one dimensional radar spectra with the buoy spectra with and without the transferfunction applied. Figure 2.a) gives the result if in the integral of equation (2) the transferfunction is assumed to be: $T = 1/A$. In figure 2.b) the result is given for a transferfunction: $T = 1/A k^{1.5}$, where $\beta = 1.5$ has been fitted for the given example. The calibration constant A is given with $35.77 \text{ m}^2/\text{Hz}$ for figure 2.a) as well as for figure 2.b).

4. The smoothing procedure

For the wave analysis 32 images of consecutive antenna rotations are used (see: [1]). The total radar observation time is 84 seconds. The wave energy contents within the analysed area ($1200 \text{ m} \times 600 \text{ m}$) is only slowly varying during the full sampling period. Therefore the parameters of each image taken during one rotation are not independent from these of other rotations. One radar image spectrum which is composed by the information of 32 consecutive images represents just one realisation of the wave field of interest. Therefore the number of degrees of freedom within a wave number interval is not more than 2.

The natural variations in the wave field parameters within a few minutes are quite big. Figure 3 shows two dimensional image spectra from four different realisations, which were taken in 7 minutes times steps intervals. Each image spectrum of this example shows different results in it's total structure as well as in the peak period and the peak direction. The direction of the energy peak changes between 210° to 260° and the corresponding lengths change between 260 m to 310 m . The directional spread at the peak measured by the buoy at this time is 30° . The peak frequency of the buoy spectra lies at 0.072 Hz corresponding to a peak wavelength of 300 m . As the variability between these image spectra is due to the variability in the wave field spectra the image spectra have been smoothed by averaging during half an hour as it was done with the buoy spectra.

The spectra shown in figures 4a to 4f are smoothed over that period of time that is given as start and end time in the picture. For most of the given results at least 6 independent samples could be used for smoothing. The significance of the energy values is therefore given by 12 degrees of freedom.

5. Results

The results of the sea state measurements, which have been evaluated for the 6 ERS-1 SAR missions of interest, are plotted in the figures 4a to 4f. The energy structure in the two-dimensional wavenumber domain may be classified into two main groups of sea state.

The first group is classified by a complicated multimodal structure. The three SAR missions taken on the 19th, 20th and 22nd of November were sampled during situations, which count to the first group. The local windsea forced by less than 10 m/sec was shorter than 90 m during these measurements. The parameters deduced from the buoy spectra give a general wave situation, that is swell dominated with significant wave heights of less than 2 m . The temporal changes in the buoy derived mean direction (fig.1.c.) and the high values in the directional spread (fig.1.d.) are clear indications for multimodal structures in the wave field. These multimodal structures are inherent in the averaged radar derived wavenumber spectra as well. At least three energy peaks with high significance are clearly determined with 12 degrees of freedom within each wavenumber interval, have been detected during this period. One swell system coming from 245° , is detected during each of the first four SAR missions. The wavelengths of this swell package change from longer than 250 m (on the 19th and 20th) down to 200 m on the 22nd. Rests of this swell are still detected on the 23rd of November with 200 m . A second swell package is detected coming from 20° with waves longer than

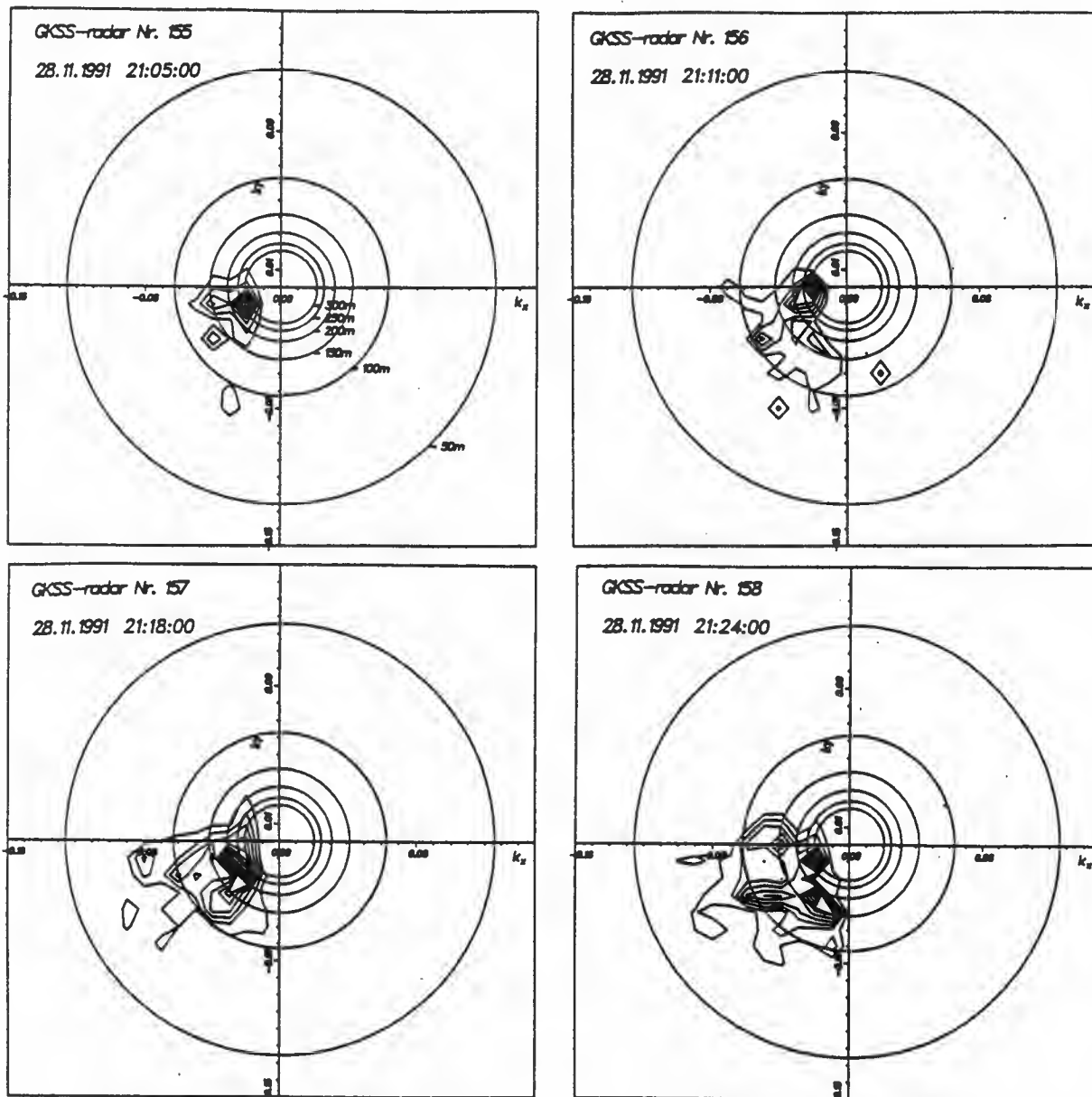


Figure 3: Four radar image wave spectra taken between 21:05 and 21:24 UTC on the 28 November 1991. Isolines are given for wave image power in 0.1 relative units. The circles mark 50 m to 300 m wave length with 50 m increments. North is pointing upwards. Directions are given in the "coming from" convention.

300 m on the 19th and 20th. This system is still detected on the 22nd with waves of 150 m length. A third package that was detected on the 19th as coming from north with a peak wave length of 100 m is very weak on the 20th and totally vanished until the 22nd. Additional swell with less significance was detected during this period, coming from the NW window with changing lengths and directions.

The second group, that has been sampled on the 23rd, the 25th and the 28th of November, has a more unimodal energy structure. The situation during these SAR missions is wind sea dominated with a very stable sea direction. The buoy derived mean direction underline the stationary wave field condition. The values of the directional spread are less than 35° (see fig 1 d) which is an additional hint for the unimodality of the sea state. The radar derived results from the 25th and the 28th are sharply peaked as well indicating a dominating wind sea

system. The example discussed in chapter 4 demonstrates the effect of the smoothing procedure. In each single realization given in fig. 3 a multi-peaked energy structure is clearly inherent. This variability is smoothed as a result of the averaging process (see fig. 4 f). The very sharply peaked energy is caused by wind waves coming from 250° with a length of 280 m. But the result from that sample which has been taken at 21:11 closest to the ERS-1 SAR mission (21:10) shows the energy peak near to 400 m coming from 270° . This indicates a swell system produced by a storm in the North East Atlantic. The spectra from the other samples are dominated by the wind sea. Thus the significance of the wind sea peak is much higher in the averaged result than the one of the swell. In [4] a comparison between these WMR results, the ERS-1 SAR spectra and spectra from a numerical wave model are discussed.

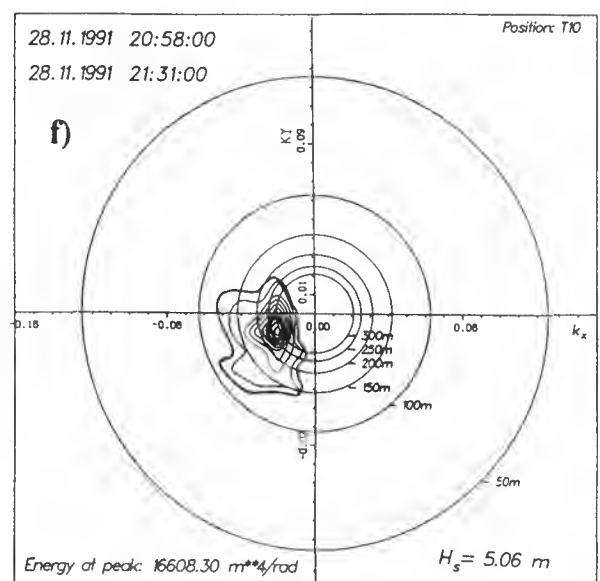
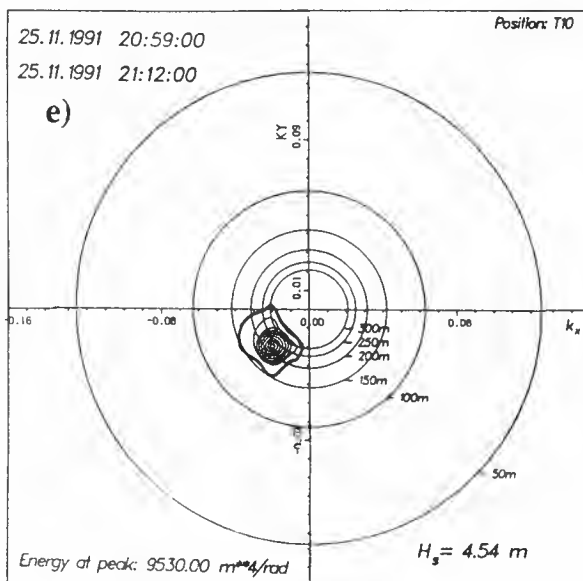
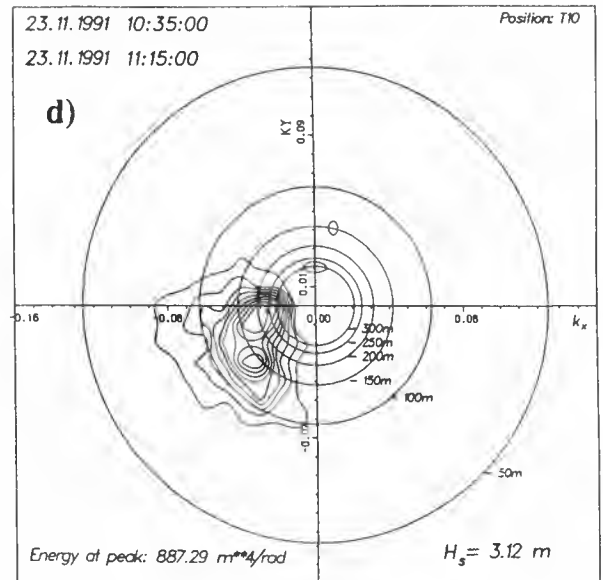
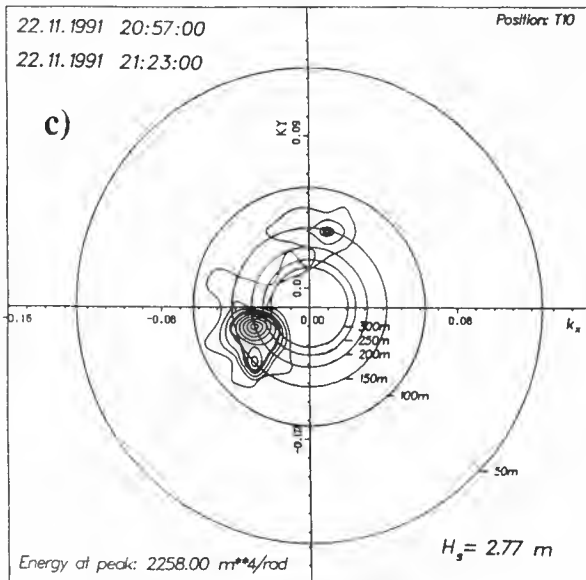
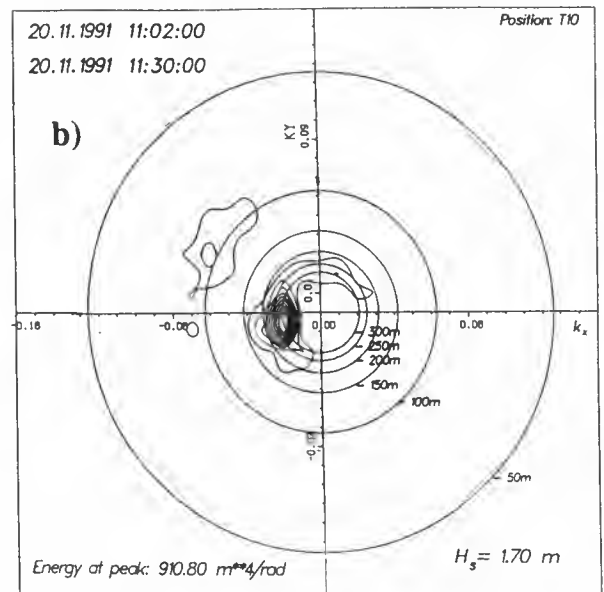
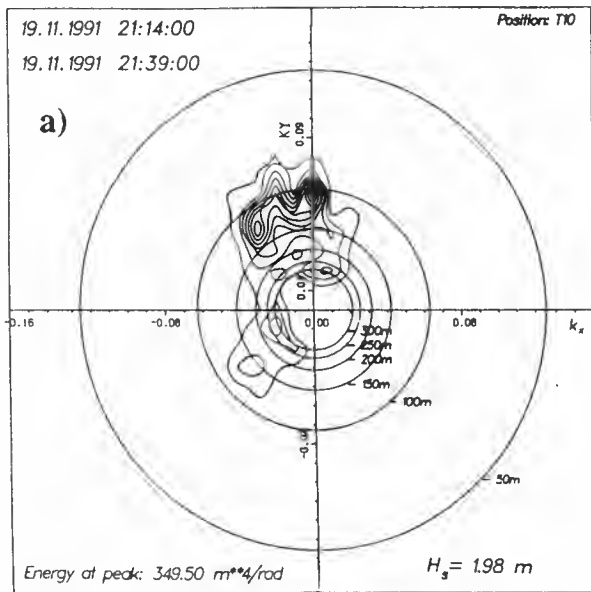


Figure 4: "Sea Truth" taken at the time of the 6 ERS-1 SAR missions in the period between November 19, 1991 until November 28, 1991. The wave energy spectra were calculated from the radar image spectra and the buoy spectra as given in the text. The energies were smoothed over six spectra each. The thick isolines gives the $10^3 \text{m}^4/\text{rad}$ and $10^4 \text{m}^4/\text{rad}$ level. Isolines are incremented by $0.1 \cdot \text{energy at peak}$. Start and Stop time of the measurements are given in the upper left corner.

6. Conclusions

The complete description of local sea state is given by the statistical expectation value of the two-dimensional spectrum. An instrument is always hampered by the finite number of collected samples so that the expectation value is reproduced within a certain statistical significance. The results from the directional wave rider are given with 16 degrees of freedom for each frequency interval. The significance of the results provided by the WMR is founded on 12 degrees of freedom for each ERS-1 SAR mission, as we averaged 6 radar image spectra to get a good estimate for the expectation value of the two-dimensional spectrum. Specially for the discussion of the wave imaging during multimodal sea states by SAR it is important to have 'sea truth' estimates with high significance to underline the complicated structures in the wave field. Such a multimodal situation is found for the first three discussed ERS-1 SAR missions. For the other three missions a one peak dominated sea state structure was detected by the WMR.

Acknowledgments: The hardware of the WMR was produced by Jürgen Dittmer from GKSS. The authors owe thanks to the crew of the R.V. Gauss, which suffered much under heavy weather conditions specially during the ERS-1 CAL/VAL REHEARSAL campaign in February 1990.

References

- [1] ZIEMER, F., "Directional Spectra from Shipboard Navigation Radar during LEWEX," in *DIRECTIONAL OCEAN WAVE SPECTRA* (Edited by R.B. BEAL) The Johns Hopkins University Press, Baltimore 1991, pp 80-84.
- [2] ZIEMER, F., and W. ROSENTHAL, "On the Transfer Function of a Shipborne Radar for Imaging Ocean Waves," in *Proc. IGARSS'87 Symp., Ann Arbor, Mich., (May 1987)*, pp 1559-1564.
- [3] LONGUET-HIGGINS, M.S., CARTWRIGHT, D.E., and SMITH, N.D., *Observation of the Directional Spectrum of Sea Waves Using the Motion of a Floating Buoy*, in *OCEAN WAVE SPECTRA*, Prentice-Hall, Englewood Cliffs, N.J. (1963), pp 111-132.
- [4] ROSENTHAL, W., ATANASSOV, V., KOCH, W., ZIEMER, F., RICHTER, K., *Sea Truth and Model Data For Surface Waves Compared With ERS-1-SAR*, this issue.

VALIDATION OF WAVENUMBER SPECTRA FROM THE ERS-1 WITH DUTCH AIRBORNE AND GROUND BASED RADAR DATA OBTAINED IN RENE91

J.C.M. Kleijweg¹, D. Schrader²

¹Physics and Electronics Lab TNO, P.O. Box 96864, 2509 JG The Hague, The Netherlands, ²Bundesamt für Seeschifffahrt und Hydrographie, P.O. Box 301220, D-2000 Hamburg 36, Germany

ABSTRACT

In the dedicated Haltenbanken experiments (RENE91) the Netherlands participated with two systems, an airborne radar SAR system called PHARS and a groundbased shipsborne radar system called SHIRA. Both systems are imaging radar systems. In RENE91 these systems are primarily used to measure two dimensional (2D) wave number spectra simultaneously with the ERS-1 overpasses. The experiments were performed in the last two weeks of November 1991. The SHIRA system was mounted together with the German shipsborne radar system (owned by the GKSS) on the German research vessel the Gauss. The Gauss deployed two wave directional buoys in the Haltenbanken area and gathered meteorological and other oceanographical data. During RENE91 the PHARS SAR system performed underflights at two reference points along the track of the ERS-1. At each reference point, two 2D wave number spectra were recorded, in a direction parallel and perpendicular to the ERS-1 track. One of the reference points was chosen in the test area of the Gauss. During the experiments the ERS-1 was in full imaging mode. This paper is about the main properties of the ERS-1, PHARS and SHIRA and the simultaneously spectra measured by the systems. A first comparison of the spectra will also be made. In this paper all the spectra shown are orientated in the geometric North position and plotted on the same wavenumber scale.

Keywords: Wave spectra, ERS-1, RENE91, Airborne SAR systems, PHARS, Shipborne systems, SHIRA.

INTRODUCTION

In response to the ESA Announcement of Opportunity in 1986 the Netherlands proposed to participate in the calibration and validation campaign of the ERS-1. In 1987 the proposal was approved by ESA under the name OA-NL6. Originally it was proposed to validate and calibrate wave-directional spectra of the ERS-1 only with SHIRA. SHIRA is a groundbased imaging radar system and designed to measure on-line two-dimensional wavenumber spectra. The system became operational in 1988. We discuss the system in the next section. In 1986 in the Netherlands plans were made to design and build an airborne SAR system with the ERS-1 parameters in mind. In 1988 the so-called PHARUS (PHased Array Universal Sar) project was started. This project is carried out in stages. In the first stage a limited prototype system, called the PHARS system has been developed. This system made its first successful flights in 1991. Shortly before RENE91 it was decided

to also use the PHARS in the experiments. Four underflights were planned between 19 and 23 November 1991. The PHARS recorded spectra in a direction along track and across track of the ERS-1 at two reference points. This is necessary since artifacts in SAR spectra due to range and azimuthal travelling waves hamper the interpretation of the spectra. We discuss these phenomena in the next sections.

THE SHIRA SYSTEM

In 1986 TNO-FEL started the SHIRA-project. SHIRA is an acronym for SHIPS RADAR and is a navigation radar system. Such a system can monitor waves if the clutter suppression is switched off. With every rotation of the antenna, a new image of the area surrounding the antenna is produced. SHIRA monitors an user specified subsection of these images for each rotation in a digital format on a PC. Repeated monitoring gives a three-dimensional database. The database contains information about wave speed and direction (the displacement of waves per antenna rotation). Applying the dispersion relationship for ocean waves, these measurements can be linked. As a result, directional spectra both in frequency and in wavenumber become available. A unique feature of SHIRA is that unlike space and airborne imaging radar systems SHIRA is capable to deliver on-line omnidirectional wavenumber spectra.



Figure 1: SHIRA mounted on the Gauss during RENE91

Figure 1 shows a picture of the Gauss on which SHIRA was mounted during RENE91. The SHIRA antenna was mounted,

approximately 16m above sea level, on a frame at starboard side of the ship (figure 1, the white antenna). The Gauss was on location between 18 and 30 November 1991. The location was a dedicated area in the Norwegian Sea between T9 and T10. Figure 2 shows a map of the test area.

SHIRA performed a great number of measurements during overpasses of the ERS-1 and airborne systems. An example of a 2 dimensional spectrum is shown in figure 7c. Table 1 gives the properties of the system.

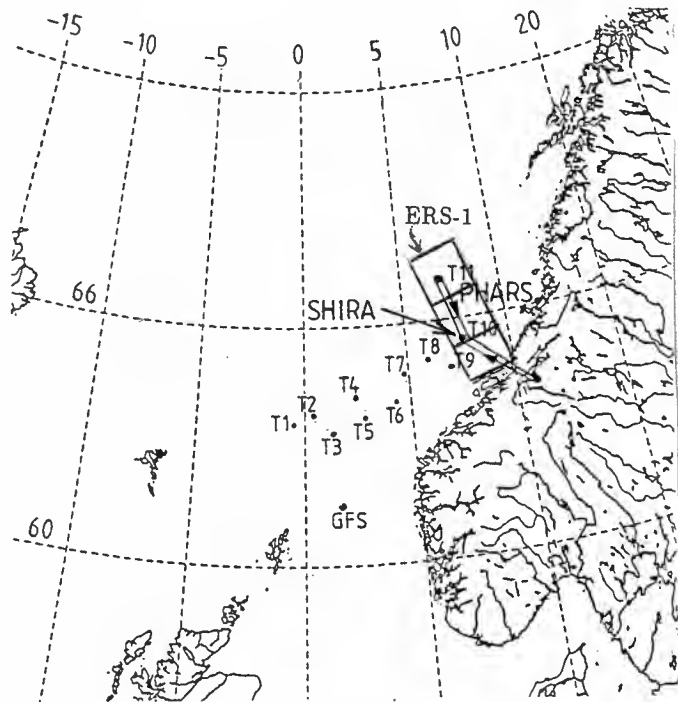


Figure 2: Location of the field campaign: RENE91

THE PHARS SYSTEM

During the RENE91 campaign the PHARS was mounted under a Swaeringen Metro 11 aircraft. The Metro II is a twin engine laboratory plane, owned by NLR (National Aerospace Laboratory). The PHARS uses the same (microwave) frequency and polarization as the ERS-1 SAR. Figure 3 shows a picture of the aircraft with the PHARS mounted underneath it. The flight attitude can be up to 6000m but from the viewpoint of sensitivity (due the limited peak power) a flight attitude of 4000m was chosen. The flight speed was 100m/sec. In RENE91 four flights on 19, 20, 22, 23 November 1991 were proposed in the dedicated Haltenbanken area concurrent the overpass of the ERS-1. The flights on 19, 20, 22 November 1991 were performed, but due a hardware failure of the PHARS system, no data could be obtained on 23 November. In total five images per day were collected, two images at reference points T10 (figure 2), two images at T11 and one image between T10 and T11. In both reference points the images were obtained in a direction parallel and perpendicular to the ERS-1 flight direction. The measurements and aircraft motions were recorded and processed off-line. The images are all geometrically and radiometrically corrected and are also corrected for artifacts such as multipath reflections on the aircraft wing and residuals of the antenna pattern. The typical



Figure 3: PHARS SAR patch antenna mounted under a Swaeringen Metro II aircraft

DATE	16	17	18	19	20	21	22	23	24	25	26	27	28	29	30
DAY	St	Sd	Md	Td	Wd	Th	Fd	St	Sd	Md	Td	Wd	Th	Fd	St
ERS-1 im.-mod				*	*		*	*		*				*	
MERLIN RESSAC				*			*			*				*	
METEO PHARS				*	*		*								
GAUSS SHIRA		*	*	*	*	*	*	*		*	*	*	*	*	

Figure 4: Wave measurement calendar of November 1991

image size of PHARS is about 6 km * 6km with pixelsizes of 2.75*2.75m and the resolution of 6*6m. To obtain 2D spectra from these images, every image was divided in 16 identical subsections. Each subsection was transformed to a wave spectrum by a Fourier transformation. Only reliable wave spectra were selected and averaged. In this way one spectrum is obtained for every image. The properties of PHARS and the spectra are listed in table 1. Two examples of along and across spectra at T10 are shown in figure 5a,b.

THE ERS-1 AMI-IMAGE MODE

Most of the time during RENE91 the ERS-1 was switched to the AMI wind/wave mode. In this mode only low-resolution wave spectra can be observed with a low coverage rate. However for six days (figure 4) in which wave measurements were planned, ESA decided to switch the ERS-1 to full imaging mode. In flight direction a strip of three images (size 300 by 100 km) were recorded. Figure 2 shows the positions of the images with the ERS-1 in ascending mode. These 18 images are available as Fast Delivery Products for the members of the geophysical calibration and validation teams. The procedure to obtain 2D spectra was similarly that for the PHARS, except that now all wave spectra could be used. Table 1 gives the wave characteristics of these spectra. Figure 6 shows an example of a 2D spectrum.

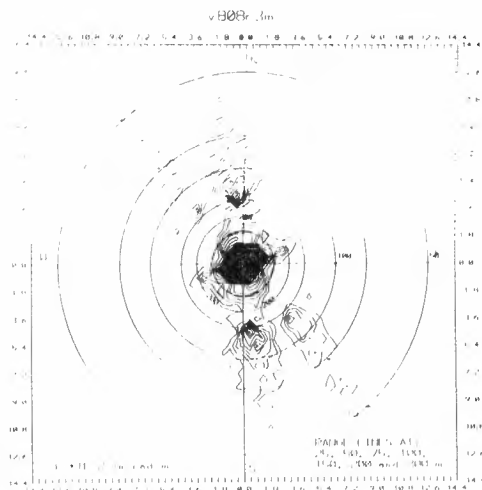
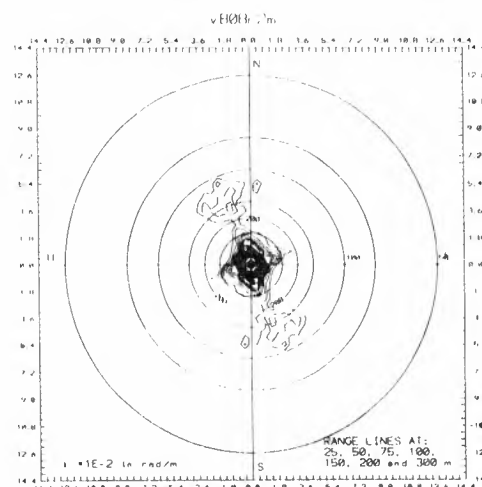


Fig.5a



5b

Figure 5: 2D wave number spectra of the PHARS. Fig.5a shows range travelling waves, fig. 5b shows azimuthal travelling waves. Date 19 Nov. 1991, position T10.

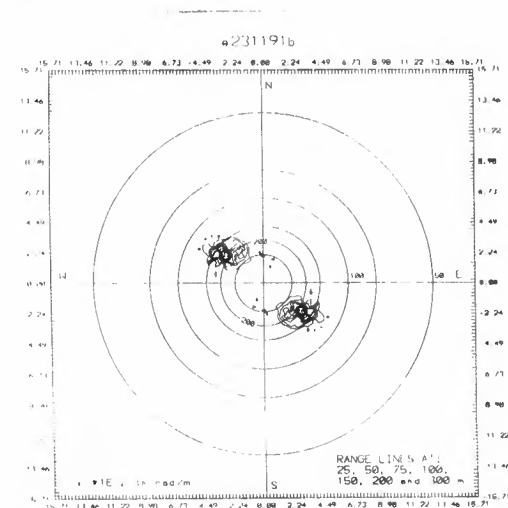


Figure 6: 2D wave number spectra of the ERS-1. Date 23 Nov. 1991.

	ERS-1	PHARUS	SHIRA	
Freq.	5.2	5.2	10	GHz
Pol.	VV	VV	HH	
inc. angle	23	50	89	deg
h/v	110	40	--	
image size	100 * 100	6 * 6	1.2 * 1.2	km
pixel size	20 * 16	2.75 * 2.75	10 * 10	m
resolution	30 * 30	6 * 6	15 * 15	rad/km
looks	3	12	--	
Wave characteristics				
length	40 - 2560	22 - 1400	20 - 1200	m
direction	0 - 180	0 - 180	0 - 360	deg
num. of aver.	16	6 - 14	1	
resolution	2.5	4.5	5.2	rad/km

Table 1: Properties of the ERS-1, PHARS and SHIRA in RENE91

DISCUSSION OF THE SAR SPECTRA

In SAR images the relatively high resolution in range direction is achieved by using the doppler frequency shift between the moving platform (SAR) and the stationary individual point scatters. If the point scatters (such as waves) are moving in the beam artifacts arise. For waves these artifacts can be distinguished in two classes:

- scale (scanning) distortion
- velocity bunching

Scale distortion arises if waves or wave components are moving parallel to the platform direction (azimuth travelling waves). The so-called defocussing (blurred image) increases if ratio between the wave velocity and platform velocity increases. This effect is for the ERS-1 SAR systems neglectable because of the relatively high platform speed of 7 km/sec in relation with the phase velocity of waves. (approx. 10m/sec).

Velocity bunching arises if waves are moving perpendicular to the platform direction (range travelling waves). The most important parameter to describe this artifact is the platform velocity to sensor-range ratio (R/V , [3]). The distortion increases if this ratio increases. For the ERS-1 SAR $R/V = 122$ sec and for the PHARS $R/V = 62$ sec which is relatively high in both cases. Due to this effect a double peak spectrum can arise. Figure 5 shows this effect in PHARS spectra. In figure 5a the waves travelling in range direction (double peak due velocity bunching) and in figure 5b the waves travelling in azimuth direction are shown. Both spectra can be compared, since these were collected shortly after each other and at the same position.

VALIDATION OF THE ERS-1 SPECTRA

Figure 4 shows that the most important days for wave measurements were: 19 and 22 November 1991. For these two days

spectra simultaneously measured by ERS-1, PHARS, SHIRA, RESSAC, and buoys are available. November 19 was a day with snow showers and no waves were detected in the ERS-1 image spectra. Therefore wave spectra of November 22, 1991 are chosen. Figure 7 shows the 2D-spectra from the ERS-1, PHARS (with the ERS-1 flight direction), SHIRA and the wave buoy. All the spectra were measured nearly simultaneously and at the same position.

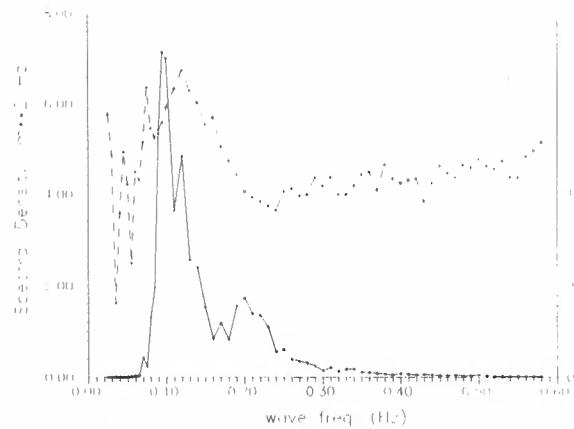
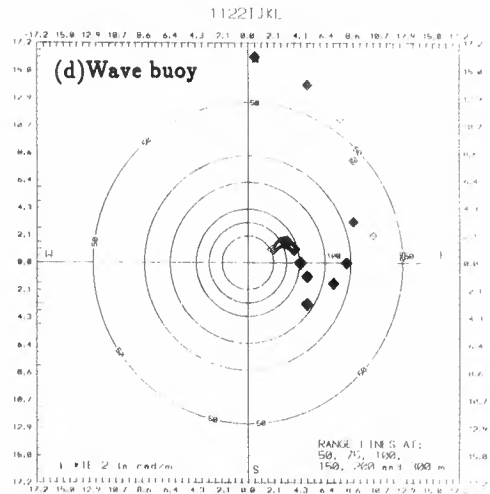
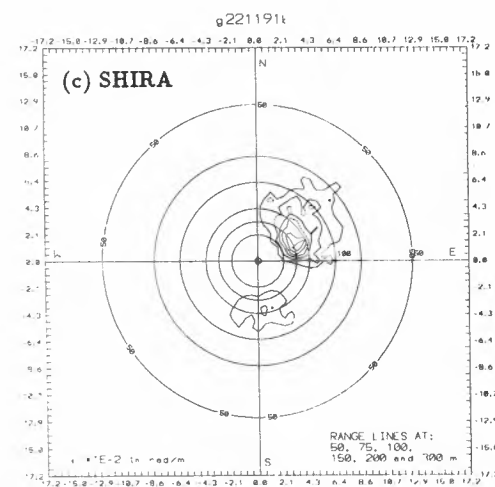
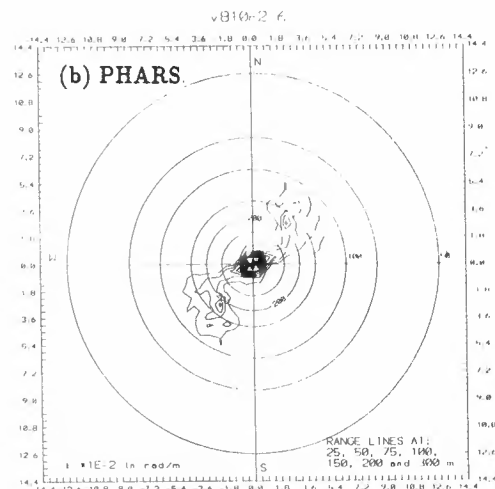
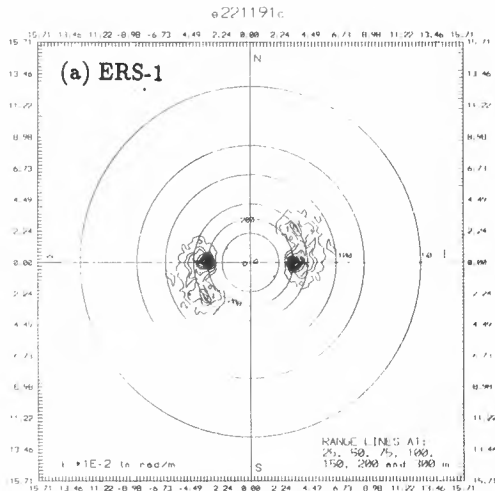


Figure 7: Simultaneously measured 2D wave number spectra from: (a) ERS-1, (b) PHARS, (c) SHIRA, (d) Wave buoy. Date 22 Nov. 1991.

As a first guess the direction and wavelength of the two highest peaks in each spectrum were estimated. Table 2 shows these values for 22 November.

From table 2 it is clear that the first (highest) peak of SHIRA and the wave buoy are comparable. It is also clear that the (first) peaks in these spectra do compare better with the second peaks in the PHARS and the ERS-1 spectra. This applies to nearly all the ERS-1 spectra. The first peak in the ERS-1 spectra is probably caused by the above mentioned velocity bunching artifact.

In all our ERS-1 spectra no azimuth travelling waves could be observed. This is remarkable because these waves are present in the PHARS, SHIRA and wave buoy spectra. At the moment it is not clear what causes this effect.

CONCLUSIONS

The Dutch contribution to the database utilized for the calibration and validation of the ERS-1 wave products with the airborne (PHARS) and the shipborne (SHIRA) radar systems has appeared to be quite valuable. The SHIRA system is a very reliable instrument and suitable for in-situ measurements of omnidirectional wave spectra. Especially the sensibility for developing (with relatively low wavelength) wavefields is good. The PHARS system gives good insight in the so-called velocity

REFERENCES

Date	First peak		Second peak	
	Wave length (m)	Wave dir. (deg.)	Wave length (m)	Wave dir. (deg.)
Nov 22 1991				
ERS-1	185	92	155	52
PHARS	180	40	160	65
SHIRA	170	71	--	--
Wave buoy	170	70	--	--

Table 2: First guess of the wavelength and direction from the first and second highest peak in the simultaneously measured spectra from ERS-1, PHARS, SHIRA and wave buoys

bunching mechanism, an artifact in the SAR imaging mechanism. This effect is for the ERS-1 stronger than for PHARS system.

In most of the investigated ERS-1 images only the range travelling waves were imaged. In the spectra of these images the most dominant peak was caused by velocity bunching and not by the waves themselves, which however, do cause the second highest peak.

A preliminary conclusion is that the sensitivity of the ERS-1 for smaller wavelengths (<100 m) is lower than for SHIRA and the PHARS which is maybe caused by the different incidence angles for the systems. This situation may improve by using full precision products of the ERS-1.

A first comparison of the investigated ERS-1 wave spectra with the wave buoys and SHIRA spectra has shown that the wave performance parameters satisfy the specifications.

In my point of view a unique database is available at ESRIN for the validation and calibration of the ERS-1 wave products, so that also calibrated waveheight spectra may be obtained. In order to transform the image spectra to these wave-height spectra an instrumental transfer function and a model is required. Further investigations are needed, to achieve this.

ACKNOWLEDGEMENT

Participation of the PHARS was possible due to financial contributions of ESA, NIVR (Netherlands Agency for Aerospace programs) BCRS (Netherlands Remote Sensing Board), NLR (National Aerospace Laboratory) and FELTNO. The authors are very grateful to Friedwart Ziemer of GKSS (Germany) and Karl Richter of BSH (Germany) for giving us the opportunity to participate with SHIRA on the Gauss and for providing us available in-situ data. We thank ESA kindly for giving the opportunity to participate in RENE91.

- [1] J.C.M. Kleijweg, "SHIRA: a mobile radar system for monitoring waves", *Conference paper UDT '91, 23-25 April 1991, Paris, 993-999*
- [2] P. Hoogeboom, P.J. Koomen, H. Pouwels, P. Snoeij, "First results from the Netherlands SAR testbed PHARS", In *IGARSS '91 proceedings, Helsinki University of Technology, vol.1, 241-244*
- [3] R. C. Beal, "Directional ocean wave spectra" *Johns Hopkins studies in earth and space sciences, The Johns Hopkins Press Ltd., London*

OBSERVATIONS WITH THE RESSAC AIRBORNE RADAR DURING RENE91

Danièle HAUSER, Gérard CAUDAL

CRPE/CNET/CNRS, 38 Rue du Général Leclerc, 92131 Issy-les-Moulineaux, France

Bertrand CHAPRON

IFREMER Brest, BP70, 29280 Plouzané, France

I- INTRODUCTION

The Synthetic Aperture Radar (SAR) of ERS1 is providing us with new ocean surface imaging over a global scale. However, the relationship between the ocean wave spectra and the SAR image spectra is still not satisfactorily determined. The imaging mechanism for a SAR is the result of a complex interplay of different mechanisms. Some of them are related to the properties of the surface (tilt modulation, hydrodynamic modulation), and others are specific to the SAR measurement technique (image smearing due to orbital motions, velocity bunching...) [1]. The latter modulation plays a key role in the formation of the image, but introduces distortions of the image, depending upon the wave direction and amplitude. The operational use of the image spectra (through assimilation into wave models for instance) requires a proper understanding of the transfer function linking the two-dimensional sea spectrum to the SAR image. Comparisons with independent measurements are therefore necessary in order to improve the methods which permit to document the two-dimensional sea spectra from SAR image spectra.

Airborne radars operating with real aperture, and therefore insensitive to the distortions related to the SAR technique, may give access to the wave field along portions of the satellite track, with a good spatial coverage. For this reason, the European Space Agency (ESA) and French Space Agency (CNES) gave support to a new project of airborne radar, called "RESSAC" (Radar pour l'Etude du Spectre des Surfaces par Analyse Circulaire), which participated to the RENE 91 validation campaign of ERS1.

II-MEASUREMENT PRINCIPLE AND DATA PROCESSING

The RESSAC radar system has been described by Hauser et al.[2]. It is based upon the same principle of measurement as the ROWS (Radar Ocean Wave Spectrometer) developed at NASA [3,4]: analysis of the reflectivity modulation due to the tilt of the long waves (wavelength larger than 30m), observed from low-incidence angle measurements. RESSAC makes use of the

Frequency Modulated/Continuous Wave (FM/CW) technique, and operates at the same frequency as the SAR of ERS1 (5.35 GHz). The radar can be mounted on two airplanes, either the Dornier 228 of DLR (Germany), or the Merlin-IV of Météo-France (France). The transmitting and receiving antennas are looking at an angle of 14° from the nadir, and perform one rotation per minute around a vertical axis. The 3dB beam width is $\pm 6.5^\circ$ in elevation and $\pm 1.7^\circ$ in azimuth. The nominal flight altitude of RESSAC is usually chosen as 6000m.

For given azimuthal direction ϕ and incidence angle θ , the radar cross-section σ° averaged over a few minutes ("smoothed" σ°) is dependent principally upon the intensity of sea waves of wavelengths smaller than a few meters, which account for most of the mean square slope. Of course this short-scale roughness is strongly dependent upon the wind intensity and (to a lesser extent) the wind direction.

Assume now that a long wave system (wavelength $\lambda > 30\text{m}$) is superimposed on those short waves. Rather than depending on θ , the reflectivity properties of the surface resolution cell now depend on the local incidence angle θ . As a consequence, the cross-section sensed by the radar will be modulated by the long waves (tilt modulation). If the along-track resolution cell is large compared to the wavelength, then it is clear that the only waves that can be detected are those which are perpendicular to the look direction of the radar, because otherwise their modulation will be averaged across the antenna beam.

Jackson et al [4] have developed a linear tilt model of this modulation (see also [2]). According to this model, it is shown that the sea surface height spectral density $F(K, \phi)$ in the look direction can be related simply to the observed modulation spectrum through:

$$K^2 F(\kappa, \phi) = L_y / \sqrt{2\pi} P(\kappa, \phi)$$

where $P(K, \phi)$ is the modulation spectrum of $\alpha\sigma^\circ(x, \phi)$, x being the horizontal distance along the look direction, and α is a function of θ depending on the smoothed $\sigma^0(\theta)$ profile, and

can be determined empirically from each observed $\sigma^{\circ}(\theta)$ profile.

The processing applied to the Ressac observations provides us with directional spectra of the surface waves, for wave lengths between 50 and 350 m, with a wavenumber resolution of 4.03×10^{-3} cpm, and for azimuth direction every 5° , between 0 and 360° (with respect to North). The effective resolution in wavelength and direction depends of the wavelength: for a 100-m wave it is of about 10 m in wavelength, and 14° in azimuth, while for a 200-m wave, it reaches 35 m and 22° , respectively. About 5 minutes of data (five complete rotations of the antenna) are used to obtain each directional spectrum. This corresponds to an approximate length of 30 km along the aircraft trajectory, owing to the average aircraft speed of 100 m/s. From these two-dimensional spectra, the non-directional spectra, and the associated significant wave height H_s , are also calculated by integrating over all the directions (and over all the wavenumber range for the significant wave height). Note that this gives a high number of degrees of freedom for the non-directional spectra (between 100 and 500, depending of the wavelength). This gives an accuracy of about 7% at the 95% confidence interval level, for a 100-m wavelength. Due to the principle of measurement, a $\pm 180^{\circ}$ ambiguity remains on the direction of propagation of the waves. New improvements in the processing are under progress in order to remove this ambiguity (also present for spectra derived from SARs).

III-SUMMARY OF THE OBSERVATIONS

Ressac was mounted on board the Merlin IV from the 2nd of October to the 8th of December, with one week off (27th October-3rd November). During this period, 27 flights were performed with Ressac on board. From these 27 flights, 24 sets of data have been provided. The data of 3 flights could not be processed (in two cases because of tape recording problems, and in one case because of a radar failure). The 24 data sets are distributed as follows: 18 correspond to missions of type 3.2 (see the presentation of the experiment, elsewhere in this document), which were defined to sample the ERS1-SAR swath during the ascending track of ERS1 on day 3, 2 correspond to missions of type 1.3 which were defined to sample the ERS1-SAR swath during the descending track of ERS1 on day 1, and 4 correspond to missions 1.4 which were defined to provide observations near or along the ERS-1 radar altimeter descending track on day 1. In all cases, Ressac performed

measurements in the vicinity of two of the directional buoys deployed in the zone (at point T10 and T11, see the presentation of the experiment elsewhere in the document). The type of sea-state encountered over the whole period is mainly characterized by a moderate significant wave height (at least near point T10): 16 cases with H_s between 2 and 4 m, 6 cases with $H_s \geq 4$ m, 2 cases with $H_s < 2$ m. Several cases correspond to swell situations (28 Nov., 17 Oct., 4 Nov., ...). However, in a number of cases, there was a complex mixture of swell and younger sea due to the frequent passages of atmospheric perturbations (13 Nov., 20 Nov., 22 Nov., 4 Dec.,...). In these cases, we observed most of the time, important spatial variations of the directional spectra, over scales of 300 to 400 kilometers along the aircraft trajectory. This is an important point with regards to the ERS-1 SAR validation: for comparisons between Sar-image spectra and measured wave spectra one must keep in mind this possible spatial variability of the wave spectra.

Figure 1 shows the peak period deduced from the Ressac observations, plotted as a function of the peak period given by the buoy. The peak period from Ressac have been obtained by using the dispersion relation in deep water, in order to convert spectra expressed in the wavenumber domain into frequency spectra. At the time this paper was written, data from the buoy were available only every 3 hours. Therefore an interpolation in time has been applied to the peak period of the buoy data in order to compare with the Ressac peak periods. Note also that the frequency spectra of the buoy were not available at that time (only three parameters were available: significant wave height, peak and average period). Therefore no check could be made of the spectral shape; in particular it was not possible to check whether there were several maxima in the frequency spectra. The results shown in Fig.1 indicate that there is an overall good agreement between the Ressac and the buoy peak periods, except for 4 data points where Ressac gives much higher peak periods. It has been verified that these data points correspond to cases where there is an artefact in the Ressac retrieved wave spectra due to a non eliminated long-wave modulation in the signal. Although this artefact is present in all the cases, it could usually be removed from the spectra because it is quite distinct from the other frequency components. Except for the above-mentioned points, the agreement for the peak period is quite good, keeping in mind that due the Fourier analysis of the signal received by

Ressac the resolution is of 2 s for a peak period of 14 s (0.7 s for a peak period of 10 s).

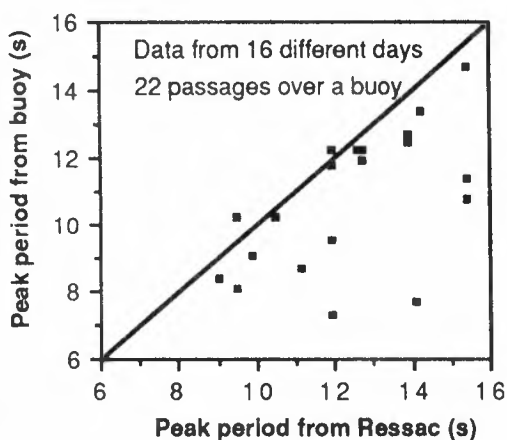


Figure 1: Comparison of the peak period of the waves, deduced from the Ressac data, and from the buoy observations. The solid line is the 1:1 line

Figure 2 shows the significant wave height obtained from Ressac, and compared to the values given by the nearest buoy (T10 or T9).

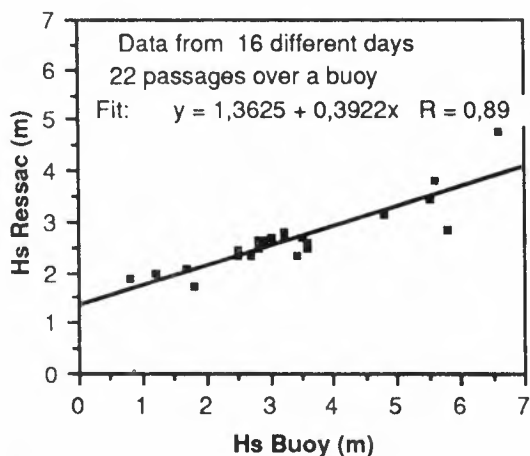


Figure 2: Comparison of the significant wave height deduced from the Ressac data and from the buoy measurements. The solid line shows the least-square fit.

Again, it must be mentioned that the buoy data have been interpolated in time (significant wave heights available every 3 hours from the buoy). It is clear from Fig.2 that the scaling procedure used in the processing of the Ressac data (parameter α mentioned in section II) is not completely adequate: there is a systematic underestimate of the significant wave heights larger than 3 m and an overestimate for H_s smaller than 2 m. This scaling problem is not yet understood. However an interesting point to

note is that a linear function relates the Ressac values to the buoy values, with a high correlation coefficient. This means that an a posteriori correction may be applied on the Ressac significant wave height. In order to go further in this analysis, it would be necessary to compare the energy density spectra from the two types of measurements. This has not been done, because the spectra from the buoy were not yet available. However, this type of analysis on data sets collected during a previous experiment (SWADE) indicated that the energy density levels are underestimated over the full range of wave frequency (or wavelength). It is likely (but this has to be verified in the next future) that for the RENE91 data set, the spectral shape is also well reproduced by Ressac, but a normalization factor is necessary to provide the absolute level of the energy density spectrum

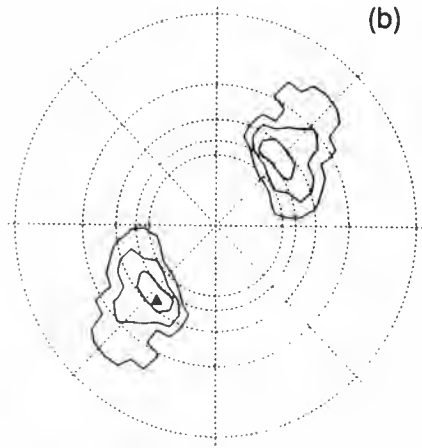
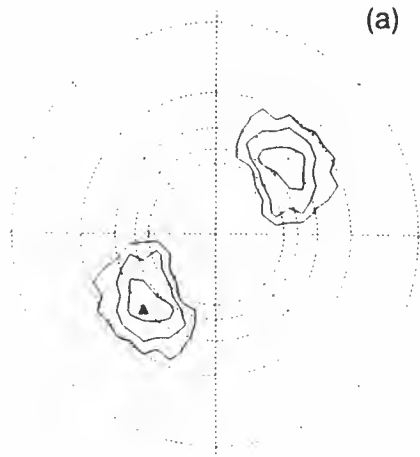
IV-EXAMPLES OF RESULTS

Since it is not possible to discuss in details all the results obtained during the campaign, we have selected three cases of observations: 28 Nov., 22 Nov., 13 Nov.. For each of them, we show slope spectra of the waves ($K^2 F(K,\phi)$), averaged over five rotations of the antenna (nearly 5 minutes of observations), and plotted as a function of wavelength, and direction.

On the 28th of November, a fairly homogeneous swell was observed by Ressac. This case corresponds to a well-defined swell propagating from South-West, i.e. approximatively in a direction perpendicular to the satellite heading (339° from North). In this case of range-travelling waves, the non-linearity and filtering effects of the SAR imaging mechanisms are the lowest. Figure 3 shows four directional spectra obtained from Ressac. Figure 3a and 3b correspond to observations made in the vicinity of buoy T10 from two different passages separated in time by about 2 hours, while Fig.3c and 3d correspond to observations made near buoy T11 also from two different passages separated in time by about 45 minutes. At T10 as at T11, the directional spectra are quite constant in time. Also the differences in the spectra between the two locations are very small, although the spectra seem to be slightly broader in azimuth and in wavelength at T10. For these four spectra, the wavelength of the peak is of about 260m, and the direction of this peak is from 225° (SW). The significant waveheight calculated from the Ressac spectra is also nearly constant (between 3.4 and 3.6 m). Figure 4 shows two examples of 2D image

SLOPE SPECTRUM Date 2811 From 191650 To 192152
 Position 64 33 7 93 Max (m²/rad) = 0.216

SLOPE SPECTRUM Date 2811 From 211257 To 211811
 Position 64 21 7 97 Max (m²/rad) = 0.263



SLOPE SPECTRUM Date 2811 From 194415 To 195130
 Position 66 39 7 12 Max (m²/rad) = 0.369

SLOPE SPECTRUM Date 2811 From 203215 To 203928
 Position 66 35 7 17 Max (m²/rad) = 0.333

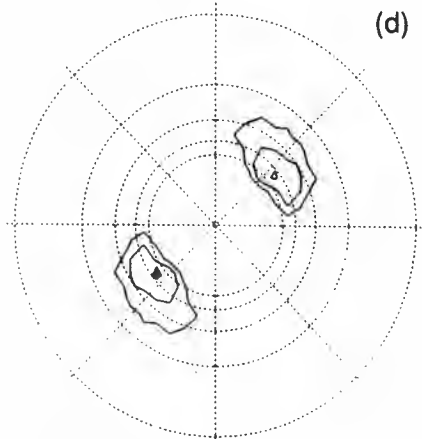
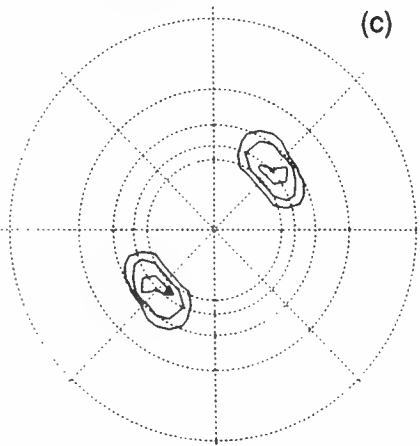


Figure 3: Polar plots of four directional spectra (expressed as slope spectra) obtained from Ressac on the 28th of November. Time and mean position of the measurements are indicated in the figures. Contours of energy density are plotted every 1.5 dB (first contour = 95% of the peak value). The circles represent isovalues of wavelength, and are plotted every 50 m from 100 m (outer circle) to 300 m (inner circle). The direction is given by the angle from North (North is towards the top of the figures). The solid triangles show the peak in each spectrum.

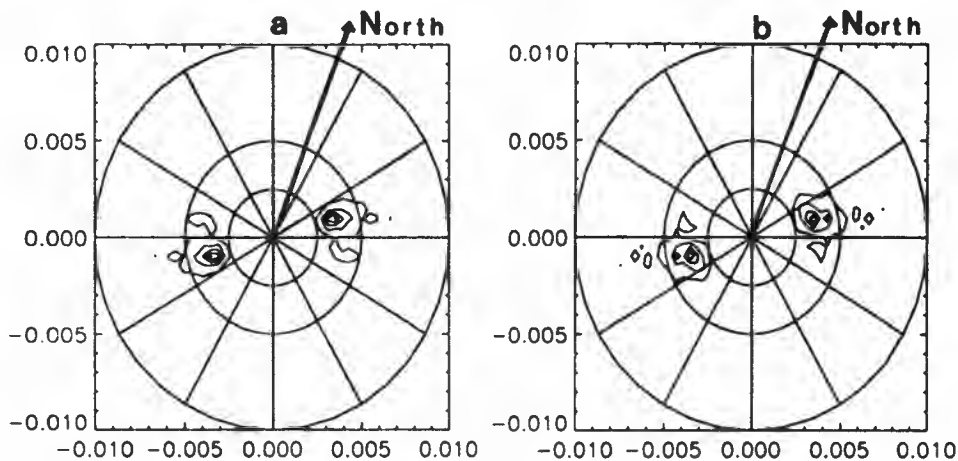


Figure 4: Image spectra obtained from one of the full SAR images on the 28th of November. These spectra have been calculated from sub-images covering 10x8 km². Fig.4a is relative to a location about 130 km North of that of Fig.3a and 3b. Fig.4b is relative to a location about 19 km South of that of Fig.3c and 3d. Same representation is used as in Fig.3, except that the circles are for wavelengths of 100 m (outer circle), 200 and 400 m, the direction is given relative to the satellite heading (339° from North), and contours are plotted every 3 dB.

spectra derived from one of the ERS-1 SAR image recorded on this day: each of these spectra have been calculated from sub-parts of the full image (over 10x8 km, i.e. 512 x 512 pixels); Fig.4a corresponds to a position about 150 km North of the location of spectra (3a) and (3b), while Fig.4b is relative to a position about 20 km South to the location of spectra (3c) and (3d). In both cases the peak of the spectrum is found in the same direction as from the Ressac observations, and the peak wavelength is of the same order of magnitude (290 m). So in this case of range travelling waves, the SAR-image provides quite consistent results.

On the 22nd of November, a wind shift occurred some hours before the wave observations: according to the observations performed by the the Norwegian research vessel Hakon Mosby (research vessel deployed for NORCSEX91 [5] at point T10), wind changed from NW to SW,S about 10 hours before our measurements, and was finally SE at the time of our observations. From measurements performed simultaneously with the Ressac flight, the airborne scatterometer "RACS" also indicates SE winds, with however a change of wind direction near T10 (changing to S -SW) just after the Ressac measurements. Three examples of directional spectra obtained from Ressac are shown in Figure 5 (near T10, near T11, and at the Northeast edge of our flight). In this case, there is an important variation in the characteristics of the 2D spectrum along the flights, and consequently along the SAR swath, although the significant wave height does not show important variations (2.3 to 2.7 m according to the Ressac measurements): near T10 (Fig. 5a), a long swell (peak wavelength \approx 220 m) from West-Southwest is present. Some evidence of shorter waves from SE to SW can also be seen. Near T11 and at the Northeast point (Fig.5b and 5c, respectively), the direction of the peak has turned to South-West, and the wavelength of the peak is shorter (\approx 170 m). The broad shape of the spectrum also indicates the presence of wind-sea from S-SE. Although in this case, the spatial variability is important, we did not found an important temporal variation at the different locations between the observations performed on the way out and the way back (separated by two hours maximum).

The 13th of November is also one of the numerous case where we observed important spatial variability. In this situation, a low pressure was located near the experimental zone. The Hakon Mosby measurements, measured several wind shifts near T10: during

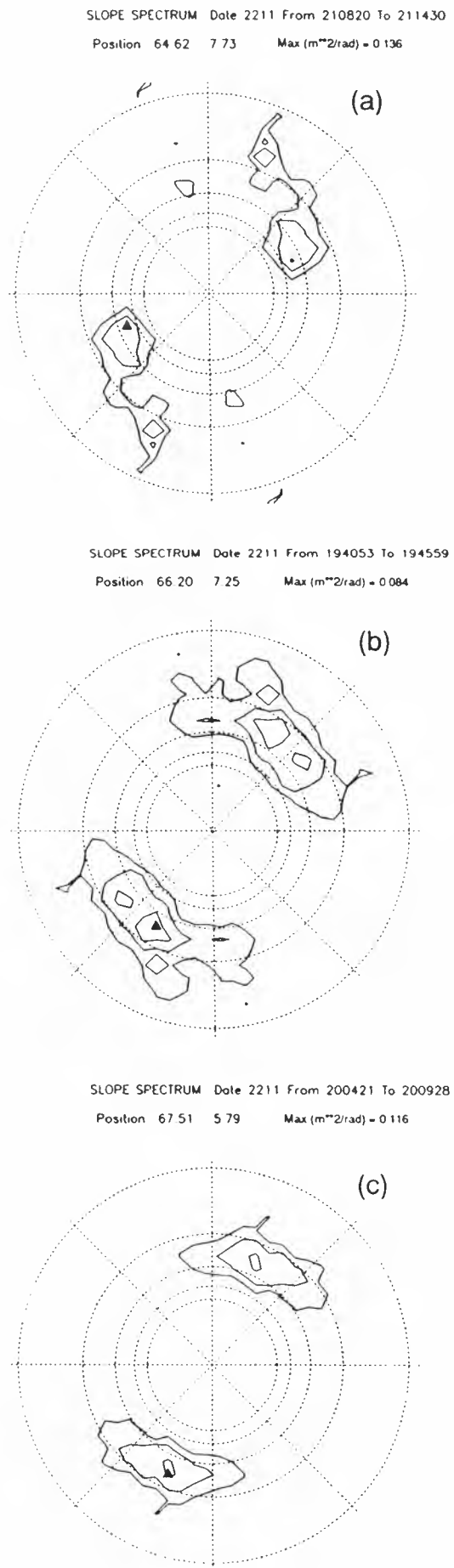
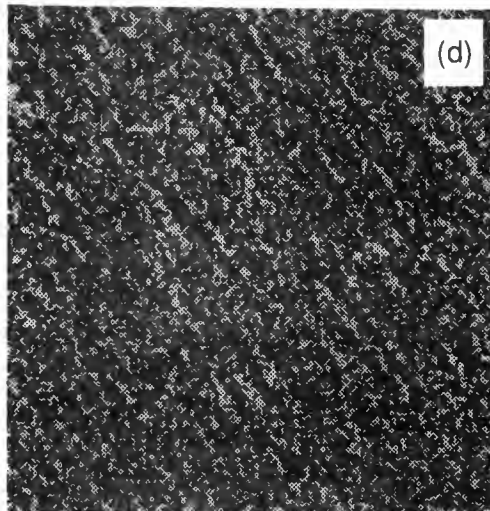
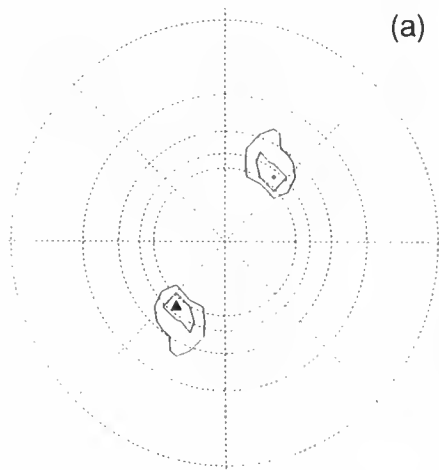
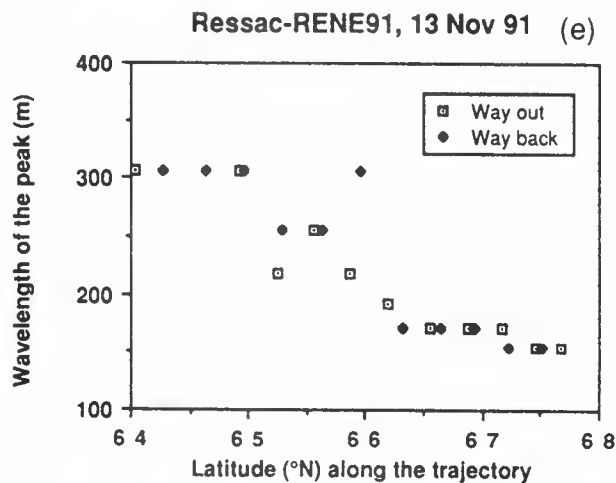
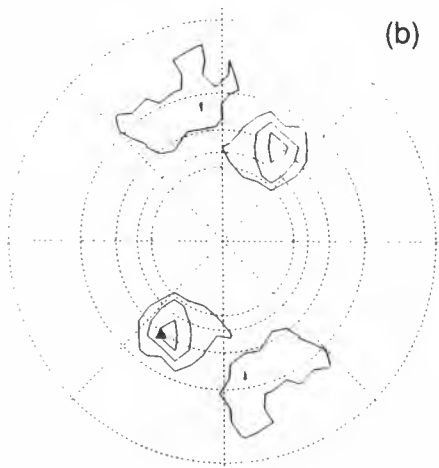


Figure 5: Same as Fig.3, but for directional spectra obtained at three different locations on the 22nd of November.

SLOPE SPECTRUM Date 1311 From 210459 To 211012
 Position 64 63 7.68 Max (m**2/rad) = 0.189



SLOPE SPECTRUM Date 1311 From 194322 To 194827
 Position 66 19 7.25 Max (m**2/rad) = 0.119



SLOPE SPECTRUM Date 1311 From 195436 To 195939
 Position 66.87 6.64 Max (m**2/rad) = 0.348

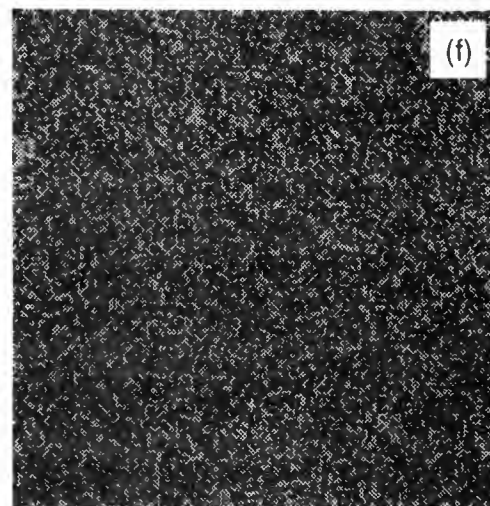
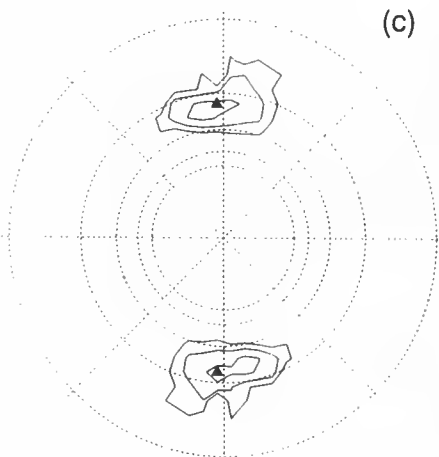


Figure 6: (a,b,c): Same as in Fig.3, but for directional spectra obtained at three different locations on the 13th of November. (d),(f): portions of the ERSI-SAR images (size of about 10x10 km), and relative to the same regions as for Fig.6a and 6c, respectively. (e): Peak wavelength retrieved from the Ressac observations and plotted versus the position in latitude. Two different symbols are used for the measurements during the way out and the way back.

the 24 hours preceding the Ressac measurements, wind turned from SE, to NE, then to SE, and then to again to NE. The directional spectra shown for this case in Fig.6 indicate the presence of swell from South-West near T10 (Fig.6a). This swell coming from South-West remains probably from the previous days. At T11 (Fig.6b), there is a mixture of South-West swell and shorter waves aligned along the Southeast-Northwest direction. North of T11 (Fig.6c), only waves along the North-South direction with wavelengths of the order of 170 m are visible. The examination of the complete set of results indicates that the evolution is progressive, with the apparition of short waves North of T10, a progressive decrease and rotation of the dominant wavelength (see also Fig.6e). Figure 6d and 6f show parts of the ERS1-SAR image relative to the same regions as in Fig.6a, and 6c, respectively. In Fig.6d, a swell signature is quite clear on the image, while in Fig.6f the image seems to show only noise. This change in the image is probably related to the change in the characteristics of the directional spectrum of the waves. Fig.6d is associated with range travelling waves, while Fig.6f is associated with nearly azimuth-travelling waves of shorter wavelength. When the numerical data corresponding to these images will be available, it will be possible to study the progressive change in the SAR image response, and to relate it to the change of the characteristics of the wave spectrum as found from Ressac.

V-CONCLUSION

A lot of information has been collected by the airborne radar Ressac during RENE91. Directional spectra of the surface waves have been derived along the swath of the ERS1-SAR. Direct comparisons of the SAR-derived spectra with the slope spectra derived from Ressac will be possible in some cases (well defined azimuth-travelling waves). However, the analysis will be much more complicated in a number of cases where we identified either range-travelling waves, or several dominant directions and wavelengths. The spatial variation of the wave field seems to be an important feature to take into account in the SAR analysis. A combination of wave-model and in situ wave observations could be helpful to make further progress in the SAR analysis.

Work is also under progress in order to derive from the Ressac data, parameters relative to the short waves (wavelength between some tens of centimeters to some meters). This is done by

combining the analysis of the σ^0 behavior as a function of incidence (in the 7-21° range of incidence angles) and azimuth angle, together with a physical model describing the interaction of the electromagnetic waves with the surface. In particular this study should provide us with information on the spectral shape and of azimuthal spread of the short waves. This information could in turn be used to improve our knowledge of the SAR modulation transfer function.

ACKNOWLEDGMENTS

The participation of Ressac to RENE91 would not have been possible without the support of the technical team of CRPE involved in this project (F. Baudin, P. Celin, P. Lancelin, G. Laurent, B. Piron), and without its active participation to the campaign. We are very grateful to the aircraft team from Météo-France, which made possible the operations of Ressac from the Merlin-IV. Thanks also to H. Branger (from IMST, France), and to G-J. Rijckenberg (from the University of Wageningen, The Netherlands) for their participation during the campaign. J. Johannessen from the NERSC of Norway kindly provided us with the data from the Hakon Mosby ship (NORCSEX'91 experiment). Finally, thanks to the organizers and to all the other participants.

REFERENCES

- [1] Alpers W.R., D.B. Ross, and C.L. Rufenach, 1981, *J. Geoph. Res.*, **86**, C7, 6481-6498
- [2] Hauser D., G. Caudal, G-J. Rijckenberg, D. Vidal-Madjar, G. Laurent, and P. Lancelin, 1992, *IEEE Trans. on Geoscience and Remote Sensing*, in press
- [3] Jackson F.C., 1981, *Radio Science*, **16**, 6, 1385-1400
- [4] Jackson F.C., W.T. Walton, and P.L. Baker, 1985, *J. Geophys. Res.*, **90**, C1, 987-1004
- [5] NORCSEX Group, 1991, *Technical report No.48, The Nansen Environmental and Remote Sensing Center.*

Data Collection or Data Management ?

(A Behind the Scenes look at the RENE '91 Campaign)

By Anne V. Edward, Serco Space Ltd.,
Earthnet Support Contract, ESA/ESRIN, Frascati, Italy.

Abstract

Data collection or data management ? Many campaigns implement the former, in the ERS-1 Geophysical Campaign (RENE '91) we undertook the latter: an active policy of data management. The overwhelming success of this campaign was made possible through our ability to access consistent, validated datasets with which to begin our analysis in near real-time. This allowed immediate feedback into the validation of the wind and wave products from ERS-1. As such the success of the campaign was a result of sound data management, and it is from here that I believe we can learn for the future.

1. Introduction

The aim of this paper is to review the philosophy adopted in the management of the diverse datasets collected during the ERS-1 Geophysical Campaign. This is supported by an explanation of the on-site implementation of the systems, and the daily operational procedures. A discussion of the results obtained in using this data management system then leads to a number of recommendations made on the basis of our experiences.

2. Background To The Campaign

The Geophysical Campaign (RENE '91) was organised by ESA for the validation of the ERS-1 wind and wave data. It was held in the Haltenbanken off the coast of Norway (See Figure 1), from September 16th to December 10th 1991. The campaign involved a number of ground truth experiments, from which data was used to validate the ERS-1 AMI, in wind and wave mode, and Radar Altimeter products.

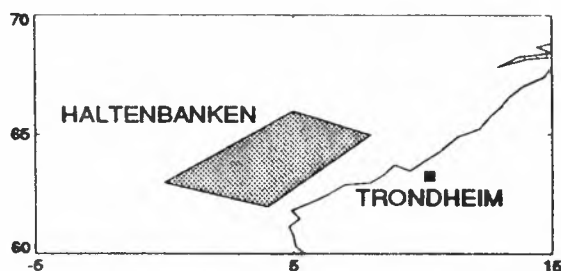


Figure 1 : The Haltenbanken, Norway

The experiments were carried on board a number of aircraft, ships, and ocean buoys, and represented a diverse collection of wind and wave measurements. Details of which are given in Table 1.

Platform Type	Experimental Platform		Experimental Data
	Owner	Instrument	
Aircraft	UK Met Office	C130	Wind measurements
	Dornier IFM	DO228 RACS	In-flight wind data Scatterometer data
	Meteo France CRPE	Merlin Ressayac	In-flight wind data Radar wave spectra
	TNO / NLR	Metro	SAR imagery
Ship	Norwegian	Met ship Mike	Wind/wave observations
	BSH TNO	GAUSS SHIRA	Wind/wave observations Radar wave spectra
	FWG	Planet	Wind/wave observations
	Nansen Centre	Hakon Mosby	Wind/wave observations
Oil Platform	Statoil	Gullfaks	Wind/wave observations Wave height/direction Radar wave spectra
Ocean buoys	OCEANOR	Tobis buoys	Wind speed/direction Wave height, period.
	GKSS	Waverider	Wave height/direction
Meteorological Analysis	ECMWF	6 hour analysis	Wind speed/direction
	DNMI	6 hour analysis	Wind speed/direction Wave field analysis
Colocation Analysis	UK Met Office	All datasets	Wind speed/direction

Table 1 : Campaign Experimental Datasets

The data collected were then used in the validation of ERS-1 wind and wave measurements. The fast delivery products used are shown in Table 2.

Instrument	Fast Delivery Product	Main parameters
AMI - Wind Mode - Wave Mode	UWI	Wind speed & direction
	UWA	Directional wave spectra
Radar Altimeter	URA	Wave height, wind speed & satellite altitude

Table 2 : ERS-1 Fast Delivery Products
(NB. All Acronyms are given in the Glossary.)

3. Concepts Behind The Data Management

In preparation for RENE '91 a rehearsal campaign was held in February 1990 from which we learnt some invaluable lessons. Primarily that simple data collection was insufficient in meeting the near real-time demands of ERS-1 validation. So in putting together a strategy for data collection during RENE '91 we looked at taking a more active part in the management of the data.

This requirement for active data management was further emphasised by the need to split the daily operations between the on-site headquarters of the campaign in OCEANOR, Trondheim, Norway and ESA/ESRIN, Frascati, Italy. This split was necessary because of the key role each had to play in the running of the campaign.

OCEANOR was the selected headquarters of the campaign management during RENE '91. As such it was the centre of the campaign's activities, and host to the majority of the experimenter teams. ESRIN meanwhile was the reception centre for the ERS-1 fast delivery products required, and offered excellent network communications with remote teams.

With these points in mind a system was developed to be installed at both sites. Important in the design were the ease of archive, preliminary validation and accessibility of the data.

In conjunction, it was recognised that the diversity of the data formats used in the rehearsal campaign limited widespread use of data. As a result, a standard format for all types of experimental data had to be established.

4. Implementation

In the concepts described above we identified four main elements of an active data management system:

1. Site Installation
2. Data Archive
3. Data Format
4. Validation System.

4.1 Site Installation

As mentioned in Section 3 management of the campaign data was split between two sites. The main installation is in ESRIN, where the system is resident on one of the main VAX systems with access to SPAN and X.25 communications.

For the period of the campaign a duplicate system was also installed at OCEANOR on their VAX system, again offering X.25 communications.

Further consolidation of the data archive, and a continuing service to the experimenter and analyst

teams is performed through the ESRIN facility. As such this is now built into the long term role of the Product Control Service, ESA/ESRIN.

The siting of the archive both in OCEANOR, and more especially in ESRIN on systems with good communications access was of prime importance. However, the mere fact that access was available did not mean it was either simple or easy. Effort was therefore put into the problems of network communication prior to the campaign. This involved time being spent in identifying network links and then fully testing connections.

4.2 Data Archive

The data archive, Pcs_Span, was developed as an archive of campaign data which Experimenters and Analysts could easily access.

It consists of a set of directories in which the data is archived, and a user interface which allows access to further campaign information. An example of the directory structure is shown in Figure 2.

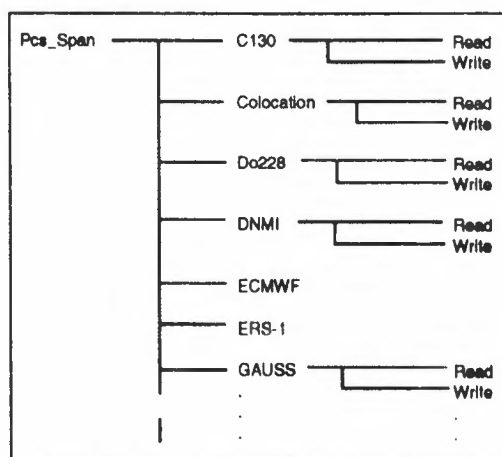


Figure 2 : The Directory Structure of Pcs_Span

The newly collected datasets were written to the *WRITE* directories by the experimenters. From here they were copied to the *READ* directories by the ESRIN team on preliminary validation of format and content. This allowed us to restrict access by the analyst teams to the *READ* directories, and hence the validated datasets.

Through the menu system there is also access to the following functions :

- mail message transfer to the system
- a directory of the data on archive
- phone calls between users on the system
- and access to details of fellow team members eg. network addresses.

This allowed a central base of information related to the campaign to be built up, and easily accessed.

4.3 Data Format

In archiving a diversity of datasets, and facilitating their use, it was important to formalise the data formats. Two of these formats, ERS-1 and ECMWF, were already in place. However the format of the experimental datasets still required development.

The ERS-1 and ECMWF formats were well understood and used as part of the normal ERS-1 operations. They are described in Reference Documents 1 and 2.

In looking at the requirements of a format for the experimental data a number of issues were considered important :

- flexibility
- ease of use
- portability
- implementation.

Flexibility – The need for flexibility resulted in the use of a numeric coding system for identification of the measured parameters. This allowed variations in written descriptions, but a definition by code number of the measurements made. A similar coding system also allowed the units of measurement to be standardised.

Ease of Use – Ease of use was important in making the format acceptable to all those taking part in the campaign. This was achieved in the use of header files describing the basic attributes of the data. These ASCII files acted as a simple description of the dataset.

Portability – Portability was essential for use of the data both during and after the campaign. Not all users work on the same computing systems, so as far as possible the format was kept simple. For example, the use of Integer*2 variables in the binary data files allows greater compatibility.

Implementation – It was a result of much consultation that the ERS-1 Geophysical Data Format was finalised in the months prior to the campaign. This allowed time for the Experimenter teams to familiarise themselves with the format in the run up to RENE '91. The details of this format are given in Reference Document No. 3.

4.4 Validation System

The validation system, Ar Mor, was developed as a validation and visualisation system for both the ground truth and ERS-1 data collected during RENE '91. The system is driven by a hierarchy of menus which allow access to the following functions :

- Data Input
- Data Selection
- Data Visualisation
- Data Analysis.

Data Input – Data Input provides the preliminary examination of all types of Pcs_Span data, and it is here that validation of the format takes place. The user may select to input any of the experimental or ERS-1 datasets listed in Tables 1 and 2.

Data Selection – Data Selection then allows the user to window in on all data loaded into Ar Mor. This windowing can be carried out in time and space in relation to any, or all, of the datasets in which the user is interested. The main facility for this data selection is shown in Figure 3.

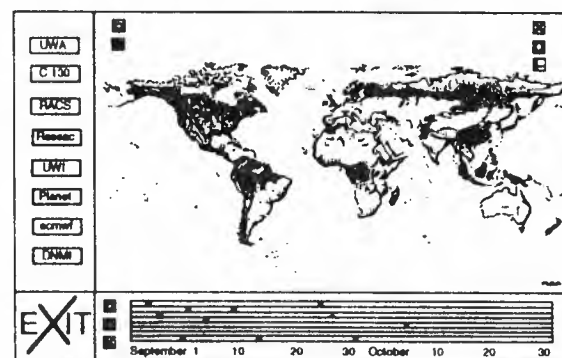


Figure 3 : Ar Mor Spatial, Time and Platform Windowing

Data Visualisation – Selected data may then be visualised in the following ways: graphs (2D and 3D), spectral plots, vector and colour maps. A few examples of these are given in Figure 4a and 4b.

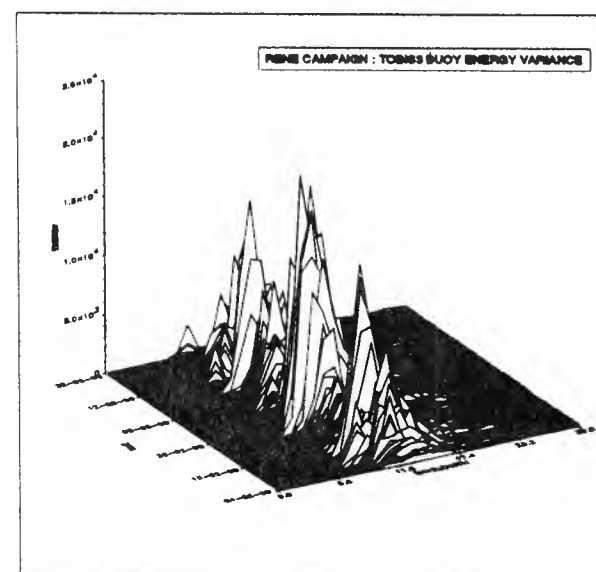


Figure 4a : Ar Mor Data Visualisation – TOBIS Buoy 3D Wave Plot

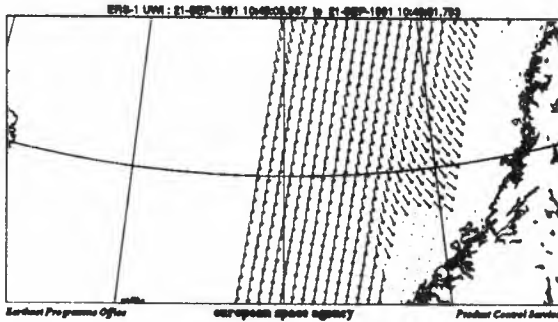


Figure 4b : Ar Mor Data Visualisation – ERS-1 UWI Wind Direction Vector Map

Data Analysis – Further analysis of the data is possible using basic statistical functions, and through access to the graphics package. Together these allow the user to summarise and compare the experimental and satellite datasets. An example is given in Figure 5.

Ressac Data : RENE '91 : Merlin : 29-11-91 : Sig. Wave Height	
Statistical Function	Output Value
Minimum	2.92000
Maximum	3.56000
Average	3.23364
Standard Deviation	0.193921
Total No. of Values	11

Figure 5 : Ar Mor Statistical Output – Ressac Significant Wave Height

5. Daily Operations

The daily operations of the data management system centred around the archiving, preliminary validation, and transfer of data between sites. This is illustrated in Figure 6 which shows the main on-line data flows during the campaign.

5.1 ESRIN

In ESRIN the main data flow was that of the ERS-1 fast delivery products from ESA ground stations. These were received as part of the normal ESRIN operations. The products relating to the Haltenbanken area were then extracted, and this subset written to the Pcs_Span archive.

The ECMWF analyses were also received on-line, as part of normal operations, and were copied daily to the Pcs_Span archive.

A link is also shown for off-site experimenter teams whose data processing could not be completed on-site at OCEANOR.

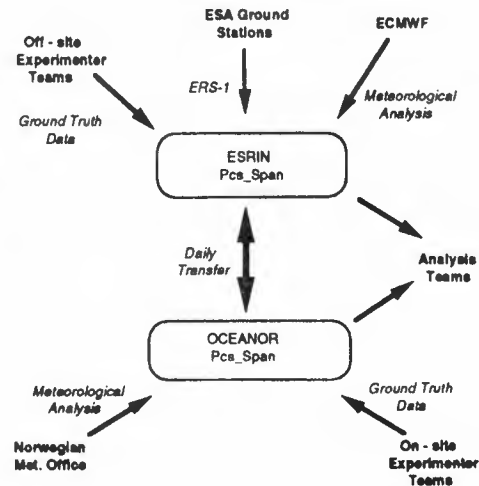


Figure 6 : On-line Data Transfer

5.2 OCEANOR

Meanwhile, in OCEANOR the Pcs_Span archive was accessed daily by the majority of the experimenters. Each of the teams, having completed their own data processing, transferred their newly collected datasets over Ethernet to Pcs_Span.

5.3 Archiving and Validation

In both ESRIN and OCEANOR the new datasets underwent a preliminary validation of format and content before being made available for use in the *READ* directories of the archive. This validation included, for example, the reformatting of the DNMI data to the ERS-1 Geophysical Data Format. Also in some cases the files had to be reformatted from IBM to VAX file structure, including the byte swapping of binary data files. However in most cases this preliminary validation was merely a routine check.

The validation process was mainly undertaken using the Ar Mor functions described in Section 4.4. Nevertheless there was a need for a number of smaller more specialised stand-alone programs. These were developed to handle the more unusual problems encountered during the operational phase of the campaign.

5.4 Data Transfer

The archiving and validation of the newly collected datasets took place at the nearest point of contact to the experimenter teams. It was then necessary to transfer this data between sites, so allowing the archives in ESRIN and OCEANOR to be kept up to date. This transfer took place daily in order to maintain consistency between sites. It also maximised real-time access to the data.

5.5 Data Access

The analyst teams had on-line access to all the data during the campaign through both Pcs_Span archives. From here they were able to copy the data

they required, and also access centralised information regarding identified problems. This type of access is still continuing through the ESRIN facility.

6. The Results of Active Data Management

Having taken an active role in the management of the data collected during RENE '91 I can identify a number of positive results.

1. Consistency
2. Validation
3. Accessibility

6.1 Data Consistency

The consistency of the datasets can be discussed in terms of their format. The RENE '91 data was made available on Pcs_Span in pre-defined formats which were well understood. This was of major importance to those in the analysis teams who did not have the day-to-day knowledge of the campaign, its operations and data collection regime. It also allowed them to bypass some of the more mundane issues of data use such as 'Is the data in the correct format?' or indeed 'In which format is the data?'

Also during the campaign a number of points were raised in the daily scientific briefs about the data content, its processing or validity. In providing centralised access points to the archive this information could be transmitted to those involved in its use.

6.2 Data Validation

In parallel to this need for data in a consistent format was the need for the data to be as accurate as possible in the circumstances. In order to fulfil this objective much of the data was subject to daily scrutiny on-site. This allowed the experimenter team to identify many of the instrument and data problems almost immediately.

For example, a problem in the definition of wind direction in the ERS-1 AMI wind mode products was identified in the first month of the campaign. In visualising the Ar Mor wind direction vector maps (an example of which is given in Figure 3) it was possible to easily recognise inconsistency between meteorological analyses and ERS-1 measurements.

6.3 Data Accessibility

The accessibility of the data is of major importance in allowing further analysis to take place in near real-time. This was accomplished through the installation of the data archive at both sites.

Remote users had access to the same datasets as those at the heart of the campaign. This provided an independent view of some of the data issues and

problems which were often not seen by the on-site teams concentrating on the operational collection of data. An example of this was the identification by an off-site team of irregularities in the buoy wind measurements.

6.5. A Summary of Results

In summarising the results we should look back at the title of this paper – Data Collection or Data Management? .

In the rehearsal campaign we operated a system of passive data collection and as such we still have an incomplete and inconsistent archive. In learning from this we adopted a strategy of active data management for RENE '91 enabling us to offer an on-line, up-to-date, and consistent archive.

So, in looking at the implications of these results we can see that removing the uncertainties of dataset consistency, validation, and accessibility allowed the analyst teams to concentrate on the aim of the campaign. In return they offered a near real-time feedback to the work of geophysical validation, so reinforcing the ongoing success of the ERS-1 mission.

7. Recommendations

Important in ensuring the success of the RENE '91 campaign was the opportunity to learn from the rehearsal. In looking to campaigns of a similar nature in the future I would like to make some recommendations.

To a large extent these are based on the lessons learnt on-site during RENE '91. They can be identified by looking again at the four elements of implementation identified in Section 4 :

- On-Site Installation
- Data Archive
- Data Format
- Validation System

7.1 On-site Installation

On-site installation of systems can seem to many an unnecessary inconvenience but in hindsight there are positive lessons to be learnt.

It allowed the data management to be coordinated at the heart of the campaign. It was here that we were able to solve the problems of data format and content. My suggestion is therefore, where possible, to coordinate your data management from the campaign centre. More importantly, it must focus on one responsible member of staff, who is able to manage the reception of data, its preliminary validation, and archive.

7.2 Data Archive

The idea of a centralised, on-line archive will also immediately appeal to people. However, the work involved in maintaining an archive on-line is quite considerable, even when done in real time. During the RENE '91 campaign there was a full-time member of staff dedicated to the archiving and preliminary validation of data. This is not an inconsiderable investment in time.

Although we did invest this time and effort in the on-line aspect of our data archive, we still found ourselves sending out a number of data tape copies to analyst teams. This was due primarily to the amount of data involved, but also because of the relative inefficiency of some of the network links. It is sensible therefore to review an on-line archive carefully in terms of the time required in implementation against the commitment to its use.

The advantages are nonetheless numerous, as discussed in Section 6. I would therefore advocate a centralised data archive, on-line if possible, as the core to any campaign data management system.

7.3 Data Format

Of fundamental importance is the definition of a clear, simple and standard format for all campaign datasets. This must be implemented and tested prior to the campaign, and rigorously imposed during operations.

The resolution of data format problems accounted for the majority of the time spent on daily operations. It should be remembered that this occurred even after spending time on defining and implementing these formats prior to the campaign. I would thus emphasise the need to invest time in experimenting with the formats to be used. This 'education' process will prove to be as important as the definition of the format itself, in the eventual use of the data.

7.4 Validation System

As Mor brought together many ideas, and as such represented an ambitious software development project. It provides functions for both preliminary validation, and complex data selection and analysis. The performance of the system in encompassing these two overall functions became a burden to its use. This was mainly due to limitations imposed by the hardware and graphics package on which the system was implemented.

During the campaign we required a simple collection of stand-alone programs, which could be easily modified in response to real-time demands. In hindsight I would suggest a more simplistic 'tool box' approach to the design of a preliminary data validation system.

The design of such a system should concentrate on the performance requirements of a data driven campaign. The more complex analysis tools can be

considered in parallel, but must not hinder this primary objective.

8. Conclusion

In conclusion I would like to return to the main thrust of this paper. If, as a participant of similar campaigns in the future you can **learn from our mistakes**, and **build on our successes** you will be able to implement a system of data management rather than a method of simple data collection. I also hope that, more importantly, you have understood some of the advantages to be reaped from being **active** in that **data management**.

Reference Documents

1. ERS-1 Ground Stations Products Specifications for Users, ESA Document : ER-IS-EPO-GS-0204, Issue 3 Revision 2, September 1991.
2. World Meteorological Organisation, Manual on Codes, Volume 1, Annex II. International Codes 1988. Section : FM 92 - VIII Ext. GRIB.
3. A. Edward, ERS-1 Geophysical Data Format, ESA Document : ER-SR-EPO-GP-1111, Issue 3 Revision 0, February 1992. (Updated Campaign Issue)

Glossary

AMI - Active Microwave Instrument
B SH - Bundesamt für Seeschifffahrt und Hydrographie
CRPE - Centre de Recherches en Physique de l'Environnement
DNMI - Norwegian Meteorological Office
ECMWF - European Centre for Medium Range Weather Forecasting
FWG - Forschungsanstalt der Bundeswehr für Wasserschall und Geophysik
IFM - Institut für Meereskunde, Univ. of Hamburg
NLR - National Aerospace Laboratory (Netherlands)
RACS - Rotating Airborne Scatterometer
RESSAC - Radar pour L'Etude du Spectre des Surfaces par Analyse Circulaire
SHIRA - Ship board Radar
TNO - Netherlands Organisation of Applied Scientific Research
URA - User Radar Altimeter FD product
UWA - User AMI Wave mode FD product
UWI - User AMI Wind mode FD product

Acknowledgements

This paper represents the work of the Product Control Service, ESA/ESRIN, in particular it focuses on the work of Martin Davison (Serco Space Ltd), Pascal Lecomte (ESA) and myself. Without the cooperation and support of the Experimenter/Analyst teams, and campaign management we could not have implemented and operated the system with such success.

Validation of the Ocean Surface Wind Field and Wave Height Measurements Derived from Data of the ERS-1 Scatterometer and Radar Altimeter (Early Results)

M. A. Goodberlet, C. T. Swift
Microwave Remote Sensing Laboratory
University of Massachusetts
Amherst, MA USA

J. C. Wilkerson
Satellite Research Laboratory
National Environmental Satellite, Data, and Information Service, NOAA
Washington, D.C. USA

Abstract—Evaluation of the launch-version algorithms used by the European Space Agency (ESA) to derive wind field and ocean wave estimates from measurements of sensors aboard the European Remote Sensing satellite, ERS-1, is accomplished through comparison of the derived parameters with coincident measurements made by 24 open ocean buoys maintained by the National Oceanic and Atmospheric Administration (NOAA). During the period from November 1, 1991 through February 28, 1992, data bases with 577 and 485 pairs of coincident sensor/buoy wind and wave measurements were collected for the Active Microwave Instrument (AMI) and Radar Altimeter (RA) respectively. Based on these data, algorithm retrieval accuracy is estimated to be ± 4 m/s for AMI wind speed, ± 3 m/s for RA wind speed and ± 0.6 m for RA wave height. After removing 180° ambiguity errors, the AMI wind direction retrieval accuracy was estimated at $\pm 28^\circ$. All of the ERS-1 wind and wave retrievals are relatively unbiased. These results should be viewed as interim since improved algorithms are under development. As final versions are implemented, additional assessments will be conducted to complete the validation.

verted buoy winds and ERS-1 winds were paired only when the ERS-1 retrieval was both within a 200 km (for AMI) or 400 km (for RA) radius of the buoy and was further than 50 km from land. Only the single AMI and RA wind retrieval from each ERS-1 overpass which was closest in distance to the buoy was retained for inclusion in the data base. Since the average wind field could change as a function of distance from the buoy, the comparison error between sensor and buoy measurements can be expected to increase with increasing separation distance. It was therefore desirable to keep the separation distance small enough so as not to affect the comparison error but, at the same time, keep it large enough to collect a sufficient number of comparisons. This decision was especially critical for the RA validation. The information in Figure 1 is given as partial justification for a 400 km comparison window. This plot indicates that for the data used in this analysis there was no significant increase in comparison error between RA and buoy measurements of wave height and wind speed for separation distances up to 400 km.

1. Introduction

Validation of environmental algorithms used to retrieve ERS-1 estimates of over-ocean wind vectors from the Active Microwave Instrument (AMI) and wind speeds and significant wave heights from the Radar Altimeter (RA) was done by comparing those derived environmental parameters with measurements of the same made by 24 of the open ocean buoys maintained by the National Oceanic and Atmospheric Administration (NOAA). The buoys are of two basic types; standard buoys which make an 8.5-minute average of the wind once every hour and continuous-average buoys which make six consecutive 10-minute averages of the wind each hour. Buoy wind measurement accuracy for both buoy types is reported in [1] to be ± 0.5 m/s for winds less than 10 m/s and $\pm 5\%$ for winds greater 10 m/s. Buoy wind direction measurement accuracy is reported to be $\pm 10^\circ$. Both types of buoys measure the ocean significant wave height using a 20-minute average once every hour with a reported accuracy of ± 0.2 m. To prevent land contamination of the over-ocean AMI and RA backscatter measurements and to insure that land did not restrict the wind fetch distance necessary for creating fully developed seas, only buoys further than 90 km from land were chosen for the validation. See Table 1 for the list of buoys used in this study.

2. Method of Comparison

Comparisons of ERS-1 wind estimates with those from the buoys was done in accordance with the following criteria. All buoy wind speeds were converted to a reference level of 10 m using the ESA supplied FORTRAN computer software called UREF v1.01 [2]. Con-

Table 1. Location of the 24 NOAA buoys used in the validation. "Alt" is the buoy anemometer height. "Dist" is the buoy's approximate distance from land. (*) beside the buoy I.D. indicates a continuous average type buoy.

<u>I.D.</u>	<u>Lat</u>	<u>Lon(E)</u>	<u>Alt(m)</u>	<u>Dist(km)</u>
32302	-18.00	274.90	5.0	1010
*41001	34.89	287.14	5.0	240
41002	32.29	284.76	5.0	310
*41006	29.30	282.62	5.0	320
41010	28.88	281.47	10.0	180
*42001	25.93	270.35	10.0	330
*42002	25.93	266.41	10.0	350
*42003	25.94	274.09	10.0	380
42019	27.90	265.00	5.0	110
*44004	38.50	289.36	5.0	300
*44005	42.65	291.44	5.0	165
*44011	41.08	293.42	5.0	280
44014	36.58	285.17	4.0	90
44026	36.02	286.52	5.0	180
*46001	56.30	211.70	5.0	270
*46002	42.53	229.61	5.0	460
*46003	51.85	204.08	5.0	370
46005	46.08	229.00	5.0	500
*46006	40.81	222.35	10.0	1100
*46035	56.96	182.27	10.0	400
51001	23.42	197.66	5.0	220
51002	17.16	202.18	5.0	250
51003	19.18	199.18	5.0	360
51004	17.43	207.49	5.0	270

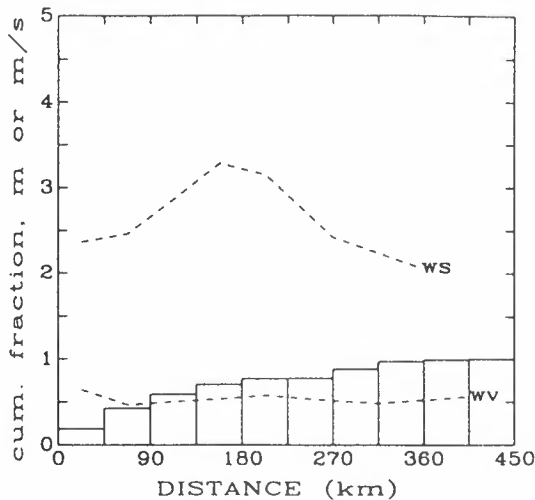


Figure 1. Cumulative histogram of the distance for RA measurements from the NOAA buoys. Dashed-line plots labelled *WS* and *WV* indicate the dependence of the RMS difference between RA and buoy measurements of wind speed (m/s) and wave height (m) upon the RA measurement distance from the buoy. The cause of the pronounced increase in RMS difference in *WS* with distance between 90 and 220 km is unknown.

To minimize the error resulting from comparisons of point measurements at the buoys with spatial averages from the satellite, it is necessary to insure equivalence of measurement by selecting the correct averaging time for the point measurement of the buoy. To this end, a vector average (for AMI) or scalar average (for RA) of the buoy measured winds in a time interval, T , centered on the ERS-1 overpass time was used for comparison with the ERS-1 wind speed retrievals. Pierson [3] suggests that when T is chosen to equal the sensor resolution cell diameter divided by the wind speed then "the averaging effect" is approximately the same for the buoy time series average and the satellite sensor spatial average. The resolution cell size for the AMI and RA is approximately 50 km and 18 km respectively. The Pierson averaging time for a buoy comparison with each of these instruments is plotted in Figure 2 as a function of wind speed. Careful application of the Pierson averaging technique is necessary since for large values of T one is likely to observe true changes in the average wind field in addition to random fluctuations about a constant wind field. As a result, the comparison error may actually increase for values of T which are too large. For this reason, T was not allowed to exceed 1 hour even when longer averaging times were specified. Errors associated with the current ERS-1 retrieval algorithms (especially for the AMI) appear to dominate the comparison error budget. Therefore, the small changes in the total comparison error resulting from the Pierson averaging can not be seen. The full effect of this technique should be apparent in later analysis when improved environmental algorithms are implemented. The comparison criteria for ocean wave estimates is similar to that for winds except that the UREF software does not apply and only the buoy measurement closest in time to the ERS-1 overpass is used.

This work is based on ERS-1 measurements made after November 1, 1991 which marked the conclusion of the engineering calibration and system check-out phase for the ERS-1 sensors. However, during the validation phase that followed, launch versions of the retrieval algorithms were revised several times. Therefore, the retrieval accuracy estimates resulting from this study represent the combined performance of several versions of

each algorithm and can only be considered tentative. A final assessment will be conducted when ESA completes current work on algorithm and model function improvement.

Using data collected during the period from November 1, 1991 to February 28, 1992, and the procedure described above, 1147 AMI/buoy coincident pairs were formed with only 577 being useful for validating AMI wind products. The balance of the 1147 coincident pairs had to be discarded because the AMI wind algorithm reported a default value of wind speed (an indication that the algorithm was unable or not allowed, as discussed below, to report estimates of wind speed and wind direction). A total of 485 coincident pairs were acquired for validating RA wind and wave products.

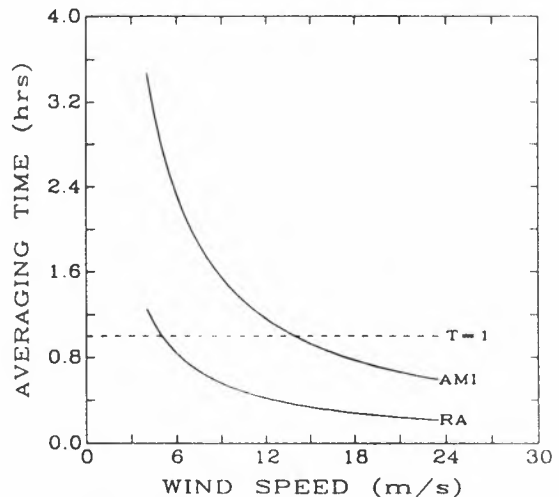


Figure 2. Pierson averaging time used to compare buoy measurements of wind speed to retrievals of the AMI and RA for the AMI measurement range of 4-24 m/s and the RA range of 4-15 m/s.

3. Analysis and Results

In the discussion that follows, "bias" refers to the average value of the quantity, (algorithm retrieval minus buoy measurement), and standard deviation, SD, refers to the root-mean-square value of the same quantity. Bias will be used to quantify the amount by which the ESA algorithms either underpredict or overpredict the true value of the environmental parameter. The SD is used to quantify the random error associated with the retrievals.

The histogram shown in Figs. 3 and 4 indicates the range and distribution of wind speeds found in the AMI and RA coincident pair data sets. Each figure contains two histograms; one for the buoy winds and one for the coincident ERS-1 algorithm derived winds. From Figure 3 it is clear that the AMI algorithm tends to bias its estimates towards low winds and does not report winds below 4 m/s. Since the AMI retrieval accuracy for low wind speeds was expected to be poor, algorithm retrievals below 4 m/s were not reported but were instead set to an invalid default wind speed of 51 m/s. The fact that the initial AMI wind algorithms underpredicted the true wind caused nearly 40% of the retrievals to appear to be less than 4 m/s when in fact only about 23% of the retrievals were made under conditions where the actual wind speed, according to buoys, was less than 4 m/s. The histogram in Figure 4 shows the RA wind speed algorithm to be performing somewhat better than the AMI algorithm. Figure 5 shows histograms of the coincident measurements of RA and buoy measured wave height and indicates a slight tendency for the wave height algorithm to favor a mean wave height of 2.5 m.

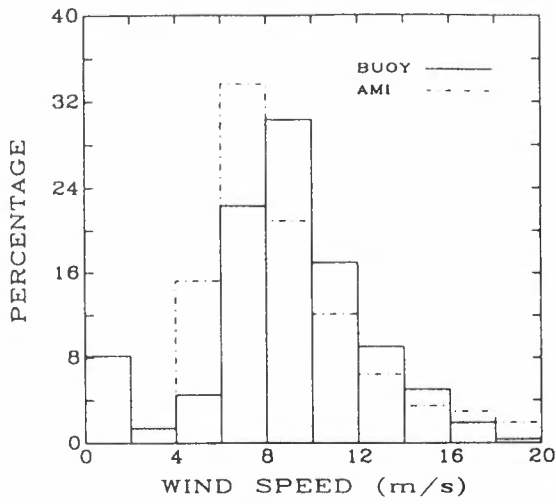


Figure 3. Distribution of buoy (solid line) and coincident AMI (dot-dash line) retrieved wind speed.

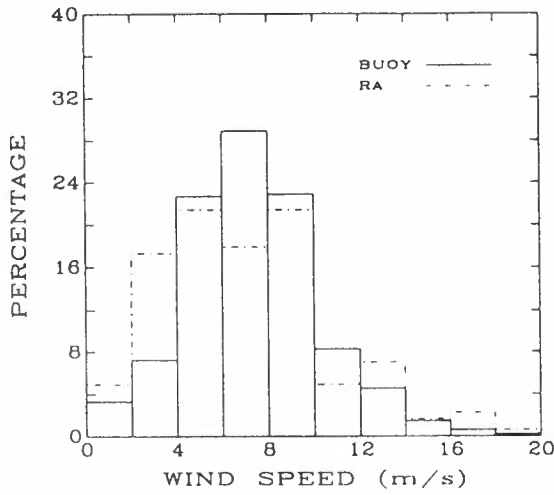


Figure 4. Distribution of buoy (solid line) and coincident RA (dot-dash line) retrieved wind speed.

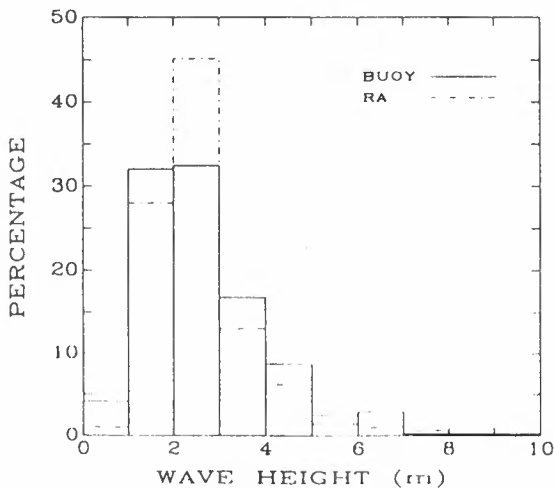


Figure 5. Distribution of buoy (solid line) and coincident RA (dot-dash line) retrieved wave height.

The scatterplots in Figs. 6, 7 and 8 indicate algorithm performance as follows: AMI wind speed: bias $+0.4$ m/s, SD 4.1 m/s; RA wind speed: bias -0.2 m/s, SD 3.0 m/s; RA significant wave height: bias -0.1 m, SD 0.6 m.

AMI wind direction is measured with respect to true north and is defined as the direction from-which the wind is blowing. Scatterplots of AMI vs buoy wind direction indicate that almost 50% of the AMI retrievals are in error by approximately 180° . The 180° ambiguity problem can be removed by using a folded scale for the scatterplot which is accomplished by subtracting 180° from both buoy and AMI wind direction when these quantities exceed 180° . Such a plot is shown in Figure 9 and in this context the AMI wind direction is found to have a bias of -1.4° and a SD of 28° .

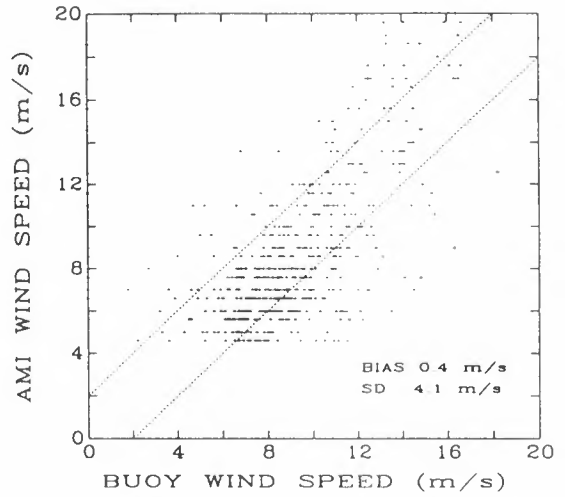


Figure 6. Scatterplot of the 577 coincident measurements of wind speed by the AMI and ocean buoys. The straight dotted lines indicate the ± 2 m/s error bounds.

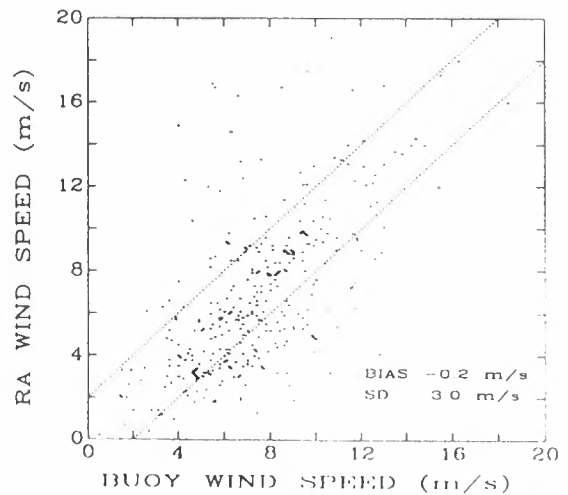


Figure 7. Scatterplot of the 485 coincident measurements of wind speed by the RA and ocean buoys. The straight dotted lines indicate the ± 2 m/s error bounds.

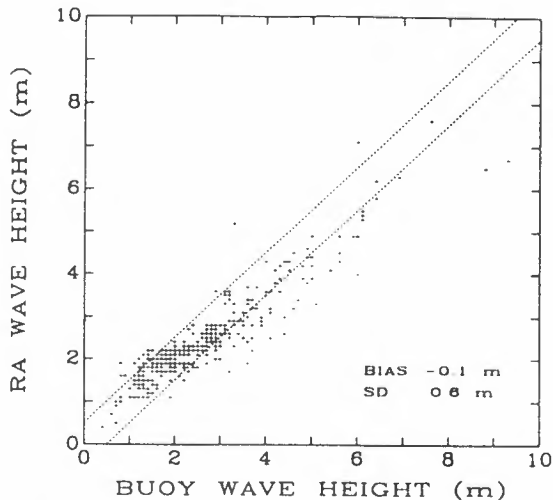


Figure 8. Scatterplot of the 485 coincident measurements of wave height by the AMI and ocean buoys. The straight dotted lines indicate the ± 0.5 m error bounds.

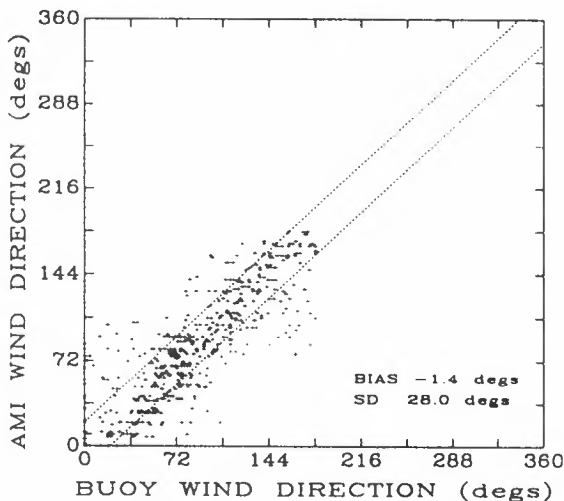


Figure 9. Scatterplot of the 577 coincident measurements of wind direction by the AMI and ocean buoys. The plotting scales have been folded to remove some 180° ambiguities in the AMI retrievals. The straight dotted lines indicate the $\pm 20^\circ$ error bounds.

4. Future Work

As more data becomes available, investigations will be undertaken to determine retrieval algorithm dependence upon such parameters as buoy type (standard or continuous-average), AMI beam incidence angle, and air/sea temperature differences. One method of studying these dependencies is to use residual plots. An example of this technique is given in Figure 10, which in general shows the AMI wind speed algorithm retrievals to be biased low at small incidence angles and to be biased high at larger incidence angles. Further evaluation of the Pierson [3] technique for averaging buoy measurements to reduce the comparison error is also planned.

Studies of buoy climatology for the NOAA network reveal an extremely low probability of occurrence for winds above 15 m/s. Therefore, aircraft underflights are planned during the 1992 hurricane season for the purpose of collecting sufficient data in the 15 m/s to 24 m/s range to complete the performance assessment of AMI wind speed algorithm.

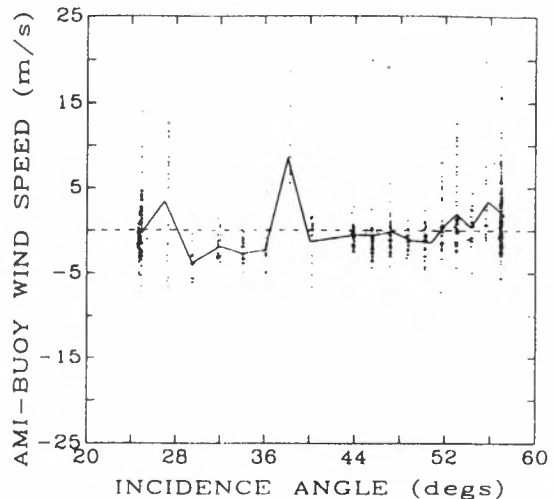


Figure 10. The difference between AMI and buoy measurements of wind speed plotted as a function of AMI fore-beam incidence angle. Note that the points in the plot fall into 19 vertical bins which correspond to the 19 beam positions in the AMI swath. The solid line is drawn through positions which are the average value of the points in each of the 19 bins.

5. Conclusions

Based on comparisons with ocean buoys during the period November 1, 1991 through February 28, 1992, the ESA operational algorithm(s) retrievals of AMI wind speed and RA wind speed are relatively unbiased with standard deviations of 4.1 m/s and 3.0 m/s respectively. After removing 180° ambiguity errors, AMI wind direction retrievals were found to be unbiased with a standard deviation of $\pm 28^\circ$. RA significant wave height retrievals are similarly unbiased with a standard deviation of 0.6 m. Because each of the ERS-1 wind speed and wave height algorithms underwent numerous changes during the validation period, the accuracy estimates presented here reflect the combined performance of several versions of each algorithm. Therefore, these performance figures can only be considered as interim assessments. As final versions of each algorithm are implemented, additional evaluation will be conducted to complete the validation.

References

- [1] Gilhousen, D.B., E.A. Meindl, M.J. Changery, P.L. Franks, M.G. Burgin, and D. A. McKittrick, "Climatic Summaries for NDBC Data Buoys and Stations", National Data Buoy Center publication, NSTL, Ms., 1990.
- [2] Ezraty, R., "Etude de L'Algorithme D'Estimation de la Vitesse de Frottement a la Surface de la Mer" IFREMER, no. 85.2.42.5000. ESA contract 6155/85/NL/BI, June 1985.
- [3] Pierson, W.J., The Measurement of the Synoptic Scale Wind Over the Ocean, *J. Geophys. Res.*, 88, 1683-1708, 1983.

AIRBORNE C-BAND SCATTEROMETER
MEASUREMENTS OBTAINED DURING UNDER
FLIGHTS OF THE ERS-1 SATELLITE IN THE GULF OF
MEXICO

S.C. Carson, R.E. McIntosh, M.A. Goodberlet
and C.T. Swift
Microwave Remote Sensing Laboratory
University of Massachusetts
Amherst, MA 01003

J.C. Wilkerson
Satellite Research Laboratory
National Environmental Satellite, Data and Information
Service, NOAA
Washington, D. C. 20233

ABSTRACT

A C-Band scatterometer was flown aboard a NOAA WP-3 aircraft during polar outbreaks over the Gulf of Mexico to collect backscatter data for comparison with coincident measurements from the Active Microwave Instrument (AMI) scatterometer aboard ERS-1. The objective was to assess ERS-1 scatterometer performance under a range of atmospheric instability conditions. Six flights produced measurements of winds from 2 to 15 ms^{-1} over a range of atmospheric stabilities (z/L) from -0.02 to -8.78. Comparison of radar cross sections from both airborne and satellite systems taken along the scatterometer's center beam show general agreement for all flights except for the lowest wind speed case of 2 ms^{-1} ($z/L = -8.78$) where the mean wind speed was half of the gust. Wind vector comparisons were possible in only four cases because ERS-1 retrievals were flag values of 51 ms^{-1} at 510 degrees for two flights. Comparisons showed rms discrepancies in wind speeds of as much as 4.8 m/s with rms direction differences as great as 80 degrees (6.7 degrees with the 180 degree ambiguity removed). In all cases, ambiguities in wind direction are due to the lack of a significant upwind /downwind ratio at C-Band. The normalized difference between the two scatterometer measurements increases dramatically for cases with $z/L < -1$ and also for cases where the time between the measurements was greater than 800 seconds.

INTRODUCTION

A C-Band scatterometer (C-SCAT) , installed on a NOAA WP-3D aircraft, was used to collect backscatter data in a series of flights over the Gulf of Mexico coincident the ERS-1 passage. The objective was to collect airborne scatterometer measurements over a wide range of wind speeds in unstable atmospheric conditions for assessment of the effect of instability on wind retrieval accuracy and

scatterometer performance. Six flights were carried out during the period November 12 - December 3, 1991 under conditions associated with polar outbreaks which produced high winds and atmospheric instability due to the strong air/sea temperature differences over the Gulf of Mexico. This operation was a joint effort by the National Oceanic and Atmospheric Administration (NOAA), and the National Aeronautical and Space Administration (NASA), and was carried out as part of the US contribution to ERS-1 validation.

INSTRUMENT

C-SCAT is a low power, incoherent pulsed scatterometer that uses a microstrip patch array antenna [1]. The antenna is positioned horizontally beneath the fuselage of the NOAA P-3 with a -2.5 degree pitch to offset the nominal upward pitch of the aircraft during flight, and its main beam can be steered from 18 to 50 degrees off nadir by changing the operating frequency from 5.75 GHz to 4.98 GHz. The operating frequency of the radar was adjusted during the course of the under flights so that nominal incidence angle of C-SCAT matched that of the center beam of the ERS-1 scatterometer to the within a degree. The patch array antenna is laminated onto a 1.3 meter aluminum disk, which is rotated via a drive shaft at approximately 20 rpm to obtain full azimuthal coverage with respect to the wind direction. The azimuthal pointing angle is measured using a 10 bit optical encoder, resulting in 0.3 degree angular resolution.

A diagram showing the measurement concept for C-SCAT is shown in figure 1.

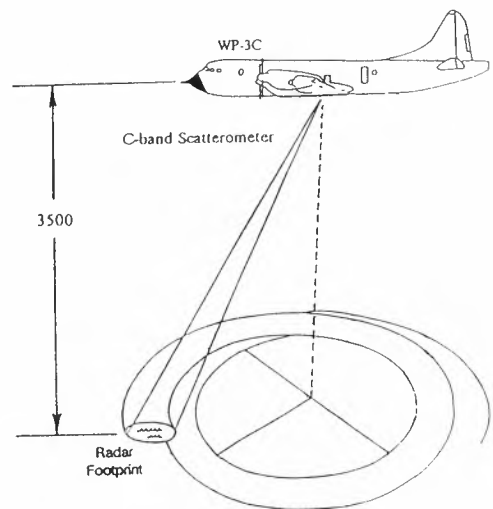


figure 1 Measurement concept for C-SCAT

CALIBRATION

C-SCAT is thermally controlled in order to minimize gain variations to 300 +/-1 K. During the collection of data, C-SCAT is internally calibrated every 90 seconds. This calibration consists of coupling the transmitter power into the receiver through an attenuator chain, followed by a separate measurement of the receiver noise.

C-SCAT was externally calibrated before and after the series of under flights. These calibration experiments were performed at the University of Massachusetts using a 1 meter corner reflector and a laser range finder. The calibration constants obtained before and after the underflights were within 0.7 dB of each other.

DISCUSSION

In order to minimize the time-dependent error inherent in comparisons of the σ^0 measurements made by C-SCAT to those made by the AMI scatterometer's center beam, flight schedules were arranged so that the aircraft arrived on station 30 minutes ahead of time and was midway through the 500 km swath and generally over a buoy as the satellite passed. See figure 2.

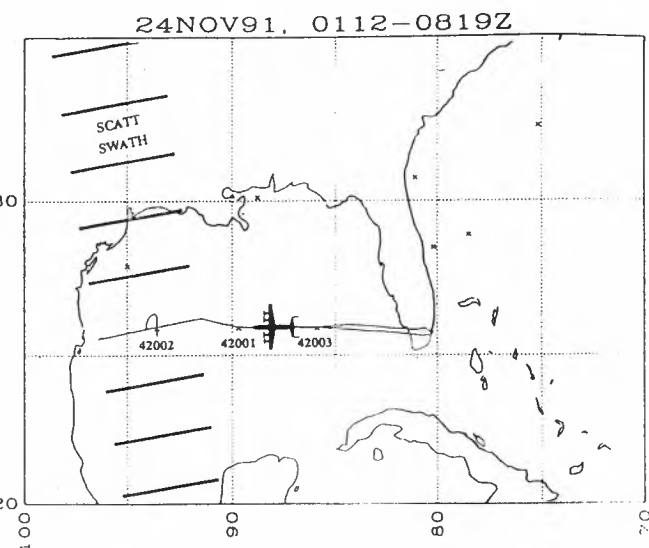


figure 2 ERS-1 underflight of Nov 24, 1991

The C-SCAT data was averaged along track to the same resolution as the AMI data, but the cross track swath of C-SCAT is completely dependent upon incidence angle and the altitude of the aircraft. The simultaneous underpasses

were performed at altitudes of 3400 to 3900 m, while the return trip across the swath was typically performed at 350 m. Nominal surface weather conditions for each flight are summarized in table 1.

Date	Wind Speed (m/s)	Gust (m/s)	Air-Sea Temp Diff (°C)	Wave Height (m)
Nov 12	2	3	-3.4	0.8
Nov 21	8	11	-5.5	2.3
Nov 24	15	17	-5.3	3.4
Nov 25	8	11	-9.4	2.3
Nov 26	5	7	-9.0	1.5
Dec 03	11	14	+0.1	2.3

Table 1 Summary of Surface Weather Conditions

The data presented in this paper do not include comparisons for the nearest range gate of the AMI scatterometer because the data taken by C-SCAT at an incidence angle of 18 degrees were noisy.

The center beam of the AMI scatterometer points at 82 degrees relative to true north on an ascending orbit, and 278 degrees relative to true north on a descending orbit. For the purposes of comparing the σ^0 measurements made by the two instruments, the C-SCAT data obtained for azimuth angles that were within +/- 3 degrees of the AMI measurements were included.

Although the antenna was installed to offset the nominal pitch of the aircraft and the pilots tried to fly as level as possible, some pitch and roll of the aircraft was experienced. In order to correct for the change in instantaneous incidence angle caused by the pitch and roll, all of the navigation data was recorded on a 1 second basis, and a time stamp was included with the radar data. A set of regression curves have been fit to the data of the form [2]

$$\sigma_{AB}^0 = A(\phi) + B(\phi) \log_{10}(\theta)$$

where θ is the incidence angle and ϕ is the azimuth angle relative to the wind direction. These curves were generated for upwind, downwind and cross wind data. They were then used to correct the data collected by C-SCAT from its initial incidence angle to the incidence angle at which the

AMI scatterometer measured the σ° of that particular cell. Fortunately, the difference in incidence angles was typically a degree or less, making the magnitude of this correction small.

The results of this analysis for the six flights are shown in figures 3 and 4. The data are plotted on a logarithmic scale and only the data from the simultaneous leg of the flight are included. The neutral stability wind speed and the Monin-Obukov stability parameter calculated from the buoy data recorded at the time of the overpass are shown on each plot. Figure 3 shows the data from all of the flights, and figure 4 shows all of the flights except November 12, 1991 as the data from this day show significantly more discrepancy between the two measurements

The unstable cases with low wind speed such as the data from November 12, 1991 show significantly more deviation than the higher wind speed cases, like the data from November 21. This is an expected result. The buoy data from November 12 shows the neutral stability wind speed was 1.6 ms^{-1} with wind gusts of 2.5 ms^{-1} . Thus, the wind speed was extremely variable in terms of deviation from the 10 minute average recorded by the buoy, both in time and space.

Figure 5 shows the normalized difference in σ° as a function of the time difference between the AMI and C-SCAT measurements for all of the days. The dashed lines indicate the mean plus one standard deviation and the mean minus one standard deviation. After approximately 800 seconds, a dramatic increase in the variance is observed.

Figure 6 shows the normalized difference between the AMI and C-SCAT measurements as a function of the stability parameter of the closest buoy reading. a dramatic increase in the variance is observed for the cases of $z/L < -1$.

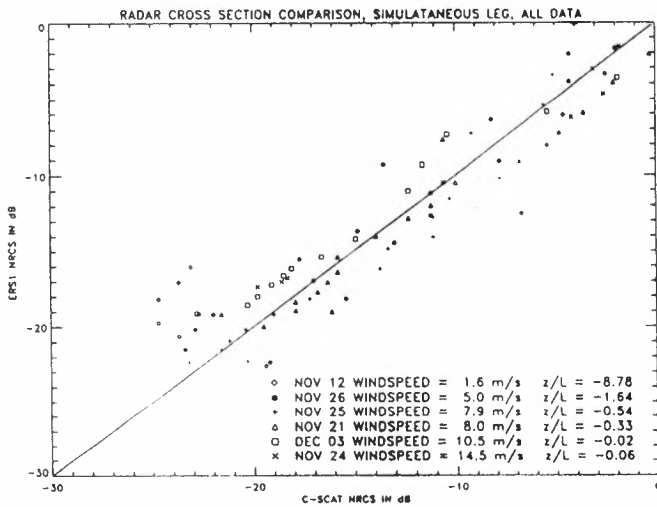


figure 3

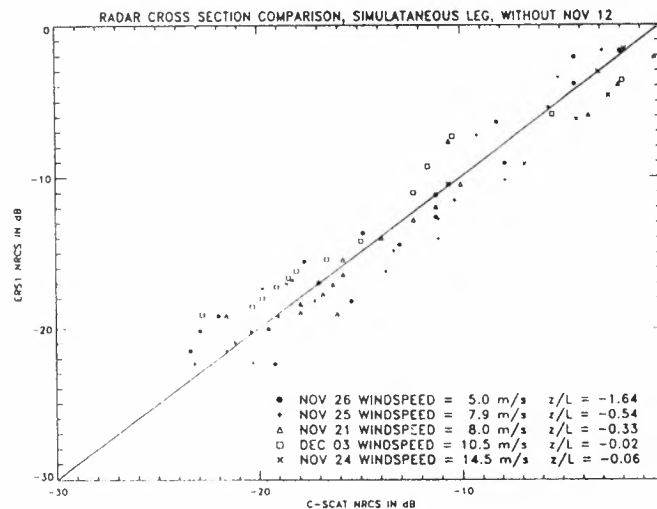


figure 4

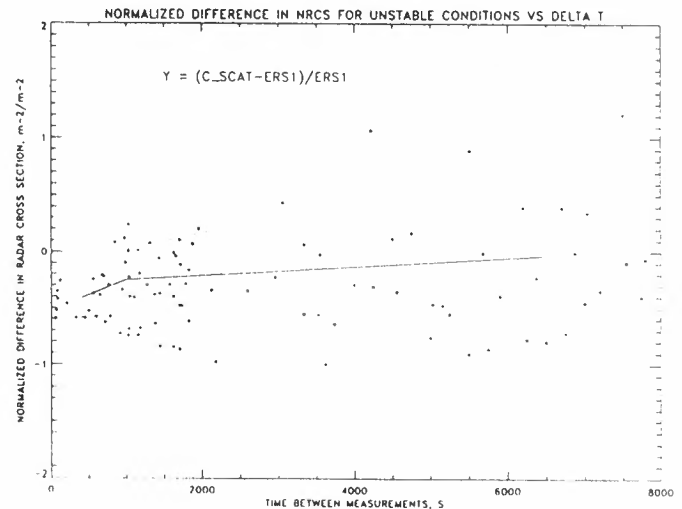


figure 5

Table 2 shows a summary of the average and rms differences in σ° and the rms differences in wind speed and direction. The wind speed and direction values for the ERS-1 satellite were flagged on November 12, and November 26. The data included in these calculations were obtained within ± 30 minutes of the overpass of the satellite. The last column of table 2 shows the difference between the σ° measured by the AMI scatterometer and C-SCAT at the exact time of over pass in dB. This data is collected at only one incidence angle for each flight, and was used to eliminate calibration differences in figures 3 and 4. The rms difference in wind direction was calculated

with the 180 degree ambiguity (ΔDir) and with the ambiguity removed (ΔDir_{res}).

Date	$\Delta\sigma_{ave}^{\circ}$	$\Delta\sigma_{rms}^{\circ}$	$\Delta Speed$ (m/s)	ΔDir degrees	ΔDir_{res} degrees	$\Delta\sigma_{opass}^{\circ}$ dB
Nov 12	0.29	0.71	-----	-----	-----	6.95
Nov 21	0.26	0.34	2.6	80.2	6.9	1.90
Nov 24	0.31	0.40	4.8	66.7	6.5	2.12
Nov 25	0.36	0.45	3.6	92.7	4.8	2.71
Nov 26	0.22	0.34	-----	-----	-----	1.82
Dec 03	0.34	0.47	3.2	76.7	6.0	3.94

Table 2 Summary of Comparisons between scatterometers

A mean offset was calculated from the data in table 2, omitting the data from November 12, yielding a relative calibration difference of 2.66 dB. This was added to the C-SCAT data in figures 3 and 4. These data indicate that the two instruments agree reasonably well for data with winds ranging from 5 to 14.5 ms^{-1} and the Monin-Obukov stability parameter in the range from the $-1.66 < z/L < -0.02$.

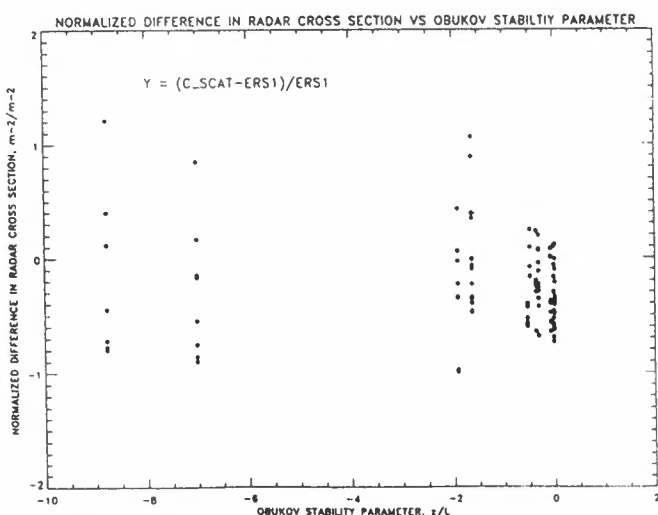


figure 6

Figure 7 shows some typical C-SCAT data versus azimuth. Each point on this plot is the average of 200 independent samples. This data illustrates the very low upwind/downwind ratio that characterizes almost all of the data taken during this measurement campaign.

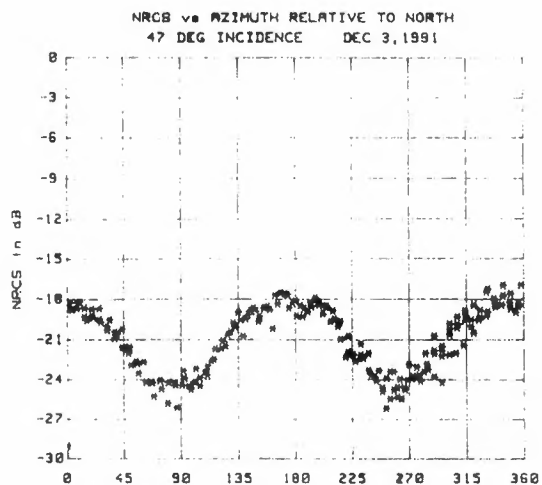


figure 7

The wind speed estimates were obtained using a power law fit of the form

$$\sigma^{\circ} = G(\theta, \phi) U(10)^{H(\theta, \phi)}$$

where G and H are fit coefficients and U(10) is the neutral stability wind speed at 10 meters. This method was chosen because it allows for a closed form solution for wind speed [2]. A one dimensional search was then performed in wind direction to minimize the rms error. This search was done in 5 degree steps. The sixth column of table 2 shows a comparison of wind direction if the 180 degree ambiguities are removed.

Figure 8 illustrates the results obtained using this method on the C-SCAT measurements for December 3, 1991. The 180 degree ambiguity is the result of the low upwind/downwind ratio discussed earlier.

CONCLUSION

A preliminary analysis of the data from this series of flights shows a 2.66 dB calibration bias, but otherwise general agreement between the airborne C-SCAT σ° measurements and the measurements made by the AMI scatterometer for all cases except for November 12. The lack of agreement on this day is probably due in large part to atmospheric conditions. The mean wind speed was roughly half of the

gust, indicating a very high degree of spatial and temporal variability. The differences in the measurement geometries of the spacecraft and the aircraft systems lead to sampling differences which can not be reconciled under these conditions. In order to achieve comparable measurements the C-SCAT data must be averaged in time to the same spatial scale as the AMI

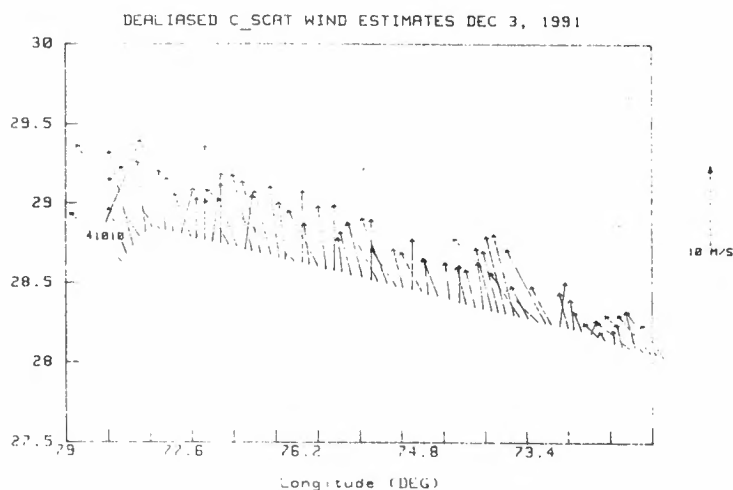


figure 8

scatterometer data. When the atmospheric conditions are extremely variable, as they were on November 12, this approach is not valid.

Examining the relative difference between the two measurements as a function of the temporal separation of the measurements shows that σ^2 of the ocean surface changes dramatically under these atmospheric conditions after approximately 800 seconds, as indicated by the increased variance as seen in figure 5. This indicates a limit on the length of time a σ^2 measurement can be assumed to be valid under these atmospheric conditions. This conclusion has implications not only for the validation of the AMI scatterometer, but also for the end users of scatterometer generated wind estimates.

Additionally the relative difference between the two measurements as a function of the Monin-Obukov stability parameter showed a marked increase in variance when $z/L < -1$. This is due to spatial and temporal variability associated with unstable atmospheric conditions. The Monin-Obukov stability parameter is roughly proportional to the inverse of the square of the wind speed, and therefore the large negative values of z/L occur at low wind speed. At low wind speed, the gust is a much larger percentage of the mean wind speed, implying a greater temporal

variability than under conditions with a high mean wind speed. Unstable atmospheric conditions may lead to phenomena such as the formation of longitudinal vortex rolls extending in the downwind direction [3]. This causes a significant increase in the spatial variability of the wind drag on the ocean surface, resulting in a highly variable radar cross section signature of the ocean surface.

The swath width of C-SCAT perpendicular to the aircraft flight path of the aircraft is on the order of 5 km. While the data can be averaged along the aircraft track to the same resolution as the AMI scatterometer data, the swath width of C-SCAT is determined by the height of the aircraft and the incidence angle. This results in the C-SCAT measurements sampling an area only a tenth as wide as the AMI scatterometer. This may lead to significant differences under unstable atmospheric conditions, when variability on subresolution size scales becomes important.

The full azimuthal coverage of the airborne measurements indicates that the 180 degree ambiguities in wind direction are the result of the lack of a significant upwind/downwind ratio at C-Band. This ambiguity must be resolved by other techniques

REFERENCES

- [1] McLaughlin, D.J., R.E. McIntosh, A. Pazmany, L.Hevizi, E. Boltinew, "A C-Band Scatterometer for Remote Sensing of the Air-Sea Interface", IEEE Transactions on Geoscience and Remote Sensing, vol. 29, pp 260-267, March, 1991
- [2] Chong-Yung Chi and F. Li, "A Comparative Study of Several Wind Estimation Algorithms for Spaceborne Scatterometers", IEEE Transactions on Geoscience and Remote Sensing, vol. 26, no.2 pp 115-121, March, 1988
- [3] Wipperman, F.K., D. Etling, and H.J. Kirstein, "On the Instability of a Planetary Boundary Layer with Rosby Number Similarity", Boundary-Layer Meteorology, vol. 15, pp 301-321, 1978

The Grand Banks ERS-1 SAR Validation Experiment

P.W. Vachon
Canada Centre for Remote Sensing
588 Booth St.
Ottawa, Ont. K1A 0E4

F.W. Dobson
Bedford Institute of Oceanography
P.O. Box 1006
Dartmouth, N.S. B2Y 4A2

J.R. Buckley
Royal Roads Military College
FMO Victoria, B.C. V0S 1B0

D. Vandemark & E.J. Walsh
Wallops Flight Facility
NASA/Goddard Space Flight Center
Wallops Island, VA 23337

Abstract

The ERS-1 synthetic aperture radar (SAR) wave spectra validation experiment was carried out over The Grand Banks of Newfoundland in November 1991. The principal objective of the experiment was to obtain complete sets of wind and wave data from a variety of calibrated instruments to allow validation of SAR measurements of ocean wave spectra. This paper describes the field program activities and summarizes the rather complex wind and wave conditions which were observed. We provide initial spectral comparisons with ERS-1 SAR image spectra. The ERS-1 SAR is shown to have reliably measured swell and range travelling wind seas as short as 100 m in wave length. Azimuth travelling wind seas were not reliably measured at any time during the experiment by the ERS-1 SAR.

1 Introduction

The European Space Agency's ERS-1 satellite [1] was launched in July 1991. One aspect of the validation of this satellite's instrument package is the assessment of the capability of the ERS-1 synthetic aperture radar (SAR) to measure geophysical phenomena related to wind and waves [2]. The subject of this paper is the "ERS-1 SAR wave spectra validation project" which is one aspect of the ERS-1 geophysical calibration and validation activities. The objective is to use the information collected during this field program to assess the capability of the ERS-1 SAR, and other SARs in general, for the reliable measurement of ocean wave spectra and the utilization of such SAR-derived spectra in operational wave prediction models.

The field component of the validation experiment was carried out from 10 to 27 November, 1991. During this time, there were 12 ascending and descending ERS-1 SAR passes over a cross-over node located on the Grand Banks of Newfoundland about 100 nm south-east of St. John's (Fig. 1).

The cross-over node formed the principal validation site and was the focus of the *in situ* measurements taken from the Bedford Institute of Oceanography (BIO) research vessel *CSS Hudson*. The *in situ* measurements were centred on grid points for the Canadian Spectral Ocean Wave Model (CSOWM) [6] (see Fig. 1; Table 1) and included up to three wave buoys (two directional Wavec buoys and one non-directional Waverider buoy), up to four meteorological buoys, two marine radars mounted on *Hudson*

Table 1: CSOWM grid point and mooring locations.

CSOWM		location	d (m)	moorings
coarse	fine			
1261	2562	N46.6 W51.0	96	Minimet, Padirt, BIO Wavec
	2519	N46.6 W50.5	94	MEDS Wavec
	2561	N46.3 W51.0	91	
	2518	N46.3 W50.5	79	Waverider
	2560	N45.9 W51.0	78	AES 4 m Discus
	2474	N45.9 W50.0	70	AES Nomad

(by Royal Roads Military College (RRMC) and MacLaren Plansearch (1991) Ltd.) for wave measurements, a bow-mounted anemometer for wind-stress measurements, and an acoustic Doppler current profiler to survey the ocean current field. The Soviet research vessel *G. Ushakov* was also on site taking meteorological measurements for a portion of the program.

In addition to the ship-based programs, at the times of the ERS-1 SAR passes the validation site was overflown by up to two aircraft radar sensors (Table 2). Specifically, the Canada Centre for Remote Sensing (CCRS) CV-580, carrying a C-band SAR, overflew the location on seven occasions, and the National Aeronautics and Space Administration (NASA) P-3, carrying a surface contour radar (SCR) or a radar ocean wave spectrometer (ROWS) and the AAFE radar altimeter, overflew the location on four occasions (nearly coincident with CCRS aircraft flights). Also, a high frequency radar station located at Cape Race, Newfoundland will provide estimates of wave height, wind and surface current on a 10-by-10 km grid over the area of radar coverage (essentially the sector from 60° to 180° (T) extending 150 km from Cape Race).

In this paper, we first review the wind and wave conditions over the duration of the field program. We then present the processing procedures and some initial spectral analysis results and comparisons from the ERS-1 and CV-580 SARs, a directional wave buoy, the RRMC marine radar, and the NASA P-3 ROWS or SCR.

2 Wind and Wave Conditions

The ERS-1 wave spectra validation program was successful in acquiring data under a variety of wind and wave conditions (Figs. 2 and 3). For example, near

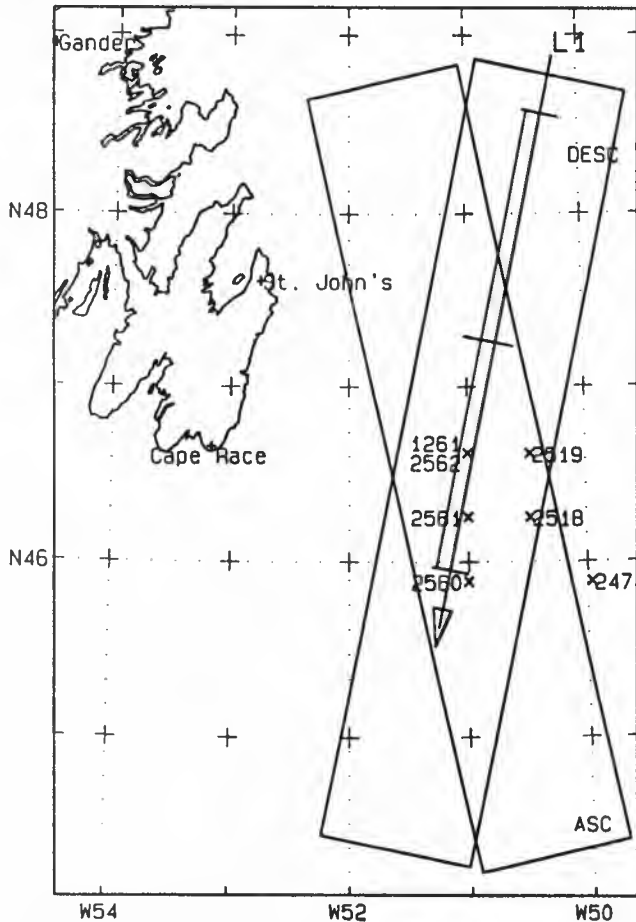


Figure 1: A map of the study area showing the extent of ascending (ASC) and descending (DESC) pass ERS-1 SAR coverage, and typical CV-580 SAR coverage (L1) for the descending ERS-1 pass. The locations of the key CSOWM grid points are indicated.

the times of the ERS-1 SAR passes, wind speeds ranged from about 4 to 15 m/s and peak wave heights up to 6 m. In addition, as many as four separate wave modes were observed and resolved by some of the wave measuring sensors (Fig. 4). While this range of conditions cannot be considered to be extreme, we will be able to study the capability of the SAR in complex real-world conditions.

3 Spectral Comparisons

3.1 ERS-1 SAR

ERS-1 C-band VV polarization SAR imagery were collected and processed to standard image products (SGF product corresponding to a six look (summed in power) scene with 8000-by-8000 samples and 12.5 m sample spacings in azimuth and ground-range) at CCRS's Gatineau station. Representative ERS-1 SAR image spectra were calculated for each over-

Table 2: ERS-1 pass times.

Nov	Abs. Orb.	Rel. Orb.	Time UTC	CV-580	P-3	CSS Hud.	RV Ush.
11	1684	11D	14:14	1		1261	
12	1691	18A	01:33			1261	
14	1727	11D	14:14	2	1	2518	
15	1734	18A	01:33	3	2	2518	
17	1770	11D	14:14	4		1261	
18	1777	18A	01:33	5	3	2519	
20	1813	11D	14:14	6	4	2519	1261
21	1820	18A	01:33			2519	1261
23	1856	11D	14:14	7		1261	
24	1863	18A	01:33			1261	
26	1899	11D	14:14				
27	1906	18A	01:33				

pass based upon a 1024-by-1024 pixel subscene chosen in the vicinity of *Hudson*. The subscene was further broken down into nine 512-by-512 pixel regions, each overlapping by 50%, which were detrended, windowed, and then two-dimensional Fourier transformed. The periodograms from the nine were averaged to create a preliminary spectrum. Subsequently, the system transfer function and speckle bias were estimated and removed [3,10] and the spectrum was high pass filtered, smoothed, rotated, and interpolated to a regular wavenumber grid in geophysical coordinates.

3.2 CV-580 SAR

CV-580 C-band VV polarization SAR imagery [8] were collected on seven different occasions during the experiment. The flights were timed such that the CV-580 arrived at the *Hudson* location at the time of the ERS-1 SAR pass. The CV-580 SAR imagery were processed in real time (nadir mode image product corresponding to a seven look (summed in voltage) swath of 4096 slant-range samples with 3.89 m sample spacing in azimuth and 4.0 m in slant-range). Representative CV-580 SAR image spectra were calculated for each overpass based upon a 512 pixel in slant-range by 2048 pixel in azimuth subscene in the vicinity of *Hudson*. The subscene location was chosen to minimize the incidence angle, maximize the wave signal-to-noise ratio, and avoided a range-oriented image artifact caused by ERS-1. The subscene was further broken down into seven 512-by-512 pixel regions, each overlapping by 50%, which were slant-range to ground-range converted, detrended, windowed, and two-dimensional Fourier transformed. The periodograms from the seven were averaged to create a preliminary spectrum. Subsequently, the system transfer function and speckle bias were estimated and removed and the spectrum was scanning distortion corrected [12], resulting in an asymmetrical spectrum. Finally, the spectra were high pass filtered, smoothed, rotated, and interpolated to a regular wavenumber grid in geophysical coordinates.

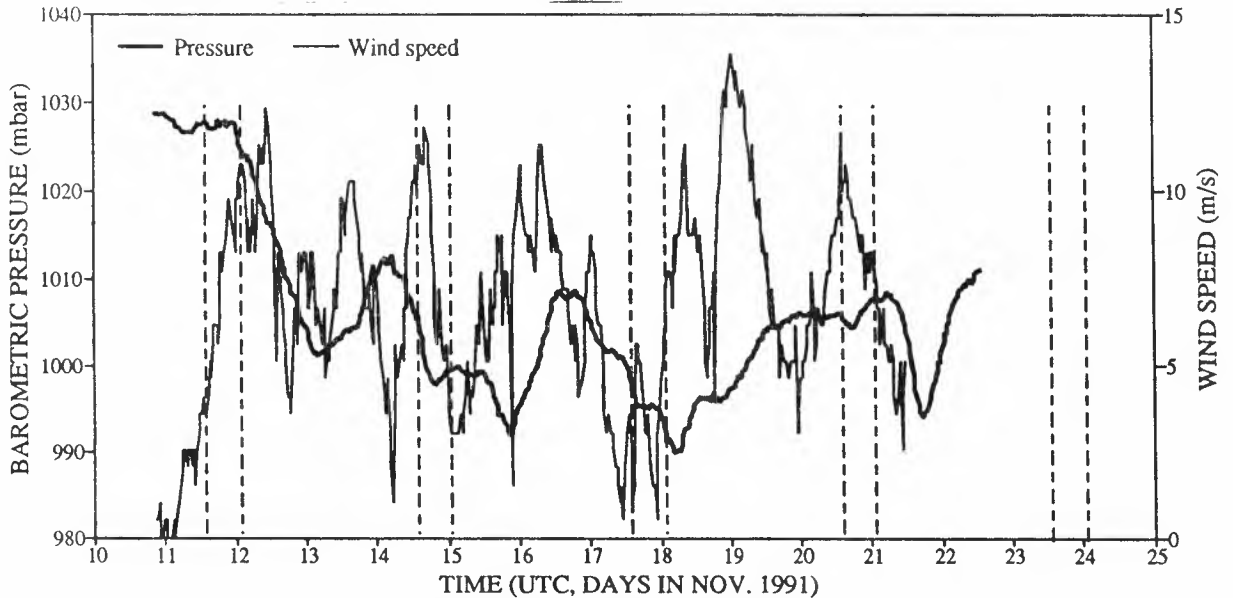


Figure 2: Time series of barometric pressure and wind speed measured by the Minimet buoy near CSOWM grid point 1261. ERS-1 pass times are marked by the vertical dashed lines.

3.3 Wavec Buoy

The Marine Environmental Data Service (MEDS) Datawell Wavec surface following heave, pitch, and roll buoy was moored at CSOWM grid point 2519 during most of the field program. Unfortunately, data were not available for the ERS-1 passes on Nov. 15 and 17 since the buoy had been removed to correct a problem with the data transmission link. Once each hour, the buoy internally recorded 4096 samples of heave, pitch, and roll at a rate of 2 Hz. The resulting time-series were Fourier transformed and cross-spectra for the three variables were calculated. Directional wavenumber slope spectra were calculated from the cross-spectra using a maximum entropy technique [9]. In this paper, we present directional slope spectra with a “going to” directional convention.

3.4 RRC Marine Radar

The RRC X-band radar system was one of two marine radar systems which were mounted on *Hudson* and dedicated to the measurement of ocean waves. The RRC system combined a standard ship navigation radar with a radar video digitizer and scan converter. The output of the digitizer was proportional to the strength of the reflected radar signal. The digitizer sampled 1024 bins along each of 1024 radials for a single radar sweep. The data were converted in real-time to a 512-by-512 pixel grid and archived. Images were collected in groups of 16 every half hour during the three hours around each ERS-1 pass.

The radial dependence of reflected radar amplitude was removed empirically from each image. Eight regions were selected, each 64-by-64 pixels in size and spaced evenly around the radar location at equal radial distances from *Hudson*. Data in each region were windowed and a three-dimensional Fourier transform

calculated. The third dimension, gained from the time sequence of images [13], assisted in resolving the 180° directional ambiguity inherent in a two-dimensional Fourier transform of image data. Spectra from all eight regions were averaged together, thus minimizing effect of the azimuthal dependence of the modulation transfer function.

3.5 NASA P-3 SCR and ROWS

A NASA P-3 flew on four occasions during this experiment. Although the ROWS was the principal instrument, the SCR was available as a back-up and was used on Nov. 14 when there was a ROWS failure. The P-3 flights were coincident with CV-580 flights, and timed such that the P-3 overflew the *Hudson* location within one-half hour of the ERS-1 SAR pass.

The ROWS is a 14 GHz pulse-compressed radar system for measurement of directional wave spectra [5]. During ERS-1 validation, the ROWS was electrically cycled between two measurement modes at a 50 Hz rate. The ROWS spectrometer mode is used to measure wave spectra, while the altimeter mode is used to derive estimates of ocean surface wave height and surface wind. The ROWS spectrometer mode, operated at an altitude of 22,000', senses radar reflectivity variations associated with ocean wave tilt as a function of slant-range, using a near-nadir pointing, conically scanning antenna. The ROWS altimeter mode switches the RF transmit and receive path to a nadir pointing broad beam-width antenna. Digitization of both modes is done using a PC-based data system.

The ROWS wave product is reflectivity modulation-variance spectra, which may be interpreted as directional wave slope spectra. Spectra are derived by Fourier transforming each of 20 azimuth sector reflectivity estimates versus range. The reflectivity estimate is the azimuthal average of 25 returns in a given sector and is converted to surface coordinates,

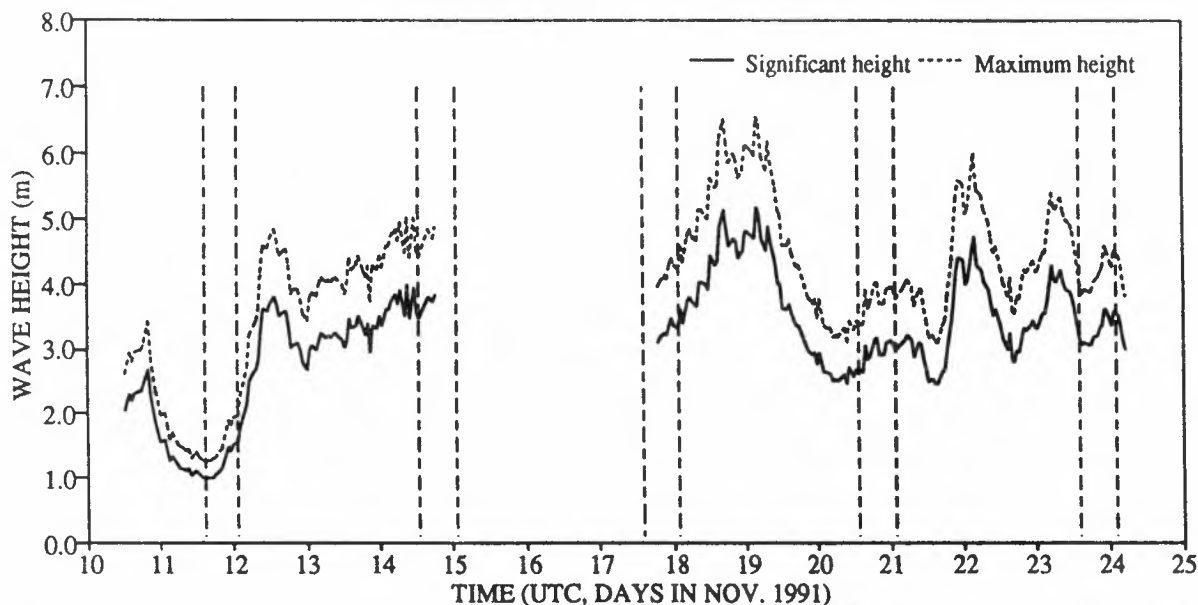


Figure 3: Time series of significant and peak wave height measured by the MEDS Wavec buoy near CSOWM grid point 2519.

motion corrected, normalized to eliminate antenna and radar cross-section contributions, and windowed. The data are high-pass filtered and smoothed. Typically, 10 to 15 revolutions are averaged to produce one spectral estimate.

The term SCR used in this paper actually refers to the replacement Scanning Radar Altimeter (SRA), a mode of the 36 GHz Multi-mode Airborne Radar Altimeter [11]. The system scans a narrow pencil beam across the aircraft ground track at 3800' altitude, and measures the slant-range to 64 points across the swath and converts them to a map of surface elevation. Post-flight data processing uses a two-dimensional Fourier transform to derive directional wave height spectra. The spectra are scanning distortion (Doppler) corrected and spectra from crossing lines are used to resolve ambiguities in the propagation direction. Typically, directional wave spectra are estimated at 6 to 7 km intervals along the aircraft flight path.

3.6 Results

In Fig. 4, we present initial spectral comparisons from our experiment. All spectra are in a directional wavenumber format using a "going to" convention. For the unimodal swell cases of Nov. 15 and 18, spectra from all available sensors appear to be similar. For the more complex cases of Nov. 14 and 20, there is little general agreement between sensors in the number and locations of spectral peaks.

The comparison between spectra from the two SARs is of interest due to the significant difference in the platform height-to-velocity ratio (h/V). It is well-known that the degree of nonlinearity in velocity bunching mapping is strongly governed by the magnitude of this key parameter. The ERS-1 SAR is characterized by $h/V \sim 120$ s, which is typical for polar orbiting SAR platforms. On the other hand,

the CCRS SAR was operated such that h/V was minimized, subject to radar and aircraft operational constraints. The aircraft SAR data is characterized by $h/V \sim 15$ s, suggesting that it should be possible to image a much wider range of ocean wave conditions without introduction of significant spectral distortion.

On Nov. 14, the CV-580 SAR, the Wavec buoy, and the SCR detected a wind sea mode of about 40 m wave length propagating towards the east. Waves of this scale are not represented in the contour plots of Fig. 4, which terminate at a wave length of 75 m.

We draw the following observations from the spectra presented in Fig. 4:

- the observed sea conditions during the experiment were very complex with up to four distinct wave modes having been present and resolved by some of the sensors;
- both SARs have accurately measured the longest scale waves (swell) present at the time of data acquisition;
- the ERS-1 SAR has not measured any azimuth travelling waves less than 200 m in wave length, which we interpret as one effect of the limitation introduced by the large h/V associated with the satellite geometry;
- the ERS-1 SAR has measured range travelling waves as short as 100 m in wave length,
- the airborne SAR has measured the shorter wave modes measured by other systems;
- the spectral contrast of the swell for the ERS-1 SAR spectra is larger than for the CV-580 SAR spectra, due to the scaling of the velocity bunching transfer function with h/V ; and

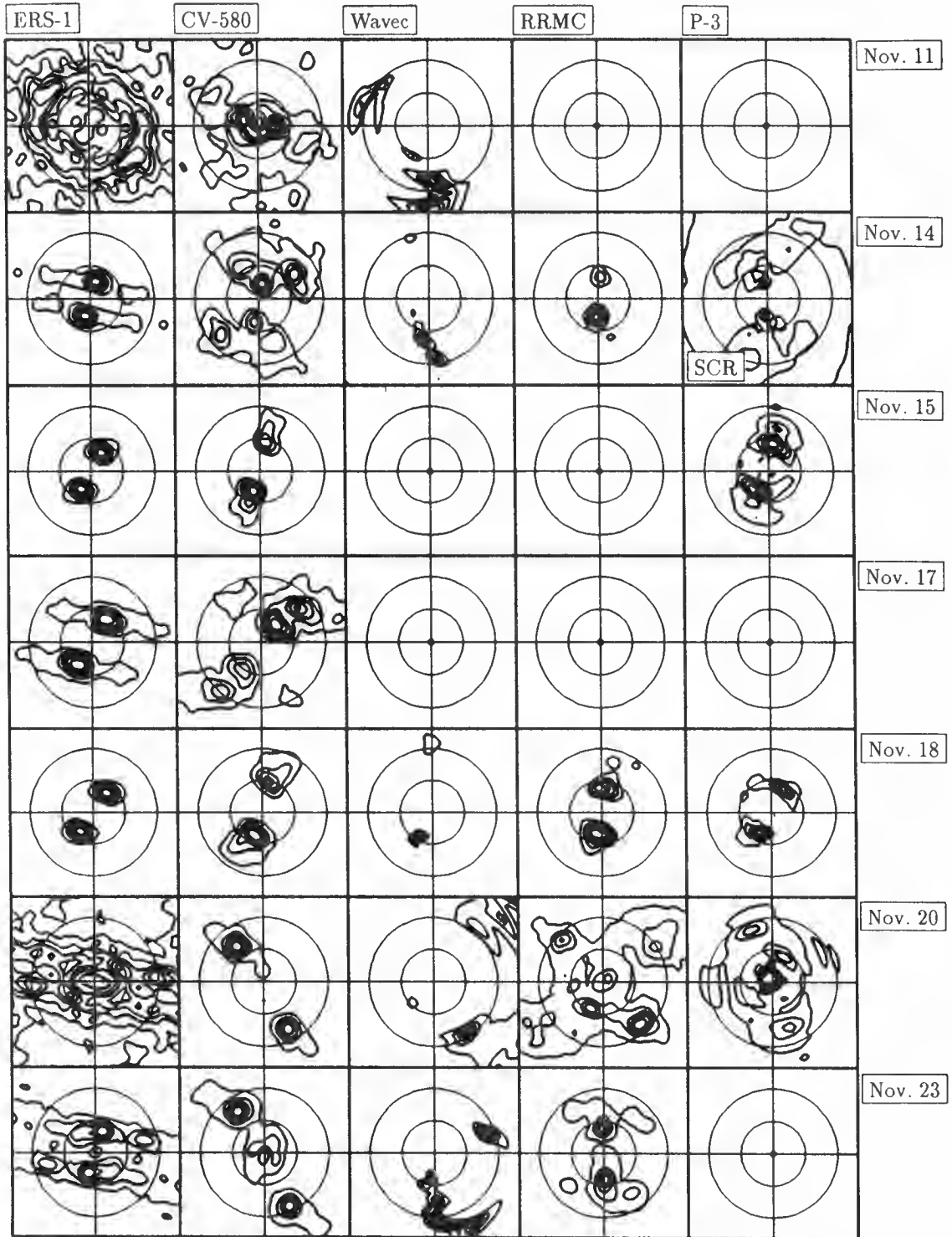


Figure 4: Initial spectral comparisons between ERS-1 SAR image spectra, CV-580 SAR image spectra, Wavec buoy slope spectra, RRMC marine radar spectra, and NASA P-3 SCR or ROWS spectra. All data were taken near the ERS-1 pass times on the indicated dates and processed as noted in the text. In each case, six contours have been used with respect to the spectral maximum. The outer circles represent constant wave lengths of 200 m (inner) and 100 m (outer). The spectra are oriented such that north is up.

- the ambiguous spectral lobe present in most of the spectra (especially those derived from imagery as an intermediate step) appear to have obliterated some genuine wave modes.

It is apparent that useful ocean wave information for swell can be provided by the ERS-1 SAR.

4 Summary

In this paper, we have summarized the ERS-1 SAR wave spectra validation project which took place over The Grand Banks of Newfoundland in November 1991. This project has provided a variety of wave information sources under many wind and wave conditions. We are now in the analysis phase of the project.

Some of the main issues we wish to address with this data set are the extraction of ocean wave information from the two sources of SAR imagery, considering both linear [10] and nonlinear [4,7] velocity bunching models, and the validation of that information against the other available wave measurements. We will then study the issues related to the assimilation of that information into ocean wave prediction models, culminating with an operational demonstration by the winter of 1994.

5 Acknowledgements

We dedicate this experiment to Nelson Freeman. We miss him greatly.

Many individuals have contributed to the successful acquisition of this data set and to the analysis which is now proceeding. In particular, we wish to note the efforts of the crews of the CCRS CV-580, the NASA P-3, and *CSS Hudson*. Site specific weather and wave forecasts were provided free of charge by AES and by Ocean Routes, Inc. during the field program. MEDS serviced the Wavec buoy and provided information from it during the field program. AES deployed and serviced their two meteorological buoys with the assistance of the Coast Guard. We thank D. Clem and B. Chapron for their efforts to secure the participation of the NASA P-3 and assistance with data processing. The SAR spectra were processed by A.S. Bhogal (CCRS), the Wavec spectra by B. Toulany (BIO), and the marine radar spectra by M. Allingham (RRMC). We thank our families for their support and encouragement.

References

- [1] Attema, E., and R. Francis, "ERS-1 calibration and validation", *ESA Bulletin*, ERS-1 special issue, No. 65, 1991, pp 80-86.
- [2] Attema, E.P.W., "The active microwave instrument on-board the ERS-1 satellite", *Proc. IEEE*, Vol. 79, No. 6, 1991, pp 791-799.
- [3] Beal, R.C., D.G. Tilley, and F.M. Monaldo, "Large- and small-scale spatial evolution of digitally processed ocean wave spectra from SEASAT synthetic aperture radar", *J. Geophys. Res.*, vol. 88, No. C3, 1983, pp 1761-1778.
- [4] Hasselmann, K., and S. Hasselmann, "On the nonlinear mapping of an ocean wave spectrum into a synthetic aperture radar spectrum and its inversion", *J. Geophys. Res.*, Vol. 96, No. C6, 1991, pp 10,713-10,730.
- [5] Jackson, F.C., "Directional Spectra from the Radar Ocean Wave Spectrometer during LEWEX", *Directional Ocean Wave Spectra*, Ed. R.C. Beal, Johns Hopkins University Press, Baltimore, 1991.
- [6] Khandekar, M.L., and R. Lalbeharry, "A forecaster's guide to the Canadian spectral ocean wave model", AES research report ARD-90-007, Atmospheric Environment Service, Downsview, Ont., Sept. 1990.
- [7] Krogstad, H.E., "A simple derivation of Hasselmann's nonlinear ocean-SAR transform", *J. Geophys. Res.*, Vol. 97, No. C2, 1992, pp 2421-2425.
- [8] Livingstone, C.E., A.L. Gray, R.K. Hawkins, and R.B. Olsen, "CCRS C/X-airborne synthetic aperture radar: an R and D tool for the ERS-1 time frame", *IEEE AES Magazine*, Vol. 3, No. 10, pp 11-20, 1988.
- [9] Lygre, A. and H.E. Krogstad, "Maximum Entropy Estimation of the Directional Distribution of Ocean Wave Spectra", *J. Phys. Oceanography*, Vol. 16, pp 2052-2060, 1986.
- [10] Monaldo, F.M., and D.R. Lyzenga, "On the estimation of wave slope- and height-variance spectra from SAR imagery", *IEEE Trans. Geoscience Rem. Sens.*, Vol. GE-24, No. 4, 1986, pp 543-551.
- [11] Parsons, C., and E.J. Walsh, "Off-Nadir Radar Altimetry", *IEEE Trans. Geosc. Rem. Sens.*, Vol. 27, No. 2, 1989, pp 215-224.
- [12] Vachon, P.W., R.B. Olsen, C.E. Livingstone, and N.G. Freeman, "Airborne SAR imagery of ocean surface waves obtained during LEWEX: Some initial results", *IEEE Trans. Geoscience Rem. Sens.*, Vol. 26, No. 5, 1988, pp 548-561.
- [13] Young, I.R., W. Rosenthal, and F. Ziemer, "Three dimensional analysis of marine radar images for the determination of ocean wave directionality and surface currents", *J. Geophys. Res.*, Vol. 90, 1985, pp 1049-1059.

VALIDATION OF ERS-1 SCATTEROMETER WIND DATA DURING CALIBRATION/VALIDATION CAMPAIGN RENE-91

A. Bentamy
IFREMER, BP 70, 29280 Plouzane, FRANCE

June 3, 1992

Abstract

On the ERS-1 satellite, a C band scatterometer is used to estimate the wind vector over the oceans. This instrument measures the normalized radar backscatter coefficient (σ^0) which depends on the wind speed and direction in a manner which varies with the incidence angle of radar on the ocean surface.

To establish scatterometer wind measuring capabilities, the best way is to compare the satellite wind estimates to in-situ wind vectors. The in-situ data were collected during the ESA geophysical validation campaign (RENE91), from a meteorological buoys deployed off the Norwegian coast. But to meet this goal, using only these ground-truth data is not sufficient. So wind vector data, obtained from meteorological model (DNMI), was also used. The analysis of σ^0 according to incidence angle, wind speed and direction indicates good agreement between the measurements of the three scatterometer beams, and the necessity of improving backscatter model proposed before flight. The comparison between scatterometer and buoy wind data was performed, and statistical parameters are given.

1 INTRODUCTION

The validation strategy is based on the comparison between the ERS-1 scatterometer derived wind speed and direction, and those measured by buoys or estimated from a numerical model, during the calibration and validation campaign, RENE91 [3]. This validation involves :

- Study of ocean normalized radar cross section (σ^0) measurements, in order to evaluate the coherence between measurements of the three scatterometer beams .
- Assessment of the actual empirical model (CMOD-2) used to estimate the scatterometer wind speed and direction. To this end we will compare measured σ^0 and simulated σ^0 with CMOD-2 from the surface wind analysis.
- Estimation and analysis of the scalar differences between buoy and scatterometer estimates of wind speed and direction.

The scatterometer data validated herein are the fast delivery products (named UWI in the ESA format [1]). These data were collected from PCS-SPAN, the database gathering all available data during RENE91, or from CER-

SAT(IFREMER), the French Processing and Archiving Facility.

The TOBIS buoys were moored at locations far enough from shore in order to avoid the effect of land. The water depth varies from 255 m (T10) to 1540 m (T1) [2]. The buoy data were also collected from PCS-SPAN and are the near-real-time ARGOS transmitted data. All the buoy data used in this study are averaged over 20 mn and evaluated at 10 m height[3].

The meteorological data consist of the 10-m wind speeds and directions obtained from numerical model developed by the Norwegian Meteorological Institute and named DNMI. Available at the main synoptic hours (00:00, 06:00, 12:00, 18:00 UTC) on a regular grid with a 50 Km mesh size, they were extracted from PCS-SPAN. To minimize the problem resulting from the comparison between satellite data, which are spatially variable, and in-situ data, which are temporally variable, the collocation procedure respects the following criteria :

1. time separation between scatterometer and buoy data is less than 20 mn
2. for each buoy, the scatterometer cell collocated is the nearest one and within 25 Km radius.

The above procedure was applied to collocate DNMI data, but with time separation less than 3 hours.

2 DNMI WIND VECTOR

It is well known that the validation results depend on the quality of the ground-truth data. If we suppose that the TOBIS buoy data have an acceptable quality, we still have to evaluate that of the DNMI data. Figure 1a and 1b indicate a full comparison between DNMI and buoy T2, T3, T6 and T10 wind speed and direction. For both, the x axis indicates DNMI data and the y axis TOBIS data. The mean value of difference is 0.10m/s and the standard deviation is about 3m/s. Figure 1a indicates that for wind speed greater than 16 m/s, buoys give higher values. Figure 1b shows good agreement between the two wind direction data sets. So, as these comparisons do not provide any significant mean difference between DNMI and buoy data, we assume that DNMI data quality is acceptable and can be used as a verification data set.

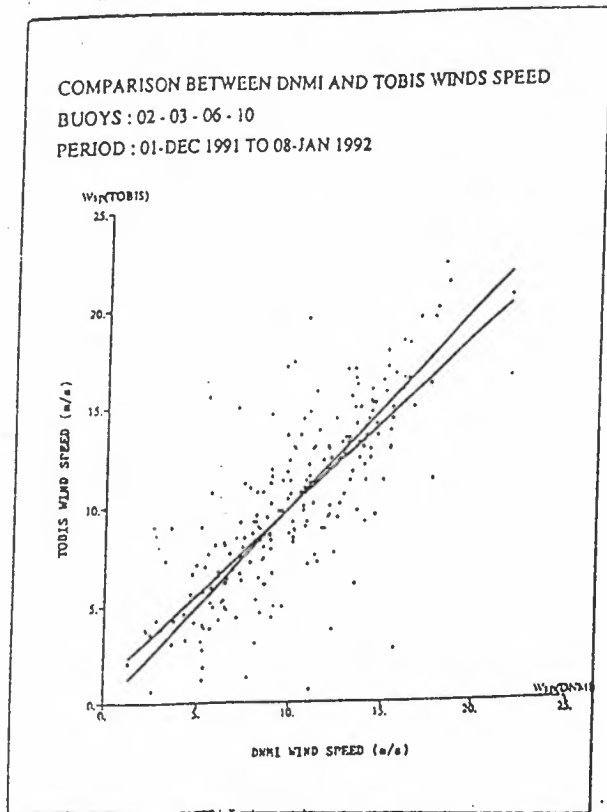


Figure 1a

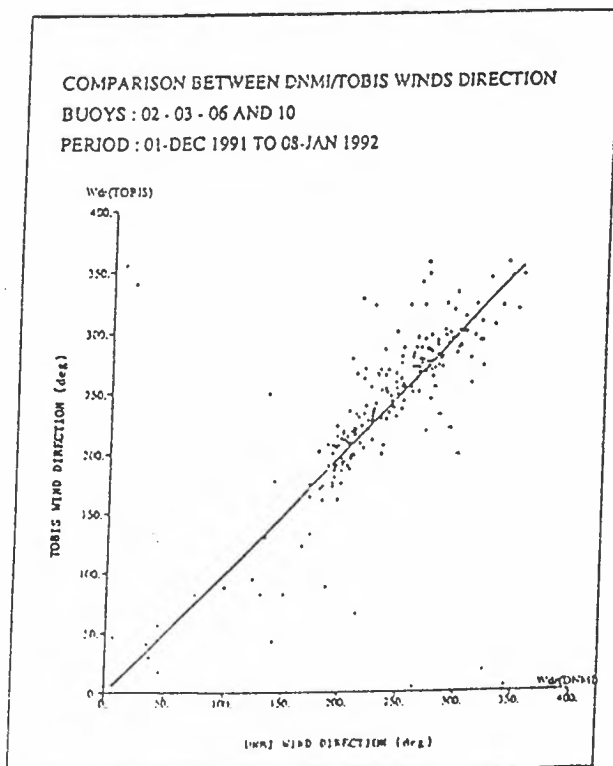


Figure 1b

3 NORMALIZED CROSS SECTION STATISTICS

The distributions of the three σ^0 were obtained for the period November 5th to January 16th. During this period 201438 UWI data were collected over the campaign area defined by 50N, 70N, 20W and 20E. The statistics are evaluated exclusively for UWI data such that σ^0 has a significant value and scatterometer derived wind speed and direction are determined autonomously. Therefore the total number of UWI data used is 68460 i.e 34% of all collected data. Table 1 gives the minimum, maximum, mean and standard deviation of each σ^0 distribution. σ_1^0 , σ_2^0 and σ_3^0 stand respectively for normalized radar cross section measured by fore, mid and aft beams. The values of the statistical parameters are in dB. Given that mid beam incidence angle varies from 17.9° to 45.4°, and that fore beam and aft beam have the same incidence angle which varies from 24.8° to 57°, it is coherent that the mean value of σ_2^0 should be greater than that of σ_1^0 and σ_3^0 . To measure the significance of the difference between σ_1^0 and σ_3^0 means, let be ϵ_{13} the difference between the two means and $Sd_{\epsilon_{13}}$ the standard error of the difference of the means. The estimation of these parameters gives [4] :

$$\epsilon_{13} = 0.04 \text{ and } Sd_{\epsilon_{13}} = 0.026$$

As ϵ_{13} is bounded by $-2 * Sd_{\epsilon_{13}}$ and $2 * Sd_{\epsilon_{13}}$, the σ_1^0 and σ_3^0 means are not statistically different.

Param	Min	Max	Mean	Sd
σ_1^0	-49.11	2.86	-14.19	4.80
σ_2^0	-32.99	2.99	-10.08	5.23
σ_3^0	-37.34	1.42	-13.74	4.84

Table 1: σ^0 STATISTICAL PARAMETERS

To advance in the statistical study of σ^0 behaviour, the mean value of each σ^0 is evaluated according to the corresponding incidence angle. Figure 2a and 2b show the behaviour of the three means respectively in upwind and crosswind cases, and for DNMI wind speeds bounded by 10 and 12m/s. Upwind and crosswind were determined using DNMI wind directions. In the first case some difference appears between the three means, especially between σ_1^0 and σ_3^0 at the first incidence angles. This result could be explained by the sample length which is less than 6. The crosswind case does not provide a significant difference between the three means. Student test[4] was applied and indicated that when the samples length is greater than 10, the means are comparable.

4 ASSESSMENT OF CMOD-2 MODEL

The ERS-1 scatterometer C band model is an empirical relationship between σ^0 and the wind vector at a height 10 m above the surface assuming neutral stability. All UWI wind speeds and directions are determined using the transfer function named CMOD-2 and which was established

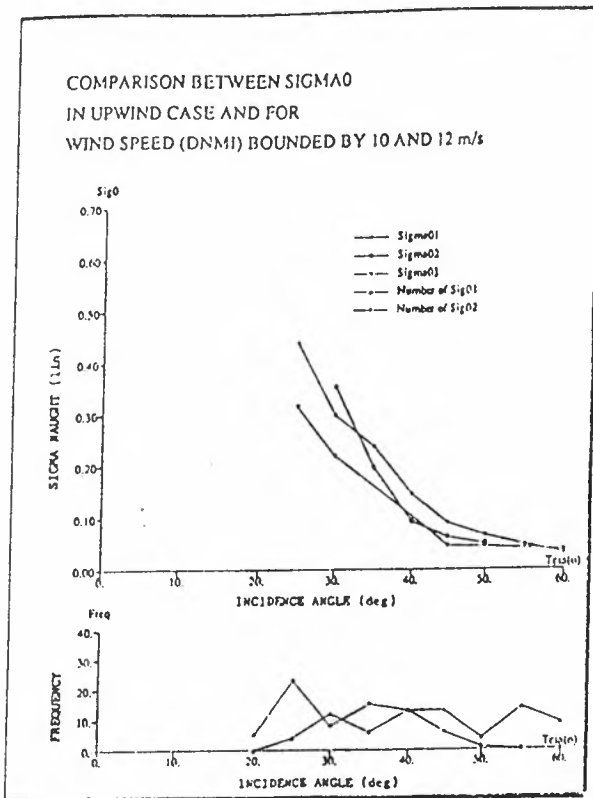


Figure 2a

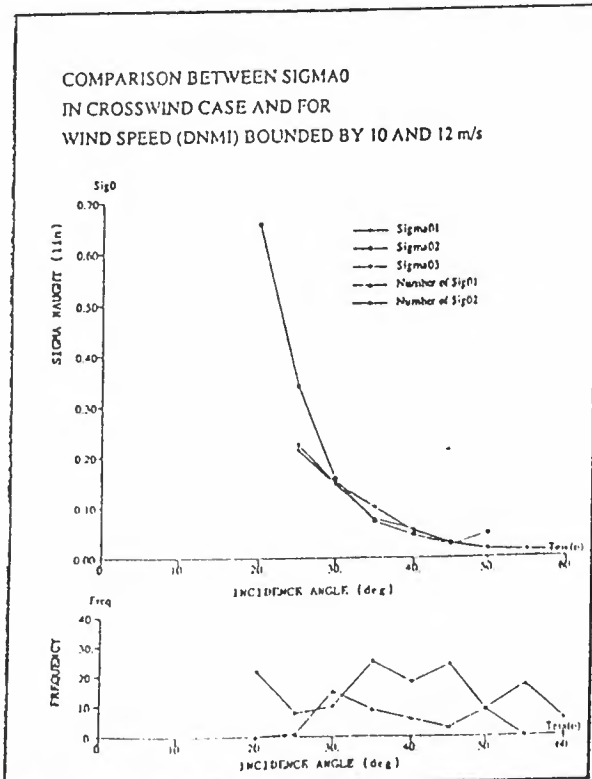


Figure 2b

before ERS-1's launch. This relationship is specified in the form :

$$\sigma^0 = B0(\theta, v) * (1. + B1(\theta, v) * \cos(\phi) + B2(\theta, v) * \cos(2 * \phi))$$

Where θ is the incidence angle, v the wind speed and ϕ is the angle between wind direction and radar azimuth.

The assessment of this model is based on the comparison between σ^0 measurements and σ^0 values computed using the above formulation, for various DNMI wind speeds and incidence angles.

The comparisons between measured and computed σ_2^0 , for an incidence angle of about 17.9° are shown by figure 3a, for collocated DNMI wind speed bounded by 4 and 6 m/s, and by figure 3b, for collocated DNMI wind speed bounded by 6 and 8 m/s. The x axis indicates the mid beam wind direction determined using mid beam azimuth and collocated DNMI wind direction. Computed σ_2^0 is represented by full line and measured σ_2^0 is represented by "+". The main result is that for this incidence angle we cannot expect to fit σ^0 measurements by CMOD-2 model and maybe by any other empirical model. Indeed, a σ_2^0 dependence of wind direction is not obvious for this low incidence angle.

Comparison made for an incidence angle of about 30.2° and for wind speeds bounded by 4 and 6 m/s (figure 4), indicates that all measured σ_2^0 do not follow the expected behaviour according to wind direction. However, in comparison with the previous case, we can see an improvement in the fit. The difference between measured and computed σ_2^0 could be explained by model calibration problem. Comparisons made for the same incidence angle but for higher wind speed, indicate that measured σ_2^0 are fitted better by CMOD-2 model.

The same comparisons were made for an incidence angle of about 45.4° and for wind speeds bounded by 4 and 6 m/s as shown by figure 5. We note that fitting measured σ_2^0 by CMOD-2 is valid, but many σ_2^0 measurements have higher values than computed ones. Similar results were obtained for other wind speed ranges. these results could be explained by the weak σ_2^0 values at this incidence angle.

As further analysis of the last result, we have, on the one hand, estimated C band-model coefficient B0 using σ^0 measurements (B0e) and, on the other hand computed B0 using CMOD-2 parameters (B0c). Figure 6 gives relative difference, evaluated for various DNMI wind speeds, between B0e and B0c as a function of incidence angle. For all wind speed bins, the difference increases from near-track to far-track. This implies that CMOD-2 model underestimates B0 values at the highest incidence angles. Thus, for an incidence angle of about 55° the difference is close to 20%. The effect of this on scatterometer wind speed determination is shown by figure 7. It represents the difference between collocated UWI and DNMI wind speed as a function of incidence angle, for each wind speed bin. This difference increases with incidence angle. At far-track it is always negative, which implies that scatterometer wind speed is overestimated at these incidence angles. This result is a consequence of scatterometer wind-vector algorithm, which is based on the optimization of the distance between CMOD-2 surface and σ^0 measurements to determine wind speed.

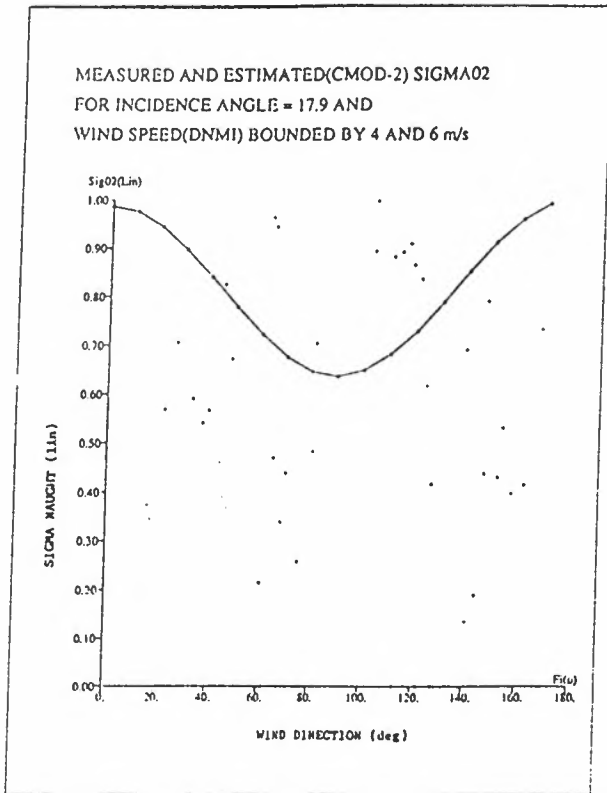


Figure 3a

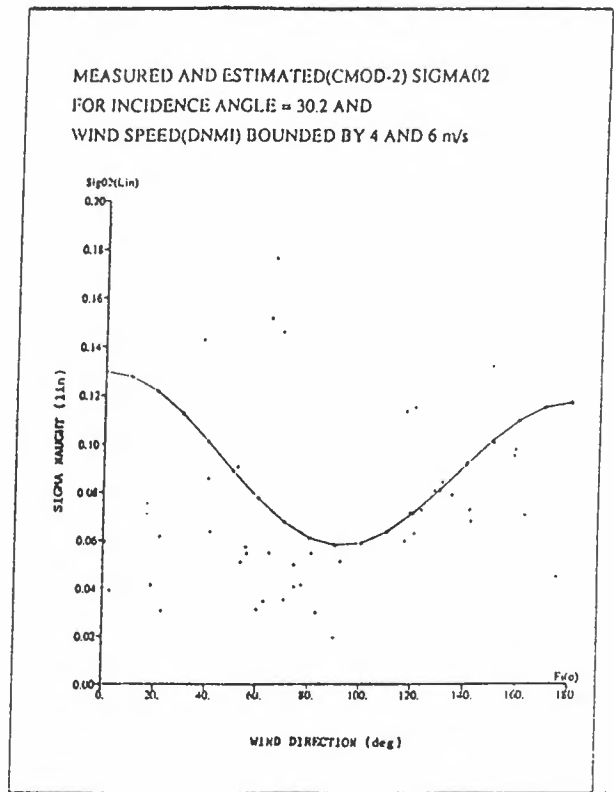


Figure 4

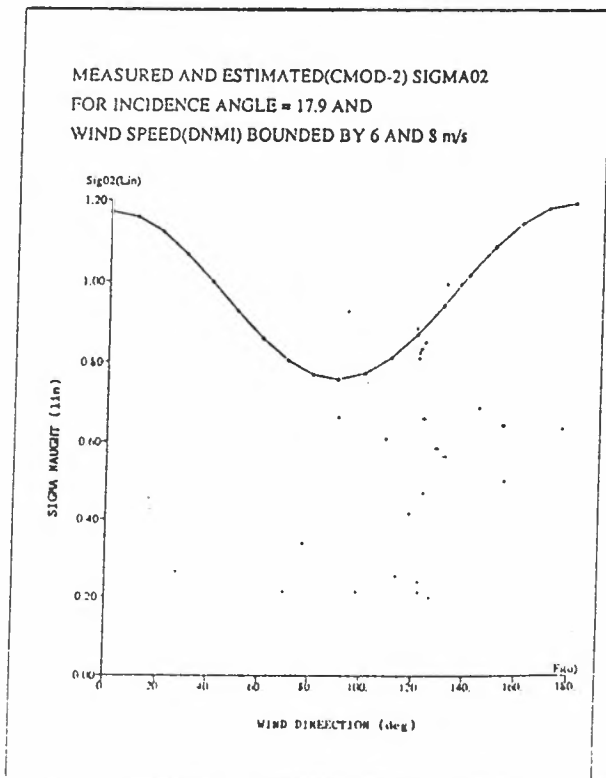


Figure 3b

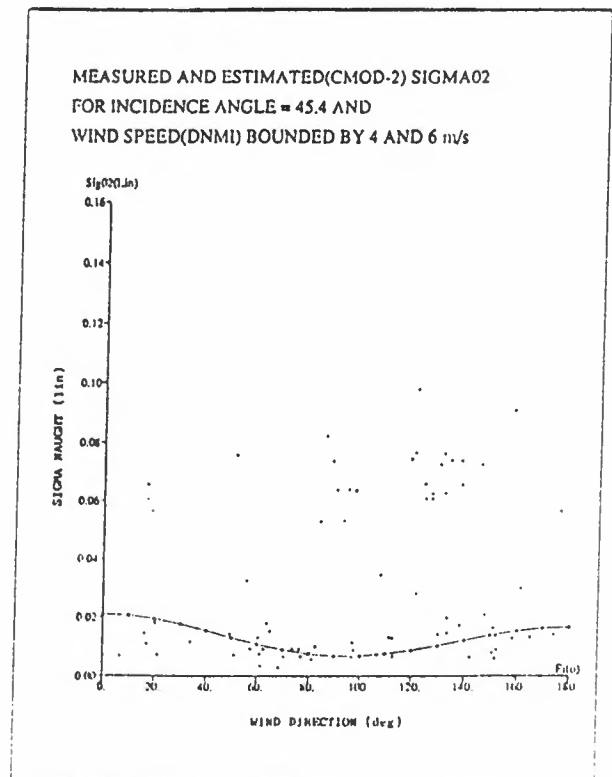


Figure 5

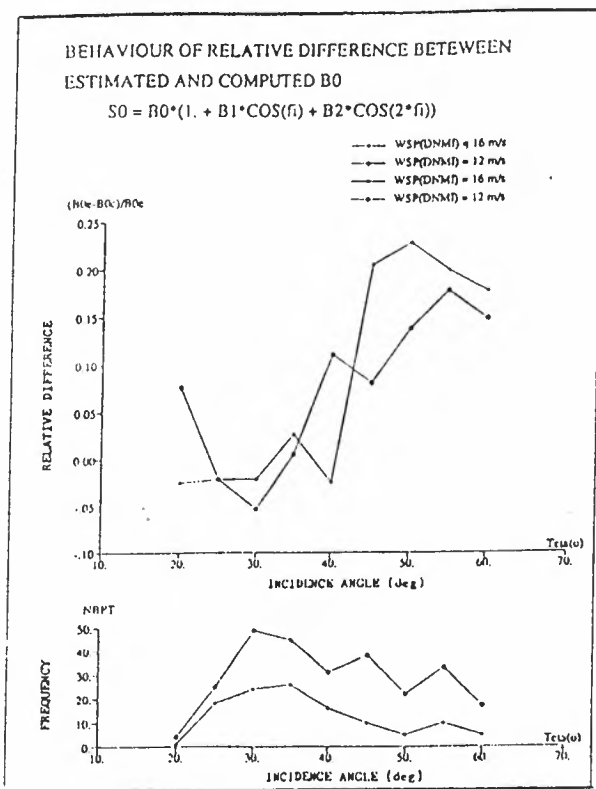


Figure 6

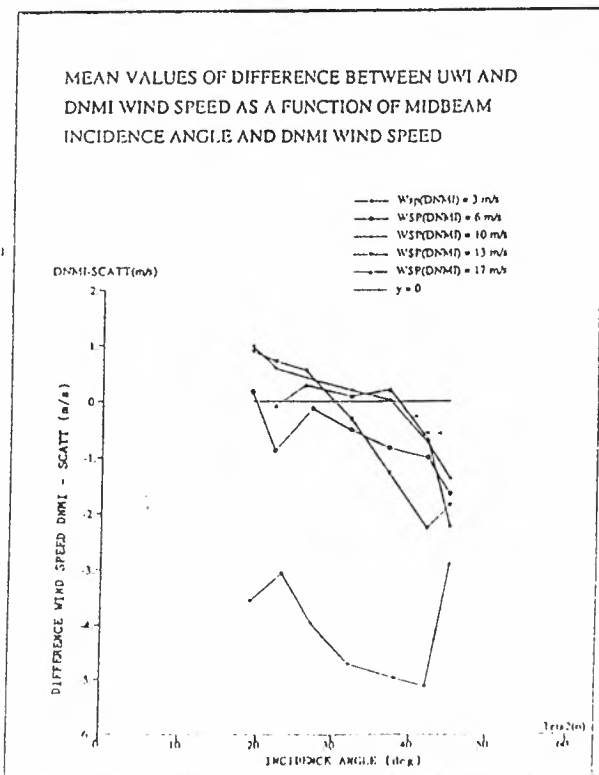


Figure 7

5 SCATTEROMETER AND TO-BIS BUOYS WIND VECTOR COMPARISONS

Using all validated buoys [3] and UWI data during 24 November 1991 to 26 January 1992, and the collocation procedure summarized in the introduction, the comparison between UWI and buoy wind speed and direction is processed with 39 collocated data. This limited data set is explained, on the one hand, by the collocation procedure itself, and on the other hand by the lack of ARGOS transmitted buoy data. Anyway, the comparison between ground-truth data and scatterometer wind speed and direction are shown by Figure 8a and 8b, where the solid line represents the perfect agreement. Figure 8a indicates that the two wind speed values have the same trend. However, scatterometer estimates are greater than buoy measured speed for wind speeds which are less than 5 m/s or which are greater than 16 m/s, and scatterometer estimates are less than buoy measured speed for wind speeds bounded by 5 and 16 m/s. This comparison result is coherent with the one obtained from DNMI and scatterometer comparison [Figure 7].

Figure 8a shows a pair of UWI and buoy wind speed such that, scatterometer gives 19m/s and buoy 4m/s. This corresponds to the collocated scatterometer cell with buoy T7. Comparison with buoy T6, the nearest one of T7, indicates that the in-situ wind speed is about 4m/s. We point out that this UWI wind speed was derived at fore beam incidence angle about 55°. This point will not be taken into account in the evaluation of statistical parameters.

All empirical models relating σ^0 to wind vector share a similar $\cos(2 \cdot \phi)$ dependence. This characteristic of scatterometer model is responsible for the difficulties in obtaining a unique solution of wind vector from σ^0 measurements. Hence two wind vectors shifted by 180° could give rise to the same set of σ^0 [5]. Comparison between UWI and buoy wind direction indicates that the most of the collocated data which are close to the perfect agreement or which are shifted by about 180° [Figure 8b]. The shift is a consequence of ambiguity removal problem.

Param	Min	Max	Mean	Sd
DW(m/s)	-7.59	3.43	-1.05	2.78
DD(deg)	-178.50	179.90	24.69	104.44

Table 2: STATISTICAL PARAMETERS OF DIFFERENCE SERIES

Table 2 gives statistical parameters of difference distribution between buoy and UWI data. DW stands for buoy wind speed minus UWI wind speed, and DD stands for buoy wind direction minus UWI wind direction. The rms of DW is 2.97m/s and of DD is 107°. These rms values are far from the wind vector measurement goal of scatterometer, which was specified as 2m/s for wind speed and 20° for wind direction. Many sources could explain this difference: instrumental error, spatial separation, temporal separation, time and space averaging [6],[7] and especially empirical model accuracy. To illustrate the last source of difference, we have evaluated the σ^0 values using CMOD-2 model and buoy wind speed and direction ($\sigma^0(CMOD-2)$), and made a

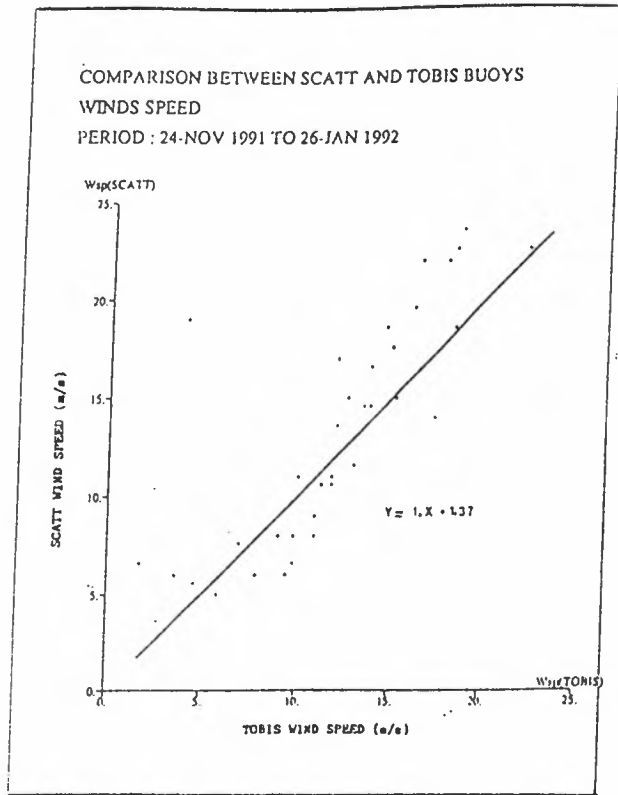


Figure 8a

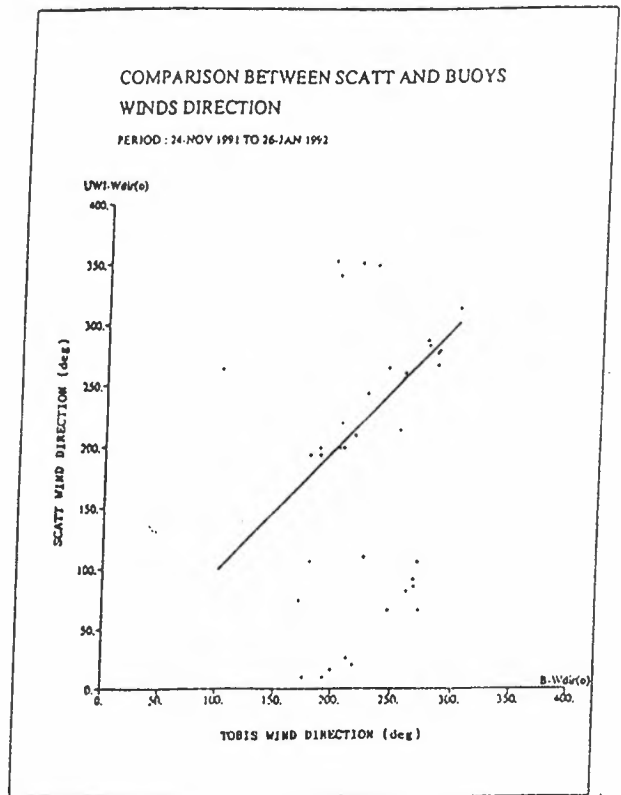


Figure 8b

comparison between these values and the measured ones. The bias (resp. standard deviation) on fore beam, mid and aft beams is respectively 0.51, 0.44 and -0.55 dB (resp. 1.86, 2.22 and 3.41 dB). So it seems difficult to derive scatterometer wind speed and direction corresponding to the specification with such model accuracy.

6 Conclusion

About two months of colocated scatterometer and either DNMI model or Tobis buoy data, were used in order to validate radar cross sections, as well as derived wind speed and direction. Comparative studies of fore beam, mid beam and aft beam σ^0 indicate that on average the three measurements could be considered comparable, and the differences between them, as a function of incidence angle and wind speed could be explained by the sample length used. Our study of CMOD-2 assessment shows that it underestimates σ^0 values at the higher incidence angles. Therefore the derived wind speeds are overestimated at far-swath. Furthermore, it has been shown that there is no obvious dependence of σ^0 measurement on wind direction at the lower incidence angles. Using TOBIS buoys data, the rms wind speed difference is about 3m/s. The rms wind direction difference is not significant because of ambiguity removal process problems. It is clear that all statistical study of difference between scatterometer and buoy data is strongly related to the model and to the algorithm used to estimate wind speed and direction. However, during the ESA calibration/validation campaign, other calibrated models were established, and indicated a better fit than CMOD-2 (see D. Offiler paper in this issue). Validation of these models using buoy data should be carried out.

References

- [1] ERS-1 Ground Stations Products Specification. Earthnet Programme Office. 26 February 1991.
- [2] ERS-1 CAL/VAL in Situ Measurements. Buoy Array Status Report. Oceanographic Company of Norway A/S. 27 November 1991.
- [3] P. Queffeuillou, A. Bentamy, Evaluation of Wind and Wave Measurements from the TOBIS Buoy Network During RENE-91. In this issue.
- [4] Von mises, Richard., Mathematical Theory of Probability and Statistics (New York : Academic Press) 1964
- [5] Cavanie A, Lecomte P., 1987. Study of a Method to De-Alias Winds from ERS-1 Data. Final Report ESA Contract 6874/87/GP-I
- [6] ESPADON Group. Steps to Be taken for Validation of In-Situ Data from Tobis buoys and Best Estimates of Wind Vector and Sea-State from ERS-1 Calibration/Validation. Contract ESTEC/IFREMER 8698/89/NL/BI. June 1990.
- [7] F.M. Monaldo, Expected Differences in the Comparison of Wind Speed and Significant Wave Height by Spaceborne Radar Altimeters. JHU/APL SIR86U-017. 1986

SESSION - II
WIND SCATTEROMETER MODELS

ERS-1 SCATTEROMETER CALIBRATION AND VALIDATION ACTIVITIES AT ECMWF:
A. THE QUALITY AND CHARACTERISTICS OF THE RADAR BACKSCATTER MEASUREMENTS

Ad Stoffelen¹, and David L.T. Anderson²

¹ European Centre for Medium-range Weather Forecasts, Reading, U.K.;

² Dept. of Atmospheric, Oceanic and Planetary physics, Clarendon Laboratory, Un. of Oxford, Oxford, U.K.

ABSTRACT

Calibration and validation activities for the ERS-1 scatterometer have been carried out at ECMWF, complementary to the "Haltenbanken" field campaign. At a Numerical Weather Prediction (NWP) centre a wealth of verifying data is available both in time and space. By using the data and resources available at a NWP centre, it is possible to contribute extensively to a satellite instrument calibration and validation exercise. We estimated noise, and characterised the scatterometer measurements in relation to wind speed and direction. The antennae configuration of the ERS-1 scatterometer proved to be crucial for this work. It is shown that a solution plane is well-defined in 3D measurement space and measurement noise is low. ESA's transfer model CMOD2 has to be extensively reformulated. In a second paper we discuss how to redefine the wind retrieval procedure given the instrumental characteristics.

Keywords: ERS-1 scatterometer, normalised radar cross section, σ^0 -to-wind transfer function, wind direction ambiguity removal, surface winds.

1. INTRODUCTION

At ECMWF there is an ongoing project to help in the calibration and validation of ERS-1 wind scatterometer data, complementary to the "Haltenbanken" field campaign off the coast of Norway. This paper reports on our part in instrumental calibration, and characterisation of the normalised radar cross sections, i.e. σ^0 , as measured by the ERS-1 scatterometer. Also conclusions are drawn on the dependence of σ^0 on wind speed and direction, and other geophysical parameters. A companion paper (Ref. 1) deals with the derivation of a σ^0 -to-wind relationship using a maximum likelihood estimation procedure, and with the retrieval of a unique wind speed and direction (wind direction ambiguity removal).

1.1 The operational wind retrieval suite

The ERS-1 scatterometer has three independent antennae pointing in a horizontal plane towards a direction of 45, 90, and 135° with respect to satellite propagation (see Figure 1). Therefore, a site in the scatterometer swath is illuminated three times, respectively by the fore, mid and aft beam. The incidence angle of the radar beam varies from 18 to 47° for the mid beam, and 22 to 58° for the fore and aft beams. The swath, approximately 500 km wide, is sampled every 25 km resulting in 19 measurement cells across the swath; along the swath the sampling distance equals also 25 km. The spatial resolution of the instrument on the earth's surface is approximately 50 km. The C-band radar frequency used is 5.3 GHz and its polarisation is vertical.

From pre-launch field campaigns an empirical relationship between σ^0 , and wind speed V and direction ϕ for neutral stratification at 10 m

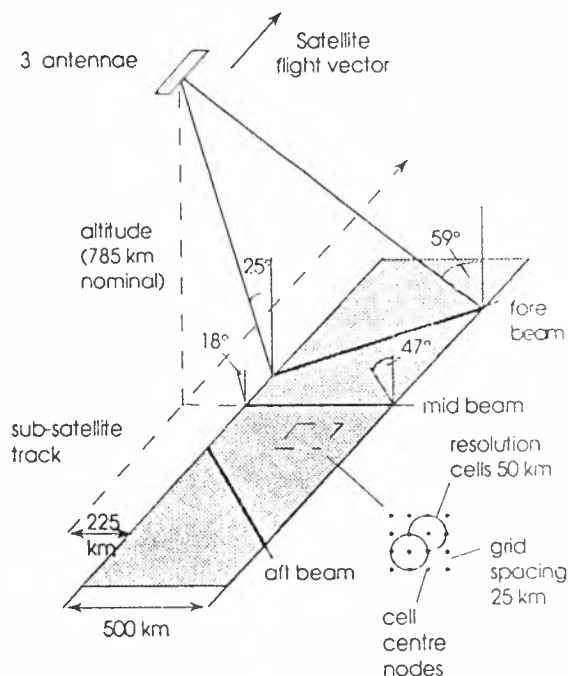


Figure 1: Wind scatterometer geometry (from: UK ERS-1 Reference Manual, Royal Aerospace Establishm., U.K.)

height was found by Long, called CMOD2 (Ref. 2):

$$\sigma^0 = 10^\alpha \cdot V^\gamma \cdot [1 + B_1 \cos(\phi) + B_2 \cos(2\phi)] \quad (1)$$

where:

$$B_1 = b_1^1 + b_1^2 \cdot V \quad (2)$$

and:

$$B_2 = b_2^1 + b_2^2 \cdot V \quad (3)$$

The coefficients α , γ , b_1^1 , b_1^2 , b_2^1 , and b_2^2 are specified by a tuning coefficient times a Legendre polynomial of order 0, 1, and 2 in $x = (\Theta - 25^\circ)/40^\circ$, with Θ the radar beam incidence angle, e.g. $\alpha = \alpha_1 + \alpha_2 \cdot x + \alpha_3 \cdot (3x^2 - 1)/2$. The resulting 18 tuning coefficients were determined from pre-launch field campaigns (Ref. 2). In this paper the first and largest term in equation (1) will be referred to as "bias term", i.e. $10^\alpha V^\gamma$, the smaller harmonic coefficient B_1 as "upwind/downwind amplitude", and B_2 as "upwind/crosswind amplitude", although the latter is strictly 50% of the average of the differences between upwind and crosswind, and between downwind and crosswind, divided by the bias term. The empirical transfer function is sketched in figure 2.

Several research groups have found σ^0 to be a function of other geophysical parameters rather than neutral 10 m wind speed and direction (e.g. Ref. 3). Globally available fields on stability, SST, and wave parameters from the WAM model can be used at ECMWF to investigate these geophysical effects statistically. Our first aim is, however, to obtain as accurate wind retrieval procedure as possible based on a σ^0 -to-wind relationship only.

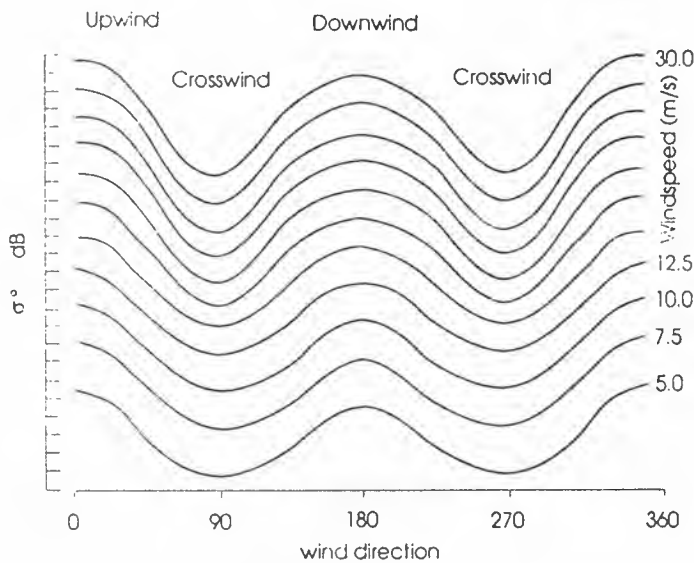


Figure 2: Relationship between wind direction and sigma naught for different wind speeds (from: UK ERS-1 Reference Manual, Royal Aerospace Establishm., U.K.)

1.2 Collocation

At ECMWF in-situ and remotely sensed data are used to define as accurately as possible the geophysical conditions at any site on the globe at regular time intervals. For each 6 hour period we collocated the ERS-1 scatterometer measurements both with the ECMWF analysis and time interpolated guess field information, and with available conventional observations, and stored the resulting files in binary format. The file containing collocations with the ECMWF meteorological model includes estimates of the model winds and simulated σ^0 s, and also relevant boundary layer information such as sea surface temperature and model 2m temperature. ERS-1 data are collocated with conventional observations including SHIP, DRIBU and SYNOP from islands (which are less than 100 km², low-lying, and away from any continent). The conventional observations are flagged against our operational guess field and wind analysis, and against a selection of high quality conventional stations. These collocation files also contain interpolated pressure, height, temperature and humidity at all model levels below 850 mb, both at the sites of the conventional observation and of the scatterometer measurement cells.

1.3 Processing

The collocation files are used to obtain statistics on the performance of the ERS-1 scatterometer. Figure 3 illustrates the data processing involved in the validation. Each process introduces its own noise characteristics to the product, and therefore interferes with the original error structure of the radar measurements. It is preferable to compare σ^0 s because one avoids uncertainties arising from the wind ambiguity removal procedure, which has to be used when comparing winds. Also in σ^0 domain it is possible to compare different beams, and different incidence angles whereas this is not possible when comparing wind speeds. For these reasons intercomparison of simulated and measured σ^0 s is the first priority exercise.

In this paper we will not give details of all the technical problems we discovered and reported to ESA, but will rather concentrate on scientifically interesting aspects of our work during the last 6 months. We will consider the noise characteristics involved in wind retrieval from the scatterometer and discuss the formulation of CMOD2. To do so, we first define the error characteristics of our comparison data.

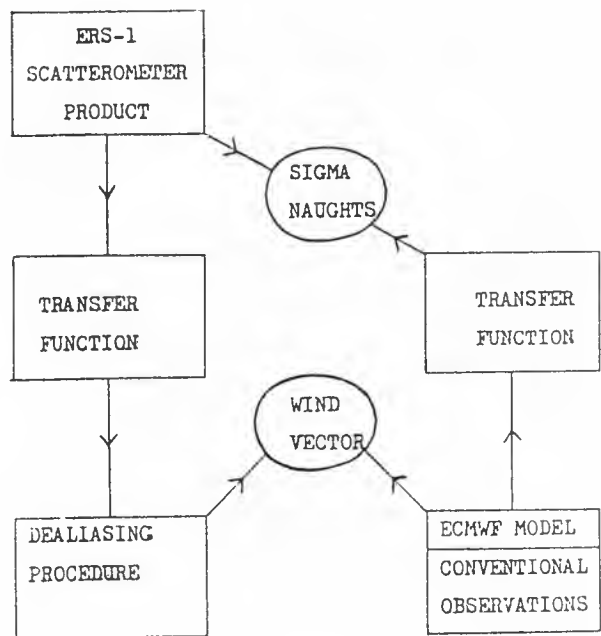


Figure 3: Data processing and validation.

2. ECMWF ANALYSIS WINDS

In order to have a uniform and complete global coverage every 6 hours, and to be able to respond quickly to operational updates in ESA's wind retrieval suite, we mainly compared the scatterometer data against σ^0 s derived from the ECMWF analysis. We produce a "white-list" of SHIP, BUOY and island wind observation stations performing within the ESA specifications for scatterometer winds in 3 subsequent months. This list is used in the subsequent (4th) month to flag high quality wind measurements. On average this list contains only approximately 80 observations, which is not sufficient to obtain a quality assessment for the scatterometer in a short time period over the full globe.

In order to use the ECMWF analysis winds as verification data set, we will need a quality assessment of the model surface winds. Figure 4 shows an example of a distribution of departures in the east-west component of the wind, of "automatic" SHIP observations from the ECMWF guess field plotted against the average of SHIP and guess field. In general the bias between conventional observations and guess field is below 10 % and positive, i.e. the conventional observations are higher than the guess field. The relative bias tends to increase above 12 m/s, most probably due to too weak extreme winds or phase errors in strong wind phenomena in the guess field. The standard deviation is rather constant over the components of the wind. We estimate the guess field error to be 2.25 m/s in the components irrespective of wind component amplitude, assuming equal portions of the standard deviation derived from figure 4 to be in SHIP observation and guess field. We found no strong regional difference, but there were some differences between the different observational systems. These differences are not easy to explain, and would need further investigation. Comparing analysis and guess field surface wind, we were led to believe that they have similar statistical properties.

3. σ^0 BIAS CALCULATIONS

Figures 5a and 5b show the average σ^0 versus incidence angle for measured σ^0 s (5a) and for values simulated with CMOD2 from the ECMWF wind analysis (5b). Figure 5c shows the ratio of the averages from figures 5a and 5b, which are for ascending tracks only. All plots are averages over a 5 day period. To achieve further independence of particular meteorological conditions we tried to sample wind direction homogeneously over all wind speeds. That we indeed sample independent of meteorology can be seen in figure 5b which shows no difference between the three beams.

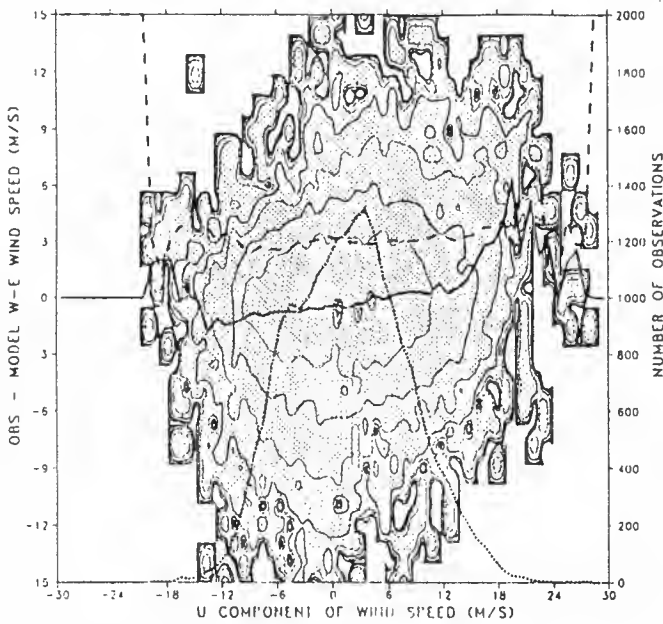
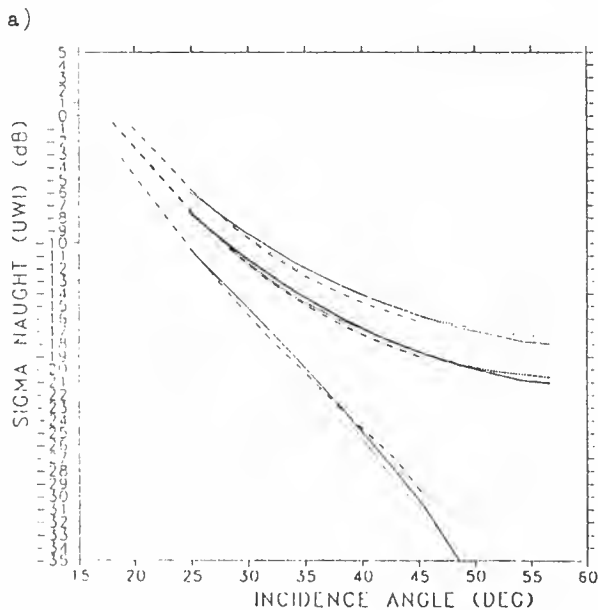


Figure 4: 2D distribution of departures in the West-East component of the wind of "automatic" SHIP from the ECMWF guess field, plotted versus the average of SHIP and guess field West-East component. The solid line shows the bias, and the dashed line the standard deviation of the departures. The dotted line is the distribution of average West-East components and is quantified on the right vertical axis. Contour levels are logarithmic and 21270 entries are used.

However, figure 5a and as a result also figure 5c show the relative instrumental beam biases. The relative beam biases were also measured by ESA over the tropical rain forest, and agree with our estimates to within 0.1 dB (Ref. 5). Absolute calibration devices (transponders) in the South of Spain didn't agree with our bias calculations, and appeared to have a sampling problem for low incidence angles.

The biases as a function of incidence angle were calculated both for ascending and descending tracks, showing no significant difference between them. This result is of importance because the day-night



temperature variations across the antennae might lead to an erroneous automatic beam gain correction. Our calculations showed this is not the case. At a later stage, ESA was able to verify our result over the rain forest.

The trend as a function of incidence angle in figure 5c results from the bias term in CMOD2. Moreover its signature is not parabolic in incidence angle, although the assumed form in equation (1-3) is quadratic. Therefore, the bias term needs to be reformulated in order to make the bias calculated in figure 5c independent of incidence angle.

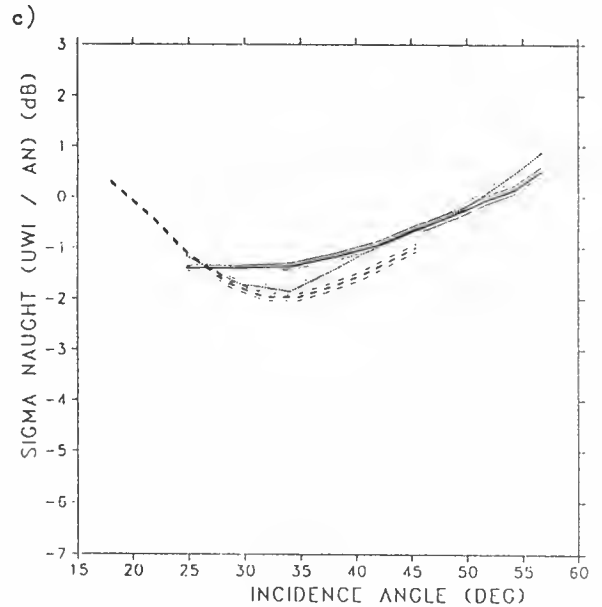
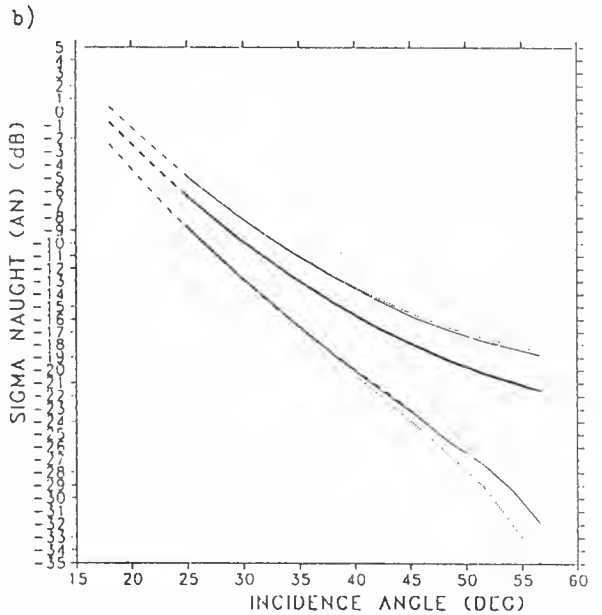


Figure 5: Average in physical space of measured (a), and with CMOD2 simulated sigma naughts (b) versus incidence angle for ascending tracks. Figure 5c shows the difference of 5a and 5b. A filter is used to obtain a flat analysis wind direction PDF. The data is global and from 21 GMT 17/10/'91 to 21 GMT 27/10/'91. The solid line shows the fore, the dashed the mid, and the dotted line the aft beam. Thin lines show +/- one standard deviation of the averages.

Comparing figure 5a with figure 5b one can see that the standard deviation of the averages (thin lines) is bigger for the measured data than for our simulated data using the model function CMOD2. This may suggest that the upwind/crosswind and to a lesser extent the upwind/downwind amplitude (variability) in CMOD2 are too small.

4. σ^0 DEPARTURES

The differences between measured and simulated σ^0 s naughts over extended areas on the globe were frequently in excess of -6 and +6 dB (the instrumental noise level specification is 0.2 dB). In light wind speed areas (below 5 m/s) one might expect errors of this size due to analysis errors in wind speed and direction, but these errors were also observed in high wind speed areas. The obvious explanations are problems with CMOD2 or with the σ^0 noise level.

By interpreting departure maps it became evident that ice or fractional ice coverage in general gives rise to σ^0 s in the same range as those measured over sea. To exclude ice areas, we used the ECMWF SST analysis field and found that on certain days a lower SST threshold of 4.5 °C still allowed ice contaminated areas. For safety we set the SST filter threshold to 6 °C.

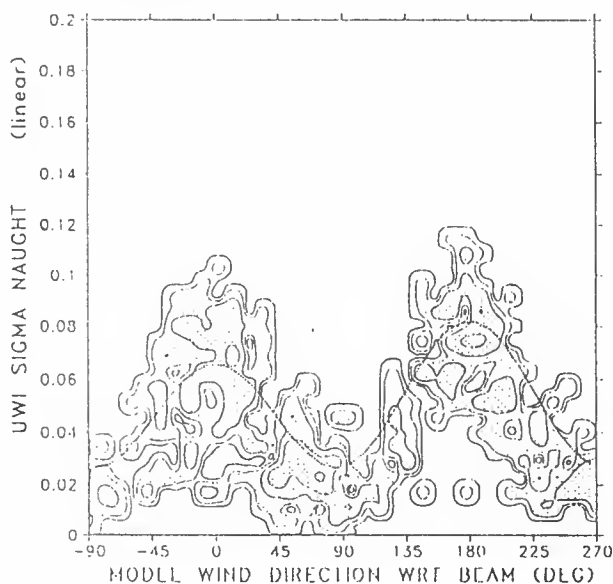


Figure 6: 2D distribution of sigma naught versus analysis wind direction, for an analysis wind speed of 15 to 17 m/s and for an incidence angle of 45.4 degrees. The dotted line shows CMOD2 (upwind is 180 degrees). The data is global and from 21 GMT 23/9/'91 to 21 GMT 3/10/'91. Contour levels are logarithmic.

Figure 6 shows the distribution of measured σ^0 s against wind direction for a particular wind speed range, incidence angle and beam. In general such plots show a high level of noise, as can be noted even at relatively high wind speeds. We found that the level of noise for upwind and downwind directions is in general bigger than for crosswind. The fact that the error in σ^0 is proportional to σ^0 helps to explain this behaviour. However, in general it is very difficult to interpret the noise characteristics seen in figure 6, because these depend both on the errors in σ^0 , wind speed and direction, and on the distribution of σ^0 , wind speed and direction. Further, for a wind speed of 5 m/s, the estimated standard deviation of error in the ECMWF wind direction is approximately 45°, i.e. equal to the difference in direction between upwind and crosswind. Except that noise is difficult to diagnose from distributions as in figure 6, the above considerations also imply that trying to estimate the transfer function behaviour by averaging, or statistically filtering σ^0 s is a very difficult task.

5. INTERNAL QUALITY CHECK; σ^0 MEASUREMENT SPACE

So far, we have indicated two reasons for a high level of noise in the calculated departures, which we still are not able to separate, i.e. a misfit of CMOD2 with the real σ^0 -to-wind relationship, and the noise level in the measured σ^0 s. To do the separation we need a way to internally check the σ^0 data.

Each triplet of measurements can in principle be plotted in a 3D space spanned by an axis system representing the fore, mid, and aft beam measurement. Given a transfer function as in equation (1-3) one can show that the triplets should lie close to a cone (solution plane) as in figure 7 (Ref. 4) for a particular cell position (Θ) across the swath. To visualise this cone we could slice through it, with a thickness comparable to instrumental noise. It is easy to show from equations (1-3) that if $B_1=0$, the sum of σ_{fore}^0 and σ_{aft}^0 equals a value related to wind speed but not direction, thus giving some physical interpretation to this particular cross-section. In reality $B_1=0$ is not valid, so the slice will represent a range of wind speeds, being lowest for downwind, and highest for upwind. Figure 8 shows a slice of constant $\sigma_{fore}^0 + \sigma_{aft}^0$, for a wind speed of approximately 9 m/s, and cell position 11 (cells are counted from the inner swath). Collocation of the points plotted with ECMWF wind speed and direction, and calculation of the probability (PDF) of selection of a particular wind speed (bin), gives us a reference to true wind speed.

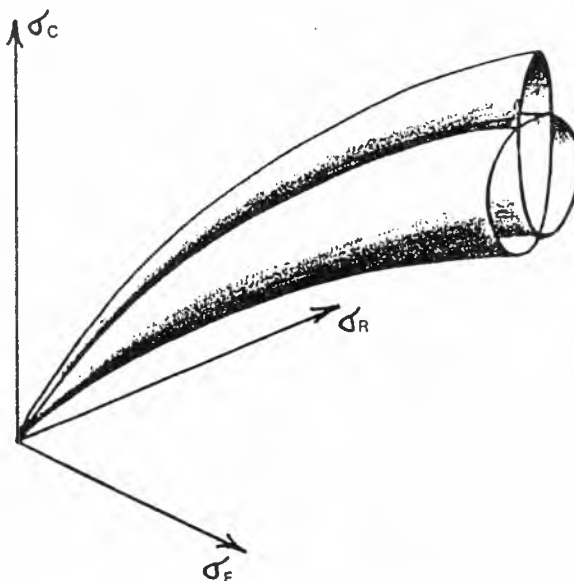


Figure 7: Plane of solution in 3D measurement space (Ref. 4).

In general, and as can be noted in figure 8 a solution plane seems to exist and to be well defined. A formulation as in equation (1-3), referring σ^0 only to two geophysical parameters (for CMOD2 they are wind speed and direction) seems sufficient. Subjectively we tried to estimate noise in σ^0 from slices at different reference wind speeds and cell positions, from the distribution of measurement points at the bottom (mid beam) and at the sides (fore and aft beam). We used the offset from the origin of the 3D space to calculate the proper noise reference σ^0 values. As shown in figure 9 the level of noise intrinsically present in σ^0 is of the order of instrumental specification (~ 5 %). Only for a reference wind speed of 3 m/s does the level of noise go up to approximately 15 % which is still a very good performance for such a low wind speed. Of course for low wind speeds geophysical effects like viscosity and surface tension will play a bigger role, and also over a 50 km diameter area wave conditions will not be very homogeneous. We can conclude from this that the ERS-1 scatterometer is performing very well, and that there is a scope for improving the σ^0 -to-wind relationship to fit the data as visualised in figure 8.

By subjectively estimating the diameter of the cone in both horizontal and vertical direction we are able to estimate the upwind/crosswind amplitude for the fore/aft and mid beam. Using simple vector algebra and ignoring the upwind/downwind amplitude for the moment we get the results as shown in figure 10. For low incidence angles the measurement noise is comparable to the upwind/crosswind amplitude, inevitably leading to reduced skill in wind direction retrieval. For higher wind speeds and incidence angles the upwind/crosswind amplitude saturates at a value of 0.6, dropping a little for the highest wind speeds and incidence angles. This behaviour cannot be described with a parabolic Θ dependence and a linear wind speed dependence as assumed in equation (3) for B_2 , indicating CMOD2 has to be revised in this respect.

Another point evident from figure 8 is the almost triangular shape of solution space. This means that higher harmonics rather than only $\cos(\phi)$ and $\cos(2\phi)$ are involved in equation (1). However, replacing $[1 + B_1\cos(\phi) + B_2\cos(2\phi)]$ by $[1 + B_1\cos(\phi) + B_2\cos(2\phi)]^{1.6}$ also allows a fit to the triangular shape.

6. WIND SPEED DEPENDENCE

The slicing method allows us to collocate σ^0 's for an approximately constant wind speed with analysis wind speeds. Knowing the 3D σ^0 offset vector for the centre of gravity of the data distribution in slices at different wind speeds, one can plot for each cell (Θ) an estimate of the bias term as a function of wind speed V . Equation (1) suggests a $\log(V)$ dependence. On doing so, we found a non-logarithmic relationship particularly at low wind speeds. However, given the uncertainty in model wind speed, and a non-symmetric error distribution for low wind speeds it is very difficult to draw any firm conclusion from the above fact.

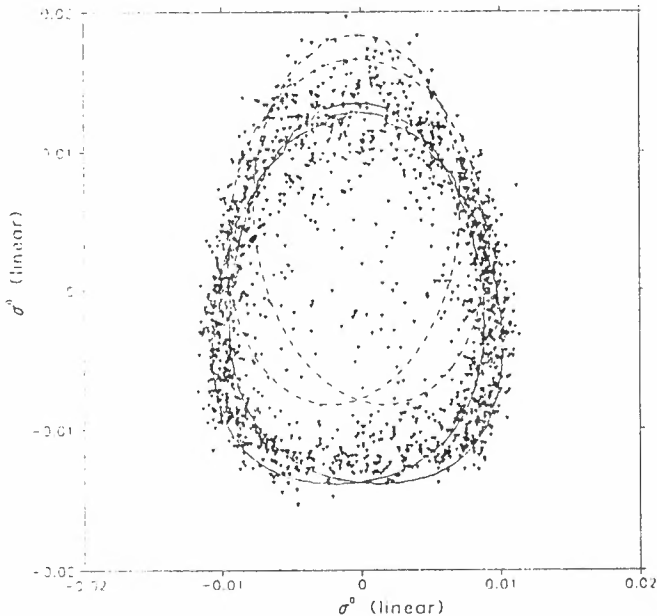


Figure 8: Cross-section through 3D measurement space for a constant fore plus aft beam sigma naught and with a thickness of two times instrumental noise. Horizontal axis is aft minus fore beam sigma naught, and vertical axis is mid beam sigma naught. Data are for cell 17 (counted across-swath from outside) and from 9 GMT 27/11/'91 to 9 GMT 27/11/'91 all over the globe. For this particular slice we estimated wind speed to be 9 m/s. The dashed curve represents transfer model CMOD2, the solid curve the model derived in Ref. 1.

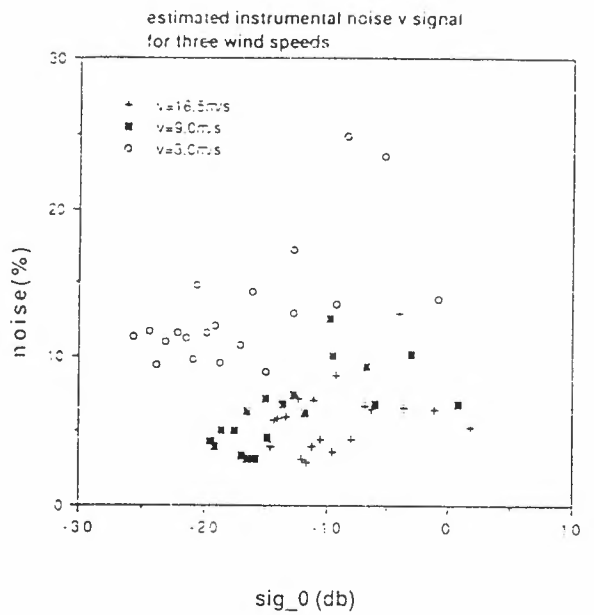


Figure 9: Sigma naught noise as a function of sigma naught for three wind speeds.

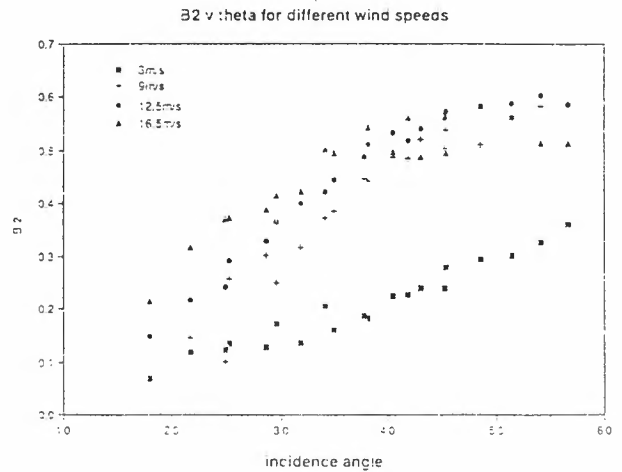


Figure 10: Upwind/crosswind amplitude versus incidence angle for four different wind speeds.

In order to study the wind speed dependence of σ^0 we compared averages of σ^0_{fore} and σ^0_{aft} to analysis wind speeds. As can be derived from equation (1) this average is independent of the upwind/crosswind amplitude, and is only slightly dependent on the upwind/downwind amplitude. Figure 11 shows a 2D histogram of wind speeds estimated from the average of σ^0_{fore} and σ^0_{aft} collocated with analysis wind speeds. From such plots it was found that the distributions as calculated with a $\log(V)$ dependence were not realistic for any value of α and γ , particularly for the lower wind speeds. Also, the resulting distributions appeared to be dependent on incidence angle. When we corrected the $\log(V)$ dependence into a $\log(V + B(\Theta))$ dependence we found that the distributions became more realistic. So far, best results have been obtained with a positive B smaller than 1.5 m/s and linearly dependent on Θ . A stronger correction, like a \sqrt{V} dependence gave unrealistic distributions for the lower wind speeds.

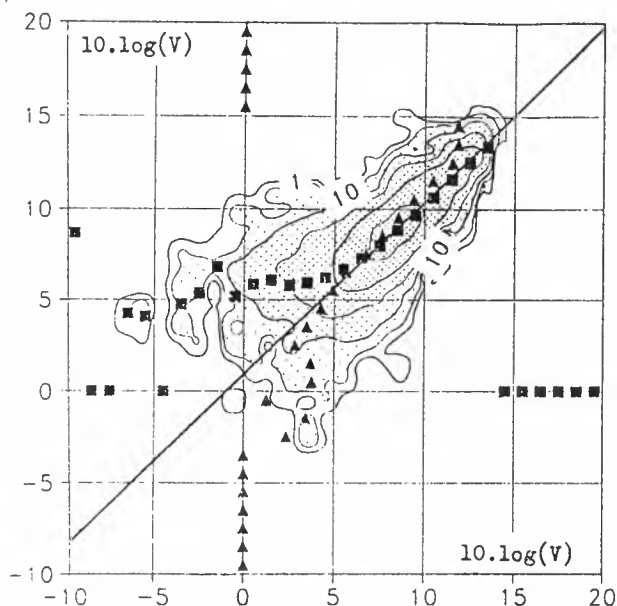


Figure 11: 2D distribution in $10.\log(V)$, where horizontally analysis wind speed and vertically a wind speed as estimated from the fore and aft beams is used. The \blacksquare are vertical averages over the distribution, and the \blacktriangle are horizontal averages over the distribution. Contour levels are logarithmic.

7. UPWIND/DOWNWIND AMPLITUDE

Although the slices in σ^0 space can provide considerable information about the geophysical processes involved in C-band radar backscattering and about σ^0 measurement characteristics, they fail to provide us a measure of the upwind/downwind amplitude. Therefore we tried to estimate this amplitude by a more straightforward method. We filtered σ^0 data to a uniform wind direction distribution over a large range of wind speeds. Then we defined an upwind bin for $|\phi| < 90^\circ$, and a downwind bin for $|\phi - 180^\circ| < 90^\circ$. The average upwind value minus the average downwind value divided by the average of upwind and downwind is then proportional to the upwind/downwind amplitude. Assuming a $\cos(\phi)$ relationship and for the remaining harmonic terms symmetry around $\phi = 90^\circ$, we find the proportionality constant to be $\pi/2$. Figure 12 shows our estimated upwind/downwind amplitude, corrected for the standard deviation of error in ECMWF analysis wind direction as a function of wind speed. This correction was not very significant because the upwind/downwind amplitude is small for low wind speeds, and it is only for low wind speeds that the wind direction standard deviation of error is large. The amplitude is in general small and negative for low incidence angle, and shows large wind speed dependence for mid range incidence angles. Again saturation can be observed for high wind speeds and incidence angles, which cannot be described by the current CMOD2 formulation, as in equation (1-3).

8. CONCLUSIONS

At a NWP centre a wealth of data is available to assist not only in the basic trouble-shooting exercise directly after launch, but also to determine the noise characteristics and behaviour of the ERS-1 scatterometer relative to wind speed and direction. In particular we found that all major terms in the formulation of CMOD2 have to be modified. In a second paper we discuss our attempts to improve the formulation of the σ^0 -to-wind relationship (Ref. 1)

The particular design of the antennae geometry for the ERS-1 scatterometer is crucial to be able to understand its performance. We were able to characterise σ^0 noise, and the upwind/crosswind amplitude by taking cross-sections through 3D measurement space. We found that two geophysical parameters (in the CMOD2 formulation these are wind speed and direction) seem sufficient to be able to describe solution space over a wide range of wave conditions for the waves

relevant to C-band radar back-scattering. In other words, the ocean topography for these waves gives a well-defined radar signature. For low wind speeds, σ^0 noise tends to increase, most likely due to more complicated geophysical processes involving surface tension, viscosity, and spatial inhomogeneities.

For low incidence angles the measurement noise is comparable to the upwind/crosswind amplitude, leading to reduced skill in wind direction retrieval. Both wind speed and direction sensitivity at the highest incidence angles seem sufficient. Therefore it might be a good suggestion for future scatterometers to move to a range of incidence angles, e.g. starting at 25° and ending at 65° .

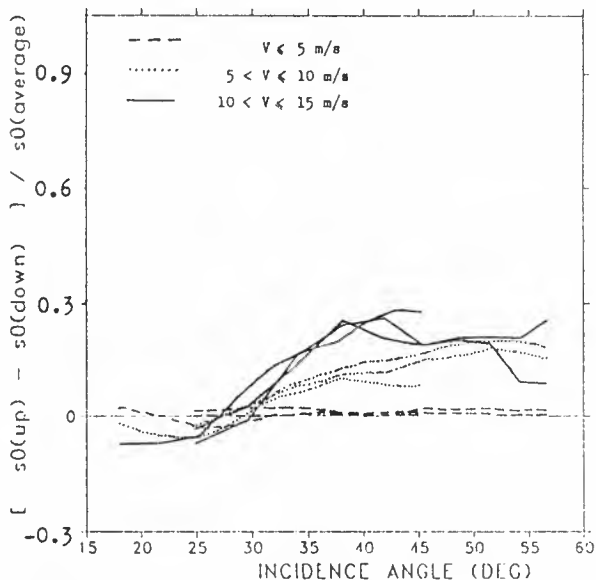


Figure 12: Upwind/downwind amplitude versus incidence angle for different wind speeds V . V is the average of scatterometer and analysis wind speed. The 3 beams are shown separately for each speed.

Acknowledgements

Numerous people contributed to this work, in particular we would like to thank Peter Woiceshyn, Ross Hoffman, John Eyre, Tony Hollingsworth, and other ECMWF staff members for their discussions on subjects involved. Also the ESA analysis and experimenters team provided a sound framework for the research to take place. Last but not least we thank ESA and ECMWF for providing us the resources for carrying out the work we have done.

REFERENCES

1. Stoffelen A., Anderson D.L.T., and Woiceshyn P.M., ERS-1 scatterometer calibration and validation activities at ECMWF: B. From radar backscatter characteristics to wind vector solutions. *Proc. European 'International Space Year' Conference*, Munich, Germany, 30 March - 4 April 1992.
2. Long A.E., Towards a C-Band radar sea echo model for the ERS-1 scatterometer. *Proceedings of a conference on spectral signatures*, Les Arc, France, December 1985, ESA SP-247
3. Donelan M.A., Pierson Jr. W.J., Radar scattering and equilibrium ranges in wind-generated waves with application to scatterometry, *Journal of Geoph. Res.*, 92, C5, pages 4971-5029, May 15, 1987
4. Cavané A., Lecomte P., Vol 1 - Study of a method to dealias winds from ERS-1 data. Vol 2 - Wind retrieval and dealiasing subroutines, *Final report of ESA contract No. 6874187/ICP-1(sc)*
5. Guignard J.-P. et al., AMI Performances, *The ERS-1 commissioning phase mid-term review*, ESA/ESTEC, Noordwijk, The Netherlands, 24-25 september 1991.

ERS-1 SCATTEROMETER CALIBRATION AND VALIDATION ACTIVITIES AT ECMWF:
B. FROM RADAR BACKSCATTER CHARACTERISTICS TO WIND VECTOR SOLUTIONS

Ad Stoffelen¹, David L.T. Anderson², and Peter M. Woiceshyn³

¹ European Centre for Medium-range Weather Forecasts, Reading, U.K.;

² Dept. of Atmospheric, Oceanic and Planetary Physics, Clarendon Laboratory, Un. of Oxford, Oxford, U.K.

³ Jet Propulsion Laboratories, Pasadena, CA, USA

ABSTRACT

Calibration and validation activities for the ERS-1 scatterometer have been carried out at ECMWF complementary to the "Haltenbanken" field campaign. At a Numerical Weather Prediction (NWP) centre a wealth of verifying data is available both in time and space. This data is used to redefine the wind retrieval procedure given the instrumental characteristics. We found that a Maximum Likelihood Estimation (MLE) procedure to obtain the coefficients of a reformulated σ^0 -to-wind relationship should use radar measurements in logarithmic rather than physical space, and use winds as the wind components rather than wind speed and direction. Doing so, we were able to derive a much more accurate transfer function than the one currently operated by ESA. σ^0 measurement space shows no signature of a separation in an upwind solution cone and a downwind solution cone. As such a signature was anticipated in ESA's wind direction ambiguity removal algorithm, reconsideration of the procedure is necessary. Despite the fact that revisions have to be made in the process of wind retrieval we show that there is a good potential for scatterometry in meteorology and climatology.

Keywords: ERS-1 scatterometer, normalised radar cross section, σ^0 -to-wind transfer function, wind direction ambiguity removal, surface winds.

1. INTRODUCTION

At ECMWF a project is being carried out in support of the calibration and validation of ERS-1 wind scatterometer data, complementary to the "Haltenbanken" field campaign off the coast of Norway. Our work is described in two papers. Part A (Ref. 1) describes the assistance we provided in instrumental calibration, and characterisation of the normalised radar cross sections, i.e. σ^0 , as measured by the ERS-1 scatterometer. We concluded that σ^0 noise is low and that 3D σ^0 measurement space is well defined. We also showed that ESA's pre-launch σ^0 -to-wind transfer function needs major reformulation. This paper (Part B) deals with (i) the derivation of a revised σ^0 -to-wind relationship using a maximum likelihood estimation procedure, and (ii) with the retrieval of a unique wind speed and direction (wind direction ambiguity removal). For a discussion of ESA's present σ^0 -to-wind transfer model formulation we refer to part A. A quality assessment of the wind data used in this paper is also given in part A.

Long provided us with his implementation (Ref. 2) of the Maximum Likelihood Estimation (MLE) procedure as described by Britt and Luecke (Ref. 3), to estimate new coefficients for the transfer function. The first part of this paper will discuss the use of this method to derive a revised transfer function. In the second part we will discuss problems involved in wind direction ambiguity removal.

2. ESTIMATION OF THE σ^0 -TO-WIND RELATIONSHIP

2.1 Method

The MLE procedure estimates the most probable σ^0 , wind speed and direction, and coefficients of an implicitly defined σ^0 -to-wind transfer function as given for example in equations (1-3) in Ref. 1. Using this MLE procedure in a straight-forward way we found that the resulting transfer functions were not significantly better than CMOD2. This result made a review of the nature of the problem, and its implementation necessary.

An assumption made in the MLE procedure is that the distributions of error in σ^0 , wind speed and direction are Gaussian. We have shown in part A (Ref. 1, figure 4) that the standard deviation of error in the components of the wind is approximately 2.25 m/s and constant over all wind speeds. Considering this figure, we assumed a symmetric error distribution in the components of the wind. The wind speed standard deviation is approximately 2.6 m/s. So, the correlation between "true" wind speed and ECMWF analysis wind speed would start to drop around 8 m/s and approach zero around 2 m/s. Beyond that, the error distributions for low wind speeds are asymmetric. Therefore, it is clear that the statistical properties of the components of the wind are much closer to the requirements of the MLE procedure, than the statistical properties of wind speed and direction.

A second consideration is the consequence of proportional errors for MLE. The expected value of the standard deviation of error in σ^0 is proportional to the "true" value of σ^0 . We will show that this type of variation in standard deviation causes the MLE procedure to fail.

Let us assume we have a 3D measurement space with axis x, y and z, where the "true" solution is a plane with $z=z_1$. Now we make an infinite number of measurement triplets (x_m, y_m, z_m) , assuming these measurements have Gaussian errors with standard deviations $\sigma_x=\sigma$, $\sigma_y=\sigma$, and $\sigma_z=\epsilon.z_1$, for x, y, and z. Given the distribution of measurements $p(x,y,z)dx dy dz$ we will estimate the solution plane $z=z_1$. Assuming we have no a priori knowledge and neglecting constant terms, we find the solution by minimising:

$$MLE = \left[\frac{z_m - z_1}{\sigma_z} \right]^2 \tag{1}$$

over all measurements. Since we don't know σ_z we have to estimate it. The best estimate seems to be $\epsilon.\sigma_1$. Now if we minimise:

$$\iiint MLE.p(x,y,z)dx dy dz \tag{2}$$

we find:

$$z_1 = (1 + \epsilon^2).z_1 \tag{3}$$

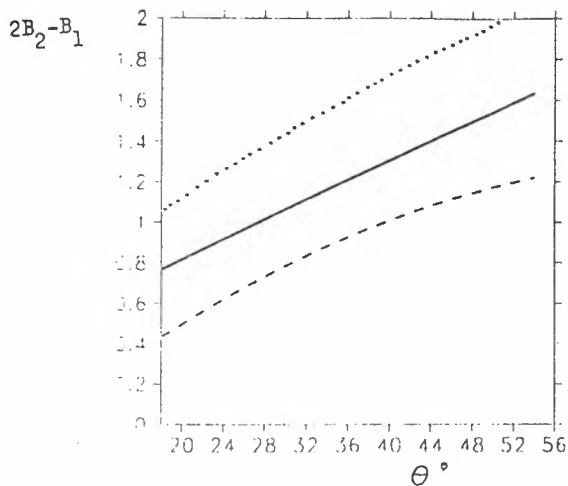


Figure 1: Upwind/crosswind amplitude as found by estimation using wind speed and direction as input (.....), using the components of the wind (-----), and for transfer model CMOD2. Wind speed is 10 m/s.

So, the theoretical solution does not match but in fact exceeds the "true" solution. In the same way, one can prove that if σ_z is estimated by e.z., a solution below the "true" plane is found.

The above example does not consider any non-linearities in solution plane. In our specific case however, the solution plane is highly non-linear as well, which will probably further degrade the performance of the estimation procedure involving parameters with proportional errors. An alternative is to do the estimation with σ^0 in dB's. The proportionality constant for σ^0 is approximately 5 %. As a consequence the σ^0 error standard deviation in dB's has an approximately constant value of 0.2 dB. The drawback of logarithmic rather than physical space, is that the σ^0 instrumental error standard deviation is expected to be Gaussian in physical space, whereas in logarithmic space the standard deviation is expected to be slightly non-Gaussian and skew. In practise, it depends on the relative non-linearity in the formulation of the transfer function in physical and in logarithmic space, as to whether it is advantageous to do the estimation in one space, rather than the other.

A non-linear surface of itself will also lead to errors in MLE. A simple example illustrates this. Assume we have a 2D measurement space with axis x and y, and a true solution $x_1^2 + y_1^2 = 1$. We now make an infinite number of measurement pairs (x_m, y_m) , which have Gaussian error standard deviations $\sigma_x = \sigma$ and $\sigma_y = \sigma$, and estimate a solution lying on a circle with $r = r_s$. Assuming no prior knowledge is present, we can define our objective function as:

$$MLE = \left[\frac{r_m - r_s}{\sigma} \right]^2 \quad (4)$$

Minimising this function over the measurement distribution $p(x,y)dxdy$, and assuming $\sigma \ll 1$ gives the solution:

$$r_s = 1 - \sigma \sqrt{\frac{2}{\pi}} \quad (5)$$

This error is first order in σ .

In a similar way it can be proved that if we try to fit the above measurement distribution with a solution like $(x + B)^2 + y^2 = r_s^2$, then we will introduce a positive term in equation (5) increasing the solution radius r_s . One could regard B as a bias misfit term.

The assumption $\sigma \ll 1$ prevents "aliasing" problems. If $\sigma = 1$ then measurements for example at $(x, y) = (0, 1)$, i.e. the top of the circle,

can either originate from "true" values at the top or the bottom, or even from anywhere on the "true" circle. The distance of the measurement point to the "true" point would be different in the cases considered. In MLE however, the likelihood that this particular point is very close to the "true" circle is infinite in all cases, since the point lies on the "true" circle.

In our estimation problem we have highly non-linear surfaces, for instance in the relation of σ^0 to wind speed, and σ^0 to wind direction. Moreover, if we are unable to estimate the bias term in CMOD2 correctly, we will have problems with the upwind/crosswind and upwind/downwind term similar to those introduced by the B term in the above problem. The "aliasing" problem will occur for low wind speeds, where the wind direction standard deviation is close to the upwind/crosswind angle difference. Finally we note that if the data selected for the estimation procedure represents an inhomogeneous distribution of the parameters involved in the estimation, then further instabilities in the MLE procedure may be introduced.

2.2 Simulation

Given the above considerations, we re-examined the estimation procedure to see whether the problem is properly posed. To this end we studied the behaviour of the MLE procedure using simulated data for which we know the true solution. Analysis winds were chosen to be "true" winds, and "true" σ^0 s were simulated from them using CMOD2. In part A we estimated the noise characteristics of both the winds and the σ^0 s to be used in the estimation of the transfer function coefficients. In our simulations we added noise to the "true" winds with a Gaussian standard deviation of 2.25 m/s in the wind components. At the time we did the simulations we were not yet able to accurately estimate the noise level in σ^0 . The noise estimates used in the simulations vary slightly, but were pessimistic (too high). Since all the problems considered above are related to the level of noise in the data, accurate noise estimates are of the utmost importance. Since we found that the selection of data used in the estimation plays an important role, we used wind distributions that were also used for tuning with real data.

In figure 1 we compare the upwind/crosswind amplitude for two simulation exercises, only different in the sense that we used wind speed and direction in one case, and wind components in the other case as input for the MLE procedure. It is evident that estimation in wind components is to be preferred, as suggested earlier.

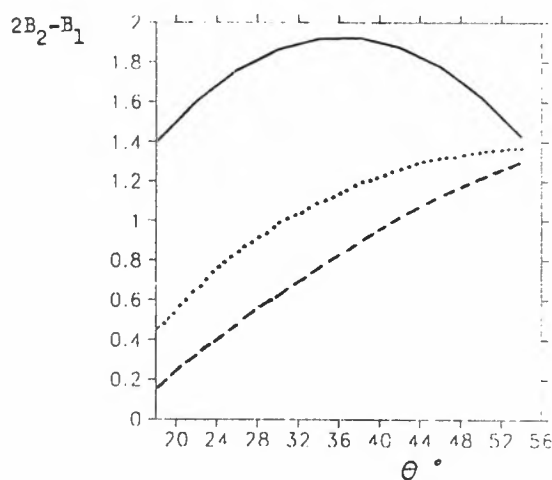


Figure 2: Upwind/crosswind amplitude found by estimation using sigma naught in physical space as input (-----), using sigma naught in logarithmic space (.....), and for the simulation model CMOD2 (-----). Wind speed is 5 m/s.

Figure 2 shows the upwind/crosswind amplitude for two simulation cases differing in only one respect: the upper curve is obtained by MLE in physical space, whereas the lower curve is obtained by MLE in logarithmic space for σ^0 . Not only does the upwind/crosswind amplitude show major differences, but the bias term and upwind/downwind amplitude are also significantly worse when estimation is made in physical space. Experiments where we varied the σ^0 error standard deviation to be either Gaussian in physical or logarithmic space did not show any significant difference in results.

In most experiments we found that the upwind/crosswind amplitude is very sensitive to slight changes in the bias term. This indicates that in reality we need a formulation for the bias term which fits the data accurately. Different but reasonably uniform wind distributions containing up to 20 000 points, gave slightly different answers after convergence of the MLE procedure. We found in general no dependence of the result on initial conditions, and in most cases 25 iterations were sufficient to converge to the solution.

2.3 Data Selection

Since we found that the MLE procedure is not particularly stable, it appears to be important to select a high quality and statistically well conditioned input data set. The following filters were tested and applied:

- ◆ Spatial correlation in the data introduces local minima in solution space, therefore input winds and σ^0 s should be spatially decorrelated. We created data sets where the spatial separation is at least 300 km between one selected data point and the next.
- ◆ Ice and fractional ice were filtered by a SST filter, if the SST is below 6 °C no data are extracted.
- ◆ We filtered the data to achieve a more uniform wind speed distribution than the usual Weibull distribution seen in nature. Although the wind direction PDF over the globe and several days varies by a factor of two with wind direction with respect to one particular beam, for all three beams together the variation is less than 10 %. Therefore after performing a limited number of tests wind direction filtering is currently not used.
- ◆ The distribution of incidence angles covered is irregular because the fore and aft beams have a range of incidence angles only partly overlapping the mid beam incidence angle range. We used a filter to achieve a more uniform coverage of incidence angles over all three beams.
- ◆ Because antenna biases were present on the scatterometer we also made a filter selecting beams in such a way to achieve equal coverage for all three beams.
- ◆ Steadiness: We used a filter selecting only those winds that are sufficiently steady over a certain time period. We compare for each selected ERS-1 scatterometer site the ECMWF guess field wind vector difference between the 3 and 6, and the 6 and 9 hour forecast. The average of both vector differences is normalised by 5 m/s plus the average of wind speed over the three times considered. The normalisation is such that this steadiness filter excludes both high and low winds, if unsteady. At present the selection threshold is set to 0.2.
- ◆ We also started experiments with time filters. Normally ERS-1 observations differing up to three hours with the analysis time are selected. Bringing the time window down to two hours has so far not shown any impact.
- ◆ The ECMWF model is believed to be more accurate in the Atlantic than for instance in the Southern Hemisphere. As described in part A (Ref. 1) we did not see any statistical difference for surface wind speed verifications between those areas. We have not yet experimented with filtering different regions of the globe.
- ◆ If a reasonable transfer model already existed, then one could reject σ^0 data if the triplet of measurements had too large a distance to the transfer model solution plane in measurement space. This filter has to be used carefully since it could severely bias the MLE result towards the transfer model used for selection. The filter is currently being investigated and was not used in the results presented here.

A typical cross-section through a selected data sample is shown in figure 3. The size of this particular sample is approximately 14.000 points, gathered over the globe over a period of 20 days, using the first 6 filters mentioned.

2.4 estimation with real data

In part A (Ref. 1) the formulation of CMOD2 is given, and it is shown that all major terms of that transfer function would need revision. Up to now we have not reached the point where we are satisfied with a formulation which describes all aspects of the σ^0 -to-wind relationship as diagnosed in the first paper. However, to show the progress made we give our preliminary formulation in Appendix A, and below the results obtained with it so far.

The formulation still contains 18 coefficients. Our experience with MLE for this problem is that more degrees of freedom lead to instability. This of course depends on how a formulation potentially can fit the data. However, because of the non-linearities in the transfer relationship our feeling is that even a perfectly formulated function with too many degrees of freedom would show aberrations after estimation. Therefore the philosophy we adopted to develop a formulation, is to constrain the solution as much as possible using the diagnostics described in part A (Ref. 1)

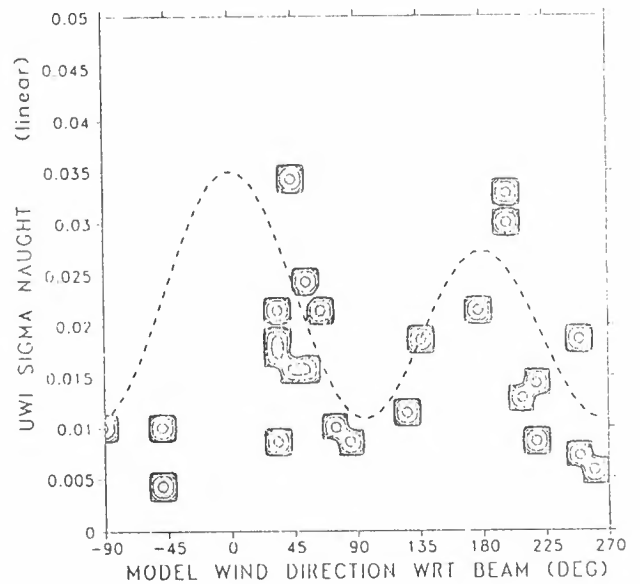


Figure 3: Selected 2D data distribution of sigma naught versus analysis wind direction, for analysis wind speeds between 9 and 10 m/s and an incidence angle of 48.6 degrees. Input data are from 6 GMT 4/11/'91 to 3 GMT 4/11/'91 and all over the globe.

Using the model formulation as in appendix A and having adapted the MLE software to work in logarithmic space for σ^0 , and in the components of the wind, we improved significantly on the performance of CMOD2 as measured by validating against independent ECMWF analysis data. The standard deviation of the difference of scatterometer retrieved winds and analysis has decreased by 20 % to approximately 2.1 m/s, and where CMOD2 is biased low by 1.1 m/s the new transfer model only has a bias of -0.2 m/s. Running ESA's wind direction ambiguity removal scheme CREO we also find a better performance for wind direction retrieval. The bias term (that part of the transfer function independent of wind direction) in the present model is such that biases as a function of wind speed and incidence angle are decreased significantly. However the upwind/downwind amplitude is still linear in wind speed and incidence angle, and so is unable to describe the saturation behaviour as can be seen in part A figure 11 (Ref. 1). Although in the present formulation the upwind/crosswind amplitude will describe saturation, it is still unsatisfactory. At high wind speeds the amplitude drops too fast. Therefore we stress again that the formulation is still preliminary, and our aim is simply to show the progress made to date.

During the "Haltenbanken" campaign off the coast of Norway high quality wind data was obtained, using an array of TOBIS buoys, and several other wind sensors, provided by a number of research groups mainly in Europe. Officer (Ref. 6) made an extensive comparison of several transfer functions over the "Haltenbanken" campaign data. For this data set CMOD2 has a wind speed standard deviation of 2.8 m/s, compared to 1.9 m/s for our model. No significant bias is present in either both model. Using Officers Slice algorithm for dealiasing (Ref. 4) the directional standard deviation is 19.9 ° for both models.

3. WIND DIRECTION AMBIGUITY REMOVAL

Comparing the operational ERS-1 scatterometer winds with the "Haltenbanken" campaign data, Officer finds a standard deviation for wind direction of 102 °. This number indicates something is wrong in the operational wind direction ambiguity removal procedure as run by ESA and named CREO (Ref. 5). Running the CREO algorithm at ECMWF we find quite a number of problems, some of which problems are related to CMOD2, and not to the ambiguity removal process itself. However, with the improved σ^0 -to-wind transfer function intrinsic ambiguity removal problems appear more clearly.

3.1 CREO

CREO performs several steps in order to obtain an unambiguous wind field:

◆ Its first step is based on minimisation of the following maximum likelihood estimator (MLE) for varying wind speed and direction:

$$MLE = \sum_{i=1}^3 \left[\frac{\sigma_{mi}^0 - \sigma_{ei}^0}{SD(\sigma_{ei}^0)} \right]^2 \quad (7)$$

where σ_{mi}^0 is the measured value, and σ_{ei}^0 is obtained from the σ^0 -to-wind transfer function for a trial value of the wind vector. The minimisation is done for each cell and the triplet of measured σ_0 s (Also σ^0 pairs can be processed). Over the full wind domain this objective function will have several local minima, with the two most probable solutions in general approximately 180 ° degrees apart, due to the small upwind/downwind amplitude in the transfer function.

◆ In the second step of CREO two fields are constructed across the full swath and a distance of 3000 km along the swath. The two fields are supposedly blowing in opposite directions. Information on potential skill in discrimination between upwind and downwind is used in this step.

◆ The third step is called "autonomous dealiasing", where the CREO algorithm tries to select one of the two fields on the basis of a sufficient difference between them in MLE averaged over all cells. Optionally this third step can be circumvented.

◆ If this is not possible, step four is to check which field is closest to a background wind field again over an area typically 500 km X 3000 km. If the large scale fit of the closest is not acceptable no solution is given. The processed areas overlap by one-thirds in order to be able to check consistency.

3.2 Performance

As shown in section 2.1 a MLE for σ^0 in physical space does not converge to the desired answer, while estimation of σ^0 in logarithmic space gives much better answers. Therefore, one might also want to pose equation (7) in logarithmic space rather than physical space. We are currently investigating the performance of CREO in logarithmic space, but do not expect dramatic changes. However, the issue whether to normalise equation (7) with a noise estimate computed from the measurement or from the solution is no longer important, because noise is virtually constant in logarithmic σ^0 space as stated earlier.

Figure 4 shows an example of dealiasied winds using the CREO algorithm at ECMWF with the σ^0 -to-wind transfer function as described at the end of section 2. Above the across-track line as indicated wind direction solutions are in reasonable agreement with the

ECMWF analysis. Below this line however, CREO wind direction solutions are 180 ° different. Verification with satellite cloud images shows there is no reason to believe in a 180 ° shift along this line. Also in numerous other occasions the same type of across-track erroneous shift lines are observed. In step 2 of CREO the wind fields are build up from the outer swath. Only at the two outermost cells, the wind direction solution of a cell in a previous across-track row is used to compute the wind direction solution for the current cell position. For all other cell positions across the swath only two previous cells in the same row are consulted in the majority of cases. This explains the type of error described above. One approach would be to extend the area of consultation when computing a wind direction solution for a particular cell over at least two across-swath rows.

Since there will be a certain probability when trying to build up two parallel but opposite wind fields that from a certain position onwards the two fields will be the same, one would rather not process large areas at the same time but areas as small as feasible with large overlap zones to check performance. Since typical surface wind patterns appear within 1000 km, the 3000 km along-swath distance used by CREO might be overdone.

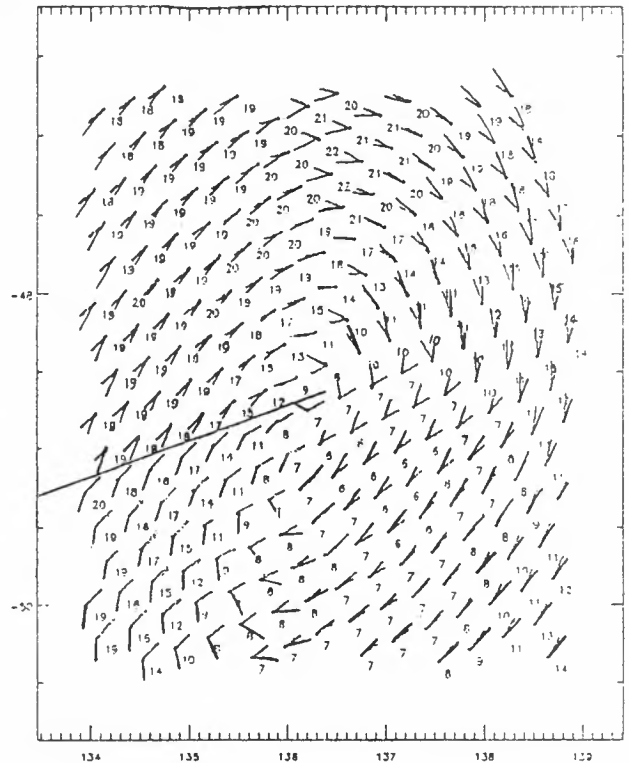


Figure 4 : Wind pattern as obtained from CREO using the transfer model discussed in section 2.4 (grey) compared to the ECMWF analysis winds (black). The numbers indicate wind speed from the scatterometer. The area is centered around 49 S and 136 E, and time is approximately 12 GMT 6/11/'91.

Equation (7) is equivalent to computing the distance in a 3D σ^0 measurement space where the axis are normalised by the measurements error standard deviation. So, interpreting slices through σ^0 measurement space, as explained in part A and shown in part A figure 8, will help us in understanding the solutions which are computed in the first step of CREO. As anticipated before launch the solution plane in σ^0 measurement space would consist of two cones intersecting along three lines (Part A, figure 7). One of the cones represents measurements for when the mid antenna beam is pointing upwind, and the other cone for when the mid beam is pointing downwind. So for this scenario, one would compute a different distance to solution plane for upwind and downwind. In reality it appears that there is no signature in σ^0 measurement space of upwind or downwind. Moreover

the upwind and downwind cone coincide (figure 5) and no skill will be present in "autonomous" ambiguity removal. Running the CREO algorithm with different σ^0 -to-wind transfer functions, having different upwind/downwind amplitudes, we indeed found that those areas which were dealiased autonomously were incorrect in about 50 % of the cases.

Since CREO relies heavily on autonomous dealiasing its philosophy has to be changed, and step 4 probably needs revision. It appears however still to be a good strategy to rely only for larger spatial scales on the meteorological guess wind field. The knowledge that autonomous dealiasing is not feasible and meteorological wind direction information has to be used anyway, is an argument to develop a full variational wind retrieval scheme (Ref. 7) and with more confidence head towards an implementation of scatterometer wind retrieval in variational analysis schemes as developed at ECMWF.

4. THE POTENTIAL OF ERS-1

We believe that the potential impact for ERS-1 scatterometer data in meteorology and climatology is large. The level of noise in the σ^0 measurements is low, and from slices through σ^0 measurement space the signature of a well defined solution plane appears.

As verified in figure 4, the ERS-1 scatterometer has the potential of accurately identifying surface meteorological features quantitatively. In this case, the ECMWF analysis and the scatterometer data agree as to the position of this storm. In a separate paper being prepared by Woiceshyn et al., this same pass picks up a wave-like disturbance not present in the ECMWF analysis. In this case, the scatterometer has the potential of improving the analysis input for subsequent forecasts.

5. CONCLUSIONS

From the necessity to change the formulation and coefficients of CMOD2, we implemented a MLE procedure provided by ESA to experiment with new formulations for a σ^0 -to-wind transfer function. We found that this procedure needed revision in order to obtain transfer functions closer to reality than CMOD2. MLE in the components of the wind rather than wind speed and direction appears to be more fruitful. Proportional errors are difficult to treat in a MLE procedure. We found that estimating σ^0 s in logarithmic space rather than physical space is very beneficial. This might also be the case for the MLE procedure as used in the first of the CREO wind direction ambiguity removal procedure, and in the 3D variational data assimilation procedure at ECMWF for the part set up to assimilate σ^0 s.

The CREO algorithm needs revision. Autonomous dealiasing was anticipated as being the major skill of the procedure. However σ^0 measurement space shows no signature at all for an autonomous discrimination of upwind and downwind solutions. Runs with CREO at ECMWF indeed indicate no skill in autonomous dealiasing of wind direction. As found in part A the upwind/downwind amplitude is not negligible (Ref. 1, figure 11) and reaches up to 15 %. The manifestation of the upwind/downwind amplitude however appears to be parallel to the solution cone in measurement space, rather than perpendicular to it as is desirable for a skilful autonomous wind direction ambiguity removal.

Although quite a few problems have to be addressed in the procedures to retrieve unambiguous ERS-1 scatterometer winds, we believe that the instrument has great potential. In σ^0 measurement space solution plane appears to be well-defined, and σ^0 noise is low. We also uncovered already cases in which the scatterometer shows small scale features not captured by the ECMWF analysis. Improved algorithms will bring a much better definition of the wind over the global ocean.

Acknowledgements

Numerous people contributed to this work, in particular we would like to thank Dave Offiler for kindly providing us valuable verification material, and Alf Long to provide us the MLE procedure. Also thanks to Ross Hoffman, John Eyre and Tony Hollingsworth for valuable discussions. The ESA analysis and experimenters team provided a sound framework for the research to take place. Not in the last place we would like to thank ESA and ECMWF for providing us the resources for carrying out the work we have done.

APPENDIX A

The preliminary formulation of the σ^0 -to-wind transfer function as tested before the conference is:

$$\sigma^0 - 10 \cdot \alpha + 10 \cdot \gamma \cdot [V + \beta + B_1 \cos(\Phi)] + 16 \cdot \log_{10} [1 + 0.42 B_2 \tanh(B_2) \cos(2\Phi)] \quad (6)$$

V and Φ are wind speed and direction. The other main dependence is as before in incidence angle Θ . The coefficients α , β , and γ are set to a tuning coefficient times a Legendre polynomial of order 0, 1, and 2, e.g. $\alpha = \alpha_0 + \alpha_1 \cdot x + \alpha_2 \cdot (3x^2 - 1)/2$. We corrected α parabolically in Θ for Θ less than 30°, and again for Θ less than 20° to obtain a bias independent of Θ . B_1 is set to a coefficient times a Legendre polynomial of order 0 and 1, plus a coefficient times wind speed and a Legendre polynomial of order 0 and 1. B_2 is set to a coefficient times wind speed and a Legendre polynomial of order 0 and 1. $B_4 = [1 + c_1 (x + c_2) (V + c_3)]$ where c_1 , c_2 , and c_3 are tuning coefficients. $x = (\Theta - 40^\circ)/25^\circ$ is used as argument for the Legendre polynomials.

REFERENCES

1. Stoffelen A., Anderson D., ERS-1 scatterometer calibration and validation activities at ECMWF: A. The quality and characteristics of the radar backscatter measurements. *Proc. European 'International Space Year' Conference*, Munich, Germany, 30 March - 4 April 1992.
2. Long A.E., Towards a C-Band radar sea echo model for the ERS-1 scatterometer, *Proceedings of a conference on spectral signatures*, Les Arcs, France, December 1985, ESA SP-247
3. Britt H.I., Luecke R.H., The estimation of parameters in non-linear, implicit models, *Technometrics*, 15, 2, 233-247, May 1973
4. Offiler D., ERS-1 wind retrieval algorithms, *UKMO MET.O 19 Branch Memorandum No. 86.*, 1987
5. Cavanié A., Lecomte P., Vol 1 - Study of a method to dealias winds from ERS-1 data. Vol 2 - Wind retrieval and dealiasing subroutines, *Final report of ESA contract No. 6874/87/ICP-1(sc)*
6. Offiler D., Personal communication, Meteorological Office, Bracknell, U.K.
7. Roquet H. and Ratier A., Towards direct variational assimilation of scatterometer backscatter measurements into numerical weather prediction models, *IGARSS 88 Proceedings*.

FROM SIMULATED DATA, TO REAL DATA

C.Gaffard*, J.M. Lefèvre** & V.Cassé*

METEO-FRANCE
*CNRM/GMAP/AAD, **SCM/PREVI/MAR
42, Avenue Gustave Coriolis
31057 Toulouse Cedex
FRANCE

ABSTRACT

A methodology which was developed on simulated data is applied to real ERS-1 data, to calibrate and validate geophysical products.

Keywords : Backscatter modelling, Rayleigh Distribution of wind speed, Numerical Weather Forecast Model, Minimization.

INTRODUCTION

Before the launch of ERS-1 we planned to validate and calibrate the geophysical data from the altimeter and the scatterometer using products from numerical weather models.

Our approach can be divided into three steps.

First we looked at the data themselves alone to study inter-beam biases as function of incidence angle.

Secondly we tuned a backscatter model of a given form using wind fields from operational analysis.

Thirdly with the hypothesis of a given distribution of the winds vectors we studied the adjustment of the retrieved backscatter model to the data and we made some suggestions to improve the fit.

In this paper after having recalled the pre-launch results and developed some statistic computations, we present the validation of sigma-naught (σ_0), then the data set used to calibrate the backscatter model, and the results of this calibration before concluding on the research work still to be done.

PRE-LAUNCH RESULTS

METEO-FRANCE is involved into the ERS-1 experiment with the aim to be able to use wind information from ERS-1 data in its numerical forecast models [1,2].

The cost function we minimized in order to calibrate the backscatter model was :

$$CF = \sum [(\sigma_{0ret} - \sigma_{0obs}) / (Kp_{obs} + \sigma_{0den})]^{**2} \\ + [(Vret - Vobs) / Kvw]^{**2} \\ + [(Dret - Dobs) / Kdd]^{**2}$$

* σ_{0obs} and Kp_{obs} were observed values

* $Vobs$ and $Dobs$ were wind data coming from numerical weather model

* $Vret$ and $Dret$ were wind data coming after the minimization

* σ_{0ret} were calculated using $Vret$ and $Dret$ plus the value of the coefficients of the backscatter model we tried to adjust

To deal with the problem of the estimation of the variance of the measurement we evaluated σ_{0den} as the arithmetic average between σ_{0ret} and σ_{0obs} .

For the minimization we used a subroutine given by the INRIA [3]. In order to use it, we only needed a subroutine to compute both a cost function and its gradient relatively to the parameters we wanted to adjust. To improve the efficiency of the minimization we used a specific norm instead of the euclidian scalar product.

We have tested this program on simulated data. We took a wind field, we interpolated it on a simulated swath of the scatterometer. Then we calculated the sigma-naught using a given backscatter model, and we added some gaussian noise. We also added some gaussian noise to the wind field, and we tried to retrieve the coefficients of the backscatter model.

For these simulations we have succeeded to retrieve the values of the coefficients in such a way that the difference between the sigma-naught computed with these values and the sigma-naught computed with the a priori given values was always less than 3%.

STATISTICAL APPROACH

At first we expected to be able to use a statistical approach as Wentz did for SEASAT [4] to evaluate the coefficients of the backscatter model. Unfortunately with the CMOD1 form [5] it was impossible to make analytical computation. But when the analysis team agreed with the CMOD2 form [6] then we decided to make these computations.

We assumed the wind direction over the world follows a uniform distribution and the wind speed follows a Rayleigh distribution. With this assumption we were able to compute for each incidence angle the expected average and the expected variance of the sigma-naught. We were also able to compute the average of the product of σ_0 for two beams.

If we note the CMOD2 form of backscatter model :

$$\sigma_0 = A \cdot V^\gamma \cdot [1 + B1 \cdot \cos(\phi) + B2 \cdot \cos(2 \cdot \phi)]$$

where $B1 = b1 + c1 \cdot V$ and $B2 = b2 + c2 \cdot V$

and A , γ , $b1$, $c1$, $b2$, and $c2$ are polynomials of order 2 in incidence angle θ ,

we obtain :

$$\langle \sigma_{0i} \rangle = A_i \cdot \langle V^{\gamma_i} \rangle \text{ and}$$

$$\langle \sigma_{0i} \cdot \sigma_{0j} \rangle = A_i \cdot A_j \cdot [\langle V^{\gamma_i + \gamma_j} \rangle \cdot$$

$$[2 + b1i \cdot b1j \cdot \cos(\Delta\phi_B) + b2i \cdot b2j \cdot \cos(2 \cdot \Delta\phi_B)] / 2 + \langle V^{1 + \gamma_i + \gamma_j} \rangle \cdot$$

$$[b1i \cdot c1j \cdot \cos(\Delta\phi_B) + b2i \cdot c2j \cdot \cos(2 \cdot \Delta\phi_B)] / 2 + \langle V^{2 + \gamma_i + \gamma_j} \rangle \cdot$$

$$[c1i \cdot c1j \cdot \cos(\Delta\phi_B) + c2i \cdot c2j \cdot \cos(2 \cdot \Delta\phi_B)] / 2]$$

where $\Delta\phi_B$ is the difference between the azimuth of the two beams i and j .

VALIDATION OF SIGMA-NAUGHT

We have computed under the hypothesis of a Rayleigh distribution (mean speed = 6.5 m/s) for the wind, $\langle \sigma_{0i} \rangle$ and $[\langle \sigma_{0i} \rangle^2 - \langle \sigma_{0i}^2 \rangle]^{0.5}$ for $i=1,2,3$ and $\langle \sigma_{0i} \sigma_{0j} \rangle$ for $(i,j) = (1,2)$ (1,3) and (3,2) using CMOD2 with the prelaunch values [6]. The figures [a1], [a2], [a3], [a4] showed for these quantities the differences between the observed sigma-naught and the result of these computations.

We were able to notice the right agreement between the beams, and the shape of the curves which showed the variations of the fit between CMOD2 and real data.

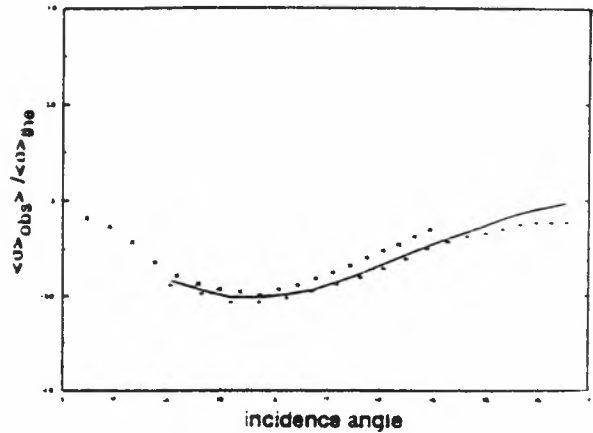


Figure [a1] : comparison for the three beams (-- for beam, * mid beam, + aft beam), between the observed mean value of sigma-naught and the processed value using CMOD2 and a Rayleigh distribution for the wind. (dB scale min=-4dB, max=+4db)

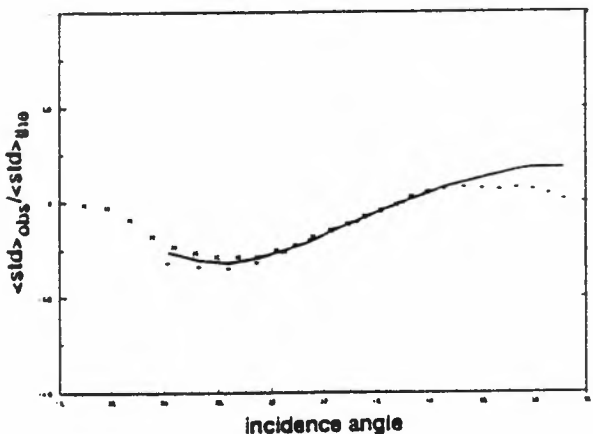


Figure (a2) : the same as fig. (a1) but for the standart deviation.

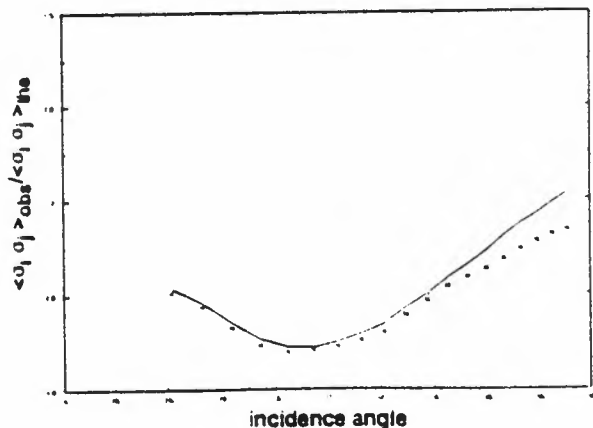


Figure [a3] : the same as fig(a1) but for the product $\langle \sigma_{0i} \sigma_{0j} \rangle$ for $(i,j)=(1,2)$ for-beam mid-beam (--), and for $(i,j) = (2,3)$ mid-beam,aft-beam (*).

DATA SET

To calibrate the backscatter model, we used the wind fields of our operational analysis. Our approach was global, without geographical selection and with a time window of $\pm 1h30$.

The sigma-naught were selected using the FDP quality control; ice points were eliminated by a geographical cut inferred from the sea surface temperature given by operational analysis.

To avoid problems of bias in our calibration process, we made a file of winds homogeneous in speed and in direction with the interpolated wind and we tried to decorrelate the data by a random choice in the available data.

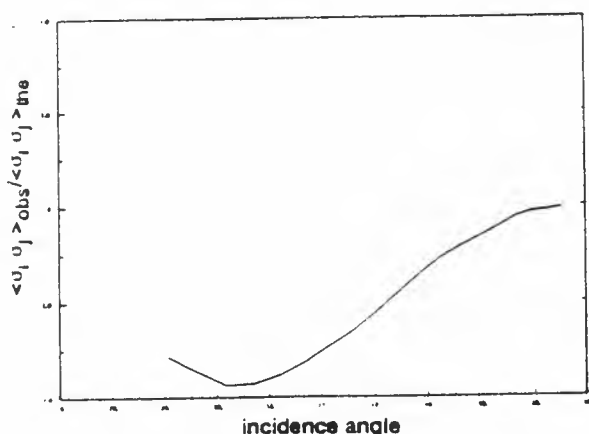


Figure [a4] : the same as fig(a3) but for the product $\langle \sigma_i \sigma_j \rangle$ for $(i,j)=(1,3)$.

CALIBRATION

With such datasets we computed sets of values for CMOD2 backscatter model.

To choose one set of values, we looked at the stability of the results, at the decrease of the cost function and at the physical consistency.

Instead of minimizing directly with the 18 degrees of freedom we processed six minimizations to determine successively the values of A , A_γ , $A_{\gamma b2}$, $A_{\gamma b2b1}$, $A_{\gamma b2b1c2}$, $A_{\gamma b2b1c2c1}$ and we studied the rate of decrease of the cost function. In order to verify if the decrease was not only due to the fitting of the data, we also used another set of data.

The results that we obtained show that the main part of the information was given by the $A_{\gamma b2}$ coefficients. The use of $b1$, $c1$ and $c2$ coefficients did not lead to an improvement of the skill for the sigma-naught processed using another set of data.

We also looked at a physical constraint : the sigma-naught had to be always positive. This condition was realized if all the extremes were positive. We were able

to compute the maxima and impose to the minima to be positive. We remarked $\phi = 0$ and π were always extrema but we also wanted them to be maxima, this condition implied the existence of another extrema ϕ_0 given by :

$$\cos(\phi_0) = -B1 / (4 \cdot B2) \text{ then } |B1| \leq 4 \cdot |B2|$$

and if we wanted that this new maxima became a minima we needed $B2 > 0$.

The value of σ_0 for ϕ_0 is

$$A \cdot \gamma \cdot [(B1^{**2} + 8 \cdot (B2^{**2} - B2)]$$

so we need $(B1^{**2} + 8 \cdot (B2^{**2} - B2) > 0$

Sometimes the use of the degrees of freedom linked with $C1$ and $C2$ led to a model which did not satisfy the physical constraints as shown on figure [b]. This effect was perhaps due to an inconsistency between the sigma-naught observed and the wind used, but there might be is a problem in the form of the model itself.

We retained a model which gave a bias of 0.8 m/s, -1.8° and a STD of 2.6 m/s, 18.1° for wind speed and wind direction respectively in an objective evaluation made by D.Offiler on the data from RENE91.

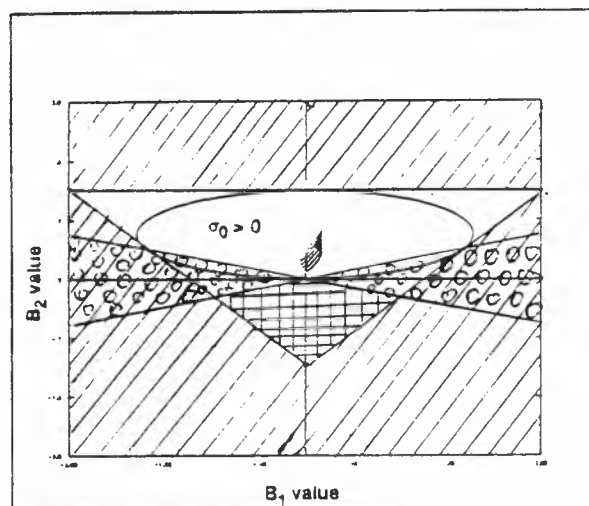


Figure (b) : physical constraints in the $B1, B2$ plane
 ☁ area where there is only two extrema
 // area where $\sigma(0)$, $\sigma(\pi/2)$ or $\sigma(\pi)$ is negative
 ⊕ area where $\sigma(\phi_0)$ is a maxima

The different curves show the evolution of $B1$ $B2$ with the incidence angle for different winds speed for a particular model. With it, for a wind speed of 4m/s and for low incidence angle we are outside the physical constraints.

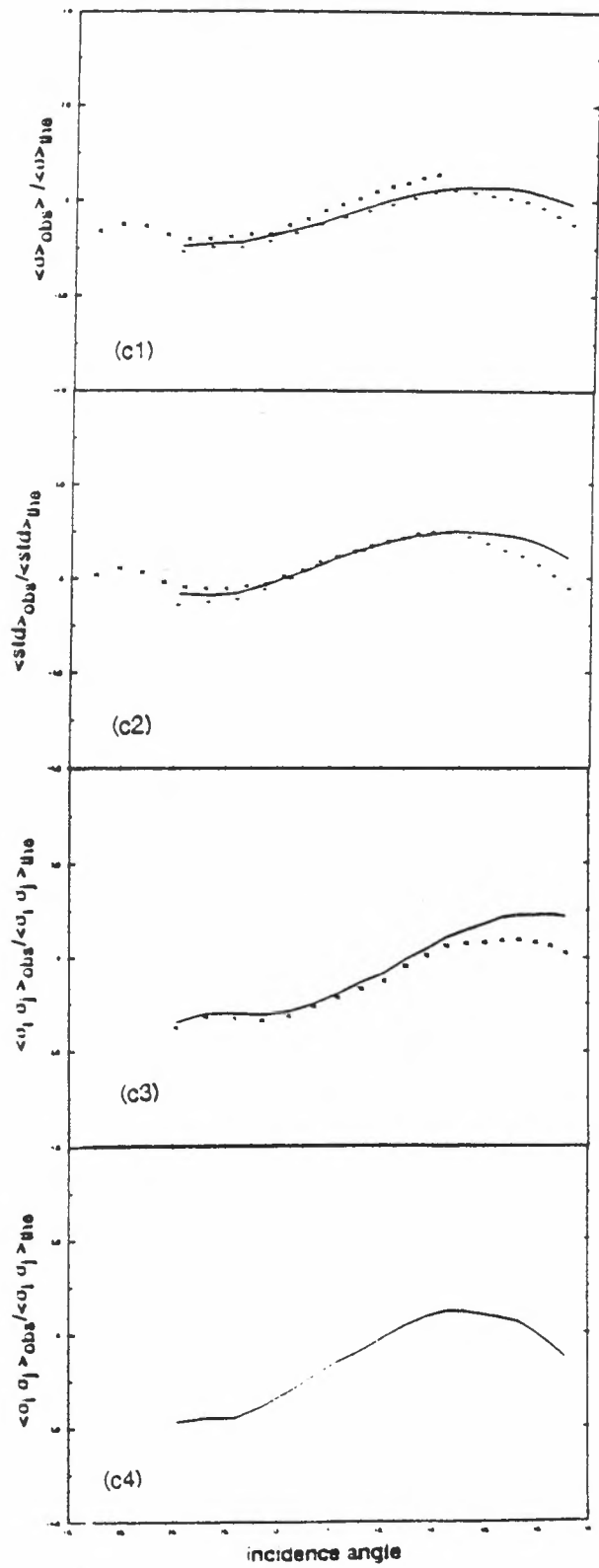


Figure (c1,2,3,4) : the same as fig(a1,2,3,4) but for the calibrated model.

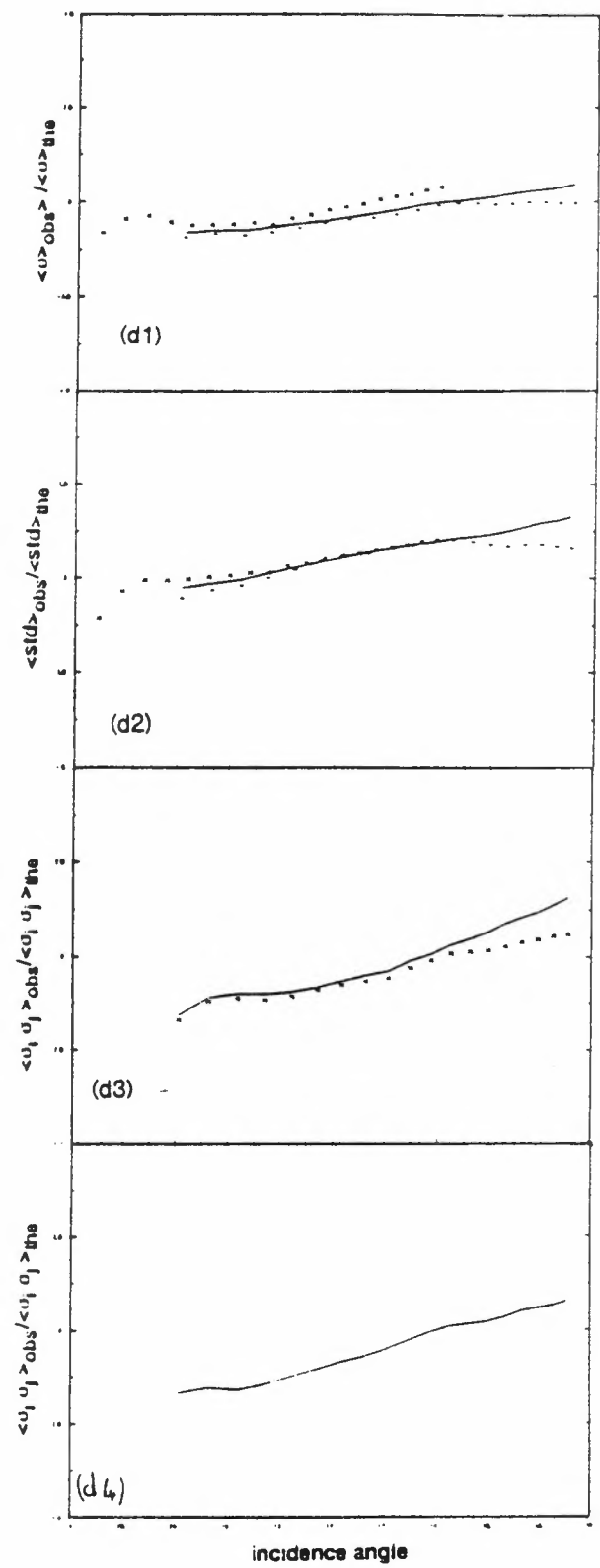


Figure (d1,2,3,4) : the same as fig(a1,2,3,4) but for a calibrated model in θ^3 .

VALIDATION OF THE MODEL

We can try to validate the backscatter model using the tools described above .

With the use of our statistical approach, we showed that if the bias between the observed sigma-naughts and those processed by our calibrated model was reduced (in comparison with those calculated by CMOD2), the variance remained high.

We also verified that the model obtained satisfied to the physic constraints.

We noticed on figures [c1], [c2], [c3], [c4] a distortion in the result with the incidence angle. This effect remained on all the backscatter models developed in CMOD2 form, for our models, as well as for the other models proposed by the other groups.

This result seemed to indicate that the form of CMOD2 was not adequate to fit the data. So we have tried to calibrate the backscatter model using a development in θ^3 for the incidence angle. The distortion was reduced like the figures [d1], [d2], [d3], and [d4] demonstrated it, but a bias remained. However this result was encouraging because it seemed to show that significant improvement could be obtained with a little adjustment on the form of the backscatter model.

ALTIMETER DATA

We have not tried to calibrate the relation between the sigma-naught and the wind speed, neither the estimation of the significative height of the waves. We have assumed the relation established for GEOSAT[7] gave acceptable results. So, in order to validate the altimeter data, we compared the ESA derived wind speed and significant wave height with data from our numerical weather and wave models. An average bias of -0.22 m and -0.16 m/s and a standard deviation of 0.9 m and 3 m/s were found respectively for the significant wave height and the wind speed.

CONCLUSION

To go from simulated data to real data, was a new challenge ! We succeeded in verifying the consistency of the data from the three beams, and in proposing coefficients for CMOD2.

A part of the difference between the observed sigma-naught and those processed with the backscatter model could be due to any error in the wind speed used. An improvement of the model could be obtained by a better selection of the data or a better evaluation of the errors made on them.

However the statistical tests seemed to indicate that the form of the model had to be changed. Now more

physical considerations are necessary to go further for the altimeter as well as for the scatterometer.

ACKNOWLEDGEMENTS

We would like to thank Patrick LELAY who developed the set of software which records and gives access to the data, and also Pierre Alain PERON, Franck DEVALLEE and Xavier DESMOULINS who worked for one year on that subject.

REFERENCES

- [1] Cassé, V., A. Ratier and H.Roquet, " Direct variational assimilation of scatterometer backscatter measurements into numerical weather prediction models", Proc. int. symp. on assimilation of observations in meteorology and oceanography, Clermont-Ferrand France, 9-13 July 1990, p153-158.
- [2] Anderson, D., A. Hollingsworth, S. Uppala and P. Woiceshyn, "A study of the feasibility of using sea and wind information from the ERS-1 satellite. Part 1: Wind Scatterometer Data", ECMWF contract report to ESA, 1987, 121p.
- [3] Lemaréchal, C., E. Panier, Modulopt, Technical note INRIA, 1984.
- [4] Wentz, F.J., S. Peteherych and L.A. Thomas, "A model Function for ocean radar cross section at 14.6 GHz.", JGR, Vol.89, n°.C3, p3689-3704.
- [5] Long, A.E., "Towards a C band radar sea echo model for ERS-1 scatterometer", Proc. 3rd int. coll. on spectral signatures, Les Arcs France, December 1985, ESA/SP-247, p29-34.
- [6] Long, A.E., Report to ERS-1 Analysis Team ESRIN 11-12 December 1990.
- [7] Witter, D.L. & D.B., Chelton, "A GEOSAT altimeter wind speed algorithm and a method for altimeter wind speed algorithm development", JGR, vol.96, n°.C5, p8853-8860.

TOWARDS AN EMPIRICAL ERS-1 WIND SCATTEROMETER MODEL

Volkmar Wismann

Universität Hamburg, Institut für Meereskunde, Troplowitzstr. 7, 2000 Hamburg 54, Germany

Abstract

During the ERS-1 Geophysical Calibration and Validation Campaign for the First European Remote Sensing Satellite (ERS-1) in the Norwegian Sea between September 15 and December 10, 1991, 46 underflights of the satellite were performed with the airborne C-band scatterometer RACS of the University of Hamburg. Wind measurements were also carried out by a network of 10 meteorological buoys, the research vessels Hakon Mosby, Planet and Gauss, a Hercules C-130 and the Dornier Do-228 aircraft.

A high-quality subset of the data obtained during the experiment was used to tune the proposed wind scatterometer model function. The given model parameters are valid for the calibration status of the ERS-1 scatterometer data before March 1, 1992.

Introduction

A C-band scatterometer is presently flying aboard the First European Remote Sensing Satellite (ERS-1) to measure ocean surface winds. In preparation for this satellite mission, the European Space Agency (ESA) has conducted a number of airborne C-band scatterometer campaigns over the North Sea, the Atlantic Ocean and the Mediterranean Sea. Based on the data collected during these campaigns an empirical prelaunch C-band wind scatterometer model for ERS-1 has been developed [1,2].

The necessity to retune this model after the launch of the satellite was generally expected since it was based on a very limited set of airborne C-band scatterometer measurements.

The ERS-1 Geophysical Calibration and Validation Campaign took place in the Norwegian Sea between September 15 and December 10, 1991. During this campaign 46 underflights of the ERS-1 were performed with the airborne C-band scatterometer RACS of the University of Hamburg [3,4]. The scatterometer was operated aboard a Dornier Do-228 aircraft of the

German Aerospace Research Establishment (DLR). The navigation system of this aircraft was also used for wind measurements during low level flights, e.g. 500 ft altitude. Wind measurements were also carried out by a network of 10 meteorological buoys of the Oceanographic Institute OCEANOR (Norway), the research vessels Hakon Mosby (Norway), Planet and Gauss (Germany) and the Hercules C-130 aircraft of the UK Meteorological Office (UK). Furthermore, wind field analyses for the experimental area were provided by the Norwegian Meteorological Office (DNMI).

The Data Set

A comparison of the wind data from the different sources showed a very high correlation for 14 of the 46 underflights of the ERS-1 satellite. Discrepancies between single measurements encountered for the other 32 underflights can be explained by great variabilities in the wind fields in space and time. In several cases the measurements of the vertical wind profile indicate that the boundary layer model, which was applied to the aircraft measurements and the wind field analyses, was not valid.

As an example of strong variations in the boundary layer the results of the measurements on October 12 are depicted in Figures 1a - 1f. Wind vector maps obtained from the scatterometer data and from the navigation system of the Do-228 aircraft are shown in Figures 1a and 1b, respectively. The measurements with the navigation system were obtained at an altitude of 500 feet, and a boundary layer model [6] was used to convert the flight level wind to the 10 meter neutral wind. The wind direction is in good agreement but for the wind speed there is a difference of 50 %. The vertical profiles of the wind speeds at position T1 and T10 are depicted in Figures 1c and 1e, respectively. A dramatic change in the structure of the wind speed profile occurred between the two reference points while there is no change in the wind directions as shown in Figures 1d and 1f.

Exact simultaneous wind measurements with the ERS-1 satellite and the aircraft can be obtained only for one

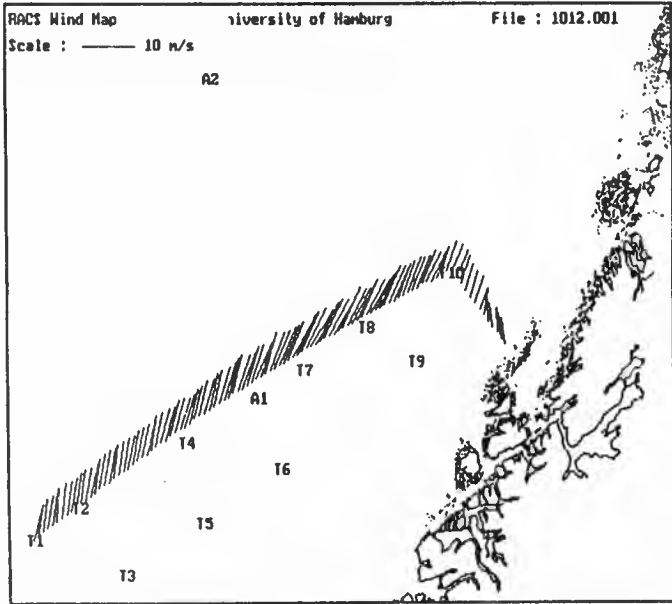


Fig.1 a : Wind vectors measured by RACS

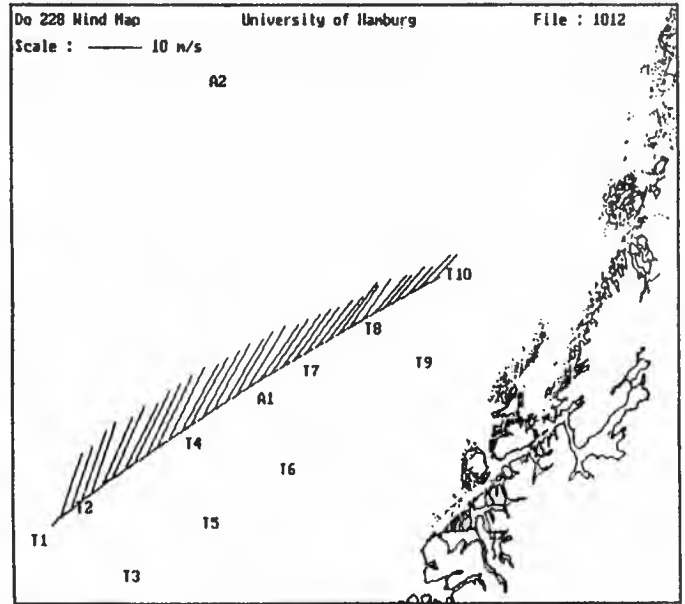


Fig.1 b : Wind vectors measured by the navigation system of the Do228

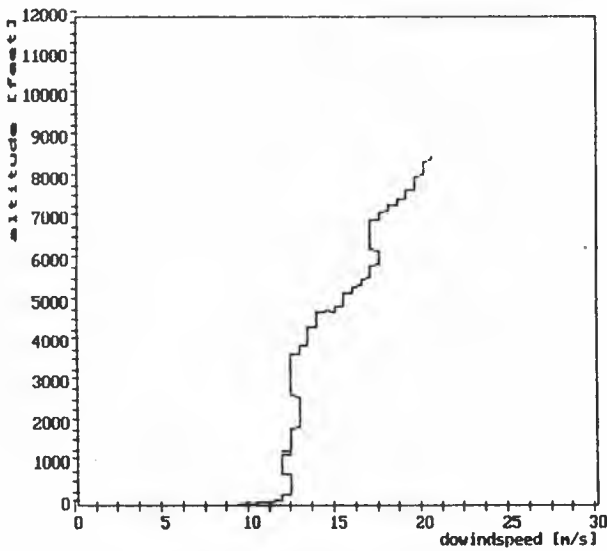


Fig.1 c : Vertical profile of the wind speed at T1

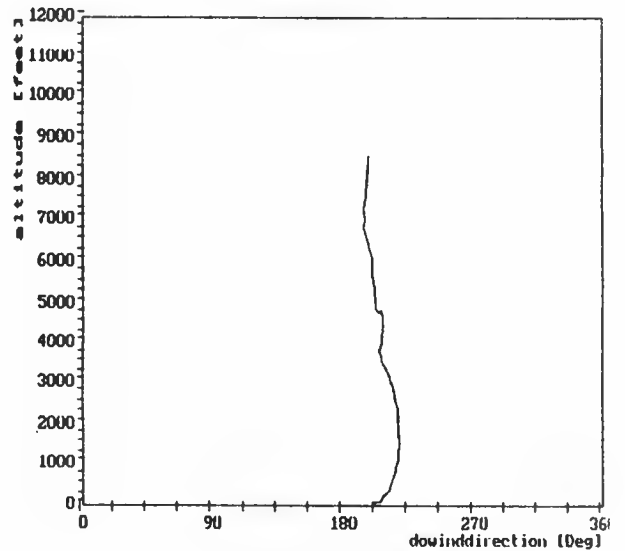


Fig.1 d : Vertical profile of the wind direction at T1

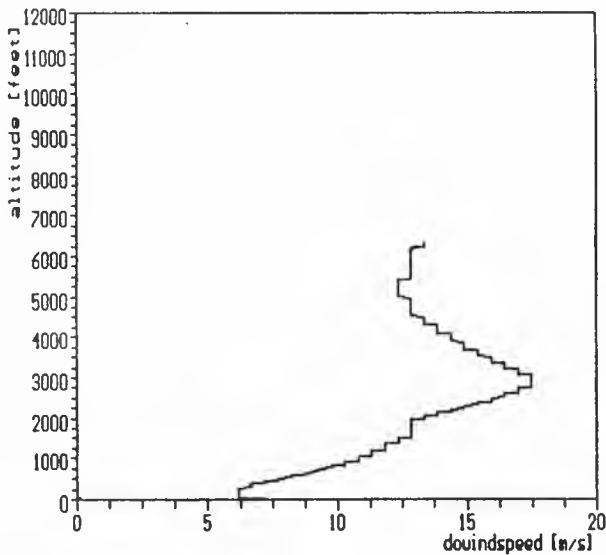


Fig.1 e : Vertical profile of the wind speed at T10

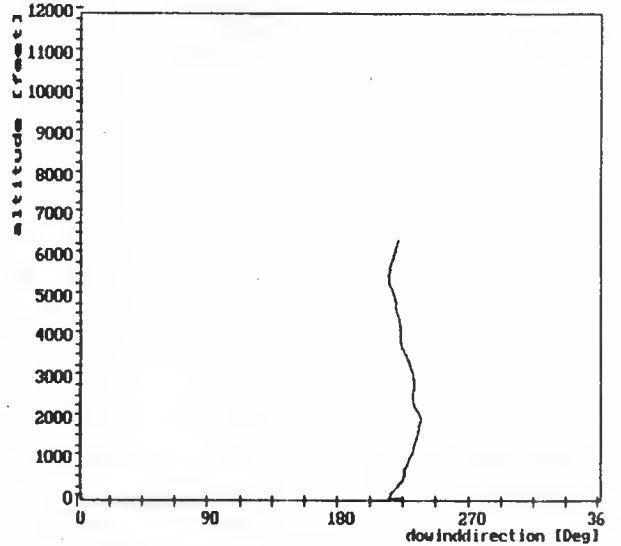


Fig.1 f : Vertical profile of the wind direction at T10

single resolution cell of the ERS-1 scatterometer due to the high speed of the spacecraft. In order to extend the data set, only underflights that showed small variabilities in the wind field in space and time were chosen for this model tuning. The second criteria was a very good correlation between the wind data from the different sources.

The result of the intensive evaluation of the in-situ data was that only the data from the following underflights of the ERS-1 were used for the model tuning :

September 28 30,

October 1, 4, 10, 16, 18, 21 22,

November 8, 14, 18, 21 and 29.

This data set contains the NRCS values measured by the ERS-1 satellite as a function of antenna look direction and incidence angle and the collocated wind speed and direction which is an average of the wind vectors obtained by RACS, the Do-228 navigation system and the DNMI wind field analyses.

The Model Function

The main difference between the prelaunch CMOD2 model function [2] and the proposed model function [7] is an independent exponential wind speed dependence for the up-, down- and crosswind antenna look direction.

The following parameters are used in the model function :

σ_0 = Normalized radar cross section of the ocean surface [linear]

Φ = Wind direction w.r.t. antenna look direction [upwind = 0 deg]

U = Wind speed in 10 meters height and neutral stability [m/s]

θ = Incidence angle of the scatterometer [deg]

The proposed model equation has the following form :

$$\sigma_0 = b_0 + b_1 \cos \Phi + b_2 \cos^2 \Phi$$

where

$$b_i = 10^{\alpha_i U \gamma_i}$$

The parameters α_i and γ_i are expanded as polynomials of the incidence angle θ

In order to minimize the computation effort the data were binned in 5 degrees for the antenna look direction

with respect to the wind direction also in 5 degrees for incidence angle and in 1 m/s for wind speed.

The coefficients of this model function were then fitted to the data using standard least square technique. They are summarized in the following table :

$$\alpha_0 = 1.173204 - 0.116702 \theta + 0.000490 \theta^2$$

$$\alpha_1 = 1.656897 - 0.146937 \theta + 0.000883 \theta^2$$

$$\alpha_2 = -1.349116 - 0.044978 \theta + 0.000121 \theta^2$$

$$\gamma_0 = 0.480203 + 0.009860 \theta + 0.000345 \theta^2$$

$$\gamma_1 = -1.788346 + 0.118614 \theta - 0.001482 \theta^2$$

$$\gamma_2 = 0.778535 + 0.033885 \theta - 0.000482 \theta^2$$

Results

The proposed wind scatterometer model was tested using the complete data set from the Calibration and Validation Campaign. Therefore the NRCS's measured by ERS-1 and the NRCS's derived from the in-situ data using the model function have been compared. In Figures 2a, 2b and 2c the difference between the actual ERS-1 NRCS measurement and the computed NRCS are plotted as a function of the actual ERS-1 NRCS measurement for upwind, downwind and crosswind, respectively.

Most of the data points are within the +/- 2 dB region. Two effects can be seen in the original colour coded plots. The scatter in the data increases with the incidence angle and decreases with wind speed. Both can be explained by the dependence of the radar cross section on incidence angle as well as wind speed and direction. The upwind / crosswind ratio of the NRCS increases with increasing incidence angle. Therefore an error in the in-situ wind direction is more important for larger than for smaller incidence angles. The same is valid for the wind speed, due to the exponential wind speed dependence of the NRCS an error in the in-situ wind speed at low wind speed leads to a greater deviation from the expected NRCS value. In addition, the variability in the wind field and therefore also the error in the measurement of the in-situ wind speed increases with decreasing wind speed.

Taking this into account, there is still a lot of scatter in the data which can partly be explained by variations in the wind field and the time differences between the ERS-1 NRCS measurements and the in-situ wind measurements. Furthermore, other environmental parameters may cause this "scatter". The airborne scatterometer measurements with RACS indicate that the angle between wind and wavefield affects the azimuthal dependence of the NRCS of the ocean surface. Differences of 5 dB in radar cross section between the two crosswind look directions have been observed. This effect is imported in the vicinity of meteorological fronts or when a strong swell is present.

Model : Wismann

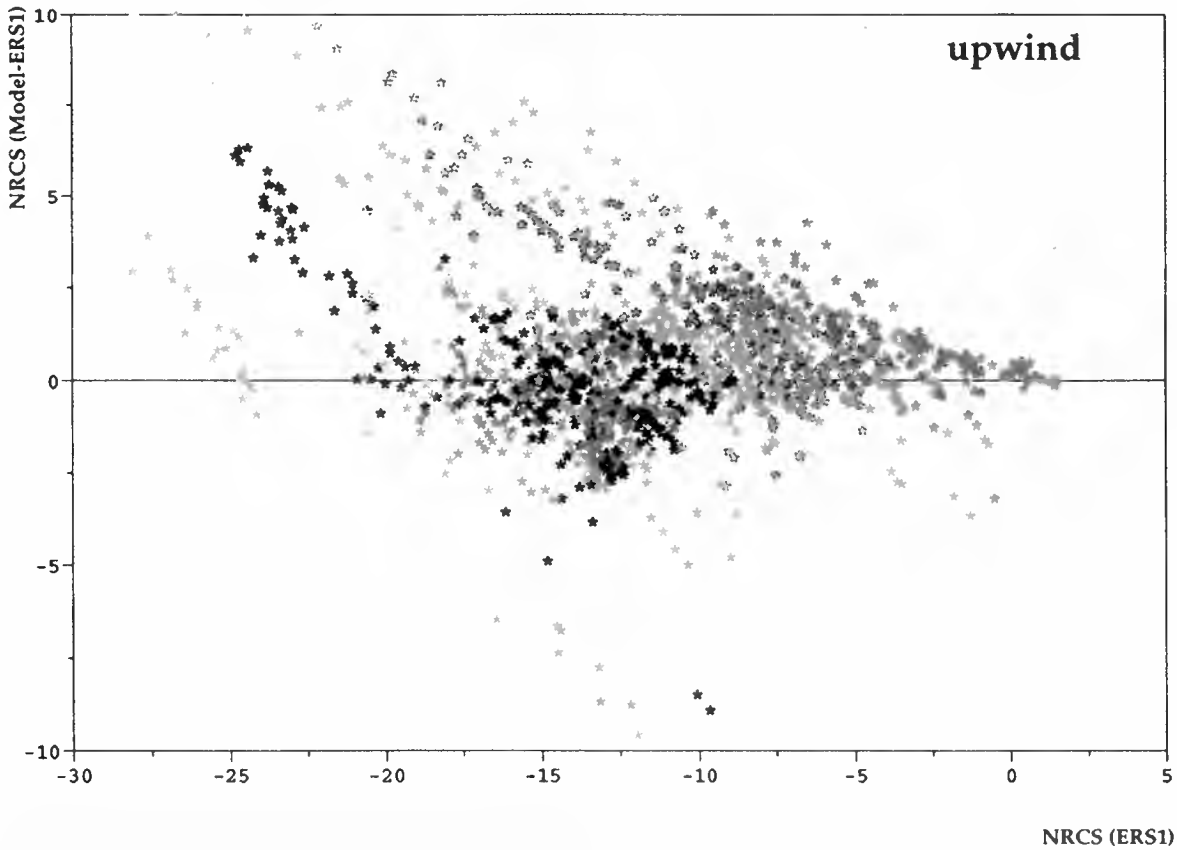


Fig 2a : Difference between the NRCS's as measured by the ERS-1 scatterometer and the from the model expected value as a function of the measured NRCS's for the upwind antenna look direction.

Model : Wismann

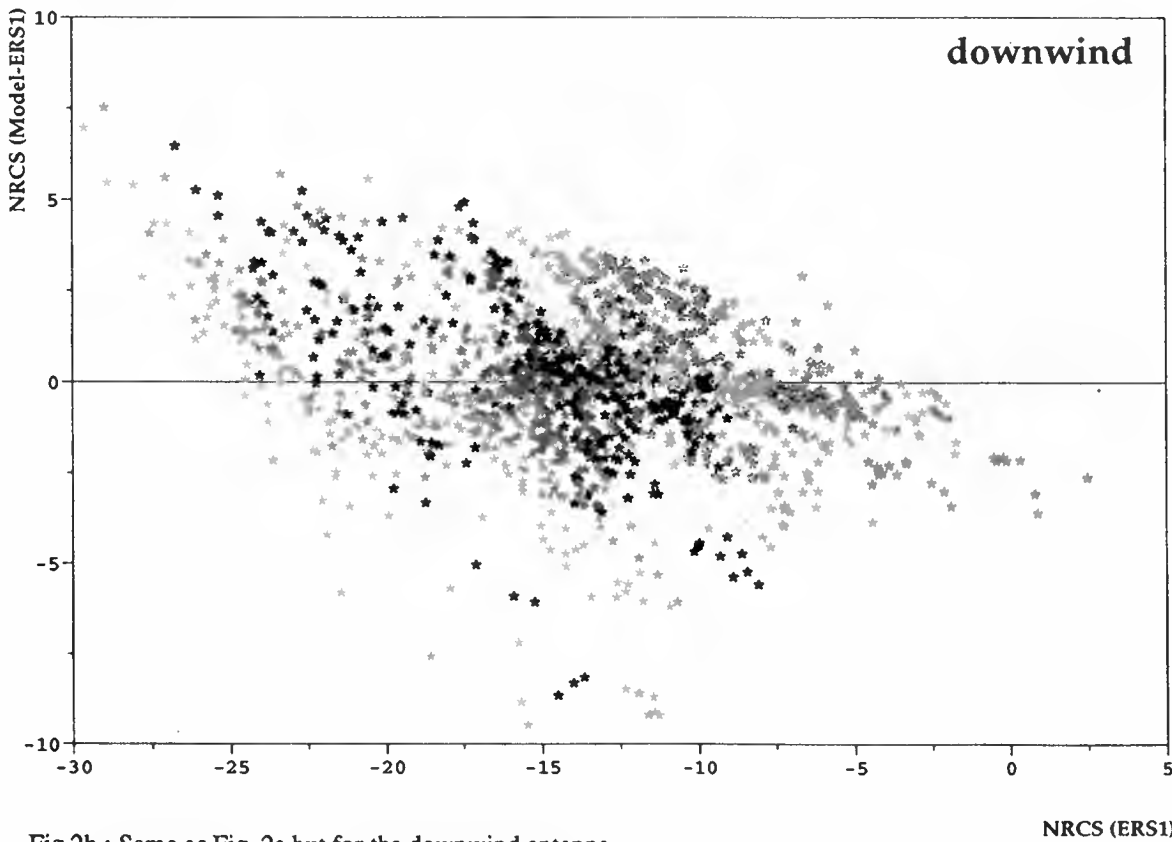


Fig 2b : Same as Fig. 2a but for the downwind antenna look direction.

Model : Wismann

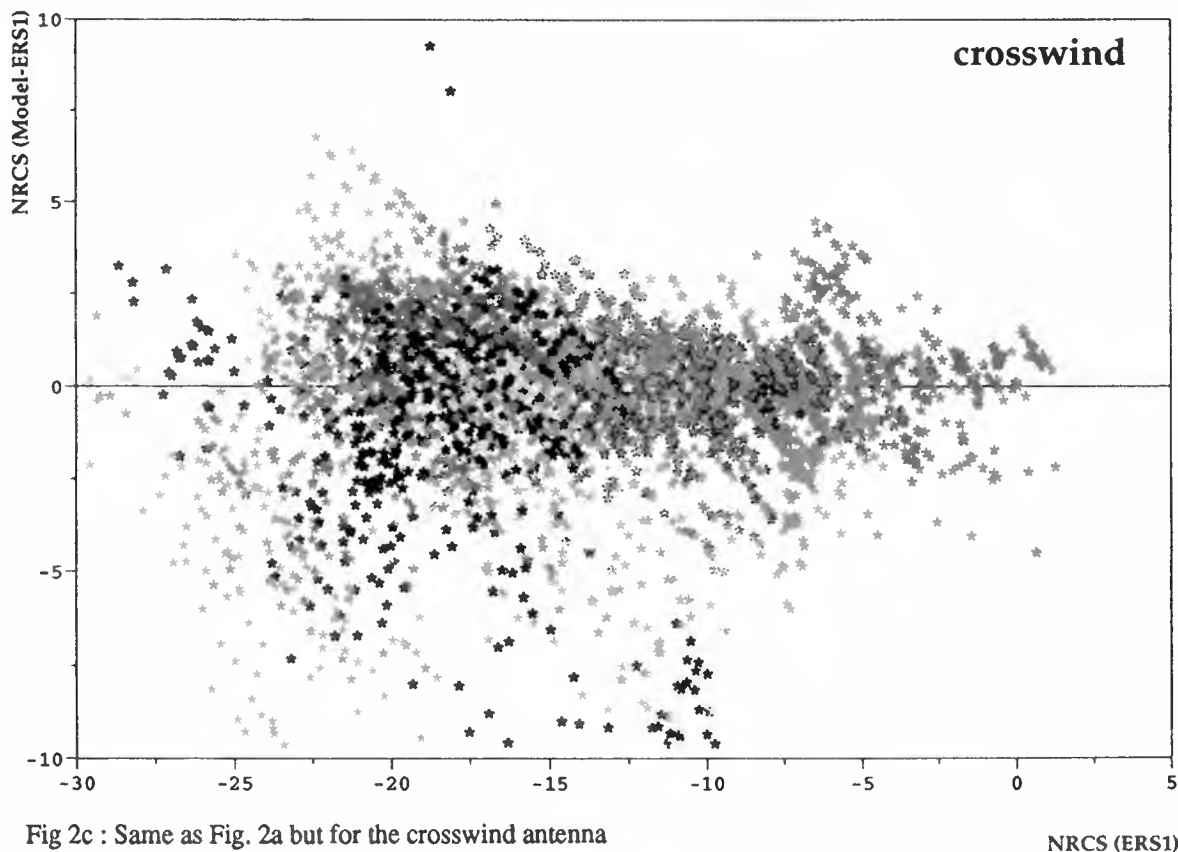


Fig 2c : Same as Fig. 2a but for the crosswind antenna look direction.

NRCS (ERS1)

It is necessary to state that the parameters given in this paper are only valid for the ERS-1 scatterometer data before March 1, 1992. On this date the calibration of the scatterometer was changed.

As soon as the reprocessed ERS-1 data for the Calibration and Validation Campaign will be available the model will be returned to the new calibration.

Acknowledgements

This research was supported by the Bundesministerium für Forschung und Technologie under grant 01QS90144 and by the European Space Agency under Contract No. 8398/89/NL/BI. We thank the crews of the Do-228 aircraft from DLR for their engaged collaboration. The wind field analyses were provided by the Norwegian Meteorological Office DNMI as their contribution to the ERS-1 Calibration and Validation Campaign.

References

- [1] Attema, E.P.W., A.E. Long and A.L. Gray: "Results of the ESA Airborne C-Band Scatterometer Campaigns, Proceedings of IGARSS' 86 Symposium, Zürich, 8-11 Sept. 1986, Ref. ESA SP-254 ESA Publications Division, pp 381-387, 1986
- [2] Long, A.E.: "Towards a C-Band Radar Sea Echo Model for the ERS-1 Scatterometer", Proceedings of the 3rd International

Colloquium on Spectral Signatures of Objects in Remote Sensing, Les Arcs, France, 16-20 Dec. 1985, ESA SP-247, pp 29-34, 1985.

- [3] Wismann, V., A.Schmidt, R.Romeiser, B.Geisler, A.Wilde and K. Boehnke: "Ocean Wind Vector Measurements with the Rotating Antenna C-Band Scatterometer during the ERS-1 Calibration and Validation Experiment", Report to ESA, Contract 8398/89/NL/BI, University of Hamburg, 1992.
- [4] Wismann, V.: "Ocean Wind Vector Measurements by the Rotating Antenna C-Band Scatterometer during the ERS-1 Calibration and Validation Experiment", Proceedings of IGARSS'92 Symposium, Clear Lake Area, Houston, Texas, 26-29 May, 1992, pp 699-702, 1992.
- [5] Wismann, V. "Wind Measurements over the Ocean with an Airborne C-Band Scatterometer during the ERS-1 Calibration and Validation Campaign", this issue.
- [6] Ezraty, R.: "ETUDE DE L'ALGORITHME D'ESTIMATION DE LA VITESSE DE FROTTEMENT A LA SURFACE DE LA MER", Contract ESA/ESTEC N 6155/85/NL/BI, 1985.
- [7] Wismann, V.: "Messung der Windgeschwindigkeit über dem Meer mit einem flugzeuggetragenen 5.3 GHz Scatterometer", Dissertation, University of Bremen, 1989.

VALIDATION AND QUALITY OF ERS-1 SCATTEROMETER WIND DATA

Y. QUILFEN

IFREMER, DRO/OS, BP70, 29280 Plouzané, France

ABSTRACT

This paper deals with the ERS-1 scatterometer wind data processed at the French Processing and Archiving Facility (Cersat, Ifremer). In addition to the fast delivery products distributed in near-real time by the European Space Agency (ESA), off-line data are generated using specific algorithms. Objectives of the work undertaken are: 1) to test algorithms and the wind transfer function used to infer the wind vector from the backscatter measurements. 2) to define rules to validate the scatterometer data. The scatterometer capabilities are shown and problems are outlined. The main difficulties are an imperfect calibration of the transfer function and the scatterometer insensitivity to the wind direction at low incidence angles. Much improvement is expected with the constitution of a large in-situ data-base to compare with the ERS-1 data.

1. INTRODUCTION

Experience with Seasat has shown that extracting the winds and removing directional ambiguities from the normalized radar cross sections (σ_0) of a two-beam scatterometer requires systematic human intervention. The three-antenna scatterometer of ERS-1 offers the possibility to determine a unique wind direction using objective criteria. An automatic dealiasing algorithm was developed at Cersat and successfully tested before ERS-1 launch [1]. The transfer function relating σ_0 to the wind vector, i.e. the C-band model, that was used was CMOD2 [2]. Since ERS-1's launch, much work has been done in order to find the best power law and to calibrate the C-band model. The model used in the present study is the

one developed by A. Long [this issue], and known as CMOD3. It is shown to be a great improvement over CMOD2. Although the choice of a model has not yet been made for use in the scatterometer software, the results obtained in this paper with CMOD3 are significant enough to show the potential and the limitation of the ERS-1 scatterometer.

1.1 THE C-BAND MODEL

Analysis of data from the Haltenbanken campaign led by ESA has provided the data set, described by D. Offiler (this issue), that was used by A. Long to infer a new C-band model formulation. The CMOD3 formulation is:

$$\sigma_0 = 10^{b_0} (1 + b_1 \times \cos\varnothing + b_2 \times \cos 2\varnothing) \quad (1)$$

where

$$b_0 = a + b \times V^{1/2}$$

$$\theta = (\theta_i - 36) / 19$$

$$\varnothing = \Phi - \Psi$$

a and b are arrangements of Legendre polynomials of order up to three in θ , b_1 and b_2 are arrangements of Legendre polynomials of order up to two in θ and V.

θ_i is the incidence angle, V is the wind speed, Φ is the wind direction, Ψ is the antenna azimuth angle.

1.2 σ_0 TO WIND PROCESSING

A detailed description of the algorithm is given in [1].

The main features are the following:

The three measurements of σ_0 from the three antenna for a given point can be considered as a surface of possible solutions constrained by equation (1). As the model will

only approximate the expected backscatter measurements, which themselves will be perturbed by noise, a maximum likelihood estimator is used to recover the wind vector. It furnishes between two and four possible solutions, named aliases, which have nearly the same speed but notably different directions. When ranked according to their maximum likelihood distance, the two first solutions (V, Φ) contain statistically the "good" wind vector. As they are nearly opposite in direction, the problem is that of resolving an upwind/downwind ambiguity.

The coefficient b_1 in (1), related to the σ_0 upwind/downwind ratio, is close to 0 and its value is not stable in the C-band model calibration process. Thus, no internal rule is efficient at the present time to resolve upwind/downwind ambiguity. The direction for a global wind field is then chosen among the aliases by comparison to external information. The dealiasing procedure used at the present time in the processing software operational at Cersat makes systematic use of the surface wind analysis of the European Center for Medium range Weather Forecasts (ECMWF).

2. DATA ANALYSIS

The analysis of scatterometer data is split in two parts.

The first one aims to estimate the accuracy of scatterometer data by comparison to the NOAA buoy data. The second one aims to highlight the statistical distribution of the scatterometer data as a function of the incidence angle and wind speed. Incidence angle and wind speed dependent bias are likely to occur for two reasons: C-band model inadequacy (analytical expression and calibration), and scatterometer inadequacy in measuring the wind vector as a result of the physics involved in the backscatter processes.

2.1 BUOY-ERS1 COMPARISONS

The buoys used in this analysis are those shown in Figure 1. These sixteen buoys were chosen by NOAA to make continuous wind measurements (integrated over ten minutes) because they are far away from the shore and are therefore suitable to compare with satellite data.

Data used are from the 4th of November to the 10th of December 1991, and from 1st of February to the 29th of February 1992. Selection of these periods depended on the availability of calibrated ERS-1 data. ERS-1 data were collocated with buoy measurements as follows: measurements falling within 25 km of a buoy observation

were retained. Buoy data were corrected to 10m reference altitude using a log-profile relation accounting for the atmospheric stability [3]. The buoy data were averaged over one hour centered on the satellite time in order to reduce the short scale variability and to make the comparison more suitable [4]. Data collocated with buoys of speed less than 1 m/s were discarded. 179 collocated measurements were thus extracted.

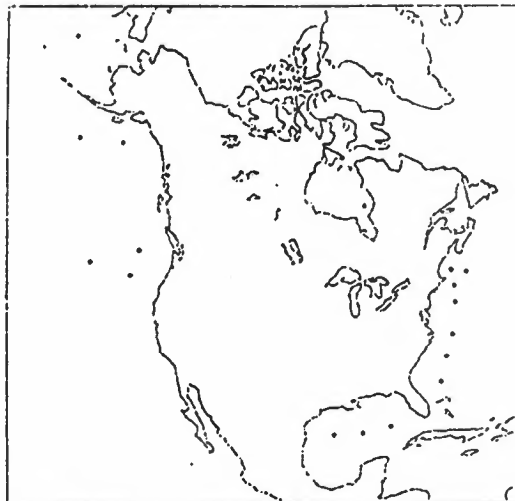


Figure 1: Positions of the NOAA buoys making continuous wind measurements.

The σ_0 were processed and the solution nearest in direction from the buoy observation was selected. This rule for dealiasing was chosen because the processing software operated at Cersat had not treated all the data for the period of time used in this study. 95% of the points determined in such a way are rank 1 or rank 2 solutions, i.e ambiguities opposed in direction and related to the best maximum likelihood estimate, showing that the dealiasing assumptions addressed in [1] and [5] are correct.

To give a measure of the scatterometer accuracy, a linear fit is performed, shown Figure 2. The root mean square of the difference between ERS-1 and buoy data is 1.61 m/s and 18.6°, which is within ESA specifications. Taking into account the buoy errors (10 % in speed and 10° [6]), time and space separation differences (about 60 cm/s and 10° [7]), and assuming the time and space sampling errors to be insignificant for the scales used (60 minutes for buoys and 50km for scatterometer) [3], the scatterometer accuracy should be about 1.3 m/s and 12°. It is difficult to separate the scatterometer errors, especially because it depends on the wind speed and incidence angle. The greatest part comes probably from the C-band model because it is not yet fully calibrated. Another part is the wind vector error derived from σ_0 noise, very low (5%),

A way to show that the scatterometer cannot give valid information on the wind direction at low incidence angles, because processes involved in the radar return are no longer only Bragg scattering mechanisms but also specular scattering mechanisms, is to calculate the distribution of the aft and fore beam radar cross-sections differences. The two beams are 90 degrees apart and when the wind is upwind for one beam (σ_0 maximum), it is crosswind for the other beam (σ_0 minimum) and the difference is maximum. What is shown in Figure 5 is the distributions for two speed ranges and for two incidence angles of $\Delta\sigma = (\sigma_1 - \sigma_3) / (\sigma_1 + \sigma_3)$. This can give a measure of the scatterometer wind direction sensitivity. When calculated using the C-band model, and assuming $b_1 \ll 1$, which is correct at low incidence angles, we have $\Delta\sigma = b_2 \times \cos 2\theta$.

Figure 5 shows the distribution of the measured values of $\Delta\sigma$, which is related to the distribution of the "true" wind direction relative to the satellite track, i.e to the wind distribution given Figure 5.b.

For low incidence angles (node 1) and for wind speeds ranging from 4 to 8 m/s (fig. 5.c) the radar return for the two lateral antennae is nearly the same whatever the wind direction. Moreover we can assume that part of the difference is noise.

For wind speeds ranging from 8 to 12 m/s (Fig 5.d), the differences increase and the form of the distribution is nearly the same as the one for high incidence angles (Fig. 5.b, node 17), showing that the wind direction can be retrieved for high winds as shown Figure 6.

The maximum of $\Delta\sigma$ are for winds oriented upwind or downwind along one beam, giving $\Delta\sigma \cong b_2$ when following the C-band model. Their values, about 0.2 for 25° of incidence and 0.35 for 52° of incidence, are of the same order of magnitude as those of the C-band model.

Although a detailed analysis of the dealiasing algorithm is not performed here, the following results can be outlined.

- 1) Dealiasing needs, at the present time, systematic use of the ECMWF wind analysis to compare with the scatterometer fields because of the low difference in the radar return for wind fields opposed in direction.
- 2) The percentage of success of the automatic processing is good (90%). Failure in dealiasing is due either to a shift in the ECMWF wind direction, or to presence of patches of wrong wind direction (180° off the "true" one) in the scatterometer field. The latter case is the most probable and is mainly due to propagation of errors from areas

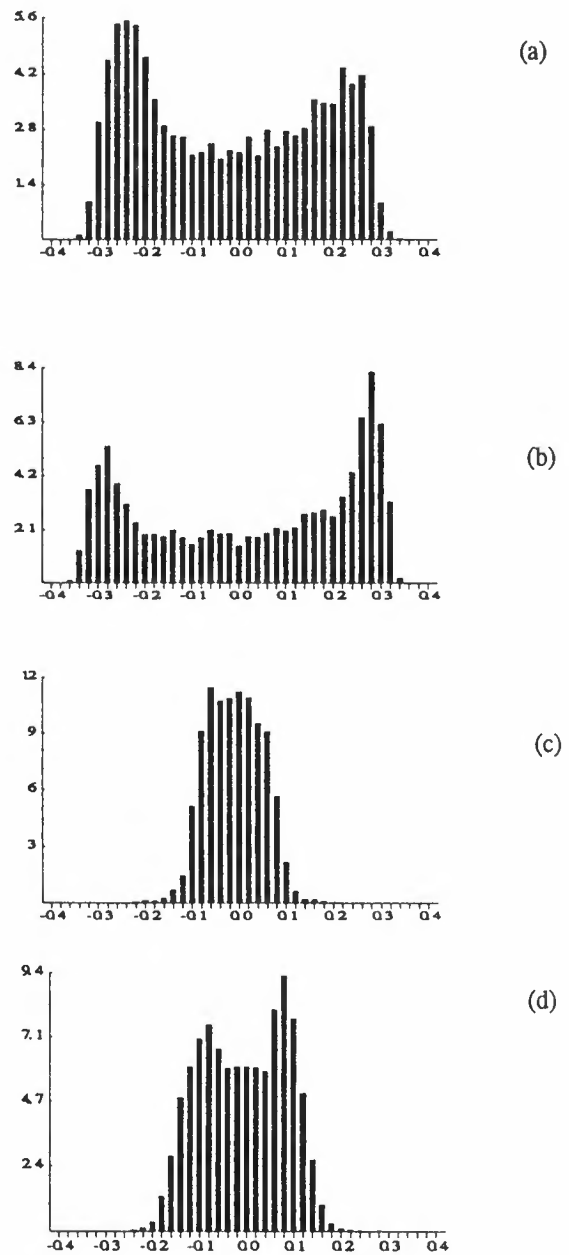


Figure 5: Distribution (%) of $\Delta\sigma$ for node 17 (outer swath) and wind speeds ranging from 4-8 m/s (a), 8-12 m/s (b) and for node 1 (inner swath), 4-8 m/s (c), 8-12 m/s (d).

of low wind direction sensitivity (low incidence or low wind speed). Work is needed in order to make this algorithm more robust.

3) Figure 6 shows cyclone ESAU which was overflowed by ERS-1 when it crossed Noumea. It shows that dealiasing works well even with strong gradients in wind direction. A striking and encouraging feature is the very

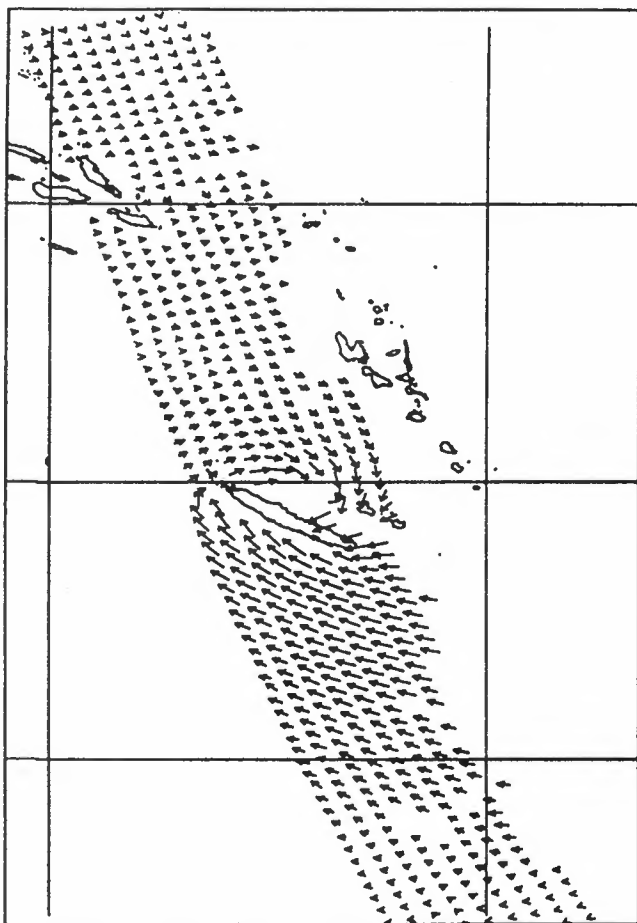


Figure 6: Cyclone ESAU as seen by ERS-1 scatterometer. February 4th 1992 at 12 h GMT. Resolution is 50km, wind speed ranges from 2 to 26 m/s.

low level of noise in wind direction, even though each point is independent of each other. It is due to the low level in σ_0 noise (5%) and to the numerical accuracy of the processing software [1].

3. CONCLUSION

This analysis of the ERS-1 scatterometer performance is preliminary because the first C-band model calibration was long to perform. This means that, even though almost a year has passed since ERS-1 launch, great improvement can still be expected in the scatterometer processing.

At the present time, first results are very promising and the ways to improve the scatterometer wind data are identified: to refine the C-band model calibration by using a global in-situ data set and to make the dealiasing algorithms more robust.

The greatest limitation in the scatterometer is its inadequacy in measuring the wind direction for the lower inci-

dence angles of the scatterometer swath, and its inadequacy to remove the 180° directional ambiguity without using external information. It is worth keeping in mind these features when using scatterometer data, as well as the scatterometer error dependence on the incidence angle when computing derivative quantities such as the wind curl.

However this paper shows that ERS-1 scatterometer data are suitable for use in fields such as climatology, ocean modeling, mesoscale meteorology and remote sensing, and that their accuracy is better than the specifications. Calibration, algorithm design and validation activities that are carried out at IFREMER will go for several years in order to improve ERS-1 scatterometer data and to prepare for ERS-2.

REFERENCES

- [1] Quilfen Y. and Cavanie A., 1991. A high precision wind algorithm for the ERS-1 scatterometer and its validation. *Proc. Igarss 91*, Helsinki, pp 873-876.
- [2] Long A.e., 1986. Towards a C-band radar sea echo model for the ERS-1 scatterometer. *Proc. on a conference on spectral signatures*, Les Arcs, December 1985, ESA SP-247.
- [3] Ezraty R., 1985. Etude de l'algorithme d'estimation de la vitesse de frottement à la surface de la mer. *Contrat ESTEC 6155/85/NL/BI*.
- [4] Pierson W. J., 1983. The measurement of the synoptic scale wind over the ocean. *J. Geophys. Res.*, 88(C3), 1683-1708.
- [5] Cavanie and Lecomte P., 1987. Study of a method to de-alias winds from ERS-1 data. *Final Report ESA Contract 6154/85/NL/BI*.
- [6] Wilkerson J.C., 1990. A study of differences between environmental reports by ships in the voluntary observing program and measurements from NOAA buoys. *J. Geophys. Res.*, 95(C3), 3373-3385.
- [7] Gilhousen D.B., 1986. An accuracy statement for meteorological measurements obtained from NDBC moored buoys. *Proc. MDS 86 Marine Data System Int. Symp.*, pp 198-204.

which value is about 30cm/s and 10° [1]. These values are yet a first estimate of the scatterometer accuracy.

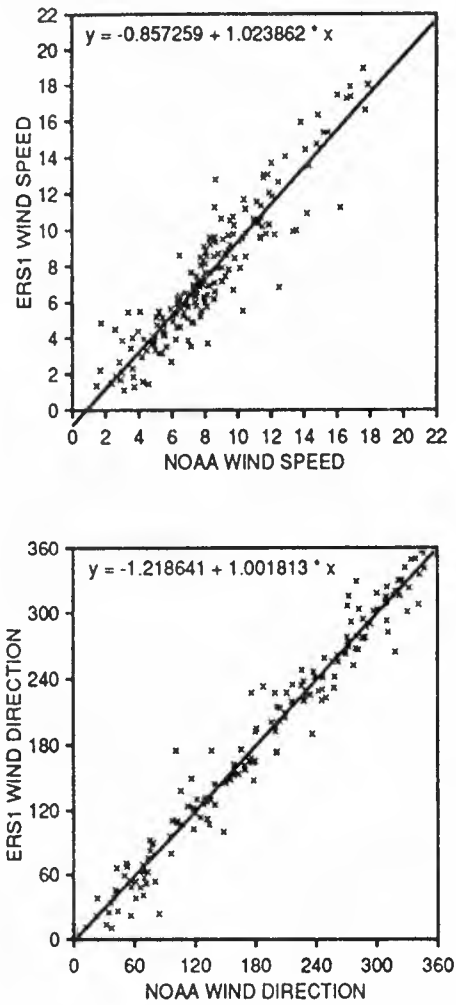


Figure 2: Linear fit between ERS-1 and buoys data

The comparison between directions is very good, showing the scatterometer capabilities in measuring the wind direction. The comparison between the wind speeds is also good, although the ERS-1 winds are biased low by nearly 0.85 m/s. This can be explained by the fact that the C-band model was calibrated using a wind analysis where the meteorological model information has great weight, thus smoothing the wind field.

As the C-band model parameters depend on the wind speed and incidence angle, a way to show this dependency on the accuracy of the scatterometer wind speeds is to compute the sum of the two lateral antenna σ_0 for the C-band model and for the scatterometer observations, removing thus the wind direction dependency. In fact this sum depends slightly on the wind direction, following the

model:

$(\sigma_1 + \sigma_3) / 2 = b_0 \times (1 + b_1 \times \cos(\varnothing + 45) / (\sqrt{2}))$
 where $b_1 \times \cos(\varnothing + 45) / (\sqrt{2}) \ll 1$ as a first order approximation. This sum depends mainly on the power b_0 , which is wind speed and incidence angle dependent. Figure 3 shows the model values, computed with the buoy wind, against the scatterometer values as a function of V for three incidence angles of the lateral antenna.

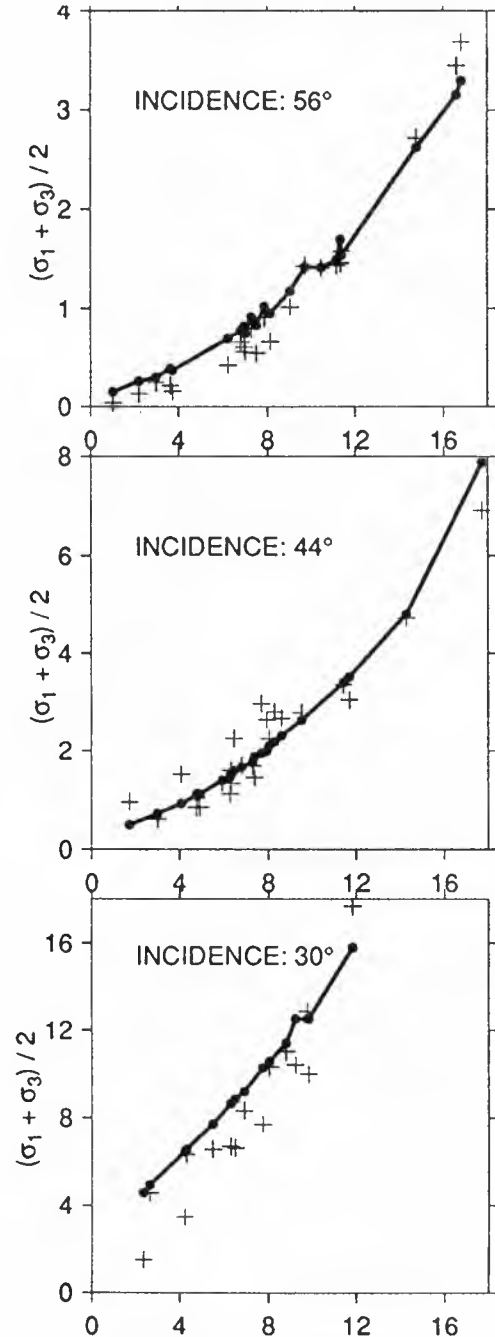


Figure 3: Model (bullet) and ERS-1 (plus) values (*100) of $(\sigma_1 + \sigma_3) / 2$ as a function of V (m/s).

This shows that the fit between the model and the observations depends on the incidence angle: it is better for medium incidence angles. At low and high incidence angles the model is higher than observations, thus giving lower values of scatterometer wind speed as seen in Figure 2.

Another interesting result is that the shape of the power law, i.e. the V exponent in the C-band model, seems to be well defined. It means that the variation of the radar-cross-section logarithmic value follows \sqrt{V} , confirming the findings of A. Long. This issue will need more examination, especially because physics involved in the backscattering at C-band are not well understood.

These findings give confidence in ERS-1 scatterometer winds and outline the need for more accurate calibration of the C-band model, especially in its dependence of the incidence angle.

2.2 THREE-DAY STATISTICS

Another way to evaluate the scatterometer data is to make statistics on a large data-set, in order to characterize the wind distribution as a function of incidence angle and wind speed. Three days of data (February 1992, 19 to 21) were processed using the operational software. The dealiasing was made by comparing the two ERS-1 ambiguous fields with the ECMWF operational wind analysis. The comparison is made by means of the normalized scalar product (NSP) between ERS-1 and ECMWF fields over areas as large as 500 km x 3000 km when not cut by low wind speed or land areas. The ERS-1 wind field is determined if the NSP is above 0.5 for one of the two ambiguous fields.

The method succeeds for 89.6% of the data, the 10.4% left undetermined were treated by an operator. The mean NSP was 0.9 which shows very good consistency between ERS-1 and ECMWF fields.

In the following analysis we use only data for which the NSP is above 0.95 in order to insure that the dealiasing algorithm worked well.

Figure 4 represents the distribution of the wind direction relative to north and relative to the satellite track for different incidence angles. The distribution relative to north calculated for the outer swath (node 17) shows the expected features, maximum for the northeast and northwest trades and for west winds. This distribution, when calculated relative to the satellite track is, as expected, nearly the same for high and medium incidence angles (nodes 17 and 10) but is trapped in the across track direction for low incidence angles (nodes 1 and 3).

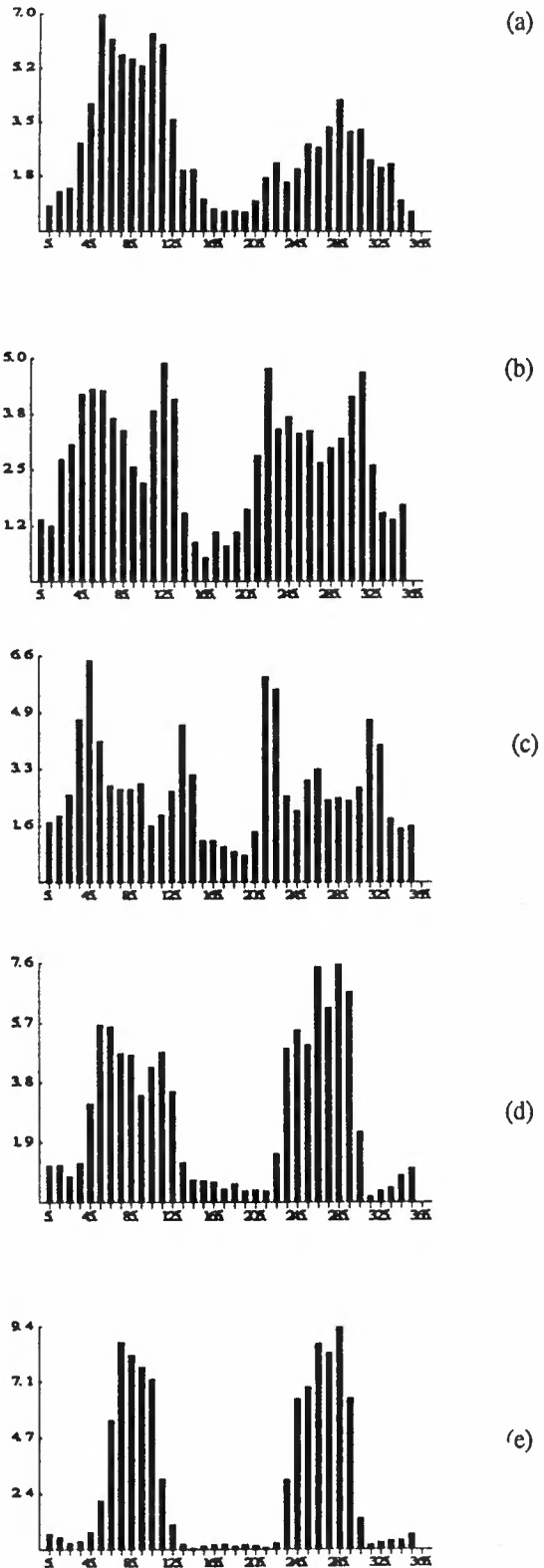


Figure 4: Distribution (%) of the wind direction between 0 and 180 ° relative to the north for node 17 (a) and relative to the satellite track for nodes 17, 10, 3, 1 (b, c, d, e)

C-band V-Polarized Radar Sea-Echo Model from ERS-1 Haltenbanken Campaign¹

A.E. Long ,

*Mathematics and Software division, ESA/ESTEC, Postbus 229,
2200 AG Noordwijk, The Netherlands.*

The ERS-1 Geophysical Calibration/Validation Campaign took place off the coast of Norway in the Haltenbanken area of the North Sea in the Autumn of 1991. Surface wind vector measurements made from a variety of platforms (aircraft, buoy, ship), were combined with a background wind field to produce an analyzed wind vector for each of the ERS-1 Scatterometer cells where σ_0 values were available. The resulting data were merged and recorded as "collocation files". Analysis of these files at ESTEC showed that half of the ~120,000 (σ_0 , wind vector) pairs were tagged as good quality and they formed a solid basis for model design. The pairs were re-classified by binning into a total of 1210 (speed-, incidence angle-, azimuth direction-) cells by cell-centering and weighted averaging over the quality tag.

The resulting plots of mean σ_0 in dB versus wind speed, v , and incidence angle, θ , were excellent and enabled a new \sqrt{v} -law (in place of the usual $\log v$ law) to be established, while its θ -dependence was closely fitted by a 3rd order Legendre polynomial. Because of incomplete coverage of some azimuth directions at the edges of the model volume (low θ in general, high v sometimes) overall estimation of the azimuth variation coefficients b_1 and b_2 were, by comparison, poorer yet good enough to produce an excellent echo-model.

Keywords: Radar, C-band, Sea-Echo Model, ESA, ERS-1, Scatterometer.

Introduction

Radar sea echo[1] has been studied for more than forty years with much of the early impetus coming from the use of radars for both military and maritime applications. Sea echo was usually studied because it was regarded as "clutter" which confused man-made targets. The advent of satellites has provided a radar platform with high stability and global coverage enabling radar to be used as a precision scientific instrument for the study and exploitation of naturally occurring phenomena which affect the radar echo. One such is surface wind. All studies of radar echo at microwave frequencies appear to show common features:

- a **rapid response** (secs) to wind speed changes
- an **increase** with wind speed, v , m/s
- a **decrease** with incidence angle, θ , defined as in optics as the angle between incident beam and local normal to the surface.
- a **sinusoidal-like** change with the azimuth angle, ϕ , the angle between the projection of the radar beam on the surface and the surface wind vector: $\phi=0^\circ$ when the beam points against the wind.

The translation of this behaviour into a quantitative echo model is the basis of wind scatterometer operation, whereby model inversion converts radar echoes into surface wind vector estimates.

The ERS-1 scatterometer has been documented elsewhere. Briefly, it is in circular orbit of period about 100 minutes, inclination 98.5° and nominal height of 785km; its three V-polarized radar beams operate at 5.3Ghz and point $45^\circ, 90^\circ$, and 135° to satellite track. Its swath width of 500km contains 19 overlapping 50km square resolution cells and incidence angles range from 18° to 55° . Coverage is essentially global over a 3-day period, apart from minor gaps due to conflicts with other instruments. To be used as a scientific instrument the beams have been painstakingly calibrated using three transponders which make point measurements near each end and middle of the swath combined with Amazon rain-forest echoes over the full swath: all beam patterns have been demonstrated to be flat and at the same level to within a maximum error of ± 0.15 dB.

An important scientific measure of radar echo is the "**normalized radar cross section**", σ_0 , which is a dimensionless property of the surface and measures the ratio of the effective echoing area per unit area illuminated.

¹ Submitted to the URSI, MICROWAVE SIGNATURE - 92 CONFERENCE, "Terrestrial Remote Sensing with Microwaves: Signatures, Techniques and Systems", IGLS - Innsbruck, AUSTRIA, July 1-3, 1992.

C-band V-Polarized Radar Sea-Echo Model from ERS-1 Haltenbanken Campaign

A model is not necessarily a complete scientific description of all the phenomena observed[2]. A balance is necessary between the main features of the observed behaviour and the use to which the model will be put. The C-band Radar Echo Model may be written in a general way as:

$$\sigma_0 = \sigma_0(v, \phi, \theta; \{U\}),$$

where $\{U\}$ is a set of unknown influences (e.g. air/sea temperature, wind/swell interaction) which are ignored in the model design. Previous work (Seasat 1978 at Ku-band[3], ESA aircraft circle-flight campaigns from 1983 onwards in the North Atlantic[4] and Mediterranean) indicated the specific model form:

$$\sigma_0 = b_0 \cdot (1 + b_1 \cdot \cos \phi + b_2 \cdot \cos 2\phi)$$

where $b_0 = 10^{\alpha(\theta)}$, $v^\gamma(\theta)$, with α and γ smooth functions of θ , and b_1 , b_2 functions of v and θ . The above are essentially the forms of ESA models CMOD1 and CMOD2

Since the time that radar measurements were first made over open sea at medium incidence angles, research has continued in parallel in the laboratory and on theoretical studies. While much progress has been made, particularly in the explanation of controlled experiments[5], an explanation of microwave radar echo from the open ocean still appears a long way off. So present model designs are almost completely empirical.

Haltenbanken Campaign Data

Over the period September 15th to December 15th 1991, a major ERS-1 Geophysical Calibration/Validation Campaign[6] took place in the Haltenbaken Area of the North Sea, with the main operation centre in Trondheim, Norway. Scientific measurements of surface conditions - waves, wind, and atmosphere - were made from a variety of platforms: five aircraft, many buoys, and three surface vessels. Emphasis was placed on covering the physical conditions in the scatterometer cells during both Ascending and Descending passes of ERS-1 in its 3-day repeat cycle.

A total of 77 ERS-1 passes were supported by surface wind vector estimation for each of the scatterometer resolution cells over open sea. The vectors came from a wind-field analysis program¹ which estimated surface-wind vector (at neutral stability and 10

metre height) by analyzing the inputs from all measuring sources, including an ever present background meteorological field acting as a sort of anchor. Depending on the number and quality of the sources, each vector was tagged with a quality measure, Q (from 0 to 99), and for each 50km square scatterometer resolution cell the wind vector, the σ_0 -triplet, and the Q -value were merged together to form a collocation and saved in the "collocation file" for that particular ERS-1 pass.

Survey of Collocation Data

The collocation data covered about 40,000 scatterometer cells. Using a minimum quality of $Q=5$, a value which would ensure corroboration from a least one sensor of the background meteorological wind-field, approximately 50% of the in total 120,000 beam/wind-vector collocations were accepted for model design and determination.

Frequent checks of the data were made by comparing the σ_0 -error with respect to some reference model, initially ESA CMOD2 but later replaced by the latest model estimated from the data, to identify major outliers (typically 10dB in error) and to give a rough and ready overview of how the data fitted the model. Counts were made over 21 error ranges and three tables produced to show wind-speed, azimuth direction and incidence angle dependence; quality weighted estimates (linear, but printed as dB) were made of mean and standard deviation of the error with respect to the Reference Model.

As an example of a comparison between raw data and a reference model, Table 1 shows the statistics of the difference between σ_0 data values and the model value predicted from model 3_h1 under the same conditions. Model 3_h1 is the most up-to-date Haltenbanken model and both it and the raw data have been calibrated to the beam patterns introduced on 1st March 1992. In the v -dependent part 1a, note the peak in the counts occurs at 8-12m/s, the very low average difference (data/model bias) except below 4m/s; and the decrease in standard deviation from low to high wind speed. Noteworthy in the θ -dependent part 1b, are the relatively few counts below 30°, the very low average difference and the smoothly increasing standard deviation (spread) with θ . Although these differences have been measured in terms of σ_0 it is not necessarily correct to infer that they arise from the radar measurements: a sizable contribution could come

¹ The wind-field analysis and generation of the collocations were done by Mr. D. Offiler of the UK Met Office, and provided as computer files in ARMOR format and stored on ESRIN's PCS_SPAN data base.

from errors in the surface wind values in spite of the care and attention applied in their estimation.

Table 1. Statistics of σ_0 differences between Haltenbanken data and model 3 h1

1a) wind speed dependence, v, ranges in m/s								
	<1	1-2	2-4	4-6	6-8	8-12	12-16	16-24
counts	391	940	5284	8055	10556	21426	9426	2431
AvgdB	-0.51	-0.35	-0.20	-0.11	0.03	0.09	0.12	-0.01
StD dB	1.53	1.64	1.40	1.26	1.22	1.16	1.04	0.95
1b) incidence dependence, ranges in degrees								
	18-20	20-25	25-30	30-40	40-50	50-60		
counts	819	1967	5228	16199	20391	13905		
AvgdB	0.07	0.16	-0.05	-0.10	0.04	0.11		
StD dB	0.83	0.91	1.03	1.14	1.22	1.30		

Re-classification (binning)

In order to reduce both the number of samples to be analyzed and their statistical fluctuations, the raw collocation samples were "re-classified" into 1210 bins centred on the following points in the following 3-dimensional model-volume space:

- θ : 18, 20, 22, 25, 30, 35, 40, 45, 50, 55, deg.
- v : 1, 2, 3, 4, 5.5, 8, 10, 12, 16, 20, 24 m/s
- ϕ : 0, 20, 40, 60, 80, 90, 100, 120, 140, 160, 180 deg.

The σ_0 binning took place as follows: each σ_0 is associated with an actual (θ, v, ϕ) in the model volume, and a corrected σ_0 , located at the grid point, was calculated from a first order Taylor expansion about the grid-point using gradients from the current Reference Model. The error is small since the relocation distance is small and the Reference Model will become a progressively better fit to the data as the model improves. There are no formal iterations taking place, but each successive analysis run represents an iteration under human control, so that the most recent model will usually be the best-fitting model. Each corrected linear σ_0 value is weighted with its Q-value and when all the samples have been processed, the weighted average for each grid point is computed. Other Q-weighted statistics are performed on linear σ_0 values, but output later as dB values.

Once the Reference Model begins to reflect the character of the data its error contribution should become much smaller. The coverage of measurements over the model's variables is important: a rough estimate of coverage, assuming the 60,000 collocations of

$Q \geq 5$ are spread evenly, should yield about 50 per bin. In practice at the extreme edges of the volume, particularly at low incidence where only the mid-beam is contributing, this may become less than 10 and even reach zero.

In much of the analysis work, the quantities of interest show a smooth θ -variation over the range 18-55 degrees. It is convenient to work in $x = (\theta - 36) / 19$, a normalized form of θ , with a full range -1 to +1. In addition, the x-dependence will usually be formulated as expansions up to some order in the set of Legendre functions: { $P_0(x)=1, P_1(x)=x, P_2(x)=(3x^2-1)/2, P_3(x)=(5x^2-3)x/2$ }.

Mean echo, b_0 , versus v and θ .

A simple method of obtaining an estimate of b_0 is to perform a Q-weighted average over ϕ . This will usually be in error due to the uneven frequency of occurrence over ϕ . A good correction ensues by taking the σ_0 at a given ϕ and calculating b_0 using the Reference Model: again this process improves as the latter improves, so it was adopted as the standard method for b_0 estimation. A third approach using the average of σ_0 on fore- and aft-beams was also used. Estimates from the first and last methods were output for cross-checking purposes, and, apart from small differences where ϕ -coverage was poor and uneven, the three estimates were almost identical.

Earlier work on sea echo[2] has shown that a likely form for b_0 is

$$b_0 = A(\theta) * B(v, \theta)$$

where A and B are smooth functions determining the purely θ and the mixed (θ, v) dependencies.

Figure 1 (the symbols) shows a plot of mean σ_0 converted to dB versus θ , for a selected set of wind speeds. Ignore for the moment the full curves. The data points are seen to form separate curves for each wind speed, with curve separation indicating a well defined v-dependence with increasing θ . The smooth decrease with θ is evident at all wind-speeds.

In order to investigate the v-dependence the above data were plotted against several different functions of v, including v itself and $\log(v)$, the law used in CMOD2. However, only when \sqrt{v} was used did the curves take on a simple straight-line form. This is shown in Figure 2 where for clarity in plotting an estimated incidence dependent curve, $10.\alpha(\theta)$ in dB, which affects only the σ_0 -level and not the curve shape, has been subtracted. The slope of the \sqrt{v} -law

C-band V-Polarized Radar Sea-Echo Model from ERS-1 Haltenbanken Campaign

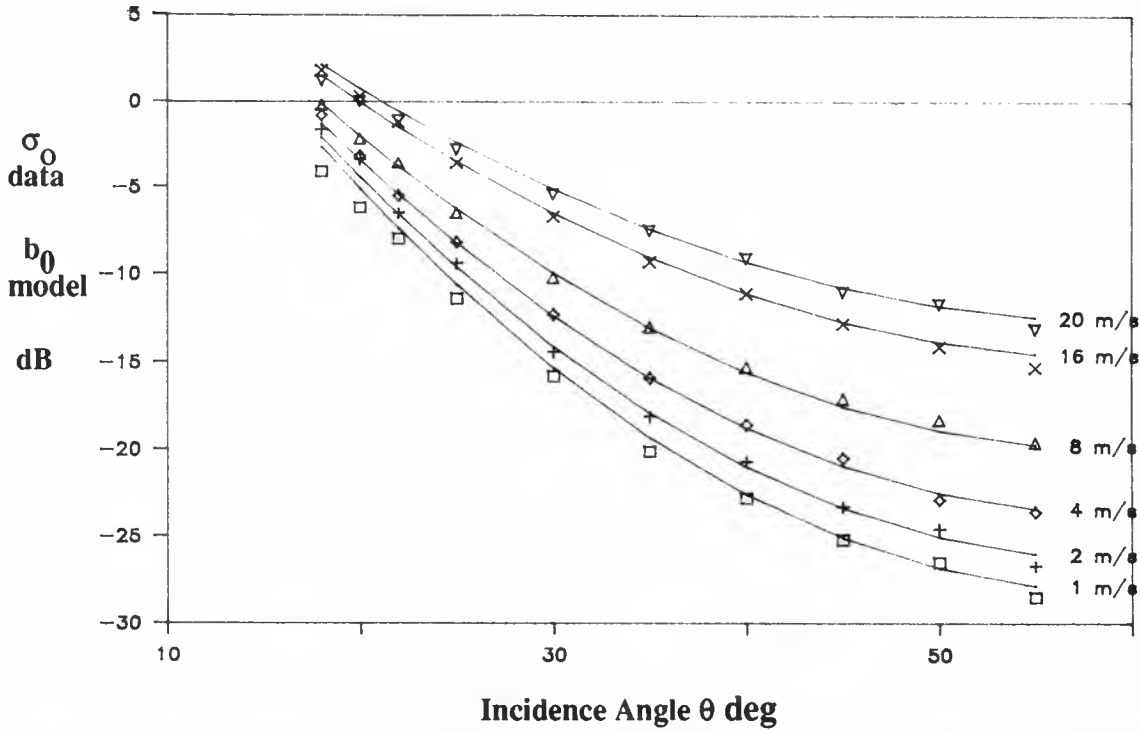


Figure 1. Mean σ_0 value from binned Haltenbanken collocated data versus incidence angle θ for wind speeds 1 to 20 m/s with data(symbols) overlaid with b_0 model plots. ($Q \geq 5$, 59,346 calibrated collocations)

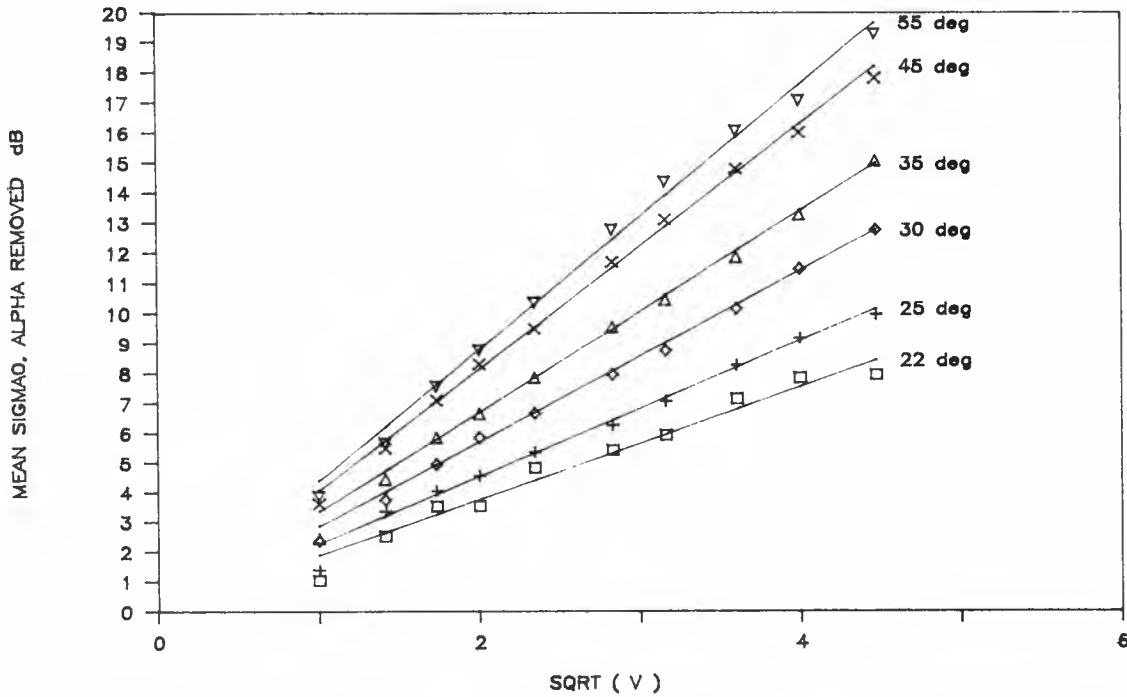


Figure 2. Square-root wind-speed law dependence of σ_0 in dB: (i) data values (symbols) and (ii) overlaid model curves $\beta \cdot \sqrt{v}$, are plotted against \sqrt{v} . A rough estimate of the pure θ -dependence law $10 \cdot \alpha$ has been subtracted out.

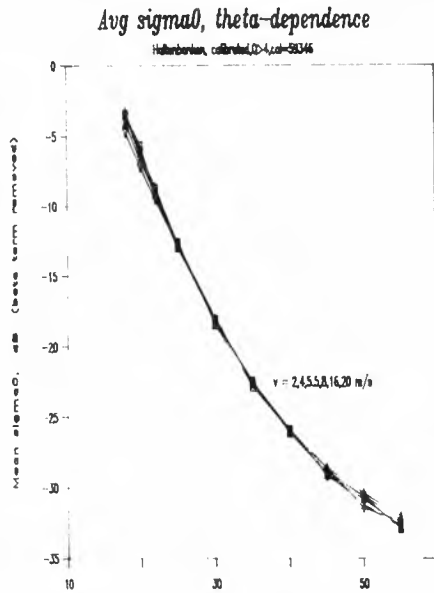


Figure 3. Binned σ_0 data as in Fig.1 except that v-dependent part of model law has been removed. All wind speed plots coalesce.

(and hence wind-speed sensitivity) increases with θ . The slopes were estimated for all θ values, (some are left out for clarity), and a continuous slope function, denoted by $\beta(\theta)$, constructed by fitting the individual slopes up to Legendre function, $P3(x)$. The full-lines have been plotted using this $\beta(\theta)$ function, whose coefficients will become part of the b_0 sub-model.

The pure θ -dependent part of b_0 can now be found by taking the data values in Figure 1 and subtracting (in dB) the appropriate v-dependent part. The result is shown in Figure 3 in which all the curves for all wind speeds have coalesced into essentially a single curve with only some small separation at extreme incidence angles where errors are expected to increase due to poorer data (beam) coverage. These composite curves have been fitted up to $P3(x)$; the resulting coefficients complete the b_0 sub-model definition.

We should now refer back to Figure 1 where the full lines shown come directly from the b_0 sub-model. Only at low incidence and very low wind speed (1m/s) is there a clearly visible discrepancy.

Modulation terms b_1 and b_2

The variation of σ_0 with ϕ may be conveniently studied by taking binned data, isolating the ϕ -varying dimension at fixed v and θ , then removing the b_0 term to isolate the azimuth modulation residue. An

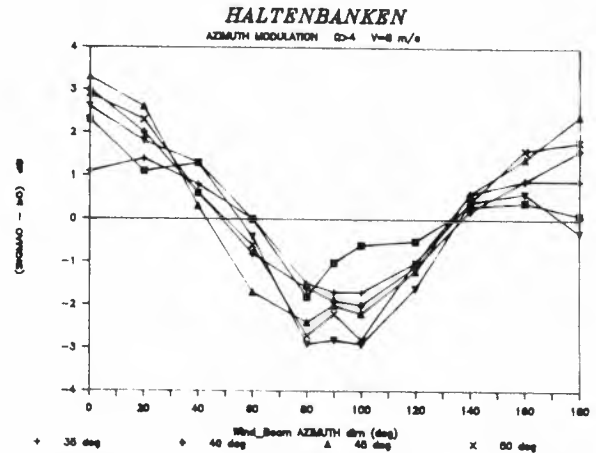


Figure 4. Azimuth variation of modulation part of σ_0 at 8 m/s and mid to high incidence angles.

example is shown in Figure 4 for wind-speed 8 m/s and $\theta = 30^\circ$ to 55° . From such curves as these the b_1 and b_2 terms may be obtained by cross-correlation estimation of the $\cos\phi$ and $\cos 2\phi$ amplitudes respectively. Unfortunately the number of samples required to yield good estimates is considerably greater than for

Table 2: Model b_1 and b_2

Table 2a. :b1 from CMOD3_H1 model							
θ deg.	m/s:	2	4	8	13	20	24
18		-0.04	-0.02	0.01	0.06	0.12	0.15
20		-0.04	-0.02	0.02	0.06	0.12	0.16
22		-0.03	-0.02	0.02	0.06	0.13	0.16
25		-0.03	-0.01	0.02	0.07	0.13	0.17
30		-0.02	0.00	0.03	0.08	0.14	0.17
35		-0.01	0.01	0.04	0.09	0.15	0.18
40		0.00	0.02	0.05	0.09	0.16	0.19
45		0.01	0.02	0.06	0.10	0.16	0.20
50		0.01	0.03	0.07	0.11	0.17	0.21
55		0.02	0.04	0.08	0.12	0.18	0.22
Table 2b. :b2 from CMOD3_H1 model							
θ deg.	m/s:	2	4	8	13	20	24
18		0.13	0.13	0.14	0.15	0.16	0.18
20		0.15	0.15	0.16	0.17	0.20	0.21
22		0.17	0.17	0.18	0.20	0.23	0.24
25		0.19	0.20	0.21	0.24	0.27	0.29
30		0.23	0.24	0.26	0.29	0.33	0.36
35		0.27	0.28	0.30	0.34	0.39	0.42
40		0.30	0.31	0.34	0.38	0.43	0.47
45		0.33	0.34	0.37	0.41	0.47	0.50
50		0.35	0.37	0.39	0.43	0.49	0.53
55		0.37	0.39	0.41	0.45	0.51	0.54

the b_0 term, so that this approach is limited to the central part of the model volume. A complementary approach is to use one's knowledge of b_0 to allow direct estimation of b_1 and b_2 from fore- and aft-beam σ_0 -pairs. This works very well but is limited to $\theta > 25^\circ$. The results of both methods were combined to produce the values shown in Table 2.

Haltenbanken model cmod3_h1

The Haltenbanken model given below is based exclusively on the Campaign data. It has been constructed from sub-models of top level b-coefficients.

cmod3_h1 model			
<u>Linear form:</u>			
$\sigma_0 = b_0 \cdot (1 + b_1 \cdot \cos\phi + b_2 \cdot \cos 2\phi)$			
<u>Variables</u>			
ϕ	= azimuth wrt upwind, deg.		
v	= wind speed m/s		
θ	= incidence angle, deg.		
x	= $(\theta - 36) / 19$		
<u>Legendre Polynomials:</u>			
$P_0 = 1,$	$P_1 = x,$		
$P_2 = (3x^2 - 1)/2,$	$P_3 = (5x^3 - 3x)/2$		
<u>b-coefficients:</u>			
$b_0 = 10 \alpha + \beta \cdot \sqrt{v},$ where			
$\alpha = c(1) + c(2) \cdot P_1 + c(3) \cdot P_2 + c(4) \cdot P_3$			
$\beta = c(5) + c(6) \cdot P_1 + c(7) \cdot P_2 + c(8) \cdot P_3$			
$b_1 = c(9) + c(10) \cdot P_1 + c(11) \cdot v$			
$b_2 = c(12) + c(13) \cdot P_1 + c(14) \cdot P_2 + [c(15) + c(16) \cdot P_1 + c(17) \cdot P_2] \cdot v + c(18) \cdot v^2$			
<u>Coefficients values:</u>			
c(1 - 3)	-2.12580	-1.48697	0.4130539
c(4 - 6)	-0.037416	0.3221361	0.1622316
c(7 - 9)	-0.043343	-0.001608	-0.027
c(10 - 12)	0.0325	0.0088	0.254
c(13 - 15)	0.120	-0.015	0.005
c(16 - 18)	0.003	-0.001599	0.00005

Conclusions

The Haltenbanken Geophysical Validation Campaign may be regarded as a huge success, due to both the enthusiasm of the experimenters and skill shown in the planning and management. ERS-1 and surface measurements yielded high quality scientific data, so that the analysis task was simplified: in the very early stages the behaviour of the binned data looked like model curves, and it is with some confidence that we feel that the current model cmod3_h1 gives a close representation of that data. The representation of the azimuth dependence (ϕ -modulation) is mainly good overall, but in places, because of lack of coverage, only adequate: more refined estimation techniques using the 3-beam σ_0 -triplets together with the b_0 sub-model should provide a substantial improvement. An attempt has been made to make the Haltenbanken data and its model stand alone. This is valuable in making comparisons with other areas in trying to decide whether or not there is a single sea-echo model which is stationary both in time and location.

Acknowledgments

I wish to acknowledge all the experimenters and support staff who made the Haltenbanken Campaign such a success. I am aware of all the hours flown on aircraft, spent on ships, and engaged in equipment maintenance; and this comes into my mind whenever I ponder over the rejection of an outlier. The analysis work I have done has been in the comfort of my own office.

References

- [1] Grant, C.R., and Yaplee, B.S., Proc IRE, vol. 45, pp. 976-982, July, 1957.
- [2] Penny, Lord W., in "Building of Scientific Models", by G.Laing, Gower Pub. Co. Ltd, 1986
- [3] Moore, R.K., and Fung, A.K., Proc IEEE, Vol 67, pp.1504-1521, 1979.
- [4] Long, A.E., Proc. 3rd International Colloquium on Spectral Signatures of Objects in Remote Sensing SP-247, ESTEC, Noordwijk, The Netherlands, pp.29-34, 1986
- [5] Halsema, D. van, et al., "First Results of the VIERS-1 experiment, Proc. of Workshop, Bergen aan Zee, May 1988.
- [6] Morin, J.C., René '91 ERS-1 Campaign Reports, Internal Reports for ESA, Nos. 1-6, GDTA No CC92001, 1992.

EVALUATION OF ERS-1 SCATTEROMETER WIND INFORMATION AT THE NORWEGIAN METEOROLOGICAL INSTITUTE

Lars-Anders Breivik

Norwegian Meteorological Institute
P.O.Box 43 - Blindern, 0313 Oslo, Norway

Abstract

Since launch of ERS-1 in July 1991 scatterometer wind information and altimeter wave information from North Atlantic has been received in real time at the Norwegian Meteorological Institute. The data has been collocated with operational numerical weather forecast model and sea wave model data and evaluated. The wind scatterometer data has been found to be capable for observing structures in the surface wind field with good accuracy, but with potentiality for improvements especially on the ambiguity removal process. Collocated information of stability and sea state from the models has been used to search for physical dependencies in the scatterometer wind formulation.

1. Introduction

As a contribution to the evaluation of the performance of ERS-1, DNMI has done a comparison study of the satellite data and DNMI's operational analysis of wind and waves. The study covers the scatterometer wind vector data (the scatt. winds), and the altimeter wind speed and wave height data. Weekly evaluation reports on the geophysical performance of these instruments has been sent to ESA from the end of August to the end of December.

The operational numerical analysis of the atmosphere combines all available meteorological observations with the knowledge of the dynamics and physics of the atmosphere incorporated in the models. The strength in using this as an calibration/evaluation (cal/val) tool is the large amount of data covering a lot of different situation.

For control of the results we have used the Oceanor buoy observations from the ESA cal/val campaign at Haltenbanken.

Beside the contribution to the cal/val, our motives for the comparison study is preparation for next step, the potential use of ERS-1 data in operational forecasts of weather and ocean state. We see the largest potential for ERS-1 data as initial information to the numerical forecasts models. To utilise this, we need knowledge of the quality and error statistics of the data.

This paper cover the evaluation of the ERS-1 wind scatterometer. Section 2 describes the evaluation tool, the numerical forecast model/analysis system while section 3 gives a brief description of the Haltenbanken buoy data. For a description of the scatterometer we would like to refer to other papers in this workshop proceedings e.g. Stoffelen and Anderson 'ERS-1 scatterometer calibration and validation activities at ECMWF'. Section 4 describes

the results of the evaluation of the scatt. wind direction in 4.1 and of the wind speed in 4.2. In section 5 the impact of some physical parameters at, and near the sea surface are discussed. Finally some conclusions are given in section 6.

2 The forecast model and the collocation of data.

The DNMI operational forecast model, LAM50S (Grønås and Hellevik, 1982), covers 121 x 97 points on a polar stereographic map with 50 km horizontal resolution at 60°N. The number of vertical levels is 18. The model area is shown on fig.1. The model area is the evaluation area for the scatterometer winds in this study. All scatterometer winds inside this area are used.

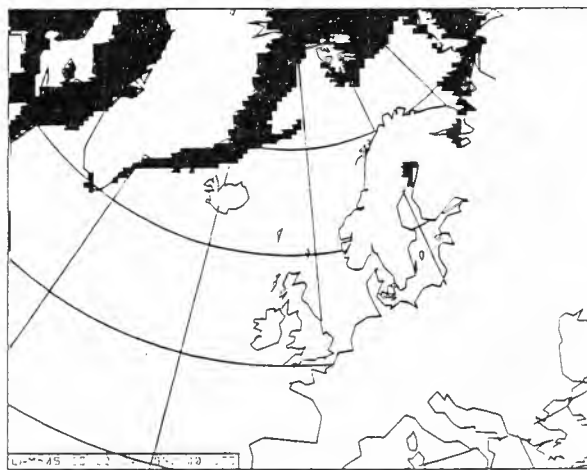


Fig. 1: LAM50S integration area. The shaded area shows the analyzed sea ice 22. April 1992.

The model is run in a six hour data analysis / assimilation cycle. In the analysis observations from a period spanning the analysis time, are used to correct a 6 hour forecast, the first guess field, made from the previous analysis (Grønås and Midtbø, 1986). The observations used are observations of wind and geopotential height available on the international meteorological data network, GTS. The analysis is three dimensional and multi variate. This means that all observations are given influence within a horizontal and vertical influence radius in the model field around the observation point under constrains concerning the dynamic balance of the atmosphere on the model scale of motion. The first guess forecast contains the information from earlier observations.

The main purpose of the analysis is to produce initial conditions for the forecast run which means that the final analysis represent the atmosphere on the model scale. It contains the inaccuracies present in the model's formulation and limitations due to model resolution.

In this study we consider the model analysis as a way of interpolating all available meteorological observations in space, by the three dimensional analysis, and in time, by the integration of the model equations describing the atmospheric motion. A weather forecast model gives the best possible representation of the atmosphere for a large area continuously in time. It makes it possible to evaluate the satellite measurements within the area at any time, independent on in situ measurements on the spot. This gives a large amount of collocated data from all kind of weather situations.

To do the comparison between the scatterometer winds and the model analyzed wind field, the model analyzed field is interpolated to scatterometer observation points and stored on collocation files. At every analysis time step, every 6 hour, collocation files are produced for all scatterometer observations in the LAM50S area within +/- 3 hours from the analysis time. The interpolation in space is linear from the four surrounding model grid points. The interpolation in time is partly performed by the model time integration in the following way: The model field is interpolated in time from the analysis and the surrounding +3 hours forecasts to the scatterometer observation time by use of a cubic spline.

The spatial resolution of the scatterometer is approximately 50 km. The scatt. winds are presented on a 25 x 25 km resolution grid. But considering the sampling resolution and the great amount of data we use the data on 50 km resolution (as the evaluation tool, the forecast model).

The scatterometer winds are collocated and compared with the model 10 m wind, $V(10)$. $V(10)$ is not a prognostic variable, but calculated every time step from the wind at the lowest model level, and by use of the models knowledge on the stability in the lowest layer of the atmosphere (Nordeng et al. 1987). As a measure of stability we use the Richarsson's number Ri .

$$Ri = \frac{g\partial\theta}{\theta\partial z} \left(\frac{\partial v}{\partial z} \right)^2$$

where θ is the potential temperature and v the wind vector. Ri describes the relation between turbulent energy loss due to static stability and gain due to vertical wind shear. The calculation of $V(10)$ from $V(h)$, where h is the lowest model level, is dependent on stability defined by the sign of Ri so that positive Ri defines the stable case and negative Ri the unstable case.

Since the scatterometer winds are derived from an empirical model function physical dependencies on stability and sea state is not taken into account. To look for physical relations we have included other parameters from the model analysis. That is the temperature at the surface $T(s)$, the temperature 2 m above the surface $T(2m)$ and the Richardssons number, Ri . We have also collocated wave parameters from DNMI's operational wave model WINCH, significant wave height and period, H_s and T_s , and wave direction D_s .

3 The Haltenbanken buoy data.

In ESA's calibration and validation campaign at Haltenbanken September to December 1991 10 buoys collecting wind and wave information was deployed. They had a long and troublesome period at the first part of the campaign. From late November between two and eight of the buoys delivered data with reasonable regularity.

In this study we have used buoy data as reference data to check the results of the main comparison between ERS-1 data and numerical analysis. We have collocated the wind observations from December 1991 with LAM50S analysis in the same way as described above for the scatterometer winds.

Each buoy is equipped with two wind sensors measuring speed and direction. If both sensors are working and not differ more than 2.5 m/s for the speed, we have taken the mean value of the observed result and given the observation a quality index 1. If they differ more than 2.5 m/s we have chosen the observation closest to the model analysis and given quality index 0. If only one sensor works this is used given quality index 0. All wind speeds less than 1 m/s are rejected. Out of a total number of 8739 buoy observations in December, 3990 was given quality index 1. But when comparing with model analysis the statistics did not change between using quality index 1 and index 0 data. The standard deviation, SD, of the buoy data are 3.4 m/s and the SD of the differences between buoy and analysis are 2.3 m/s for both cases. Also the root mean square differences, RMS, remains unchanged. As conclusion for the rest of this study, we use all data.

4. Evaluation results for scatterometer wind.

We will in this section give the results of the evaluation study of the scatterometer wind measurements (hereafter scatt.-wind) and the numerical model analysis (hereafter the analysis). Our study is limited to look at the ESA-derived wind vectors.

To avoid erroneous scatterometer data due to sea ice we use information from the analysis's to leave out data in sea ice area. In the model the ice edge is updated on the basis of NOAA satellite pictures. Fig. 1 shows the ice edge in the integration area 22. april 1992.

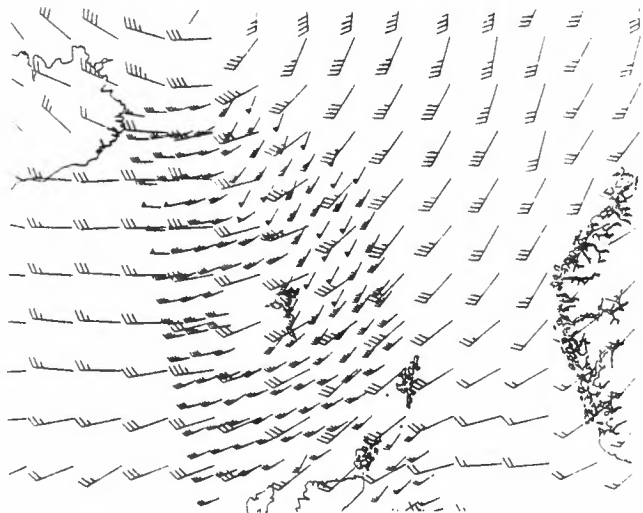


Fig. 2: LAM50S analyzed wind field and scatt. wind field (small arrows) 28. February 1992 00 UTC.

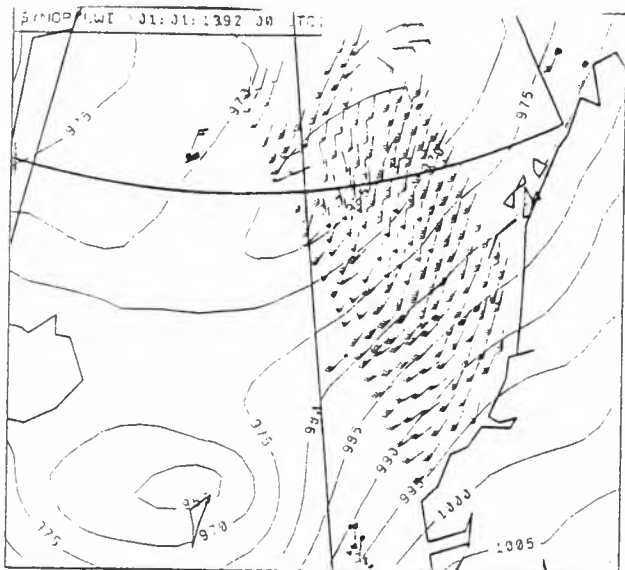


Fig. 3: LAM50S analyzed mean sea level pressure isobars and scatt. wind field and SHIP observations (arrows with head) New Year Day 00 UTC.

Fig. 2 shows scatt. winds, small arrows, between Iceland and Scotland, plotted together with analyzed 10 m wind 28. February 1992, 00 UTC. The wind arrows in this and in the following similar plots are standard meteorological symbols where a short mark symbolise 5 knot wind speed, a long mark 10 knot, a black triangle 50 knot, and a square 100 knot. The details, consistency, and quality of the scatt. wind field looks very convincing. The scatterometer insist on a sharper curve of the wind field east of Iceland and between 5 and 10 knots higher wind speeds for most of the area.

Fig. 3 shows scatt. winds outside the Norwegian coast 00 UTC 1. January 1992. An extreme storm is approaching the coast, while an other low pressure centre is east of Jan Mayen. The scatt. winds are plotted together with mean sea level pressure isobars of the analysis and some ship observations of wind, small arrows with head. The analyzed position of the storm centre and curving of the isobars is consistent with conventional observations. The scatt. winds describes the structure of the field very nice in most parts of the track. There are however problems with wind direction north of the low pressure centre. Here the real wind bend around along the isobars, while the scatterometer winds keep on the opposite direction.

4.1 Comparison of scatt. and model analyzed wind direction

On fig.4 a and b the difference in wind direction between scatt. and the analysis are binned in 10 degrees intervals from 0 to 180. The vertical axis gives the percent of the total number of cases in each difference interval. The figure is made from the results in December 1991. The bars shows a characteristic U-shape which has been similar for all results from the evaluation period, autumn/winter 1991/92. In extracting wind from the scatterometer, the first step gives no unique solution, but up to four different solutions with different directions. The solutions are given rank after some probability criteria. In most cases two solutions will have quit similar probability, but differe 180 degrees in direction due to difficulties in upwind / downwind discrimination of the scatterometer model function. The second step, the ambiguity removal, consist of choosing of the right solution. The skill depends

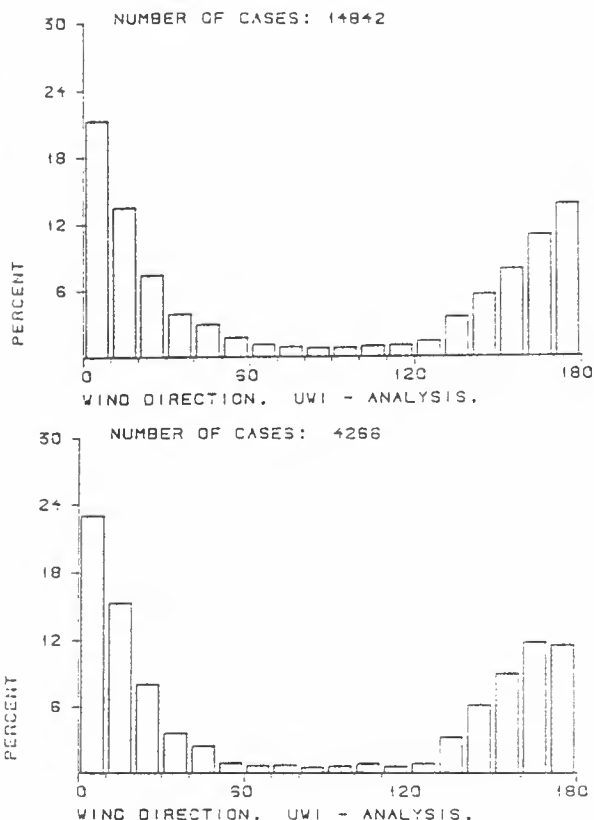


Fig. 4: Relative occurrence (percent) of wind direction differences between scatt. and analysis binned in 10 degrees intervals from 0 to 180 for a: all data and b: ambiguity removed.

in most cases on the capability to find the right solution from these two. The ambiguity removal method used by ESA, CREO (Cavnin and Lecocome 1987) is a method based on maximum likelihood estimates of varying wind speeds and direction.

The u-shape of fig.4 demonstrate the difficulties in the ambiguity removal process. In fig.4.a all available data are used. It means that if the ambiguity is not removed, rank 1 is chosen. About 35 percent is within 20 degrees difference, while about 24 percent is between 160 and 180 degrees wrong. Taking only the results when the ambiguity has been removed autonomously (without use of a meteorological back ground field), this is not much changed, as seen in fig.4.b. Here 38 percent is within 20 degrees and still about 24 percent more than 160 degrees.

The wind direction problem is also illustrated on the plot of fig.3 where ambiguity removed scatt. winds are plotted together with analyzed isobars and conventional wind observations. It is from a situation when a severe storm is approaching the norwegian west coast on New Year Day 00 UTC 01.01.92 and the centre of the storm is seen over Faeroes. There is an other low pressure centre between Norway and Jan Mayen, and the satellite measures the wind in a swath across this centre. The real wind is mainly blowing along the isobars with lower pressure to the left. The scatt. winds are very good, but going from south to north, crossing the low pressure centre, the ambiguity removal process seems to keep the consistence in wind direction and miss the turn of the wind around the low pressure centre. The winds remains correct in speed but 180 degrees wrong in direction. The same problem has been observed in a number of other cases. The ambiguity removal process fail in choosing the right wind direction around a storm centre and miss the important curvature of the wind field. The

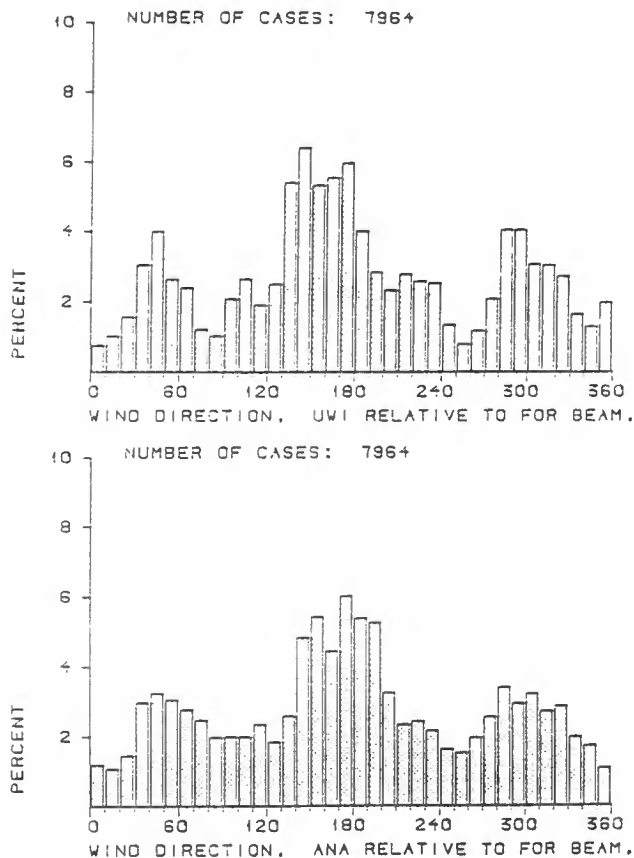


Fig. 5: Relative occurrence (percent) of wind directions measured relative to mid beam look angel. a: for scatt. b: for analysis.

problem is severe, when considering independent use of the results, because it is an example of situations where correct information are most needed. It emphasise the need for further work on dealiasing. Experience with SEASAT in 1979 showed problems with preferred wind directions due to antenna geometry. The angular distribution relative to the antenna look angel showed peaks in 90° intervals (Anderson et.al. 1988). This problem was connected to the two antenna geometry on SEASAT and is not expected to be a problem for ERS-1. To check this, we have on fig.5 a and b for December plotted histograms for the occurrence of wind directions relative to forward antenna. Fig.5.a shows the results for the scatt. wind, while fig.5.b shows the results for the analysis. For this comparison we have only used the results where the difference between analysis and scatt. is less than +/- 90°. If there are no 'scatterometer preferred' directions, fig.5.a and b shall be very similar. This is also the case. The peaks in occurrence are around 160° and 300° relative forward antenna are due to the dominating wind directions. There is a dominant wind direction from south west during the period for the collocated cases in the North Atlantic.

4.2 Comparison of scatterometer and model analyzed wind speed

After some corrections in the first part of the mission, the quality of the scatt.-winds has been quit unchanged since november and until spring 92.

In this report we will study the results from December 1991. The total number of entries in the collocation files where for December 14732. This include all data so that when the ambiguity has not been removed, the

rank 1 solution is used. Among all the data the ambiguity has been removed in 5006 cases. The qualitative differences of the wind speed results between all data including rank 1 and the dealiased data has been variable but in general small. For the comparison in this study we use all data.

Fig. 6.a shows scatter diagrams for scatt. wind speeds and model analysis. The squares shows the mean values of scatt. in 1 m/s intervals of analysis, while the triangles shows mean analysis in 1 m/s intervals of scatt.

The first thing to notice is that there are no scatt. winds bellow 4 m/s. The wavelength of the ERS-1 scatterometer is 5.7 cm. This is rather big compared to e.g. the wavelength of the scatterometer at SEASAT, wavelength = 2.1 cm. The relative long wavelength for the ERS-1 scatterometer reduces sensitivity to small wind speeds. The scatt. winds where found unreliable for wind speeds lower than 4 m/s and dropped.

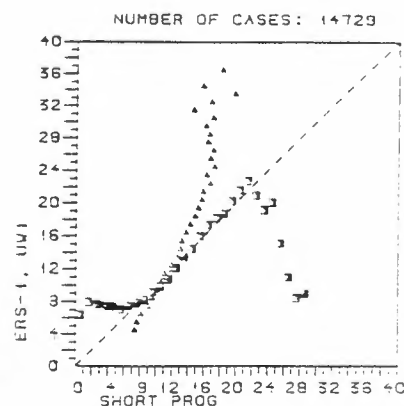
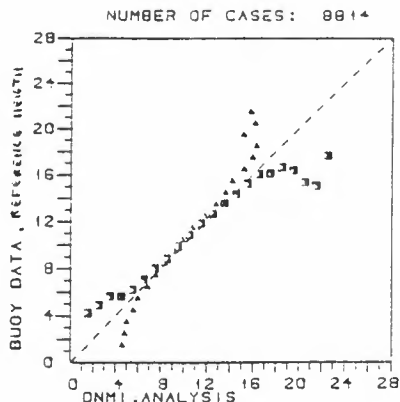
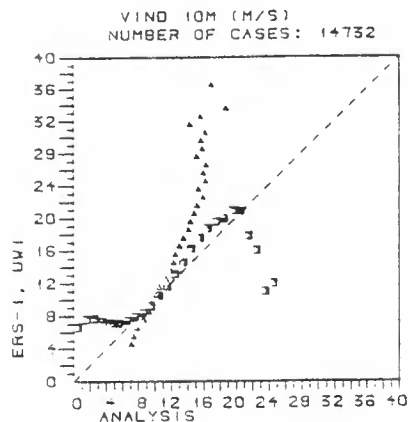
Table 1.a shows statistical parameters obtained by comparing scatt. wind speeds with model analysis. For the calculations of the statistics the data is not used if the model analyzed wind speed is below 4 m/s.

The scatt. wind speed has a positive bias relative the analysis of 0.8 m/s. The standard deviation of the differences, SDE, are 3.7 m/s and the root mean square difference, RMS, is 3.8 m/s. The correlation is 68.3 percent.

The results presented in fig. 6.a and in table 1.a is representative for the general results for the whole period. Compared to the model analysis of 10 m wind speed the present scatterometer wind speed is to high. To check the result we have compared the model analysis with the RENE-91 Haltenbanken buoy data for the same month, December 1991. The results are presented in fig. 6.b and table 1.b in the same manner as for the scatt. data. The buoy data used is interpolated to 10 m reference height by a assuming neutral conditions and a logarithmic wind profile. Wind speeds down to 1 m/s are used. The mean difference between buoy and model is + 0.4 m/s. The standard deviation of the differences, STE, is 2.5 m/s and the correlation is 81 percent. If we remove all wind speeds less than 4 m/s, as for scatt., the mean difference, buoy - model, becomes 0.6 m/s and the STE 2.3 m/s.

The model analysis of 10 m wind speed is a bit lower than both scatterometer and buoy measurements. We did suspect the value of the 10 m wind speed to be a bit too low in the analysis. The model 10 m wind is used as input to run DNMI's operational wave model WINCH. The wave model is very sensitive to the quality of the wind input. On the basis of long experience from wave model results we know that the surface wind is a bit to low at the analysis time, and that this is corrected after a short time of model integration (Magnar Reistad pers.com.). This is probably due to properties of the intermittent analysis system, and it can not be corrected until a continuously assimilation procedure which use the dynamic equations of the model as a constrain has been developed. At present, the problem is cured after some step of model integration.

In fig 6.c we have not used the analyzed winds but the model winds from a short prognosis, between +3 and +9 hours from analysis time. The statistical parameters are given in table 1.c. The mean difference between short model forecast and scatt. is a reduced to 0.3 m/s, and STE is 3.8 m/s. The correlation is slightly reduced from the analysis, but only by 1 percent, to 67.3 percent.



ALL DATA:
 numb. of entries: 14732
 mean analysis: 10.5
 mean ERS: 11.2
 bias (ERS-ana): 0.8
 sde (ERS-ana): 3.7
 rms (ERS-ana): 3.8
 sd (ana): 3.5
 sd (ERS): 5.1
 correlation: 68.3

BUOY WIND: REFERENCE HEIGHT
 V(BUOY), V(ANA) > 1 m/s
 numb. of entries: 8814
 mean analysis: 10.4
 mean buoy: 10.8
 bias (buoy-ana): 0.4
 sde (buoy-ana): 2.5
 rms (buoy-ana): 2.5
 sd (ana): 4.0
 sd (buoy): 4.0
 correlation: 81.0

SHORT FORECAST:
 ALL DATA:
 numb. of entries: 14729
 mean analysis: 10.9
 mean ERS: 11.2
 bias (ERS-ana): 0.3
 sde (ERS-ana): 3.8
 rms (ERS-ana): 3.8
 sd (ana): 3.9
 sd (ERS): 5.1
 correlation: 67.3

Upper row:

Fig. 6, a,b,c: Scatter diagrams of wind speeds. A square denotes mean value of the vertical parameter in 1 m/s intervals of the horizontal parameter, and the triangles denotes mean values of the horizontal parameters in intervals of the vertical. Fig. 6.a is scatt. compared to analysis, fig. 6.b is RENE buoy data compared to analysis, and fig. 6.c is scatt. compared to short forecast.

Lower row:

Tab. 1, a,b,c: Statistical parameters comparing wind speeds from a: model analysis and scatterometer, b: model analysis and RENE-91 buoys and c: model short forecast and scatterometer.

Our conclusions are that the scatterometer, by the present model function 'CMOD2' gives quite reasonable wind speed results up to approx. 25 m/s.

3.3 Further evaluation of wind speed

The model function, 2.1, include three variables, incidence angle, θ , and wind speed and direction 10 m above sea level. It is likely that other physical parameters influence the relationship between the measured σ^0 and the wind at 10 meter level. Among these are stability and wave steepness.

- The relation between the surface stress, described by σ^0 , and the wind 10 meter above the surface level is dependent on the stability (Offiler 1988). The model function is derived empirically for all kind of situations and supposed to be valid for neutral conditions. Since the air over the ocean in most cases are well mixed this is probably a good approximation.

- In the presence of long waves, the backscatter will be modulated because incidence angle is now to be measured relative to the local tilted surface plane (Barthel 1990). In addition hydrodynamic effects resulting from wave-wave interactions act to modulate the backscatter by changing the short wave energy density.

We have collocated the scatt. winds with different parameters from the atmospheric model analysis, and in this section we will discuss some results. Comparison between analysis and RENE buoy data is used as reference. The discussion will turn out to be just as much on the quality of the model parameterisation as on the scatt. wind quality.

We found the differences between analysis and scatt. to be dependent on incidence angle, θ . In fig.7 the differences are binned in intervals of 5 degrees of mid beam incidence angle from 15 to 50 degrees for the period from 1. November to 10. December 1991. The horizontal axis is the mid.beam intervals, while the vertical axis is the difference scatt. - analysis, represented by the bars in each interval. The dashed line show the relative occurrence of cases in the intervals. The scatterometer model function needs a better tuning for the θ dependence.

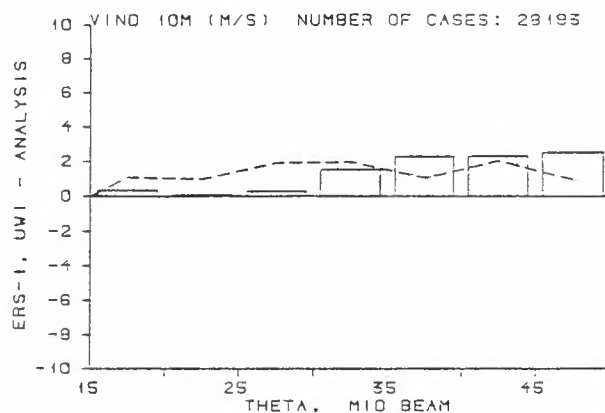


Fig. 7: The bars denotes mean differences of scatt. wind speeds and analyzed wind speeds binned in 5 degrees intervals of mid beam incidence angle. The dashed line gives the relative number of occurrences in the intervals.

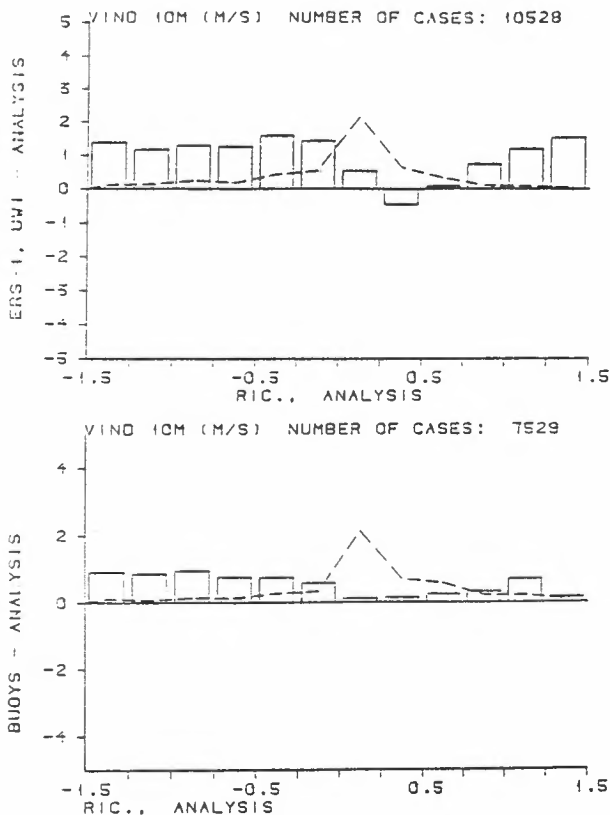


Fig. 8: The bars denotes mean differences of observed wind speeds, 8.a: scatt., 8.b: RENE buoys, and analyzed wind speeds binned in 25 intervals of analyzed Richardson's number, Ri . The air is considered stable for $Ri > 0$ and unstable for $Ri < 0$. The dashed line gives the relative number of occurrences in the intervals.

In fig.8.a, made similar to fig.7, the differences between scatt. and analyzed wind speeds are binned in intervals of the model analyzed Richardson's number, Ri , in the closest to sea surface model level. As described in section 1 Ri is a measure of the stability. The differences are largest for the unstable region, $Ri < 0$. Using a short forecast instead of an analysis gives a similar result. In fig 8.b the same type of plot is made for the RENE buoy data. The two plots are qualitatively very similar, but the differences are larger for the scatt. data. Similar plots, but using model temperature differences between 2 m and surface, gives similar results, positive differences for the unstable case and only small differences for the stable case.

The scatterometer winds and the buoy measurements could be too high for the unstable case. This is not likely since both are assumed valid for neutral conditions. The model wind speeds are corrected for stability in a manner that increase the near surface speed for the unstable cases due to the well turbulent mixing of the air. The conclusion at this stage is therefore that the 10 m model wind is too low and that this is general problem in well mixed air of unstable cases and particularly for the analysis.

We have also, since January 1992, collocated the data with wave parameters from DNMI's operational wave model. The wave data chosen are peak period and direction and significant period and height. Using the dispersion relation for deep water a set of wave parameters can be derived. The evaluation work is on going.

Conclusions.

The scatterometer winds are promising. On basis of calibration and validation exercises performed by various centres we hope and expect the new scatterometer model function to improve the wind speed and direction to a level that will make them useful as input data for assimilation in numerical forecast models. We suspect that the most difficult part will be ambiguity removal especially in important cases as storms as shown in section 4.1.

Our first attempt to find physical dependencies of the scatterometer winds, resulted in improved knowledge of the evaluation tool, the numerical model. The assumption in the scatterometer model function of well mixed neutral conditions is, on the average, good. We will keep collocating the data operationally and, getting the improved wind results, we will try to isolate the different effects, and concentrate on wave dependencies.

References

- Anderson, D., A. Hollingsworth, S. Uppala and P.M. Woiceshyn, *A study of the feasibility of using sea and wind information from ERS-1 satellite. Part 1: Wind scatterometer data.* ECMWF contract report to ESA, 1987.
- Barthel K., K. Hasselmann and S. Hasselmann, *Use of wave model as a validation tool for ERS-1 AMI wave product and as an input for the ERS-1 wind retrieval algorithms.* Max-Planck-Institut für Meteorologie, report no. 55, contract report to ESA, 1990
- Cavanie, A. and P. Lecomte, 1987. *Vol 1 - Study of a method to dealias winds from ERS-1 data. Vol 2 - Wind retrieval and dealiasing subroutines.* Final report of ESA contract No. 6874/87/CP-I(sc).
- Grønås, S and O.E. Hellevik, 1982. *A limited area prediction model at the Norwegian Meteorological Institute.* Techn.Rep. No. 61, DNMI, Oslo.
- Grønås, S and K.H. Midtbø, 1986. *Four dimensional data assimilation at the Norwegian Meteorological Institute.* Techn.Rep. No. 66, DNMI, Oslo.
- Nordeng, T.E., M. Reistad and A.K. Magnusson, *An optimum use of atmospheric data in wind wave generation.* Techn.Rep. No. 68, DNMI, Oslo.
- Offiler, D., *Wind field and surface fluxes.* NATO ASI Series- Vol. 298, 1988

Validation and Comparisons of Alternative Wind Scatterometer Models

D. Offiler, Meteorological Office, Bracknell, UK

Abstract

This paper explains the techniques used to validate the performances of various candidate C-band radar backscatter models in retrieving wind vectors from the ERS-1 scatterometer. A comparison of their performances is described, enabling a selection to be made of one model which will replace the current version used for the operational fast delivery processing.

1 Introduction

Comparisons between the ERS-1 fast delivery (FD) scatterometer winds and those from other sources show systematic differences, particularly at low and high wind speeds and with position across the swath. Given the good absolute engineering calibration, the high stability and low noise of the basic backscatter measurements, the transfer model must be deficient in properly describing the true relationship between the measured backscatter and near-surface wind vector.

In order to design and test the wind retrieval algorithms prior to launch, there was a requirement to have a transfer model valid for C-band radar frequencies; the empirical 'CMOD1' model was derived by Long [1] from aircraft 'circle-flight' backscatter measurements. With additional data from later campaigns, a modified formulation and associated coefficient set, known as 'CMOD2', was devised. This is the transfer model currently used for the FD processing.

Since the satellite commissioning phase, several groups have attempted to tune the CMOD2 coefficients — or have used alternative formulations — using the backscatter coefficients, σ^0 , measured by the ERS-1 scatterometer and various sources of collocated wind information. These sources include the *RENE-91* campaign *in situ* winds, analyses derived from that campaign's data or global numerical weather prediction (NWP) model analyses. The details of these tuning studies and their resulting models are presented elsewhere in these proceedings.

This paper describes the method used to reprocess the measured σ^0 values into winds using these alternative wind transfer models, the validation of their performances and a comparison between them. Finally, one of the candidates is selected to replace CMOD2 in the FD processing scheme.

2 Objectives

The objective of this study was to select the 'best' transfer model — with 'best' here meaning *the model which*

produces the highest quality wind retrievals. The criteria for 'highest quality' are similar to those in validating traditional meteorological data sources, such as from ships — e.g. the overall 'errors' in terms of bias and standard deviation of wind speed and direction separately, or by the rms vector, when compared to the true winds. Of course, since we do now know the true winds, but only an estimate from other sources, our comparison can only be stated to be a difference from the (independent) estimate.

Because the models are required to perform equally well over a wide range of conditions (i.e. at least over the wind speed range 4–24ms⁻¹, over all wind directions and over the whole width of the swath), the comparison statistics have been broken down by wind speed and incidence angle to detect any trends with these parameters. In addition, performances in terms of ambiguity removal skill (particularly upwind-downwind selection) have been analysed.

For the purposes of this paper, no account has been taken of the models' abilities to predict the measured σ^0 values given an estimated surface wind vector, since this is considered to be 'engineering' tuning, rather than geophysical.

3 Retrieval processing

The UK Met. Office has been actively involved in this transfer model validation study because

1. we already re-process the 'UWI' FD product in near real-time on an operational basis. This is done so that the full ambiguous set of retrieved winds is available for ambiguity removal, using our own NWP analyses or short-period forecasts as a selection criterion. Thus the re-processing software and environment were available without needing any modification
2. the required data are readily available — both the direct FD products and NWP wind fields, or the UWI products and collocated analyses made during the *RENE-91* campaign
3. we are not ourselves involved in model tuning, so may be considered to be a neutral 'referee'.

3.1 Algorithms

The retrieval algorithms used in the Met. Office's processing are different from those used by ESA in the FD system. During their development of our own algorithms, throughput was an important consideration, but without loss of wind quality. The principal differences are:

- for global retrievals, an ice-edge analysis is used to flag cells which could be ice contaminated
- the use of a look-up table to extract σ° as a function of wind speed, relative wind direction and incidence angle
- the use of a look-up table of coefficients used to directly estimate wind speed from the measured σ° triplets as a function of (guess) direction and incidence angle
- the use of the *measured* σ° as a scaling factor in the residual (cost function) calculation, rather than the *model* value
- the residual is scanned only in wind direction (in coarse steps of 15°); the wind speed being estimated directly. This means we need to find the minima in only a 1-d function rather than a 2-d surface
- once the coarse minima have been identified, the actual directional position of the residual's minimum is found by interpolation using a local polynomial fit
- although four solutions (residual minima) are searched for, there may be fewer distinctly different ones. Solutions within some tolerance of another solution, and having a larger residual, are discarded
- only cells with a retrieved wind speed of less than 0.5ms^{-1} are rejected (4ms^{-1} in the FD processing). Unlike the FD, there is no rejection for retrievals having exceeded some arbitrary threshold of their lowest residual solution (which is assumed to indicate a poor fit to the model because of gross errors in the σ° measurements)
- cells with fewer than 2 beams operating are still retrieved (though with reduced quality). Such cells are not, however, used in compiling the statistics for this study.

The ambiguity removal scheme is also different to the FD processing in that

1. METEO — a background wind is used as a selector for the possible solutions
2. AUTO — the 'SLICE' modal field filter is applied *after* the background selection to correct cases where the background directions may be in error, thus ensuring consistent directions over the 2-d swath.

In order to compare the FD winds as delivered — containing only one solution per cell, but having a high percentage of incorrectly selected solutions — a crude form of ambiguity 'removal' has been applied; in cases where the FD and the background directions differ by more than 90° , it is assumed that an upwind/downwind selection error has occurred and 180° is added to the ESA wind direction prior to calculating the difference statistics.

3.2 The models

Several models (i.e. transfer functions and associated coefficient sets) from various groups have been tested. In some cases, more than one set of coefficients have been

supplied as tuning progressed; results from only the 'best' (criteria discussed in Section 2) sets are reported here.

The final models considered, and their names given for the purposes of this study, are:

CMOD2	ESA, pre- ERS-1 original, using 'circle-flight' data.
CMOD2.Z	ECMWF, using global analyses during November 1991
CMOD2.I2	IFREMER, using <i>RENE-91</i> Tobis buoy and DNMI data
CMOD2.M3	Meteo-France, using global analyses
CMOD3.L3	ESA, new formulation, using <i>RENE-91</i> analyses
CMOD3.L4	ESA, CMOD3 formulation but based on post-March 1992 beam calibrations.
CMOD4.W2	IFMEE, using <i>RENE-91</i> Do-228, RACS and DNMI winds
CMOD5.E2	ECMWF, new formulation

Each model has been implemented in its analytic form with the given coefficients. Using this form, look-up tables of σ° have been generated as functions of wind speed, relative wind direction and incidence angle. During this process, the model in both forms has been validated by ensuring that sensible values for σ° is generated over the whole range of the table, and that the interpolated tabular values compare with the analytic values at arbitrary (random) positions in the model's range without significant error.

The look-up table of coefficients for direct wind speed retrieval are generated by a second-order polynomial regression of the logarithm of wind speed against σ° in dB for a range of wind directions and incidence angles. Again, this table is validated by a Monte Carlo simulation of 'true' and retrieved wind speeds over the table's range.

Each model has then been used in turn to reprocess (a) the UWI products saved during the *RENE-91* campaign over the Haltenbanken area and (b) the operational FD products on a daily basis. In the case of CMOD3.L4, which is tuned to the latest (March 1992) beam calibrations, corrections to the *RENE-91* σ° values have been applied to give an equivalent 'post-calibration'; for all other models, the original σ° s have been used.

3.3 Comparison winds

The primary source of background data for comparing with the scatterometer winds are the analyses derived from the *RENE-91 in situ* measurements; the derivation of these winds is fully described in [2]. These winds are considered to be the best estimate of the true winds, combining several data sources over an extended period of time. They contain a reasonable range of surface conditions, and should not have any systematic errors; the analysis was also tuned to give a grid resolution comparable to the scatterometer cell separation. All 77 collocation datasets have been used, with no screening for synoptic features, homogeneous conditions, etc, but only

cells where the analysis Quality Index is ≥ 5 have been used in the statistics.

A secondary source is the Meteorological Office's operational NWP analyses and short term (up to 9 hour) forecast wind fields, as used in the day-to-day UWI product processing scheme. Complete products containing any 2-beam data, land- or ice-flagged cells, or individual cells where the background wind is below 1ms^{-1} are rejected from the statistics.

A third source is the equivalent NWP wind fields from the European Centre for Medium-Range Weather Forecasting (ECMWF). A subset of the models was used to reprocess the FD data from a limited number of complete days using a version of the FD software at ECMWF. Additional parameters available from this package have also been considered in this study.

In each case the same backgrounds used in the validation were used for the ambiguity selection, so we should not be surprised that the ambiguity removal skill in 'METEO' mode is high! In the case of the 'ambiguity corrected' original FD winds, the skill, by definition, is 100%.

3.4 Validation statistics

For each cell meeting a set of selection criteria described above, the differences between the retrieved scatterometer wind (RET) and the collocated background (BG) are binned by BG wind speed and by incidence angle in the swath. The basic statistical parameters include:

- mean RET minus BG (bias) in wind speed
- standard deviation of the differences (SD) in wind speed
- bias in wind direction
- SD in wind direction
- root-mean-square (rms) absolute vector difference

These parameters, as well as being binned, are also averaged over all incidence angles and over winds $4\text{--}24\text{ms}^{-1}$, weighted by the observation density distribution; the same values would be obtained by an overall statistical analysis without binning. This procedure gives most emphasis to the areas where there is most data, as would be the case if we were analysing global ship data, for instance. However, this could favour models which retrieve well in mid-range, but poorly at say high wind speeds where there are few observations, so unweighted averages across all bins have also been calculated.

In addition, a *a posteriori* validation of the ambiguity removal skill using only the residual value for each solution is calculated as a 'percentage correct'. This can be considered as a measure of the upwind-downwind ratios in the model. In the ECMWF processing, other diagnostic parameters are output, including the number of cells with 'no solutions', and ambiguity removal skills after 'AUTO' and 'METEO' stages.

In order to assist in the objective relative ranking of the models in retrieved wind quality, a number of summary indices or 'Figures of Merit' (FoM) have been devised:

1. the (weighted) rms vector difference; this value can indicate correlations in speed and direction differences on a cell basis when compared to the individual overall rms speed and direction differences which are not correlated. The lower this value is, the better the wind retrieval quality.
2. a weighted FoM, based on a combination of the overall speed and direction bias and SD values (weighed by observation density). The W-FoM has a value such that if the scatterometer geophysical specifications were exactly met (overall a zero bias, with standard deviations of 2ms^{-1} and 20°), then the W-FoM value would be unity. The higher the figure the better.
3. an unweighted FoM, based on a combination of the average (unweighted) rms speed and direction over all bins. Again, if the specifications were met, a value of one would be obtained, with higher U-FoM values indicating better quality in terms of wind retrieval.
4. a ranking FoM, which is based on the relative ranking of each model on a variety of parameters from the ECMWF processing, and summing the parameter rank scores for each model. Here, a low value indicates that the model performed relatively 'better' over a range of criteria than models with a higher R-FoM value. Note that not all of the models have been tested by ECMWF.

4 Results

There is no space in this paper to show more than a summary of the results on which the selection of one model was based. Figure 1 is a graph showing the performances of each model in terms of wind speed; the upper left graph shows the speed bias and the upper right the SD, both as functions of BG wind speed, averaged over all incidence angles. The lower graphs similarly show the speed bias (left) and SD (right) as a function of incidence angle, averaged over wind speeds $>4\text{ms}^{-1}$. Looking at the SD plots, there is clearly a spread in performances, with the original FD and reprocessed CMOD2 value having the highest values; conversely, CMOD4.W2 has the lowest SD as functions of both BG speed and incidence angle, though there is a trend to larger absolute bias values at higher wind speeds. CMOD5.E2 appears to be the next best in retrieving wind speeds, but CMOD3.L3 shows low biases and least variation in all four plots.

Figure 2 shows equivalent graphs for differences in wind direction. Here, there is much less spread from model to model, though most of the new models improve on the old CMOD2. As might be expected, there is a trend from large direction differences at very low wind speeds to smaller differences at high wind speeds, though the biases are increasing. There are also systematically larger differences at low incidence angles (inner edge of the swath), perhaps indicating a physical limitation in the radar backscatter sensitivity to relative wind direction. The CMOD2.M3 model appears to have the best wind direction retrieval over most of the plots;

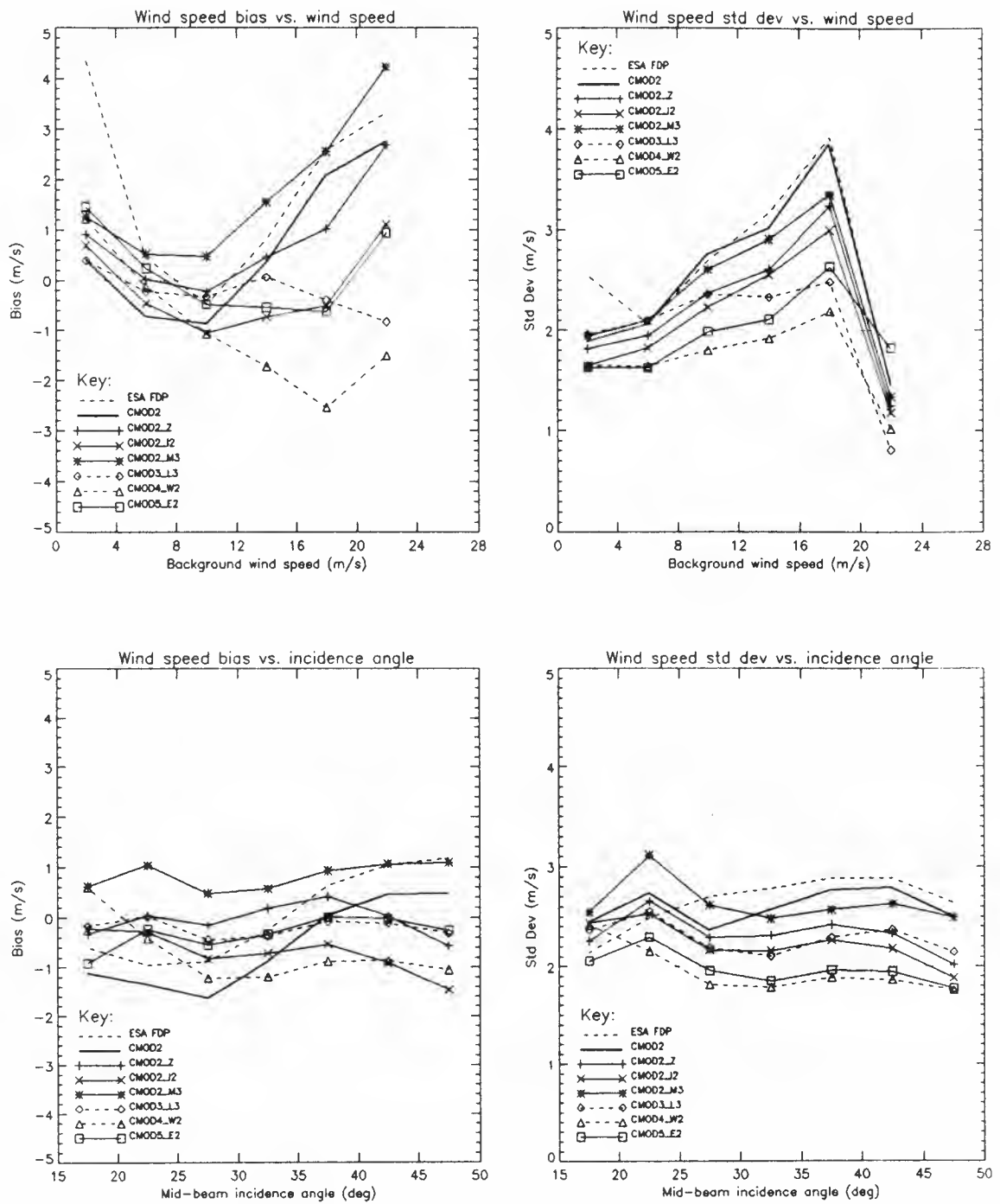


Figure 1: Summary graphs of wind speed differences from *RENE-91* analyses for various alternative wind transfer models.

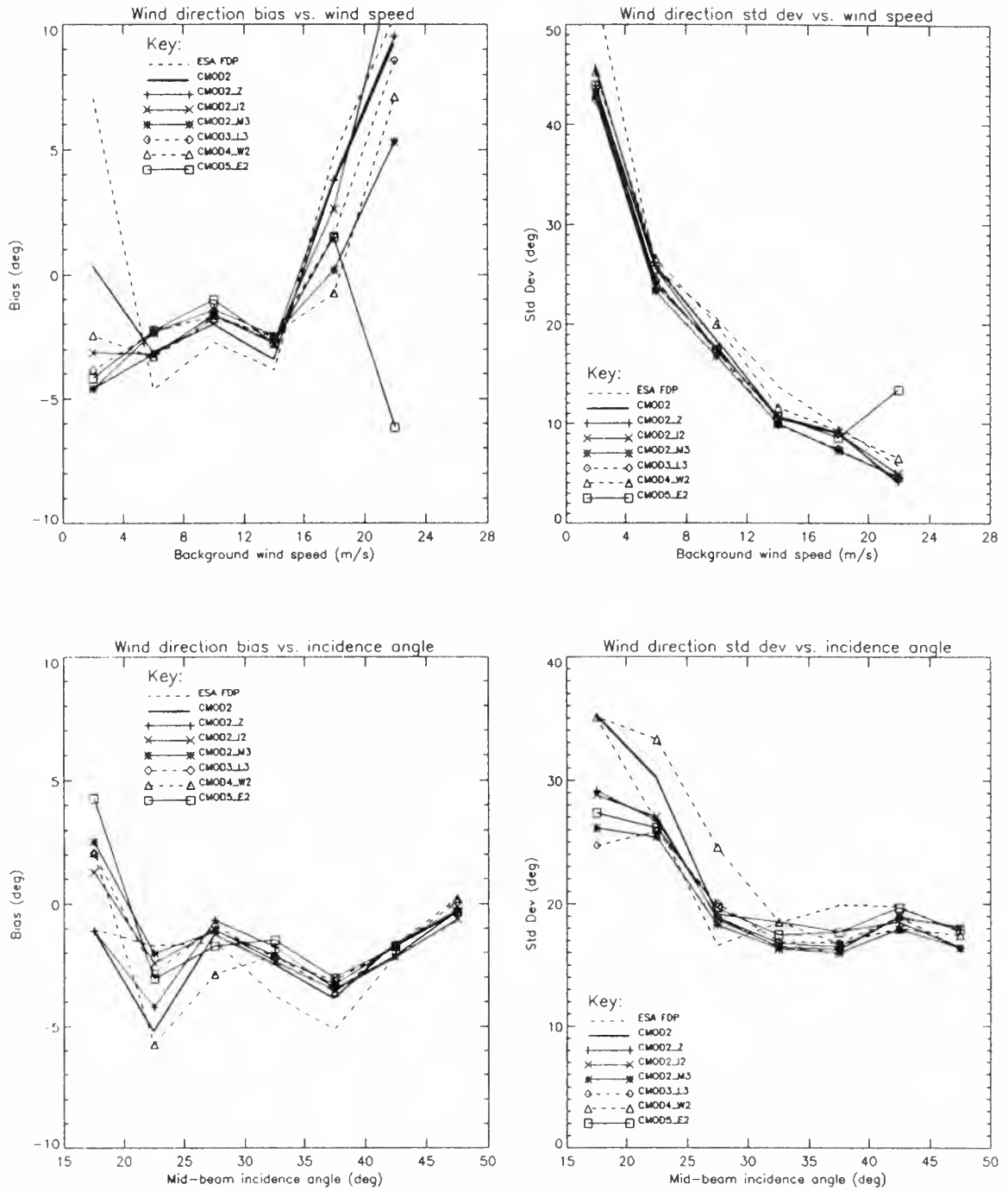


Figure 2: Summary graphs of wind direction differences from *RENE-91* analyses for various alternative wind transfer models.

CMOD4-W2, although having the smallest SD for speed, has the largest SD for direction.

Table 1 shows the weighted statistics, averaged over all incidence angles and for wind speeds $4\text{--}24\text{ms}^{-1}$ when compared with the collocated *RENE-91* analyses. Table 2 shows a sub-set of these statistics for daily FD comparisons against the NWP analyses, averaged over a two week period in March.

These figures confirm our impressions from the graphs that

- the new models all perform significantly better than CMOD2 in retrieving wind speed (CMOD4-W2 best), and all but one are better at retrieving wind direction (CMOD4-W2 worst).
- no one model is best at retrieving both parameters
- three out of four of our objective comparison indices (those based on weighted statistics) suggest that CMOD5_E2 is the 'best' model
- the unweighted FoM indicates that CMOD3.L3 (or L4) performs 'best' over the whole range of conditions, regardless of the observation distribution.

Analysis of results from the ECMWF runs showed that the high R-FoM value for CMOD3.L3 reported here was due in part to a large percentage ($\sim 20\%$) of retrievals were that being rejected. The reasons for this — whether due to the model or to the FD retrieval software — are under investigation at ECMWF.

5 Conclusions

Given that it was desirable that the known deficiencies in the existing CMOD2 model should be corrected for FD processing as soon as possible, CMOD5_E2 has been recommended to ESA as the 'best' transfer model for retrieving wind vectors and from those models so far proposed. This model shows good performance over most of the parameter ranges, and without side-effects when tested with a version of the FD software. ESA have recently accepted this recommendation, and are expected to implement the new model within the FD processing scheme in the near future.

However, it should be stressed that all of the latest models perform significantly better than the pre-launch CMOD2 version — several meet the product specification of 2ms^{-1} and 20° in most bins — and any one of them could have been selected if different criteria or emphasis on the statistical parameters had been chosen.

It should also be noted that the new model is recommended only on the basis of the 'first operational, geophysically calibrated' model; which implies that improvements should still be possible. Indeed ESA's beam calibration updates made on 1 March 1992 have been shown to have introduced an immediate 1ms^{-1} overall bias shift in the FD products, which will have to be removed by further tuning (as has been done with CMOD3.L4).

It is also recommended that since some models are better at wind speed retrieval, and other at wind direction, etc, that the strengths of the various models — or their

detailed formulation — should be combined into a 'super-model'. It is then to be expected that the FD geophysical product specifications will be met everywhere.

6 Acknowledgements

My thanks are extended to all the participants for providing their model formulations and update coefficients to meet the deadlines placed upon the study. The author also gives special thanks to Dr Peter Woiceshyn of JPL (currently at ECMWF) for running the FD package and providing the summary results for use in this study.

References

- [1] AE Long. Towards a C-band radar sea echo model for the ERS-1 scatterometer. In *Proceedings of the 3rd International Colloquium on Spectral Signatures of Objects in Remote Sensing, Les Arcs, France, December 1985*, pages 29–34. ESA SP-247, 1986.
- [2] D Offiler. Wind measurements from the MRF C-130 and the derivation of analyses from RENE-91 winds. In *ERS-1 Geophysical Calibration Workshop, Penhors, France, 26–30 April, 1992*. ESA, 1992.

Model Ident	Speed		Direction		Vector RMS	Rank 1 %	FoM	
	Bias	SD	Bias	SD			W	U
FDP(r)	0.2	2.9	4.0	101.7	12.6	62.4	—	—
FDP(a)	0.2	2.9	-2.9	20.3	4.3	100.0	0.77	0.69
CMOD2	-0.4	2.8	-2.3	20.2	3.9	51.6	0.79	0.73
CMOD2.Z	0.1	2.3	-2.0	19.0	3.5	51.2	0.90	0.82
CMOD2.I2	-0.7	2.2	-2.1	18.9	3.5	50.8	0.91	0.84
CMOD2.M3	0.8	2.6	-1.8	18.1	3.8	52.5	0.85	0.80
CMOD3.L3	-0.2	2.3	-1.8	18.9	3.4	52.0	0.92	0.89
CMOD3.L4	0.1	2.3	-1.6	18.4	3.4	48.1	0.93	0.89
CMOD4.W2	-0.9	1.9	-2.3	21.1	3.5	47.6	0.92	0.82
CMOD5.E2	-0.2	2.0	-1.7	19.5	3.3	51.3	0.97	0.86

Table 1: Summary results of comparisons between *RENE-91* analyses and scatterometer data reprocessed using various transfer models. FDP = CMOD2 fast delivery product (r) as received and (a) after 180° ambiguity removal. Note that the FDP(r) ‘Rank 1’ is a count of ‘correct’ wind directions after ESA’s ambiguity processing.

Model Ident	Speed		Direction		W	FoM		R
	Bias	SD	Bias	SD		U	R	
FDP(a)	-1.1	2.7	1.8	24.3	0.73	0.62	—	—
CMOD2	-1.3	2.6	1.4	22.7	0.77	0.62	154	—
CMOD2.Z	-0.7	2.4	1.3	20.6	0.86	0.64	85	—
CMOD2.I2	-1.3	2.3	1.3	21.2	0.86	0.63	90	—
CMOD2.M3	0.2	2.7	1.5	20.9	0.81	0.63	—	—
CMOD3.L3	-0.7	2.3	1.5	21.4	0.85	0.64	121	—
CMOD5.E2	-0.9	2.2	1.1	21.1	0.89	0.63	74	—

Table 2: Summary results of comparisons between UK Met. Office NWP analyses and daily scatterometer data reprocessed using various transfer models, averaged over the two week period 15–30 March 1992. (Not all models were available for testing during this period.) FDP(a) = CMOD2 fast delivery product after 180° ambiguity removal. N.B. The R-FoM values are derived from ECMWF reprocessing for 6,7 November 1991 and 10,11 March 1992.

Sensitivity Study - Scatterometer Retrievals With Wave Age Parameter

Peter Woiceshyn* and Peter Janssen**

European Center for Medium Range Weather Forecasts
Shinfield Park, Reading, Berkshire RG2 9AX, England

**Permanent Affiliation
KNMI
deBilt, the Netherlands

*Permanent Affiliation
Jet Propulsion Laboratory
California Institute of Technology
4800 Oak Grove Drive
Pasadena, CA 91109, USA

Abstract

The operational retrieval algorithms for C-band scatterometers relating the radar backscatter measurements to surface wind vectors have been customarily empirical. We performed a preliminary sensitivity study at ECMWF which has shown a large reduction in scatter of the ERS1 scatterometer data when wave age is included in the retrieval algorithm for the situation of medium to high winds, i.e., "young wind waves".

This research study was possible because ECMWF now has the WAM wave forecast model running operationally. This permits ready access to wave parameters necessary for inclusion in the ERS1 scatterometer wind retrieval process. The long range objective would be to recommend the implementation of this new model operationally where wave models are available, such as at ECMWF and at NOAA.

Introduction

The ERS1 scatterometer is a 3 antenna instrument radiating in vertically polarized C band (5.3 GHz) on one side of the spacecraft producing data across a swath of 500 km. The swath is organized in nineteen 50kmx50km resolution cells across it at a spacing of 25 km. The 3 antennas are separated by 45 degrees with the forward antenna being 45 degrees from the right side of the ground track of the ERS1 spacecraft. The centroids of measurements from each of the antennas are maintained in each measurement cell through yaw steering

of the spacecraft. The 3 backscatter measurements (one from each of the antenna) at each measurement cell presents the capability for the computation of statistical estimates of the "distance" (using sum of squares (SOS) or maximum likelihood (MLE) estimates) between model and measurements to estimate the most probable selection of a wind vector based on instrument/transfer function skill alone. In comparison, SEASAT had two measurements and this computation was not possible.

SEASAT in 1978 demonstrated the potential and value of scatterometer wind field data for meteorological and oceanic applications and research. This is well illustrated by one our images of SEASAT scatterometer wind fields on the cover of Aviation Week & Space Technology, March 13, 1989 issue, that were derived from about 8 orbits of data. (This same image showing weather patterns with streamlines appears elsewhere including the cover of the supplement (titled Spaceship Earth) inside the magazine Geographical, March 1991.) The geophysical evaluation of the SEASAT data including scatterometer were published in a special issue of the J. Geophys. Res., Vol. 87, dated April 30, 1982.

The scatterometer does not measure the wind speed directly since the scatterometer's radiation mainly probes the high frequency waves at the surface that are driven by the wind. The 'geophysical' measurement made by the scatterometer is the normalized radar cross-section, σ^0 (the parameter which we call 'backscatter' in this pa-

per). For C band radiating scatterometers, such as the ERS-1 AMI, σ^o is customarily related to the wind speed at some reference height above the surface (10 meters) via an empirically-based σ^o -to-wind transfer function model that relies totally on *in situ* and airborne experimental data. Further, these winds have been modified to correct for the influences of heat and moisture fluxes at the surface using the surface layer model of Ezraty (E. Attema, ESA-ESTEC, personal communication) and are thus called "neutral" winds. At this time, ECMWF plans to use the σ^o 's directly in their assimilations while the UK Met Office does not.

One can estimate the friction velocity, u_* , from estimates of the "neutral" drag coefficient, C_D , and the "neutral" wind speed. The difficulty in estimating u_* (and wind stress) from scatterometer has been one of choosing the proper C_D algorithm. Estimates of C_D over the ocean for the same neutral wind vary considerably (Geernaert *et al.*, 1986). Global measurements of u_* are not available for the development and calibration of a σ^o -to- u_* transfer function model. So the parameter, neutral wind, has been traditionally the parameter of choice in the σ^o -to-wind model parameterization.

Several studies, *e.g.*, Geernaert *et al.*, have shown that variations in the magnitude of C_D can be modelled in the C_D formulation by including the wave age parameter, ξ , such as was also done by Kitaigorodskii (1973), Donelan (1982), Maat *et al.* (1991), Nordeng (1991), and others. The physics of the wind waves are partially described by the input of energy from the wind. The input of energy from the wind is proportional to ξ^{-1} and the 2-dimensional wave spectrum (Cavaleri *et al.*, 1991). It was found that the major influence of ξ on C_D were for estimates of C_D for medium to high winds (Geernart *et al.*, 1986).

A preliminary attempt to postulate SEASAT backscatter to a C_D formulation is described in Woiceshyn *et al.* (1984). The C_D in this case did not involve the wave age parameter as described in the above papers. Nevertheless, the C_D chosen for the Woiceshyn *et al.* study was determined by Kondo (1975) to be related empirically to a "sea state dependent" roughness parameter, z_o . In this instance, z_o was determined from rms height measurements of high frequency waves at a tower off the coast of Japan. The correlation of the backscatter-to-wind measurements to that of the C_D -to-wind measurements was about 0.98. In another limited study using collocated

SEASAT and buoy data, Glazman, Pihos, and Ip (1988) demonstrated that wind speed biases in wind retrievals from SEASAT can also be reduced if the large-scale component of the wave field can be accounted for in the σ^o -to-wind retrievals.

In the companion paper by Janssen and Woiceshyn (which we now call J&W) we reflected on the associated physics of the scatterometer/wind-sea measurement process. In J & W we postulated that the backscatter reflects in some way the state of the high-frequency wind waves. We noted that the spectrum of the gravity-capillary waves generated by the wind depended not only on the magnitude of the wind, the duration of the wind, the previous history of the sea state, and the fetch over which the wind is blowing, but is determined by a number of physical processes -- namely wind input, nonlinear three and four wave interactions (which are enhanced by the presence of shear currents), etc. Further, we noted that for high winds when the waves are sufficiently steep, nonlinear processes are dominant so that the state of the gravity-capillary waves is mainly determined by gravity waves.

We therefore feel obliged to investigate the sensitivity of the scatterometer wind retrievals on the wave age parameter, ξ . In this paper we conduct sensitivity study in wind speed retrievals by incorporating the wave age parameter in current empirical retrieval algorithms such as CMOD2. Two tests are performed to answer the following questions: (a) what results to the scatter in the data particularly for medium to high winds (*i.e.*, for a relatively "young" sea state, *e.g.*, $\xi < 25$), and (b) what are the results when such a restriction as stated in (a) is not applied. The ξ that will be used in this study is defined as that by Maat *et al.* (1991), *i.e.*, the ratio C_p/u_* , where C_p is the phase velocity of the waves at the peak of the spectrum. This study is a preliminary attempt to include some wave physics in the backscatter transfer function that could influence the values of winds retrieved from the scatterometer measurements.

In J&W we describe a scatterometer retrieval algorithm that relates backscatter to wave age. There, we describe the basis for our approach, we tune the coefficients from data, and follow through with preliminary retrievals of the surface marine winds from the ERS1 AMI scatterometer backscatter data.

The Sensitivity Analysis

The pre-launch CMOD2 formulation (Long, 1991) relating scatterometer backscatter, σ^0 , to wind speed and direction was derived from field experiment data from aircraft-borne C band scatterometers. (This is the basis of the currently delivered ESA data product.) The first post-launch revisions to the scatterometer model were confined to refinements to the estimates of CMOD2's coefficients as a result of comparisons to available data sets, e.g., the analysis fields and conventional data available at the numerical weather prediction centers, and the data obtained from ESA campaign's *in situ* instrumentation on board ships, buoys, and aircraft off the coast of Norway, and from the Norwegian meteorological service's regional analysis. The model-refinement activities were conducted by ESA's ERS-1 Cal/Val analysis team members from ECMWF, ESA, IFREMER, METEO-France, and the University of Hamburg. For some investigators (notably from ESA, ECMWF, and the University of Hamburg), revisions of the CMOD2 coefficients were still not adequate to explain the empirical behavior of the ERS-1 scatterometer backscatter σ^0 relative to wind speed and direction.

The CMOD2_Z model, an early post-launch ECMWF model, referred to in this paper has the same formulation as CMOD2 except for the coefficients. For brevity, the details of the Legendre and ordinary polynomials are not included here. The formulation is:

$$\sigma_{linear} = b_0 (1 + b_1 \cos \varphi + b_2 \cos 2\varphi) \quad (1)$$

$$\text{where } b_0 = 10^\alpha U^\gamma$$

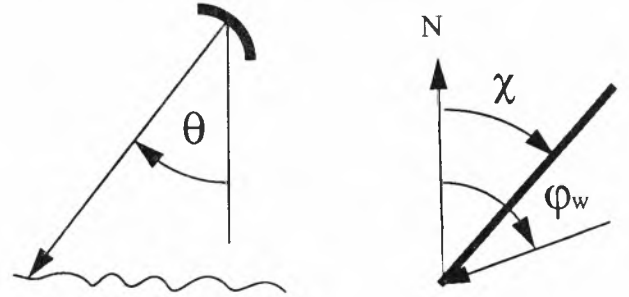
U = wind speed at 10 m height above the sea surface and is corrected for moisture and heat fluxes

$\varphi = \chi - \varphi_w$, where χ is the antenna look angle of the scatterometer antenna with respect to North and φ_w is the wind direction.

α , γ , b_1 , and b_2 are expanded as Legendre polynomials of θ to a total of 18 coefficients (some of which may be 0)

θ is the incidence angle, the angle difference between ERS1 nadir and scatterometer measure-

ment cell location at the sea surface



For completeness, we repeat here some equations in the J & W paper that are pertinent to this sensitivity study.

The wave age parameter is defined as $\xi = C_p/u_*$. Here, C_p is peak phase speed

$$C_p = \frac{g}{\omega_p}, \quad \omega_p = 2\pi f_p \quad (2)$$

and f_p is the peak frequency.

We collocate peak phase speeds C_p from the operational WAM model (WAMDI Group, 1989) running at ECMWF with the ERS1 scatterometer measurements in the ECMWF files that were prepared by Ad Stoffelen. The Stoffelen files include the ECMWF analysis winds collocated with the ERS1 UWI data, i.e., the CMOD2 determined wind data from scatterometer. We now call the CMOD2 wind speed U as U_{scat} .

In view of the previous discussion regarding the wind input to the waves we give, however, a slightly different interpretation to the parameter, U_{scat} . We assert that

$$U_{scat} \sim \frac{1}{\xi} \quad (3)$$

Then, from U_{scat} and the phase speed C_p we obtain the friction velocity u_* ,

$$u_* = 0.0022 C_p U_{scat} \quad (4)$$

This was converted to 10 m height wind speeds using a sea state dependent roughness length formulation obtained during HEMAX (Maat et al., 1991)

$$z_0 = \frac{\alpha u_*^2}{g}, \quad \alpha = \frac{0.45 u_*}{C_p} \quad (5)$$

while for low winds, the usual viscous roughness length was obtained. Thus

$$U_{10} = \frac{u_*}{\sqrt{C_D}}, \text{ and} \quad (6)$$

$$C_D = \left(\frac{k}{\ln \left(\frac{10}{z_0} \right)} \right)^2 \quad (7)$$

The wind speed we obtained in this manner was compared with the ECMWF analysis wind speeds. When wave age was used, a much higher wind speed correlation was found with the ECMWF analysis wind speeds than when U_{scat} winds are compared to the same ECMWF analysis wind speeds.

For young waves ($\xi < 25$, *i.e.*, medium to high winds), the standard deviation was reduced by nearly 30 percent when ξ^{-1} was simply substituted for U in the CMOD2 backscatter to wind transfer function model. Examples of this are shown in Figures 1 and 2. Figure 1 displays pairs of scatter plots and 2-dimensional histograms for scatterometer data derived from 3 types of σ^0 -to-wind transfer functions for the condition $\xi < 25$. Each of the comparisons are made to collocated ECMWF analysis wind speeds plotted along the horizontal axis. The top panel represents scatter and histogram for the data derived with the prelaunch CMOD2 model. The middle set of panels are comparisons for the post-launch model function, CMOD2_Z, an early model developed by Ad Stoffelen at ECMWF. The bottom pair of plots represents the data derived from the equations above. Both the standard deviation and scatter are considerably reduced for the condition of wave age < 25 . The peak phase velocity, C_p , to compute the wave age was obtained from the operational WAM wave model at ECMWF. Figure 2 is the case for ξ both below and above 25, *i.e.*, all the data. Again, our wave age model reduced the scatter for medium to high winds, but in this case some bias is introduced at lower winds for "old" waves having a large swell component.

Discussion and Conclusions

The results from this sensitivity experiment showed a large reduction in ERS1 wind speed scatter compared to wind speeds estimated from both pre-launch and post-launch scatterometer model function algorithms when all of these were plotted against collocated ECMWF analysis winds. The large positive impact in the medium to high wind speed regime suggests that there is potential in the use of wave age in scatterometer wind retrieval algorithms. It should be noted, however, that in order to obtain a reliable retrieval algorithm that ξ is certainly not the whole story. We expect that in order to obtain a reliable retrieval algorithm, the high frequency wave spectrum would have to be obtained explicitly and its dependence on environmental parameters such as slicks, air-sea temperature differences, etc. (which are all important for low winds) may have to be considered. Work on the influence of some these parameters are in progress. Nevertheless, we thought it of interest to pursue our simple approach and to develop a scatterometer algorithm based on wave age. This work is reported in the paper by Janssen and Woiceshyn in these proceedings.

Acknowledgements

We appreciate the help from many colleagues including Ad Stoffelen, David Anderson, Ross Hoffman, and Tony Hollingsworth and his Staff at ECMWF for the many discussions related to this paper. We also thank Evert Attema and his Cal/Val analysis team for their valuable comments. The work described herein was performed at ECMWF. Part of this work was supported by the Jet Propulsion Laboratory, California Institute of Technology, through an agreement with the National Aeronautics and Space Administration.

References

- Cavaleri, L., L. Bertotti, and P. Lionello, "Wind Wave Cast in the Mediterranean Sea," *J. Geophys. Res.*, **96**, 10,739-10,764, 1991.
- Donelan, M. A., "The dependence of the aerodynamic drag coefficient on wave parameters," in *First Conference on Meteorology and Air-Sea Interaction of the Coastal Zone*, pp. 381-387, American Meteorological Society, Boston, Mass., 1982.
- Geernaert, G. L., K. B. Katsaros, K. Richter, "Variation of the drag coefficient and its dependence on sea

- state," *J. Geophys. Res.*, **91**, 7667-7679.
- Glazman, R. E., G. G. Pihos, and J. Ip, "Scatterometer wind speed bias induced by the large-scale component of the wave field," *J. Geophys. Res.*, **93**, 1317-1328, 1988.
- Kitaigorodskii, S. A., "The physics of air-sea interaction," translated from Russian by A. Baruch, Israel Programs for Science Translations, Jerusalem, 1973.
- Long, A.E., ERS-1: C-Band and Sea-Echo Models, *ESA Report ESTEC/WMA/9104, Revision 1*, April 8, 1991.
- Maat, N., C. Kraan, and W. A. Oost, "The roughness of wind waves," *Boundary-Layer Meteorology*, **54**, 89-102, 1991.
- Nordeng, T. E., "On the Wave Age Dependent Drag Coefficient and roughness length at sea," *J. Geophys. Res.*, **96**, 7167-7174, 1991.
- WAMDI Group, "The WAM model - a third generation ocean prediction model," *J. Phys. Oceanogr.*, **18**, 1775-1810, 1988.
- Woiceshyn, P. M., M. G. Wurtele, D. H. Boggs, L. F. McGoldrick, and S. Peteherych, "A new parameterization of an empirical model for wind/ocean scatterometry," Proceedings of the URSI Commission F Symposium and Workshop, Shores, Israel, May 14-23, 1984, *NASA Conf. Publ. CP-2302*, 57-74, 1984.

Figures

- Figure 1. Scatter plots (left column of panels) and associated 2-D histograms. Left column of panels from top to bottom show scatter plots of CMOD2, CMOD2_Z, and data from wave model wind speeds vs. ECMWF wind speeds collocated to ERS-1 locations. Scatter plots are for young waves ($\xi < 25$). On each of the scatter plots, the number of points, the mean value, the standard deviation, and the correlation are noted.
- Figure 2. Same as Figure 1., except data for all values of ξ are plotted

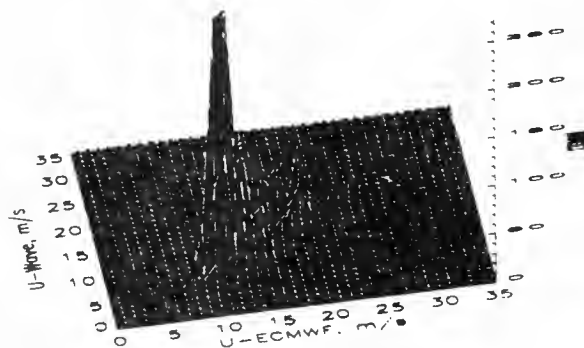
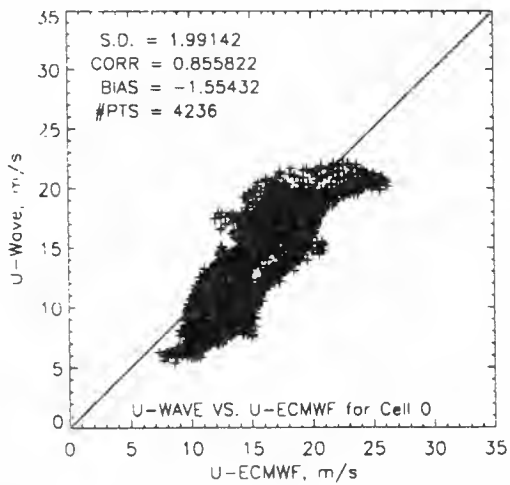
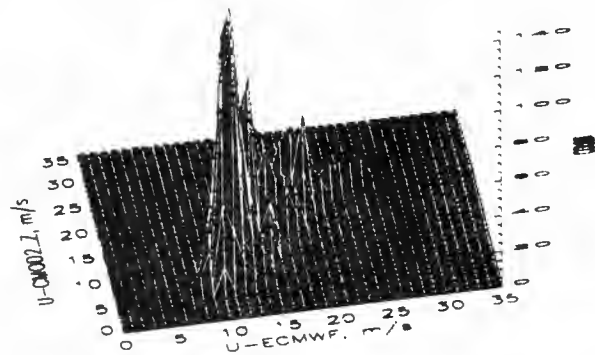
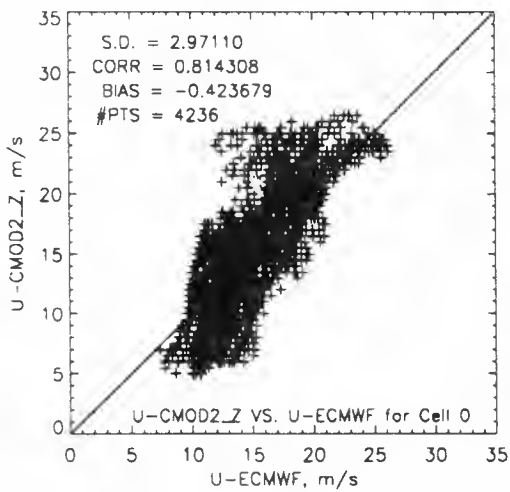
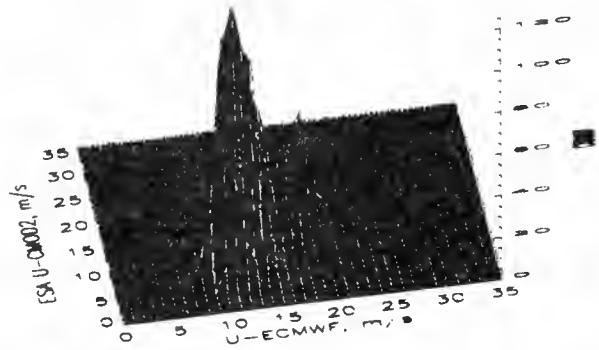
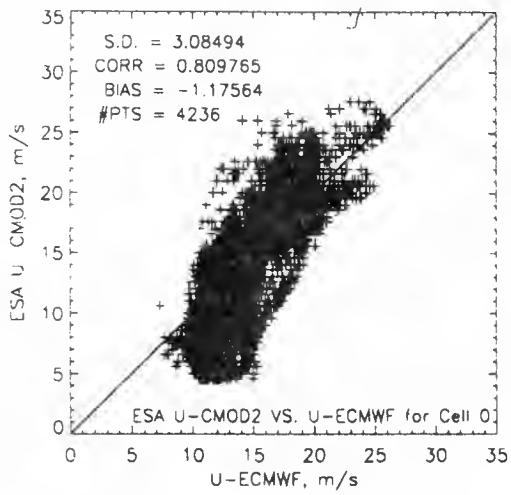


Figure 1

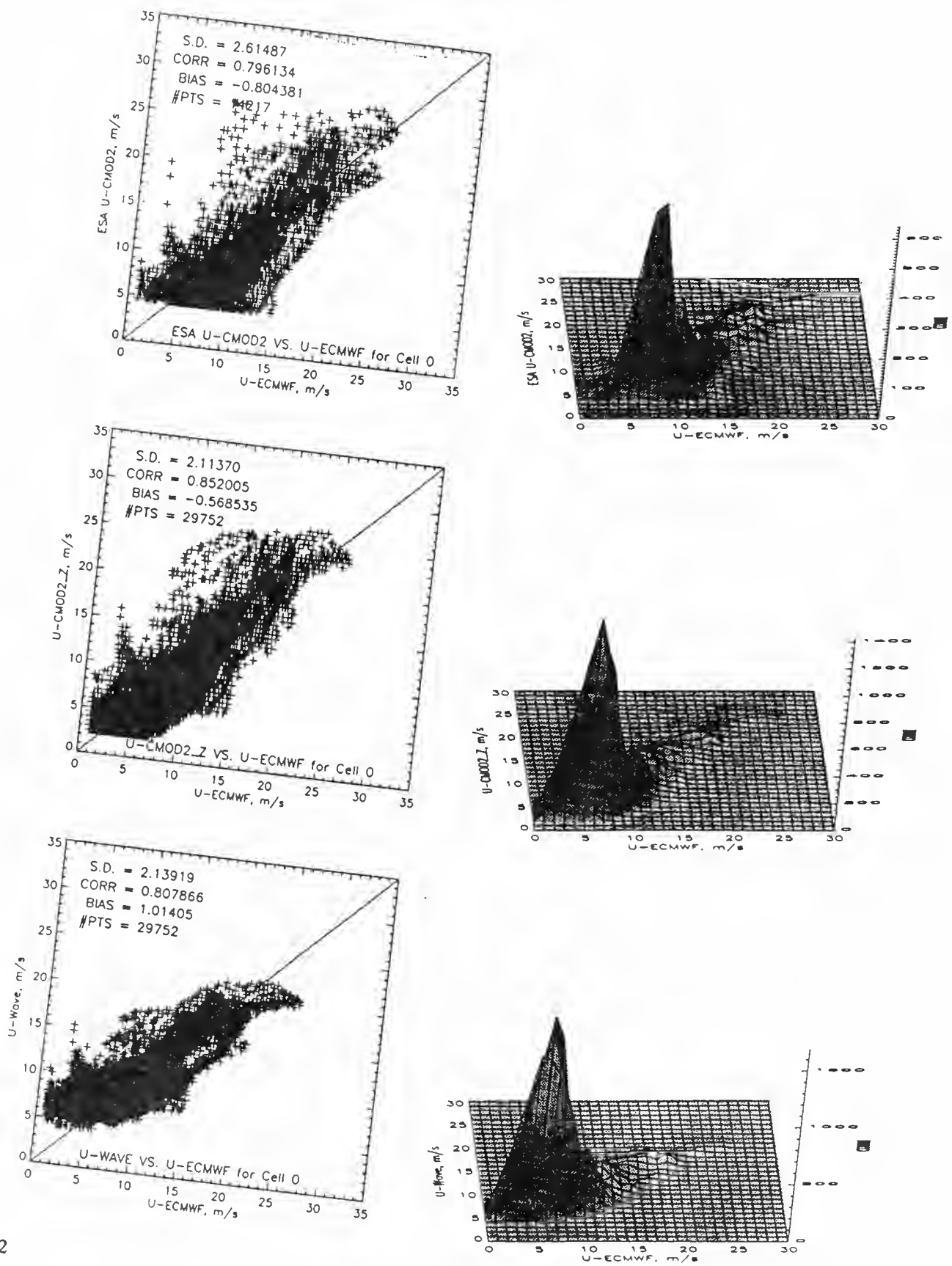


Figure 2

Wave Age and the Scatterometer Wind Retrieval Algorithm

Peter Janssen* and Peter Woiceshyn**

European Centre for Medium-Range Weather Forecast
Shinfield Park, Reading, Berkshire RG2 9AX, England

*Permanent Affiliation
KNMI
deBilt, the Netherlands

** Permanent Affiliation
Jet Propulsion Laboratory
California Institute of Technology
4800 Oak Grove Drive
Pasadena, CA 91109, USA

Abstract

A backscatter to "wave age" transfer function is proposed to retrieve wind vectors from scatterometer over the ocean. In this report, we apply this model to the ERS1 AMI scatterometer. The basic form of the angular dependence of the transfer function comes from Bragg scattering theory. However, some modifications are introduced in the formulation such as upwind/downwind differences in the backscatter measurements evident in the data. Values of the coefficients are obtained by tuning to a subset of ECMWF-analysis surface winds and ERS1-scatterometer measurements that were collocated. Preliminary results of applying the "wave age" transfer function to a large sample of high-resolution data of 6 Nov 1991 resulted in a rms error of 1.50 m/s and a rms wind direction error of 19 degrees. This is well within the required geophysical specifications of 2 m/s and 20 degrees. The introduction of the "wave age" as an intermediate parameter to obtain an estimate of surface marine wind vectors appears to be quite promising. This formulation is a preliminary attempt to include some wave physics in the backscatter transfer function and interpretation of the measurements.

Introduction

It is customary to relate the backscatter measurements of radar scatterometers to the local wind at some arbitrary height above the sea surface. In the case of ERS1 it is 10 meters and in the case of SEASAT it was 19.5 meters. However, on reflection of the associated physics of the measurement process, it should be realised that this is an empirical assumption since the backscatter reflects in some way the state of the high-frequency wind waves. The spectrum of the gravity-capillary waves generated by the wind depends not only on the wind, but is determined by a number of physical processes -- namely wind input, nonlinear three and four wave interactions (which are enhanced by the presence of shear currents), viscous dissipation due to slicks (cf. VIERS-1). However, for high winds when the waves are sufficiently steep, nonlinear processes are dominant so that the state of the gravity-capillary waves is mainly determined by gravity waves. This is illustrated in Fig.1 where we have plotted frequency spectra for a friction velocity ranging from $u_* = 0.1$ to 1 keeping the wave age parameter $\xi = C_p/u_*$ fixed. Here C_p is the peak phase speed and f_p is the peak frequency.

$$C_p = \frac{g}{\omega_p^2}, \quad \omega_p = 2\pi f_p \quad (1)$$

It is therefore tempting to investigate the dependence of a backscatter algorithm on the wave age parameter ξ . Thus, for wind waves, one would expect a relation between the backscatter σ_0 and ξ . In a separate paper in these proceedings (Woiceshyn and Janssen) we investigate a possible dependence and a sensitivity study. There we collocated peak phase speeds C_p from the operational WAM model running at ECMWF with the ERS1 scatterometer measurements in the ECMWF files that were prepared by Ad Stoffelen. The Stoffelen files include the ECMWF analysis winds collected with the ERS1 UWI data, i.e., the CMOD2 determined wind data from the scatterometer. We call the CMOD2 wind speed U_{scat} .

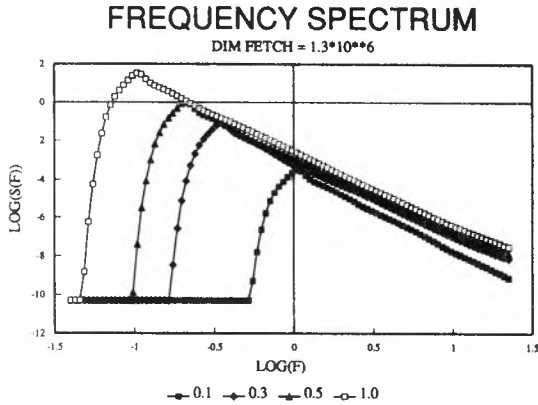


Figure 1

In view of the above discussion regarding the state of the high-frequency waves we give, however, a slightly different interpretation to the parameter U_{scat} , we assert that

$$U_{scat} \sim \frac{1}{\xi} \quad (2)$$

Then, from U_{scat} and the phase speed C_p we obtain the friction velocity u^* ,

$$u^* = 0.0022 C_p U_{scat} \quad (3)$$

This was converted to 10m height wind speeds using a sea state dependent roughness length formulation obtained during HEMAX (Maat et al)

$$z_0 = \frac{\alpha u_*^2}{g}, \quad \alpha = \frac{0.45 u_*}{C_p} \quad (4)$$

while for low winds, the usual viscous roughness length was obtained. Thus

$$U_{10} = \frac{u_*}{\sqrt{C_D}}, \quad C_D = \left(\frac{k}{\ln \frac{z_0}{z_0}}\right)^2 \quad (5)$$

The wind speed we obtained in this manner was compared with the ECMWF analysis wind speeds. When wave age was used, a much higher wind speed correlation was found with the ECMWF analysis wind speeds than when U_{scat} winds are compared to the same ECMWF analysis wind speeds.

For young waves ($\xi < 25$, i.e. medium to high winds), the standard deviation was reduced by nearly 30 percent when ξ^{-1} was simply substituted for V in the CMOD2 backscatter to wind transfer function.

This suggests that there is potential in the use of wave age in scatterometer wind retrieval algorithms. It should be noted, however, that in order to obtain a reliable retrieval algorithm that this is certainly not the whole story. We expect that in order to obtain a reliable retrieval algorithm, the high frequency wave spectrum would have to be obtained explicitly and its dependence on environmental parameters such as slicks, air-sea temperature differences, etc. (which are all important for low winds) may have to be considered. Work on the influence of these parameters is in progress (VIERS-1 group).

Nevertheless, we thought it of interest to pursue our simple approach and to develop a scatterometer algorithm based on wave age. This work is reported in the next sections.

Wave-Age Scatterometer Algorithm Description and Tuning

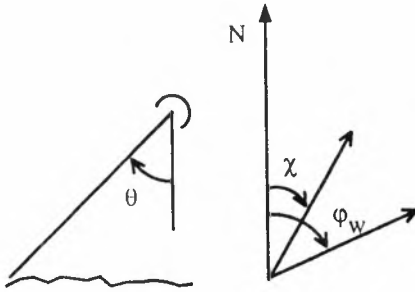
We propose to use the following algorithms,

$$\sigma_m^o = \alpha + \beta \log \xi + 10 \log F(\theta, \varphi) \quad (6)$$

where ξ is the wave age and F is an angle factor for incidence and azimuth dependencies of the radar backscatter,

$$F = \frac{1}{\sin^4 \theta} (5t^4 + 4t^2 + \gamma t + 1) \quad (7)$$

The parameter γ represents the upwind - downwind difference, $t = \cos \varphi$, $\varphi = \chi - \varphi_w$, χ is the look angle, φ_w is the wind direction and θ is the incidence angle (see sketch)



It should be emphasized that the choice of the angular distribution function F is not easy to justify. If one would (in a strict sense) believe in Bragg scattering as the dominant mechanism then the backscatter would depend on the value of the spectrum at $k_w = 1/2 k_r \sin \theta$ and at angle φ . With a spectrum Φ of the shape

$$\Phi(k, \theta) = E(k) \frac{2}{\pi} \cos^2 \varphi$$

where we take the Phillips spectrum for high frequencies

$$E(k) = \frac{1}{2} \alpha_p k^{-4}$$

and a \cos^2 directional distribution, we would obtain that the backscatter: Σ ($\sigma_m = 10 \log \Sigma$) looks like

$$\Sigma \sim \frac{\alpha_p}{k_R^4 \sin^4 \theta} \cos^2 \varphi \quad (8)$$

Then dependence of Σ on environmental parameters would be given by the dependence of α_p on wave age, viscosity, etc. However, intuitively, one would expect that also waves making an angle with the look direction of the scatterometer antenna beam would give a contribution to the backscatter. As a result the resonance condition becomes

$$k_w \cos \varphi = \frac{1}{2} k_R \sin \theta \quad (9)$$

and as a result the backscatter Σ becomes

$$\Sigma \sim \frac{\alpha_p}{k_R^4} F(\gamma = 0) \quad (10)$$

In "F" we have added an empirical factor γ which represents the upwind - downwind difference and which will be determined by tuning to a data set. Note that the entire wave age dependence is contained in the Phillips constant α_p . Since there is always a debate about the sensitivity of the Phillip's constant on wave age we will determine β (and of course also α) by tuning.

We obtain a best estimate for α , β and γ by minimizing the cost function

$$J = \Sigma (\sigma_m - \sigma_0)^2 \quad (11)$$

where σ_0 is the observed backscatter and σ_m is derived from collocated ECMWF wind speeds using equations (6), and (7).

The minimum is found if the gradient of J with respect to α , β , and γ vanishes,

$$\frac{\partial J}{\partial \alpha} = \frac{\partial J}{\partial \beta} = \frac{\partial J}{\partial \gamma} = 0 \quad (12)$$

Thus, taking the derivative of J we have

$$\frac{\delta}{\delta\alpha}J = 0 \Rightarrow \Sigma(\sigma_m - \sigma_0)\frac{\delta}{\delta\alpha}\sigma_m = 0 \quad (13a)$$

$$\frac{\delta}{\delta\beta}J = 0 \Rightarrow \Sigma(\sigma_m - \sigma_0)\frac{\delta}{\delta\beta}\sigma_m = 0 \quad (13b)$$

$$\frac{\delta}{\delta\gamma}J = 0 \Rightarrow \Sigma(\sigma_m - \sigma_0)\frac{\delta}{\delta\gamma}\sigma_m = 0 \quad (13c)$$

where

$$\frac{\delta}{\delta\alpha}\sigma_m = 1$$

$$\frac{\delta}{\delta\beta}\sigma_m = \ln \xi$$

$$\frac{\delta}{\delta\gamma}\sigma_m = \frac{10}{F} \frac{t}{\sin^4 \theta}$$

Note that (13a) implies that the mean difference between model and observed backscatter vanishes (no bias). It is however not easy to solve (13) straightforward, because γ occurs in a complicated manner. We therefore solved (13) by means of Newton-Raphson iteration. By using a coarse set of collocations provided by Ross Hoffman we obtained the following results for α , β , and γ .

$$\alpha = -10.78$$

$$\beta = -11.62$$

$$\gamma = -0.652$$

We will use these coefficients in our retrieval algorithms. In passing, we note that the value of β thus found would imply the following wave age dependence of the Phillips constant

$$\alpha_p \sim \xi^{-1.2}$$

which is not unreasonable when compared with Heinz Gunther's fits of the Jonswap data.

Retrieval Algorithms

The retrieval algorithm procedure is outlined below. We minimize at every measurement location the cost functions

$$H = \sum_{i=1}^4 (\sigma_m - \sigma_0)^2$$

where the summation is over the number of antenna beams involved. In general, this gives 4 minima (a possibility of 6 when wind direction is parallel to the mid antenna beam illuminated at the surface) with their associated cost

$$cost(n_c) = \sum_b [(\sigma_m - \sigma_0)^2]^{\frac{1}{2}}, \quad n_c = 1, \dots, 4$$

These solutions were generated by first choosing as an initial guess the ECMWF model wind speed and direction from the analysis fields

$$\phi = \phi_{mod} + (n_c - 1) * 90$$

Thus, $n_c = 1$ 'usually' gives the solution with direction that is closest to the ECMWF analysis direction. This is the solution which is chosen in the first instance. If the cost of the other solutions is, however, significantly lower, such that

$$| cost(n_c) - cost(1) | > 5 < \Delta\sigma >$$

where $<\Delta\sigma>$ is the mean error over the three beams, we choose the solution n_c . Furthermore, we only allow solutions where the cost is small enough ($< 5 * <\Delta\sigma>$). Otherwise, if the cost values were too big, we consider the model function/observation retrieval has failed to obtain a solution.

We applied the retrieval algorithm to a much larger, high resolution data set of 6 Nov 1991. Results are presented in Fig. 2 and 3. The statistics are presented in Table I.

	Speed (m/s)	Direction (deg.)
bias	-0.75	-4
rms error	1.50	19
correlation	83 %	

Table 1

Of the chosen solutions 83% have directions within 45 degrees from the ECMWF analysis directions.

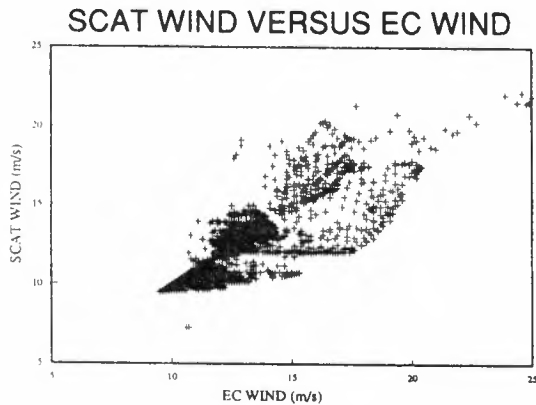


Figure 2

Conclusions and Comments

Preliminary results from this "wave age" scatterometer transfer function appear to be promising based on this limited evaluation. We attempted to include some wave physics that possibly may modify the ocean surface and thus the backscatter measurements, and hence the estimate of the retrieved marine wind vectors. The traditional wind retrieval transfer function approach has normally been a purely empirical one for the C-band scatterometers.

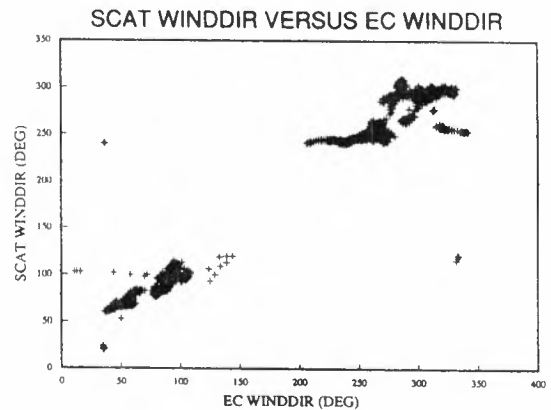


Figure 3

Acknowledgements

We wish to thank ESA for ERS1 and its data, and ECMWF for providing the computer resources, the WAM wave model data and the wind analysis data. We particularly wish to express our appreciation to Tony Hollingsworth and his staff at ECMWF for their counsel related to this paper. We also thank Evert Attema, ESA-ESTEC, for the privilege of serving on his Cal/Val analysis team. This permitted timely positive interaction with other team members regarding this paper.

The work described herein was performed at ECMWF, Reading, Berkshire, England. The writing and publication of this paper was partially supported by the Jet Propulsion Laboratory, California Institute of Technology, through an agreement with the National Aeronautics and Space Administration.

References

Maat, N. , Kraan, C. & Oost, W.A. "The Roughness of Wind Waves", *Boundary Layer Met.* 54, 89-103.

SESSION - III

RADAR ALTIMETER VALIDATION

THE HEIGHT CALIBRATION OF THE ERS-1 RADAR ALTIMETER

C. R. Francis

ESA/ESTEC,
2200AG Noordwijk,
The Netherlands

Abstract

During August and September 1991 a coordinated campaign of many different types of measurements was made in order to perform a height calibration of the ERS-1 Radar Altimeter. This followed extensive preparatory campaigns over the previous years. The basic scenario required the satellite to overfly a small oceanographic research platform in the Northern Adriatic Sea, off the shore from Venice. This has been surveyed into the same network as a set of European Satellite Laser Ranging (SLR) stations, by a series of GPS campaigns. Additionally a new site for a mobile SLR station was established in the area. Local measurements of sea level were made at the platform during the overflights, together with additional environmental measurements. Following the measurement campaign all of the data sets, including the altimeter data themselves, have been carefully processed and cross-checked against other data sources, where possible, to ensure consistency. Eventually it has been possible to determine the bias in the altimeter measurements to a high level of accuracy.

Introduction

The height measurements from the ERS-1 Radar Altimeter (RA) have a sub-millimetre long-term stability, and a noise level of about 2 cm [1]. An overall system calibration to this level was not possible before launch, so it has been necessary to determine the height bias error after launch, by means of a dedicated measurement campaign. Maintaining control of all the elements contributing to this calibration is a delicate task, but had been achieved before [2].

The requirements for the calibration included:

1. The objective was *engineering* calibration, geophysical effects being minimised wherever possible.
2. Both the accuracy and the precision should be maximised, with an overall goal of 5 cm for the combined error.
3. The calibration should avoid potential single-point failures and be resistant to the effects of single errors.

At its most basic, the statement of the calibration procedure is to independently measure the distance from the satellite to the sea-surface, while the altimeter is measuring the same path, with suitable corrections for propagation effects. The independent measurement was made in two steps, firstly from the satellite to a suitable tracking network, and secondly from this to a point on the sea-

surface. The key practical elements of the approach were:

1. The comparison overflight point was an oceanographic research platform in the open sea.
2. Measurements of sea-level (tide), winds, waves, tropospheric and ionospheric density were made on the platform.
3. Several Satellite Laser Ranging stations (SLR) surrounding the comparison site enabled a quasi-geometric solution for the trajectory.
4. Dedicated campaigns to measure the three-dimensional positions of all the reference points, and the local geoid, were made.
5. There was a high degree of redundancy in the system to aid error resistance.

An illustration of the calibration area is shown in Figure 1.

The satellite made northward passes directly over the "Acqua Alta" platform (see Figure 2) located about 14km offshore from Venice. This platform is a tower fixed to the sea-bed in about 16m of water, at a position 45°18.78'N, 12°30.55'E.

ERS-1 was launched at 01:46:34 on 17 July 1991, from Kourou in French Guyana. The RA was first switched on for test measurements on 25 July 1991 and on the following day, when the Commissioning Phase orbit was acquired. The RA was not switched on again until 28 July 1991 when continuous operations started, eleven days after launch. This was the first pass over the calibration site, and the next pass, on 31 July 1991, became the first pass of the campaign. During the calibration campaign, which lasted until 17 September 1991, the RA operated correctly on all passes.

The satellite was tracked simultaneously by several SLR sites which became known as the European Calibration Network (ECN), at Grasse, Graz, Herstmonceux, Matera, Zimmerwald and a new mobile laser site at Monte Venda, in the hills south of Padova, about 60km to the west of the tower. This site was selected for a number of reasons, including better weather due to its altitude above the coastal plain and its solid connection into the

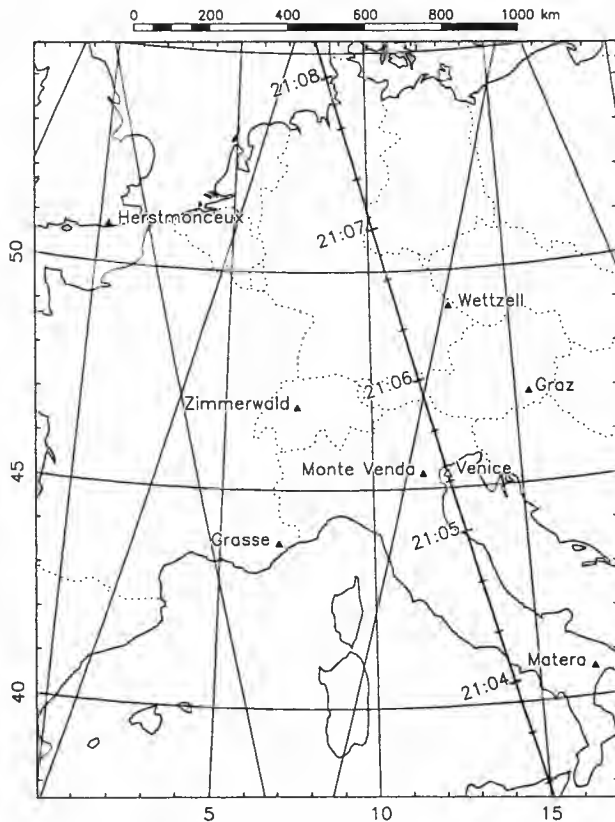


FIGURE 1. The track of ERS-1 over the Northern Adriatic sea and the calibration site, with time marks given in UTC. The positions of the European Calibration Network of laser sites is also marked.

continental crust. The six lasers provide a network surrounding the Venice tower with a favourable topology and provided redundancy in the system. Analysis had shown [3] that useful results would be obtained with various sub-sets of the lasers. This was a major contribution to the reliability of the method.

The northbound pass over the calibration site is shown in . This pass was over the sea for about 25sec before the tower overpass, which was adequate for the altimeter to acquire the sea-surface. The northward pass had the further advantage that it was at night, which is favourable for many SLR systems and has a smaller ionospheric effect.

The Three-Dimensional Network

A regional network has been established in campaigns spread over four years [4,5], by GPS measurements. The origin of the network is the SLR site at Monte Venda whose coordinates were determined independently by (a) direct LAGEOS laser ranging, and (b) dual-frequency GPS survey involving other European laser/GPS stations. This has enabled the determination of all the reference points (SLR's and platform) in a new reference frame (ERS90B, [6]). Analysis of the extensive set of dual-frequency GPS measurements was made by two independent institutes (DUT and AUIB) to trap errors. The final results, using different software, are in close



FIGURE 2. The *Acqua Alta* platform during the campaign. The microwave radiometer is being calibrated.

agreement, with an error ellipse of 5cm vertically for the platform solution.

A combination of the GPS measurements, conventional levelling and astrogeodetic measurements have also enabled the definition of a detailed regional geoid [7]. This has allowed the distribution of RA measurements across-track to be compensated.

Finally a series of painstaking surveys on the platform itself have enabled the determination of the relationship between the tide-gauge readings and the distance from the platform reference point to the actual sea-level.

Local Measurements

During each calibration pass measurements of the local environment were made on the platform. There were two tide gauges, an upward-looking microwave radiometer, a full set of meteorological instruments and a dual-frequency GPS receiver. Measurements were also made at other sites in the region, mentioned later.

The primary tide gauge on the platform [8] was designed to have a rapid response yet to effectively filter wave motion. This was used as the reference for the calibration. It records its readings on a paper chart. The second gauge records at 5 minute intervals, and telemeters data to the shore. Similar gauges provide telemetered

data from 3 coastal sites around the platform which were used as quality control for the primary gauge.

The tropospheric corrections were made by analysis of the microwave radiometer data. The processing algorithm used at the University of Rome makes use of the two-frequency brightness temperature measurements and the surface pressure. Estimates were also made from the surface measurements of temperature, pressure and humidity. The combined tropospheric delay for each pass is shown in Figure 3.

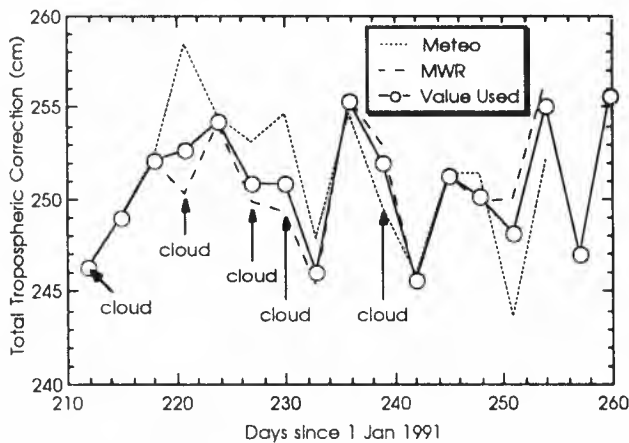


FIGURE 3. Tropospheric corrections during the calibration campaign.

Ionospheric corrections were derived from the dual frequency GPS measurements made on the platform, and by Faraday Rotation measurements made from Florence. For the August passes ionospheric measurements from the DORIS system on the SPOT 2 satellite (which is in a very similar orbit to ERS-1) have been made available. Figure 4 shows the summary of ionospheric corrections used for the calibration passes. There are discrepancies amongst the different measurement techniques, but the absolute values are rather small.

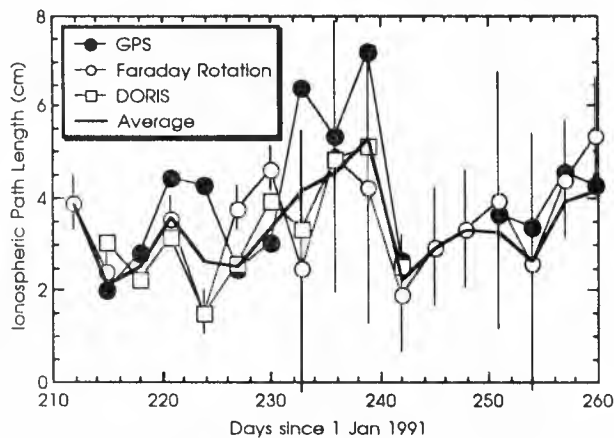


FIGURE 4. Ionospheric corrections during the calibration campaign.

Orbit Determination

Table 1 shows the coverage by European lasers of each of the calibration passes and the availability of reprocessed altimeter data. In the analysis so far the three Eastern European stations have not been used. The passes selected were those with Monte Venda and one other laser, and of course with available RA data.

Station	July		August							September									
	28	31	3	6	9	12	15	18	21	24	27	30	2	5	8	11	14	17	
Monte Venda		
Grasse
Graz			
Matera	.			.															.
Wetzell					
Zimmerwald		
Herstmonceux
Borowiec					
Potsdam
Riga		
Altimeter

TABLE 1 Tracking coverage by European lasers, and the availability of altimeter data, during the campaign.

The precise orbit was computed in two steps, both using the DUT/SOM version of the NASA GEODYN II orbit determination software. First, a 4-day long arc solution was generated using ERS-1 so-called quick-look normal points from a global network of satellite laser ranging systems. Secondly, this orbit serves as *a priori* information for the determination of a short-arc orbit over the "Acqua Alta" and the European Calibration Network. This procedure maximises the orbit accuracy over the calibration site and minimises the possibility of obtaining an unrealistic or non-converging orbit solution. Once they became available the short-arc orbits were based on high-quality full-rate SLR data.

The RMS of the residuals, which indicates how well the computed orbit fits to the observations, ranges from 0.3–6.2 cm per pass with an average of 1.9 cm, and consists for a large part of remaining system noise in the normal points.

Altimeter Measurements

For each of the calibration passes the altimeter data were specially preprocessed in a reference, retracking processor at ESTEC. This processor uses a least squares fit to the classical Brown Model [9] for radar altimeter echoes over ocean surfaces. It is independent of the on-board tracking performance, which proved to be fortunate in this area, as low prevailing wind speeds often led to specular radar echoes distorting the mean echo shape. This had a significantly degrading effect on the on-board tracker, but were effectively filtered out by the reference processor. A further characteristic of this processor was its optimum use of internal calibration data and instrument characterisation data.

Retracked RA data at the full 20Hz rate produced from this processor were found to be fully decorrelated, with a white noise spectrum up to the alias frequency of 10Hz, and an RMS noise level of 10cm. This corresponds to a 1Hz noise level of 2.5cm. The stability of the

retracked data was guaranteed by the handling of all available characterisation data.

The retracked data were distributed to DUT/SOM where they were included in the overall calibration solution. Although the altimeter measurements have a noise of nearly 10 cm, the interpolation of the sea level could be performed up to about 2-cm accuracy.

Results

A total of 10 calibration passes have been processed, and the resulting altimeter height bias values per pass are shown in Figure 5 as a function of the cross-track position of the point of closest approach.

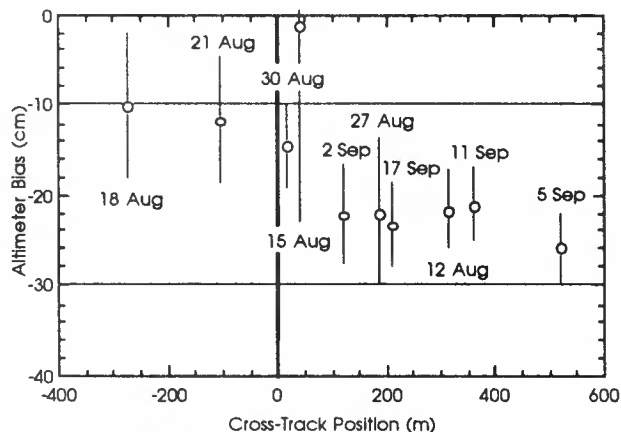


FIGURE 5. Individual estimates of altimeter bias, per pass, determined during the calibration campaign. The 1 σ error bars are shown.

The measured value of the deflection of the vertical at the platform is 1.6 arcseconds. When a line of this slope is introduced into the set of bias values the resulting bias value at the position of the platform itself is -19.2cm , and the associated standard deviation is 6cm. In addition to this there must be included an uncertainty for static errors which cannot be averaged out in this way. Such errors have zero mean, otherwise they would be removed.

Consequently the current estimate of the ERS-1 RA height bias is $-19.2 \pm 8\text{cm}$.

Analysis of the calibration data set is continuing, with the intention of improving the determination of the bias value. Additionally the static elements of the calibration system can be remeasured (by definition they are *static*) with consequent improvement in the confidence in the bias value.

Acknowledgements

The work described in this report has been performed, over a period of several years, by a large team from the following establishments: Agenzia Spaziale Italiana (I); Centre d'Etudes et de Recherches Géodynamiques et Astronomiques (F); Delft University of Technology/Kootwijk Observatory for Satellite Geodesy and Section Orbital Mechanics (NL); Deutsches Geodätisches Forschungsinstitut (D); European Space Agency; ETH Zürich (CH); Institut für Angewandte Geodäsie (D); Institut für Navigation Stuttgart (D); Istituto Geografico Militare Italiano (I); Istituto di Ricerca sulle Onde Elettromagnetiche

(I); Istituto Studio Dinamica Grandi Masse (I); James Rennel Centre for Physical Oceanography (GB); Telespazio SpA (I); Università di Padova (I); Università di Roma "La Sapienza" (I); Universität Bern (CH); Universität Graz (A).

References

- [1] Francis, C.R., ERS-1 Altimeter In-Orbit Performance, *ESA Technical Note*, (in preparation).
- [2] Kolenkiewicz, R., and C. F. Martin, SEASAT altimeter height calibration, *J. Geophys. Res.*, **87**, C5, 3189-3197, 1982.
- [3] Francis, C.R. and B. Duesmann, ERS-1 Altimeter Calibration, *ESA ER-TN-ESA-RA-0003*, Issue 3, 128 pp. July 1, 1988.
- [4] Caporali, A., G.F. Dallaporta, F. Facchinelli and G. Zambon. Rete GPS nel Territorio Veneto. Monografie delle Stazioni di Misura, *TN 126 Consiglio Nazionale delle Ricerche*, Istituto per lo Studio della Dinamica delle Grandi Masse, Venezia, 1990.
- [5] Gurtner, W., The GPS Campaigns 1990/1991, *ERS-1 Radar Altimeter Calibration Team Meeting*, Berne, 20 December 1991.
- [6] Wakker, K. F., R. Scharroo and B. A. C. Ambrosius, Some Results of the ERS-1 Radar Altimeter Calibration, *Proc. ESA Symposium on Spacecraft Flight Dynamics*, Darmstadt, ESA SP-326, 1991.
- [7] Caporali, A., G. Bianco, A. Cenci, G. Dallaporta, M. Fermi, R. Maseroli and M. Pierozzi. Combined Regional Geoid Determination for the ERS-1 Radar Altimeter Calibration (paper in preparation).
- [8] Cavaleri, L. and S. Curiotto. A fast response shallow water tide gauge, *Il Nuovo Cimento*, Serie 1, **2C**, pp. 273-287, 1979.
- [9] Brown, G. S., The Impulse Response of a Rough Surface and its Applications. *IEEE Trans Ant. Prop.*, **AP-25**, 1, 1977.

VALIDATION OF ERS-1 IN THE ICELAND-FAEROES REGION OF THE NORTH ATLANTIC

P.D. Cotton¹, M.A. Srokosz², T.H. Guymer¹, R.T. Tokmakian¹

¹James Rennell Centre for Ocean Circulation, Gamma House, Chilworth Research Centre, Southampton SO1 7NS, UK;

²RSADU, James Rennell Centre, Gamma House, Chilworth Research Centre, Southampton SO1 7NS, UK;

ABSTRACT

During September 1991 scientists from RSADU (the Remote Sensing Applications Developments Unit), JRC (The James Rennell Centre for Ocean Circulation) and IOSDL (The Institute of Oceanographic Sciences, Deacon Laboratory) carried out a research cruise on the RRS Charles Darwin, in the Iceland-Faeroes region of the North Atlantic. This campaign was dedicated to validation of ERS-1 data, particularly scatterometer and altimeter winds, altimeter waveheight, altimeter ocean topography and sea surface temperature (SST) and atmospheric water vapour from the ATSR. Most of the measurements taken on the cruise were made in a triangle whose vertex coincided with an altimeter cross-over point. The eastern and western sides of the triangle were coincident with the sub-satellite track of ERS-1. Surface moorings were deployed at the southern corner of the triangle (directional Waverider, current meter buoy and sonic anemometer buoy), and at the north western corner (meteorological toroid buoy). Hydrographic, wave and surface meteorological measurements were made from the ship along the sides and in the interior of the triangle. Two radiosondes were launched per day, some of which were timed to coincide with ERS-1 overpasses, the aim being to provide comparisons of atmospheric water vapour content with the ATSR. Initial results of intercomparisons between these data and ERS-1 data are discussed.

1. INTRODUCTION

On September 6th 1991 the NERC (the Natural Environment Research Council) ship RRS Charles Darwin sailed from Troon in Scotland to make *in situ* measurements of the ocean that could be used to calibrate and validate the oceanic observations being made by the sensors on ERS-1. The Darwin returned to Barry in Wales on September 28th 1991.

The main objective of the cruise was the provision of an independent, high quality data set to allow the validation of geophysical oceanographic measurements made by the sensors on ERS-1, including altimeter significant wave height, wind speed, and sea surface topography measurements, scatterometer wind speed and direction measurements, and sea surface temperature (SST) measurements made by the Along Track Scanning Radiometer (ATSR). Other objectives, the results of which will not be discussed within this paper, were the validation of measurements of the integrated water vapour content of the atmospheric column, made by the microwave sensor on the ATSR instrument, the investigation of the relationship between wind stress at the sea surface and radar

backscatter as measured by the scatterometer (including the effect of wave conditions on this relationship), and *in situ* observations of the Iceland-Faeroes oceanographic front.

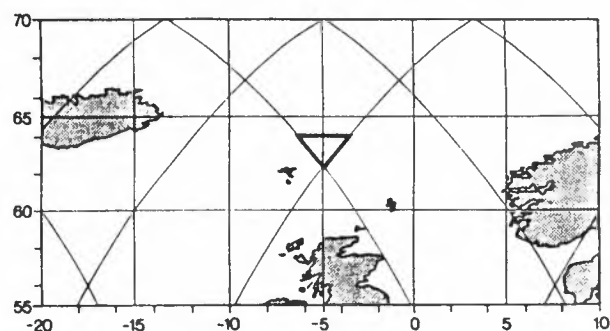


Figure 1. ERS-1 ground tracks and the Charles Darwin survey triangle in the North Atlantic (September 1991).

Most of the measurements taken on the cruise were made round a triangle to the east and north of the Faeroes, the eastern and western sides of which were coincident with the ground track of ERS-1 (figure 1). Three (directional Waverider, VAESAT-sub-surface current meter, and sonic anemometer) were deployed at the southern corner of the triangle (62°18.6'N, 4°55.8'W), coincident with an altimeter cross-over point, and a meteorological toroid buoy was deployed at the north western corner of the cruise triangle (63°57.6'N, 6°18.6'W). From the ship, CTD (conductivity, temperature and depth), XBT (expendable bathythermograph), ADCP (acoustic doppler current profiler), PES (precision echo sounder), thermosalinograph, SBWR (shipborne wave recorder) and MultiMet measurements were made along the sides and in the interior of the triangle.

A range of sea and weather conditions was encountered during the cruise, from light winds and low waves through to storm force 10 winds and 5 metre waves, leading to good calibration and validation data for comparison with ERS-1 wind and wave measurements. One day was lost sheltering amongst the Faeroes during a force 10 storm, and wind (force 9) and wave conditions on another day prevented two CTD stations on the second survey being made.

On arrival at the study area it was planned to deploy the various moorings, to follow this with a CTD / XBT / ADCP survey round the triangle coincident with an ERS-1 overpass, and then to sit on station making meteorological measurements and also carry out a brief SST survey. After

this a repeat of the CTD / XBT / ADCP survey round the triangle was to be carried out (again coincident with an ERS-1 overpass) and finally the moorings recovered before heading for home. This strategy was carried out fairly successfully. To some degree the need to have the Darwin in the right place at the time of the ERS-1 overpasses constrained the way and order in which measurements were made.

Two problems were encountered with the moorings that were deployed. The directional Waverider buoy was trawled by fishermen a few days after deployment. Fortunately the SBWR on Darwin was available to make wave measurements for comparison with ERS-1. The second problem was the overturning of the sonic anemometer buoy shortly after deployment. This was the first time the buoy had been used, so the deployment was more by nature of a trial. The buoy was recovered successfully and the data it had acquired, prior to overturning, were of good quality.

The data collected on the cruise are presently being analysed at both the Rennell Centre and IOSDL and will eventually be compared with the off-line ERS-1 oceanographic data products. At the time of writing only fast delivery (FD) data products were available, and the algorithms that were used to produce geophysical data were only provisional. This means that any comparisons made with the *in situ* data can only be regarded as provisional until re-processed FD or off-line data are made available by ESA. Then a full intercomparison of ERS-1 data and the *in situ* data from the cruise should be possible.

2. ALTIMETRIC SIGNIFICANT WAVEHEIGHT

The aim on cruise RRS Charles Darwin 62A was to obtain significant wave height (H_s) data from a directional Waverider buoy moored at the cross over point of the ascending and descending ERS-1 ground tracks to the east of the Faeroes (see Figure 1), together with some additional comparisons from the shipborne wave recorder (SBWR) on the Darwin, for comparison with the ERS-1 altimetric measurements of H_s . Unfortunately, the Waverider was trawled by fishing boats working in the vicinity after two ERS-1 overpasses, and only data from the SBWR were subsequently available for comparison with ERS-1 altimetric H_s . However, the Waverider drifted towards Norway and was eventually recovered by a Norwegian vessel. Being satellite transmitting, its progress was followed and data were received during this period, leading to a further three measurements useful for comparison with ERS-1 data, obtained when the Waverider drifted onto the satellite ground track during an ERS-1 overpass. Together with the nine SBWR / ERS-1 comparison points, this gave a total of twelve data points for analysis. [In theory there should have been ten SBWR / ERS-1 comparisons as the satellite was in a three day repeat and the ship was on station for just over fifteen days. Being at a cross over point leads to two comparisons every three days, giving a total of ten in fifteen days. Unfortunately, on the night of September 13th ERS-1 was switched off, thus reducing the number of comparisons by one.]

After an initial study of the surface data, it was found that the SBWR data were biased about 0.5m high compared to the Waverider data (based on a comparison of the two types of measurement when the ship was by the Waverider during a twenty four hour period, prior to the Waverider being trawled). Consequently the SBWR data have been adjusted for this bias (the Waverider being believed to be a more reliable instrument than the SBWR).

The ERS-1 data used for comparison were FD data obtained

in near real-time from the UK Met. Office via the Mullard Space Science Laboratory (UK). During the time of the cruise, on September 17th, ESA changed the H_s FD algorithm and after the cruise, on November 11th, they made a further change to the algorithm, these changes have been allowed for in the calculations presented below. SBWR and Waverider buoy H_s values are based on half-hour wave records, while the ERS-1 values are the one second FD value (7km along-track) co-incident with the SBWR measurement.

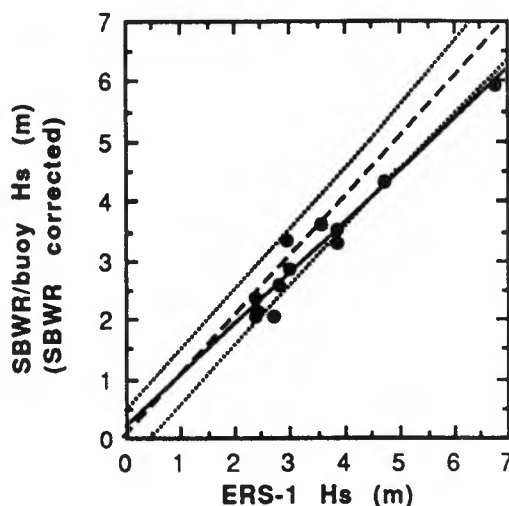


Figure 2. Scatter plot of shipborne wave recorder/buoy measurements versus ERS fast delivery significant wave height. The lines of perfect fit (dashed), least squares fit (solid), and the product specification limits (dotted) are indicated.

This gave the results shown in Figure 2, showing a good agreement between the satellite and ground truth data. Least squares fits of straight lines (with non-zero and zero intercepts) to the data give equations 1-4:

$$H_s(\text{SBWR}) = 0.862H_s(\text{ERS-1}) + 0.191 \quad (1)$$

(0.070) (0.256)

$$H_s(\text{SBWR}) = 0.912H_s(\text{ERS-1}) \quad (2)$$

(0.023)

$$H_s(\text{ERS-1}) = 1.088H_s(\text{SBWR}) + 0.006 \quad (3)$$

(0.088) (0.296)

$$H_s(\text{ERS-1}) = 1.090H_s(\text{SBWR}) \quad (4)$$

(0.027)

the figures in brackets giving the standard error of the estimate of the coefficients above them. These results show that statistically, based on this rather limited dataset, there is no evidence for any difference between the *in situ* (SBWR and Waverider) measurements of H_s and those made by the ERS-1 altimeter (FD data), if an intercept is included in the fit (at the 95% significance level). However, with zero intercept, the difference in the slope of the line from unity is significant (at the 95% level), so the question of agreement between *in situ* and ERS-1 H_s is problematical.

Alternatively these results can be expressed as a mean difference ($H_s(\text{ERS-1}) - H_s(\text{SBWR}) = 0.28 \pm 0.33$, showing a positive bias in favour of ERS-1, and a standard deviation (0.33) which compares favourably with the ESA accuracy specification of 0.5m or 10%. A word of caution is required though, it has been necessary to adjust the ERS-1 H_s values to take account of the FD algorithm changes made by ESA, but until re-processed FD data are available from ESA for comparison with the *in situ* measurements it would be unwise to make definitive statements about the accuracy of the ERS-1 H_s values.

2. ALTIMETRIC WIND SPEED

Similarly to the H_s comparisons, it was hoped to make use of an experimental sonic anemometer buoy, moored at the ERS-1 cross over point, to obtain data co-incident with the ERS-1 altimeter values of U_{10} (wind speed at 10m height above the sea surface). Unfortunately, problems with the buoy precluded this and data were obtained from the propeller-vane anemometers on the main and foremasts of the ship (a total of nine comparisons). In addition, three further comparisons were obtained from the anemometers on a toroid buoy moored at the north west corner of cruise survey area. As the different *in situ* measurements were made at different heights above the sea surface, they were adjusted to 10m values under the assumption of the existence of a neutral stability logarithmic boundary layer. Thus the wind speed at a height z above the sea surface is given by equation 5:

$$U(z) = (u^*/\kappa) \ln (z / z_0) \quad (5)$$

where u^* is the wind friction velocity, κ is von Karman's constant and z_0 is the roughness length. Thus

$$U(10) = U(z) \ln (10 / z_0) / \ln (z / z_0) \quad (6)$$

with z and z_0 in metres (here z_0 was taken to be 0.001m). Equation 6 was then used with the appropriate value of z for each anemometer.

Again, as with the H_s comparisons, near real-time ERS-1 FD values of altimetric U_{10} were used, for which ESA made algorithm changes on September 17th and November 24th. Account has been made for these algorithm changes in the data comparisons presented here. Half-hour averages of ship wind speed and one second ERS-1 FD U_{10} values are used in the analysis (one hour averages of ship wind speed were also used, and the corresponding results were little different from those based on half-hour averages). Figure 3 shows a scatter plot of the resulting data set. Fitting straight lines to the data (with non-zero and zero intercepts) gives equations 7-10:

$$U_{10}(\text{Ship/Buoy}) = 1.032U_{10}(\text{ERS-1}) - 0.482 \quad (7)$$

(0.115) (1.352)

$$U_{10}(\text{Ship/Buoy}) = 0.992U_{10}(\text{ERS-1}) \quad (8)$$

(0.030)

$$U_{10}(\text{ERS-1}) = 0.861U_{10}(\text{Ship/Buoy}) + 1.670 \quad (9)$$

(0.096) (1.125)

$$U_{10}(\text{ERS-1}) = 0.99U_{10}(\text{Ship/Buoy}) \quad (10)$$

(0.030)

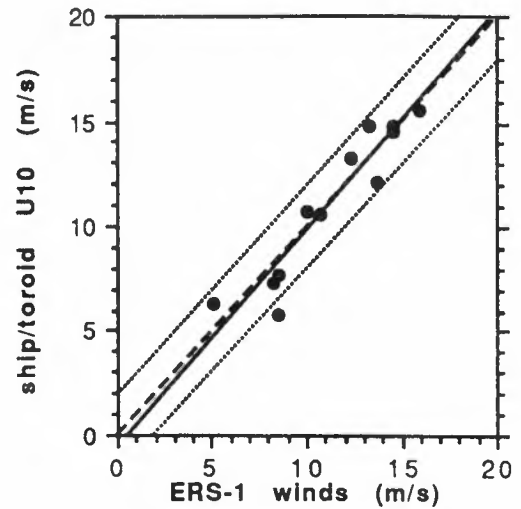


Figure 3. Scatter plot of ship/buoy wind speed (corrected to U_{10}) versus ERS fast delivery wind speed. The lines of perfect fit (dashed), least squares fit (solid), and the product specification limits (dotted) are indicated.

These results show that statistically, based on this rather limited dataset, there is no evidence for any difference between the *in situ* (ship and toroid) measurements of U_{10} and those made by the ERS-1 altimeter (FD data). As before, these results can be expressed as a mean difference ($U_{10}(\text{ERS-1}) - U_{10}(\text{Ship/Buoy}) = 0.12 \pm 1.20$, again showing a slight positive bias in favour of ERS-1, and a standard deviation (1.20) which compares favourably with the ESA accuracy specification of 2 ms^{-1} or 10%. The same proviso as for the H_s results must apply to these conclusions.

4. SEA SURFACE TOPOGRAPHY

4.1 Hydrography

For comparison with the altimetric sea surface topography from ERS-1, two hydrographic surveys, comprising CTD, XBT and ADCP measurements, were conducted around the triangle described in figure 1. On the first survey CTD stations were approximately 40 kilometres apart, with XBT drops every 10 kilometres (three between each CTD station and two along the top of the triangle). The spatial sampling is close to the 7 kilometres (one second) along track sampling of the altimeter. The second survey had similar CTD sampling, but the number of XBT drops reduced to one between CTD stations. The CTD measurements were made to the full depth of the ocean and the XBT drops only sampled the top 700 to 1300 metres of the water column (depending on the type of XBT used).

The CTD and XBT data from the two surveys have been combined to show the density structure of the sections of the survey. The density structure of a section is used to calculate the dynamic height of the sea surface, which can be compared with the altimetric sea surface topography. Figure 4 shows the density section for the western side of the triangle from the first survey. An upturning of the isopycnals, indicating the Iceland-Faroes front, can be seen at about 63.2°N and also at about 64°N . If the feature moves, the resulting change in surface height (the sea surface anomaly) should be visible in the altimeter data.

From the two surveys, the expected height change of the feature is on the order of 20 cm over a distance of 10 kilometres.

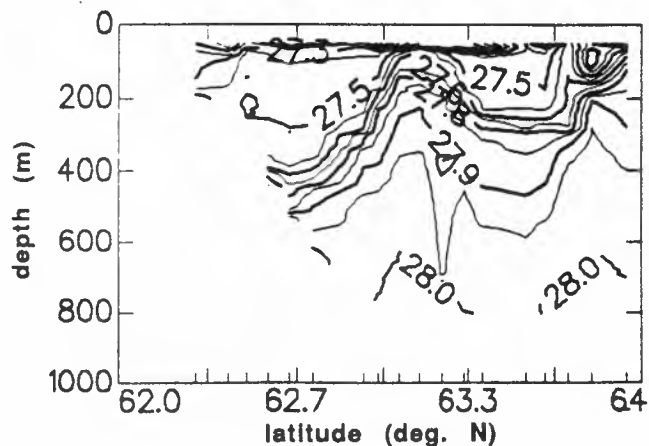


Figure 4. Results of the first hydrographic survey of the western side of the survey triangle (figure 1), from combined CTD and XBT data. Contours of constant density (as σ_{θ}) are plotted against depth and latitude.

4.2 ERS-1 sea surface topography

The ERS-1 FD altimetric height data for the period of the RRS Charles Darwin cruise in September 1991 has been used for the analysis described below. There are five repeat passes over the western side of the survey triangle and six repeat passes over the eastern side (one less on the western side due to ERS-1 being switched off on the night of September 13th). The FD height data contains no orbit information and no corrections (tides, tropospheric, ionospheric, inverse barometer, and so on).

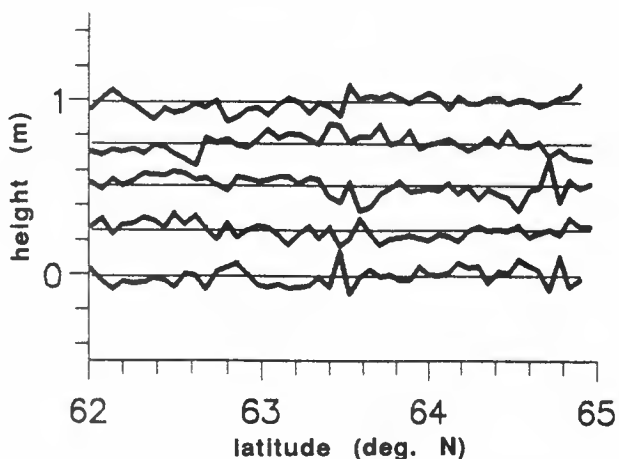


Figure 5. Height residuals from 5 ERS-1 overpasses on the western leg of the cruise triangle (figure 1). The dates of the passes are, from top to bottom, the 28th, 25th, 22nd, 19th and 16th of September (1991) respectively. The tracks are offset for readability.

A preliminary assessment of the data consisted of correcting the altimeter height data as follows. An orbit from Delft University (Wakker, pers. comm.) and tidal signal (Cartwright-Ray model, based on Geosat data) were removed from the altimeter height values. No other corrections were applied to the height data. The standard colinear repeat track method was then applied to remove the mean geoid and sea surface signal. A tilt plus bias orbit correction was used to remove the final orbit error from the height data. The height residuals, from the western track,

are plotted in Figure 5. The height residuals for each pass are offset for clarity. The standard deviation of the residual height signal for both sets of passes was calculated giving a value of 35 centimeters for the western track, and 43 centimeters for the eastern track.

The western track (Figure 5) shows signals that might be the signatures of frontal features at 63.5°N and at 64.6°N, on the order of 10-20 centimetres, consistent with the height anomaly deduced from the hydrographic data above.

4.3 Geosat data

Given the limitations of the ERS-1 height data available for analysis, particularly the lack of corrections, it seemed appropriate to look at Geosat altimeter data in the same area to try to improve our understanding and interpretation of the ERS-1 data. By using Geosat data, it is possible to test the effect on the height residuals of only using a small number of repeat passes to calculate the mean topography. It should be borne in mind that ERS-1 was in a 3 day repeat orbit, while Geosat was in a 17 day repeat orbit. This difference on its own may affect the detectability of a "frontal" signal in the height residuals due to the time scales on which the oceanographic features change (essentially the height residuals give information on changes in the sea surface topography, which may not be large in any 3 day period, but might be significant over 17 days). The two Geosat passes (one ascending, one descending) used in the analysis had a crossover point somewhat to the north of the ERS-1 crossover point (due to the different orbit patterns of the two satellites the ground tracks differ).

The same colinear repeat track analysis was applied to the Geosat data as was applied to the ERS-1 data. The orbit for Geosat is the GEM-T2 model and the tidal correction was the Cartwright-Ray model. The solid earth tide and dry tropospheric corrections were from the Geosat GDR. No other corrections were made. The repeat tracks for the August to November period in the first year of Geosat data were analysed. The mean sea surface was computed only from these repeat passes. Examination of the resulting residuals showed results similar to those for the two ERS-1 tracks. One set of repeat passes showed some indication of a "frontal" signal, the other did not. The standard deviations of the height residuals for the two sets of passes were 28 and 35 centimetres, not too dissimilar to the values obtained from the ERS-1 data.

To test the effect a better estimate of the mean would have on the detectability of "frontal" signals in the height residuals, the analysis was repeated for the track with the frontal signal, but using the whole of the first year of Geosat data to compute the mean. In this case, the "frontal" signals were much stronger (of about 25 centimetres amplitude) and therefore more easily seen in the residual data. Clearly, using a short period mean removes some of the frontal signal. The Geosat analysis over the August to November period shows this problem, so it is to be expected that our analysis of the ERS-1 data (for part of September) would be severely affected in this way.

5. ATSR SEA SURFACE TEMPERATURES

Sea surface temperature data were obtained from a thermosalinograph (TSG) and a trailed thermistor. Problems were encountered with the latter leading to large drifts with time. Therefore, for this paper, only the TSG data have been considered. The TSG consists of a conductivity cell and temperature sensor measuring water taken from the non-toxic ship supply with an intake at 5m below the water line. These temperatures were compared with those obtained from

the tops of CTD casts every few tens of kilometres and were found to agree to a few hundredths of a degree Kelvin, encouraging confidence in the TSG values. The temperatures were sampled every 30s (equivalent to ~ 150m spatial resolution). Bucket SSTs were obtained every 3 hr as a further check on the data. The ATSR data used are the 0.5° product provided by the Rutherford Appleton Laboratory.

Ideally, for validation, a number of spot comparisons at the time of satellite overpass would have been obtained between the TSG value and the ATSR data for the pixel containing the ship. However, conditions were generally too cloudy to enable SST retrievals from an Infra-Red (IR) spaceborne sensor and only one or two points would have resulted. Instead, the following approach was adopted. Occasions on which a relatively cloud-free ATSR image was obtained were identified and one of these (1145 GMT on 22 September), when the ship was part-way through conducting a CTD triangle survey, was selected for further analysis. From the $0.5^\circ \times 0.5^\circ$ ATSR product SSTs were extracted for boxes intersected by the ship's track. The TSG data were then averaged over 50 km segments of ship track and compared with the ATSR data in the relevant 0.5° box. On some occasions the ship went through the same box on successive occasions giving more than one 50 km average; when this occurred a simple mean was taken. When the location of the TSG mean was close to the boundary of two 0.5° boxes a mean of the ATSR values was used. As a result of this process 10 comparisons were obtained over the period 19-23 September.

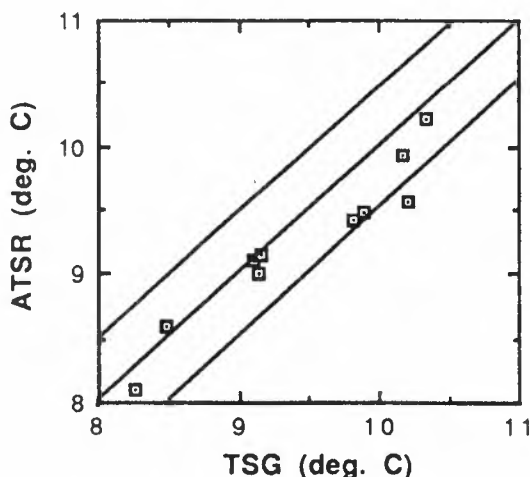


Figure 6. Ship / ATSR sea surface temperature comparison, the solid lines mark a perfect fit and the ESA product specifications.

Figure 6 is a scatter plot comparing the two temperatures over the range 8 - 10.5 °C; this range occurred as a result of the CTD triangle being located in a portion of the Iceland-Faeroes Front. A tendency for the ATSR to underestimate compared with the TSG is seen with a mean difference (ATSR - TSG) of -0.20 ± 0.23 °K. The bias is explainable in terms of the surface skin effect whereby the temperature of the top micron or so, which is what is measured by an IR radiometer, is lower than the bulk temperature measured by all in-water instruments. The effect is produced by a combination of evaporative and radiative cooling and can be as large as 0.6 °K under certain circumstances. It is also possible for surface temperatures to be higher than those at 4 or 5m depth. In sunny, calm conditions absorption of solar radiation can produce a diurnal warming of the surface

layer of 2 °K or so. Such an effect is not observed on this occasion, consistent with the wind being strong throughout the period (up to 18 m/s) and extensive cloud being present. The size of the standard deviation, 0.23 K, is also very encouraging when compared with the accuracy specification of 0.5 K for 0.5° squares and a scientific goal of 0.3 K.

6. FURTHER WORK

Given the uncertainty associated with applying corrections to the altimeter wind speed and wave height FD data to take into account ESA's FD algorithm changes, final comparisons and conclusions will only become possible once ESA makes available the re-processed FD data (based on their "final" algorithms). Furthermore, similar comparisons need to be carried out with the H_5 and U_{10} data that will appear in the off-line altimeter product from the French PAF (when available), in order to test the quality of the off-line estimates of significant wave height and wind speed.

Similarly, any final comparison of topography data must await the delivery of the ERS-1 altimeter off-line product for the whole of the commissioning period (August to December 1991). This will provide both the corrections necessary to improve the quality of the height data and sufficient repeat passes to make an improved estimate of the mean. Once available, a full comparison will be possible, giving a better indication of the utility of the ERS-1 height data for ocean circulation studies.

Future work with the ATSR data will focus on comparisons with 1 km resolution data and identifying other ATSR passes which can be used. Other cruises have since carried an IR radiometer and comparisons based on *in situ* skin temperatures will be conducted.

Similar sets of measurements to those described in this paper have been made in the Tyrrhenian sea (October-November 1991) as part of the TEMPO (Tyrrhenian Eddy Multi Platform Observations) programme, and analysis of these data will provide further data for validation purposes. The TEMPO campaign includes plans for further cruises in 1992.

A number of Southern ocean cruises are planned for the Austral summer of 1992-93. The planning of these cruises includes provision for the acquisition of ground truth data to enable further altimeter, scatterometer, and SST validations during expected high sea states.

7. CONCLUSIONS

The results of the initial and limited comparison of altimeter wave height and wind speed data with ground truth measurements suggest that the ERS-1 FD H_5 and U_{10} values agree with the *in situ* observations (at least statistically no significant difference is discernible). The FD algorithm changes implemented by ESA during September and November 1991 led to improvements in the agreement, which is reassuring.

From the topographical analysis we can conclude that the *in situ* data suggest the existence of frontal structures which should be visible in the residual height data from the ERS-1 altimeter. There is some indication that such frontal features in the Iceland-Faeroes region can be seen in the ERS-1 data. We have also seen that, despite severe limitations on the ERS-1 sea surface topography data used in the analysis (in particular, the lack of corrections), the standard deviations

of the height residuals for the two ERS-1 tracks compare favourably with the Geosat values. There is, however, some indication (visually) that the ERS-1 data from September are "noisier" than the Geosat data, which may reflect the lack of adequate corrections to the data.

The results of the preliminary SST comparison, using a single ATSR pass, has shown that the ATSR meets its accuracy specifications even when compared with bulk temperatures rather than a radiometric skin temperature. It is surprising that such good results should have been obtained when in situ data obtained over a 4-day time window have been compared with data from one satellite overpass. This indicates that SSTs varied little with time, at least when averaged over the 50 km scale. The results also suggest that the atmospheric correction scheme for the ATSR was

working well.

ACKNOWLEDGEMENTS

The authors are grateful to T. Forrester, E. Kent, and M. Yelland (JRC) for carrying out much of the processing on the data presented here, and to P. Challenor (JRC) for his help in getting the ERS-1 FD data out to the ship during the cruise.

Funding for much of the analysis has been provided by the UK Earth Observation Data Centre project. The Waverider buoy was funded by the CEC under its MAST programme.

ERS-1 RADAR ALTIMETER VALIDATION WITH THE WAM MODEL

B Hansen¹ and H Günther^{1,2}

¹ European Centre for Medium-Range Weather Forecasts (ECMWF), Reading

² GKSS Forschungszentrum Geesthacht, Geesthacht

Abstract

The third generation WAM wave model in connection with a wave data assimilation system was used to study the radar altimeter during the calibration/validation phase of ERS-1. The data quality control system in particular was applied to check the wave and wind measurements and provide technical support to ESA in real time. Extensive comparisons of model computations with ground truth and satellite were done.

1. INTRODUCTION

A special project was carried out at ECMWF in cooperation with 8 other European institutes to implement the third generation WAM wave model into the operational environment and to prepare the system for the use of satellite data. The overall objective of this project was to set up a system which can be operationally used for global wave analysis and forecasts.

This includes an on-line monitoring of the model performance by comparison with buoy measurements and satellite data and a wave data assimilation system in combination with an extensive data quality control package.

The necessary calibration/validation of a satellite sensor requires large amounts of ground truth data which should cover the full range of possible events. Especially the number of reliable wave measurements is very limited and because of financial restrictions, the set-up of special experiments is only possible at a few sites. In contrast to that model data are cheap and provide global data sets for comparison. Therefore the combination of both seems to be an optimal cal/val data set.

Before model data can be used for this purpose, the performance of the model has to be proved. Therefore

chapter 2 presents the verification of the WAM-Model forced by analyzed winds of the ECMWF atmospheric model with buoy measurements. Chapter 3 describes the altimeter processing, particularly the internal quality control method. Altimeter wave height and wind speeds are compared with WAM-model and ECMWF T213 results, respectively, in chapter 4.

2. THE WAM WAVE MODEL

The wave model used in this study is the cycle 4 of the third generation wave model WAM-Model (WAMDI 1989, Günther *et al.*, 1991). The model will be operationally applied at ECMWF 1 July 1992. Since 1987 the WAM-Model runs daily for 24 h with analyzed ECMWF surface winds and for 24 h with forecasted surface winds. The wave model works on a regular 3° Gaussian Grid covering the globe from 60°S to 69°N. Figure 1 shows a typical wave height and direction map. The model has been verified in the last years against buoy and GEOSAT measurements (Zambresky, 1989; Romeiser, 1982). Since September 1992 the comparison with buoy data is routinely carried out using wave data available in quasi real time via the global telecommunication network (GTS).

Figure 2 shows wave height comparisons at three different sites in December 1991. The sites are representative for the Gulf of Alaska (2a) with mainly wind waves, the swell dominated area around Hawaii (2b), and the US East coast (2c) where both sea and swell are present. The excellent agreement between model and measurements is also demonstrated in Table 1 which shows the comparison statistics for the period September to December 1991. The negative bias of about 10 cm indicates a very small underestimation of the model. Scatter indices around 20% are regarded as very good model performance as well. The 31% at the US East coast results from buoys very close to the coast line which is poorly resolved in a 3° model.

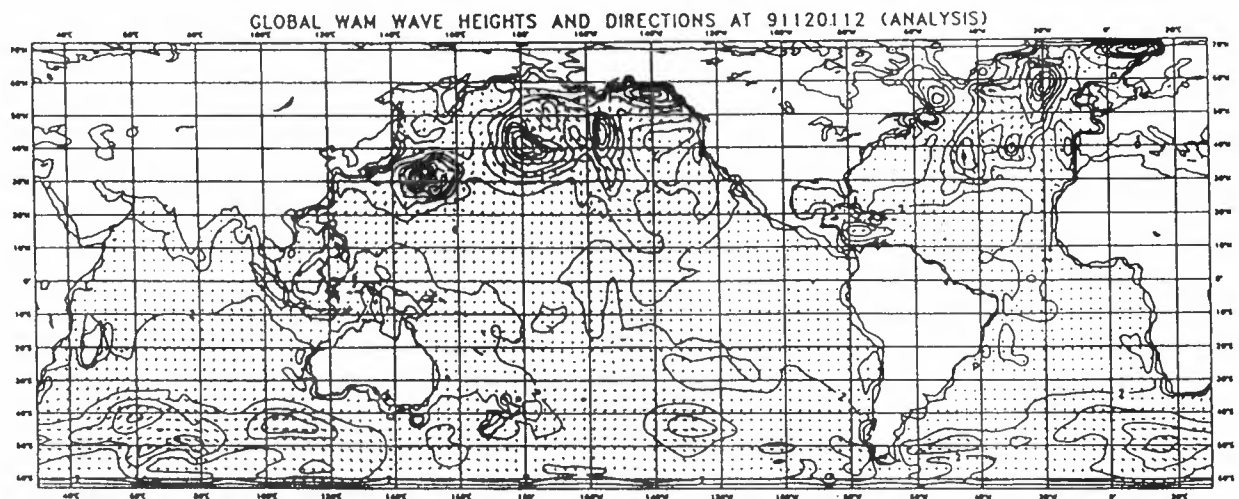


Fig. 1 Map of significant wave height and mean wave direction (1 December 1991)

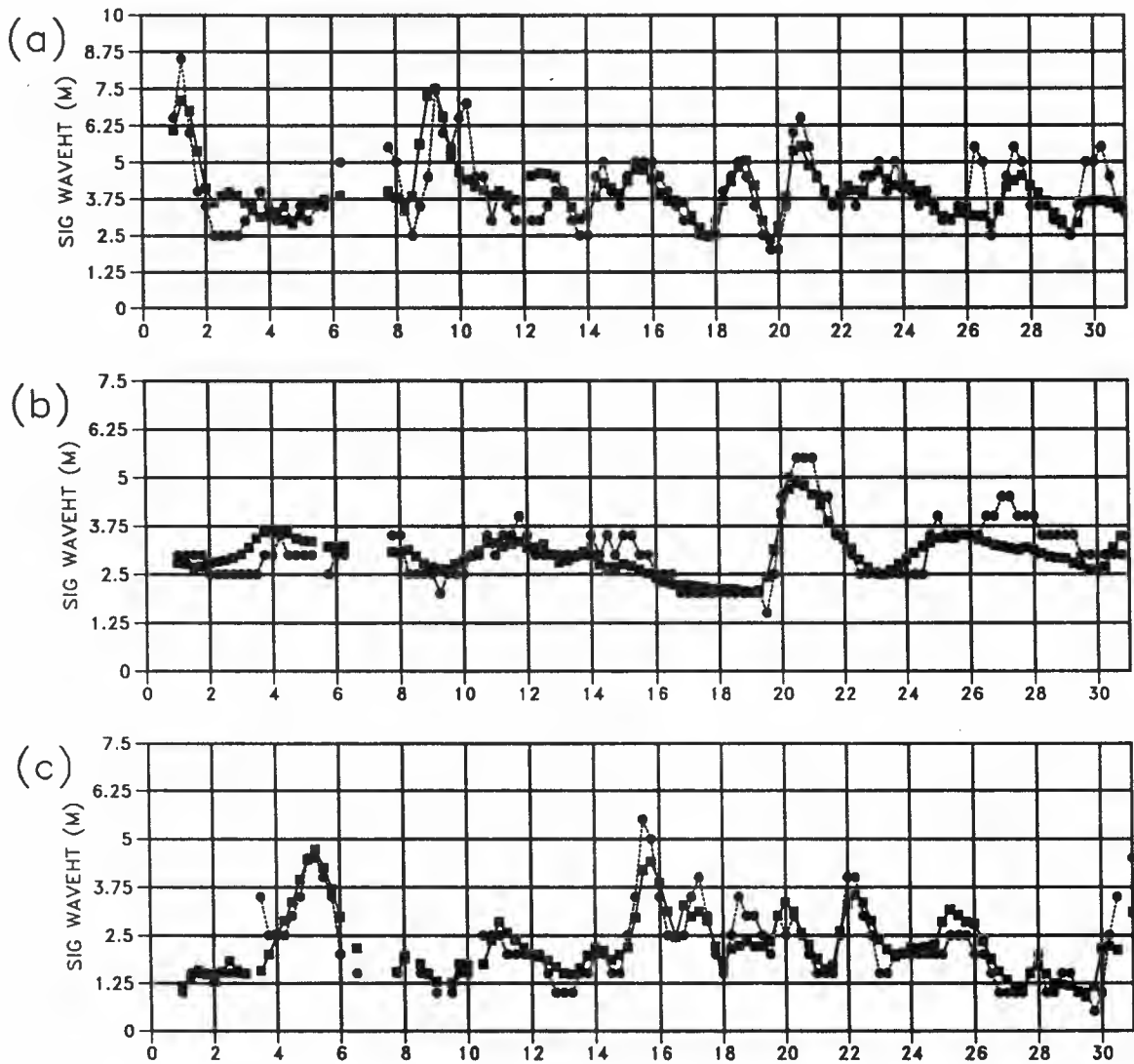


Fig. 2 Timeseries of measured (circles) and computed (squares) significant wave heights in December 1991
 (a) Buoy 46001 (56.3 N, 148.3 W) (Gulf of Alaska)
 (b) Buoy 51003 (19.3 N, 160.8 W) (Hawaii)
 (c) Buoy 44008 (40.5 N, 69.4 W) (US East Coast)

	Alaska	Hawaii	US East C
Number	1932	1478	3150
Mean			
Buoy (m)	3,34	2,39	1,64
Bias (m)	-0.13	-0.05	-0.08
STD (m)	0.71	0.41	0.51
Scatter (%)	21	17	31

Table 1: Comparison statistic with buoy wave height measurements from September to December '91. Bias is model - buoy.

3. ALTIMETER DATA

The ERS-1 fast delivery products URA have been received at ECMWF via the GTS network since August 1991. The data coded in FM94-BUFR format are passed on by the operational data acquisition system to the assimilation system of the WAM-Model. The wave measurements have been processed by the quality control (QC) part of the system but have not influenced the model analysis.

The purpose of the QC is to check the consistency of the data and to identify unreliable observations. The wind speed measurements of the radar altimeter are not checked and passed the QC whenever the wave height has been accepted. The QC, similar to the one used in *Bauer et al., 1992* for SEASAT providing a QC-flag for each observation, works in four steps:

- 1) identify all observations which:
 - are not related to a sea point of the wave model
 - are below 0.4 m significant wave height (H_s)
 - are above 20.1 m H_s (saturation level)
- 2) identify spikes within a sequence of continuous observations. A sequence is defined by 20-30 consecutive observations where the time difference between each observation has to be less than 3 seconds. Observations are classified as spiky if:

$$|H_{s_i} - \overline{H_s}| \geq 2 * STD \text{ and } |H_{s_i} - \overline{H_s}| > 1.$$

$$H_{s_i} \text{ is also classified as spiky if } |H_{s_2} - H_{s_1}| > 2 \text{ and } H_{s_n} \text{ is classified as spiky if } |H_{s_{n-1}} - H_{s_n}| > 2$$
- 3) identify short sequences. A short sequence is defined as a sequence where the number of observations is less than 20
- 4) identify sequences where the variance is too large, i.e. where $STD \geq 0.1 * \overline{H_s}$ and $STD \geq 0.5$

Each observation which remains unidentified by one of these criteria is regarded as reliable.

In addition the QC provides a reduced data set for the comparison of radar altimeter versus wave model. Therefore the mean values for the time, the location, H_s and the wind speed of each accepted sequence are computed and passed through for comparison purposes. The QC statistics as shown in Table 2 have been forwarded to ESA each week during the cal/val phase. Every 6 hours about 14 400 observations are received of which 53% were related to sea points of the wave

Day	Time	Total	Land ¹	Sea	Range ²	Spikes ³	Short ⁴	Variance ⁵	Sea data accepted %	
1	00	13552	4245	9307	650	456	310	60	7821	84.0
1	06	8343	3758	4585	230	205	118	30	4002	87.3
1	12	18865	7288	11577	858	555	433	0	9731	84.1
1	18	18357	8439	9918	330	474	413	30	8671	87.4
2	00	20049	7697	12352	847	612	309	30	10554	85.4
.
.
.
30	00	13398	5082	8316	334	428	230	30	7294	87.7
30	06	12983	6420	6563	332	302	181	30	5718	87.1
30	12	21406	9797	11609	691	535	341	90	9952	85.7
70	18	21833	11147	10686	316	489	360	60	9461	88.5
Mean		14410	6753	7658	435	316	237	24	6586	86

- ¹ Observations not related to a model sea point
- ² Observations related to a sea point but rejected by (1)
- ³ Observations related to a sea point but rejected by (2)
- ⁴ Observations in sequences with less than 20 observations
- ⁵ Observations rejected by (4)

Table 2: QC statistics for November 1991. RA measurements are grouped in 6 hour periods.

model. From this data 86% passed the QC, 6% were already rejected in step 1 of the QC, 5% were identified as spikes, 3% were observations in short sequences and less than 0.5% were rejected by step 4 of the QC.

As mentioned before most of the rejected data could be identified as measurements over ice or land. But a very few data are rejected by the variance test (4), because of strong wave height gradients along the sub satellite track. A further tuning of these variance criteria may be necessary, but will not affect the already excellent data rate. As the criterion to identify spikes is based on the technical characteristics of the radar altimeter this has to be tuned as well to have a criterion based on natural variability.

4. VALIDATION

Whereas the QC only checks the internal data consistency, the altimeter performance is monitored by comparison with global wave model fields. The mean H_s and wind speed values as computed by the QC are collocated with, in space (3°) and time (6 h), interpolated WAM-Model wave heights and with analyzed T213 surface wind speeds, which have forced the wave model. The collocation files are analyzed in two different ways. First six hourly colour plots are visually inspected and second weekly statistics are computed.

During the cal/val the results of these comparisons were weekly reported to ESA and have been very effective in identifying errors and problems in the altimeter software and model function.

In August 1991 the global mean altimeter wave height was about 1 m higher than computed by the model and the standard deviation was about 0.5 m. The investigation of the detected bias led to the discovery of a programming error in the altimeter processing software at the ground stations. After correction the statistics changed to a reduced bias (about 0.25 m) but a very large standard deviation (> 1.0 m) in late September. The reason was the use of different software versions at different ground stations. In October and November 1991 the wave height bias changed to about 0.3 m and the standard deviation returned to 0.5 m. A detailed analysis showed that the altimeter wave heights were nearly 20% lower than the model independent on the wave height bands. This 20% coincides with the correction which was applied to the theoretical altimeter model function because of results from prelaunch calibrations.

Since December 1991 the final calibrated and validated altimeter measurements have been received. The global comparison with the WAM-Model wave heights is shown in Figure 3 together with the corresponding statistics. The global bias -0.05 m with a standard deviation of 0.48 m is very small. The slope of the symmetric regression line indicates that high sea states are underestimated by the radar altimeter. The same behaviour as already observed in the GEOSAT altimeter data (*Guillaume and Mognard, 1992*) is confirmed by two facts. First the WAM-Model buoy comparison always shows an under estimation by the model, whereas the altimeter heights are always lower than the model values. Second the biggest differences are in the Northern Hemisphere (north of 22° N), where most of the high sea states occur (cf Table 3). In the tropics, where most of the wave heights are between 2 and 3 m, differences are small. In the Southern Hemisphere (south of 22° S) the model is

probably too low because of the artificial model boundary at 60° S and because of a too low model wind (cf Table 4), which does not allow the full wave height to be developed in the main storm area of this region.

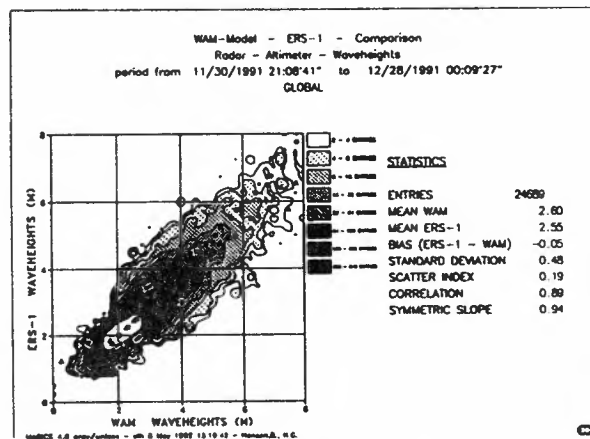


Fig. 3 Global comparison of altimeter and WAM-Model wave height in December 1991.

	North H	Tropics	South H
Number	5613	7812	11264
Mean WAM (m)	3.45	2.12	2.5
Bias (m)	-0.28	-0.05	0.07
STD (m)	0.63	0.33	0.44
Scatter (%)	18	16	18

Table 3 Regional comparison statistic of altimeter and WAM-Model wave heights in December '91. Bias is altimeter - model.

The comparison of the model and altimeter wind speeds was carried out in parallel to the wave height validations. Figure 4 and Table 4 present the final global and regional statistics for December 1991. The global agreement is surprisingly quite well. But the regional trend in the bias may indicate that the model winds are too low in the Southern Hemisphere, where only a few data exist for the atmospheric analysis.

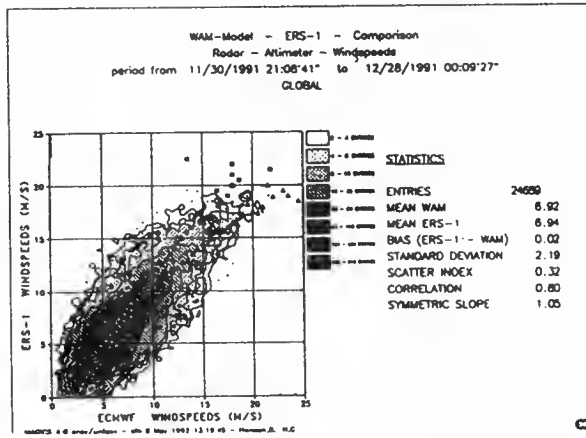


Fig. 4 Global comparison of altimeter and T213 wind speeds which drove the WAM-Model in December 1991.

	North H	Tropics	South H
Number	5613	7812	11264
Mean T213 m/s	8.82	5.66	6.84
Bias (m/s)	-0.11	-0.1	0.17
STD (m/s)	2.33	1.92	2.28
Scatter (%)	26	34	33

Table 4 Regional comparison statistic of altimeter and ECMWF-T213 model wind speeds in December 1991. Bias is altimeter - model.

Figures 5 and 6 summarize the development of the performance of the radar altimeter wind and wave measurements between the beginning in August 1991 and the end of the cal/val phase in December 1991. The dependency of the bias of the wave height measurements on the sea state has been clearly visible since November where the wave height calibration was already finished. From November the mean wave height as computed by the WAM-Model in the Northern Hemisphere was much higher compared to the global mean. Since the same time the altimeter is biased much lower for the Northern Hemisphere than for the full globe.

The replacement of the 3-branch Brown wind model with the Witter and Chalton wind model in early September did not affect the overall statistics. But at the end of November ESA carried out tuning operations using the ECMWF surface wind fields. These are clearly visible and the good agreement of the satellite measurements with the ECMWF winds at the end of the cal/val phase is a result of these tuning operations. Detailed information about the calibration process of the wind and wave measurement is given in Francis, 1992.

SIGNIFICANT WAVE HEIGHT

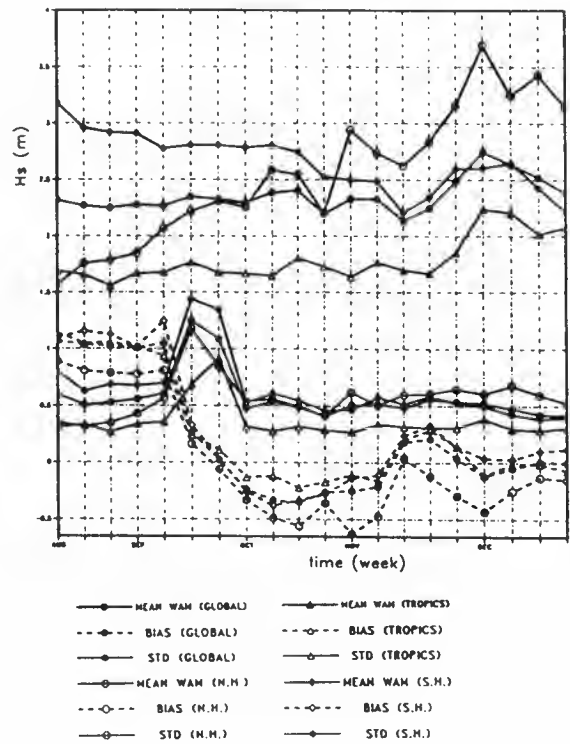


Fig. 5 Development of RA wave height measurements in the cal/val phase of ERS-1. Global and regional validation against the WAM-Model. Bias is RA - model.

WIND SPEED

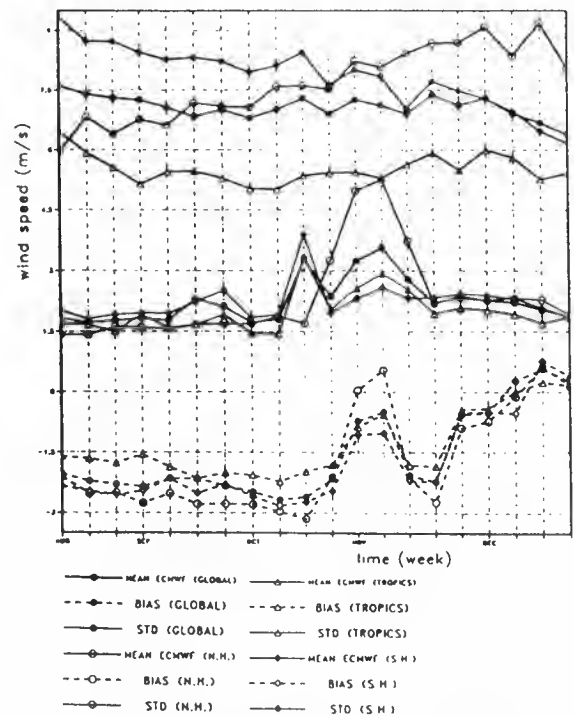
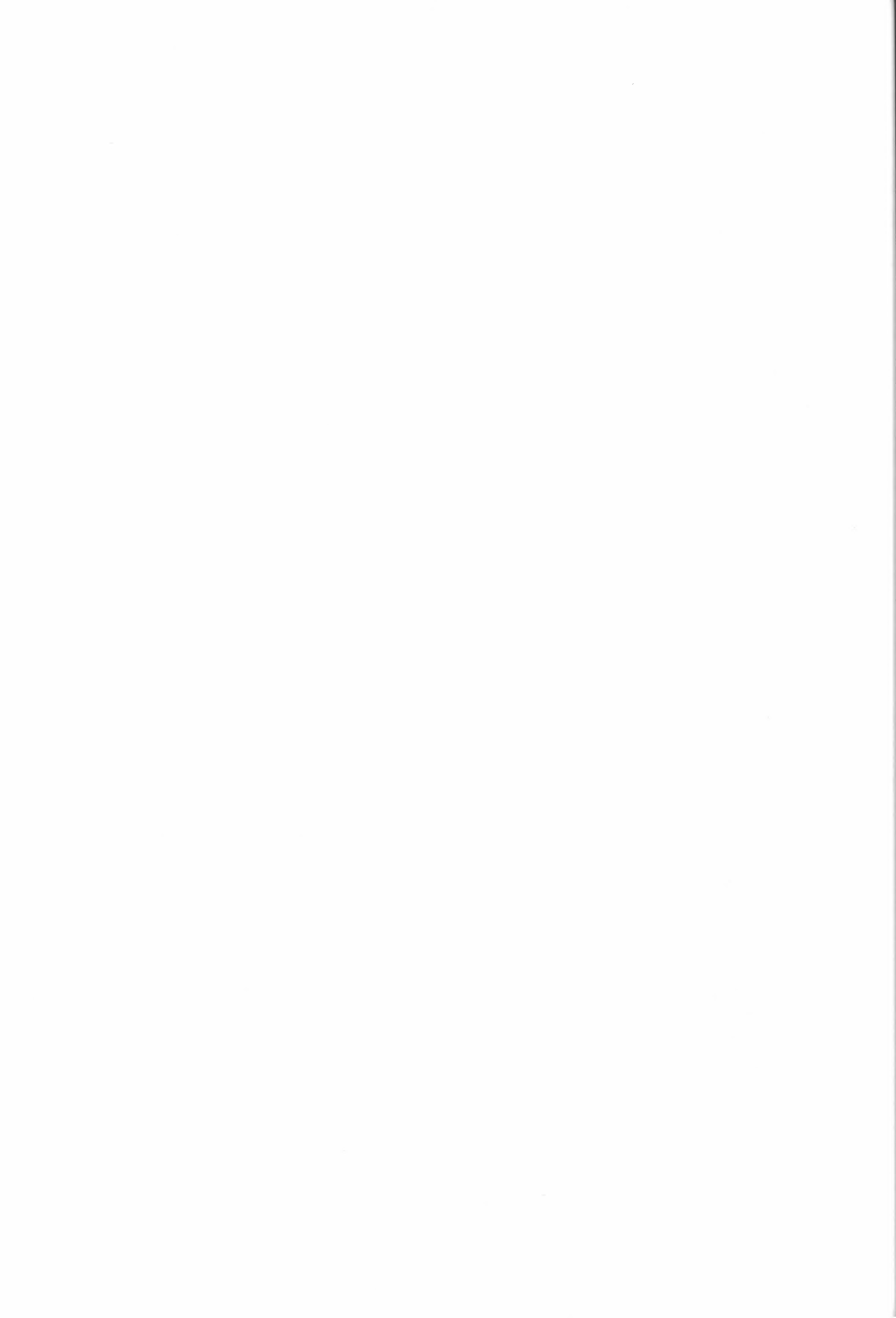


Fig. 6 Development of RA wind speed measurements in the cal/val phase of ERS-1. Global and regional validation against ECMWF T213 Model. Bias is RA - Model.



VALIDATION OF ERS-1 ALTIMETER WAVE AND WIND FAST DELIVERY PRODUCT

P. Queffeuilou

IFREMER, BP 70, 29280 Plouzane, FRANCE

J. M. Lefevre

METEO-FRANCE/SCEM, 42 Av. G. Coriolis, 31057 Toulouse, France

June 5, 1992

Abstract

The ERS-1 radar altimeter data are processed in near real time in the dedicated European Space Agency acquisition stations to generate wave height and wind speed Fast Delivery Products. Validation of these products was achieved in two different manners. The first one consisted of comparisons with wave and wind measurement from the buoy network deployed in the Norwegian Sea during the dedicated validation experiment, RENE-91. The second test was performed using the french wave and weather numerical models output over one month. After the last major modification of the real time processing (november 11th), the altimeter and buoy significant wave height measurements are found to be strongly correlated (mean difference of 0.42 m with a 0.46 m standard deviation), however some underestimation of altimeter is still observed. Altimeter and model data are also in good agreement. For wind speed, good agreement is found with the model (mean difference of 0.16 $m s^{-1}$ and 2.9 $m s^{-1}$ std) but results are not so good when comparing to the near real time buoy data. In a last section some examples are given to illustrate quality and usefulness of altimeter wind and wave for models.

Keywords : wind, wave, ERS-1, altimeter, validation

INTRODUCTION

The ERS-1 radar altimeter data are processed in near real time in the dedicated European Space Agency acquisition stations to generate wave height and wind speed Fast Delivery Products (fdp) [1]. These products are obtained using simplified algorithms and have to be validated. This was one of the goals of the ERS-1 calibration and validation dedicated experiment, RENE-91. During this experiment, a network of ten wind and wave measuring buoys was deployed by the OCEANOR company in the Norwegian Sea, from september 15th,

1991, to the end of february 1992. IFREMER was in charge of the evaluation of the wind and wave buoy data and with the validation of altimeter and scatterometer fast delivery products. A first evaluation of in-situ measurements was achieved, using the ARGOS transmitted buoy data [2] and showed that the significant wave height (swh) measurements were of good quality and that, though the wind data were found homogeneous over the buoy network, their absolute accuracy was still questionable for high wind and sea state conditions. Nevertheless, both wave and wind buoy data were used to validate the altimeter fdp, but to improve the confidence in the results, particularly for the wind product, the altimeter fdp were also compared to wave and wind outputs of VAGATLA and EMERAUDE models of METEO-FRANCE. Results of these validation studies are presented hereunder.

ALTIMETER WAVE HEIGHT VALIDATION

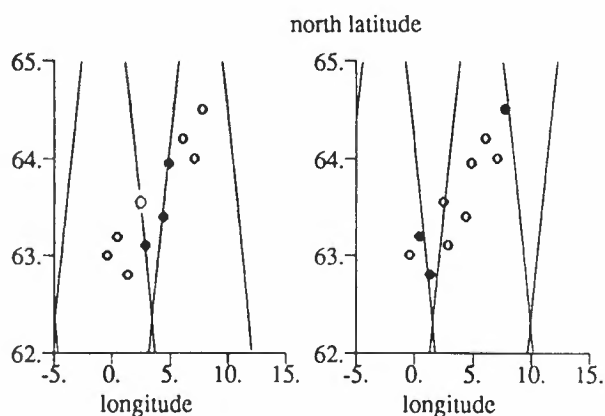


Figure 1: ERS-1 altimeter tracks for the *validation* (left) and *ice* (right) orbit cycles over the RENE-91 buoy network.

Buoy and altimeter collocated data. The wave buoy network was operated from mid-september 1991

to the end of february 1992. During this time period ERS-1 experienced two different 3-day orbit repeat cycles: the so-called *validation* orbit, from launch till december 10th, and the *ice* orbit, after december 25th, change from one orbit to the other one corresponding only to a phase shift, as shown on Figure 1.

For altimeter fdp validation, only the buoys located close to the ground tracks were selected in order to avoid biases due to the spatial variability of the wave field. This constraint combined with the wave buoy data return during the involved time periods [2], results in selectionning a set of six buoys, shown as full circles on Figure 1. A colocation procedure was then applied, collecting the altimeter data within 150 km of the buoys. The buoy swh, estimated from 34 min long wave records, is available every 3 h for the ARGOS buoy data used in this study and the collocated buoy data sets were then selected so that the difference between times of buoy and altimeter measurements be less than 1 h 30 min. An example of such collocated data, over about 50 days, is shown on Figure 2. The buoy (full line) and the fdp altimeter (■) swh are reported on the lower graph. Each individual altimeter fdp is an average over 1 s and for each data the standard deviation (std) of swh within the 1 s time period is also computed: this value, shown on the upper graph, allows to detect passes with high noise level on swh, if any. In the given example this altimeter 1 s standard deviation is less than 1 m. For comparison, the

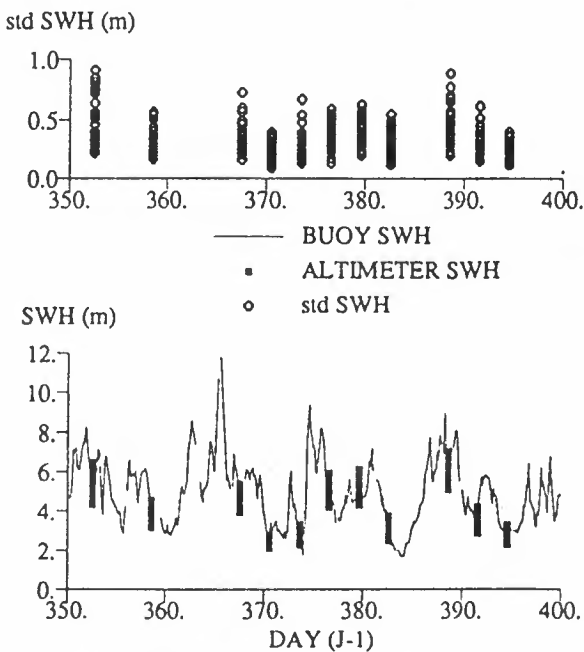


Figure 2: Example of buoy and collocated altimeter swh data together with standard deviation of individual altimeter data.

distance was then restricted to 50 km, each side of the buoy, the fdp altimeter data flagged as non valid were

discarded and each collocated altimeter data set (15 individual data points) was averaged along the track.

Results. For swh analysis, two time periods were considered in order to take into account changes that occurred in the fdp processing algorithm implemented in acquisition stations and particularly the major change, on november 11th, 1991, consisting in a removal of a 20% swh correction [3]. The two time periods analyzed here are respectively from 1991/09/18 to 1991/10/31 and from 1991/11/27 to 1992/02/23.

Scatterplots comparing buoy and altimeter swh for these two periods are shown on Figure 3 and statistics are given in Table 1. The first remark is that

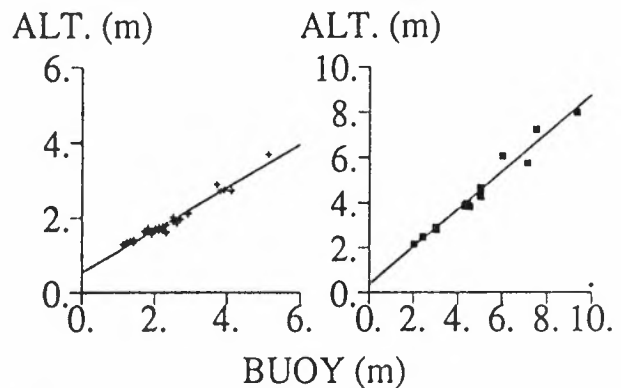


Figure 3: Comparison of buoy and altimeter fdp swh for two time periods : from 1991/09/18 to 1991/10/31 (left) and from 1991/11/27 to 1992/02/23 (right).

time period	n	mean m	std m	cor %	a	b m
before nov.	33	0.48	0.39	97.8	0.57	0.54
after nov.	13	0.42	0.46	98.3	0.84	0.37

Table 1: Mean value and std of swh differences, buoy minus altimeter, for the two time periods, correlation and regression coefficients $Alt = a * Buoy + b$.

the correlations between buoy and altimeter data are very high. Then, obviously, for the first period, the altimeter swh was strongly underestimated for high sea state, the slope coefficient of the linear regression line being only 0.57. The major fdp processing modification, applied in november, improved considerably the swh altimeter data, though a slight underestimation of higher sea states is still observed (slope coefficient of 0.84). For this data set, the mean value of differ-

ences between buoy and altimeter swh is 0.42 m with a standard deviation of 0.46 m.

Wave model comparisons. An independent check of the altimeter swh measurements was performed using output data of the METEO-FRANCE numerical wave model, VAGATLA. Description and validation of this model can be found in [4]. The data set was selected during one month (december 1991) over the North Atlantic Ocean. First the altimeter data were averaged along ground tracks in boxes of size comparable to the model mesh (about 150 km). Then, the data were processed in order to control their quality: bad data as those contaminated by land were eliminated. In this process, the fdp altimeter data flag was not used because it can lead to occult interesting feature of the altimeter signal, therefore only the standard deviation was used as an indicator of the spatial homogeneity of the measurements. Only altimeter data within a six hour time window centered at the time of the model fields (00, 06, 12 and 18 UT) were collected and compared to the corresponding field. About 10^5 altimeter data were processed and 27% were rejected because of the quality control. After averaging, about four thousand values were compared with model data. Resulting scatterplot of mean values within each swh class is shown on Figure 4, together with the standard deviations observed on model and altimeter data within each model swh class, the length of horizontal or vertical segments being proportionnal to twice the std.

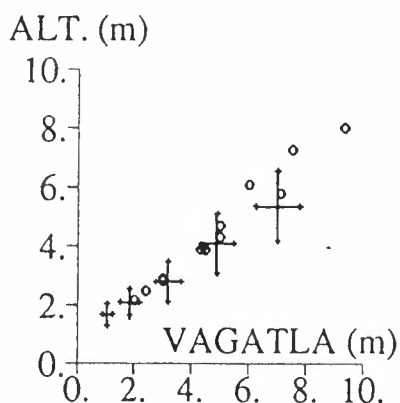


Figure 4: Comparison of VAGATLA model and altimeter swh.

The buoy and altimeter comparison data set of the previous section was also reported, as open circles, on Figure 4, showing similar results for the two comparisons: some underestimation of altimeter swh, for highest values. Note also that for highest values the model swh are less than buoy measurements, this being certainly due to some space and time smoothing effect induced by the model. The mean value of differences between model and altimeter swh is 0.22 m with a standard deviation of 0.91 m. The mean value and the

standard deviation were found to be strongly dependent on swh, as shown in Table 2. For instance the std increases from 0.31 m for the lowest swh class (0.5 m to 1.25m) to 1.15 m for the 6 m to 9 m class.

swh m	n	mean m	std m
0.5-1.25	255	-0.61	0.31
1.25-2.5	1581	-0.26	0.44
2.5-4.0	1028	0.38	0.65
4.0-6.0	741	0.80	0.93
6.0-9.0	263	1.66	1.15
9.0-14.0	13	1.52	2.53

Table 2: Statistics on differences, VAGATLA minus altimeter swh, within each class of model swh.

ALTIMETER WIND SPEED VALIDATION

Same types of analysis as above were achieved for validation of the altimeter wind fast delivery product.

Buoy comparison. The wind buoy comparison data set was limited by internal buoy processing problems encountered at the beginning of the RENE-91 experiment, the buoy wind data being available only after the end of november [2]. The in-situ wind speed data used hereunder is the 10 m neutral wind speed, as transmitted in near real time by the buoys. As for wave, altimeter data were selected within 50 km from the buoys, but the time window was set, in a first approach, to 20 min, the elementary buoy data being an average over 20 min. Over the 26 point data set selected in this way, the mean value of differences, buoy minus altimeter wind speed, was found to be -2.5 ms^{-1} , with a 2.1 ms^{-1} standard deviation. The data set, reported as open circles on Figure 5, shows an overestimation of the altimeter wind speed or, inversely, an underestimation of buoy wind speed measurements. The relatively large scatter observed among the data is certainly due to the short time window (20 min) used, in comparison with the plus or minus 50 km space window.

Model comparison. Independently of the above comparisons, the altimeter wind speed measurements were tested versus the EMERAUDE numerical weather model of METEO-FRANCE. Colocation and data processing were the same as those used for wave analysis (see above wave section). Scatterplot of mean values within wind speed classes is shown on Figure 5, together with standard deviation of altimeter data (vertical segments) and model data (horizontal segments). The relation between the two data sets is quasi linear

for speed higher than 4 ms^{-1} and the data are closer to the perfect agreement than the buoy comparison data. Over the whole data set, the mean value of wind speed differences (model minus altimeter) is 0.16 ms^{-1} , with a standard deviation of 2.9 ms^{-1} . Some statistics, within the model wind speed classes, are given in Table 3: as for wave comparison, biases and std increase with the class level, for instance value of std increases from 2.7 ms^{-1} in the 1.5 ms^{-1} - 3.0 ms^{-1} class to 3.3 ms^{-1} in the 15 ms^{-1} - 20 ms^{-1} class.

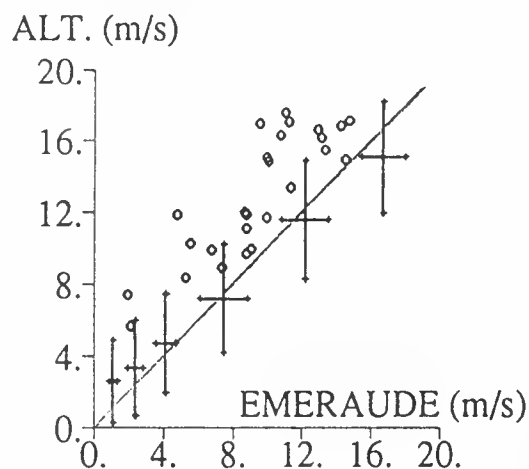


Figure 5: Comparison of buoy (open circles) and EMERAUDE model (+) with altimeter wind speed fdp.

speed ms^{-1}	n	mean ms^{-1}	std ms^{-1}
0.5-1.5	43	-1.51	2.25
1.5-3.0	253	-0.97	2.70
3-5	584	-0.60	2.71
5-10	1951	0.19	2.81
10-15	841	0.61	3.03
15-20	195	1.61	3.27
20-30	16	4.43	2.43

Table 3: Statistics on differences, EMERAUDE minus altimeter wind speed, within each class of model wind speed.

EXAMPLES OF WAVE AND WIND ALTIMETER MEASUREMENTS

In this last section, quality and usefulness of altimeter wave and wind fdp are illustrated by two examples. The first one is relative to a storm induced, over the Norwegian Sea, by a deep low pressure system (960 mb, centered on the south west of Norway on

october 17th), resulting in a strong northerly airflow. This storm was a short and intense event since, from buoy (located $64^{\circ}\text{N } 44^{\circ}\text{8E}$) measurements [2], swh is shown to increase from 4 m, on october 17th at 0500 UT, to a maximum value of 12.7 m, on the 18th at 0800 UT, and then to decrease back to 4 m, on the 19th at 2100 UT. An altimeter track was available on 18th at 2040 UT, and the along track wave measurements were corrected using coefficients of Table 1. Altimeter wave

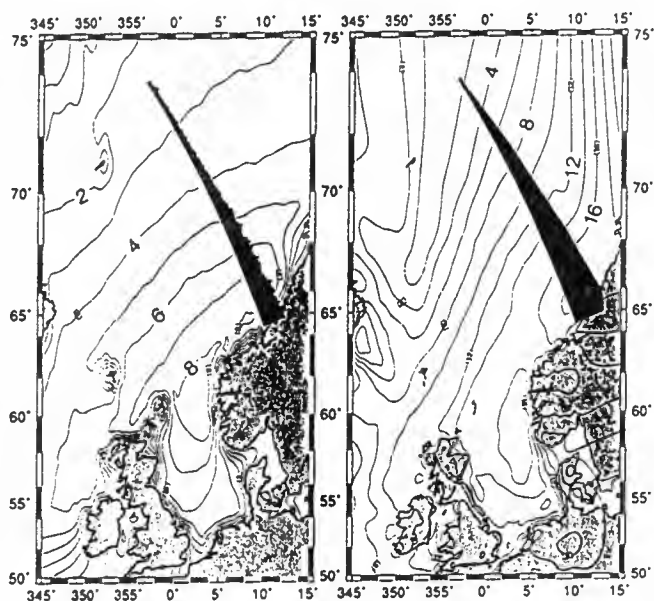


Figure 6: Wave (left) and wind (right) data for the october 18th storm: altimeter track at 2040 UT and isolines from DNMI model analysis on 19th at 0000 UT.

and wind speed data are reported on maps of Figure 6, together with isolines deduced from the Norwegian Meteorological Institute (DNMI) wave and wind models [5], these model data being available in the RENE-91 data base. Shaded areas perpendicular to the tracks are proportionnal to altimeter measurements. Model contour maps indicate wave and wind maximum values of about 8 m and 18 ms^{-1} , immediatly west off Norway, and decreasing respectively to 3 m and 2 ms^{-1} towards north-west.

Plots of Figure 7 compare altimeter measurements and along track interpolated model data. The noise level on altimeter measurements is observed to be low, with some increase with wind speed or with swh. For wind speed, over the 2 ms^{-1} - 18 ms^{-1} range, the agreement is very good and even surprising. For swh the agreement is not as good as for wind, the altimeter swh being larger than the model one. This might be due perhaps to some model boundary conditions because the maximum value of sea state was observed very close to the coast. An other explanation might

be that, during this storm, the swh increase was very steep and too fast to be correctly modelled.

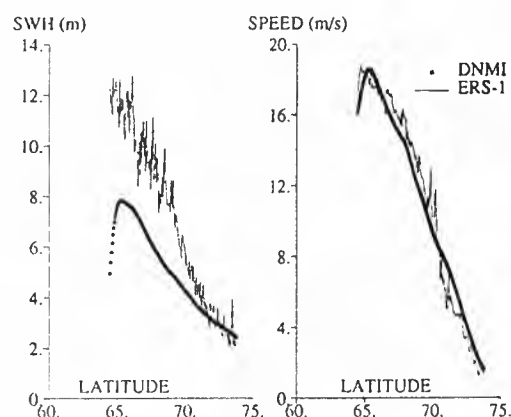


Figure 7: Altimeter wave and wind data (full lines) and along track interpolated DNMI model data (■), as a function of latitude.

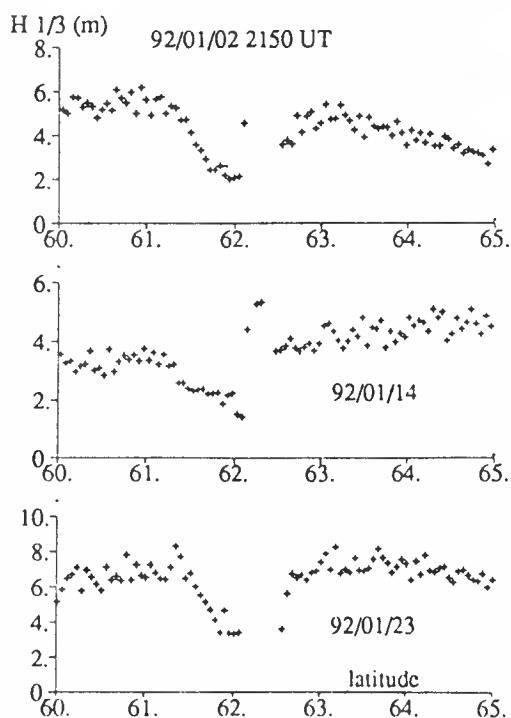


Figure 8: Altimeter swh measurements for three different passes along a track, east of Faroe Islands.

The second example illustrates the sheltering effect that islands can induce on sea state. Figure 8 shows altimeter swh measurements along a ground track, east

of the Faroe Islands, for three passes separated in time respectively by 12 and 9 days. The sheltering effect of Faroe Islands corresponds to the swh decrease observed between latitudes 61° and 62° (The spikes observed on some of the profiles, just after 62°, as also on Figure 9, result from land contamination). The swh decrease can be sharp, as observed for the third profile: from 8 m to 3 m over about 70 km distance. Amplitude and rate of decrease change from one pass to another in a way depending to the wind direction as illustrated by Figure 9. The two first swh profiles are plotted together with the DNMI wind field: the sheltered low sea state area clearly increases from the left case to the right case, due to wind direction change from South-West to West which induces an enlargement of the sheltering area because of the main north to south shape of the islands.

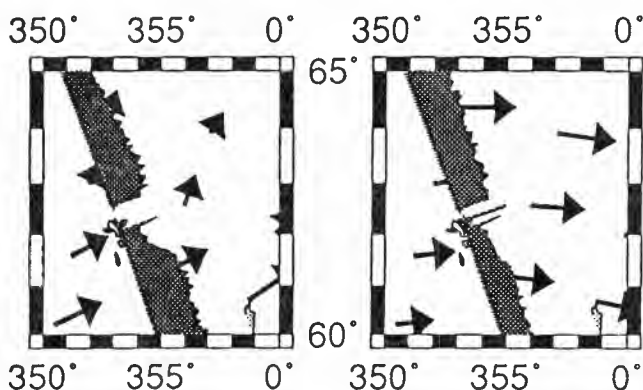


Figure 9: Altimeter tracks and swh measurements together with DNMI model wind fields on 92/01/02 (left) and 92/01/14 (right), corresponding to the two first profiles of Figure 8.

CONCLUSION

ERS-1 altimeter wave and wind speed fast delivery products were tested using comparisons with the RENE-91 buoy network and with french wave and weather numerical models. The altimeter swh are well correlated with buoy and model data. Large underestimation of altimeter swh was observed on data before the major change in fdp processing (november 11th). The processing modification improved considerably the data quality, however some underestimation of highest wave is still observed (about 16%) and a linear correction is proposed. On average, mean values of differences were found to be equal to 0.42 m and 0.22 m, respectively for comparisons with buoys and model, with standard deviation of 0.46 m and 0.91 m. For wind speed, good agreement is found with the model (mean difference of 0.16 ms^{-1} and 2.9 ms^{-1} std) but

results are not so good when comparing to the near real time buoy data. Wind speed model comparison corresponds to smooth data, in time and space, and it seems suitable to further investigate the instantaneous altimeter wind data in comparison with the RENE-91 buoy onboard stored data, if available, or with other buoys.

REFERENCES

- [1] ESA Earthnet, 1991 : ERS-1 Ground Stations Products Specification, Doc. No: ER-IS-EPO-GS-0201, 26 february.
- [2] Queffeuilou P. and A. Bentamy , 1992 : Evaluation of wind and wave measurements from the TOBIS buoy network during RENE-91, this issue.
- [3] Francis R., 1992 : Radar altimeter performance, ERS-1 commissioning phase final review, vol. 2, ESTEC, 14-15 April.
- [4] Guillaume A., 1990 : Statistical tests for the comparison of surface gravity wave spectra with application to model validation, *J. Atmos. Oceanic Technol.*, vol 7, n 4, pp 551-567, August 1990
- [5] Breivik L. A., Haugen J. E. and M. Homleid, 1992 : Experience with increased resolution in numerical weather prediction, Technical report No. 94, DNMI, PB 45 0313 Blindern, Oslo, Norway.

SESSION - IV

SAR WAVE AND CURRENT OBSERVATION

OCEAN WAVE IMAGING BY ERS-1 SYNTHETIC APERTURE RADAR: FIRST RESULTS FROM THE HALTENBANKEN CALIBRATION/VALIDATION CAMPAIGN

Claus Brüning, Werner Alpers, Andreas Wilde

Universität Hamburg, Institut für Meereskunde,
Tropelwitzstr. 7, 2000 Hamburg 54, Germany

ABSTRACT

Synthetic aperture radar (SAR) images of the European ERS-1 satellite were obtained over the Norwegian Sea during the ERS-1 Haltenbanken Calibration/Validation Campaign in November 1991. SAR image spectra calculated from the full-swath SAR images are compared to simulated SAR image spectra computed from ocean waveheight spectra measured by a directional waverider buoy. The SAR imaging of ocean waves is described by the velocity bunching model. It predicts strong nonlinear mapping distortions for wave components propagating in flight (azimuth) direction. This is seen in all SAR images analyzed. Even one example is shown where azimuthally travelling waves with a mean wavelength of 128 m are completely smeared out and not imaged at all by ERS-1 SAR. On the other hand, range travelling waves can be imaged by ERS-1 SAR down to wavelengths of 59 m as evidenced by an image obtained over the Mediterranean Sea.

INTRODUCTION

The first European Remote Sensing Satellite (ERS-1) launched on July 17, 1991, carries a C-band synthetic aperture radar (SAR) operating at VV-polarization and at an incidence angle of 23 degrees. Since July 27, 1991, SAR images obtained from this instrument are routinely acquired. During the Calibration and Validation Campaign carried out in the Haltenbanken area of the Norwegian Sea from September 15 to December 10, 1991, a number of SAR images were taken over this area. At present, only fast delivery SAR images processed at the ground station of the European Space Agency (ESA) at Kiruna (Sweden) are available

to us. We have analyzed six ERS-1 full-swath SAR images acquired between Nov. 19 and 28, 1991. Simultaneously two-dimensional waveheight spectra were measured by a directional waverider buoy moored within this area at 64°30.082'N, 7°41.79'E. Furthermore, we have analyzed one SAR image acquired over the Mediterranean Sea (Strait of Bonifacio) which shows range travelling waves with a mean wavelength of 59 m.

SAR image intensity spectra are calculated from these images and compared to simulated SAR image intensity spectra computed from the measured ocean waveheight spectra. In these calculations the velocity bunching theory as described in [1]-[5] is used.

It is well known that the imaging of ocean surface waves by space-borne SAR is often nonlinear. Image distortions are caused by the wave motions. Especially waves that have a significant component in flight or azimuth direction are heavily distorted. Often waves are completely smeared out and become invisible on SAR images.

Because of this nonlinearity the well-known methods applicable to linear imaging cannot be applied to the calculation of SAR image spectra from ocean waveheight spectra. In general, it is not permissible to use the linear transfer function concept for relating ocean waveheight spectra to SAR image spectra. Methods capable of describing nonlinear imaging are the Monte-Carlo simulation technique [4],[5] and the nonlinear integral transform method [6],[7]. In this paper we use the Monte-Carlo simulation technique for mapping ocean waveheight spectra into SAR image spectra. Although this method is more costly in

computer time, it is more exact than present versions of the integral transform method since it includes the azimuthal image smear caused by the orbital acceleration and the sub-resolution scale orbital velocity spread.

THE SAR OCEAN WAVE IMAGING MODEL

According to the generalized velocity bunching model the relationship between the ensemble averaged SAR image intensity $I(\underline{x})$ and a given realization of the ocean wave field is described by [4],[5]

$$I(\underline{x}) = B \iint \sigma(\underline{x}_0) (\rho_{aN}(\underline{x}_0))^{-1} \exp \left\{ \pi^2 (x - x_0 - \frac{R}{V} u_r(\underline{x}_0))^2 / \rho_{aN}^2(\underline{x}_0) \right\} \delta(y - y_0) dy_0 dx_0 \quad (1)$$

Here R denotes the target range, V the platform velocity, $\sigma(\underline{x}_0)$ the normalized radar backscattering cross section, $\delta(y - y_0)$ the impulse response function in ground range direction and B a normalization factor. The coordinate system is chosen in such a way that the x -axis points into the flight (or azimuth) direction. The term $(R/V)u_r(\underline{x}_0)$ represents the azimuthal image shift of a scatter element induced by the radial orbital velocity u_r associated with the long ocean waves. The degraded azimuthal resolution for incoherent N looks ρ_{aN} is given by

$$\rho_{aN}(\underline{x}_0) = N \rho_a \left[1 + \frac{\pi^2 T^4}{N^2 \lambda_0^2} a_r^2(\underline{x}_0) + \frac{1}{N^2} \frac{T^2}{\tau_s^2} \right]^{\frac{1}{2}} \quad (2)$$

where $\rho_a = \lambda_0 R / (2VT)$ denotes the nominal single-look azimuthal resolution, λ_0 the radar wavelength and T the full-bandwidth, single-look SAR integration time. The second term in the square root expression represents the degradation in azimuthal resolution due to the large-scale orbital acceleration $a_r(\underline{x}_0)$ and the third term the degradation due to the sub-resolution scale orbital velocity spread which is parameterized by the scene coherence time τ_s [4] with $\tau_s = 0.02$ s.

We assume that Bragg scattering theory is applicable to describe the radar backscattering at the ocean surface at the incidence angle of 23 degrees and that the modulation of the normalized radar cross section (NRCS) by the long ocean waves is describable by a linear modulation transfer function (MTF), which is called here RAR (real aperture radar) MTF, R^{RAR} . It consists of two terms, the tilt MTF and the hydrodynamic MTF:

$$R^{RAR} = R^{Tilt} + R^{Hyd} \quad (3)$$

The tilt MTF results from the tilting of the Bragg waves by the long waves and can easily be calculated from Bragg theory in conjunction with the two-scale wave model [2]. The hydrodynamic MTF is less well known. A theoretical value can be calculated by using weak hydrodynamic interaction theory [8] which contains the relaxation rate μ as the only free parameter. However, it is questionable whether this theoretical MTF is the optimum MTF to be used in the SAR imaging model.

In this investigation we use the theoretical MTF for calculating the SAR image spectra from the ocean waveheight spectra. The simulated SAR spectra shown in the figures are obtained by using the theoretical RAR MTF with $\mu = 0.5 \text{ s}^{-1}$. This seems to be a realistic value for the relaxation rate of C-band Bragg waves [9]. In parallel, we also have performed simulations with $\mu = 0 \text{ s}^{-1}$ and $\mu = 100 \text{ s}^{-1}$, which are not shown here. The relaxation rate $\mu = 0 \text{ s}^{-1}$ gives a hydrodynamic MTF which has maximum modulus and whose phase is equal to zero (maximum modulation occurs at the crest of the waves [8]). The relaxation rate 100 s^{-1} yields a very small hydrodynamic MTF such that the total RAR MTF is practically equal to the tilt MTF.

The range bunching modulation which also enters into the SAR imaging mechanism [10] is neglected in the present analysis.

MONTE-CARLO SIMULATIONS

The Monte-Carlo simulation method used here consists in generating individual realizations of the ocean wave field from the measured ocean waveheight spectrum as described in detail in [4]. The complex wave amplitudes are assumed to be Gaussian distributed variables. A realization of the wave field consisting of 128×128 pixels (with a pixel spacing of 16 m) is imaged by applying the SAR imaging model given by eq. (1). The SAR image spectrum is then obtained by averaging the

individual SAR image spectra calculated from 50 realizations of the ocean wave field. The final SAR image spectrum is smoothed by applying a 3 x 3 triangle filter.

SAR DATA ANALYSIS

Full-swath SAR images of ocean waves (SAR Fast Delivery Products, ERS-1.SAR. UI 16) of six ERS-1 passes acquired on Nov. 19, 20, 22, 23, 25 and 28, 1991, over the Haltenbanken area of the Norwegian Sea (see Fig. 1) have been analyzed. They have a nominal ground range resolution of 33 m and a nominal azimuthal resolution of 33 m (3 incoherent looks). The full-swath ERS-1 SAR image covers an area of approximately 100 km x 100 km. SAR image intensity spectra are calculated from sub-images of 512 x 512 pixels with a pixel spacing of 16 m. Each sub-image is subdivided into 9 overlapping scenes of 256 x 256 pixels. The instantaneous SAR image intensity spectrum is calculated by squaring the Fourier coefficients of the Fourier transform of individual SAR scenes. Then the mean SAR image spectrum is calculated by averaging over 9 instantaneous SAR image spectra. The final SAR image spectrum is corrected for the ERS-1 SAR

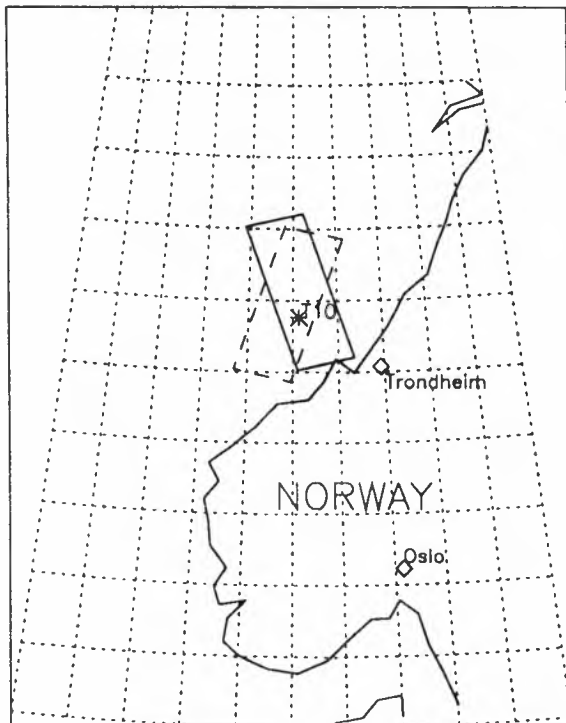


Fig. 1: Area in the Norwegian Sea (Haltenbanken) where the ERS-1 SAR data analyzed in this paper were collected during ascending (solid lines) and descending (dotted lines) passes. T10 is the location of the buoy.

stationary wavenumber impulse response function. This is done by fitting one-dimensional fourth order even polynomials to the spectra in azimuth as well as in ground range direction at $k_x=2\pi/32 \text{ m}^{-1}$ and $k_y=2\pi/32 \text{ m}^{-1}$, respectively. These high wavenumber lines were selected because this part of the SAR image spectrum should contain no wave information. The two polynomials are evaluated at each gridpoint of the SAR image spectrum yielding the correction matrix. This matrix is normalized and values less than 1/3 are set equal 1/3 in order to suppress the noise in the high wavenumber region. Finally, the SAR image spectrum is divided by this matrix which represents an approximation of stationary wavenumber impulse response function in both directions. Fig. 2 shows a cut through the center of this matrix in azimuth (solid line) and ground range (dotted line) direction, respectively. It is evident from Fig. 2 that the azimuthal resolution of the ERS-1 SAR is better than the ground range resolution.

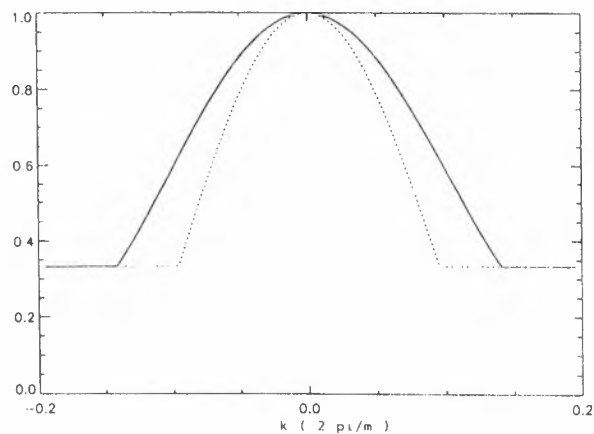


Fig. 2: Cut through the center of the spectral impulse response correction matrix in azimuth (solid line) and range (dotted line) direction.

The final SAR image spectrum is obtained by smoothing over 5 x 5 spectral points applying a triangle filter and by subtracting the background noise.

This procedure is applied to all analyzed SAR image spectra except to the spectrum of Nov. 19, where no noise is subtracted, because it contains no discernible wave information.

The mean wavelength and mean wave propagation direction are obtained by calculating the center of gravity around the spectral peak. In this calculation all spectral values which are larger than half the value of spectral peak are taken into account.

MEASUREMENT OF OCEAN WAVEHEIGHT SPECTRA

During the ERS-1 overflights considered here two dimensional ocean wave height spectra were measured at the position $64^{\circ}30.082'N$, $7^{\circ}41.79'E$ by a moored Datawell directional waverider buoy [11]. It measures the orbital motion of the wave field in the wavelength range between 600 m and 6 m in deep water from which estimates of ocean waveheight spectra in frequency/direction space are calculated.

We have transformed the waveheight spectra from frequency/direction space into wavenumber space by using the deep water dispersion relation neglecting the influence of ocean currents.

RESULTS

Figure 3a, 4a and 5a show three examples of ocean waveheight spectra measured by the directional waverider buoy on Nov. 25, 20 and 23, 1991, respectively. The waveheight spectra are calculated from time series recorded on Nov. 20 and 23 between 10:38 and 11:08 UTC, on Nov. 19 and 25 between 20:38 and 21:08 UTC, and on Nov. 22 and 28 between 20:08 and 20:38 UTC. All spectra shown in the figures are plotted in a coordinate system where the x-axis points into the satellite flight direction.

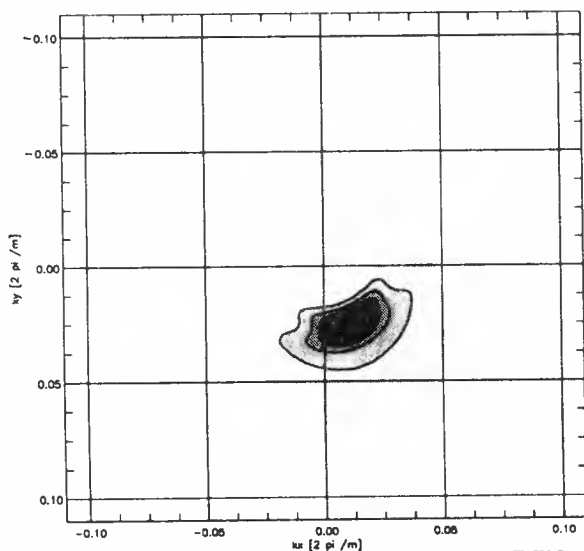


Fig. 3a: Ocean waveheight spectrum measured by the directional waverider buoy on Nov. 25, 1991, between 20:38 and 21:08 UTC.

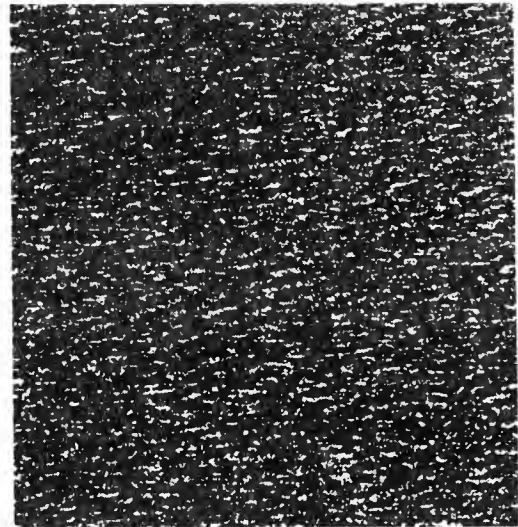


Fig. 3b: ERS-1 SAR image acquired on Nov. 25, 1991, at 21:10:13 UTC over the position of the directional waverider buoy.

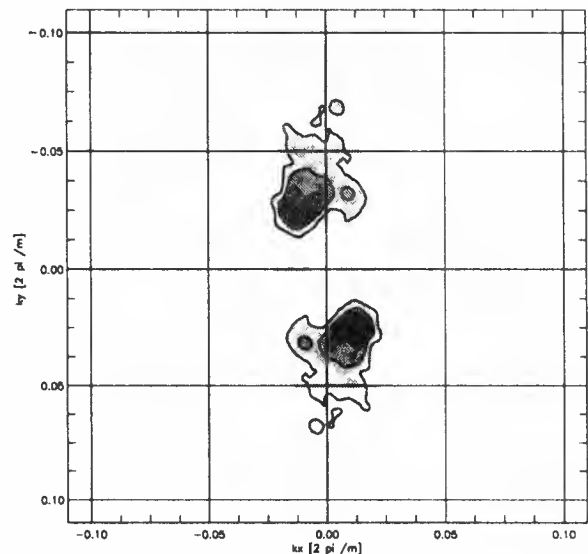


Fig. 3c: SAR image spectrum calculated from the ERS-1 SAR image shown in Fig. 3b.

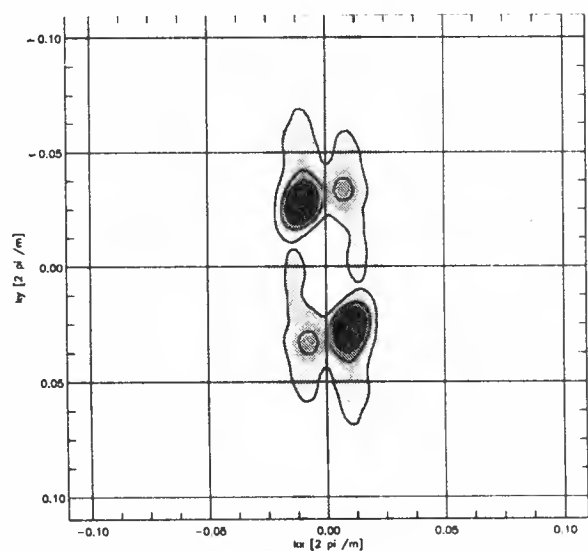


Fig. 3d: SAR image spectrum simulated from the ocean waveheight spectrum shown in Fig. 3a.

Fig. 3b shows a sub-image covering an area of approximately 8.2 km x 8.2 km of the full-swath ERS-1 SAR image acquired on Nov. 25 at 21:10:30 UTC over the position of the buoy. Wave patterns can clearly be delineated on this SAR image.

The corresponding SAR image intensity spectrum is depicted in Fig. 3c. Note the characteristic cigar-like shape of the SAR spectrum. It is caused by the orbital motion of the ocean waves which results in an azimuthal cut-off of the SAR image spectrum. The measured ocean waveheight spectrum and the simulated SAR image spectrum are shown in Fig. 3a and 3d, respectively. The mean ocean wave propagation direction is 67 degrees off the flight direction, the mean wavelength 221 m, and the significant waveheight 4.5 m. Although the form of the ocean waveheight spectra is strongly distorted by the SAR imaging process [5], the mean wavelength and direction are not changed significantly.

By comparing Fig. 3c and Fig. 3d, one notes that the measured and simulated SAR spectra agree quite well. The mean wavelengths and directions of the measured and simulated spectra are 222 m / 66 degrees and 211 m / 69 degrees, respectively (see also Table 1).

Another example is depicted in Fig. 4. The SAR image was acquired on Nov. 20, 1991, at 10:48 UTC over the position of the buoy during a descending ERS-1 pass (flight direction towards 201°N). The ocean wave field consisted of a swell travelling at 227 degrees off the ERS-1 flight direction (i.e., towards 68 degrees N, since the SAR looks to the right of the flight direction) and a low energy wind sea travelling at approximately 340 degrees off this direction (see Fig. 4a). The significant waveheight was 1.70 m. The measured and simulated SAR image spectra are shown in Fig. 4b and 4c, respectively. The mean wavelength and mean wave direction of the swell are well reproduced by the simulation within the experimental and computational limits (see Table 1).

The wave height spectrum measured on Nov. 23, 1991, at 11:08 UTC, shown in Fig. 5a, has a mean wavelength of 171 m and a significant waveheight of 3.1 m. The corresponding measured SAR image spectrum obtained at the position of the buoy is shown in Fig. 5b. The spectral shape of the measured spectrum is well reproduced by the simulated one depicted in Fig. 5c. However, when comparing the mean wavelength calculated from the ERS-1 SAR data with the one obtained from the simulation, one notes that the measured one is 192 m while the simulated one is only 159 m (see Table 1). This is a difference of 17%. The

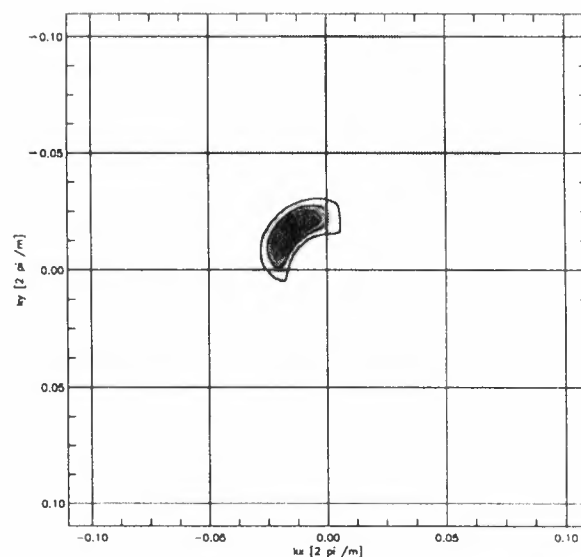


Fig. 4a: Ocean waveheight spectrum measured by the directional waverider buoy on Nov. 20, 1991, between 10:38 and 11:08 UTC.

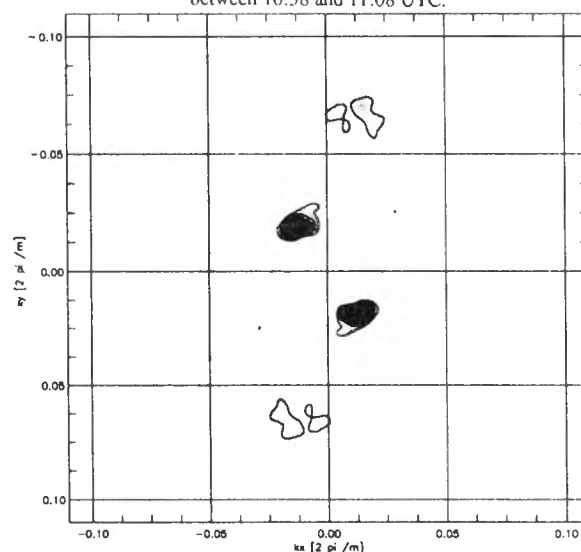


Fig. 4b: SAR image spectrum calculated from the ERS-1 SAR image acquired on Nov. 20, 1991, at 10:48 UTC.

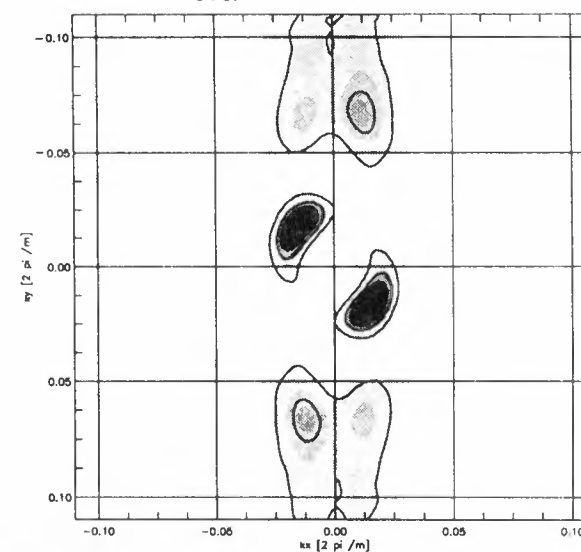


Fig. 4c: SAR image spectrum simulated from the ocean waveheight spectrum shown in Fig. 4a.

most likely reason for that is that on Nov. 23, the variability of the SAR mean wavelength of different scenes is extremely large ($\lambda_m = (183 \pm 16)$ m, with a minimum and maximum value of 145 m and 230 m, respectively, see Fig. 5d). The simulated mean wavelength is well within the 95% confidence limit. Fig. 5d gives an impression how the mean SAR spectral parameters vary along a swath on Nov. 23, 1991. The arrows indicate the mean wavelength and direction relative to the satellite track at the position on the swath, while the satellite was flying from the bottom to the top of the plot. The numbers on the right hand side give the mean wavelengths in m for the corresponding positions. The whole scene is 300 km x 100 km, and the satellite heading is 201 degrees N.

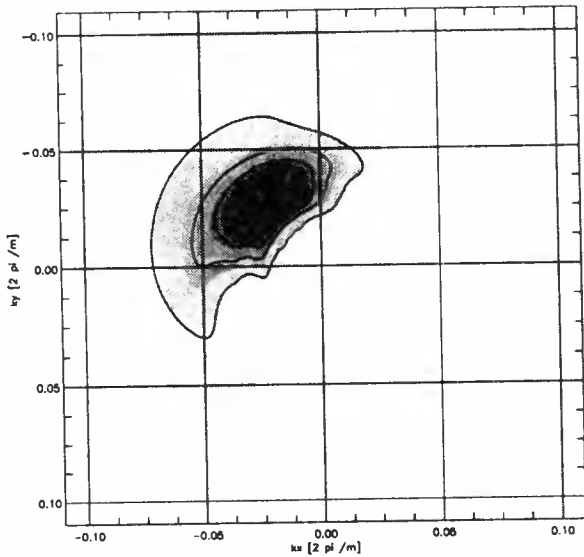


Fig. 5a: Ocean waveheight spectrum measured by the directional waverider buoy on Nov. 23, 1991, between 10:38 and 11:08 UTC.

Table 1 Mean wavelength, λ_m , and mean propagation direction, ϕ_m , of the ocean waveheight spectra measured by the directional waverider buoy, of the measured ERS-1 SAR image spectra and of the simulated SAR image spectra at the position of T10 (Fig. 1), which is $64^{\circ}30.082'N$, $7^{\circ}41.79'E$.

DATE	TIME OF ERS-1 SAR DATA TAKE [UTC]	SATELLITE HEADING [deg.N]	OCEAN WAVE SPECTRUM MEASURED		SAR SPECTRUM MEASURED		SAR SPECTRUM SIMULATED	
			λ_m [m]	ϕ_m [deg.]	λ_m [m]	ϕ_m [deg.]	λ_m [m]	ϕ_m [deg.]
Nov 19, 1991	21:10:30	339	128	177	--	--	--	--
Nov 20, 1991	10:48:02	201	278	227	271	235	268	228
Nov 22, 1991	21:10:31	339	193	97	172	83	184	93
Nov 23, 1991	10:48:03	201	171	229	192	244	159	254
Nov 25, 1991	21:10:30	339	221	67	222	66	211	69
Nov 28, 1991	21:10:29	339	263	85	256	83	235	85

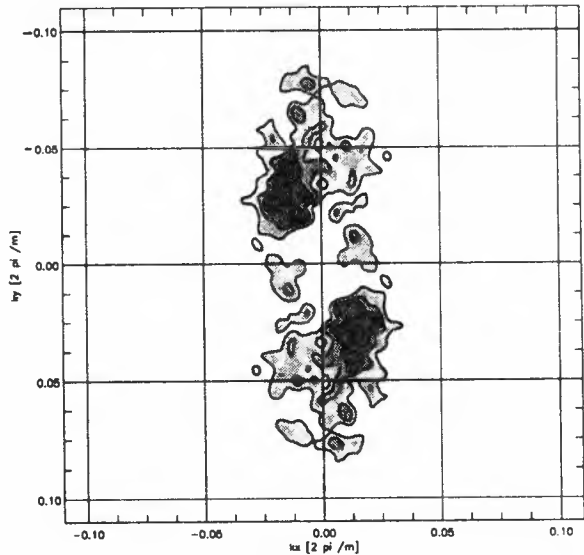


Fig. 5b: SAR image spectrum calculated from the ERS-1 SAR image acquired on Nov. 23, 1991, at 10:48 UTC.

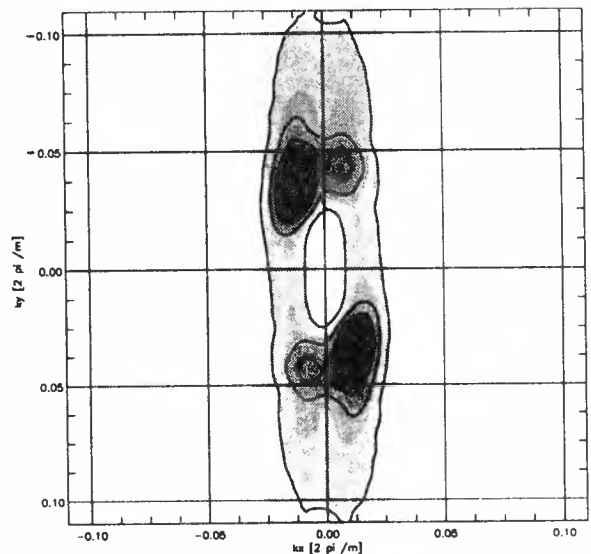


Fig. 5c: SAR image spectrum simulated from the ocean waveheight spectrum shown in Fig. 5a.

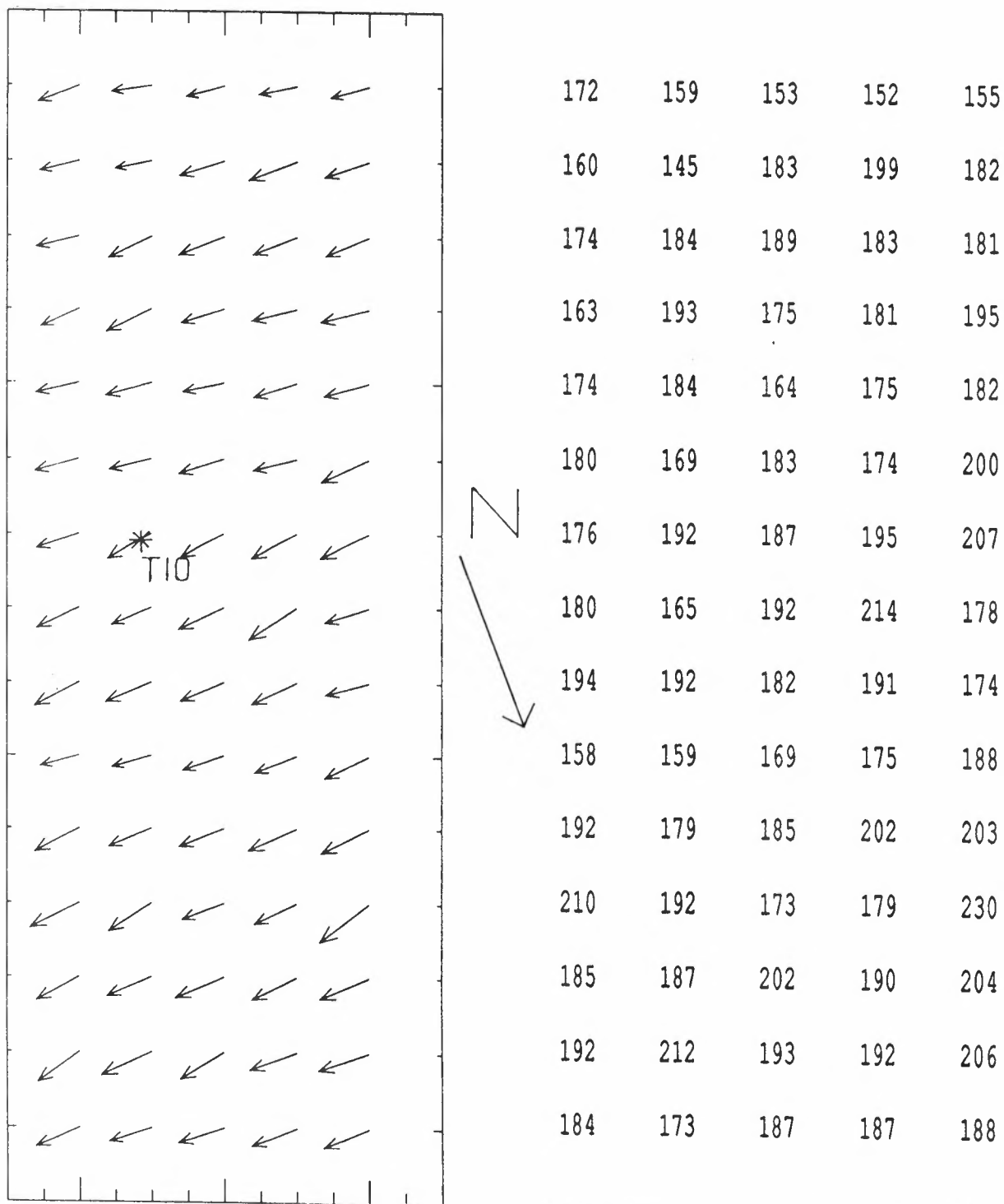


Fig. 5d:

Mean wavelength, λ_m , and mean propagation direction, ϕ_m , calculated from measured ERS-1 SAR image spectra obtained on Nov. 23, at 10:48 (area according to Fig. 1, descending pass). The arrows indicate the mean wavelength and direction relative to the satellite track at the position of the swath. The numbers on the right hand side give the mean wavelengths in m for the corresponding positions.

A scenario where ocean waves are not imaged at all by ERS-1 SAR was encountered on Nov. 19, 1991, at 21:10:30 UTC. The ocean waveheight spectrum measured by the directional waverider buoy at the time of the overflight (ascending pass, flight direction towards 338°N) shows azimuthally propagating wind sea with a mean wavelength of 128 m and a very low energy swell with a wavelength of approximately 340 m (Fig. 6a). The significant waveheight was 2.00 m. The measured ERS-1 SAR image spectrum is shown in Fig. 6b. Neither the measured nor the simulated SAR image spectra (not shown here) contain any obvious wave information.

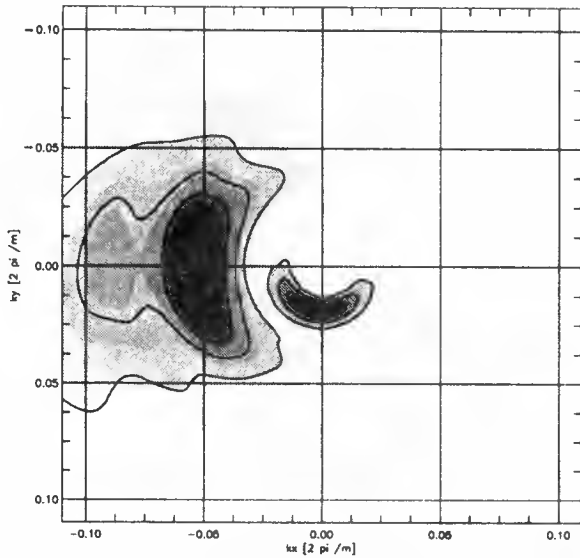


Fig. 6a: Ocean waveheight spectrum measured by the directional waverider buoy on Nov. 19, 1991, between 20:38 and 21:08 UTC.

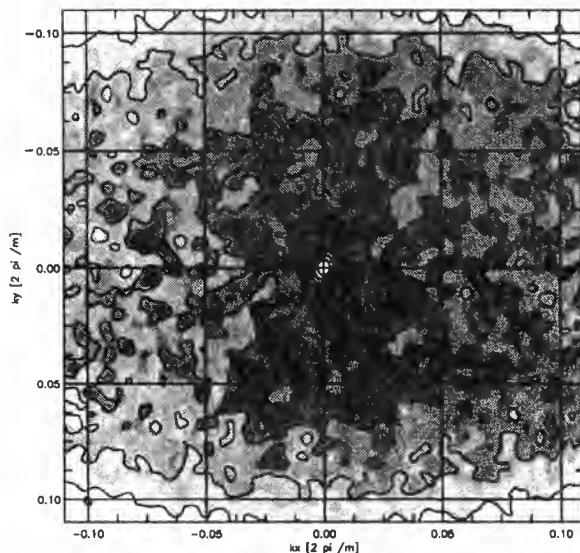


Fig. 6b: SAR image spectrum calculated from the ERS-1 SAR image acquired on Nov. 19, 1991, at 21:10:30 UTC. No waves can be delineated clearly.

On the other hand, we have found one ERS-1 SAR image which shows nearly range travelling waves with mean wavelength of approximately twice the theoretical ERS-1 SAR ground range resolution of 33 m (in fact the range resolution is better than 33 m). The image was taken on Oct. 31, 1991, at 21:36:55 UTC over the Strait of Bonifacio in the Mediterranean Sea. We have calculated a SAR image spectrum from an area of 8.2 km x 8.2 km centered around 41.30°N, 9.30°E which is north-east of the Strait of Bonifacio in the Tyrrhenian Sea. This spectrum which is shown in Fig. 7 has a mean wavelength of 59 m. The wind speed reported by land stations on the west coast of Corsica and Sardinia was 13-15 m/s from N. However, it is well known that the

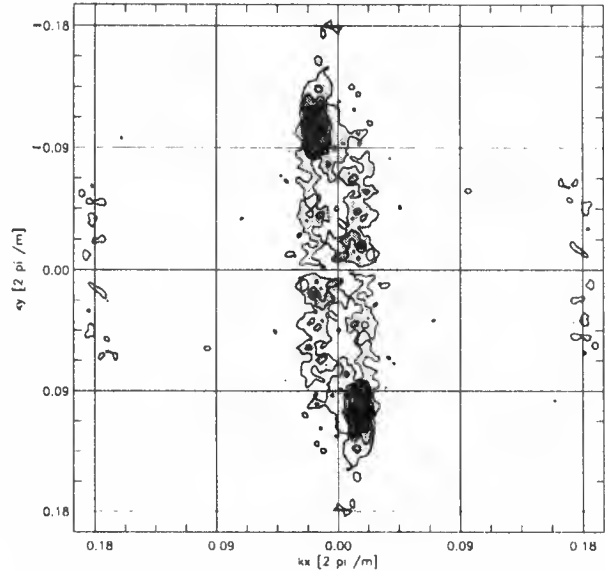


Fig. 7: SAR image spectrum calculated from the ERS-1 SAR image acquired on Oct. 31, 1991, at 21:36:55 UTC over the Mediterranean Sea (41.30°N, 9.30°E).

wind field exhibits strong spatial variations in the vicinity of the Strait of Bonifacio, since the Strait acts as a funnel to the wind. E.g., the wind speed measured by the meteorological station at Bonifacio at the southern tip of Corsica at 21:00 UTC was 8 m/s from 40 degrees N.

We have also calculated the SAR image spectrum from an area 40 km south of the above mentioned area. This spectrum does not show waves.

The results of the analysis of the remaining two SAR scenes obtained over the Haltenbanken area on Nov. 22 and 28, 1991, are summarized in Table 1 with respect to the mean wavelength, λ_m , and the mean wave propagation direction, ϕ_m . The significant waveheight on these days was 2.80 m and 5.10 m, respectively.

DISCUSSION

Table 1 shows that for the data obtained on Nov. 20, 22, 25 and 28, 1991, the mean wavelength and direction of the measured and simulated SAR image spectra agree quite well. Also the shape of the spectra is well reproduced in most cases (see Fig. 3c, 3d; Fig. 4b, 4c and Fig. 5b, 5c). We have noticed that for waves travelling near to the range direction the form of the simulated SAR image spectrum is very sensitive to the choice of the real aperture radar modulation transfer function (RAR MTF). In general, simulations carried out with a hydrodynamic MTF where the relaxation rate is set equal to 0.5 s^{-1} fit the measured SAR image spectra better than the simulations carried out with $\mu=0 \text{ s}^{-1}$ and $\mu=100 \text{ s}^{-1}$.

For the data obtained of Nov. 22, 1991 the agreement between the spectral shape of the measured and simulated SAR image spectra is not as good as for the other days. The measured SAR image spectrum is unimodal (apart from the 180 degrees ambiguity) whereas the simulated SAR images spectrum has a bimodal form. This disagreement is very likely due to the inadequately measured wave height spectrum that serves as input for the SAR simulation model. On Nov. 22, 1991, the spectrum measured by the buoy shows a large directional spread which is an indication for a second wave system not resolved by the buoy. Indeed, simultaneous wave measurements carried out by a ship radar show two wave systems having almost the same peak wavelength travelling roughly 150 degrees apart (F. Ziemer, private communication).

CONCLUSION

This first analysis of full-swath ERS-1 SAR images carried out with Fast Delivery SAR Data collected over the Haltenbanken area of the Norwegian Sea clearly shows the ability of the ERS-1 C-Band SAR to image ocean surface waves. Due to the large R/V ratio of the ERS-1 SAR, which is, like for Seasat, approximately 130 s, the imaging is often non-linear. Short azimuth travelling waves are smeared out by the nonlinear velocity bunching process, they are not imaged by ERS-1 SAR. Range travelling waves, however, are imaged down to wavelengths of 60 m.

This investigation shows that the Monte-Carlo simulation technique based on the velocity bunching model is able to reproduce the measured ERS-1 SAR image spectra in great detail. This gives additional confidence in our proposed SAR ocean wave imaging model.

ACKNOWLEDGMENTS

We thank F. Ziemer (GKSS, Geesthacht) and K. Richter (BSH, Hamburg) for collecting and processing the directional waverider data and ESA for supplying copies of the ERS-1 SAR Fast Delivery Products.

This research was supported by the Bundesministerium für Forschung und Technologie, Contract Nr. 01 QS 9014.

REFERENCES

- [1] W.R. Alpers and C.L. Rufenach, "The Effect of Orbital Motion on Synthetic Aperture Radar Imagery of Ocean Waves", IEEE Trans. Antennas Propagat., vol. AP-27, pp. 685-690, 1979.
- [2] W. Alpers, D.B. Ross and C.L. Rufenach, "On the Detectability of Ocean Surface Waves by Real and Synthetic Aperture Radar", J. Geophys. Res., vol. 86, pp. 6481-6498, 1981.
- [3] K. Hasselmann, R.K. Raney, W.J. Plant, W.R. Alpers, R.A. Shuchman, D.R. Lyzenga, C.L. Rufenach and M.J. Tucker, "Theory of Synthetic Aperture Radar Ocean Imaging. A MARSEN View", J. Geophys. Res., vol. 90, pp. 4659-4686, 1985.
- [4] W.R. Alpers and C. Brüning, "On the Relative Importance of Motion-Related Contributions to the SAR Imaging Mechanism of Ocean Surface Waves", IEEE Trans. Geosci. Remote Sensing, vol. GE-24, pp. 873-885, 1986.
- [5] C. Brüning, W.R. Alpers and K. Hasselmann, "Monte-Carlo Simulation Studies of the Nonlinear Imaging of a Two-Dimensional Surface Wave Field by a Synthetic Aperture Radar", Int. J. Remote Sensing, vol.11, pp.1695-1727, 1990.
- [6] K. Hasselmann and S. Hasselmann, "On the Nonlinear Mapping of an Ocean Wave Spectrum into a SAR Image Spectrum and its Inversion", J. Geophys. Res., vol. 96, pp. 10713-10729, 1991.
- [7] H.E. Krogstad, "A Simple Derivation of Hasselmann's Nonlinear Ocean-SAR Transform", J. Geophys. Res., vol. 97, pp. 2421-2425, 1992.
- [8] W. Alpers and K. Hasselmann, "The Two-Frequency Microwave Technique for Measuring Ocean Wave Spectra From an Airplane or Satellite", Boundary Layer Meteorol., vol. 13, pp. 215-230, Appendix A, 1978.
- [9] E.A. Caponi, D.R. Crawford and H.C. Yuen, "Modulation of Radar Backscatter From the Ocean by a Variable Current", J. Geophys. Res., vol. 93, pp. 12249-12263, 1988.
- [10] J.F.R. Gower, "'Layover' in Satellite Radar Images of Ocean Waves", J. Geophys. Res., vol. 88, pp. 7719-7720, 1983.
- [11] F. Ziemer, W. Rosenthal, K. Richter, D. Schrader, "Two-dimensional wave field measurements as sea truth for ERS-1 SAR", this issue.

Sea Truth and Model Data For Surface Waves Compared With ERS-1-SAR

W. Rosenthal, V. Atanassov, W. Koch, F. Ziemer
GKSS Forschungszentrum Geesthacht GmbH

K. Richter

Bundesamt für Seeschifffahrt und Hydrographie

Abstract

On 28th Nov. 1991 SAR imagery of ERS-1 is available for significant wave height between 5 m and 6 m. The seastate is measured by directional sensitive wave buoys and navigational radar and modelled by the numerical wave model HYPAS. The two dimensional SAR image spectra and tentatively obtained wave spectra derived with an empirical transfer function are shown together with the ground truth.

1. Introduction

The partners of the CAL/VAL-Project D6 : GKSS-Research Center, Norwegian Meteorological Institute, Bundesamt für Seeschifffahrt und Hydrographie, Forschungsanstalt für Wassershall und Geophysik der Bundeswehr mobilized several ships, buoys and other sensor platforms to determine the performance of the ERS-1 sensors for measuring ocean waves. A

description of gathering two dimensional wave spectra with a WMR (Wave Monitoring Nautical Radar) has been described in another presentation of this seminar [Zierner et al., 1992] .

In the following we describe the status of our work towards the three aims:

1. Determine the spatial variability of ocean wave SAR-image spectra.

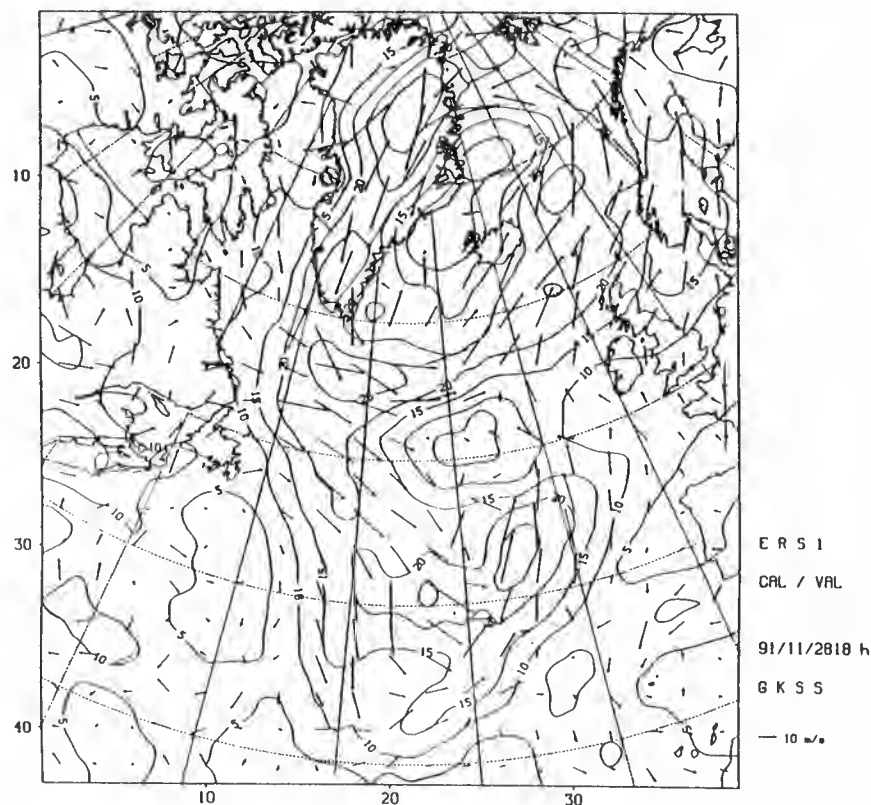


Figure 1: Coarse grid area of the wave model with the wind field on 28 November, 18:00 h UTC

2. Develop an empirical transfer function from ocean wave spectra to SAR-image spectra:

$$(1) I(kx',ky') = T * E(kx,ky)$$

$$T = T(kx',ky';kx,ky;\delta,\Pi)$$

I = Image spectrum

E = Wave energy spectrum

δ = satellite flight direction

Π = other parameters, e.g. windspeed and wind direction

3. Develop inversion techniques to determine T^{-1} or convenient approximations.

To achieve these aims we shall use the following eight data sets:

1. Two dimensional image spectra in wave number space from neighbouring areas within the ERS-1-SAR image.
2. One dimensional spectra in frequency space of energy and mean direction from a directional waverider at station T10 of the Tobis buoy array (64° 30' N; 7° 42' E).
3. One dimensional spectra of energy and mean direction from a pitch-roll buoy at station T9 of the Tobis buoy array.

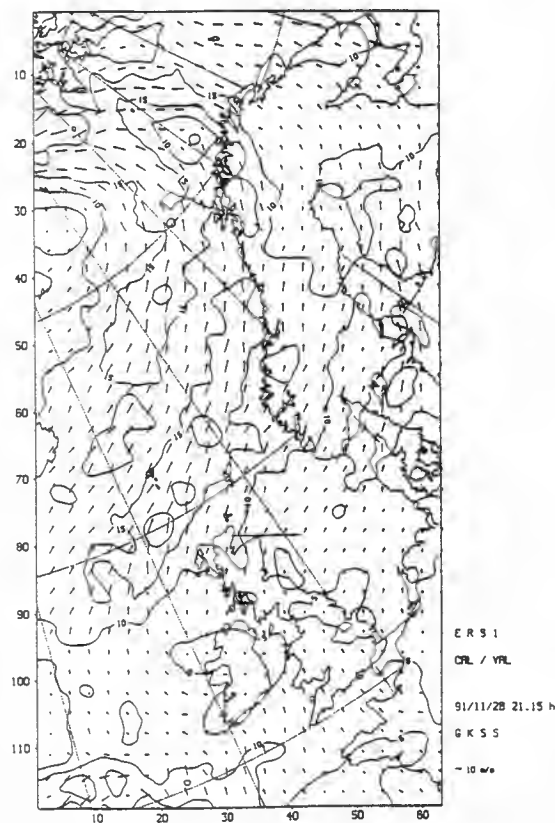


Figure 2: Fine grid area of the wave model with the wind field on 28 November, 21:15 h UTC.

4. One dimensional spectra from the Tobis buoys.
5. Three dimensional marine radar spectra in frequency-wave-number-space from the research vessels GAUSS and PLANET.
6. Three dimensional spectra from a radar mounted on the oil production platform GULLFAKS.
7. Two dimensional wave spectra from the numerical wave model 3GWAM as it has been run at the ECMWF (Günther, Hansen 1992).
8. Two dimensional wave spectra from the numerical wave model HYPAS as it has been implemented for the Bundesamt für Seeschifffahrt und Hydrographie at the German weather service.

To explain our methods in this status report we selected data from the 28. November 1991 for which SAR imagery is available on an occasion with significant wave heights between 5 m and 6 m and a wind sea dominated spectrum documented by the data of the wave buoys. For brevity we concentrate on a description of the data sets 1,2,5,8 mentioned above.

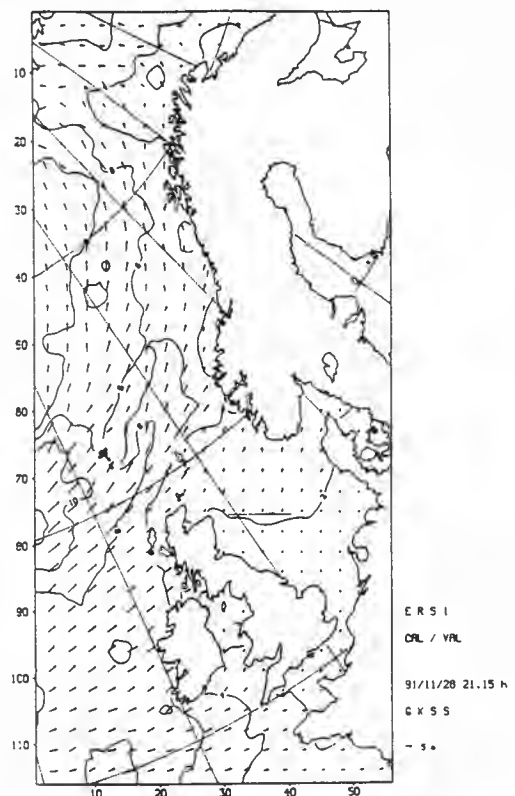


Figure 3: Isolines of significant wave height at 21:15 h UTC

2. Modelling wind and waves for the CAL/VAL period demonstrated for the event on 28 Nov. 1991 (data set 8).

To drive an ocean wave model the history of the surface wind field has to be known with sufficient accuracy. For the

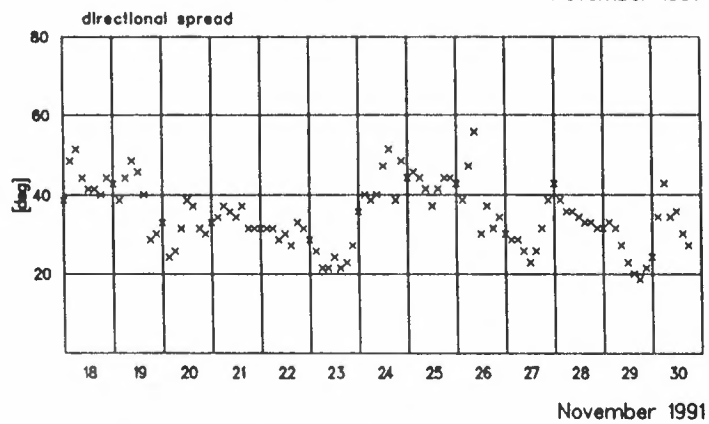
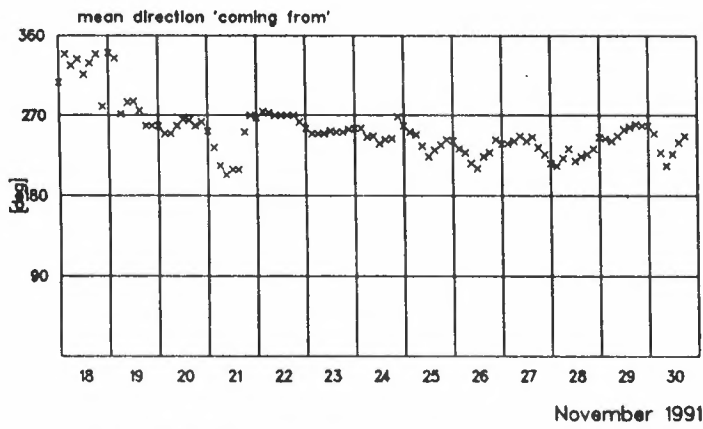
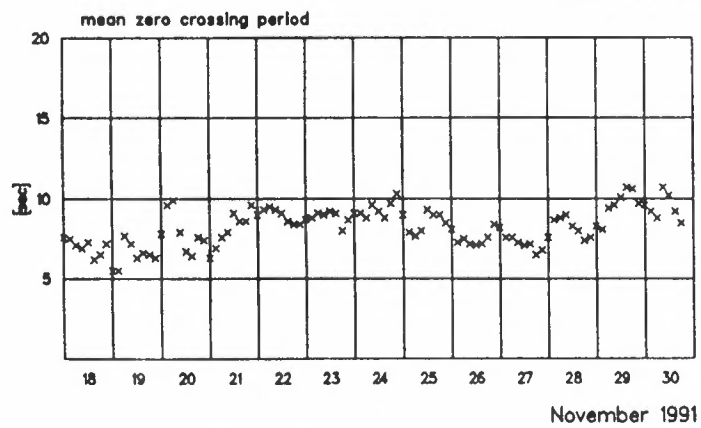
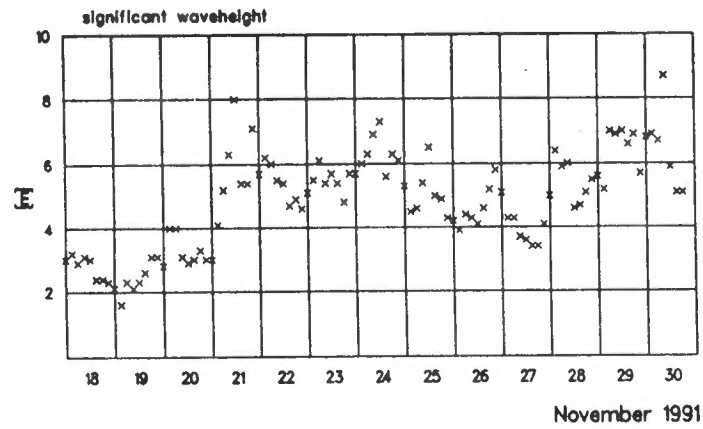


Figure 4 a - d: Time series of integrated parameters. Model computations for grid point 25,45 of fig. 7. See Ziemer et al. for parameter definitions

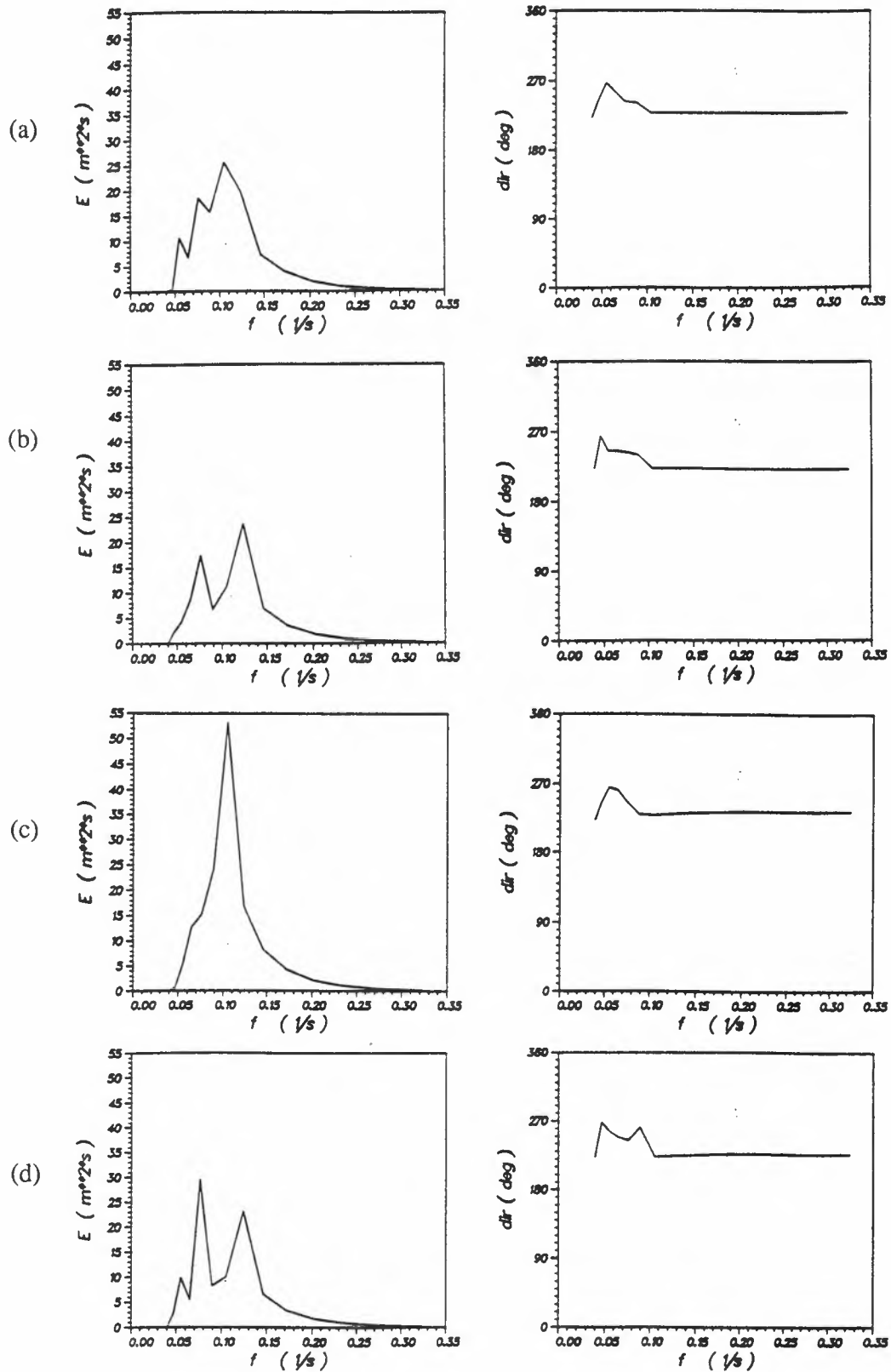


Figure 5 a - d: The one-dimensional model spectrum at the grid point north of T10 (a), south of T10 (b), west of T10 (c) and east of T10 (d).

CAL/VAL campaign the windfield from the LAM of the Norwegian Meteorological Institute is available at ESRIN. However a wave model has to be used with a numerical windfield generated in the same way as it has been done in the validation phase of the wave model or it has to be recalibrated with the new source of numerical windfields. We therefore followed our extensively tested procedure to produce wind fields used successfully in various wave hindcast projects. The method is summarized as follows.

- a. Digitisation of the isobars from the hand analysed working charts of the Seewetteramt Hamburg (German Weather Service), given in 6 hourly intervals.

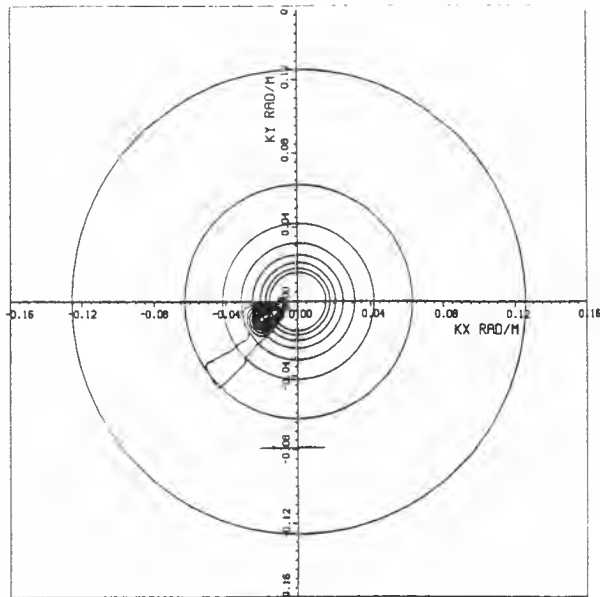


Figure 6 a: The two-dimensional model spectrum at the next grid point north of T10

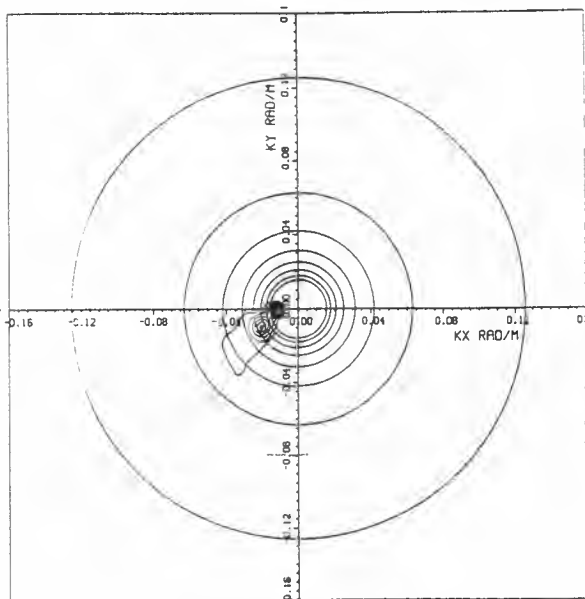


Figure 6 b: The two-dimensional model spectrum at the next grid point south of T10

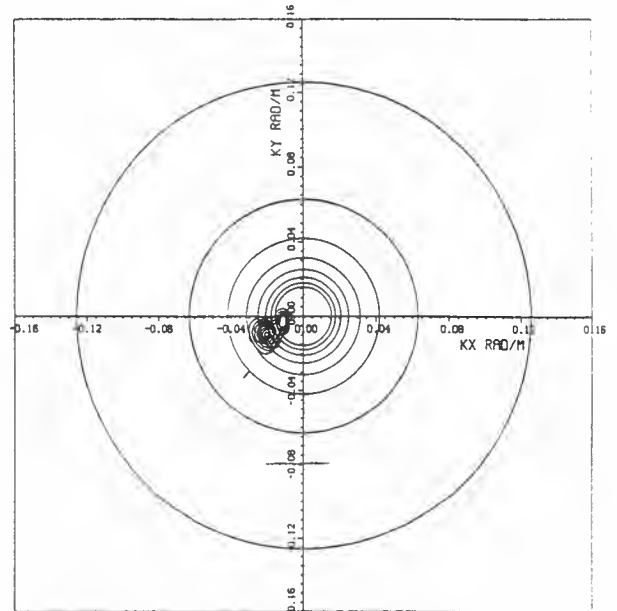


Figure 6 c: The two-dimensional model spectrum at the next grid point west of T10

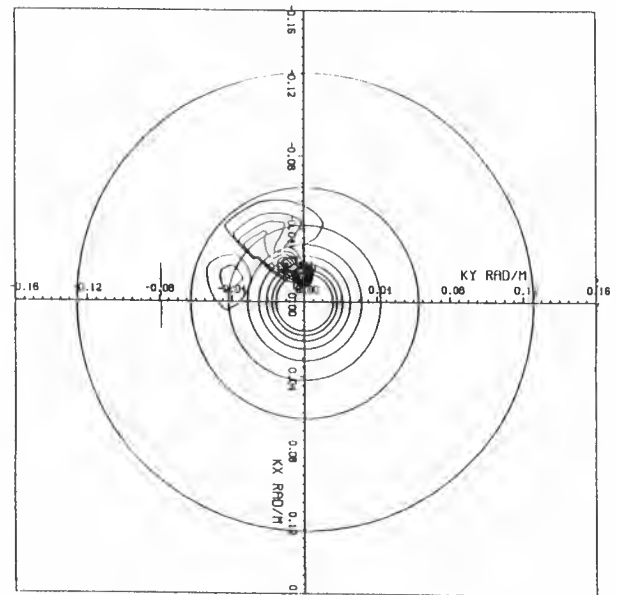


Figure 6 d: The two-dimensional model spectrum at the next grid point east of T10

- b. Interpolation of the isobars to a computational grid of 30 km. Computation of the windfield by a modified Sverdrup-Hesselberg-procedure. Interpolation of the windfield in time to match the time steps of the wave model.
- c. By the numerical wave model HYPAS the CAL/VAL area is covered with a grid of 30 km resolution. The internal time step of the model is 15 min. To catch the influence of the complete North Atlantic Ocean a coarse grid model with a grid size of 150 km and a time step of one hour has been run to provide boundary values at the border of the fine grid. The wave height error that can be achieved with

our model set up is estimated to be 15 % for significant wave heights above 5 m. It can be shown (Günther, Rosenthal 1989) that the error contained in the wind field (which we estimate to be a standard error of 2 m for the wind speed) is the limiting factor for the error of the hindcasted wavefield. An increase in grid resolution therefore cannot improve the accuracy significantly.

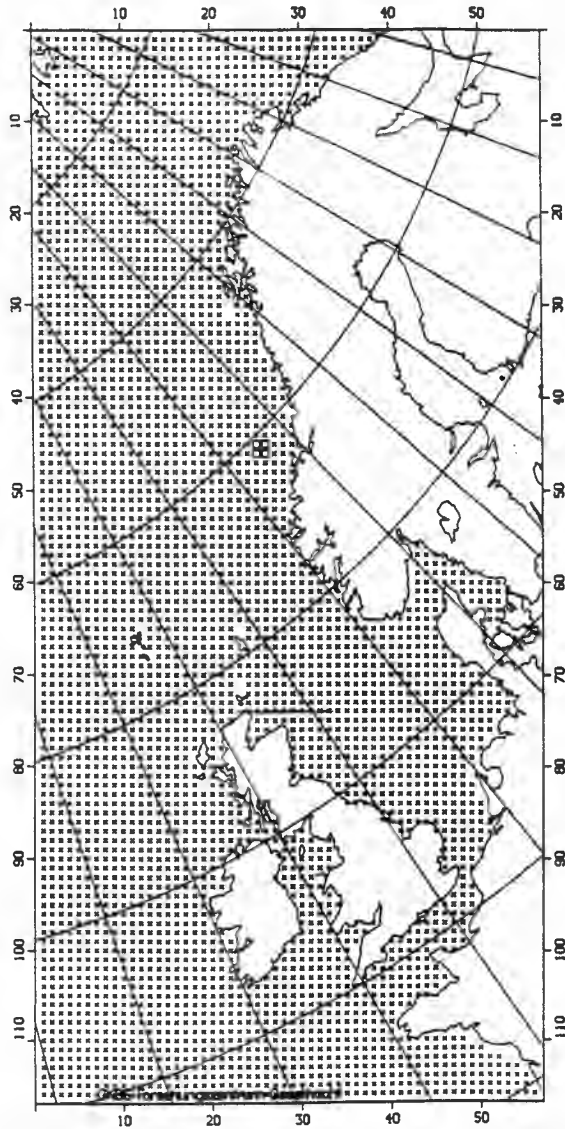


Figure 7: Grid position of the model points for fig. 5 and fig. 6

The windfield at 18.00 UTC is shown in fig. 1 for the coarse grid. For the fine grid we interpolated the windfield to the model time step that is next to the time of the SAR image. The fine grid wind field is shown in fig. 2. The history of the wind field shows a rather stationary isoline pattern with a slowly decreasing wind speed from 12.00 hours until 24.00 hours. The wind in the CAL/VAL area is blowing from SW with a wind-speed of about 15 m/s and the situation looks homogeneous

enough that one might expect an ideal wind wave situation with a typical deep water wind wave spectrum that propagates approximately parallel to the local wind direction. As it turns out the situation is more complicated.

Fig. 3 gives the isolines of significant wave height at 21.15 UTC. The arrows indicate the mean wave direction averaged over all frequencies and directions. For the CAL/VAL area we see waves coming from SW and significant wave height between 5 m and 6 m. A time series of modelled wave parameters for position T10 is given in fig. 4. This may be compared with fig. 1 of Ziemer et al.

To give an impression of the variation of the one-dimensional spectra in space we plotted in figs. 5 a, b, c, d the computed one-dimensional spectra of four nearest model gridpoints to the Tobis buoy location T10. The respective twodimensional spectra are shown in figs. 6 a, b, c, d. Fig. 7 indicates the position of the four grid points.

3. Measuring waves for the CAL/VAL event on 28 Nov. 1991

The System WMR exploits the information from a navigational radar to produce three-dimensional and unambiguous two-dimensional spectra. The corresponding directional waverider measurements from the CAL/VAL period are described in these proceedings in the presentation of Ziemer et al. In their fig. 2 the buoy measured one-dimensional spectra are compared with the respective radar data. The comparison between both data is excellent.

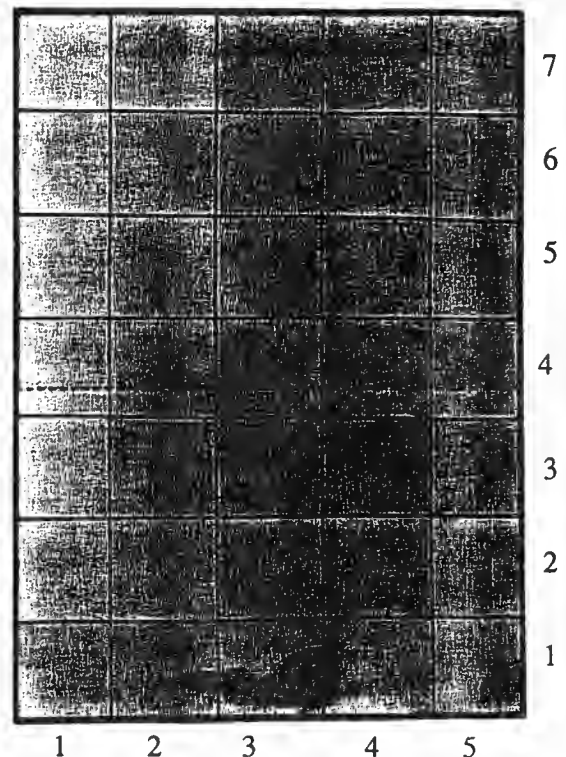


Figure 8: Partition of the most southern SAR image on 28 November, 21:10 h UTC (different scale in along track and cross track direction)

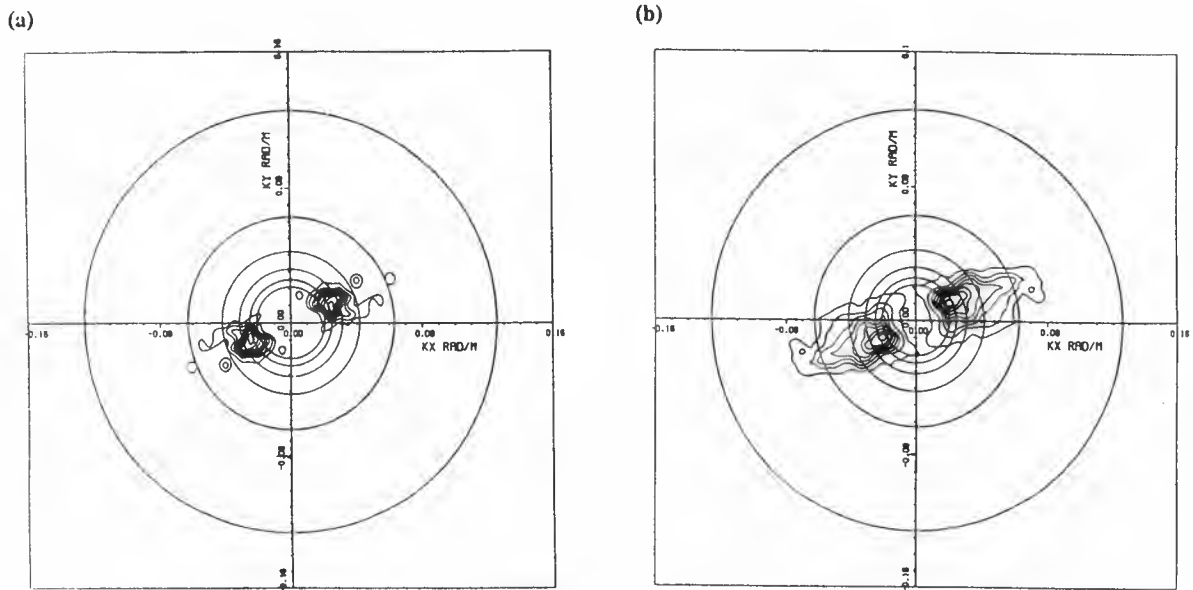


Figure 9: Sample (a) and averaged (b) image spectra obtained from the center of subarea (7,3)

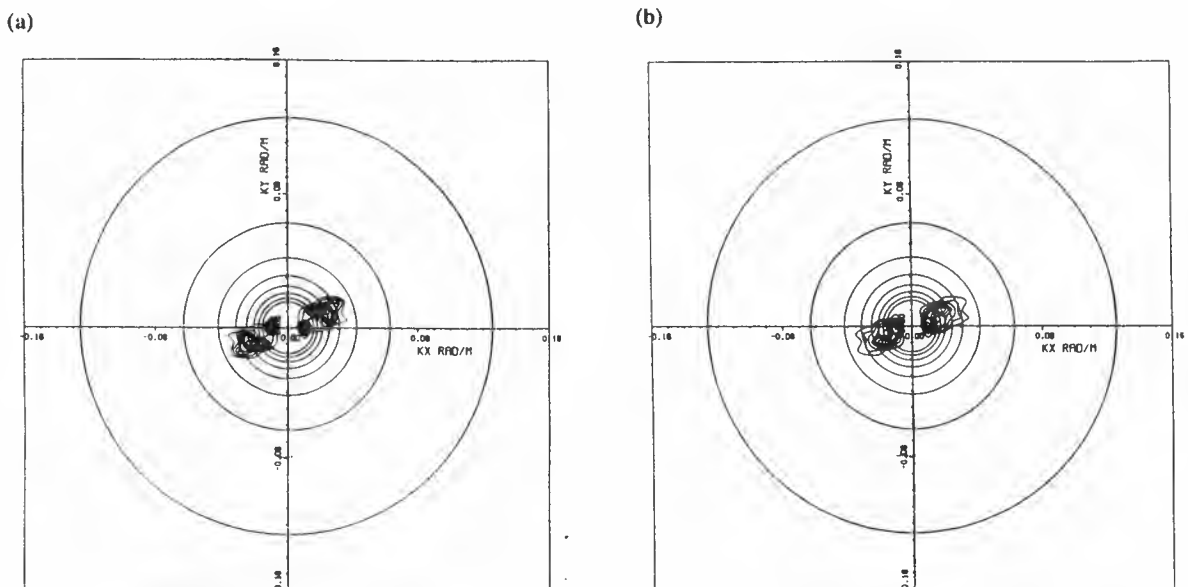


Figure 10: Sample (a) and averaged (b) ocean wave spectra reconstructed from the image spectra of fig. 9

4. Comparing modelled and measured wave data

The measured wave data are subject to the so called statistical sampling variability. This expresses the fact that there is variability in the spectral parameters in spite of stationary weather conditions and stationarity of other possible influences from outside. To keep the variability small averaging of spectra in space or time is necessary, assuming respectively homogeneity or stationarity of the external conditions. A numerical wave model does not have this feature of sampling variability. By construction it resembles the expectation value for the spectrum under the given external conditions. That causes much less spatial and temporal variance in model hindcasts than in actual measured data. As an example we can imagine ideal or-

thogonal fetch conditions. In this case two locations with the same fetch would give identical model results while tow sensors at the same fetch would give different results caused by the sampling variability.

With these facts in mind from figs. 5 and 6 we must draw the conclusion that the situation is not ideally homogeneous since the modelled expectation values of spectra from the corners of a square with 30 km side length show large variations.

The situation is neither especially stationary. This is shown by fig. 3 of [Ziemer et al.]. Also the half-hour averaging in fig.4 f of the same paper indicates a superposition of waves from different origins.

The different wave trains are nicely hindcasted by the numerical model which gives the statistical expectation values for the spectral data. In fig. 6 we can observe the local windsea with a peak at about 0.12 Hz and a swell from SW with a frequency near to 0.05 Hz. This low frequency energy is present also in the buoy data and in the WMR spectra shown in [Ziemer et al.].

5. The ERS-1 SAR data

For convenience we divided the original high resolution SAR image (ERS-1 fast delivery product UI-16, 21.10 UTC) into 7x5 subareas named by their row (1-7, bottom first) and column (1-5, most left first) numbers, as shown in fig. 8. The three subareas closest to the T10 location, namely those with row and column number (7,2), (7,3) and (7,4), have been subsequently treated. In the middle of each subarea a square with side length of 5120 m is divided into 20 rectangular parts of size 1280x1024 m; the latter are subjected to a 2D Fourier transform to obtain image sample spectra. An example for such spectrum, corresponding to the middle of subarea (7,3), is demonstrated in a north up wavenumber frame in fig. 9 a; this sample spectrum has only two degrees of freedom for each grid point in the wavenumber plane and it represents, therefore, a description of the local image grey level variation rather than a close estimate of the expectation image spectrum. The latter, derived by averaging 20 sample spectra, is plotted on fig. 9 b; it has an estimated relative error of about 0.3 (90% confidence) for each spectral value.

Although the reconstruction of ocean wave spectra from SAR imagery runs into difficulties of different nature we have nevertheless applied a procedure described in Lyzenga (1987), after slight modification and involvement of additional parameters. Fig. 10 a,b demonstrates reconstructed ocean wave spectra corresponding to the image spectra of fig. 9 a,b. The reconstructed wave spectra show the correct orientation with respect to direction and the two peaks of swell and wind sea detected by the other instruments and hindcasted by the numerical model.

6. Summary

The comparison of SAR-image-spectra with sea truth and with model results of ocean wave spectra gives encouraging results towards the development of an empirical transfer function to derive wave spectra from their respective SAR-image spectra

Acknowledgement

The support of the Alexander von Humboldt Foundation for one of the authors (V.A.) is gratefully acknowledged.

References

- Ziemer, F., W. Rosenthal, K. Richter, D. Schrader, "Two-Dimensional Wave Field Measurements as Sea Truth for ERS-1 SAR", this issue.
- Günther, H., W. Rosenthal, Interpretation of wave model validation statistic. Proceedings of the 2nd International Workshop on Wave Hindcasting and Forecasting, Vancouver, April 25-28, 1989, Published by Environment Canada, Atmospheric Environment Service, 4905 Dufferin Street Downsview, Ontario M3H5T4.

H. Günther and B. Hansen, The WAM Model and ERS-1. In Proceedings of European 'International Space Year' Conference 1992; Space in the Service of the Changing Earth. Munich, Germany, March 30 - April 4, 1992

D.R. Lyzenga, The Physical Basis for Estimating Wave Energy Spectra from SAR Imagery, John Hopkins APL Technical Digest, vol. 8, pp. 65-69 (1987).

DIRECTIONAL WAVE SPECTRA BY INVERSION OF ERS-1 SAR IMAGERY

H. Johnsen¹⁾, G. Engen¹⁾, H.E. Krogstad²⁾ and S.F. Barstow³⁾

- 1) FORUT Information Technology, P.O. Box 2806, Elverhøy, N-9001 Tromsø, Norway
 2) SINTEF Industrial Mathematics, N-7034 Trondheim-NTH, Norway
 3) OCEANOR A/S, P.O. Box 2514, N-7002 Trondheim, Norway

ABSTRACT

In this paper we present analysis of full resolution ERS-1 SAR wave imagery from the Haltenbanken area recorded during the calibration-validation phase in November-December 1991. Enhanced wave spectra are obtained using first-guess wave spectra either from the numerical wave model WINCH operated by the Norwegian Meteorological Institute, or synthesized from non-directional wave data and meteorological conditions. The inverted spectra are compared to *in situ* directional wave data. It is concluded that the wave imagery from ERS-1 appears to be of excellent quality, and as soon as the RAR modulation transfer functions are properly understood, satellite SAR data will be an important tool for *enhancing* and *extending* conventional wave measurements and results from numerical wave models.

1. INTRODUCTION

The closed form "forward" non-linear ocean-to-SAR spectral mapping [1] represents a major breakthrough in our understanding of the SAR imaging process of ocean waves. A simple derivation of the transform along with some of its analytic properties are discussed in [2], and the derivation is extended to include the range bunching effect in [3]. The "many-to-one" property of the forward transform necessitates an inverse formulation when an ocean spectrum is to be extracted from a SAR image spectrum. A functional minimisation procedure utilising first guess wave spectra was given in [1]. A modified iteration procedure which appears to be more stable has been derived in [3] and is briefly reviewed below.

ERS-1 has turned out to provide excellent imagery of ocean wave fields. Below we report results from six passes over the Haltenbanken area during NORCSEX'91 [4], all showing ocean waves. The SAR spectra from the images have been used as input to the inversion procedure and compared to directional and non-directional wave spectra measured by buoys.

We conclude that the inversion algorithm is very promising although the results demonstrate that the current models for RAR modulation along the range direction are inadequate.

2. THE SAR INVERSION PROCEDURE

The ocean-to-SAR spectral transformation is a sequence of linear and non-linear filters [2]. The SAR image spectrum, S , is obtained from the ocean wavenumber spectrum Ψ by

$$S = V \circ T \circ \Psi$$

where T is the backscatter "RAR" modulation and V the bunching effects due to the surface motion (azimuth) and elevation (range). Scanning distortion is not significant for a satellite carried SAR. Apart from a δ -function contribution at $\mathbf{k}=0$, the SAR spectrum may be expressed as

$$S(\mathbf{k}) = \int_{\mathbf{x}} G(\mathbf{x}, \mathbf{k}) e^{-i\mathbf{k}\cdot\mathbf{x}} d^2x$$

with

$$G(\mathbf{x}, \mathbf{k}) = e^{\mathbf{k}'(\rho_{dd}(\mathbf{x}) - \rho_{dd}(0))} \mathbf{k} \{ 1 + \rho_{Ij}(\mathbf{x}) + i \mathbf{k}'[\rho_{Id}(\mathbf{x}) - \rho_{Id}(-\mathbf{x})] + [\mathbf{k}'(\rho_{Id}(0) - \rho_{Id}(\mathbf{x}))](\mathbf{k}'(\rho_{Id}(0) - \rho_{Id}(-\mathbf{x}))) \}.$$

Here $I(\mathbf{x})$ denotes the (hypothetical) backscatter image and $\mathbf{d}(\mathbf{x})$ the shift vector. The various correlation functions $\rho_{..}$ (scalar or matrix-valued) may all be computed from the ocean wavenumber spectrum and the accompanying transfer functions [2].

The corresponding *quasi-linear* form of the transform [1] is

$$S_{ql}(\mathbf{k}) = \frac{1}{2} e^{-\mathbf{k}'\rho_{dd}(0)} \mathbf{k} \{ | i \mathbf{k}'T_d(\mathbf{k}) + T_I(\mathbf{k}) |^2 \Psi(\mathbf{k}) + | i \mathbf{k}'T_d(-\mathbf{k}) + T_I(-\mathbf{k}) |^2 \Psi(-\mathbf{k}) \}.$$

where T_d is the shift and T_I is the backscatter transfer function.

The least understood mechanism in the forward transform appears to be the *hydrodynamic modulation*. The modulation seems to depend on the surface wind, and a wind dependent expression for the hydrodynamic modulation transfer function was derived in [5]. The derivation is based on a linear description of the interaction between short waves, wind and longer waves using a linear wind model. This transfer function has been applied in the present case where the input wind is taken from weather charts and model data.

The inversion algorithm used below follows with slight modifications the approach in [1]. The cost-functional is minimised in an iterative fashion where, on each step of the iteration, the exact functional derivative of the quasi-linear transform is used to determine the search direction. At step n of the iteration, the functional has the form

$$J = \int_k \{ |\Delta S(\mathbf{k}) - S_0(\mathbf{k})|^2 W_s(\mathbf{k}) + |\Delta \Psi(\mathbf{k}) - \Psi_0(\mathbf{k})|^2 W_\psi(\mathbf{k}) \} l^2 k + (\Delta \mu)^2 W_\mu$$

where

$$\Psi_0 = \frac{\alpha \Psi_n + \beta \Psi_{a \text{ priori}}}{\alpha + \beta} - \Psi_n$$

$S_0 = S_{SAR} - S_n$, $S_n = V \circ T \circ \Psi_n$, and μ is the variance of the shift. The weight functions control the relative weighting between the three terms in the cost-function. Here $W_s(\mathbf{k}) = \gamma \exp[-k_x^2 / 2\sigma_x^2 - k_y^2 / 2\sigma_y^2]$, $\gamma=8$, $\sigma_x = 4\text{m}^{-1}$, $\sigma_y = .3\text{m}^{-1}$, $W_\mu = 1$, whereas W_ψ is a half-plane weighting defined by the centre of gravity of the *a priori* wave spectrum. Furthermore, the parameters α and β allow for a change in the relative weighting between the *a priori* spectrum and the latest updated spectrum. Apart from two examples with $\alpha=\beta=1/2$, we have used $\alpha=1$ and $\beta=0$, which means that the *a priori* spectrum is only used as a first guess and then neglected in subsequent iterations. This puts minimal constraints on the wave spectrum and represents the case of closest match between the SAR spectrum and the result from the non-linear transform.

The cost-functional is minimized with respect to the ocean wave spectrum. After each iteration, the increment $\Delta \Psi$ is calculated from the derivative of the quasi-linear transform, and then added to the current iterate followed by a full non-linear transform. The process is repeated until convergence, *i.e.* until the difference in the cost-functional between two successive iterations is less than a certain pre-defined limit. A detailed derivation of the update equations for $\Delta \Psi$ is given in [3]. The current algorithm has been implemented on an HP work station using the IDL® programming language.

3. THE ERS-1 SAR DATA

The ERS-1 SAR data used below have been received and processed into full-resolution Fast Delivery Image Format at Tromsø Satellite Station. Location, orientation and time are listed in Table 1 and also shown in Fig. 1.

From each scene a sub-image covering roughly 20x20 km² is selected. The sub-image power spectrum of the relative image modulations, $(I-\langle I \rangle) / \langle I \rangle$, is estimated using the periodogram method with 50% overlap and followed by a box-car smoothing. The final spectrum has an RMS spectral variability of 1%, corresponding to about 900 degrees of freedom. The spectra are then corrected for the stationary SAR system response function using featureless ocean scenes, and finally the speckle noise level is estimated and removed from the spectra.

4. OCEAN CONDITIONS AND IN SITU WAVE DATA

During the Cal-Val period, wave and wind observations were taken by an array of wave buoys located in the Haltenbanken area [6], see Fig. 1. Significant wave heights (H_s) were about normal for the time of year averaging about 3.5 m. During

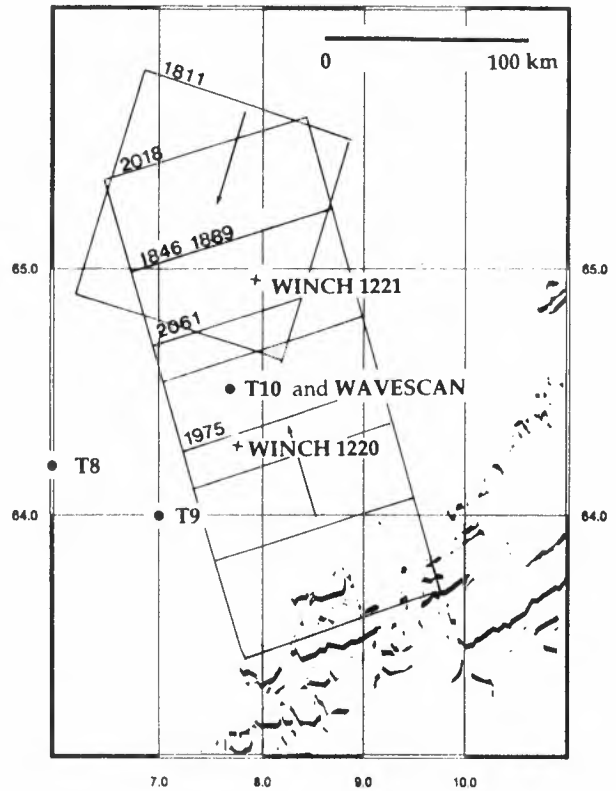


Fig. 1: Location of SAR images, wave buoys and grid points for the WINCH model (T8-10: non-directional "Tobis" buoys. WAVECSAN: heave/pitch/roll buoy).

Table 1: Full resolution ERS-1 scenes

Orbit	Date and time	Centre position	Azimuth dir.
1811	20 Nov. 10.17	65.2N, 7.5E	197 deg.
1846	22 Nov. 21.10	64.6N, 8.1E	343 deg.
1889	25 Nov. 21.10	64.7N, 8.0E	343 deg.
1975	01 Dec. 21.10	64.0N, 8.5E	343 deg.
2018	04 Dec. 21.10	65.0N, 7.8E	343 deg.
2061	07 Dec. 21.10	64.3N, 8.3E	343 deg.

November, weather was of a westerly type with low pressure systems moving from the Atlantic into the Norwegian Sea. The wind and the wind sea were mostly south to westerly together with ever-present Atlantic swell. From early December high pressure built up over the southern Norwegian Sea resulting in variable wind directions. Fairly strong south westerlies out in the Atlantic to the south west of Iceland resulted in continuing background swell.

No wind or directional wave measurements were available before 23rd November so it is difficult to be sure of the detailed wave conditions. On the 20th at 21 UTC wave heights were relatively low at about 1.7 m with probably quite a complicated directional spectrum, the wave height data from station T9 suggests a 13 sec. Atlantic swell and a local wind sea (westerly) peaking at 7 - 8 sec.

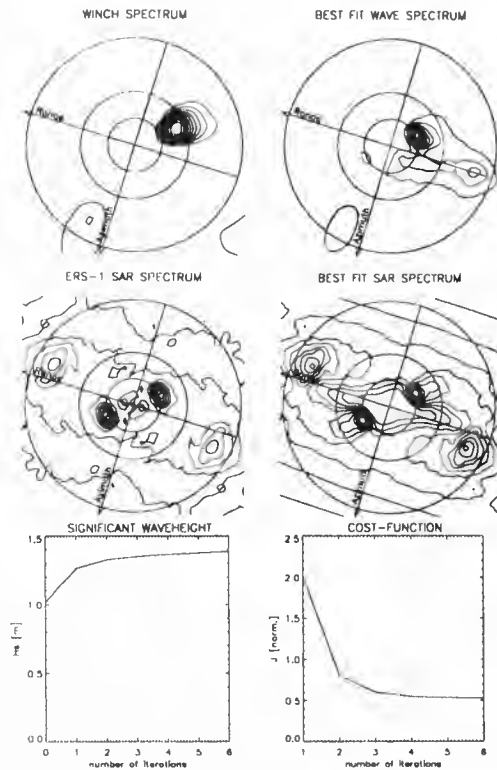


Fig. 2: Inversion for image from Orbit 1811 (20Nov91), $\alpha=\beta=1/2$.

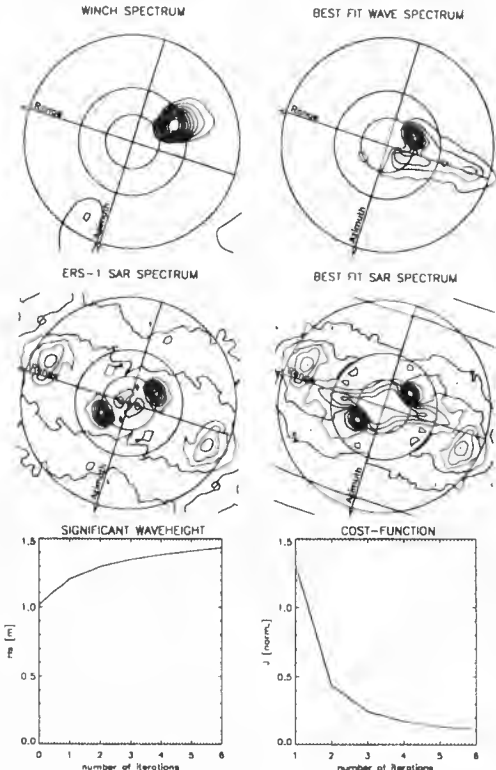


Fig. 3: Inversion for image from Orbit 1811 (20Nov91), $\alpha=1, \beta=0$.

On the 22nd at 21 UTC wave height was around 2.5 m with north westerly swell from a storm which had moved past the previous day peaking at 9 - 10 secs. and an increasing local wind sea veering from south east to south west across a front lying east-west over Haltenbanken. The local sea probably had not exceeded 6 -7 secs. in wave period at this time due to the short duration. A secondary Atlantic swell was possibly also present.

Directional wave measurements are available from the WAVESCAN buoy from the 25th November event so that a more accurate ground truth is then available. At 21 UTC on that day waves were predominantly south westerly with a significant wave height of 3.5 m and peak period around 12 secs. Wind speed was very low locally (< 1 m/s), a temporary lull in the otherwise strong southwesterlies, as a frontal system approached Haltenbanken. On the 1st December high pressure had built up, winds were moderate and westerly as were the waves with 2.7 m significant wave height measured by WAVESCAN.

By the 4th December the high was located between Scotland and Iceland and fairly strong northerlies resulted at Haltenbanken. Crossing seas were present with a continuing westerly swell (11 secs.) together with the northerly wind sea (8 secs.) giving H_s of 2.4 m. By the 7th December the high had moved south and was positioned over the southern North Sea. A powerful low was located west of Svalbard and winds were as a result strong and westerly in the Norwegian Sea. At Haltenbanken winds were south westerly and near gale force at the time that the image was taken. The wave spectrum was bimodal with a westerly swell at 11 - 12secs. and a local wind from south west at about 7 secs.

5. RESULTS

From an application viewpoint, the important question is whether SAR derived wave spectra can provide additional information about the directional ocean wave spectrum. This can only be answered by comparing the results from the inversion procedure to simultaneous *in situ* buoy or other relevant measurements of the wave spectrum. In the graphical presentations below, all spectra are wavenumber spectra with circles representing wavelengths of 300m, 150m and 75m from inner to outer. Geographic north is upward, the positive azimuth axis is the satellite flight direction, and the positive range direction is the radar look direction. The *a priori* spectrum is denoted WINCH, whereas BEST FIT spectra are results from the inversion. The development of the significant wave height and the cost functional with the iteration number are also shown.

The *a priori* spectra are based on the WINCH wave model for the orbits 1811 and 2018. For the other cases, directional wave spectra have been synthesized by means of non-directional data and weather charts, see Sec. 4. As a test, the WAVESCAN data were not used in this construction.

For orbit 1811 (Nov. 20) $H_s=1.7$ m and the modulation is weak. However, the SAR image spectrum still shows two modes (denoted *swell* and *wind sea*, for simplicity), see Fig. 2. In the result from the inversion, the wavelength of the swell mode appears to be shifted towards longer wavelengths, but having the same direction as the model spectrum. The dominant wind mode system is dramatically changed, and a new wave system is observed with a peak wavelength of 90m. This

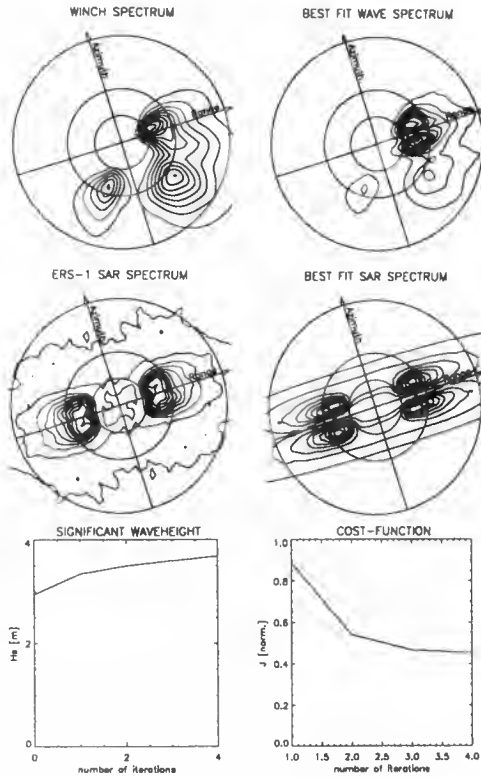


Fig. 4: Inversion for image from Orbit 2018 (4Dec91), $\alpha=\beta=1/2$.

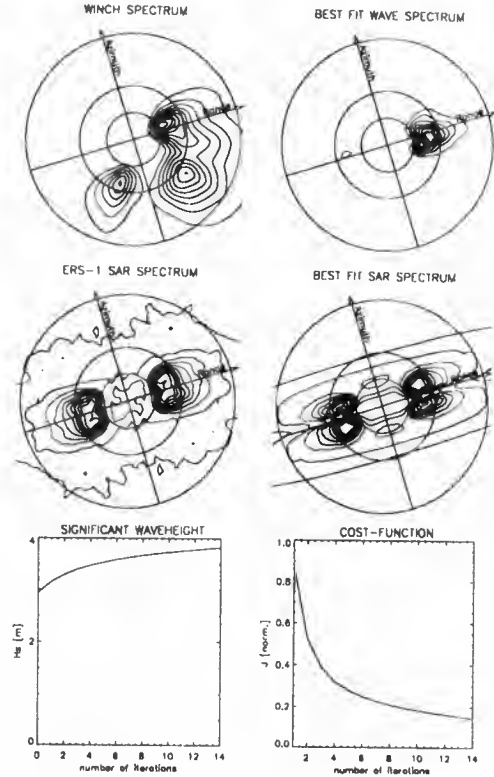


Fig. 5: Inversion for image from Orbit 2018 (4Dec91), $\alpha=1, \beta=0$.

system is actually observed in the non-directional data from that date, see Sec. 4. The second wind mode system observed in the WINCH spectrum remains unchanged during the inversion because it is not observed by the ERS-1 SAR. The inversion shown in Fig. 2 has been run with $\alpha=\beta=1/2$, and Fig. 3 shows the corresponding results if the WINCH spectrum is neglected in the cost-function ($\alpha=1, \beta=0$).

On Dec. 4 (orbit 2018), the buoys give $H_s=2.4\text{m}$ and a strong modulation is observed, see Fig. 4. Also here, $\alpha=\beta=1/2$. The peak of the swell mode is somewhat shifted towards shorter wavelengths, but the wind modes shown in the WINCH spectrum are only observed in the SAR image spectrum through their

contribution to the observed azimuth cut-off. The inversion with $\alpha=1, \beta=0$ is shown in Fig. 5. Obviously, the wind modes are not reproduced in this case.

For the remaining four cases, the WINCH spectra were (currently) not available, and the *a priori* directional distributions had to be synthesized from weather charts. The *cos-2s* directional distribution was used as a basis, but since the spectra were temporarily converted to the WAVESCAN data format (four directional Fourier coefficients), the resulting *a priori* spectra turned out to be artificially bimodal in three of the cases. However, this bimodality vanishes completely in the inverted spectra as shown in figs. 6-9, thus demonstrating the effectiveness of the inversion procedure. The inversion used $\alpha=1, \beta=0$ for all these cases. On November 22 the Atlantic swell gives a more important contribution than suspected from the weather charts (sec. 4).

Directional data from WAVESCAN exist from November 25, and first guess spectra, results from the inversion procedure, and corresponding WAVESCAN spectra are compared in Fig. 10. It is immediately clear that although the first guess spectra are rather bad in some cases, the results from the inversion are much closer to the WAVESCAN spectra. It is also obvious that the inverted spectra are too large along the range direction. This can immediately be attributed to a too weak RAR modulation in the range direction. In order to match the measured SAR spectrum, the inversion procedure enhances the wave spectrum too much in that direction. This effect apparently also causes the significant wave height to increase above the most probable value as summarised in Table 2. Obviously, putting more weight on the *a priori* spectrum will tend to stabilise the significant wave height.

Table 2: Summary of significant wave heights.

a: $\alpha=\beta=1/2$, b: $\alpha=1, \beta=0$

Orbit	A priori estimate (m)	Inversion result (m)	Ground truth (m)
1811a	1.0	1.4	1.7 ± 2
1811b	1.0	1.4	1.7 ± 2
1846	2.6	2.7	2.6 ± 2
1889	3.5	4.4	3.5 ± 3
1975	2.7	2.8	2.7 ± 2
2018a	3.0	3.8	2.4 ± 2
2018b	3.0	3.6	2.4 ± 2
2061	2.5	2.4	2.5 ± 2

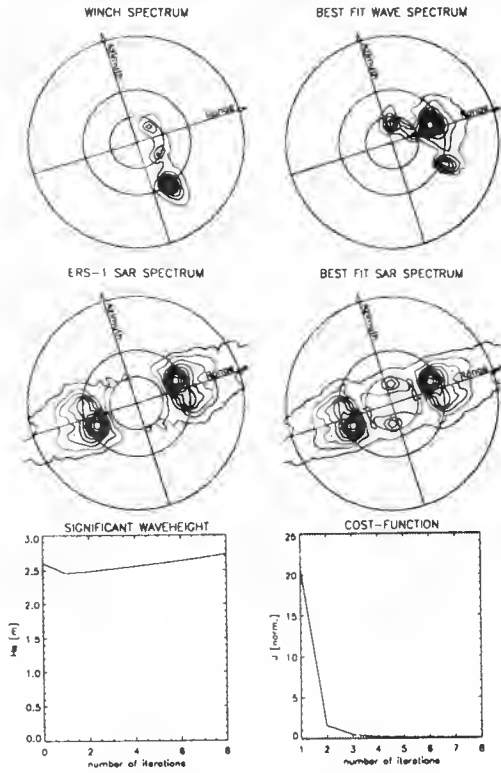


Fig. 6: Inversion for image from Orbit 1846 (22Nov91), $\alpha=1, \beta=0$.

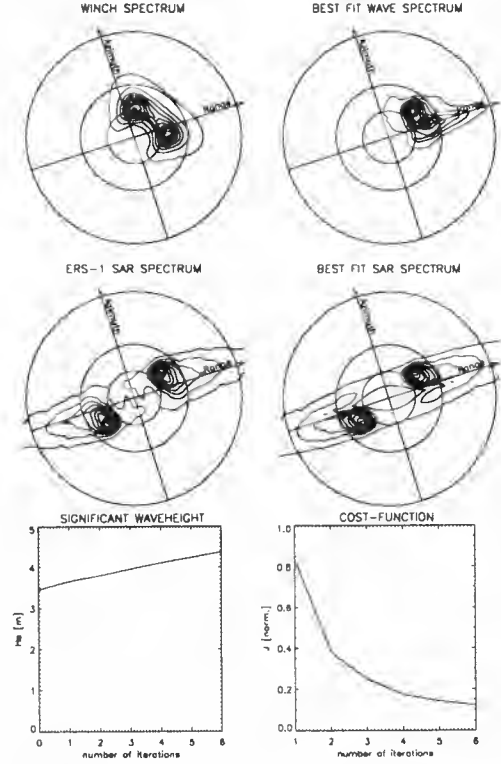


Fig. 7: Inversion for image from Orbit 1889 (25Nov91), $\alpha=1, \beta=0$.

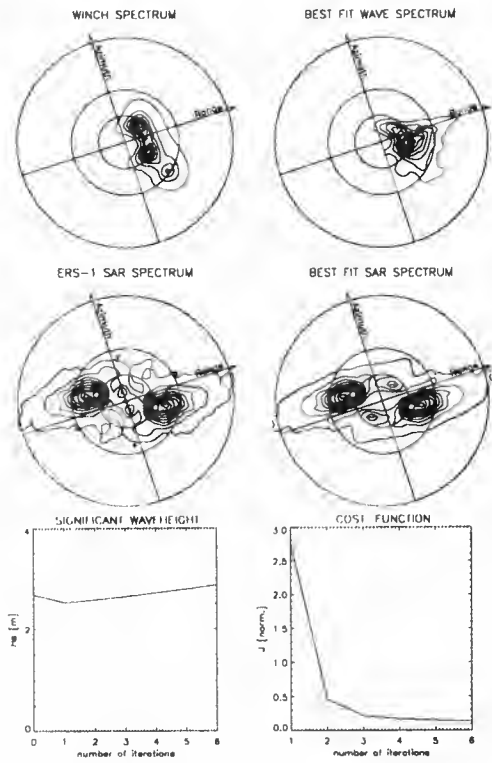


Fig. 8: Inversion for image from Orbit 1975 (1Dec91), $\alpha=1, \beta=0$.

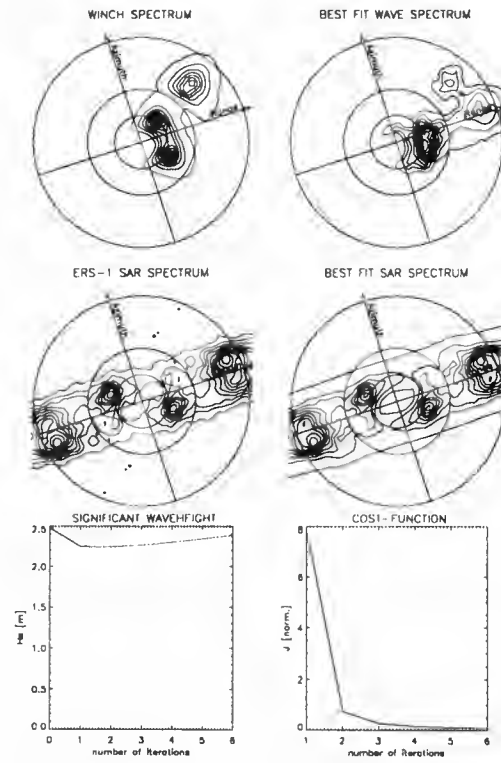


Fig. 9: Inversion for image from Orbit 2061 (7Dec91), $\alpha=1, \beta=0$.

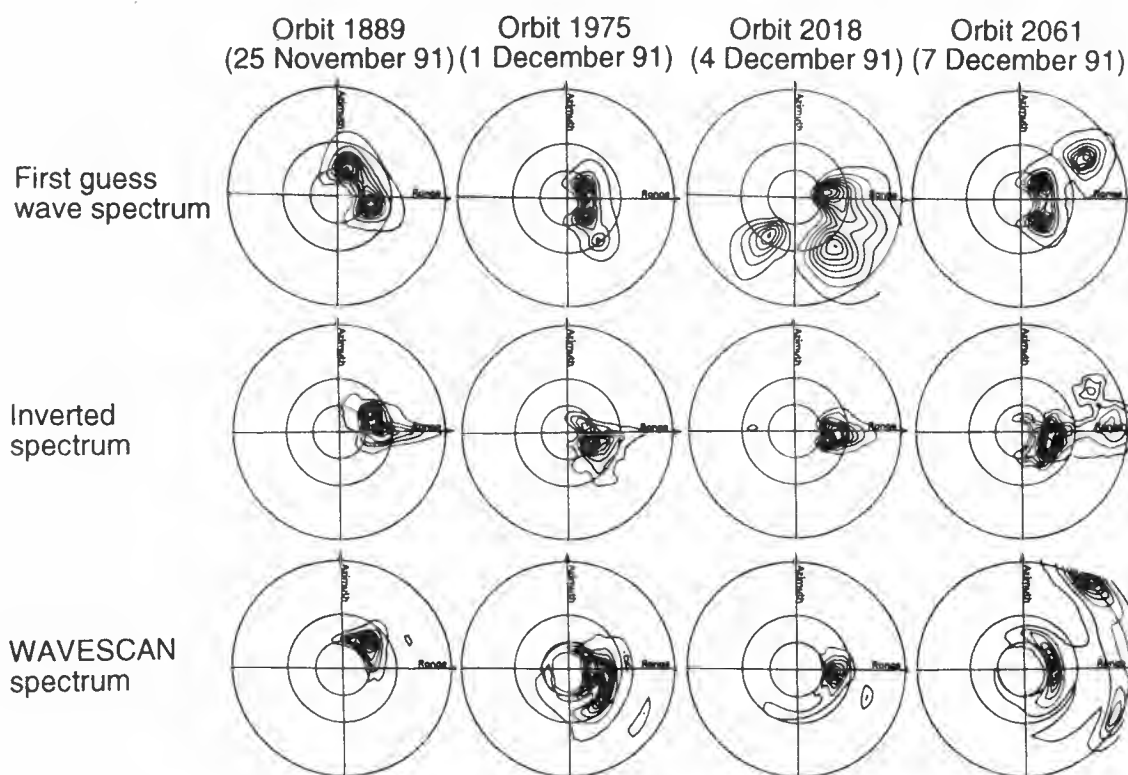


Fig. 10: A comparison between first guess spectra, the results from the inversion and the WAVESCAN spectra.

6. CONCLUSIONS

The present paper has demonstrated the possibility of using SAR wave imagery for enhancement of instrumental and numerical wave data. The forward transform and an inverse formulation with a priori spectra from numerical wave models or simply intelligent guesses seems to be a promising way of utilizing the SAR data for ocean surveillance. Clearly, the ERS-1 wave mode products will be valuable from this point of view.

The current implementation of the inversion algorithm appears to be both stable and robust. Typically 6 to 20 iterations are needed to obtain a reasonable convergence. This means that the inversion may be carried out within seconds on a modern super-computer.

The RAR modulation in the range direction seems to be the central remaining question which has to be resolved before the inversion algorithm can be taken into routine use.

Acknowledgments We thank Tromsø Satellite Station for providing the SAR images, The Norwegian Meteorological Institute for providing WINCH directional spectra and meteorological charts, and OCEANOR A/S for providing buoy wave data. This research was carried out under NTNf/Norwegian Space Centre Contract No. 8.3.303.91.2 with additional funds from the Ocean Surveillance Centre (HOV), Bergen.

REFERENCES

1. Hasselmann, K., Hasselmann, S., 1991, On the non-linear mapping of an ocean wave spectrum into a Synthetic Aperture Radar image spectrum and its inversion, *J. of Geophys. Res.*, **96**, No. C6, pp.10,713-10,729.
2. Krogstad, H.E., 1992, A Simple Derivation of Hasselmann's Non-linear Ocean-Synthetic Aperture Radar Transform, *J. of Geophys. Res.* **97**, No C2, pp 2421-2425
3. Engen, G., H. Johnsen and H.E. Krogstad, 1992, Inversion of Synthetic Aperture Radar Ocean Image Spectra, *IGARSS'92*, Houston, May 1992.
4. NORCSEX Group, 1991, NORCSEX'91 Science and Operation Plan, Nansen Environmental and Remote Sensing Center, October 1991.
5. Engen, G., 1991, Et studium av de ulike modulasjonsmekanismene i et SAR havbølge inversjons-system, Thesis, Univ. of Tromsø, December 1991.
6. Bern, T. I. and S.F. Barstow, 1992, Wind and Wave Measurements During Extreme Situations. These Proceedings.

COASTAL OCEAN STUDIES WITH ERS-1 SAR DURING NORCSEX'91

J.A.Johannessen¹⁾, R.A.Shuchman²⁾, K. Davidson³⁾, Ø.Frette¹⁾, R.Onstott²⁾, O.M.Johannessen¹⁾

¹⁾ NERSC, Bergen, Norway; ²⁾ ERIM, Ann Arbor, Mi., US; ³⁾ NPS, Monterey, Ca., US.

ABSTRACT

The NORwegian Continental Shelf EXperiment-NORCSEX'91 was conducted between 6-29 November 1991 during the commissioning phase of ERS-1. In this period about 30 SAR scenes were obtained at a regular interval of three days and complemented with *in-situ* observations of wind-wave-current and their interaction collected from ship and moorings. The integrated data base reveal that SAR images document expressions of; 1) mesoscale ocean current circulation pattern including frontal boundaries and eddies; 2) wave-current refraction; 3) internal waves; and 4) rapid mesoscale wind field variations. In some cases impact of radar imaging geometry on these image expressions are found. The expressions of oceanic circulation features are limited by both high and low wind speed. These preliminary results will be presented and discussed.

ERS-1, C-band SAR, Current boundaries, Wind fronts

1. Introduction

The Norwegian Continental Shelf Experiment NORCSEX'91 was conducted off the west coast of Norway centered to Haltenbanken (64°30'N, 9° E) from 6-29 November 1991. The primary objectives of NORCSEX'91 was to demonstrate and validate the ERS-1 detection capabilities of:

- * current boundaries including eddies;
- * near surface mesoscale wind fronts;
- * sea state conditions;

and their interaction in weather conditions ranging from moderate to extreme. In particular the study focused on the ERS-1 C-band SAR imaging capabilities. This required access to a dedicated fast processing and distribution system. At the Norwegian national receiving station, Tromsø Satellite Station (TSS), data were received and processed to a geocoded image on a CESAR processor at an approximate speed of 6-8 minutes per 100 km * 100 km scene. Subsequently full resolution (16 m by 20 m) and low resolution (80 m by 100 m) images were transmitted to Nansen Center in Bergen via NORSAT B/Idun telecommunication satellite system (2 MegaBit/s) with Spacetec as operator in Tromsø. At NERSC these data were further processed and value added on an image processing system, and interpreted images were finally faxed to R/V Håkon Mosby within 3 hours of SAR data acquisition. This ensured possibilities to steer the ship into regions where the SAR images expressed interesting features. In turn near synoptic collection of ground truth data were obtained providing the geophysical data necessary to offer improved interpretations of the images.

The paper is outlined with a short description of the NORCSEX'91 field campaign including a data overview in section 2; preliminary results of the SAR detection capabilities in section 3; and a brief summary in section 4.

2. Data overview

The experimental region including an indication of the SAR swath from the ascending track is shown in Figure 1.

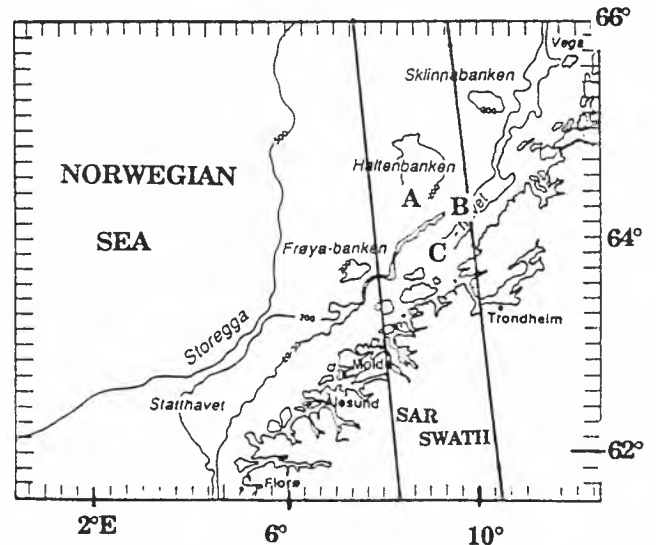


Figure 1. Map of the experimental region and the overlapping SAR swath.

An overview of the multiplatform- and multisensor data collection is given in Table 1 including satellites, ship and moorings. Table 2 provides an overview of available SAR data collected within the experimental area from 20 October to 7 December. The comments indicate the main features identified in the images.

PARAMETER	OCEAN CURRENT FRONTS EDDIES	SURFACE WAVES WAVES SWELL	INTERNAL WAVES	NEAR SURFACE WINDS	AIR-SEA STABILITY
SHIP					
ADCP	X			X	
SEASOAR	X				
WEATHER STAT.				X	X
SCATTEROMETER	X		X	X	X
VIDEO CAMERA		X	X		
MOORINGS					
CURRENT	X				
ERS-1					
AMI IMAGE MODE	X	X	X	X	X
ALTIMETER	X	X	X	X	
ATSR	X				X
DMSP				X	
SSM/I				X	
NOAA					
AVHRR	X				X
Complementary Operation service by HOV center	X	X	X	X	

Table 1: Overview of platforms/instruments and corresponding primary observed geophysical quantities/features.

In regards to the SAR detection capabilities of current features and wind fronts the most important geophysical quantities to measure are the upper ocean currents, the boundary layer stability, the near surface wind vector in vicinity of the SAR detected frontal boundaries. The temporal and spatial variations of these quantities were regularly measured from a ship mounted Acoustic Doppler Current Profiler (ADCP), towed undulating Seasoar (CTD), six current meter moorings separated upto 100 km, thermistors and sonic- and cup- anemometers. In addition the wind wave and swell field were monitored from directional wave buoys and Tobis buoys.

Date.	Time (UTC).	Data Source	Comments
21.08	21:10:10	Tromsø	Cyclonic eddy.
20.10	21:10:10	Tromsø	Dominated by wind.
23.10	21:10:10	Tromsø	Current shears and internal waves.
26.10	21:10:10	Tromsø	Strong current shears.
29.10	21:10:10	Tromsø	Oil spill and current shears.
01.11	21:10:13	Kiruna	Internal waves and current shears.
04.11	21:10:10	Tromsø	Dominated by wind.
07.11	21:10:16	Kiruna	Wind front.
10.11	21:10:15	Kiruna	Wind streaks and current shear.
13.11	21:10:09	Kiruna	Wind and current fronts.
16.11	21:10:10	Tromsø	Wind front.
19.11	21:10:10	Tromsø	Current front and wind front.
20.11	10:47:55	Tromsø	Wind fronts and rain cells.
22.11	21:10:10	Tromsø	Current shears.
23.11	10:47:55	Tromsø	Current shears.
25.11	21:10:10	Tromsø	Current shears and internal waves.
28.11	21:10:10	Tromsø	Wind front.
01.12	21:10:09	Tromsø	
04.12	21:10:10	Tromsø	Current shears.
07.12	21:10:10	Tromsø	Weak current shears.

Table 2. Overview of available NORCSEX'91 SAR data

Near surface current of order 1 m/s was observed in the Norwegian Coastal Current flowing northeastward along the coast. The sea surface temperature changed from about 9°C in this current to about 8°C in the North Atlantic Norwegian Current located further offshore. On the other hand the current shear across this relatively weak temperature front was of the order of 10^{-4} s^{-1} . Throughout the first 18-20 days of the field campaign unstable stratification on the average of about -3°C was encountered in the atmospheric boundary layer. Passages of several storms were encountered with 10 minutes average wind speed exceeding 20 m/s sometimes accompanied by significant waveheights of about 8-10 m. Between these storms the winds occasionally dropped to less than 2-3 m/s. The corresponding upper ocean and lower atmospheric interaction provided a variety of sea surface conditions that are manifested in the series of collected SAR images. We will address some of these image manifestations in more details in the next section.

3. SAR Image expressions

The vertical polarization C-band SAR instrument primarily senses the spatial distribution of the 0.07 m short gravity waves on the ocean surface at a resolution of about 30 m through a resonant Bragg backscattering mechanism (Ref. 1). The illuminated area (swath width) on ground is 100 km, and is displaced about 200 km off the satellite sub-track corresponding to a center radar incidence angle of 23°. The Bragg scattering waves are developed in

response to the wind stress. These short waves are in turn modulated by longer gravity wind waves and swell (Ref. 2). However, as demonstrated in Seasat SAR and numerous airborne SAR images, the spatial distribution of these short gravity waves is also correlated with a number of significant larger scale processes including local wind field variations, mesoscale circulation patterns and internal waves (Refs. 3-6). Among the most frequently reported circulation features detected in SAR images are mesoscale and sub-mesoscale eddies, in particular in the Gulf Stream, along the marginal ice zones and in shelf and coastal currents. In addition, the presence of pollutant oil spill and natural slicks at the sea surface can be expressed as dark features in SAR images, through damping of the Bragg waves (Refs. 7, 8).

The motivation behind the study reported here is to document that wind, current and internal wave modulated frontal structures can be distinguished and classified in SAR imagery. This is schematically illustrated in Figure 2 where the SAR manifests the surface roughness change due to wind shift as a steplike transition zone from low to high backscatter intensity induced by the change in wind speed and direction. On the other hand the backscatter modulation induced by wave-current interaction along a current front or eddy can be expressed as a narrow, bright or dark curving signature. These fronts are again distinguished from internal waves since they are expressed as a chain of regularly spaced bright and dark backscatter zones.

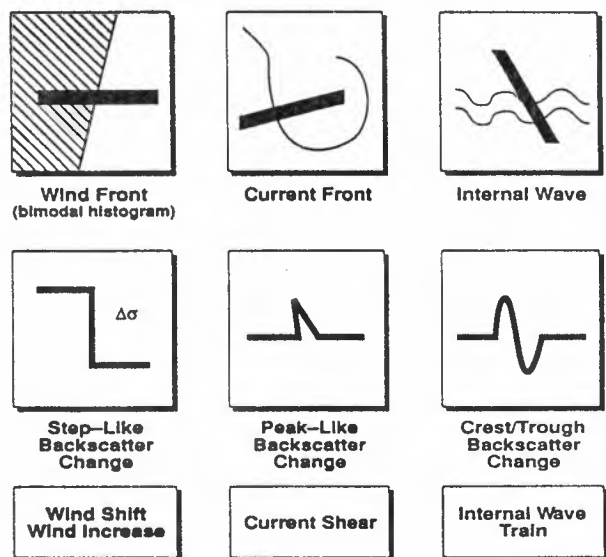


Figure 2. Proposed SAR image classification system.

SAR DETECTED FRONTS: In Figure 1 the labels A, B and C mark the specific geographical locations within the first 100 Km * 100 Km ascending SAR scene after the crossing of the land-ocean border. They respectively represent the sites where expressions of current boundaries, internal waves and a cyclonic eddy are repeatedly identified in SAR images (see also Table 2). In general the Norwegian Coastal Current in region A is steered northeastward between the bank and the coast, while a weak anticyclonic flow of mostly Atlantic water usually appears to be trapped on the bank. In turn a current front with cyclonic current shear is formed at the boundary between the two characteristic currents (Ref. 9). This is documented in the temporal variations of the near surface current as obtained at the two current meter moorings located on each side of the front (Figure 3a), and in the spatial changes of the

upper ocean current across the front as obtained from the ship mounted ADCP (Figure 3b) during NORCSEX'91. The maximum current exceeds 1.2 m/s in the NCC while the current shear across the front reaches up to $0.5 \cdot 10^{-3} \text{ s}^{-1}$. The average semidiurnal tidal current in the region was estimated from the moorings to be about 0.10 m/s.

In the SAR image obtained on 26 October an expression of a meandering frontal boundary is seen extending across the image from near to far range (Figure 4). A few places the front splits into several meandering fronts, and narrow zones are expressed by either elongated high or low backscatter return. We interpret these expressions to be the manifestation of the above mentioned current front including meanders and eddies. The interaction of the shearing current along the front and the surface waves can lead to changes in the surface roughness which are detected by the SAR. The apparent shifts from high to low backscatter may be caused by effects of imaging geometry. The largest spectral perturbations, or departures from equilibrium spectra with the local wind, typically occur at wavelengths of the order of 1 m (Ref. 10). Both at longer wavelengths where the group velocity becomes much larger than the current speed, and at shorter wavelengths where the relaxation effects play a predominant role, this spectral perturbation decreases. This is supported by a comparison of a collection of multispectral SAR images obtained with the NASA DC-8 C-, L- and P-band SAR flight of the Norwegian Coastal Current last summer where the P-band (0.68 m) is clearly most sensitive to surface roughness variations induced by current fronts.

overpasses the wind speed remained between 4-10 m/s, while the boundary layer stratification remained unstable (-3°C) up to 20 November when it gradually became neutral as a result of temperature increase in the air.



Figure 4. 100 km * 100 km SAR image obtained on 26 October. Expression of several frontal boundaries are clearly identified. Resolution is 100 m. Directions of range and azimuth are marked.

Further analyses of the SAR detection capabilities of current boundaries will be done by employing the SAR image simulation model discussed in Ref. 10.

SAR DETECTED INTERNAL WAVES: The SAR expressions of internal waves identified in region B are located close to a shallow topographic plateau extending northeastwards from the island of Frøya. We assume that they are generated by tidal interaction with the steep slope along this plateau. From the SAR image we estimate that the internal waves have a wavelength of about 3 km and they extend westwards from the generation region near the plateau. That means that they are propagating in a direction opposing the strong northeastward NCC.

The oceanographic conditions across the internal wave train were sampled with towed Seasoar and ADCP. The spatial variations in the temperature- and salinity profiles reflect the shape of the internal wave with an amplitude of about 5 m centered at the mean pycnocline depth of 20 m. The wavelength of about 3-4 km agrees with that estimated from the SAR image. Regular variations in the upper ocean currents of about 0.10-0.20 m/s furthermore reflect the circulation pattern in the upper mixed layer induced by the propagating internal wave train.

Detailed analyses of the near surface wind stress variations and the complementary surface roughness changes obtained from the scatterometer measurements will provide opportunities to study the behavior of the surface layer across this internal wave train.

SAR DETECTED EDDY: The 5 km cyclonic eddy in region C (Figure 1) was depicted in the first SAR image received at Tromsø Satellite Station at 21:10 UTC on 21 August 1991 (Figure 5). The SAR image manifests the existence of the eddy by the dark low backscattering lines (with a width of 200 m to 500 m) outlining a cyclonic spiral with an approximate diameter of 5 km. Apart from standard weather observations along the coast reporting southwesterly wind between 3-5 m/s, no surface data are

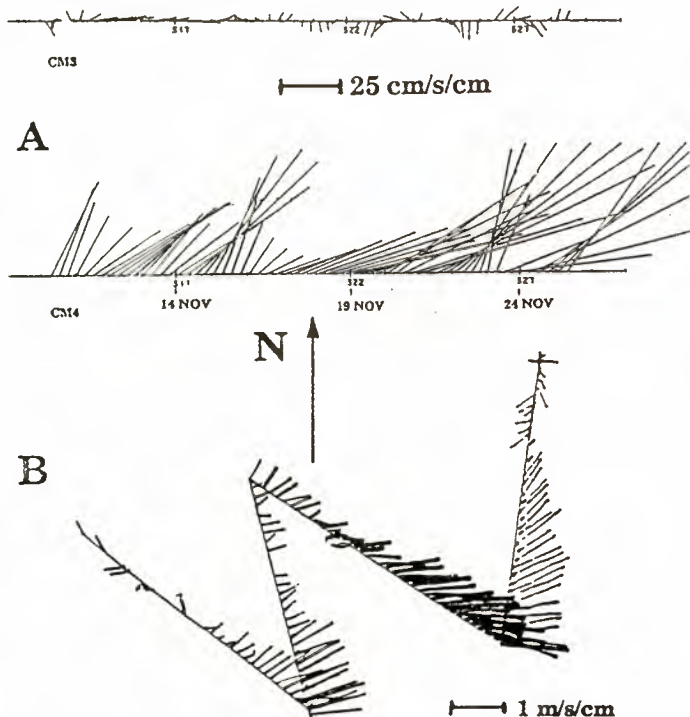


Figure 3. a) Comparison of temporal variations in the current at 25 m depth below surface at CM3 and CM4; b) spatial variations in the current at 15 m depth between CM3 and the coast.

From the sequence of 19 SAR scenes regularly collected between 20 October and 7 December evidence of frontal expressions assumed to be modulated by the wave-current interaction along the shearing frontal boundary are clearly identified in 6 images (see Table 2). During all these SAR

available to offer sufficient analysis of the physical (and biochemical) conditions in the eddy, in particular along the dark spiraling lines. In spite of this we interpret the low backscattering lines to be expressions of small scale turbulence aligned in the direction of the larger scale eddy orbital motion. This turbulence leads to convective motion in the water that can bring organic material present in the upper layer to the surface where it can remain as a microlayer of natural surface film (Refs. 8, 11). As the concentration of this surface film (surfactant molecules) increases due to for example converging currents, it can reach sufficient pressure to inhibit growth of capillary and short gravity waves at C-band. This damping of the small scale surface roughness prevents the radar echos from the surface to maintain its strength leading to manifestation of dark features or surface slicks. This imaging mechanism is characteristically different from that suggested to be dominant for the frontal boundary expressions reported above. Again these expressions of dark spiral lines are expected to disappear at higher winds (10 m/s) since wind induced mixing in the upper layer will redistribute the surface slicks and prevent such damping.



Figure 5. SAR image of 5 km cyclonic eddy assuming expressed by presence of surface slicks.

We lack a sequence of SAR images to study the temporal characteristics of this eddy, i.e. is it forming, fully developed or decaying. In turn we cannot precisely determine if the 5 km in diameter spatial dimension represents the fully developed size of the eddy. Despite this the synoptic SAR image manifestations of surface convergence in the eddy and its rotational direction are clearly of importance for studies of mesoscale coastal circulation. The combination of such SAR detected mesoscale eddies and results of numerical ocean circulation models is shown to be a powerful technique in coastal ocean studies (Ref. 12).

WIND FRONTS: In Table 2 it is also commented that several SAR images manifest the presence of wind fronts. As schematically illustrated in Figure 2 they have a distinct "steplike" backscatter expression. In Figure 6 the SAR obtained on 20 November indeed shows this characteristic expression. Comparison to analyzed wind fields from this day are in good agreement. The center of the low pressure is located to the northeast of the SAR image, and the wind direction in the scene is almost parallel to the frontal orientation as indicated by the streak pattern in near range.

The analyzed map shows that the wind changes gradually from 15 m/s to 10 m/s while the SAR image indicates that the wind speed undergoes a series of steplike decrease across the scene from near to far range.

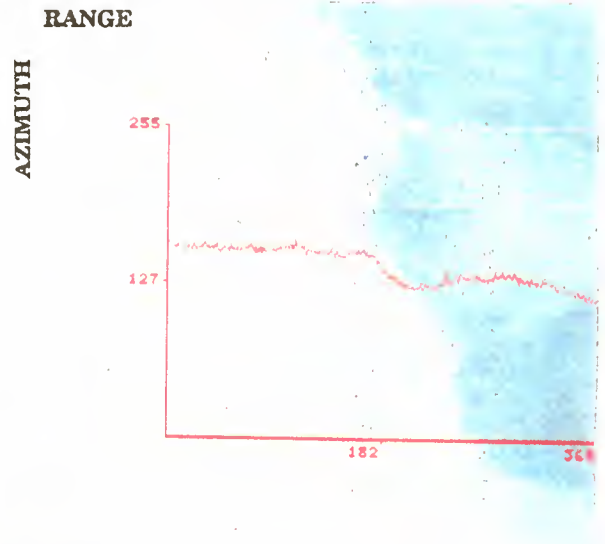


Figure 6. SAR image obtained on 20 November showing the steplike change in radar cross-section in correspondance with the rapid change in wind speed.

On 13 November another wind front was imaged by the SAR and this time it was crossed with the ship. A blowup of the SAR scene with the backscatter profile superimposed is shown in Figure 7a, and the corresponding wind speed measurements across the front from the ship is shown in Figure 7b indicating that the wind speed varied between 2-6 m/s.

Further discussion of different characteristic mesoscale wind field variations in this coastal region will be provided during the presentation.

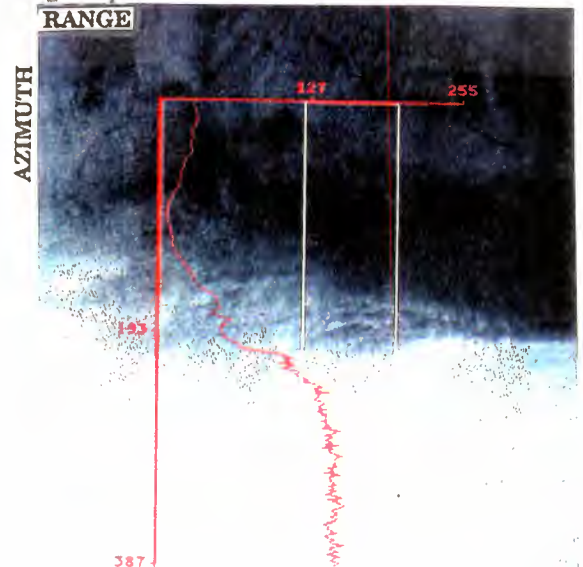


Figure 7. a) SAR image obtained on 13 November with the backscatter profile averaged within the "white box" superimposed.

SESSION - V
SPECIAL TOPICS

INTERPRETATION OF ERS-1 SCATTEROMETER DATA OVER SEA ICE

Alain Cavanié, Francis Gohin

Centre IFREMER de Brest, FRANCE

ABSTRACT

ERS-1's three-beam scatterometer is designed for, and dedicated to, the measurement of winds at sea. But since it directly measures backscattering coefficients over its 500km-wide swath, it also offers new possibilities for remote sensing of sea ice on regional or polar cap scales; full use of this potential will be possible only after sufficient data is collected and analyzed to evaluate the importance of seasonal variations in backscattering coefficients on regional scales. At present, we have already developed tools, based on the isotropic return and the incidence angle dependence determined over smooth first year ice, which can serve in the automatic detection of ice covered areas, avoiding erroneous computations of winds over such regions. Much work still remains ahead, but the scatterometer data appears to offer a useful complement to passive microwave data such as that furnished by the SSM/I, since it varies as a function of the ice surface's roughness.

INTRODUCTION

ERS-1's scatterometer was designed as an instrument dedicated to the measurement of surface winds over oceanic areas. This required that the backscattering coefficients obtained from this three-beam instrument be highly accurate, since they vary almost linearly with wind speed. The 50kmx50km footprint of the instrument was chosen small enough to correctly sample regional scale variations of the windfields. Since ERS-1 is yaw-steered, forward and rear beams, separated by 90 degrees in azimuth, have the same incidence angles to better than 0.1 degrees. Consecutive 19x19 point products, covering an area of about 500kmx500km, completely cover the earth's surface from 60 degrees of latitude to the poles over a three-day period, taking into account separately the northward or southward passes.

These aspects are all rather positive for the monitoring of seasonal and interannual behaviour of sea ice on regional or polar cap scales, which we are interested in. Certainly, SSM/I and previous passive microwave sensors have furnished a major contribution to this field, but active microwave data should somehow be complementary since it is strongly modulated by the ice surface roughness. The objective of this paper is certainly not to give conclusive evidence confirming this idea but to show, by the presentation of selected data, that it is not completely unfounded.

DATA AT POINT OR PRODUCT LEVELS

The scatterplot (Fig.1) of backscattering coefficients of the forward and rear beams, $S(1)$ and $S(3)$ respectively, taken over the Weddell sea during mid-november 1991, shows that isotropy of the radar return is generally quite well respected, although a few points may be influenced by proximity to the land masses of Antarctica. The fact that ERS-1 is yaw-steered allowed all points across the track to be included in this scatterplot, since incidence angles are practically the same for forward and rear beams.

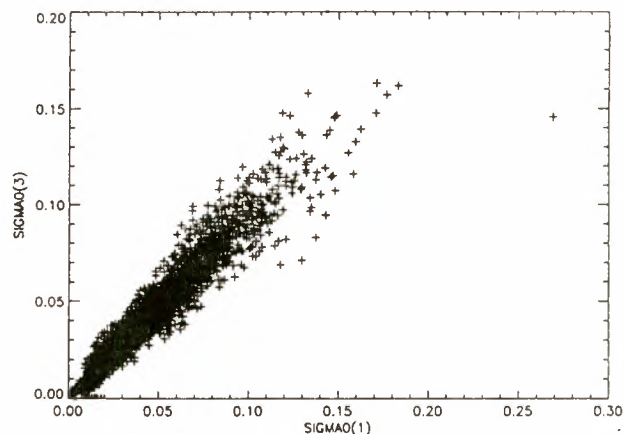


Figure 1: Scatterplot of backscattering coefficients of the forward and rear beams over Weddell sea first-year ice

Data of a product of which roughly half is over open water and half over Weddell sea first year ice is presented in Figure 2. Backscattering coefficients of the three antennas (Fig.2a) show a rapid decrease of radar return as a function of incidence angle both over water and over sea ice; of course they are different from each other at same incidence angles over water, since backscattering over wind waves is strongly anisotropic. The $S(1)$ versus $S(3)$ plot (Fig.2b) clearly shows the straight line behaviour of points over sea ice, well separated from points over water. This difference in behaviour is enhanced when the parameter of anisotropy, defined as $(S(1)-S(3))/(S(1)+S(3))$ is plotted (Fig.2c) as a function of the mean backscattering coefficient $(S(1)+S(3))/2$.

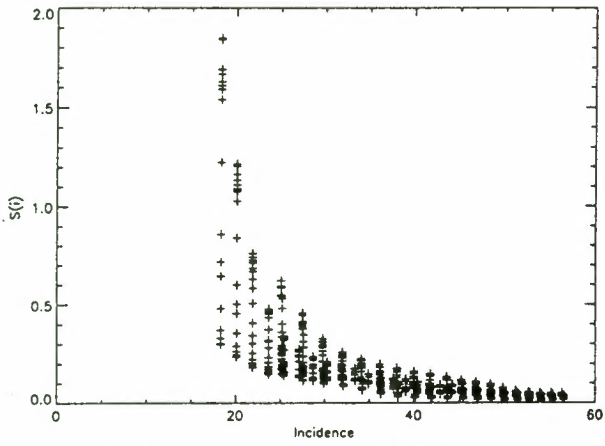


Figure 2a

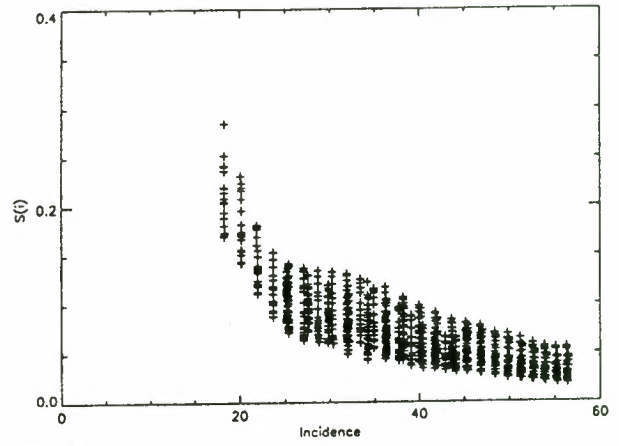


Figure 3a

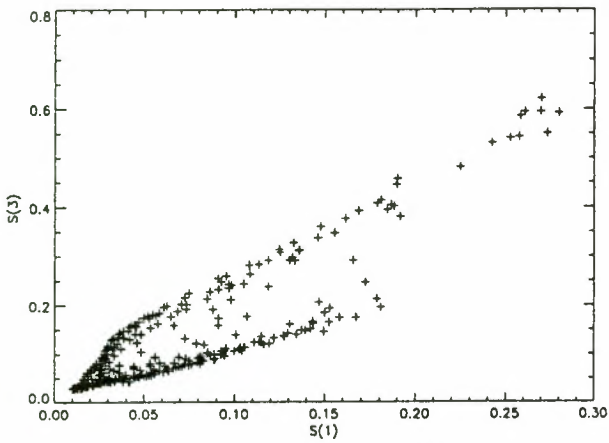


Figure 2b

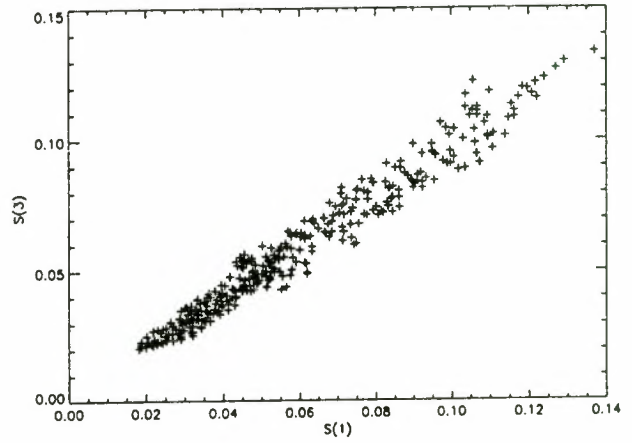


Figure 3b

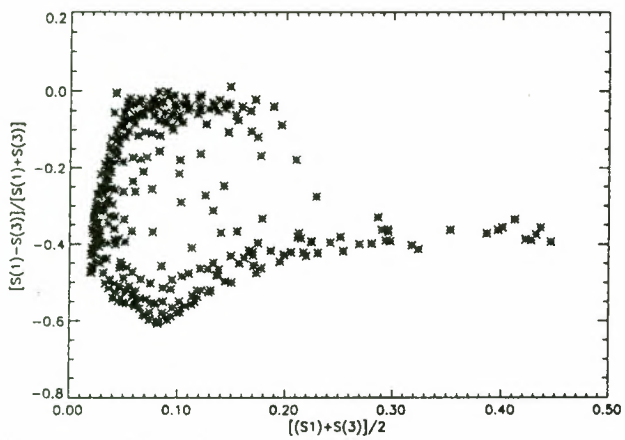


Figure 2c

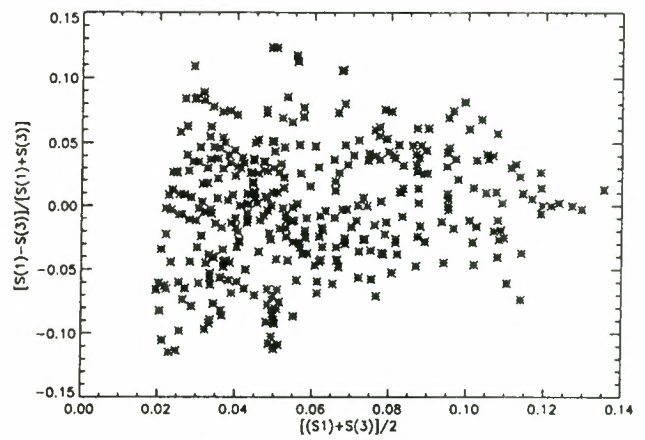


Figure 3c

Data of the next product along the scatterometer swath is entirely over Weddell sea first year ice (Fig.3) and it is instructive to compare the two datasets. Clearly the backscattering coefficients are much smaller over ice than over water, but decrease more slowly as a function of incidence angle and are the same for all three antennas, which could be expected because of isotropy, if the region is suitably uniform (Figures 2a and 3a). The wind-over-water points of Fig.2b have disappeared in Fig.3b where all points lie neatly close to the $S(1)=S(3)$ line. Finally, data of Fig.3c, because of a change in vertical scale, appears at first sight quite noisy compared to that of Fig.2c. In fact, it must be remembered that the measured backscattering coefficients have a standard error of approximately six percent, mainly due to speckle, which largely accounts for the vertical extension of the cloud of points.

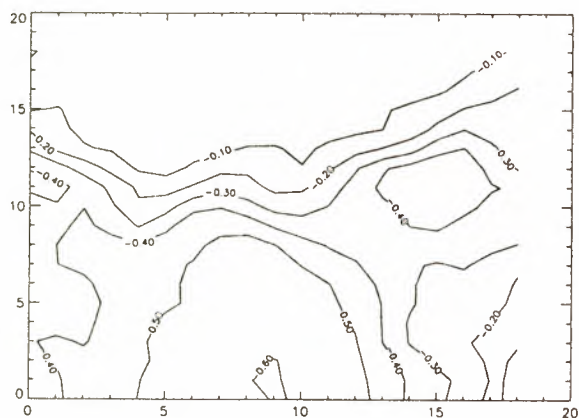


Figure 4: Isolines of the parameter of anisotropy around the ice edge

Isolines of the parameter of anisotropy for the product which straddles the marginal ice zone are plotted in Figure 4, which covers the 475kmx475km area of the product. A strong gradient of this parameter is observed at the ice-water boundary, very small values of the parameter occurring over sea ice. A similar plot, not shown, over the area of the following product, shows values of the parameter close to zero and no significant gradient, as might be expected over smooth first-year ice.

DATA AT REGIONAL OR POLAR CAP LEVELS

Because, as previously noted, normalized backscattering coefficients over sea ice are strongly incidence-angle dependent, scatterometer data cannot be used directly in its totality to map regional variations, because gradients across the swath, due to this effect, swamp regional variations in the properties of the ice. This difficulty can be circumvented by assuming that backscatter over sea ice is the product of two functions, of which one depends only on incidence angle and the other only on the physical properties of the ice. The incidence-angle dependent function can then be determined empirically from a sufficient number of points over a region of homogeneous ice, either from the mean of data points in small incidence angle bins, or by integrating the logarithmic derivative of backscattering coefficients, estimated from the difference between central and side antenna values, separated in incidence angle by about ten degrees. As might

be hoped, both methods, tested over the Weddell sea area, led to very similar values.

False-color maps of the backscattering coefficients corrected for the incidence-angle effect have been produced for both polar caps, using the scatterometer data collected during mid-november 1991. The empirical scheme for incidence-angle compensation efficiently suppressed cross-track gradients and left no visible discontinuities at adjacent swath limits. Comparisons with ESMR atlases show that strong backscattering is associated with multi-year ice, weak backscattering with first-year ice as reported by the ESMR monthly maps. An exception to this is the marginal ice zone, where backscattering coefficients increase, either because wave action breaks the ice, increasing its roughness, or because much of the zone is still open water which the wind roughens.

CONCLUSION

ERS-1's scatterometer data over sea-ice offers many different opportunities for engineering and scientific applications. Over zones of uniform and isotropic backscatter, such as the Weddell sea, intercomparisons of the different antennas can be rapidly carried out and a rough check of standard error on the backscattering coefficients made. The marginal ice zone can be geographically located and its evolution monitored, present limitations being the rather large footprints of the antennas. Empirical compensation curves necessary to reduce the incidence-angle effects over individual polar caps are fairly easy to determine and quite efficient; once applied, they allow the production of regional maps which can be interpreted as a function of ice roughness.

These conclusions, however promising, are not to deny that many questions, and therefore much work, still lie ahead. Can rational explanations be given for the differences in incidence-angle compensating functions, and are these functions seasonally varying? In the space of the three antenna backscattering coefficients, is the ice region separate from the wind-generated surface, and sufficiently so that automatic ice detection be possible using a simple and efficient algorithm? To what extent is active microwave data, produced by the scatterometer, complementary to passive microwave data of the SSM/I, and to what extent is it simply redundant? Answers to these questions seem within our reach, once sufficient data is acquired, and the wind model is correctly specified.

REFERENCES

- [1] Cavanié A. and Lecomte P., Study of a method to de-alias winds from ERS-1 data. Final Report, ESA contract 6874/87/GP-I(sc). 1987
- [2] Zwally H., Cosimo J., Parkinson C., Campbell W., Carsey F., and Gloersen P., Antarctic sea ice, 1973-1976: Satellite passive microwave observations. NASA SP-459. 1983
- [3] Parkinson C., Cosimo J., Zwally H., Cavalieri D., Gloersen P., and Campbell W., Arctic sea ice, 1973-1976: Satellite passive microwave observations. NASA SP-489. 1987

WORKSHOP CONCLUSIONS

WORKSHOP CONCLUSIONS AND FUTURE PLANS

Evert Attema
ESA/ESTEC
Postbus 229, 2200 AG Noordwijk,
The Netherlands

1. GENERAL CONCLUSIONS

Workshop participants were in broad agreement that the Geophysical Campaign (RENE-91) had been very successful, and provided a very valuable dataset for current and on-going studies.

The data archive, PCS_SPAN, had, and would continue to provide an excellent mechanism for central storage and experimenter access to the large datasets acquired during the RENE-91 campaign. The archive is still being added to, and would be maintained by ESA for as long as it serves a useful purpose.

Reprocessing of ERS-1 wind scatterometer data for Haltenbanken was taking place currently at ESRIN, with completion due within a few weeks. The wind scatterometer ECMWF model was under test at ESRIN, with work still going on to tune the model.

The time required to implement software changes for the scatterometer once an improved model is agreed should be approximately 3 months. In the case of the SAR, there is provision for new software changes every 3 months.

Results presented at the workshop demonstrate how many of the ERS-1 geophysical data products meet the pre-launch specifications, however there are a number of problem areas still needing special attention. The validation status for each geophysical data product is briefly reviewed under the following headings.

2. RADAR ALTIMETER DERIVED WINDSPEED

Results presented by *Cotton et al.* and *Queffelec et al.* show high correlations between ERS-1 FD

product windspeed, and both in-situ and model windspeeds. It was reassuring to hear that the small adjustment in instrument gain (0.8dB) implemented in the FD processing algorithm by ESA in September and November 1991 led to improvements in windspeed measurement accuracy. Although the results presented are very good, the number of in-situ datapoints used in the analyses is rather small. Further extended analysis of altimeter windspeed data with RENE-91 buoy data is planned and this could significantly increase the number of datapoints.

3. RADAR ALTIMETER DERIVED SIGNIFICANT WAVE HEIGHT

Hansen et al. described how radar altimeter wave heights were compared with outputs from the oceanographic WAM model running operationally at ECMWF. Following some initial minor modifications to the FD processing algorithms, the results have been good. However, still there is a slight tendency for the altimeter measurements to be low in comparison with the SWH measurements from the WAM model. Also, there seems to be an underestimation of high sea states; similar to that found during Geosat studies.

Confirmation of the accuracy of ERS-1 derived SWH measurements has been provided by results from the in-situ studies described by *Cotton et al.* and *Queffelec et al.*. Analysis of measurements obtained by the James Rennell Centre for Ocean Circulation, Southampton, showed that ERS-1 SWH was biased 0.5m high in comparison with wave-rider data. The analysis of collocated buoy and aircraft measurements made during RENE 91 has given similar results.

4. SCATTEROMETER DERIVED WINDSPEED & DIRECTION

There were 8 different papers presented during Session II on wind scatterometer models, and several different validation methods have been developed for the derivation of ocean surface wind vectors from the scatterometer data. Meteorological model outputs have been used in 2 different ways.

Firstly, meteorological model outputs have been used to simulate sigma nought values using model windspeeds. These simulations provided useful inputs for engineering calibration, and also indicated that the pre-launch wind scatterometer model needed some tuning. After the removal of statistical biases through model tuning, the spread in simulated sigma nought values still tended to exceed the instrument design specification. It was shown that this spread was not caused by scatterometer measurement errors, but was due to resolution mismatch and representativity errors of the meteorological model output for this type of analysis. Subsequent analysis and model tuning was undertaken using the actual satellite data rather than satellite-model collocations.

Secondly, meteorological model outputs have been used by a number of investigators to evaluate the wind field data products obtained from the scatterometer. These indicate that even the pre-launch wind retrieval models give promising results, but further analysis is needed once an up-date wind retrieval model has been established.

The large RENE-91 dataset has provided an excellent basis for developing an echo-model. A number of different models have been proposed as up-dates of the pre-launch wind retrieval model. *Offiler* presented results of a statistical analysis which show that the new models perform substantially better than the pre-launch model. A model proposed by ECMWF (*Stoffelen et al.*) performed marginally better than its competitors and was therefore implemented in the ESA FD processing system. With this model the wind scatterometer data products satisfy the design accuracy of 2 m/s for windspeed and 20° for wind direction. Analysis is continuing to study model differences. Eventually, this will lead to further model up-dates and wind scatterometer performance enhancement.

Another outcome of the model tuning activity is that the in-orbit observed radar signature of the ocean makes it more difficult to estimate wind direction unambiguously than expected on the basis of the pre-launch model. A revised algorithm has been developed which uses meteorological forecast models to resolve wind direction ambiguity.

5. DIRECTIONAL OCEAN WAVE SPECTRA

To-date, the validation results for the derivation of wave spectra from SAR images are mainly from dedicated campaigns. The use of global wave models has also commenced, but extensive analysis is awaiting software up-dating of the ERS-1 SAR wave mode ground processor.

Results were presented from both the RENE campaign using the Haltenbanken test site (*Ziemer et al.*, *Kleijweg et al.*, *Hauser et al.*, *Brüning et al.*, *Johnsen et al.*, and *Rosenthal et al.*), and from the Grand Banks validation campaign (*Vachon et al.*). Preliminary conclusions are all based on the analysis of the ERS-1 SAR image mode, and indicate that swell (wavelengths > 200m) is well imaged, but shorter azimuth travelling waves suffer from linear and non-linear distortion introduced by the SAR imaging mechanism. Non-linear inversion methods to overcome these are being developed (*Brüning et al.*).

6. FUTURE ACTIVITIES

Although the period of intense activity has now been completed, scientific analysis will continue and some experimenters have plans for extending their work with new ship data collection programmes.

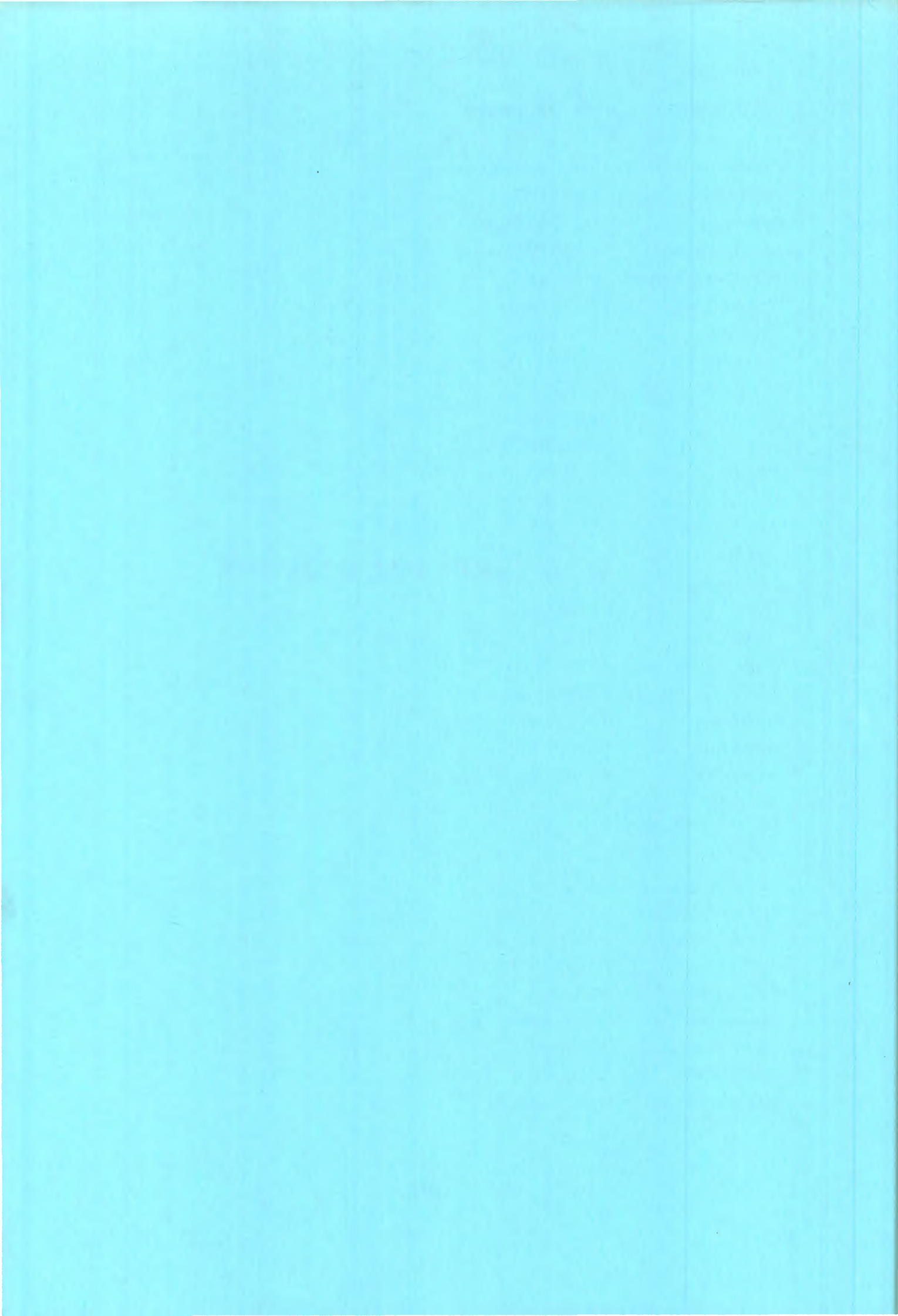
Clearly, more time is needed to digest fully the results presented on wind scatterometer models during the workshop. Three different datasets have been used; the Global dataset, the Haltenbanken dataset, and a subset of the Haltenbanken dataset. Results from the 3 datasets seem to be consistent, but there is a need to check this.

ESTEC, ECMWF and other groups will continue with efforts to improve models. The plan is to continue with experimenter teams, but to review the membership and combine teams into one group.

In recognition of the processing delays and special difficulties being experienced with the validation of ocean wave spectra, ESA proposes to form a small sub-group of experimenters to specifically look at SAR and the derivation of wave spectra

As far as future work is concerned, opportunities for checking results against new ground data will be more limited. However, it was noted that there are plans within the meteorological/oceanographic community for future experiments, and efforts will be made to have ESA participation in order to gain access to some new measurements. It was mentioned that GKSS have plans for more measurements in the Haltenbanken area in November. Also, in autumn 1993 there are plans for a major French experiment (SEMAPHORE), which will include some aircraft measurements.

WORKSHOP PARTICIPANTS



LIST OF WORKSHOP PARTICIPANTS

Werner Alpers	Univ. Hamburg, Germany
Evert Attema	ESA/ESTEC, The Netherlands
A.Bentamy	IFREMER, France
Tom-Ivar Bern	OCEANOR, Norway
Lars-Anders Breivik	DNMI, Norway
Vincent Casse	CNRM, France
G.Caudal	CRPE, France
A.Cavanie	IFREMER, France
P. Cotton	JRC/OC, UK
Mark Doherty	ESA/ESRIN, Italy
Anne Edward	ESA/ESRIN, Italy
R.Ezraty	IFREMER, France
Heinz Finkenzeller	DLR, Germany
Richard Francis	ESA/ESTEC, The Netherlands
Catherine Gaffard	CNRM, France
Mark Goodberlet	Univ. Massachusetts, USA
Bjorn Hansen	ECMWF, UK
Danièle Hauser	CRPE, France
Jonny Johannessen	NERSC, Norway
Kristina Katsaros	IFREMER, France
Jan Kleiweg	TNO, The Netherlands
Harald Krogstad	SINTEF, Norway
Alfred Long	ESA/ESTEC, The Netherlands
Jac Louet	ESA/ESTEC, The Netherlands
Jean-Claude Morin	GDTA, France
David Offiler	Met. Office, UK
P.Queffeulou	IFREMER, France
W.Rosenthal	GKSS, Germany
Ad Stoffelen	ECMWF, UK
Paris Vachon	CCRS, Canada
John Wilkerson	NOAA, USA
Volkmar Wismann	Univ. Hamburg, Germany
Peter Woiceshyn	ECMWF, UK
Mike Wooding	RSAC, UK
Friedwart Ziemer	GKSS, Germany



